Study of Generalized Parton Distributions and Deeply Virtual Compton Scattering on the nucleon with the CLAS and CLAS12 detectors at the Jefferson Laboratory (Virginia, USA)

Baptiste Guegan

UNIVERSITE PARIS-SUD

RENSSELAER POLYTECHNIC INSTITUTE

A thesis submitted for the degree of Doctor of Philosophy in Physics

Study of Generalized Parton Distributions and Deeply Virtual Compton Scattering on the nucleon with the CLAS and CLAS12 detectors at the Jefferson Laboratory (Virginia, USA)

Examining Committee:

Dr. Eric VOUTIER

Dr. Valery KUBAROVSKY

Dr. Bruno ESPAGNON

Pr. Jim NAPOLITANO

Pr. Joel GIEDT

Supervisors:

Dr. Michel GUIDAL

Pr. Paul STOLER

Author:

Baptiste GUEGAN

L'essentiel est invisible pour les yeux.
Le Petit Prince (1943), Antoine de Saint-Exupéry

Acknowledgements

I would like to gratefully thank my supervisor Michel Guidal for his support and his guidance throughout the three years of my PhD. Your wide-ranging knowledge and your logical way of thinking have been of great value to me and to the accomplishment of this thesis. Thank you for the time you spent answering my questions, even between two tennis lessons or two poker games. It was a great pleasure to work with you. I thank you for your understanding and for your constant good mood. Don't forget that the sausages are not the only choice in the menu. Whenever you want for another Atlantic City trip ! Merci.

I would like to sincerely thank my supervisor Paul Stoler, for having given me the opportunity to complete my PhD between l'Institut de Physique Nucléaire d'Orsay and Rensselaer Polytechnic Institute. Thank you for your patience, your constant encouragements and your detailed and constructive comments on my work. Thanks.

A million thanks to Silvia Niccolai for the million of questions you so kindly answered. I learned so much working with you daily. Your rigor and your endless motivation helped me a lot in accomplishing my work. It was a great pleasure to exchange with you through the last few years. I am sure that Evelyne Thomas knows how chatty you are, but no need to yell, I am here ! Your tiramisu is good, but I prefer when you Sing Sing Sing ! All the best for your two rascals. Grazie.

Hyon-Suk Jo has been for me an invaluable daily help. Your numerous advices and (de)constructive remarks helped me a lot to improve my work. I thank you for your willingness to help people even when you have no time. I can not count the number of discussions and fights we had about the analysis, but it was always benefic to me in the end. My only remaining question is: what happened in Cyprus?

I would like to thank all the members of the physics group at IPNO. I wish "bon vent" to Daria Sokhan on her Scottish adventure (Paris is already missing you). Many thanks to Carlos Munoz for the time he spent to answer my questions (but I am still waiting for the sangria). A special dedication to El Magnifico Alejandro Marti with who it was a pleasure to share the office (stooop shaking your knees !!). I would like to welcome the newcomers of the group: Camille Desnault, Brice Garillon, Mohammad Hattawy, Rafayel Paremuzyan and Raphaël Dupré. I wish you all good success in your future work.

I would like also to thank all the members of JLab I have been involved with. First, many thanks to Nicholas Saylor with whom I shared the analysis of the e1-DVCS2 data set. I thank all the e1-DVCS analysis group for their constructive remarks during all the meetings: Harut Havakian, Valery Kubarovsky, FX Girod, Volker Burkert, Franck Sabatié and Alex Kubarovsky. Many thanks to Mikhail Myurov and Maurizio Ungaro for their huge help in solving important problems in the analysis. Also a special dedication to the great people I met at JLab: Azenath Etile, John German, Jason Bono, Miguel Angel Lopez Ruiz, Dipak Rimal, Rupesh Silwal and Vadim Guzey.

Of course, I thank Jacques Van de Wiele for everything I have learned from our numerous discussions. Your rigor and your knowledge stand as an inspiration and example to me. I also thank Egle Tomasi, Samuel Wallon, Lech Szymanowski and Cédric Lorcé for interesting and constructive discus-

sions.

I do thank all the great computing staff of IPNO. Among all the team, I especially thank Florent Mellac (Mr Ktas), Yann Aubert (Mr Marathon Man), Vincent Lafage (Mr Compilation), Laure Amélie Couturier (Mme data recovering) and Gérard Lalu (Mr Linux) for their disponibility and their help during my three-years fight against my dark computing side.

Last, but not least, I would like to finish by a personal French note. Je remercie mes parents pour leur support continu tout au long de mes années d'étude. Ce travail ne se serait jamais fait sans leur soutien sans faille. Merci pour votre patience et votre compréhension dans les jours de désarroi. Merci aux frangin-frangine pour m'avoir appris à travailler dans le bruit. Un gros poutou à ma marraine, ma bonne fée. Merci enfin à tous les membres de ma précieuse famille.

Contents

APPENDIX

Chapter 1

Introduction

The mass of the visible universe consists at 99% of the nucleons mass. However, after almost a century of research, their inner structure is still not fully comprehended. Since the discovery of the proton in 1919 by E. Rutherford [Rut19] and of the neutron in 1932 by J. Chadwick [Cha32], our understanding of the nucleon structure has constantly evolved. Until the 1960s, protons and neutrons were thought to be elementary particles that were interacting strongly to form the nucleus. But in 1964, a drastic transformation appeared in our picture of the nucleon. M. Gell-Mann [GM64] and G. Zweig [Zwe64] postulated the existence of quarks, particles that would compose the hadrons[1]. A few years later, to describe the results of the Stanford Linear Accelerator (1968-1969), J. Bjorken [BP69] and R. Feynman [Fey69] developed the parton model in which the nucleons are composite particles made of constituent quarks that interact strongly.

In 1973, a quantum field theory of the strong interaction is formulated by D. Politzer, D. Gross and F. Wilczek [GW73, Pol73]. The quarks carry a color charge and are bound together by interacting vector bosons, the gluons. The fundamental theory that describes the strong interactions between partons (quarks and gluons) within the hadron is the quantum chromodynamics (QCD). A characteristic property of QCD is asymptotic freedom, which means that the running coupling constant is small at high energies and large at low energies. Equivalently, at small distances QCD is well described in terms of weakly interacting quarks and gluons, while at large distances, of the order of 1 fm, the theory becomes non-perturbative and quarks are confined. It means that quarks can not be observed as free particles. We can only observe color singlet bound states of quark-antiquark pairs (mesons) like the pion, or of three quarks or three antiquarks (baryons) like the proton and the neutron.

In 1979, a strong evidence for a gluon radiated by a quark is found at PETRA [Col79], proving for the first time the existence of the gluon and confirming crucial predictions of QCD. Our understanding of the nucleon structure thus consists of a "soup" of quarks and gluons that form the nucleons with the strong interaction of QCD.

In 1989, the EMC collaboration [col89] found that approximately 30% of the nucleon spin arises from the spin of the quarks. This result gave rise to the so called "spin crisis" and raised some fundamental questions. It is established that the nucleon is formed by quarks and gluons but how these latter determine the properties of the nucleon is still not precisely understood. We know that the mass of the nucleon is of the order of one GeV, but when we sum up the masses of the three constituent quarks, we get a mass of around 10 MeV [MS10]. Where does the remaining mass come from? How do the electromagnetic properties of the nucleon arise from its inner constituents? Where does the spin of the nucleon come from? What is the origin of quark confinement? Many are the questions to which we still do not have answers. Understanding the structure of the hadrons in terms of quark and gluon

[1] Mesons and baryons are collectively denoted as hadrons and, being composed of quarks, are subject to strong interactions.

degrees of freedom remains an outstanding challenge.

A powerful way of investigating strongly interacting particles is to probe them with a well known particle, for instance the electron. To study the fundamental degrees of freedom of the nucleon, namely the quarks and gluons, we use the electromagnetic probe because the electron is a structureless particle and is unsensitive to the strong interaction. The electromagnetic interaction is precisely described by quantum electrodynamics (QED), which is one of the most accurate physical theories constructed up to now (for instance, agreement between data and theory to within ten parts in a billion (10^{-8}) [ea03b] was found for the magnetic moment of the electron).

A large part of what we have learned on the inner structure of the nucleon until now arises from the scattering of high-energy leptons on the nucleon. We distinguish three main processes of lepton-nucleon scattering:

- Inclusive scattering (IS), that we can write as $lN \to lX$, consists in the detection of the scattered lepton and no particles of the final hadronic state. In the frame where the particles are going at the speed of light along the z-axis, inclusive scattering allows to access the Parton Distribution Functions (PDFs). They can be interpreted as the longitudinal momentum distributions of the partons inside the nucleon (independently of their transverse localisation).
- Semi-Inclusive Deeply Inelastic Scattering (SIDIS), that we can write as $lN \to lhX$, consists in the detection of the scattered lepton and one hadron (a pion or a kaon for instance) of the final state. The SIDIS processes allow to access the Transverse Momentum-Dependent parton distributions (TMDs) that provide information about the nucleon structure in both the longitudinal and transerse momentum space.
- Exclusive scattering, consists in the identification of all the particles of the final state. The simplest process is the elastic scattering (ES) $lN \to lN$. It gives access to the Form Factors (FFs) which can be interpreted as the transverse localisation of partons in the nucleon (independently of their longitudinal momentum).

Studying these processes allows us to get more information about the inner structure of the nucleon. For example, elastic experiments allowed us to calculate precisely the spatial extention of the nucleon through the measurement of the charge distributions [MH56]. With unpolarized deeply inelastic scattering (DIS), we learned that only 45% of the nucleon momentum is carried by the quarks, the rest being carried by gluons [SVS88].

A new theoretical description (Generalized Parton Distribution (GPD)) appeared about fifteen years ago. With the exclusive leptoproduction of a photon $lN \to lN\gamma$ or a meson, we are able to reveal much more information about the structure of the nucleon. These processes allow us to extract four GPDs: H, E, $\tilde{H}$, $\tilde{E}$, defined for each quark flavor (u, d, s), and corresponding to each of the four possible helicity-spin configurations of the proton and the quark. The GPDs can help to answer some of the questions mentioned at the beginning. For instance, X. Ji showed [Ji97] that the GPDs appear in a sum rule which gives access to the total angular momentum of the partons, thus contributing to solve the nucleon spin problem. Also, they allow to access the meson content of the nucleon and they provide a correlation between the transverse position and the longitudinal momentum of the partons, allowing a three-dimensional description of the nucleon.

The processes of leptoproduction of a meson have the property to be sensitive only to specific GPDs. Vector mesons are sensitive to the GPDs H and E, while pseudo-scalar mesons are sensitive only to the GPDs $\tilde{H}$ and $\tilde{E}$. Morever, because of their different parton content, the mesons are sensitive to different flavor combinations of GPDs. For instance, the pseudo-scalar meson π^0 is sensitive to a combination of the GPDs of the u and d quarks, while the vector meson ϕ is sensitive to the GPDs of the s quarks. Meson electroproduction channels thus allow one to make a flavor decomposition of the GPDs.

The exclusive leptoproduction of a real photon is considered to be the "cleanest" way to access the GPD. This process is called Deeply Virtual Compton Scattering (DVCS) $lN \to lN\gamma$, and is sensitive to all the four GPDs. Measuring the DVCS cross section is one of the main goals of this thesis. Combining the results from experiments using proton and neutron targets, the flavor decomposition of the GPDs can also be performed.

Extracting the four flavor-separated GPDs is a non-trivial task that requires to measure different observables (cross-sections, spin and charge asymmetries) from different processes. A combination of all these measurements is then to be used in global-fitting procedures to extract the informations related to the GPDs.

To achieve the measurements of exclusive processes, some specific experimental conditions are necessary. Because of their very small cross section (∼nbarn), a high-intensity lepton beam is required. In addition, a large-acceptance detector with good angular and energy resolutions is needed to ensure the exclusivity of the measurement and to access a large phase space. These conditions are fulfilled at Jefferson lab.

In this thesis, we present the work performed to extract on a wide phase-space the DVCS cross-section from the JLab data at a beam energy of 6 GeV. This thesis consists of the following parts:

- A theoretical introduction to GPDs and DVCS.
- A presentation of the JLab facility.
- The data quality checks and corrections using the elastic scattering for the study of DVCS on the proton at 6 GeV, and the extraction of the elastic cross section to check the normalization of the data.
- The extraction of the DVCS beam-polarized and unpolarized cross sections and the beam spin asymmetry.
- The extraction of the quantities related to the GPDs from our data, and a first interpretation of the results.
- A study about a neutron detector that is planned to be installed in the future CLAS12 detector at JLab GeV. This detector will allow to study DVCS on the neutron.

Chapter 2

Physics motivation

2.1 Elastic scattering

Electron-proton elastic scattering experiments started in the 50's at the Stanford linear Accelerator. Physicists continue to work on this process in order to understand the structure of the nucleon. We give in this section a brief summary of the present knowledge in this domain, which is of particular interest for the study of the GPDs.

The Born term (Fig. 2.1) of the elastic process consists of the scattering of a lepton (an electron) off a nucleon (a proton) via one virtual photon exchange. Higher-order radiative correction graphs (Bremsstrahlung, vertex, self energy, 2γ exchange ...) contribute also to the process, but are not described here (see reference [PPV07] for more details).

We define the elastic scattering (ES) process as: $l(k) + N(p) \rightarrow l'(k') + N'(p')$, with $k = (E, \overrightarrow{k})$ ($k' = (E', \overrightarrow{k'})$) the four-vector of the incoming (outgoing) electron respectively, and p (p') the four-vector of the incoming (outgoing) nucleon respectively.

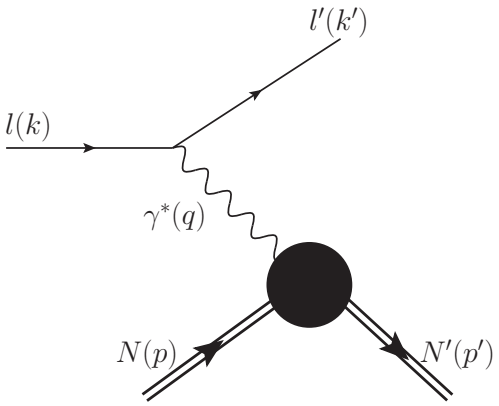

Figure 2.1: Elastic scattering.

The conservation of the four-momenta at each vertex of the diagram can be written as: $q = k - k' = p' - p$. We introduce the momentum transfer squared q^2, which represents the virtuality of the photon: $q^2 = (k - k')^2 \simeq -4EE'sin^2\frac{\theta_e}{2}$. It is a negative quantity for any energy and scattering angle θ_e of the outgoing electron. The kinematical region associated to $q^2 < 0$ is called the space-like region, while the

one for $q^2 > 0$ is the time-like region. This latter can be accessed in the crossed process (Drell-Yan process) when a quark of one nucleon and an antiquark of another nucleon annihilate, creating a virtual photon which then decays into a leptons pair.

To calculate the amplitude of the process $ep \to e'p'$, we introduce structure functions, called form factors, which parametrize the complex inner structure of the nucleon. The unpolarized differential cross section for electron-proton elastic scattering (Rosenbluth formula [Ros50]) can be written as follows:

$$\left.\frac{d\sigma}{d\Omega}\right|_{lab} = \frac{\alpha^2}{4E^2 sin^4\frac{\theta_e}{2}}\frac{E'}{E}\left[\left(F_1^2(q^2) - \frac{q^2}{4M^2}F_2^2(q^2)\right)cos^2\frac{\theta_e}{2} - \frac{q^2}{2M^2}\left(F_1(q^2)+F_2(q^2)\right)^2 sin^2\frac{\theta_e}{2}\right] \quad (2.1)$$

where $d\Omega = sin\theta_e\, d\theta_e\, d\phi$ is the solid angle (in steradian) into which the electron is scattered, α is the electromagnetic coupling constant ($\alpha = \frac{e^2}{4\pi} \sim \frac{1}{137}$) and M is the proton mass. F_1 and F_2 are respectively the Dirac and Pauli form factors (FFs). They are real functions which depend upon the scalar q^2 only. F_1 is linked to the charge distribution inside the nucleon, and is related to helicity conserving processes. F_2 expresses the existence of an anomalous magnetic moment and is related to helicity non conserving processes. They are normalized according to the experimental results:

- The charge of the proton is 1 and its measured magnetic moment is $\mu_p = 2.7928$ in nuclear magneton-units ($\mu_N = \frac{e\hbar}{2M}$). Therefore, the anomalous part of the magnetic moment for the proton is $\kappa_p = 2.7928 - 1 = 1.7928$. In the static limit ($q^2 = 0$), it follows:

$$\begin{cases} F_1^p(0) = 1 \\ F_2^p(0) = 1.7928 \end{cases} \quad (2.2)$$

- Concerning the neutron, the charge is equal to zero and the measured total magnetic moment is $\mu_n = -1.9130 = \kappa_n$, so that we have:

$$\begin{cases} F_1^n(0) = 0 \\ F_2^n(0) = -1.9130 \end{cases} \quad (2.3)$$

We show in Fig. 2.2 the results for the extraction of the FFs obtained from recent polarization experiments, that measured the Q^2 dependencies of the FFs from $Q^2 \approx 1$ GeV^2 to be: $F_1 \approx \frac{1}{Q^4}$ $F_2 \approx \frac{1}{Q^6}$.

Interpretation of the form factors

Recently, a relativistic interpretation of the FFs has been developed (the Sachs FFs interpretation in the Breit frame is also discussed in Appendix A.1). In the infinite momentum frame, where the nucleon is moving with a very large momentum along the z-axis, the Dirac form factor F_1 can be related [Mil07] to the quark charge density in the transverse plane for an unpolarized nucleon through the two-dimensional Fourier transform:

$$\rho(b_\perp) = \int \frac{d^2q}{(2\pi)^2} e^{iq\cdot b_\perp} F_1(q^2) \quad (2.4)$$

with $b_\perp$ the impact parameter that represents the transverse distance of the partons relative to the center of mass. The Pauli form factor F_2 is linked to the quark charge density in the transverse plan for a transversely polarized nucleon [CV08].

In Figs. 2.3 and 2.4 are shown the charge density distributions $\rho(b_\perp)$ of the proton and of the neutron. The proton density peaks at 0 with a long positive tail suggesting a long-range positive charged pion cloud. The neutron charge density has a negative contribution at large distance due to a negative pion cloud, a positive contribution around 0.5 fm, and a negative core at small $b_\perp$.

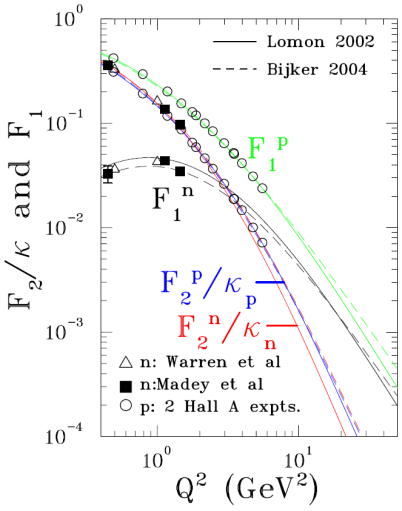

Figure 2.2: The FFs F_1 and F_2 for the proton and the neutron obtained from double-polarization experiments only. F_1 and F_2 are obtained from the experimental FF ratios using fitted values to G_M^p and G_M^n (see Appendix A.2). The proton data are fitted from [Kel04]. The neutron data Madey et al. [ea03c] are fitted from [Kel04], and the data Warren et al. [ea04b] are fitted from [ea02b]. The curves are the vector meson dominance fits of [L.01] and of [RI04]. Figure extracted from [PPV07].

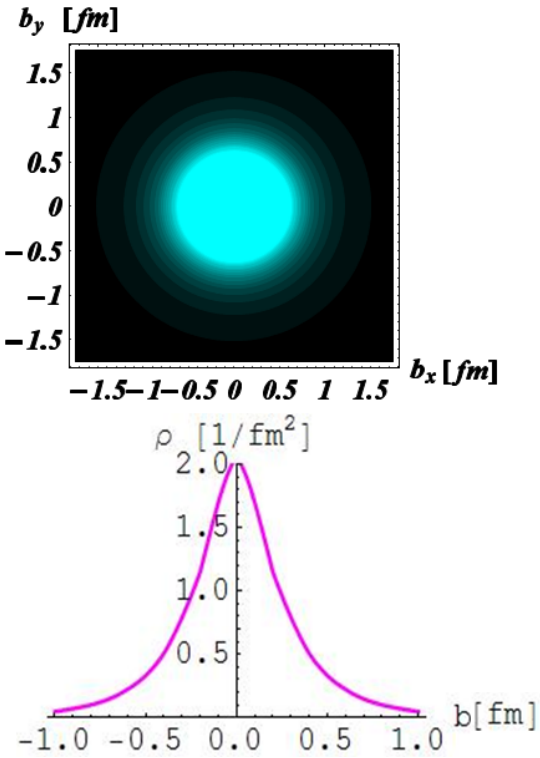

Figure 2.3: Upper panel: quark transverse charge density in an unpolarized proton [VW10]. Lower panel: $\rho(b_\perp)$ [Mil07] using the Fourier transform of the FFs parametrization of [BBBA06].

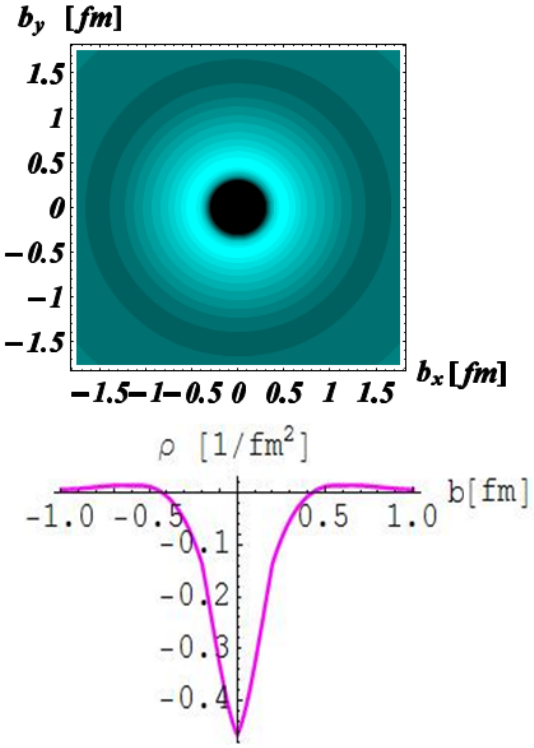

Figure 2.4: Upper panel: quark transverse charge density in an unpolarized neutron [VW10]. Lower panel: $\rho(b_\perp)$ [Mil07] using the Fourier transform of the FFs parametrization of [BBBA06].

2.2 Inelastic scattering

A photon of vituality Q^2 can "see" a short-distance region of the nucleon with a spatial resolution of the order $\Delta b_\perp \sim \hbar/\sqrt{Q^2}$. Therefore, by increasing Q^2 up to 2 GeV^2 - 3 GeV^2, we are able to resolve the inner constituents of the nucleon with a spatial precision of around 0.1 fm - 0.05 fm, which is much smaller than the typical size of the nucleon (∼1 fm).

During the photon-nucleon interaction, the electromagnetic interaction time τ_e is much shorter than the typical strong interaction time τ_s between proton constituents: $\tau_e \sim \frac{1}{E_{\gamma*}} \sim \frac{2\,x_B\,M}{Q^2} \ll \tau_s \sim \frac{1}{\Lambda_{QCD}}$, with $\Lambda_{QCD} \approx 200$ MeV. Therefore, during the process, the picture of the nucleon appears to be "frozen", and at first order one can consider that the virtual photon interacts with only one free parton of the nucleon, while interaction between partons is neglected. At large momentum transfer ($Q^2 \gg M^2$), i.e short-distance scale, the asymptotic freedom property of QCD states that the coupling constant is small enough ($\alpha_s \approx 0.3$ at 2 GeV) to allow to perform perturbative calculations and to extract the dominant diagrams.

In a lepton-nucleon collision at large momentum transfer Q^2, the proton has a high probability to break up so that the hadronic final state is very complicated. This process is called Deeply ($Q^2 \gg M^2$) Inelastic ($W^2 \gg M^2$) Scattering (DIS). Because this hard scattering can produce many particles, the final state is not fully detected experimentally, i.e. $ep \to eX$. In such a case, only the energy and the angle of the scattered electron are measured.

We define the inclusive scattering process (Fig. 2.5) as: $l(k) + N(p) \to l'(k') + X$.

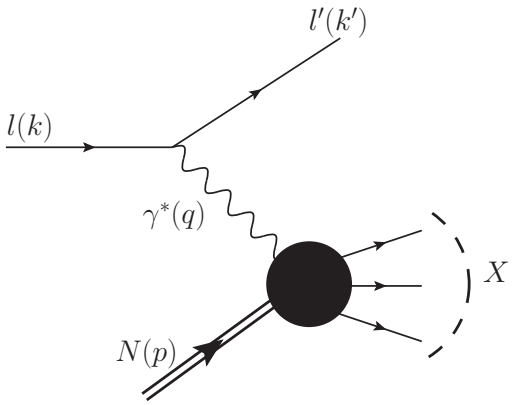

Figure 2.5: Inclusive lepton-nucleon inelastic scattering: only the final lepton is detected.

If the energy of the incoming lepton is known, an inclusive process can be described by two kinematical quantities. We introduce two independent variables that are combinations of the laboratory variables. Neglecting the electron mass, we have:

$$\begin{cases} \nu = \frac{-q\cdot p}{M} = E - E' & (\geq 0) \\ q^2 = (k-k')^2 \simeq -4EE'sin^2\frac{\theta_e}{2} & (\leq 0) \end{cases} \tag{2.5}$$

The invariant mass W of the (unobserved) hadronic final state is defined as:

$$W^2 = (p+q)^2 = M^2 + 2M\nu + q^2 \Longleftrightarrow W^2 - M^2 = 2M\nu + q^2 \tag{2.6}$$

For an elastic process, we have $W^2 = M^2$, while for an highly inelastic one we have $W^2 \gg M^2$.

The unpolarized inelastic cross section (see also Appendix B.1) can be written as:

$$\frac{d^2\sigma}{d\Omega d\nu} = \frac{\alpha^2}{4E^2 sin^4\frac{\theta_e}{2}} \frac{E'}{E} \left(W_2 \, cos^2\frac{\theta_e}{2} + 2W_1 \, sin^2\frac{\theta_e}{2} \right) \tag{2.7}$$

where $W_{1,2}(\nu, q^2)$ are the structure functions of the nucleon and depend upon the two independent variables ν and q^2.

It has been shown at SLAC-MIT (1968-1969) that in the deeply inelastic region, where W^2 is large compared to M^2, the inelastic cross section is not suppressed as much as the elastic one, as can be seen in Fig. 2.6. The measured cross section was compatible with the one expected if the proton were a point-like particle. As W increases, the ratio $\frac{\sigma}{\sigma_{MOTT}}$ tends to become flatter, which gives rise to the idea that the scattering happened on a point-like object inside the nucleon. The effort of interpretation of this result has given rise to the parton model [BP69, Fey69].

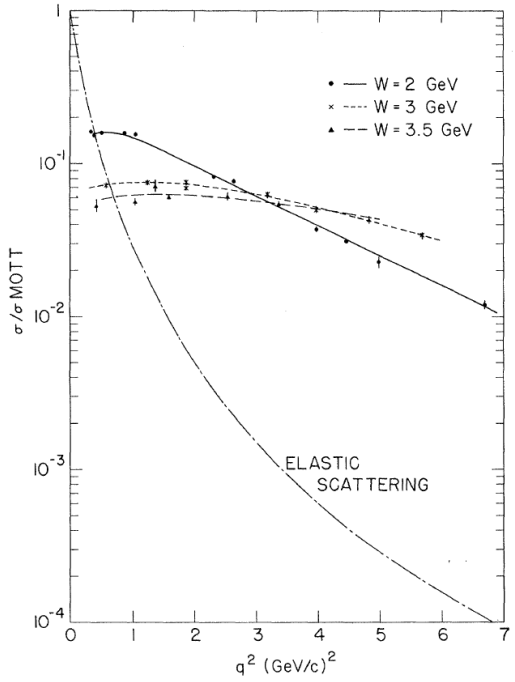

Figure 2.6: Comparison of the ratio $\frac{\sigma}{\sigma_{MOTT}}$ for different W values (plot from [BFK$^+$69]). For the elastic cross section, the ratio drops sharply as q^2 increases. In contrast, as we go further from the elastic region ($W \gg M$), the ratio tends to become flatter, showing a similarity with the Mott cross section (scattering on a point-like particle).

Relating Eq. 2.7 to the elastic scattering off a point-like particle (see also Appendix B.2) gives rise to two main equations:

$$W_1(\nu, Q^2) = \sum_q e_q^2 \frac{q(x)}{2M} \equiv \frac{1}{M} F_1(x) \tag{2.8}$$

and:

$$W_2(\nu, Q^2) = \sum_q e_q^2 x \, q(x) \equiv F_2(x) \tag{2.9}$$

where $x = x_B = \frac{Q^2}{2M\nu}$ the Bjorken variable, e_q is the quark charge and $q(x)$ describes the probability that the struck parton q carries a fraction x of the longitudinal proton's momentum p. These functions

are called the parton distribution functions (PDFs). In the Bjorken regime where $\{-q^2, \nu\} \to \infty$ with x_B fixed, the structure functions $W_{1,2}(\nu, q^2)$ scale, they do not vary with q^2.

However, in QCD, the scaling property is violated because the radiation of gluons produces an evolution in Q^2 of the structure functions. As Q^2 increases, more and more gluons are radiated, which in turn split into $q\bar{q}$ pairs, leading to the growth of the gluon and the $q\bar{q}$ sea quark density at low x. The Q^2 evolution of the PDFs are given by the DGLAP[1] equations [Dok77]. This property is illustrated by the experimental data shown in Fig. 2.7.

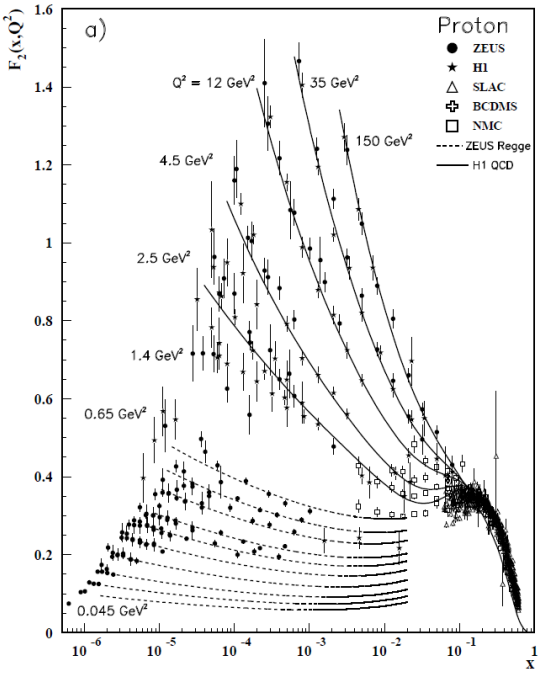

Figure 2.7: Proton structure function $F_2^p(x, Q^2)$ for different Q^2 values, showing a large Q^2 dependance at small x. Curves are from ZEUS and H1 parametrizations for lower and higher Q^2 respectively [eaPDG08].

The structure functions $F_{1,2}$ describe the longitudinal momentum distributions of the partons in the nucleon target. This property is related to the assumption that the transverse momentum of the partons is small in the infinite-momentum frame of the nucleon. F_1 and F_2 are linked by the Callan-Gross relation: $2xF_1(x) = F_2(x)$. This has been checked experimentally [Pic95] and implies that the partons involved in the DIS are fermions. Because of this relation, only one structure function is necessary to describe the longitudinal momentum distribution of the quarks inside the nucleon.

For a beam and a nucleon target both longitudinally polarized, the study of the cross-section difference under the reversal of the nucleon spin direction (indicated with the double arrow) $d^2\sigma^{\rightrightarrows} - d^2\sigma^{\rightleftarrows}$ allows the measurement of the polarized structure functions: g_1 and g_2. The scaling result g_1 for the longitudinally polarized DIS is expressed as:

$$g_1(x) = \frac{1}{2} \sum_q e_q^2 \, \Delta q(x) \tag{2.10}$$

[1] Dokshitzer, Gribov-Lipatov, Altarelli-Parisi.

with $\Delta q(x) = q_+(x) - q_-(x)$. $q_\pm(x)$ are the densities of the quarks whose spin orientation is parallel or antiparallel to the longitudinal spin of the nucleon (in the unpolarized DIS case, $q(x) = q_+(x) + q_-(x)$). The leading-twist information is contained inside g_1. The polarized structure function g_2 is a higher-twist contribution and is linked to g_1 by the Wandzura-Wilczek relation [WW77].

The data used to extract the PDFs over a large x domain are coming from fixed target experiments performed at JLab ($l\,N$), COMPASS ($\nu\,N$) and from the colliders HERA ($e^{\pm}\,p$) and Tevatron ($p\,\bar{p}$). The agreement between the QCD predictions and the data allows one to extract the PDFs. Fits are performed to the data on F_2 to extract the PDFs. One can see the results on Fig. 2.8 at $Q^2 = 20$ GeV^2 and $10,000$ GeV^2. At large x, u and d valence quarks distributions dominate. As x decreases, the contribution of the sea dominates.

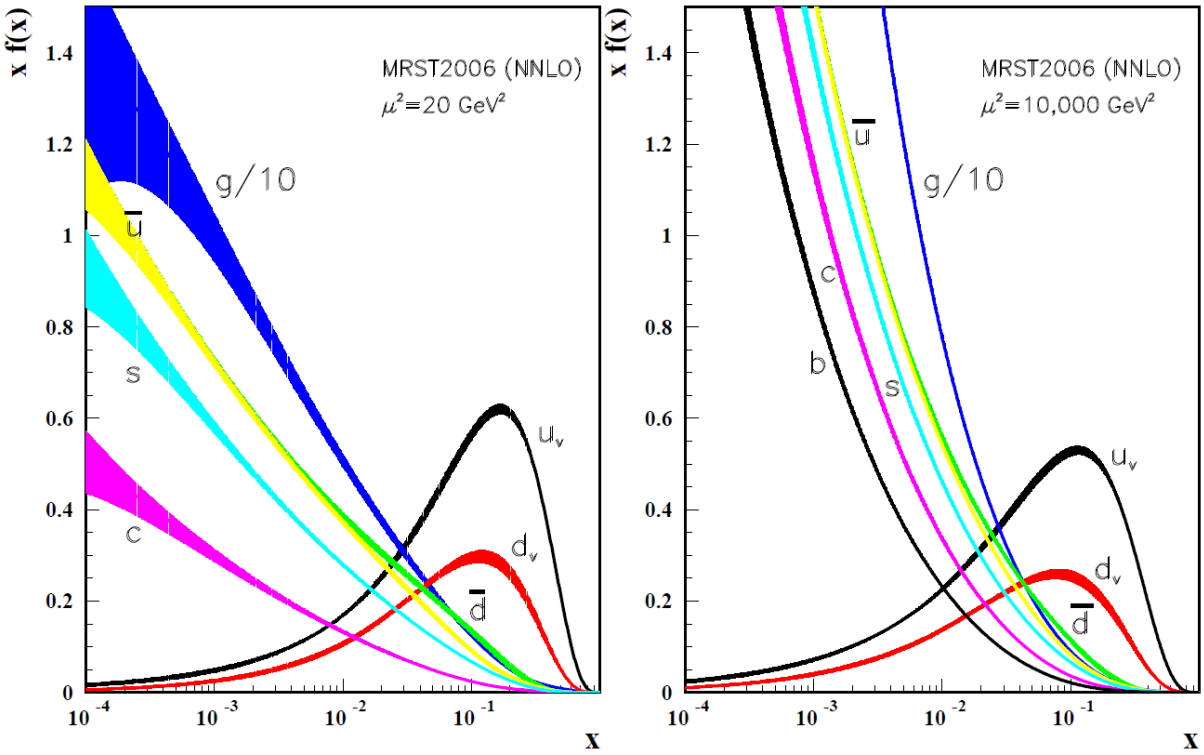

Figure 2.8: Distribution of x times the unpolarized parton distribution $q(x)$ (for q= u_v, d_v, $\bar{u}$, $\bar{d}$, s, c, b, g), and their associated uncertainties using the NNLO MRST2006 parametrization for $Q^2 = 20$ GeV^2 and $10,000$ GeV^2 [eaPDG08].

Knowing the PDFs, one can extract an important result about the proton momentum distribution in terms of quarks and gluons. The following sum rule holds:

$$\int_0^1 dx\, x\,[u(x) + \bar{u}(x) + d(x) + \bar{d}(x) + s(x) + \bar{s}(x)] = 1 - \sigma \tag{2.11}$$

where σ is interpreted as the fraction of the proton momentum that is not carried by the quark. This sum-rule has been computed by EMC collaboration [SVS88]. They found: $1 - \sigma = 0.465 \pm 0.023$. Therefore, quarks contribute to only about half of the total momentum of the nucleon. The rest of the proton momentum is carried by the gluons.

2.3 Exclusive process: DVCS

Elastic and DIS experiments allow one to access respectively the electromagnetic FFs related to the quark spatial charge distribution in a transverse plane, and the PDFs that carry information on the longitudinal momentum distribution of the quarks in the nucleon.

Deeply Virtual Compton Scattering (DVCS) allows us to obtain more information about the nucleon constituents. It provides an access to new structure functions, the Generalized Parton Distribution (GPDs), that correlate the spatial parton distribution in the transverse plane and their longitudinal momentum fraction. We can thus achieve a three dimensional picture (tomography) of the nucleon.

Approximately fifteen years ago, D. Muller et al. [MRG+94], X. Ji [Ji97] and A. Radyushkin [Rad96] showed that in the Bjorken regime it is possible to factorize the DVCS amplitude into two parts. One can seperate a "hard" part which consists of the virtual Compton process at the quark level ($\gamma^* q \to \gamma q$) that is perturbatively calculable in QED, and a non perturbative "soft" part which is parametrized in terms of four GPDs at leading twist and leading order.

Some examples of QCD diagrams for the DVCS process are shown in Fig. 2.9. At leading order[2] and leading twist[3], the cross section is dominated by the single-quark scattering, shown in panel (a). Other subprocesses are suppressed. The diagram in panel (b) gives rise to higher order contributions in α_s proportional to $\ln(Q^2)$. Panel (c) is an example of a diagram supressed by a factor $\frac{1}{Q}$ (higher twist contribution) when the virtual quark interacts with the nucleon through gluon exchange. The last panel (d) shows the gluon handbag diagram that gives access to the gluon GPDs. Because gluons do not couple directly to photons, a quark loop has to be introduced, which has two extra contributions in α_s compared to the single-quark diagram. The gluon contribution is more important at low x_B values and compensates for the α_s suppression. However, in the physical region accessible at JLab ($x_B \in [0.1, 0.5]$), we probe mostly the valence quark constituents of the nucleon so that we can assume we are not sensitive to the gluon contribution. Hereafter, we will therefore focus on the single-quark "handbag" dominant process (a).

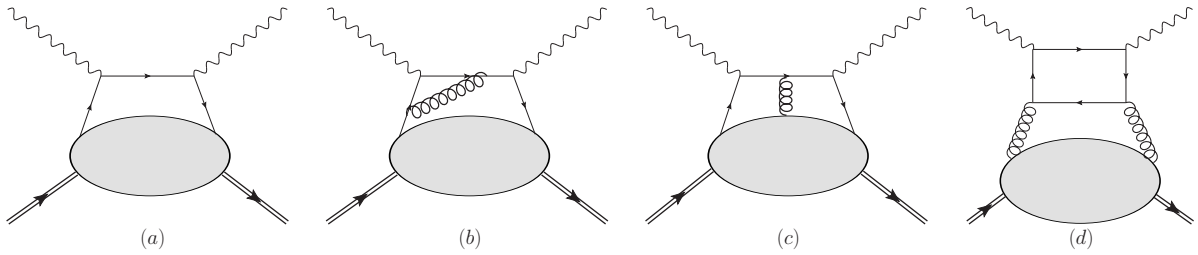

Figure 2.9: QCD diagrams for the DVCS process.

Figure. 2.10 shows the "handbag" diagram for the DVCS process on a nucleon: $eN \to e'N'\gamma$. An initial nucleon of momentum p absorbs a virtual photon of momentum q emitted by the incoming electron, producing in the final state an outgoing real photon of momentum $q' = q - \Delta$ and a recoil nucleon of momentum $p' = p + \Delta$. The quark that absorbs the virtual photon becomes virtual and propagates perturbatively. This quark then radiates a real photon (Compton process) and returns to the nucleon left in its ground state.

[2] Perturbation theory allows one to express an amplitude in terms of a power series in the (small) parameter α_s, where $\alpha_s = \frac{1}{\beta_0 ln(Q^2/\Lambda^2_{QCD})}$.

[3] Twist is equal to $dimension - spin$ of an operator. It allows one to classify terms in a $\frac{1}{Q}$ expansion. Twist n correspond to power-suppressed corrections in $\frac{1}{Q^{n-2}}$ with respect to the leading twist $n = 2$ for DVCS.

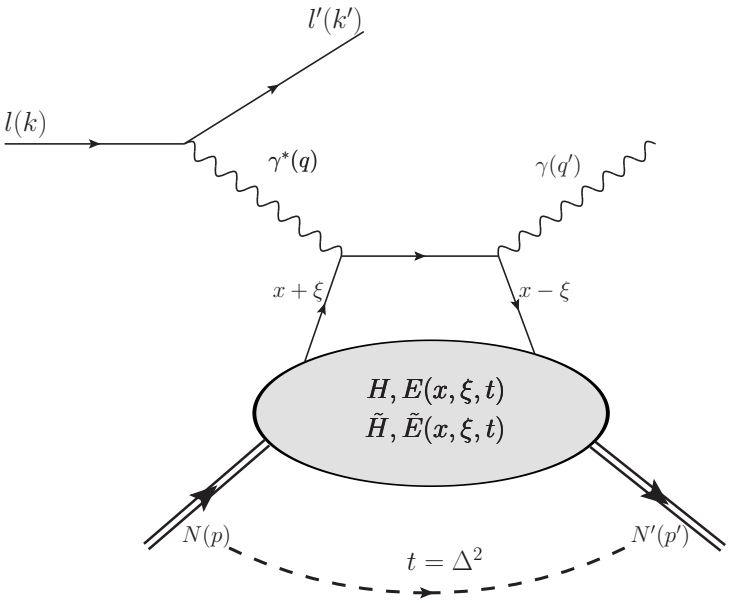

Figure 2.10: Handbag diagram of the DVCS process in the DGLAP region $x \in [\xi, 1]$, corresponding to the scattering on a quark.

The quantities $x+\xi$ $(x-\xi)$ of Fig. 2.10 refer to the longitudinal momentum fractions of the initial (final) quark respectively. x is the proton momentum fraction of the struck quark, and -2ξ is the longitudinal momentum fraction of the transfer Δ. These momentum fractions are defined in the infinite momentum frame relative to the average nucleon momentum $P = \frac{p+p'}{2}$ such as $k^+ = x\,P^+$ and $\Delta^+ = -2\xi\,P^+$, where $(+)$ is the plus component of the light cone vectors (for more details, one can also refer to Table C.2 of Appendix C). In the Bjorken limit, ξ is related to the standard deep inelastic Bjorken variable x_B via the formula $\xi \sim \frac{x_B}{2-x_B}$. The variable $t = \Delta^2 = (p'-p)^2$ is the squared momentum transfer between the initial and final nucleons.

One can find in Appendix C the explicit derivation of the DVCS amplitude at leading twist and leading order of perturbation. The DVCS cross section in the twist-three approximation calculated and decomposed in angular harmonics can be found in [BMK02].

In Appendix C, we define the light-cone frame where particles go at the speed of light along the z-axis and we show that in this frame the lower blob of Fig. 2.10 can be represented by the matrix element of a bilocal quark operator, which can be expressed in terms of four GPDs as:

$$\frac{P^+}{2\pi}\int dz^- e^{ixP^+z^-}\,\langle p'|\bar{q}_b\left(-\frac{z}{2}\right)q_a\left(\frac{z}{2}\right)|p\rangle\Big|_{z^+=\vec{z}_\perp=0}$$

$$\begin{aligned} = \;& \frac{1}{4}\Big\{(\gamma^-)_{ab}\left[H^q(x,\xi,t)\bar{u}(p')\gamma^+u(p) + E^q(x,\xi,t)\bar{u}(p')i\sigma^{+\kappa}\frac{\Delta_\kappa}{2m_N}u(p)\right] \\ & + (\gamma_5\gamma^-)_{ab}\left[\tilde{H}^q(x,\xi,t)\bar{u}(p')\gamma^+\gamma_5 u(p) + \tilde{E}^q(x,\xi,t)\bar{u}(p')\gamma_5\frac{\Delta^+}{2m_N}u(p)\right]\Big\} \end{aligned} \tag{2.12}$$

The first line is the Fourier integral along the light-cone distance z^- of a quark-quark correlation function. It represents the process where a quark is taken out of a nucleon of initial momentum p at the space-time point $z/2$, and is put back in a final nucleon of momentum p' at the space-time point $-z/2$.

This process takes place at equal light-cone time ($z^+ = 0$) and at zero transverse separation ($z^\perp = 0$) between the quarks.

The second line of this equation corresponds to the vector part (γ^μ stucture) of the current and the last line corresponds to the axial part ($\gamma^5\gamma^\mu$ stucture). These two structures are parametrized in terms of four GPDs: H, E, $\tilde{H}$, $\tilde{E}$. They are called the quark helicity conserving GPDs (the so called chiral-even GPDs) because the helicity of the struck quark is conserved during the process.

As discussed in Appendix C, the others structures are suppressed at leading order and leading twist because of an odd number of γ matrices in the trace computation of the amplitude. At higher order, these structures are kept and lead to the quark helicity flip GPDs (the so called chiral-odd GPDs), not described in this thesis.

For each quark flavour (u, d, s), there are four GPDs, H, E, $\tilde{H}$, $\tilde{E}$, corresponding to each of the four possible helicity-spin configurations of the proton and the quark (Fig. 2.11). The GPDs H and E are independent of the quark helicity and are therefore called unpolarized GPDs whereas $\tilde{H}$ and $\tilde{E}$ are dependent of the quark helicity and are called polarized GPDs.

H and $\tilde{H}$ conserve the proton spin, whereas E and $\tilde{E}$ flip of the proton spin. In the latter case the overall helicity is not conserved (the proton changes helicity but the quark does not), and the angular momentum conservation implies some orbital angular momentum to be present.

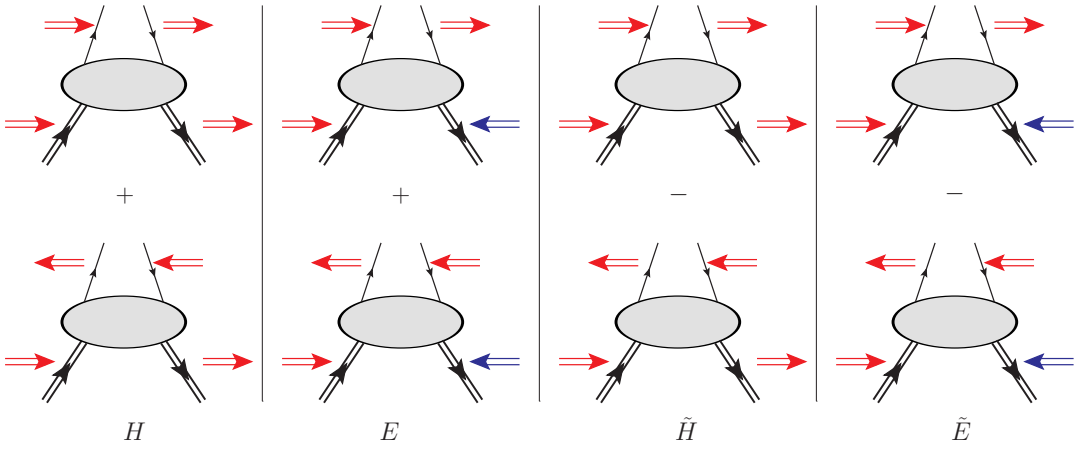

Figure 2.11: The four nucleon/quark helicity states and associated GPD. Arrows show the helicity states of the proton and of the quark. Blue arrows indicate the flip of the proton spin. The GPDs H and E are independent of the quark helicity and consist of the linear sum of the proton and quark helicity states. The GPDs $\tilde{H}$ and $\tilde{E}$ depend on the quark helicity and consist of the difference of the proton and quark helicity states.

GPDs depend upon three variables: x, ξ and t. GPDs represent the probability amplitude of finding a quark (anti-quark) in the nucleon with a longitudinal momentum fraction $x+\xi$ and of putting it back into the nucleon with a longitudinal momentum fraction $x-\xi$. GPDs are defined for ξ and $x \in [-1, 1]$. The relative values of these two variables allow one to distinguish the interaction between the virtual photon and the nucleon in three different regions (Fig. 2.12):

- The regions $x > \xi$ and $x < -\xi$ are called the DGLAP region. It corresponds to the QCD evolution equation in Q^2 for the PDFs defined in the DIS reaction. If $x \in [\xi, 1]$ ($x \in [-1, -\xi]$), both momentum fractions $x + \xi$ and $x - \xi$ are positive (negative) and the GPDs describe the emission and the reabsorption of a quark (antiquark) with different momenta.

- The region $|x| < \xi$ is called the ERBL[4] region [ER80]. It corresponds to the QCD evolution equation in Q^2 for the Distribution Amplitudes (DAs). In this region $x+\xi$ is positive (corresponds to a quark) and $x-\xi$ is negative (corresponds to an anti-quark). This region is sensitive to the meson content (i.e $q\bar{q}$) of the nucleon and is not accessible in the DIS process (because $\xi \to 0$ in the forward limit). The GPDs represent then the probability amplitude of finding a $q\bar{q}$ pair in the nucleon.

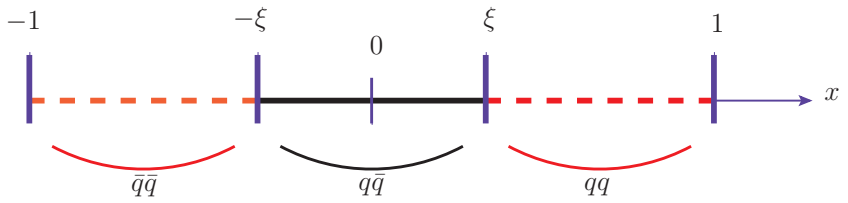

Figure 2.12: Representation of the three regions in x with respect to ξ of the GPDs. The DGLAP regions (in red) correspond to a scattering on a pair of quarks if $x > \xi$, and on a pair of anti-quarks if $x < -\xi$. The ERBL region (in black) corresponds to a scattering on a quark-antiquark pair.

Fig. 2.13 is an illustration of a GPD model in the two kinematic regions discussed above - the ERBL and DGLAP. When $\xi \to 0$, the DGLAP region dominates and we can recognize the typical shape of the PDFs that diverge for small momentum fraction x. For large values of ξ, the ERBL region dominates and the GPD H tends to the asymptotic shape of a meson distribution amplitude.

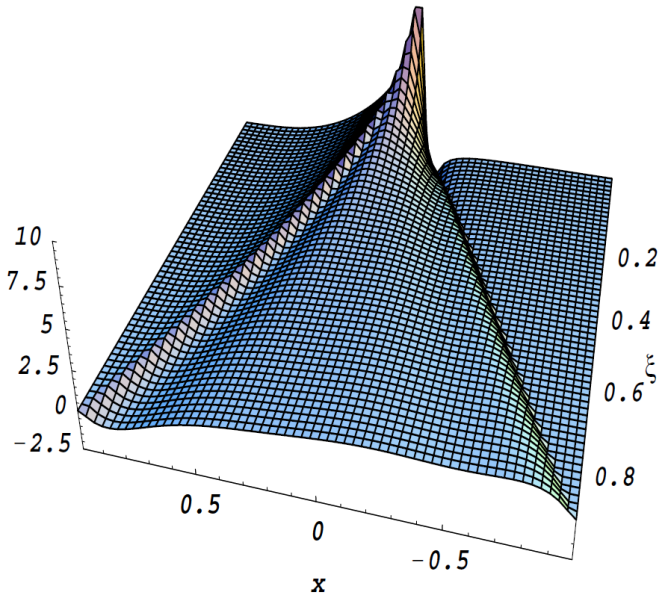

Figure 2.13: The GPD $H(x,\xi,t)$ as a function of x and ξ, at $t = 0$. $x > 0$ ($x < 0$) corresponds to quark (anti-quark) distribution.

[4] Efremov-Radyushkin, Brodsky-Lepage.

2.3.1 Properties of the GPDs

Forward limit and link with the PDFs

In the forward limit ($\Delta = p - p' = 0$), the optical theorem (illustrated in Fig. 2.14) links the imaginary part of the DVCS amplitude to the DIS cross section. One has for each quark flavor q:

$$H^q(x,0,0) = q(x) \quad ; \quad \tilde{H}^q(x,0,0) = \Delta q(x) \tag{2.13}$$

where $q(x)$ and $\Delta q(x)$ are respectively the unpolarized and polarized PDFs introduced in Section 2.1. There are no similar equations for the GPDs E and $\tilde{E}$ because of the pre-factor $\frac{\Delta}{2m_N}$ ($= 0$ in the forward limit) in Eq. 2.12. E and $\tilde{E}$ are new functions that can be accessed only in exclusive processes.

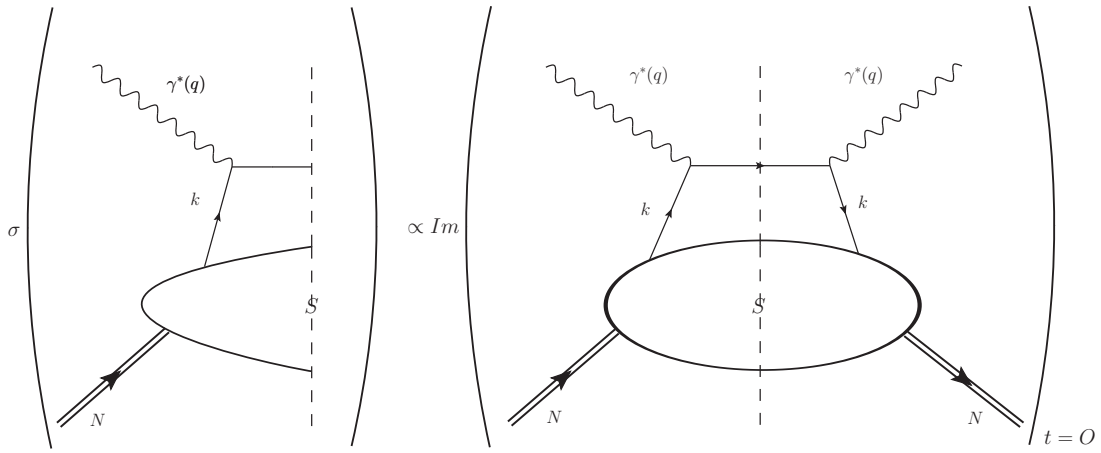

Figure 2.14: Illustration of the optical theorem linking the DIS cross section with the imaginary part of its forward limit amplitude, equivalent to the double DVCS process (production of a virtual photon in the final state instead of a real photon).

First moment of the GPDs and link with the FFs

Model-independent sum rules link the first moment in x of the GPDs to the elastic FFs [Ji97]. Integrating Eq. 2.12 over x and using the Fourier property $\int dx\, e^{ixz^-} = 2\pi\delta(z^-)$, one finds:

$$\int dx \int \frac{dz^-}{2\pi} e^{ixz^-} \langle p'|\bar{q}_b(0)\, q_a(z)\, |p\rangle \Big|_{z^+=\vec{z}_\perp=0} = \langle p'|\bar{q}_b(0)\, q_a(0)\, |p\rangle \Big|_{z^+=\vec{z}_\perp=0} \tag{2.14}$$

The second term of this equation corresponds to the local non-forward matrix element used in elastic scattering to describe the hadronic process with the FFs. So the integration of Eq. 2.12 over x gives rise to four relations between the GPDs and the FFs:

$$\begin{aligned} \int_{-1}^{1} dx\, H^q(x,\xi,t) = F_1^q(t) \quad ; \quad \int_{-1}^{1} dx\, E^q(x,\xi,t) = F_2^q(t) \qquad \forall\xi \\ \int_{-1}^{1} dx\, \tilde{H}^q(x,\xi,t) = G_A^q(t) \quad ; \quad \int_{-1}^{1} dx\, \tilde{E}^q(x,\xi,t) = G_P^q(t) \qquad \forall\xi \end{aligned} \tag{2.15}$$

where $F_1^q(t)$ and $F_2^q(t)$ are the Dirac and Pauli FFs, and $G_A^q(t)$ and $G_P^q(t)$ are the axial and pseudoscalar FFs presented in section 2.2.

In Fig. 2.15, we summarize the two previous properties by showing a representation of the links that exist between the GPDs, the FFs (via the first moment) and the PDFs (via the forward limit).

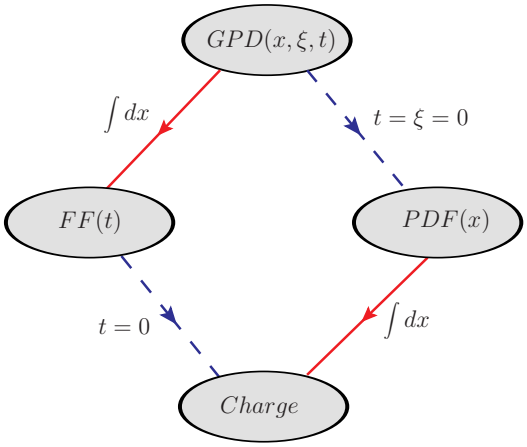

Figure 2.15: Links between GPDs (from DVCS), FFs (from ES) and PDFs (from DIS).

Second moment of the GPDs and link with the orbital momentum

Generalizing Eq. 2.14 to higher moments in x gives rise to the polynomiality property of the GPDs which states that the x-integrals of $x^n H^q$ and of $x^n E^q$ are polynomials in ξ of order n (for n even[5]) or $n+1$ (for n odd[6]) [Ji98, Die03, Gui08b], where ξ appears only in even powers. This is the reason why we do not observe a ξ dependence for the first moment in x of the GPDs in Eqs. 2.15.

The second moment of H^q and E^q are of the form [Die03]:

$$\begin{aligned} \int_{-1}^{1} dx\, x H^q(x,\xi,t) &= A^q(t) + 4\xi^2 C^q(t) \\ \int_{-1}^{1} dx\, x E^q(x,\xi,t) &= B^q(t) - 4\xi^2 C^q(t) \end{aligned} \tag{2.16}$$

so that:

$$\int_{-1}^{1} dx\, x[H^q(x,\xi,t) + E^q(x,\xi,t)] = A^q(t) + B^q(t) \tag{2.17}$$

Ji derived a sum rule [Ji97] that links in the forward limit ($t \to 0$) the second moment in x of the GPDs H and E to the total (spin + orbital) angular momentum carried by the quarks J_{quarks}:

$$\sum_q \int_{-1}^{+1} dx\, x[H^q(x,\xi,t=0) + E^q(x,\xi,t=0)] = \sum_q [A^q(0) + B^q(0)] = 2\, J_{quarks} \tag{2.18}$$

Ji also showed that there is a gauge-invariant decomposition of the nucleon spin that can be written as:

$$\frac{1}{2} = J_{quarks} + J_{gluons} \tag{2.19}$$

where J_{gluons} is the total contribution of the gluons to the spin of the nucleon. J_{quarks} can be decomposed as: $J_{quarks} = \sum_q (S_q + L_q)$, where L_q is the quark orbital momentum and

$$S_q = \frac{\Delta q}{2} = \frac{1}{2}\int_0^1 dx\, [q_+(x) - q_-(x)] \tag{2.20}$$

[5] For the GPD H, if n even: $\int_{-1}^{1} dx x^n H^q(x,\xi,t) = a_0 + a_2\xi^2 + a_4\xi^4 + \cdots + a_n\xi^n$.

[6] For the GPD H, if n odd: $\int_{-1}^{1} dx x^n H^q(x,\xi,t) = a_0 + a_2\xi^2 + a_4\xi^4 + \cdots + a_{n+1}\xi^{n+1}$.

is the contribution of the quark intrinsic spin to the nucleon spin. Δq has been measured by the EMC collaboration [col89] using DIS with polarized muons on a polarized proton target. They found that $\sim 30\%$ of the nucleon spin arises from the spin of the quarks. Therefore, if one can extract the second moments of the GPDs, this sum rule will then give access experimentally for the first time to the quark orbital momentum contribution to the nucleon spin.

Recently, Wakamatsu [Wak10] has proposed a gauge invariant extention to the decomposition of Ji by introducing the separation[7] of the total angular momentum of the gluons in terms of spin and orbital angular momentum contributions: $J_{gluons} = \Delta g + L_g$. So far, the information that we have about the gluons contribution to the nucleon spin arises from COMPASS [Col06], STAR [Col08] and PHENIX [Col09] experiments. They have measured the gluon spin contribution Δg and found a result compatible with zero $\Delta g \sim 0$, though with large error bars. Similarly to J_{quarks}, the contribution J_{gluons} could be accessed by measuring the gluons GPDs at very small x_B, and would allow to access indirectly the gluon orbital momentum contribution to the nucleon spin.

2.3.2 Impact parameter interpretation of the GPDs

It has been shown [Bur03] that the t-dependence of the GPDs can be related to the transverse spatial distribution of the partons in the nucleon. As we saw in Sec. 2.3.1, the FFs correspond to the GPDs but integrated over the momentum fraction x. If one uses the same Fourier-transform interpretation for the GPDs as for the form factors (Eq. 2.4), it is then possible to interpret the GPDs as an x-decomposition of the form factors: we have access to the FFs at different values of x, rather than integrated over x.

For $\xi \to 0$ ($t = -\Delta_\perp^2$ is purely transverse), the 2-dimensional Fourier transform of the GPD $H_q(x, 0, t)$ is equal to the distribution $q(x, b_\perp)$ which provides a simultaneous measurement of the longitudinal momentum x at a given tranverse position (impact parameter $b_\perp$) for unpolarized quarks and target:

$$q(x, 0, b_\perp) = \int \frac{d^2\Delta_\perp}{(2\pi)^2} e^{ib_\perp \Delta_\perp} H^q(x, 0, -\Delta_\perp^2) \tag{2.21}$$

If the target is transversely polarized, the impact parameter dependent PDF $q(x, 0, b_\perp)$ is no longer axially symmetric and the transverse deformation is described by the gradient of the Fourier transform of the GPD $E^q(x, 0, t)$. For a transversely polarized target in the $+X$ direction, we write:

$$q_{+X}(x, 0, b_\perp) = q(x, 0, b_\perp) - \frac{1}{2M} \frac{\partial}{\partial b_y} \int \frac{d^2\Delta_\perp}{(2\pi)^2} e^{ib_\perp \Delta_\perp} E^q(x, 0, -\Delta_\perp^2) \tag{2.22}$$

The two distributions $q(x, b_\perp)$ and $q_{+X}(x, b_\perp)$ are presented for different values of x in Figs. 2.16 (quark u) and 2.17 (quark d). We see that inside a transversely polarized proton along $+X$, the term related to $E^q(x, 0, t)$ introduces a positive "shift" in Y of the parton distribution for the u quark while the shift is negative for the quark d.

We also see that as x increases the quark distributions tend to be concentrated at small values of $b_\perp$, reflecting the fact that the distribution of the valence quarks is located in the core of the nucleon.

So the information coming from the PDFs of the DIS experiments and the FFs measured in ES are now unified into the GPD framework. This gives the possibility to have a three dimensional (2 spatial and 1 momentum) picture of the nucleon, as can be seen on Fig. 2.18.

2.3.3 Compton Form Factors

The four GPDs $(H, \tilde{H}, E, \tilde{E})$ depend on the three variables x, ξ, and t, but only ξ and t are accessible experimentally. Equation 2.23 (see also Appendix C) corresponds to the DVCS amplitude at leading

[7] the Wakamatsu decomposition is gauge invariant, however the interpretation of J_{gluons} in terms of spin and orbital angular momentum contributions is valid only in the light cone gauge, i.e. the one defined by $A^+_{phys} = 0$.

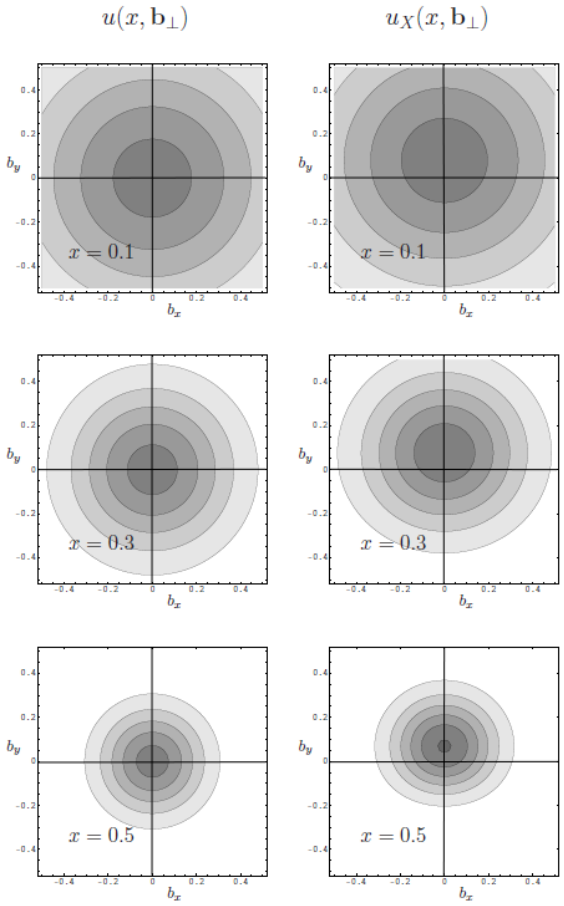

Figure 2.16: Distribution of the u quark in the transverse plane for $x = 0.1$, 0.3, and 0.5. Left column: $u(x, b_\perp)$ quark distribution for unpolarized protons. Right column: unpolarized quark distribution $u_{+X}(x, b_\perp)$ for transversely polarized protons. Figure taken from [Bur03].

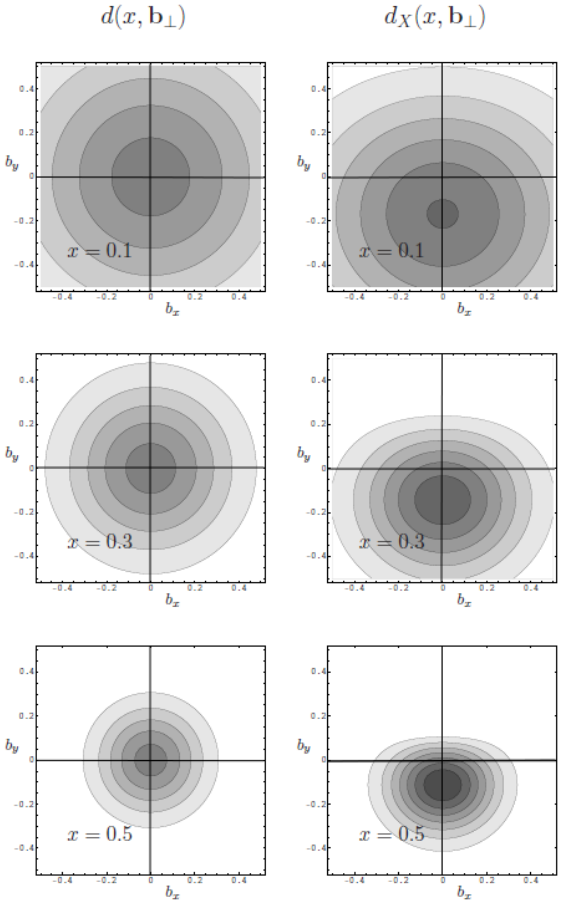

Figure 2.17: Distribution of the d quark in the transverse plane for $x = 0.1$, 0.3, and 0.5. Left column: $d(x, b_\perp)$ quark distribution for unpolarized protons. Right column: unpolarized quark distribution $d_{+X}(x, b_\perp)$ for transversely polarized protons. Figure taken from [Bur03].

order and leading twist. One can see that the amplitude is proportional to an integral over x of the GPDs (the two terms $\frac{1}{x-\xi+i\epsilon}$ and $\frac{1}{x+\xi-i\epsilon}$ come from the quark propagator between the virtual and the real photons).

$$
\begin{aligned}
i\mathcal{M} = -i \sum_q (|e|Q_q)^2 \epsilon^*_\mu \epsilon_\nu \Bigg\{ & \\
(p_1^\mu p_2^\nu + p_1^\nu p_2^\mu - g_\perp^{\mu\nu}) \int_{-1}^{1} dx \left[\frac{1}{x-\xi+i\epsilon} + \frac{1}{x+\xi-i\epsilon} \right] \times \frac{1}{2P^+} \left[H^q(x,\xi,t)\bar{u}(p')\gamma^+ u(p) + E^q(x,\xi,t)\bar{u}(p') i\sigma^{+\alpha} \frac{\Delta_\alpha}{2m_N} u(p) \right] & \\
+ i\epsilon^{\mu\nu+-} \int_{-1}^{1} dx \left[\frac{1}{x+\xi-i\epsilon} - \frac{1}{x-\xi+i\epsilon} \right] \times \frac{1}{2P^+} \left[\tilde{H}^q(x,\xi,t)\bar{u}(p')\gamma^+\gamma_5 u(p) + \tilde{E}^q(x,\xi,t)\bar{u}(p')\gamma_5 \frac{\Delta^+}{2m_N} u(p) \right] \Bigg\} &
\end{aligned}
\tag{2.23}
$$

As a consequence, one can not have access to the x-dependence of the GPDs, and the GPDs can not be measured directly from DVCS experiments.

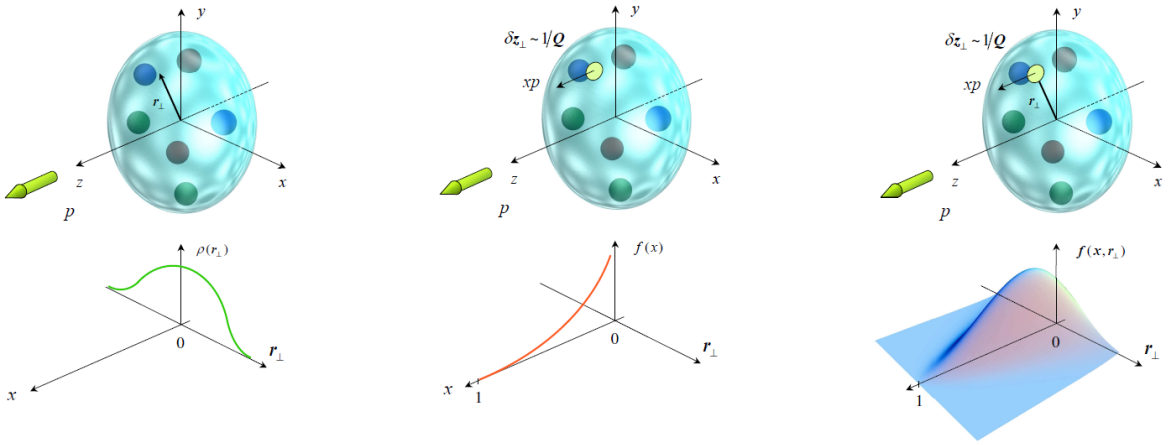

Figure 2.18: From left to right: probabilistic interpretation of FFs (quark spatial charge distribution in the transverse plane) measured in ES, PDFs (quark longitudinal momentum distribution) measured in DIS, and GPDs (correlation of the two previous distributions). For $\xi \to 0$, the GPDs are interpreted as the probability amplitude of finding a quark (anti-quark) at a distance $b_\perp$ from the nucleon center with a longitudinal momentum fraction x. Figure taken from [BR05].

The amplitude is complex and can be decomposed as:

$$\mathcal{M}_{DVCS} \propto \int_{-1}^{1} dx \frac{f(x,\xi,t)}{x \pm \xi \mp i\epsilon} = \mathcal{P} \int_{-1}^{1} dx \frac{f(x,\xi,t)}{x \pm \xi} \pm i\pi f(x = \mp\xi, \xi, t) \tag{2.24}$$

where $f(x,\xi,t)$ stands for any of the four GPDs, and $\mathcal{P}$ for the Cauchy principal value integral.

This decomposition leads to the eight quantities presented in Table. 2.1, called the Compton Form Factors (CFFs). In this definition, the 8 CFFs are all real functions. They are combinations of weighted GPDs integrated over x and of GPDs at the line $x = \pm\xi$. They correspond respectively to the real part and to the imaginary part of the DVCS amplitude.

Real part	Imaginary part
$\mathcal{H}_{Re}(\xi,t) = \mathcal{P}\int_0^1 dx[H(x,\xi,t) - H(-x,\xi,t)]\, C^+(x,\xi)$	$\mathcal{H}_{Im}(\xi,t) = H(\xi,\xi,t) - H(-\xi,\xi,t)$
$\mathcal{E}_{Re}(\xi,t) = \mathcal{P}\int_0^1 dx[E(x,\xi,t) - E(-x,\xi,t)]\, C^+(x,\xi)$	$\mathcal{E}_{Im}(\xi,t) = E(\xi,\xi,t) - E(-\xi,\xi,t)$
$\tilde{\mathcal{H}}_{Re}(\xi,t) = \mathcal{P}\int_0^1 dx[\tilde{H}(x,\xi,t) + \tilde{H}(-x,\xi,t)]\, C^-(x,\xi)$	$\tilde{\mathcal{H}}_{Im}(\xi,t) = \tilde{H}(\xi,\xi,t) + \tilde{H}(-\xi,\xi,t)$
$\tilde{\mathcal{E}}_{Re}(\xi,t) = \mathcal{P}\int_0^1 dx[\tilde{E}(x,\xi,t) + \tilde{E}(-x,\xi,t)]\, C^-(x,\xi)$	$\tilde{\mathcal{E}}_{Im}(\xi,t) = \tilde{E}(\xi,\xi,t) + \tilde{E}(-\xi,\xi,t)$

Table 2.1: The eight Compton form factors. The terms corresponding to the real part of the DVCS amplitude are weighted by: $C^\pm(x,\xi) = \frac{1}{x-\xi} \pm \frac{1}{x+\xi}$.

The CFFs depend only on ξ (or equivalently on x_B) and t, and are the quantities that can be

extracted from DVCS experiments. Model-independent fitting procedures have been developed which, for a given experimental point $(x_B, -t)$, keep the CFFs as free parameters and extract them from the DVCS experimental observables [Gui08a, Mou09].

Let us mention here that the x-dependence of the GPDs can be accessed with the double DVCS (DDVCS) process, which consists in the scattering of a spacelike virtual photon from the nucleon with the production of a virtual photon in the final state. The DDVCS provides an additional lever arm, which allows us to vary both the quark momenta x and ξ independently [GV03].

2.3.4 The Bethe-Heitler process

In addition to the DVCS amplitude, the cross section for the exclusive electroproduction of a photon ($eN \to eN\gamma$) also receives a contribution from the Bethe-Heitler (BH) process (Fig. 2.19). In this case, the real photon is emitted either by the incoming or by the scattered electron but not by the nucleon itself, unlike for DVCS.

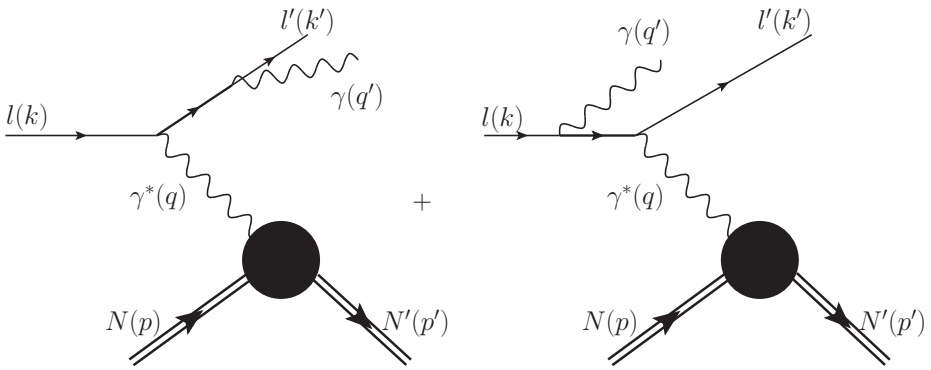

Figure 2.19: Bethe-Heitler process.

The BH process is not sensitive to GPDs, but is experimentally indistinguishable from the DVCS process and interferes with it. The amplitude $\mathcal{M}$ for the $eN \to eN\gamma$ reaction is the sum of the DVCS $\mathcal{M}_{DVCS}$ and Bethe-Heitler $\mathcal{M}_{BH}$ amplitudes:

$$\mathcal{M}^2 = |\mathcal{M}_{BH}|^2 + |\mathcal{M}_{DVCS}|^2 + \mathcal{I} \tag{2.25}$$

with the interference term $\mathcal{I} = \mathcal{M}_{DVCS}\mathcal{M}^*_{BH} + \mathcal{M}^*_{DVCS}\mathcal{M}_{BH}$.

If we set the mass of the electron to zero, the invariant amplitude of the BH process is equal to:

$$\begin{aligned} i\mathcal{M} &= \bar{u}(k')\left\{(-ie\gamma_\mu)\left[i\frac{\not{k}-\not{q}'}{(k-q')^2}\right](-ie\gamma^\nu)\epsilon^*_\nu + (-ie\gamma^\nu)\epsilon^*_\nu\left[i\frac{\not{k}'+\not{q}'}{(k'+q')^2}\right](-ie\gamma_\mu)\right\}u(k)\frac{-i}{q^2} \\ &\times \bar{u}(p')(ie\Gamma^\mu)u(p) \end{aligned} \tag{2.26}$$

where Γ^μ parametrizes the hadronic current in terms of the FFs (Eq. A.5). As the nucleon form factors are well known at small t, the BH process is precisely calculable theoretically.

One notes the two poles of the amplitude coming from the propagators:

$$\begin{aligned} (k-q')^2 &\sim -2E_eE_\gamma[1-cos(\theta_{e\gamma})] \\ (k'+q')^2 &\sim 2E_{e'}E_\gamma[1-cos(\theta_{e'\gamma})] \end{aligned} \tag{2.27}$$

The BH cross section diverges in the $m_e = 0$ limit for either $\theta_{e\gamma}$ or $\theta_{e'\gamma} \to 0$, corresponding to the case when the real photon is emitted in the same direction as either the incoming electron or the outgoing electron. In these regions, the BH process dominates completely over the DVCS process.

2.3.5 Access to GPDs with DVCS observables

Different observables from the DVCS process have to be measured to extract the information related to the GPDs. For instance, a polarized beam allows to measure two independent observables: the unpolarized cross section $\sigma_{unp} = \sigma^{\rightarrow} + \sigma^{\leftarrow}$ and the difference of polarized cross sections $\sigma_{pol} = \sigma^{\rightarrow} - \sigma^{\leftarrow}$ for opposite beam helicities.

The unpolarized and the polarized cross section are:

$$\begin{aligned} \sigma_{unp} &\propto |\mathcal{M}_{BH}|^2 + 2\,\mathcal{M}_{BH}\,Re(\mathcal{M}_{DVCS}) + |\mathcal{M}_{DVCS}|^2 \\ \sigma_{pol} &\propto 2\,\mathcal{M}_{BH}\,Im(\mathcal{M}_{DVCS}) \end{aligned} \tag{2.28}$$

In a first approximation, the term $|\mathcal{M}_{DVCS}|^2$ can be neglected in the analysis compared to the term $|\mathcal{M}_{BH}|^2$, which is much more important. As a consequence, the observable σ_{unp} gives mainly access to the real part of the DVCS amplitude, i.e an integral over x of a combination of GPDs (see Table. 2.1). The observable σ_{pol} gives access to the imaginary part of the DVCS amplitude which is a combination of the GPDs at the point $x = \pm\xi$.

The ratio of the two previous observables defines the Beam Spin Asymmetry (BSA): $\mathcal{A}_{LU} = \frac{\sigma^{\rightarrow} - \sigma^{\leftarrow}}{\sigma^{\rightarrow} + \sigma^{\leftarrow}}$. Experimentally, the asymmetry has the advantage compared to the other observables that the normalization factors (acceptance of the detector for instance) cancel.

	Sensitivity	Experiment
$\sigma_{unp} = \sigma^{\rightarrow} + \sigma^{\leftarrow}$	$\propto \mathcal{H}_{Re}$	H1 ((2001) [ea01b], (2005) [ea05a], (2008) [ea08b]) ZEUS ((2003) [ea03d], (2009) [ea09b]) Hall-A ((2006) [ea06a]) Hall-B (E1-DVCS experiment: data under analysis [BEG$^+$03])
$\sigma_{pol} = \sigma^{\rightarrow} - \sigma^{\leftarrow}$	$\propto \mathcal{H}_{Im}$	Hall-A ((2006) [ea06a]) Hall-B (E1-DVCS experiment: data under analysis [BEG$^+$03])
$\mathcal{A}_C$	$\propto \mathcal{H}_{Re}$	HERMES ((2007) [ea07], (2008) [ea08a], (2009) [ea09a])
$\mathcal{A}_{LU}$	$\propto \mathcal{H}_{Im}$	HERMES ((2001) [ea01a], (2009) [ea09a]) Hall-B ((2001) [ea01d], (2008) [ea08c])
$\mathcal{A}_{UL}$	$\propto \mathcal{H}_{Im}, \tilde{\mathcal{H}}_{Im}$	Hall-B ((2006) [ea06b]) HERMES ((2010) [ea10a]) Hall-B (Eg1-DVCS experiment: data under analysis [BEJN05])
$\mathcal{A}_{LL}$	$\propto \mathcal{H}_{Re}, \tilde{\mathcal{H}}_{Re}$	HERMES ((2010) [ea10a]) Hall-B (Eg1-DVCS experiment: data under analysis [BEJN05])
$\mathcal{A}_{UT}$	$\propto \mathcal{E}_{Im}$	HERMES ((2008) [ea08a]) Hall-B proposal [ea12]
$\mathcal{A}_{LT}$	$\propto \mathcal{H}_{Re}, \mathcal{E}_{Re}$	HERMES ((2011) [ea11a]) Hall-B proposal [ea12]

Table 2.2: Main sensitivity of the experimental obsvervables to CFFs, and references to published or ongoing analysis.

One can also measure beam charge and target polarization observables. Table 2.2 shows for a particular beam polarization (unpolarized (U) or longitudinally polarized (L)), associated with a (unpolarized (U), longitudinally polarized (L), or transversely polarized (T)) target, the sensitivity to different CFFs. The unpolarized cross section and the double spin asymmetries give access to the CFFs corresponding to the real part of the DVCS amplitude (left column of Table 2.1). The difference of polarized cross sections and the single spin asymmetries give access to the CFFs corresponding to the imaginary part of the DVCS amplitude (right column of Table 2.1).

In Table 2.2, we list the DVCS observables and the CFFs that dominantly contribute to them. Notice that the CFF $\tilde{E}$ is not present in this table. We stress that each observable has a particular sensitivity to a CFF, but nevertheless all the CFFs actually contribute to the amplitude. To extract the CFF $\tilde{E}$ with enough precision, one will first need to have strong contraints on the others CFFs.

2.3.6 GPDs parametrization

We describe in this section the parametrization of the GPDs adopted by the VGG model (Vanderhaeghen, Guichon and Guidal [VGG98, VGG99, GPV01, GPRV05]). Since the first article in 1998, the model has constantly evolved and we describe here its latest version, where the GPDs are parametrized using the double distribution ansatz, the D-term and a Reggeized t dependence. The parametrization of the (x, ξ) dependence, based on the double distributions, will be first described. We will then discuss the t-dependence parametrization and finally we will introduce the D-term.

Parametrization of the x and ξ dependence

The (x, ξ) dependence of the GPDs can be parametrized using the double distribution formalism that has first been introduced by Radyushkin [Rad96, Rad97]. The relation between the $GPD^q(x, \xi)$ and the double distributions $DD^q(\alpha, \beta)$ is given by the change of variables:

$$GPD^q_{DD}(x,\xi) = \int_{-1}^{1} d\beta \int_{-1+|\beta|}^{1-|\beta|} d\alpha\, \delta(x-\beta-\alpha\xi)\, DD^q(\beta,\alpha). \tag{2.29}$$

The idea of Eq. 2.29 is to introduce two new variables α and β, that are used to linearly correlate x and ξ. The polynomiality condition (Sec. 2.3.1) of the GPDs implies that the n^{th}-moment in x of the GPD is a polynomial in ξ of order n. In the most simple case, this property can be satisfied by using a Dirac delta function integral: $\int dx\, f(x)\, \delta(x-\xi) = f(\xi)$, that implies a one-to-one correlation between x and ξ. The order of x is then linked to the order of ξ and the polynomiality condition is automatically satisfied up to the order n. However, a more general form can be written and the two variables can be linearly correlated as: $x = \beta + \alpha\xi$. The parametrization of the GPDs consists then in finding a function, the so-called double distribution, constrained by the GPDs limits (forward limit at $\xi = 0$ where GPDs reduce to the PDFs, and the limit $\xi = 1$ in the case of the GPDs reduce to a DA) and integrated over all the possible values of β and α. As momentum fractions, β is integrated from -1 to 1, and α from $-1 + |\beta|$ to $1 - |\beta|$ because $|x| = |\beta + \alpha\xi| \leq 1 \Rightarrow |\beta| + |\alpha| \leq 1$.

Because $\Delta^+ = -2\xi P^+$, the longitudinal momentum fraction of the initial quark $(x+\xi)P^+$ becomes $\beta P^+ - (1+\alpha)\frac{\Delta}{2}$. Fig. 2.20 illustrates this change of variables. The DD can be interpreted as the

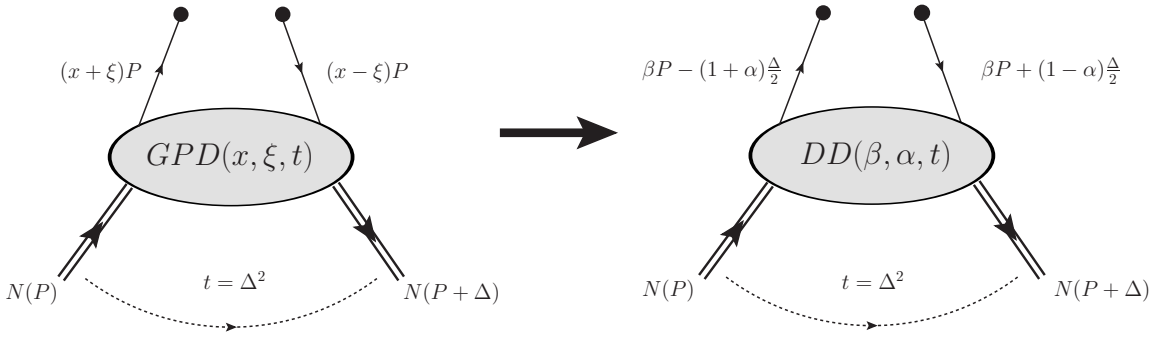

Figure 2.20: Illustration of the change of variable $(x, \xi) \to (\beta, \alpha)$ as defined in the double distribution.

probability amplitude to find a quark with the momentum fraction β of the average proton momentum

P, plus the fraction $-(1+\alpha)/2$ of the momentum transfer Δ.

The shape of the DD is constrained by two limits:

- $P \neq 0$ and $\Delta = 0$: the process reduces to its forward limit ($t = 0$) and we access the PDFs. The β dependence must therefore contain the unpolarized quark distribution $q(x)$ for the GPD H, and the polarized quark distribution $\Delta q(x)$ for the GPD $\tilde{H}$.
- $P = 0$ and $\Delta \neq 0$: the DDs are interpreted as the probability amplitude to find in a nucleon a $q\bar{q}$ pair of momenta $(1+\alpha)\Delta$ and $(1-\alpha)\Delta$. The α dependence of the DDs can therefore reduce to a meson distribution amplitude and parametrize the probability amplitude to find a meson in the nucleon.

The parametrization of the DDs must therefore include the PDFs (in the limit $\Delta = 0$) and the DAs (in the limit $P = 0$). Such a function taking into account these two limits has been proposed by Radyushkin [Rad97]:

$$DD^q(\beta,\alpha) = h(\beta,\alpha)\, q(\beta) \tag{2.30}$$

where $q(\beta)$ is the parton distribution function and $h(\beta,\alpha)$ is the profile function defined as:

$$h(\beta,\alpha) = \frac{\Gamma(2b+2))}{2^{2b+1}\Gamma^2(b+1)} \frac{[(1-|\beta|)-\alpha^2]^b}{(1-|\beta|)^{2b+1}}. \tag{2.31}$$

The free parameter b characterizes the strength of the ξ dependence of the GPDs. The limit $b \to \infty$ corresponds to the absence of any ξ dependence, i.e $\mathrm{GPD}^q(x,\xi) \overset{b\to\infty}{=} q(x)$.

Parametrization of the t dependence

The VGG model uses a Regge-like approach to correlate (x,ξ) and t, adopting a $x^{-\alpha' t}$ behavior. The t dependence of the double distribution $DD^q(\beta,\alpha)$ for the GPD H and E is parametrized as:

$$H^q(\beta,\alpha,t) = h(\beta,\alpha)\, q(\beta) \times \beta^{-\alpha'(1-\beta)t} \tag{2.32}$$

$$E^q(\beta,\alpha,t) = h(\beta,\alpha)\, q(\beta) \times (1-\beta)^{\eta_q}\, \beta^{-\alpha'(1-\beta)t} \tag{2.33}$$

The parameter α' is constrained by the sum rules (Eqs. 2.15) that link the GPDs to the FFs. A fit to the FFs data gives a Regge slope $\alpha' \approx 1$ GeV^{-2} [GPRV05]. The $(1-\beta)$ factor in the exponentials allows to reproduce the Dirac form factor $F_1(t)$ at large t, which drops like $\approx 1/t^2$.

For the GPD E, the model is modified: an additional $(1-\beta)^{\eta_q}$ term is added to reproduce the Pauli form factor $F_2(t)$, that has a faster fall-off than $F_1(t)$ at large t, and drops as $\approx 1/t^3$. The power η_q is determined from a fit to the nucleon form factor data.

VGG has a different approach for the parametrizations of $\tilde{H}$ and $\tilde{E}$. $\tilde{H}$ is simply parametrized as $\Delta q(x) \times G_A(t)/G_A(0)$ (where $G_A(t)$ is the axial form factor, see also Appendix A.1), which means that at $t = 0$, $\tilde{H}$ reduces to $\Delta q(x)$ as it should. This ansatz also satisfies the form factor sum rule. The parametrisation of the GPD $\tilde{E}$ is different because there is no DIS constraint (forward limit) for the x-dependence. The GPD $\tilde{E}$ is associated to a pseudo-scalar (γ_5) structure, the same that one finds for a pion t-channel exchange. Because of the proximity of the pion pole at $t = m_\pi^2$, an idea is to model the $\tilde{E}$ by the t-channel pion-exchange whose behaviors (normalization, x_B, t dependences,...) are well-known. The GPD $\tilde{E}$ can thus be parametrized as $\tilde{E} = \theta(\xi - |x|)\, G_P(t) \frac{1}{\xi}\Phi(\frac{x}{\xi})$, where θ is the unit step function ($\theta = 1$ if $\xi - |x| \geq 0$, $\theta = 0$ if $\xi - |x| < 0$), G_P is the pseudoscalar form factor and Φ corresponds to the pion distribution amplitude. The pion exchange contributes only in the region $-\xi \leq x \leq \xi$, and therefore to the real part of the DVCS amplitude.

Equations 2.32 and 2.33 suggest that the t slope of the GPDs becomes sharper and sharper as β decreases, as discussed in Sec. 2.3.2. Because t is the conjugate variable of the impact parameter $b_\perp$ and

β is linked to the momentum fraction, the picture of the nucleon shown in Fig. 2.21 can be described as:

- For large momentum fraction β, the t slope (and so the impact parameter) of the GPDs is small. It means that the valence quarks that have large momentum fraction are localized in the core of the nucleon (small $b_\perp$).
- For small momentum fraction β, the t-slope of the GPDs becomes large, which means that the distribution of the sea quarks that have small momentum fraction can extend to large values of $b_\perp$.

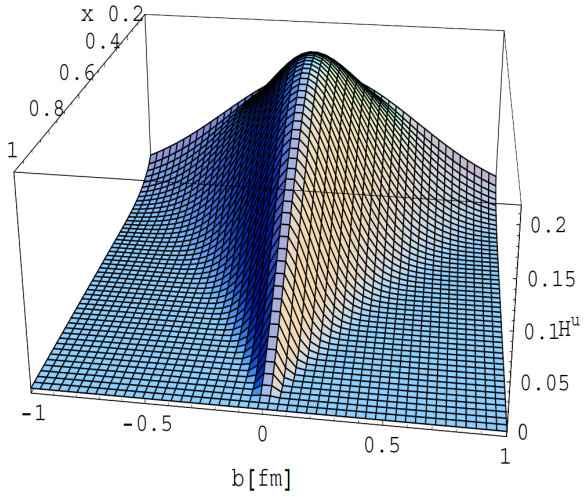

Figure 2.21: Two dimensional distribution of the GDP $H(x,0,t)$ for the quark u, shown as a function of the longitudinal momentum fraction x and the transverse impact parameter $b_\perp$. This three dimensional picture of the nucleon computed by the VGG model shows that the partons having large momentum fraction are localized in the core of the nucleon (small $b_\perp$) while partons with small momentum fraction are spread over the nucleon radius.

D-term

The form of the parametrization purely based on DDs does not fully satisfy the polynomiality property of the GPDs. This relation implies that for n odd, the n^{th} moment in x of the GPDs is a polynomial in ξ of degree $n+1$. However, the δ function in the double distribution (Eq. 2.29) imposes a linear relation between x and ξ and implies that the n^{th} moment in x is, at most, a polynomial in ξ of order n. The last term of the polynomial corresponding to ξ^{n+1} is therefore missing in the double distribution. To restore this property, an additional term has been introduced in Eq. 2.29 by Weiss and Polyakov [PW99]. The so called D-term contribution to $H(x,\xi)$ and $E(x,\xi)$ has the following form:

$$H^{D_{term}}(x,\xi) = \theta(\xi-|x|)\, D(\frac{x}{\xi}) \tag{2.34}$$

$$E^{D_{term}}(x,\xi) = -\theta(\xi-|x|)\, D(\frac{x}{\xi}) \tag{2.35}$$

The D-term is therefore defined in the region $-\xi < x < \xi$, which corresponds to the ERBL region describing the exchange of a $q\bar{q}$ pair. The opposite sign between H and E is linked to the opposite sign in Eq. 2.16.

The function $D(x/\xi)$ can be written in the form of an expansion of odd Gegenbauer polynomials which are the standard basis functions on which the DAs are decomposed:

$$D(\frac{x}{\xi}) = N(1-(\frac{x}{\xi})^2)[C_1^{3/2}(\frac{x}{\xi}) + d_3 C_3^{3/2}(\frac{x}{\xi}) + d_5 C_5^{3/2}(\frac{x}{\xi})] \tag{2.36}$$

where the parameters $N = -4/3, d_3 = 0.3, d_5 = 0.1$ are coming from the chiral quark-soliton model [GPV01]. One can notice that the D-term is equal to 0 at the lines: $x = \pm\xi$, so that it does not contribute to the imaginary part of the DVCS amplitude. The t-dependence of the D-term is unknown. In practice, $D_{term}(\frac{x}{\xi})$ is multiplied by the form factor $F_1(t)$ having a $1/t^2$ behavior.

$(x,\ \xi,\ t)$ dependence

To summarize, the complete parametrization of the GPDs in the VGG model can be written in the form:

$$GPD^q(x,\xi,t) = \int_{-1}^{1} d\beta \int_{-1+|\beta|}^{1-|\beta|} d\alpha\, \delta(x-\beta-\alpha\xi)\, DD^q(\beta,\alpha,t) + D_{term}(\frac{x}{\xi},t) \tag{2.37}$$

where $DD^q(\beta,\alpha,t)$ is defined as in Eqs. (2.32, 2.33) and $D_{term}(\frac{x}{\xi},t)$ as in Eqs. (2.34, 2.35).

2.3.7 DVCS measurements

DVCS cross sections have been measured in two different kinematic regimes. Data from H1 and ZEUS were obtained with the HERA collider operating with 27.5-GeV positrons and 820-GeV protons, providing a cross section measurement at high energy ($30 < W < 140$ GeV, $2 < Q^2 < 100$ GeV^2). JLab Hall-A measured the unpolarized (σ_{unp}) and the difference of polarized cross sections (σ_{diff}) at low energy ($W \approx 2$ GeV) (Fig. 2.22). These measurements allowed us to get first constraints to extract $\mathcal{H}_{Re}$ and $\mathcal{H}_{Im}$ (see Fig. 2.23). The data seem to indicate that the t-slope of $\mathcal{H}_{Im}$ (related to the PDFs in the forward limit) increases with x_B decreasing (from JLab to HERMES kinematics). It means that the valence-quarks (high x) tend to remain in the center of the nucleon while the sea quarks (low x) extend to the periphery of the nucleon. In contrast, the t dependence of $\mathcal{H}_{Re}$ seems to increase from negative to positive values. The cross section that we study in this thesis will be used to constrain the CFF $\mathcal{H}_{Re}$ in the JLab kinematics, and therefore will fill the empty box in the middle of this figure. One can notice that $\tilde{\mathcal{H}}_{Im}$ is smaller than $\mathcal{H}_{Im}$, which is expected for a quantity that is related to the polarized PDFs (in the forward limit). We observe a weak t-dependence compared to $\mathcal{H}_{Im}$, and a very small sensibility to the x_B variations. The small t-dependence of $\tilde{\mathcal{H}}_{Im}$ compared to $\mathcal{H}_{Im}$ suggests a narrower axial charge distribution ($\tilde{\mathcal{H}}$ is related to the axial structure $\gamma_5\gamma_\mu$) than the electromagnetic charge in the nucleon.

The first asymmetry measurement $\mathcal{A}_{LU}$, which has a particular sensitivity to $\mathcal{H}_{Im}$, has been published by the HERMES collaboration in 2001 at the average kinematics $\langle x_B\rangle = 0.11$, $\langle Q^2\rangle = 2.6$ GeV^2 and $\langle -t\rangle = 0.27$ GeV^2, using a 27.5-GeV positron beam (Fig. 2.24). In the same year came the JLab Hall-B publication of $\mathcal{A}_{LU}$ at the average kinematics $\langle x_B\rangle = 0.19$, $\langle Q^2\rangle = 1.25$ GeV^2 and $\langle -t\rangle = 0.19$ GeV^2, using a 4.2-GeV electron beam (Fig. 2.25).

Both asymmetries clearly show $\sin\phi$ modulation, in a relatively good agreement with a theoretical prediction. The asymmetry observed was about 20-30%. The fact that models predicted such an amplitude was an encouraging sign that we were indeed sensitive to the handbag diagram and to the GPDs formalism (in particular the BH does not produce asymmetry). Notice that the two amplitudes have opposite sign because HERMES and JLab used respectively positron and electron beams. The discrepancy observed between data and theoretical calculations can be attributed partly to the fact that the theory is calculated at a well-defined kinematic point whereas the data have been integrated over several variables and wide kinematic ranges. Also, at these rather low Q^2 values, higher-twist and higher-order corrections could be important and need to be quantified and introduced in the models.

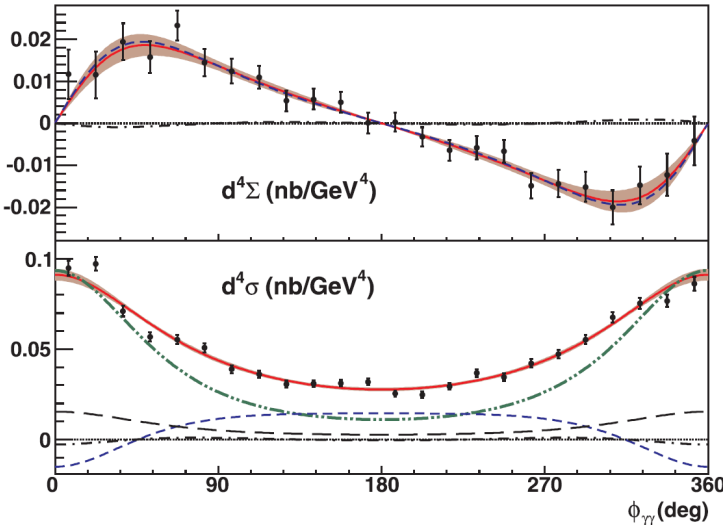

Figure 2.22: σ_{diff} (top panel) and σ_{unp} (bottom panel) cross sections measured in Hall-A as a function of the angle ϕ between the leptonic and hadronic planes at the average kinematics $\langle x_B \rangle = 0.36$, $\langle Q^2 \rangle = 2.3$ GeV^2 and $\langle -t \rangle = 0.28$ GeV^2. The red curves are the fits to the data. The dot-dot-dashed (green) line is the $|\mathrm{BH}|^2$ contribution to σ_{unp}. Short-dashed (blue) and long-dashed (black) curves are two different azimuthal contributions of twist-2 to σ_{unp} (see Ref. [ea06a]). The dot-dashed curves are the twist-3 contribution, showing a negligeable contribution to the cross section.

Since 2006, Hall-B and HERMES have carried out additional asymmetry measurements using longitudinally and transversely polarized targets. Hall-B published the first spin asymmetry with a longitudinaly polarized target $\mathcal{A}_{UL}$ (Fig. 2.26). This is the first observable showing a sensitivity to $\tilde{\mathcal{H}}_{Im}$ (see Fig. 2.23).

HERMES published in 2008 the first spin asymmetry with a transversely polarized target $\mathcal{A}_{UT}$, the observable with the main sensitivity to $\mathcal{E}_{Im}$, and the least known of the CFFs.

The GPD experimental program, launched more than 10 years ago, intends to carry out several measurements of DVCS observables in order to better constrain the GPD models. The current experimental program at JLab aims to double the statistics of the dedicated DVCS cross-section experiment [BEG$^+$03] (in order to reduce the error bars and the size of the bins). It also plans to measure the single and double spin asymmetries with a longitudinaly polarized target [BEJN05] in a new kinematic region.

For the future, DVCS dedicated experiments have already been accepted [NKAM11, HWMCR12, BEG$^+$12] or proposed [ea12] with the future CLAS12 detector, using an 11-GeV electron beam and a higher luminosity. This will cover a broader kinematic region at higher Q^2 and lower x_B than available at 6 GeV. The expected kinematic region is presented in Fig. 2.27.

The COMPASS experiment at CERN also has a dedicated program to study GPDs. With a 200 GeV muon beam and a recoiling detector allowing to detect all the particles of the final state, it aims at studying DVCS at very small x_B and sufficiently large Q^2.

As can be seen in Figs. 2.27 and 2.28, COMPASS will measure exclusive reactions in a kinematic rang from $x_B \approx 0.01$ to about 0.1, which cannot be explored by any other existing or planned facility in the near future. COMPASS would thus explore the uncharted x_B domain between the HERA collider experiments H1 and ZEUS and the fixed-target experiments as HERMES and the planned 11 GeV upgrade of the JLab accelerator.

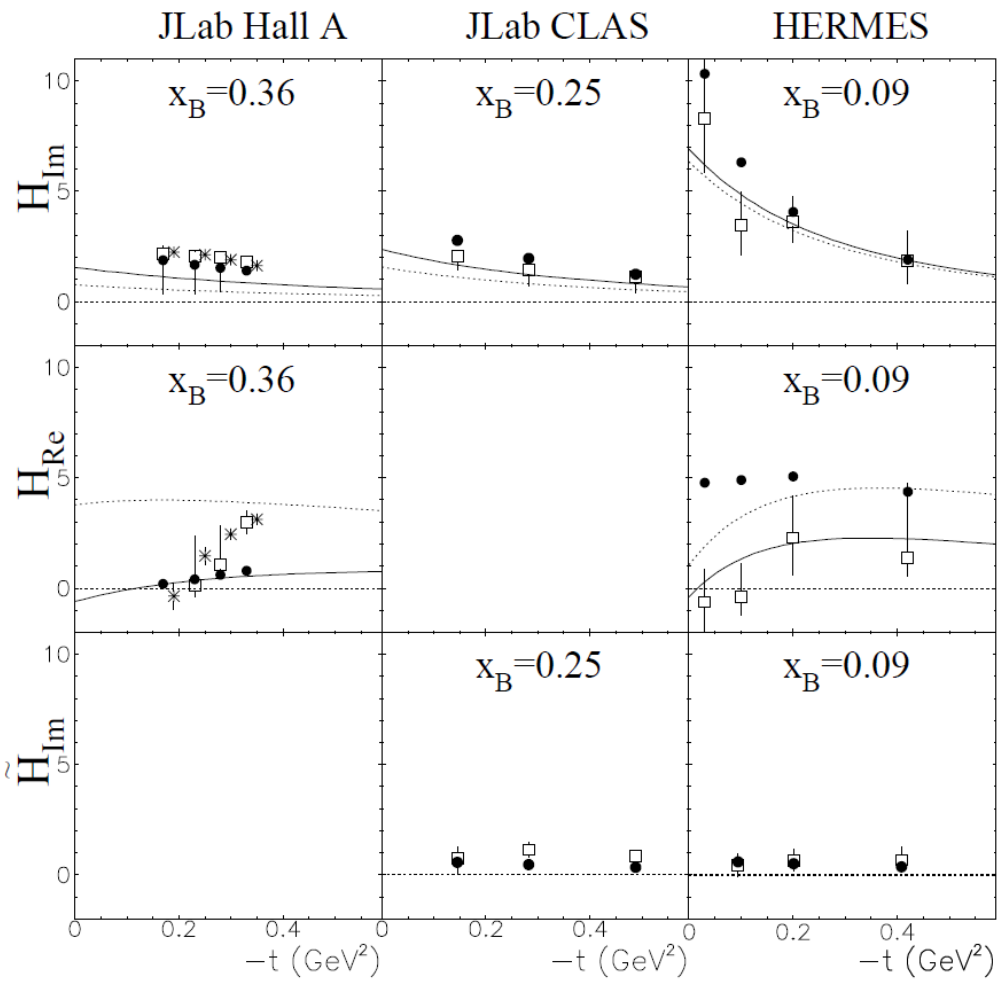

Figure 2.23: The CFFs $\mathcal{H}_{Re}$, $\mathcal{H}_{Im}$ and $\tilde{\mathcal{H}}_{Im}$, as a function of $-t$. The empty squares are the results of the fits [Gui10] using the data from JLab and HERMES. The stars are the result of the CFF fit from [Mou09]. The curves are the model-based fit of [KM10]. The solid points show the predictions of the VGG model [VGG99, GPV01, GPRV05].

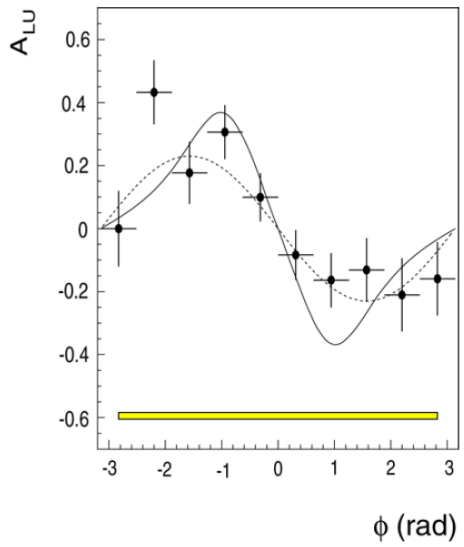

Figure 2.24: DVCS beam-spin asymmetry $\mathcal{A}_{LU}$ as a function of the ϕ angle (in radians) at the average kinematics $\langle x_B \rangle = 0.11$, $\langle Q^2 \rangle = 2.6$ GeV^2 and $\langle -t \rangle = 0.27$ GeV^2. The dashed line is a $\sin\phi$ fit. The solid line is the theoretical GPD calculation of the VGG model with twist-3 effects [KPV01].

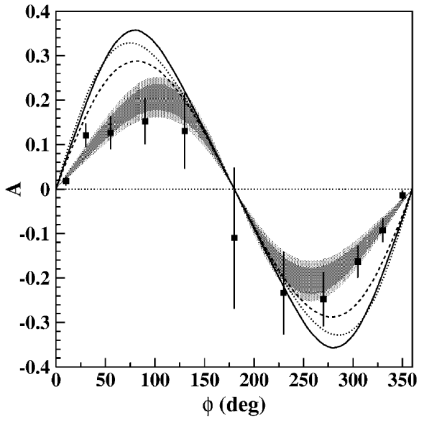

Figure 2.25: DVCS beam-spin asymmetry $\mathcal{A}_{LU}$ as a function of the ϕ angle (in degrees) at the average kinematics $\langle x_B \rangle = 0.19$, $\langle Q^2 \rangle = 1.25$ GeV^2 and $\langle -t \rangle = 0.19$ GeV^2. The shaded regions are the statistical (+ systematic) errors of the fitted function: $\mathcal{A}(\phi) = \alpha sin(\phi) + \beta sin(2\phi)$. The curves are VGG-model calculations: leading twist without ξ dependence (dashed curve) [VGG99], leading twist with ξ dependence (dotted curve) [VGG99], and including twist-3 effect [KPV01].

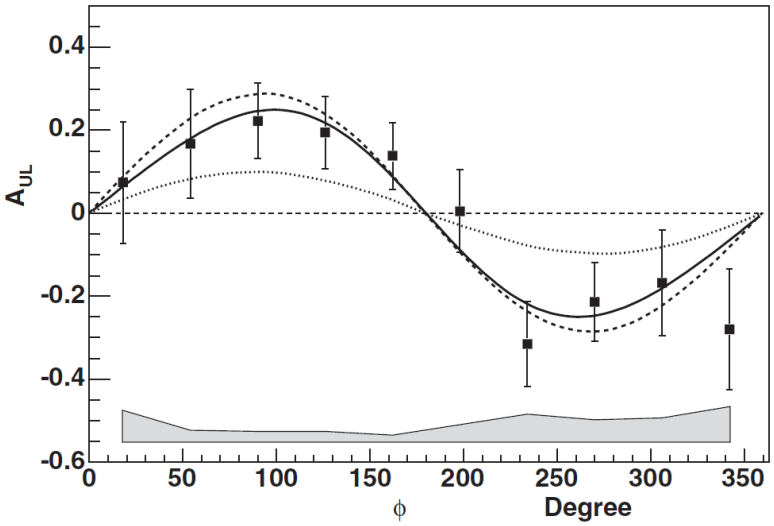

Figure 2.26: Azimuthal ϕ dependence of the longitudinal DVCS target-spin asymmetry $\mathcal{A}_{UL}$. The solid line is a fit to the data: $\mathcal{A}(\phi) = \alpha sin(\phi) + \beta sin(2\phi)$, with $\beta \approx 0$. The dashed curve is the VGG model [VGG99] prediction with $E = \tilde{E} = 0$ and twist-3 contribution. The dotted line is the expected asymmetry for $\tilde{H} = 0$, showing the sensitivity of $\mathcal{A}_{UL}$ to $\tilde{H}$.

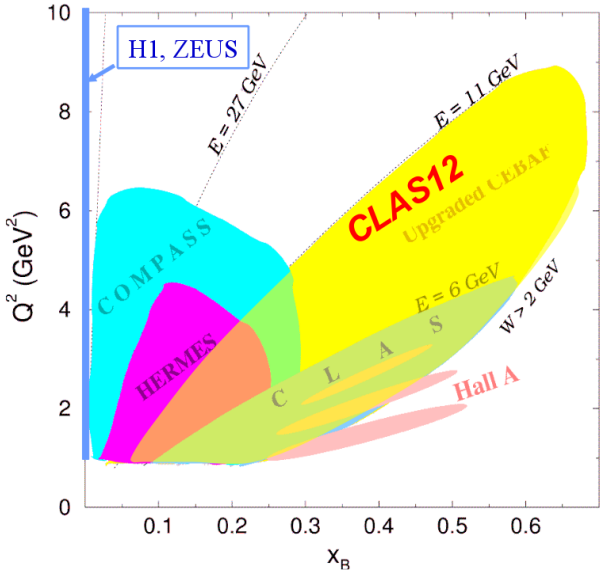

Figure 2.27: Kinematic domain-Q^2 as a function of x_B (in linear scale) for measurements of hard exclusive processes at JLab (Hall-A, CLAS at 6 GeV and 11 GeV), COMPASS, and HERMES fixed-target experiments and at the HERA collider experiments H1 and ZEUS.

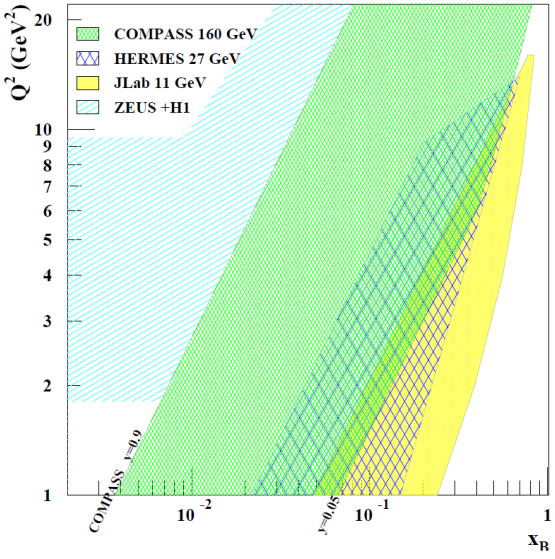

Figure 2.28: Kinematic domain-Q^2 as a function of x_B (in logarithmic scale) for measurements of hard exclusive processes at COMPASS, HERMES and JLab fixed-target experiments and the HERA collider experiments H1 and ZEUS.

Chapter 3

Experimental apparatus

In this chapter, we review the characteristics of the detector CLAS, that acquired the data of the e1-DVCS experiment [BEG+03]. The data taking has been performed in two intervals: 36 days during spring 2005 and 34 days from October 2008 to January 2009. This experiment aims at studying DVCS using the CEBAF (Continuous Electron Beam Accelerator Facility) 6-GeV polarized electron beam and the CLAS (CEBAF Large Acceptance Spectrometer) detector.

We will gegin by describing the electron accelerator and the toroidal magnet. We will then review the standard equipement of the CLAS detector: the Drift Chambers (DC), the Cherenkov Counters (CC), the Scintillator Counters (SC) and the Electromagnetic Calorimeters (EC). We will also discuss the two extra parts that have been added specifically for the experiments: the Inner Calorimeter (IC) and the solenoid.

3.1 The CEBAF accelerator

CEBAF (Fig. 3.1) is a high intensity and high duty factor electron accelerator whose maximum energy is around 6 GeV. It consists of an electron injector (67 MeV) and two super-conducting linear accelerators (linacs) connected to each other by recirculation arcs which contain steering magnets.

The electron beam makes up to five successive orbits (gaining around 600 MeV with each pass through a linac) so that, depending on the number of recirculations, its energy can increase up to a maximum of 6 GeV.

After each pass, the beam can be divided by a transverse radio-frequency (RF) separator into three beams delivered simultaneously to experimental halls of JLab: namely, Hall A, B and C. Each of these halls can run with its own beam intensity and energy, allowing to perform simultaneous measurements with different settings.

Halls A and C operate at very high luminosity ($L \sim 10^{38}$ cm^{-2}s^{-1} which corresponds to a beam intensity of 200 μA) and the reaction products are detected in high-resolution spectrometers with small acceptances. More precisely, Hall-A has an identical pair of high-resolution spectrometers that can detect particles with a maximum energy of 4 GeV with a momentum precision $\frac{\Delta P}{P} \sim 10^{-4}\%$. Hall C has two asymetric spectrometers that allow to detect high momentum particles with a good precision $\frac{\Delta P}{P} \sim 10^{-3}\%$.

Because of its large acceptance, the CLAS detector in Hall-B has to run with a lower beam intensity to allow the data acquisition. Typically, for a liguid hydrogen target, the beam intensity is around 20-30 nA and the corresponding luminosity is $L \sim 10^{34}$ cm^{-2}s^{-1}.

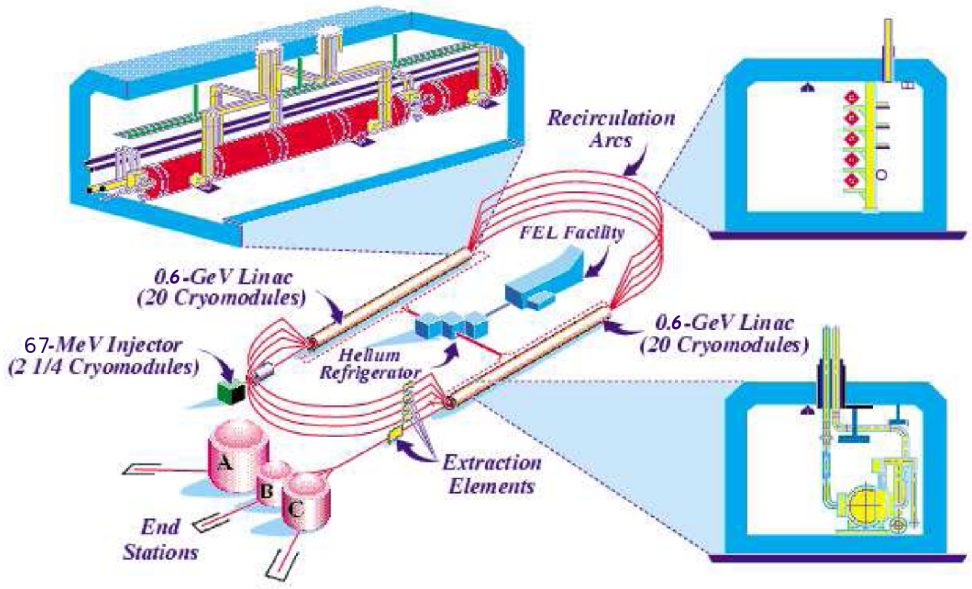

Figure 3.1: Configuration of the Continuous Electron Beam Accelerator Facility (CEBAF) with the halls A, B and C.

3.2 CLAS

CLAS [ea03a] (Figs. 3.2 and 3.3) provides identification and kinematics measurements for charged and neutral particles. It has a radius of around 5 meters and its structure comprises six superconducting coils, located around the beamline, that produce a toroidal magnetic field. CLAS has a structure of layered detectors that are split into six symetrical sectors.

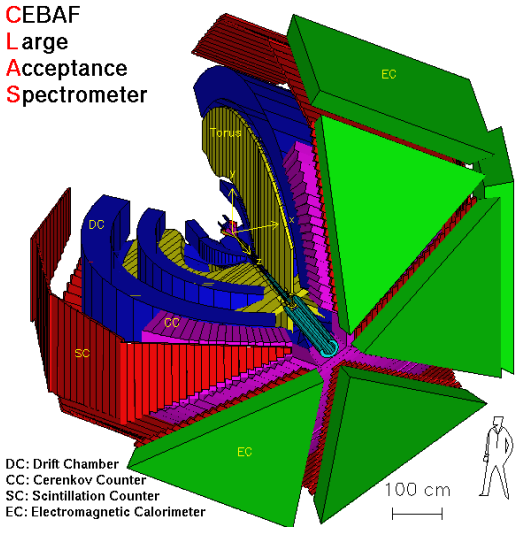

Figure 3.2: Schematics of CLAS. Four of the six CLAS sectors are displayed, with their different layers of sub-detectors.

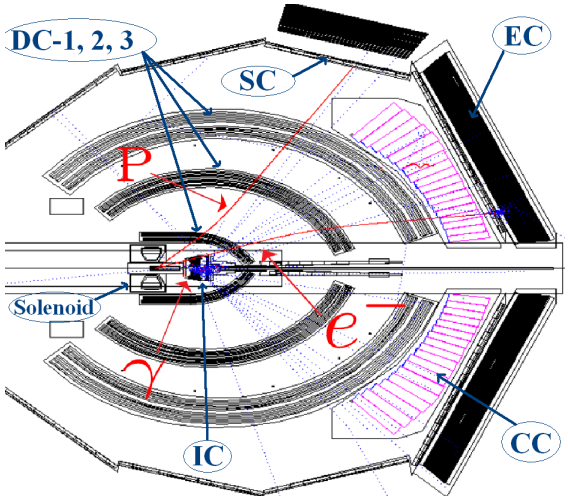

Figure 3.3: Typical $ep\gamma$ event in a side view of CLAS. The solenoid and the Inner Calorimeter, that are not part of the standard CLAS equipement, can be seen in the central part.

This detector has a large acceptance covering most of the solid angle, particularly adapted for the study of exclusive processes. Charged particles can be detected between 5° and 140° and neutral particles between 8° and 45°. Momentum resolution is of the order of the percent ($0.5\% \leq \frac{\Delta P}{P} \leq 2\%$) and angular resolutions are $1 \leq \Delta\theta \leq 1.5$ mrad and $2 \leq \Delta\phi \leq 3$ mrad. Time resolution is $100 \leq \Delta t \leq 250$ ps.

A particle coming from the vertex of the interaction crosses several layers of detectors that track it and allow its identification. These detectors consist of:

- 3 layers of drift chambers that allow the momentum measurement of charged particles via the tracking in the magnetic field
- Cherenkov counters which allow to distinguish electrons from pions
- the scintillators provide information for the triggering and the time-of-flight of the particles
- identification and energy measurements of charged and neutral particles are provided by electromagnetic calorimeters, located in the forward region

We will now review the different parts of the CLAS detector.

3.3 Torus Magnet

The magnetic field is generated by six superconducting coils arranged in a toroidal geometry around the electron beam line. It was designed to induce a radius of curvature approximately constant for charged particles, providing a momentum resolution approximately constant. Fig. 3.4 shows the magnetic field lines generated between two coils: a high magnetic field ($\approx$ 20 kG =2 Tesla) at forward angles bends the particle path where the momenta is large, and a lower field (100 G) at backward angles bends the particle path where the momenta is generally smaller.

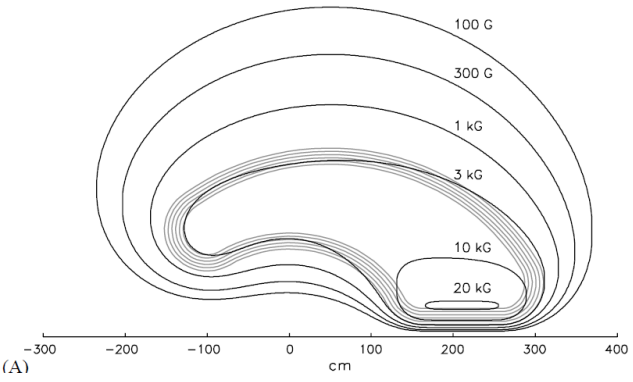

Figure 3.4: Side view of the CLAS magnetic field.

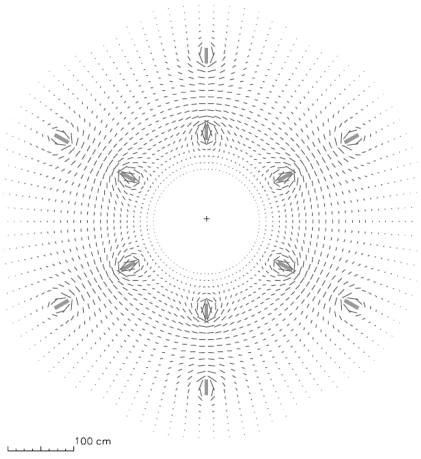

Figure 3.5: Transverse view of the CLAS magnetic field

Fig. 3.5 shows the magnetic field map in the transverse plan. The path of charged particles is bent along a constant ϕ direction, except around the coil where a large deviation of the field lines can be observed.

The center of CLAS is an almost field-free region that causes a minimal deflection to a charged beam and allows the use of a polarized target.

3.4 Drift Chambers (DC)

Charged particles with a momentum higher than 100 MeV are tracked by 18 drift chambers [ea00b] (covering the polar-angle range from 8° to 142°) arranged in three radial layers (regions) around the target. The wire layers in each region are grouped into two superlayers of six wire layers each (Fig. 3.6). One is aligned along the direction of the magnetic field (axial), and the other is tilted by 6° (stereo) to provide azimuthal information. Due to space constraints, the stereo superlayer of region 1 is an exception to this rule and consists of four wire layers only.

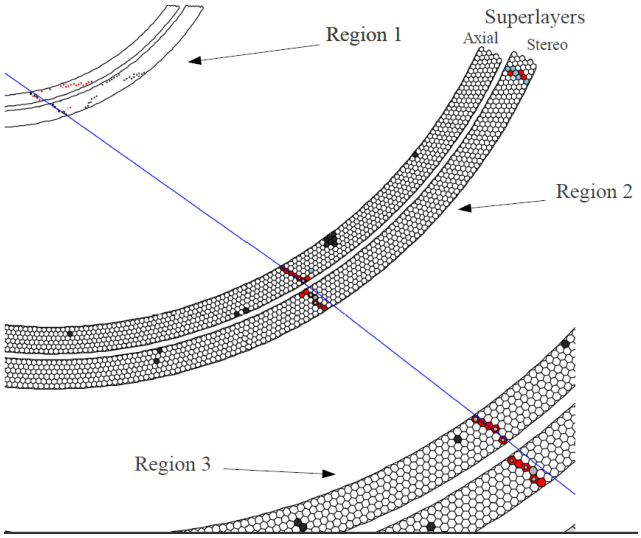

Figure 3.6: The three regions (with two superlayers each) of Drift Chambers.

The first region is located at around 70 cm from the target where the magnetic field is low. The second region is located in a high magnetic field at approximately 2 m from the center of CLAS. The third region is located beyond the coils, at around 4 m from the target. This large spacing between the layers is intended to allow a significant bending of the trajectory of high energy charged particles. Knowing the radius of curvature (R) and the magnetic field (B), it is then possible to calculate the momentum of the particle ($p = BqR$).

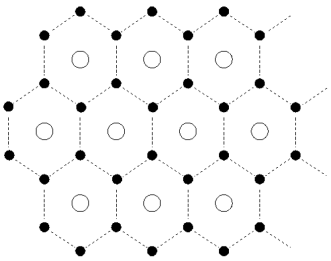

Figure 3.7: Configuration of the wires in the drift chambers. White points correspond to the sense wires and black points correspond to field wires (at a high negative potential).

The signals are triggered by the avalanche of electrons produces by the passage of charged particles in a mixture of Argon and CO_2 gas. The detection is ensured by layers of wires with a strong difference

of potential, whose structure is shown in Fig. 3.7. A layer of sense wires is followed by two layers of field wires, forming cells of hexagonal cross-section. The size of the cells gradually increases according to the distance from the target.

Each wire is linked to a Time to Digital Converter (TDC). The timing signals are used to calculate the drift time and velocity of the charged particles. This information is used to determine the distance of closest approach to each triggered wire, allowing the reconstruction of the track. An example of the tracking through the three DC regions is shown if Fig. 3.6.

The momentum resolution of the drift chambers is $\frac{\Delta P}{P} \sim 2\%$, and the angular precision is ≤ 2 mrad.

3.5 Cherenkov counters (CC)

Cherenkov counters [ea01c] are used to distinguish electrons from pions. Each sector of CLAS has 18 The Cherenkov counters, covering the polar-angle range $8° \leq \theta \leq 45°$. The counters consist of two symmetrical modules (Fig. 3.8 and 3.9). Each module contains an elliptical and a hyperbolic aluminium mirror that focus the emitted photons to a Winston light cone. The light is then collected by a photomultiplier tube (PMT).

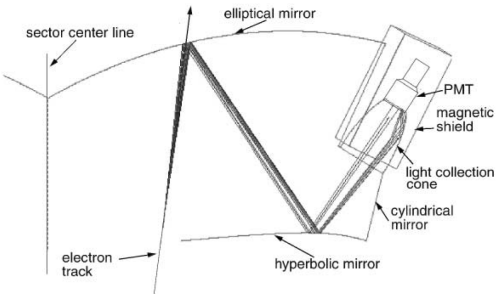

Figure 3.8: Optical arrangement of one of the 216 optical modules of the CLAS Cherenkov detector. The optical and light collection components are also displayed.

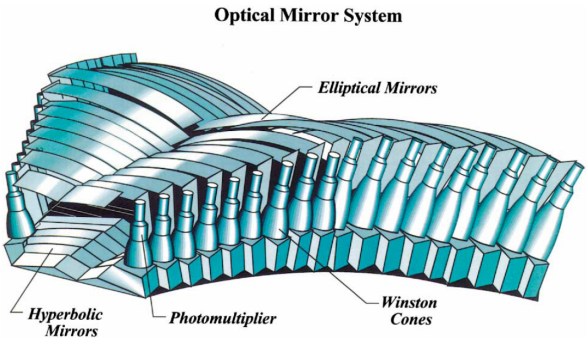

Figure 3.9: Schematic of the optical modules in one of the six sectors.

Cherenkov radiation is produced when a particle passing through a medium has a velocity greater than the one of the light in this medium ($v > c/n$ with n the refractive index). Cherenkov counters are filled with perfluorobutane (C_4F_{10}), which is a gas with a high refractive index $n = 1.00153$. The energy threshold necessary for a particle of mass m to produce Cherenkov light in a medium of index n is: $E_{min} = \frac{mc^2}{\sqrt{1-(\frac{1}{n})^2}}$. In these conditions, pions with momentum smaller than 2.5 GeV do not emit light, while electrons emit light for any momentum above 10 MeV.

An electron traversing the active volume of the detector results in typically 5-6 photoelectrons. Above 2.5 GeV, the discrimination is made by the electromagnetic calorimeters.

3.6 Time of Flight scintillators (TOF)

Time measurement [ea99] is performed by the TOF scintillators. They are located after the drift chambers and are used to identify charged hadrons like protons, pions or kaons. Knowing the time of flight and the momentum of the charged particles from the drift chambers, we can calculate its mass and thus identify it. Each sector comprises 57 organic plastic scintillators perpendicular to the beam direction (Figs. 3.10 and 3.11) covering the θ angular range 8° to 142°. The paddles are all 5-cm thick and vary

in length from 32 cm to 445 cm, going from the forward to the backward angles.

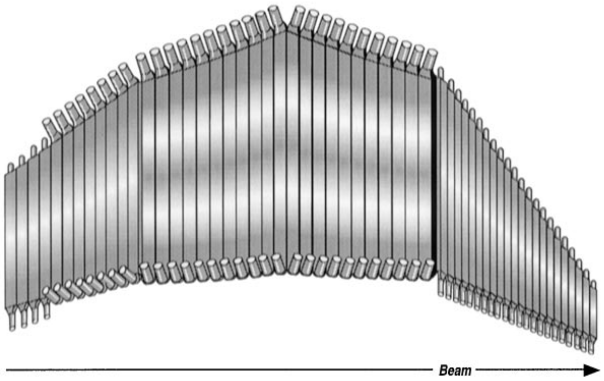

Figure 3.10: View of a sector of the CLAS TOF.

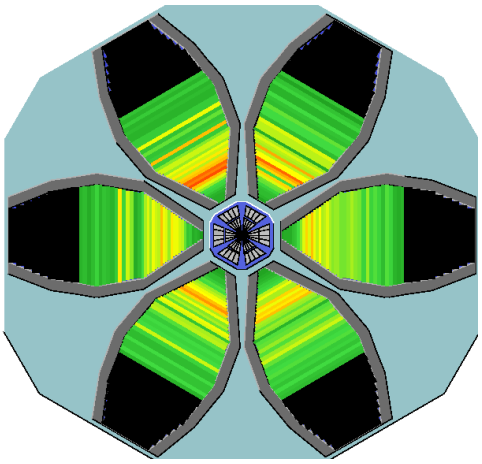

Figure 3.11: TOF detector in the X-Y plane.

The scintillation light produced during the interaction in the scintillator is read out by PMTs optically connected to each end of the paddle, allowing to use the time difference between them to find the hit position. For all events, precise determination of the interaction time or event start time is required. The event start time is derived from the arrival time of the electron at the TOF counters.

The particles detected at large angle have generally longer time of flight so that the requirement for time resolution is reduced (the width of the counters at large angles was increased). The average time resolution is approximately equal to 150 ps.

3.7 Electromagnetic Calorimeter (EC)

Each sector of CLAS is equiped with one electromagnetic calorimeter which covers the polar angles $8^\circ \leq \theta \leq 45^\circ$. It is a sandwich calorimeter, consisting of alternate sheets of lead, providing a high-Z material to produce electromagnetic showers, and scintillators to measure the energy and timing of particles.

Each calorimeter has a triangular shape and consists of a succession of 39 lead-scintillator layers. Each layer consists of a lead sheet followed by a strip of 36 scintillators parallel to one side of the triangle. The layers of scintillator strips are successively rotated by 120°, giving three possible orientations (U, V, and W) that provide stereo information on the location of the energy deposition (Fig. 3.12). The overall calorimeter thickness is equal to 16 radiation lengths, allowing the recovery of the electromagnetic shower.

In order to perform the electron-pion discrimination above 2.5 GeV (below that value, the discrimination is done by the Cherenkov counters), the 39 layers of the calorimeters are separated into two stacks. The inner part is composed of 5 groups of 3 oriented planes, and the outer is composed of the remaining 8 groups. Electrons leave almost all their energy in the inner stack, while pions which are minimum-ionizing particles, deposit their energy constantly all along the calorimeter.

The scintillators are connected via optical fibers to the PMTs placed on the back of the calorimeter. The electromagnetic calorimeters, in addition to the information coming from the scintillators and the Cherenkov counters, are used to trigger the acquisition when an electron deposites an energy above 0.5 GeV. ECs also provide a way to detect neutral particles (photons and neutrons) above 0.2 GeV.

The energy resolution of the EC is $\frac{\Delta E}{E} \sim \frac{10\%}{\sqrt{E}}$ and time resolution is ~ 500 ps.

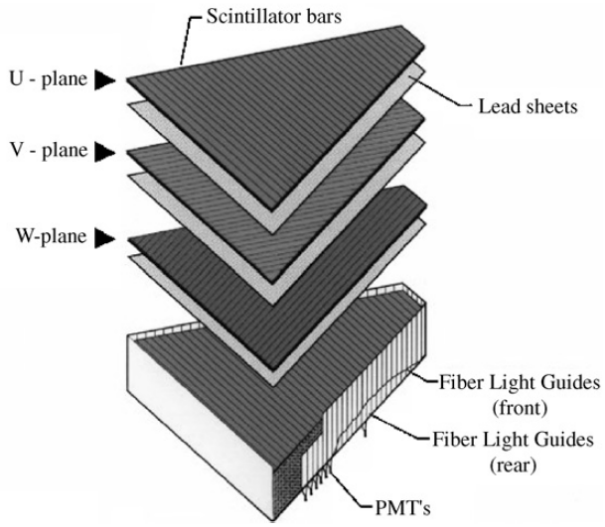

Figure 3.12: Configuration of the Electromagnetic Calorimeter of CLAS.

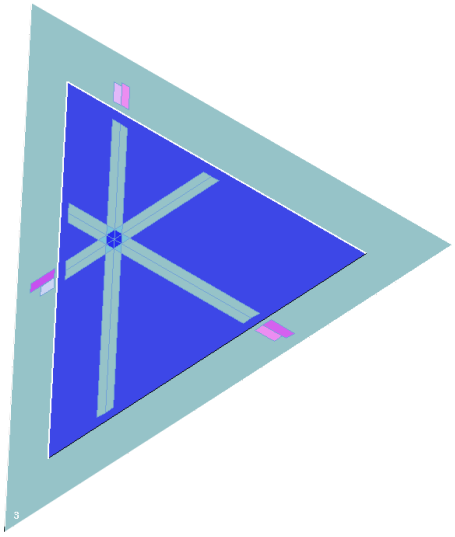

Figure 3.13: Exemple of an event in EC, where the three U, V, W orientation of the paddles can be seen.

3.8 Inner Calorimeter (IC)

Because most of the DVCS photons are emitted at forward angles, the acceptance of the EC only is not sufficient to detect them. In order to study the DVCS channel $ep \to ep\gamma$, a new calorimeter has been introduced covering the forward region at low angle: $5° \leq \theta \leq 15°$. It is located around the beam line 57.5 cm downstream of the target and before the first drift chambers region. The location of the IC can be seen in Fig. 3.3. The calorimeter consists of 424 lead-tungstate crystals (PbWO4), about 16 cm long (Fig. 3.14). This length corresponds to roughly 18 radiation lengths so that almost all the electromagnetic shower is deposited in the calorimeters.

The Energy resolution is around 3% at 2-5 GeV and the angular resolution is around 3 to 4 mrad. Additionnal information on IC calorimeter can be found in Ref.[Jo07].

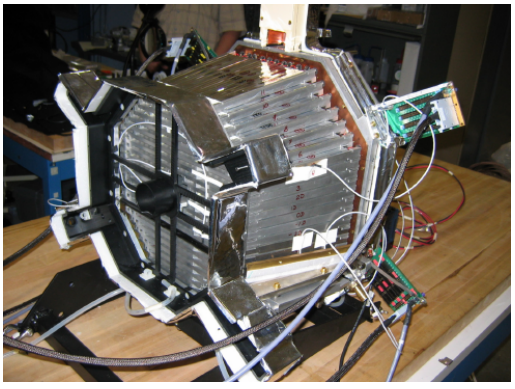

Figure 3.14: Picture of the Inner Calorimeter used to detect the DVCS photons at low angle.

3.9 Solenoid

Moller electrons are low-energy electrons produced by the scattering of the electron beam on the target's electrons. They introduce a lot of noise, especially in the first region of the DC and in the IC calorimeter, as can be seen on Fig. 3.15 (left).

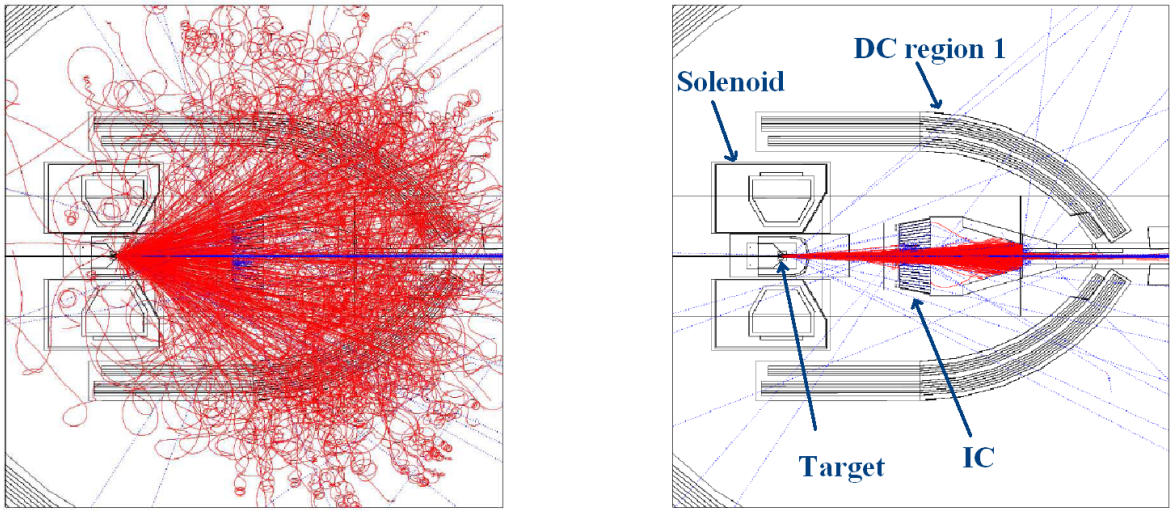

Figure 3.15: The solenoid aims to focus the Moller electrons at really low angles to prevent them from reaching the first region of the DC. Figure taken from [Jo07].

To reduce this noise, a solenoid magnet has been implemented in the central part of CLAS. It focuses these low energy electrons at very low angle (into the central hole of IC), "protecting" the IC and DC. The effects can be seen on Fig. 3.15 (right).

Chapter 4

Data quality checks and corrections using elastic scattering

We describe in this chapter the data quality checks and corrections that have been performed using the elastic channel $ep \to ep$ prior to the DVCS cross-section analysis.

4.1 Particle identification

We first present the cuts applied to identify the electrons and the protons. This selection is common to both the elastic and the DVCS channels.

4.1.1 Electron selection

The electrons are used to trigger the data acquisition of CLAS. They also give the "start" time for the time measurement necessary to identify the other detected particles. We present here the cuts applied to negatively charged particles (information provided during the reconstruction) to identify the electrons:

- Vertex position: a cut is applied on the reconstructed longitudinal vertex position V_z. In this experiment, the liquid hydrogen target was 5 cm long and was positioned at -57.5 cm with respect to the CLAS center. We apply a cut ± 3.5 cm around the target center to remove bad reconstructions. Figure 4.1 shows the vertex position and the cuts.
- minimum p_e: during the data acquisition, the minimum threshold for the deposited energy in EC was fixed at 0.6 GeV. A conservative cut is applied on this value to remove potential bad reconstructions. In this analysis, the minimal electron momentum value is fixed at 0.8 GeV. Figure 4.2 shows the momentum distribution for the negatively charged particles.
- EC fiducial cuts: the edges of the calorimeter are regions where the electromagnetic showers are truncated and thus the deposited energy can not be reconstructed correctly. We remove these regions by applying cuts on the local coordinates U, V, W of the calorimeter (Sec. 3.7). Figure 4.3 shows the distributions for $40 < U < 400$ cm, $V < 360$ cm and $W < 390$ cm.
- CC fiducials cuts: similarly to EC, the edges of the CC have to be suppressed from the analysis because of their low efficiency. For the Cherenkov detector, this boundary is defined by the edges of the mirrors, beyond which the optical collection efficiency for Cherenkov light rapidly drops. A special coordinate system has been developed according to Ref. [OVT] where the angles θ and ϕ of the intersection of the particles with CC are calculated as seen from the center of CLAS. The effect of these cuts can be seen in Fig. 4.4.

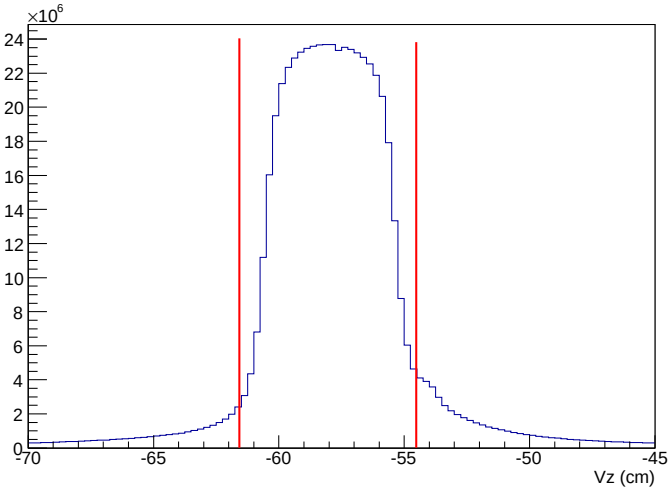

Figure 4.1: Longitudinal vertex position for negatively charged particles. The red lines indicate the cuts applied.

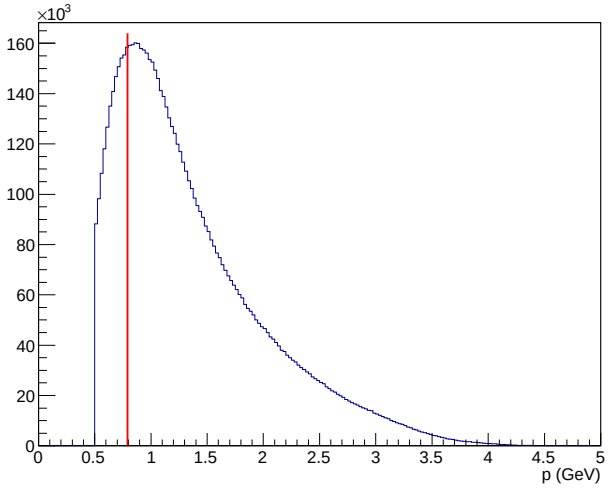

Figure 4.2: Momentum p for negatively charged particles. The cut at 0.5 GeV corresponds to a pre-analysis cut. The cut applied in this analysis is displayed in red and corresponds to $p > 0.8$ GeV.

- SC cuts: fiducial cuts should also be applied to the SC in principle. However, we did not develop dedicated fiducial cuts because the cuts applied to the CC are sufficient to remove the edges of the SC where the efficiency is not good. In addition, the electrons are detected only in the first "θ" panel of each sector. This panel covers the θ angle up to $\approx 45°$. In this region, we did not notice any low-efficiency paddles. We will see that for protons that are detected also by the second panel of each CLAS sector, there are low efficiency paddles which have to be removed from the analysis.

- E_{inner} cut: as mentioned in Sec. 3.7, the EC consists of both an inner (≈15 cm thick) and an outer (≈24 cm thick) stack which allows the discrimination between electrons and pions by providing

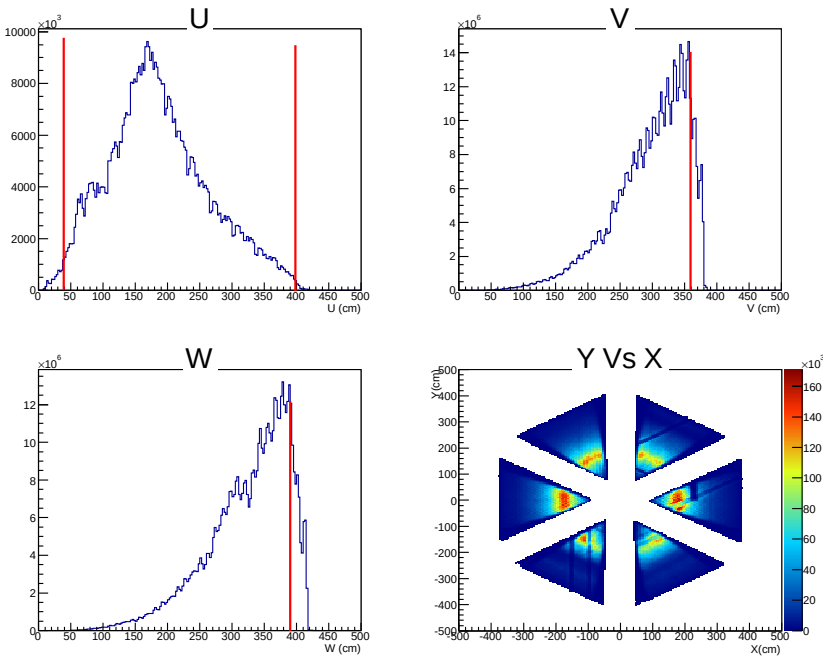

Figure 4.3: U, V and W distributions for negatively charged particles. The cuts we apply are shown in red. The bottom right plot is the Y versus X distribution after the fiducial cuts.

a longitudinal profile of the energy deposited by the particles. Because pions are minimum-ionizing particles, they deposit a constant amount of energy independently of their energy along the calorimeter thickness ($\approx$ 2 MeV/cm). This can be seen in Fig. 4.5 with the peak around $E_{inner} \approx 30$ MeV and $E_{outer} \approx 50$ MeV. To remove these pions, one applies the cut $E_{inner} > 60$ MeV.

- E_{tot}/p Vs p cut: as can be seen in Fig. 4.6, the reconstructed energy of the electrons in the calorimeters represents around 25% of the total energy. The remaining 75% are lost in the sheets of lead producing the electromagnetic showers. The cuts are applied to the fraction E_{tot}/p as a function of p. For each slice in p, E_{tot}/p is fitted with a gaussian distribution. One extracts the mean value $\mu(p)$ and the width $\sigma(p)$ for different bins in p, and one then applies a 2.5 σ cut $|E_{tot}/p - \mu(p)| < 2.5\,\sigma(p)$, where:

$$\mu(p) = 0.2297 + 4.0835 \times 10^{-2}\,p - 1.1774 \times 10^{-2}\,p^2 + 1.1605 \times 10^{-3}\,p^3 \quad (4.1)$$

$$\sigma(p) = \sqrt{(1.7588 \times 10^{-2})^2 + \left(\frac{3.3941 \times 10^{-2}}{\sqrt{p}}\right)^2} \quad (4.2)$$

- Photo-electrons cut: below a momentum of 2.5 GeV, the discrimination between electron and pions is performed by the Cherenkov counter. In this energy region, the pions are not supposed to emit any photo-electrons. However, the scattering of pions from the electrons of the Cherenkov gas produces low energy electrons, called δ-electrons, that emits a small number of photo-electrons. As can be seen on Fig. 4.7, the signal N_{phe} deposited by the electrons can be fitted with a Poisson distribution peaking around 6 photo-electrons. The large peak around 1 photo-electron is coming from the δ-electrons produced by the pions. To remove this indirect pion contamination, we apply the cut $N_{phe} \times 10 > 25$.

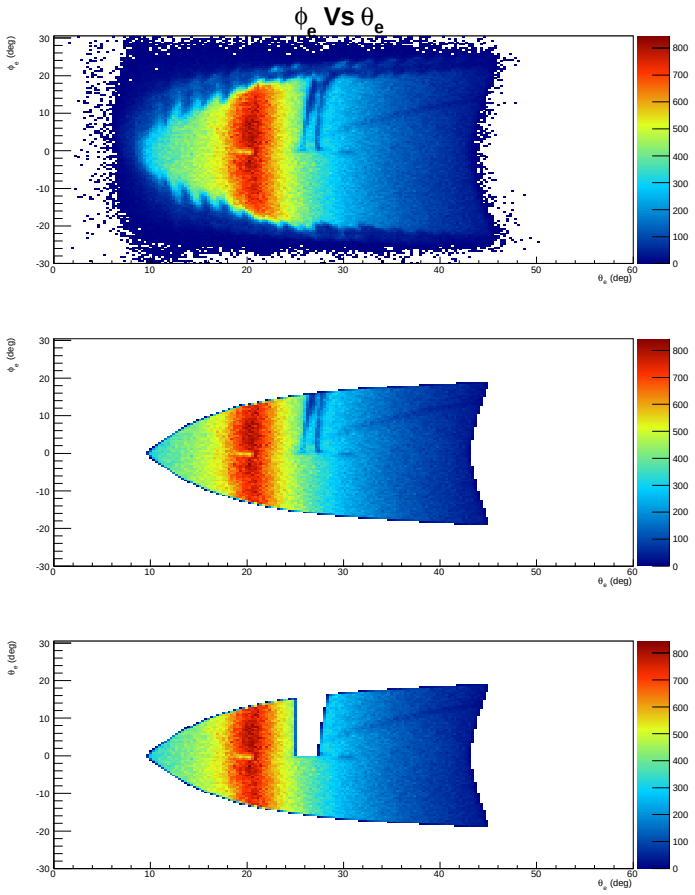

Figure 4.4: Occupancy of the CLAS Cherenkov detector for one of the six sectors, as a function of the angles ϕ versus θ defined with respect to the CLAS center. The top and middle plots are respectively before and after fiducial cuts. The bottom plot shows a fiducial cut applied on the data to remove a Cherenkov counter with very low efficiency.

- DC and IC shadow cuts: some regions of the drift chambers have very low detection efficiency and must be removed from the analysis. Fig. 4.8 shows the status of the first region of the drift chambers before any fiducial cuts. The events too close to the DC edges are cut out by applying fiducial cuts. The result can be seen in Fig. 4.9. Moreover, additional cuts are applied to remove the events too close to the inner calorimeter. These event are suppressed by removing the "shadow" that the IC produces on the DC (one can visualize these cuts in Fig. 4.9).

4.1.2 Proton selection

Once the "good" electron of the event has been identified according to the previously listed cuts, we can start the identification of the proton. We first require a positively charged particle. The additional cuts that we will describe hereafter aim at seperating the protons from the other positively charged particles.

- $\Delta\beta$ cut: the β is reconstructed by using the correlation of the time of flight information coming from the SC and both the momentum and the path length from the DC. This information leads to two possible ways of estimating it: β_{meas} is measured with the path length l and the time of

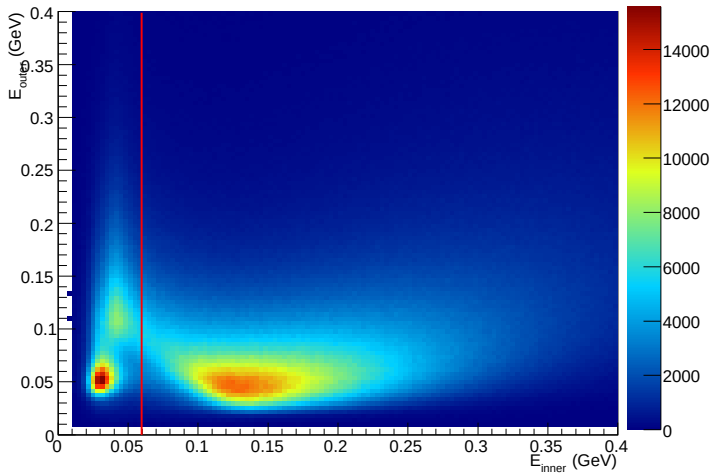

Figure 4.5: Deposited energy in the two stacks of the EC: E_{outer} vs E_{inner} (GeV). The cut removes the π^- that are minimum-ionizing particles and deposit a constant amount of energy along the inner and outer stack. The π^- energy deposit distributions peak at $E_{outer} \approx 50$ MeV and $E_{inner} \approx 30$.

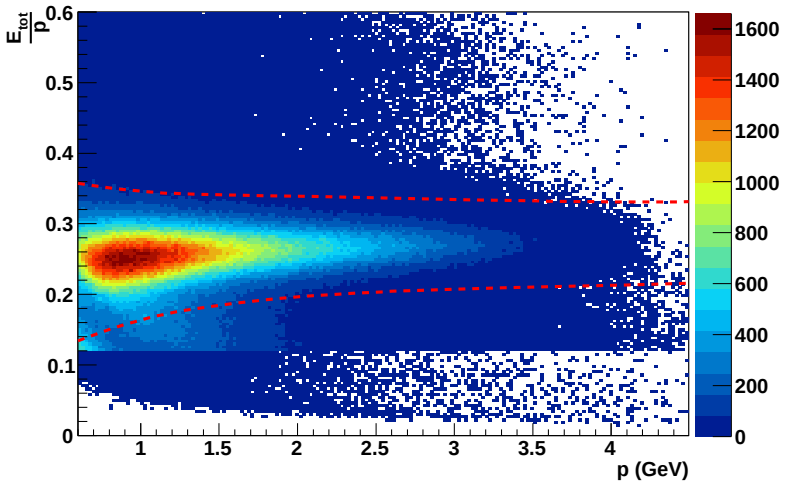

Figure 4.6: E_{tot}/p as a function of p. The distribution is fitted by a Gaussian for different slices in p. The cuts are then applied at 2.5 σ.

flight t_{TOF}: $\beta_{meas} = \frac{l}{ct_{TOF}}$. The second is calculated with the momentum p and attributing to the particle the mass m_p of the proton: $\beta_{calc} = \frac{p}{\sqrt{p^2+m_p^2}}$. The β_{meas} is shown in Fig. 4.10 as a function of the momentum p. One can see that the proton signal comes along with other positively charged particles signals such as e^+, π^+ or K^+, which must be removed from the analysis.

The difference $\Delta\beta = \beta_{meas} - \beta_{calc}(m_{proton})$ is shown in Fig. 4.11. It allows one to identify the particles of mass m_p. One applies the cut $|\Delta\beta| < 0.05$ corresponding to a 5-σ cut. This cuts allows to discriminate the protons from other positively charged particles for any value of p, except for

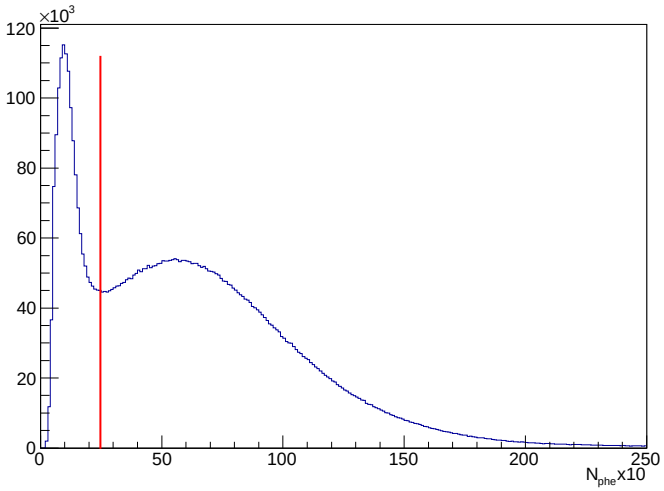

Figure 4.7: Number of photo electrons detected by CC. The red line corresponds to the cut at $N_{phe} \times 10 > 25$.

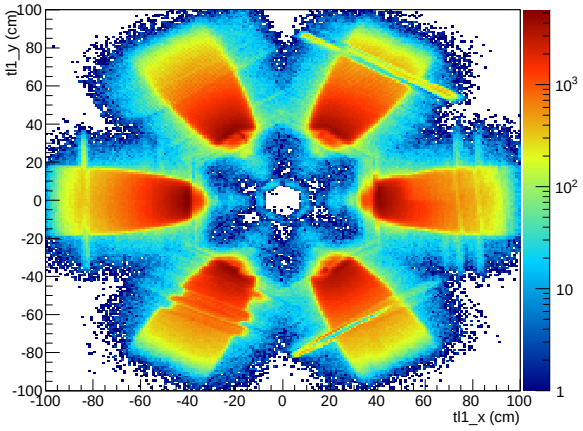

Figure 4.8: DC local coordinates for negatively charged particles detected in the DC region 1 for the six sectors of CLAS, before the fiducial cuts.

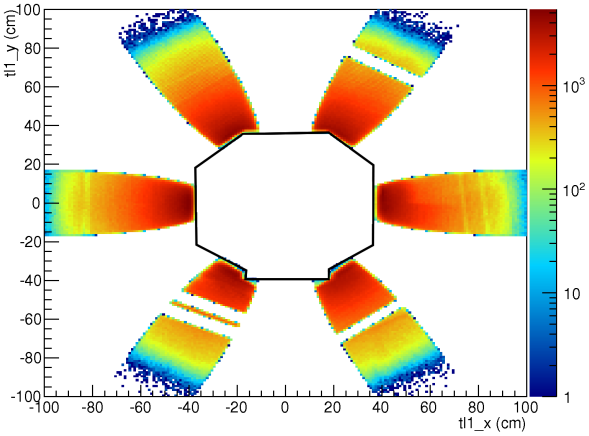

Figure 4.9: Same as Fig. 4.8 but with the fiducial cuts applied to all sectors. The IC-shadow cut can also be seen in black.

the π^+ whose signal merges into the proton one starting from approximately 2.5 GeV. However, the kinematical regime of the DVCS channel does not allow to reach proton momenta bigger than 2.5 GeV.

- Fiducial cuts: the same procedure used to apply the DC cuts to the electrons have been applied to the protons. In addition, the SC fiducial cuts have been developped for the first two panels of each sectors. The two remaining panels of each sector (see Fig. 3.3) cover a polar angle $\theta > 70°$ which a DVCS proton can not reach. Fig. 4.12 shows the status of the first two panels of SC before the fiducial cuts. The low-efficiency paddles and the edges of the detector have to be removed. The effects of the cuts can be seen in Fig. 4.13.

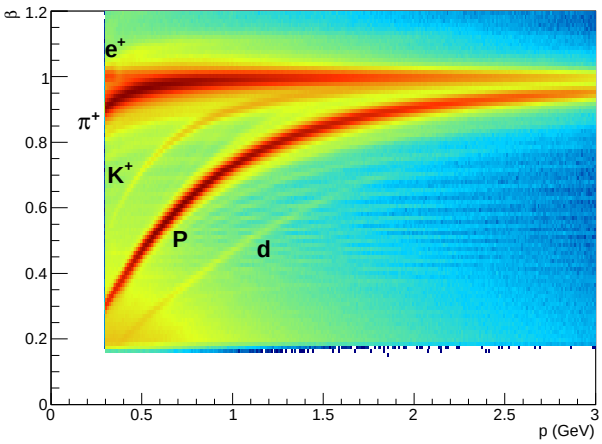

Figure 4.10: β_{meas} for positively charged particles, as a function of the momentum.

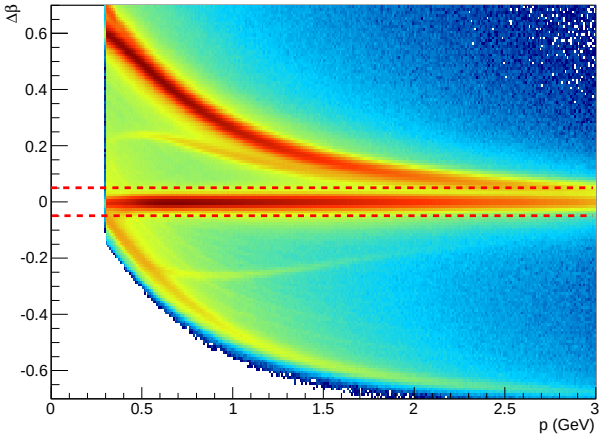

Figure 4.11: $\Delta\beta(m_{proton}) = \beta_{meas} - \beta_{calc}(m_{proton})$ calculated for positively charged particles, as a function of the momentum. We apply the cut $|\Delta\beta(m_{proton})| < 0.05$, shown in red, to select the protons.

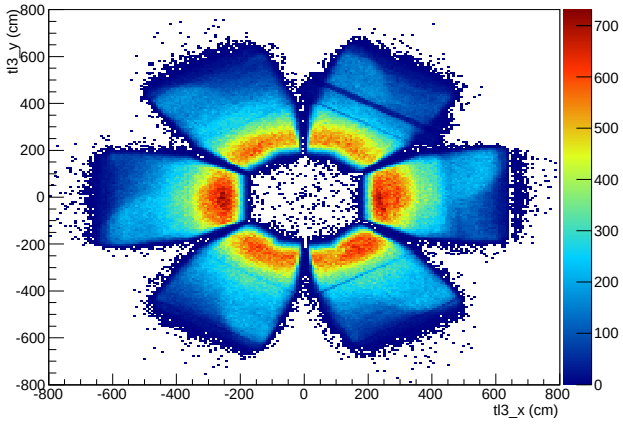

Figure 4.12: SC local coordinates for positively charged particles detected in the first two panels of the six sectors of CLAS, before the fiducial cuts.

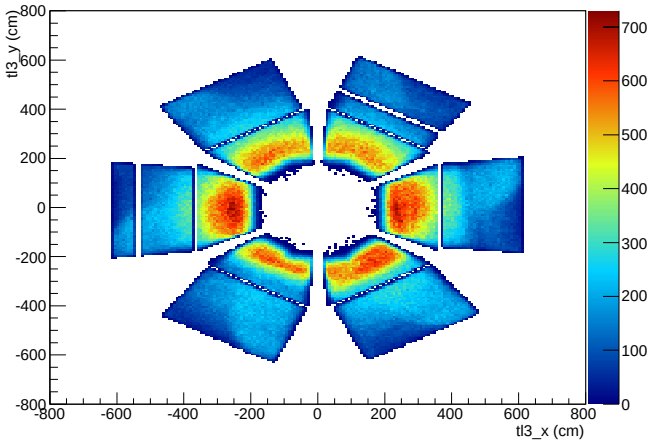

Figure 4.13: Same as Fig. 4.12, but after applying the fiducial cuts to all sectors.

4.1.3 Elastic channel selection

After applying the particle identification cuts presented in the previous section to select a good electron and a good proton, we apply two more cuts in order to isolate elastic events. Firstly, in a two-body reaction the electron and the proton have to be in the same plane. It means that the difference of azimuthal angles $\Delta\phi$ between the two particles has to be 180°. We apply a 3-σ cut ($\sim 2.5°$) around 180° to the $\Delta\phi$ distribution. Fig. 4.14 shows the azimuthal angle between the electron and the proton. Secondly, we also apply a cut on the invariant mass W (Fig. 4.15), which peaks at the proton mass for the elastic events. A 3-σ cut on this quantity corresponds to ~ 0.16 GeV.

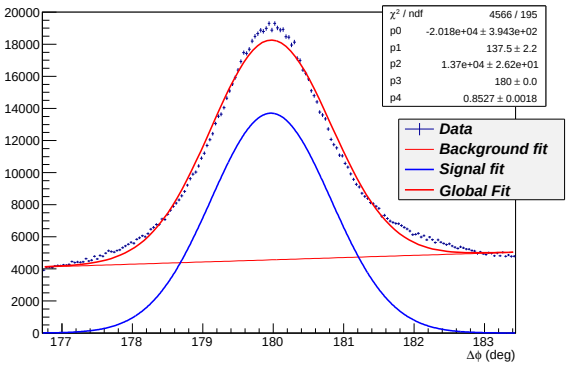

Figure 4.14: $\Delta\phi$ distribution for elastic events fitted with a Gaussian (parameters $p_{2,3,4}$) plus a linear background (parameters $p_{0,1}$).

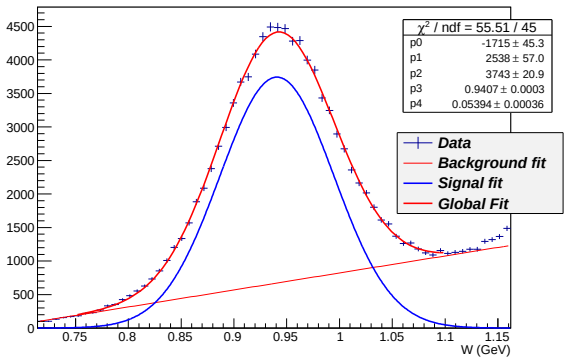

Figure 4.15: W distribution for elastic events fitted with a Gaussian (parameters $p_{2,3,4}$) plus a linear background (parameters $p_{0,1}$).

Fig. 4.16 shows ϕ as a function of θ for electrons and protons detected in CLAS. The electrons tend to go at relatively small polar angles ($\approx 22°$), while the protons recoil typically at higher θ ($\approx 35°$). Fig. 4.17 shows the same distributions with the fiducial cuts applied to remove the low efficiency regions of the different sub-detectors (DC, CC, ...).

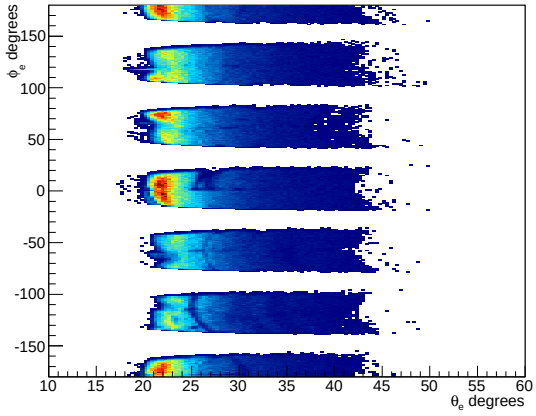

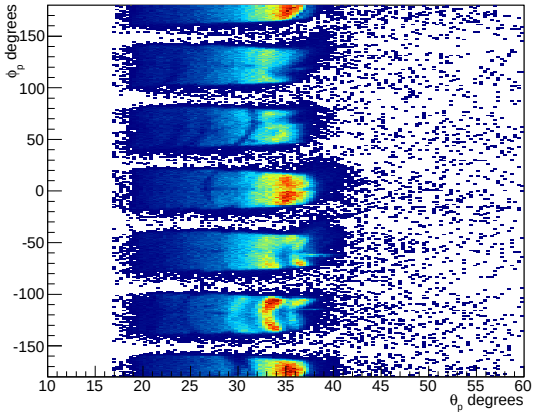

Figure 4.16: ϕ as a function of θ for both electrons (left) and protons (right). Most of the electrons are in the region: $20° < \theta_e < 25°$, while most of the protons are in the region: $32° < \theta_p < 37°$.

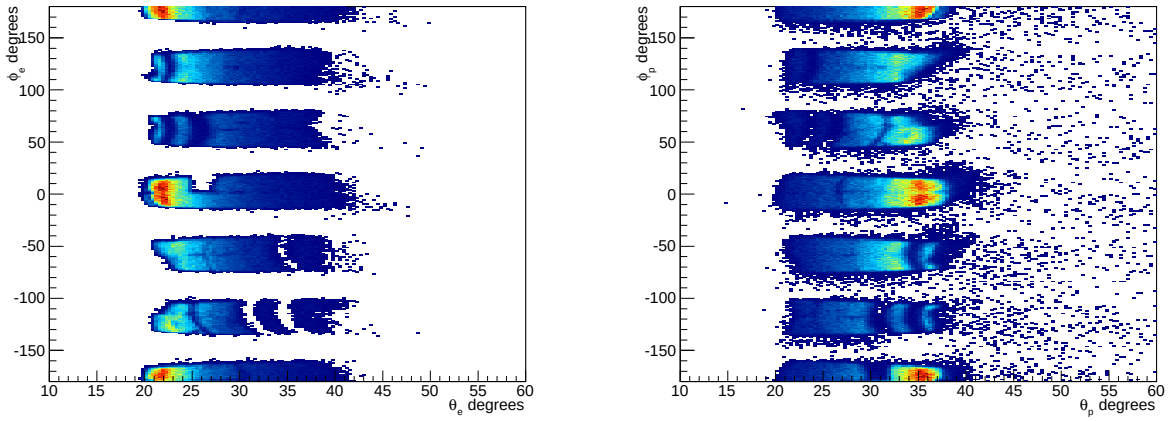

Figure 4.17: Same as Fig. 4.16 with the fiducial cuts applied to remove the low efficiency regions of the various CLAS subdetectors.

4.2 Beam-energy study with the elastic channel

For the DVCS channel, it is important to know precisely the value of the beam energy as the DVCS cross section can vary extremely rapidly as a function of the x_B, q^2, t ... kinematical quantities (in which the value of the beam energy enters). As an example, Fig. 4.18 shows the sensitivity of the Bethe-Heitler cross-section (which interferes with the DVCS) to the $x_B = \frac{Q^2}{2M_p(E-E')}$ variable.

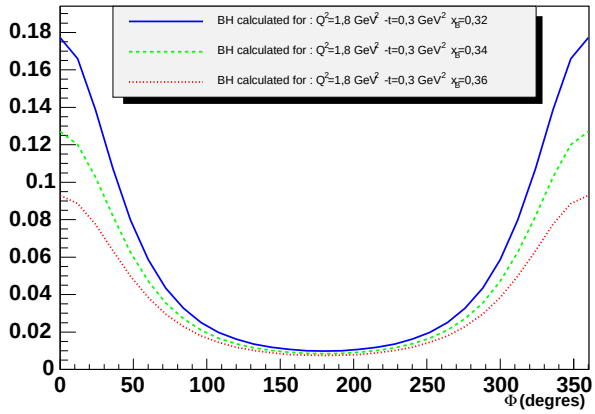

Figure 4.18: 4-fold differential Bethe-Heitler cross section $\frac{d^4\sigma}{dQ^2 dx_B dt d\Phi}$ (nb/GeV^4) as a function of Φ in the bin: Q^2=1.8 GeV^2, $-t$=0.3 GeV^2 and for three different values of x_B: x_B =0.32 (blue curve), x_B =0.34 (green curve) and x_B =0.36 (red curve). Around $\Phi = 0°$, we can see a factor 2 between x_B =0.32 and x_B =0.36. Figure extracted from Ref. [Jo07].

The beam energy can be extracted from the analysis of the elastic scattering $ep \rightarrow ep$ with the knowledge of only a couple a kinematical variables. It can be shown that knowing the scattering angles of the two final-state particles, it is possible to calculate the beam energy with the following formula:

$$E_B = M_p . \left[\left(\frac{1}{tan(\theta_p).tan(\frac{\theta_e}{2})} \right) - 1 \right] \tag{4.3}$$

The beam energy is reconstructed using all the elastic events of the data set. The result is shown in Fig. 4.19. The mean value of the reconstructed beam energy for the e1-DVCS2 experiment is $E_B = 5.883 \pm 0.035$ GeV.

We have also computed the beam energy for each of the six CLAS sectors. The energy distribution was fitted for each sector with a gaussian curve. We find that the shift of the beam energy follows a sinusoidal shape (Fig. 4.20). The amplitude of this sinusoid is about 35 MeV. The sector dependence for the $\Delta\phi = |\phi_e - \phi_p|$ distribution is shown in Fig. 4.21. A similar oscillation is observed with an amplitude of approximately 0.6°.

Different tests have been carried out in order to understand these sector dependencies:

- We simulated a shift of the electron beam in the transverse plane (the beam axis is along z) of 0.5 cm in the x direction, and we checked if this could possibly reproduce the data. According to the results of these simulations, it was not possible to recover the sector dependence that we observe in the data.
- We implemented a tilt of the electron beam by 0.2° around the axis that defines the middle of

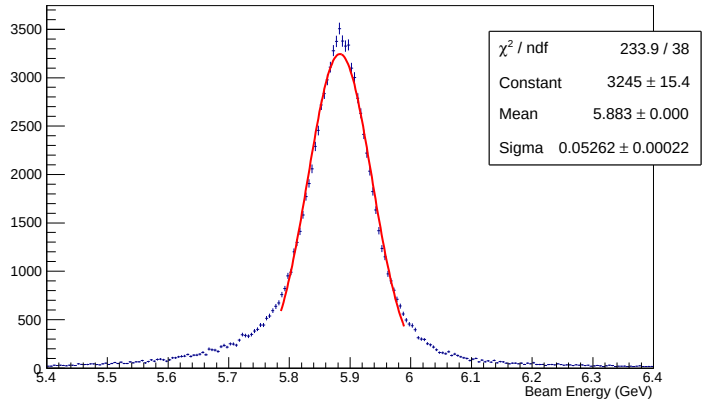

Figure 4.19: Reconstructed beam energy from the elastic events.

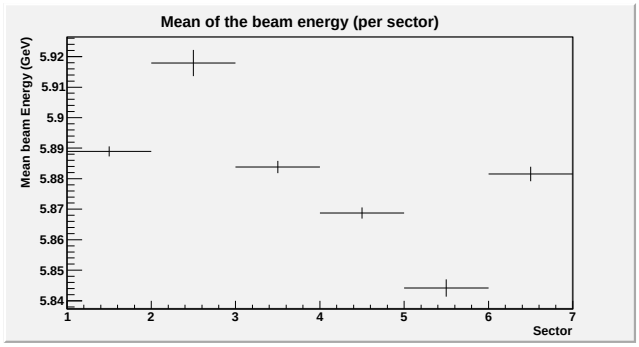

Figure 4.20: Beam energy as a function of the sector.

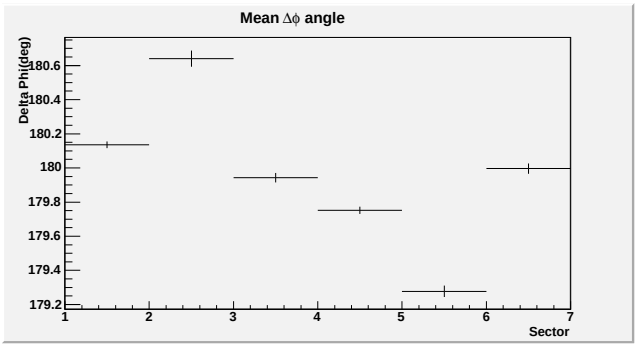

Figure 4.21: $\Delta\phi$ as a function of the sector.

sectors 2 and 5. As we can see in Fig. 4.22, the sector dependence of the $\Delta\phi$ distribution is well reproduced. However, this method did not allow to reproduce the beam energy distribution.

- We modified the torus and solenoid magnetic fields. According to our simulations, a rotation of the torus field is not the cause of such sector discrepancy, as we did not observe a $\Delta\phi$ or a beam energy dependence for moderated angles of rotation. We also applied a rotation of the solenoid field. It is then possible to recover the beam energy distribution of the data (Fig. 4.23) for a rotation of around 2.5°. However, the $\Delta\phi$ distribution was not reproduced using this method.

Therefore, it is in principle possible to reproduce the data by two complementary procedures. A tilt of the beam direction (or equivalently a tilt of the CLAS longitudinal axis) can explain the sector dependence of the $\Delta\phi$ distribution while the tilt of the solenoid can explain the beam energy distribution.

However in practice, the tilt of the beam direction has to be rejected because it would mean that the elastic cross section would be sector dependent as well, and this was not observed. To explain the beam energy distribution, we have to rotate the solenoid field by approximately 2.5° in order to find the same behavior as in the data. But according to position measurements that have been performed on the solenoid, such a tilt is not possible quantitatively and this explanation is not acceptable.

Our last approach was to introduce a shift (rather than a tilt) of the solenoid. It was observed

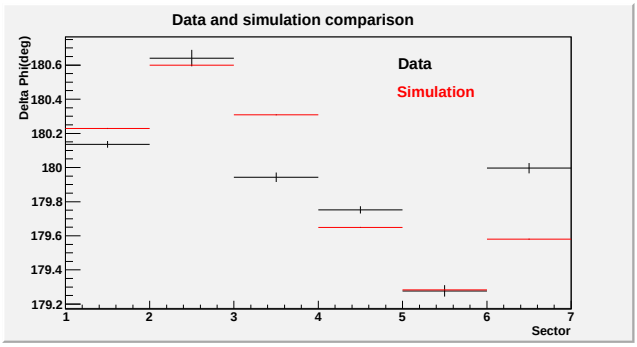

Figure 4.22: $\Delta\phi$ as a function of the sector number, for simulation (red) and data (black). A tilt of 0.2° of the beam direction is applied.

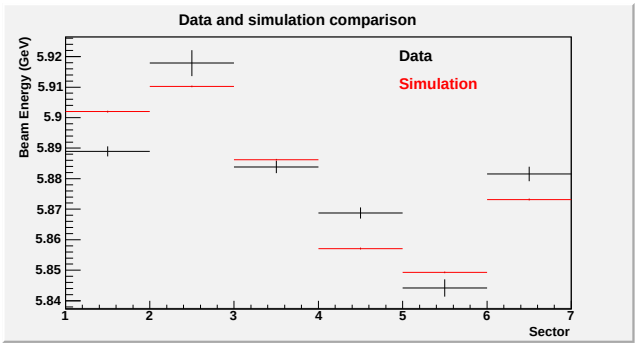

Figure 4.23: Beam energy as a function of the sector number, for simulation (red) and data (black). A tilt of 2.5° of the solenoid field is applied.

that with a 4 mm shift of the solenoid in the direction $\phi = -63.3°$, we were able to reproduce the sector dependence of the beam energy. The result obtained is compatible with the result shown in Fig. 4.23. This last explanation was approved as to be the most probable and the shift of the solenoid has been implemented into the reconstruction code and applied to the whole DVCS2 data set. The sector dependence is reduced significantly and the beam energy value is $E_B = 5.883 \pm 0.01$ GeV. The result can be observed in Fig. 4.24.

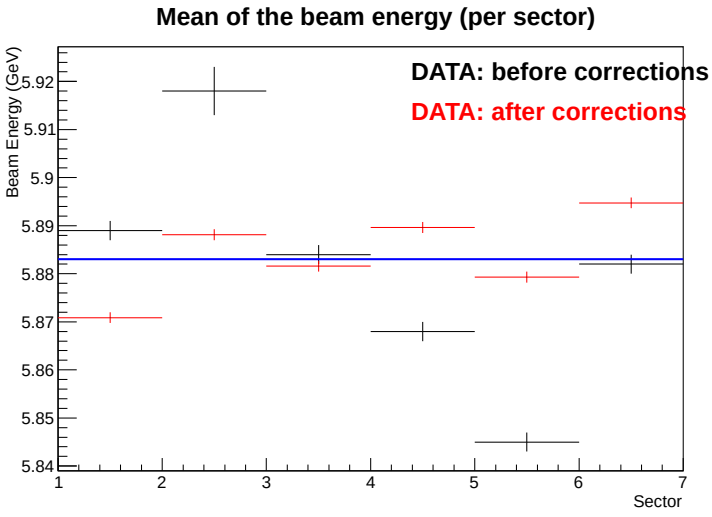

Figure 4.24: Mean of the beam energy as a function of the sector number. The uncorrected data are in black. The corrected data taking into account a shift of the solenoid are in read.

The sector dependence of the $\Delta\phi$ distribution being of a different nature, the shift of the solenoid did not allow to correct it. Despite the different tests performed, we did not find any suitable explanation and no particular correction has been implemented to the data to removed the sector dependence of $\Delta\phi$.

4.3 Sector 5 analysis

We show in this section an extra problem that we have encountered during the data analysis of the elastic process. Figure 4.25 shows the momentum P plotted as a function of θ of the protons, for sectors 4 and 5. The distribution in sector 5 presents two large shifts (called A and B hereafter) at scattering polar angles $\approx 35°$. We note that such effect is not observed with the electrons spectra because they are mainly scattered at lower angles, typically 22°.

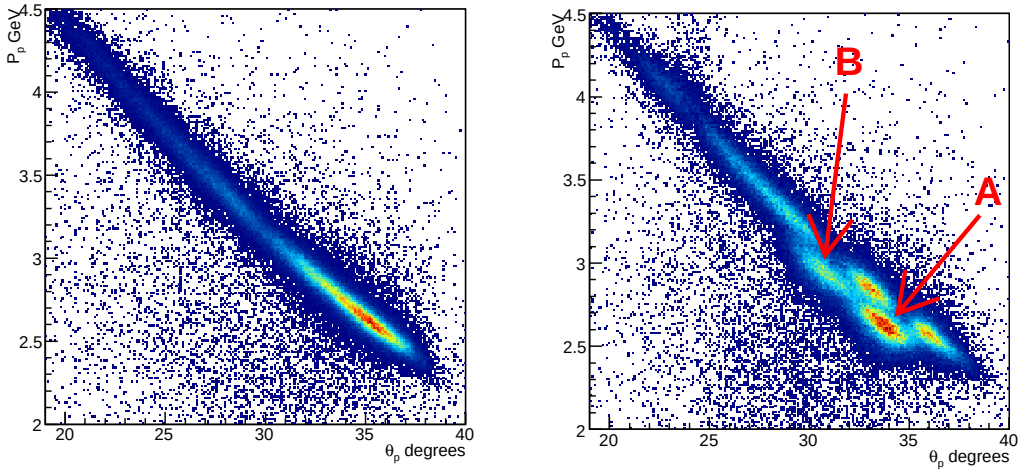

Figure 4.25: P vs θ of the protons, for sector 4 (left) and sector 5 (right). Sector 4 shows a regular correlation between P_p and θ_p as expected for an elastic process, while sector 5 shows two important shifts.

The events coming from the shift region A have been isolated and studied one by one with the CLAS Event Display (CED) software in order to detect some patterns. Figure 4.26 shows a small amount of elastic events accumulated in the region A of the sectors 4 and 5. The wires fired by the elastic events are almost aligned in the DC region 2. By comparing sectors 4 and 5, one can notice that in the sector 5 there is a strip of dead wires on the left side of the elastic track (pink arrows).

The inefficiency of these wires has been double checked with a larger amount of statistics without restricting ourselves to the elastic process. Figure 4.27 shows the wire occupancy of the DC region 2 in sector 4 and sector 5. One can see that a complete strip of six wires is inefficient. Only a few hits have been detected by these wires. A dead connector linking six successive wires seems to be the main reason to explain such problem.

Figure 4.28 shows the consequence of the problem. The six dead wires on the left side of the elastic trajectory prevent the reconstruction code from fitting correctly. Because the left side of the elastic track can not be recorded, the resulting fit is shifted systematically to the right and produces a bad reconstruction of the tracks.

This right-shift of the fits is in agreement with the smaller reconstructed proton angle θ_p that we observe in the data. These badly reconstructed tracks passed the reconstruction stage because the χ^2 was set too high in the code. A way to correct this problem would be to recook the whole DVCS2 statistics with a smaller χ^2 limit, but this would require months of computing. A alternative solution is simply to remove these badly reconstructed tracks by applying fiducial cuts. We choose to work with the last solution and the effects of these cuts are shown in Fig. 4.29.

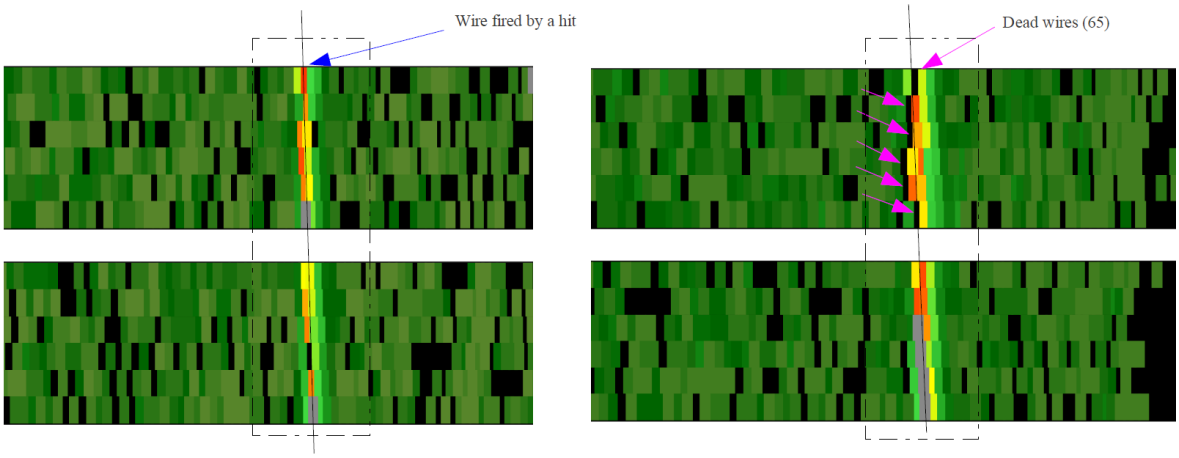

Figure 4.26: Elastic events accumulated and displayed with CED, in DC region 2 of sector 4 (left) and sector 5 (right). The dashed rectangles show where the elastic events are mainly located when we select the elastic events from the region A. The fired wires are aligned.

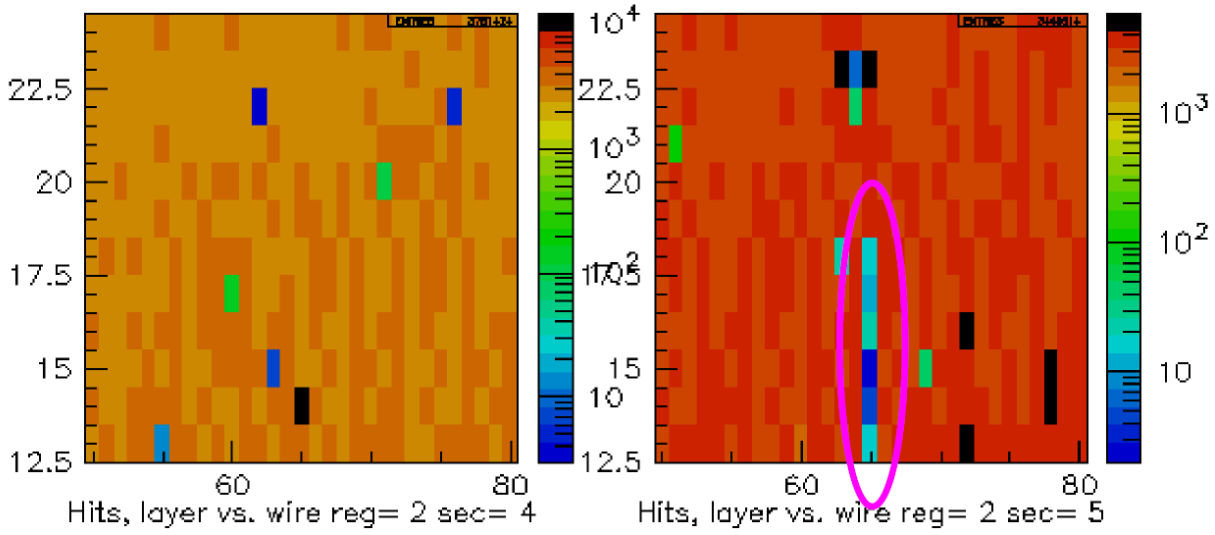

Figure 4.27: Occupancy of the DC region 2 for sector 4 (left) and sector 5 (right). No particular reaction has been selected for these figures. One can see a strip of dead wires (id=65) confirming what we observe with limited statistics for elastic events.

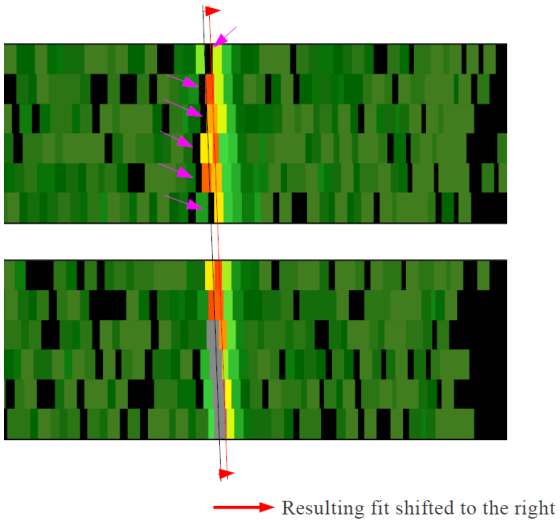

Figure 4.28: The strip of dead wires on the left side of the elastic distribution shifts the fit to the right.

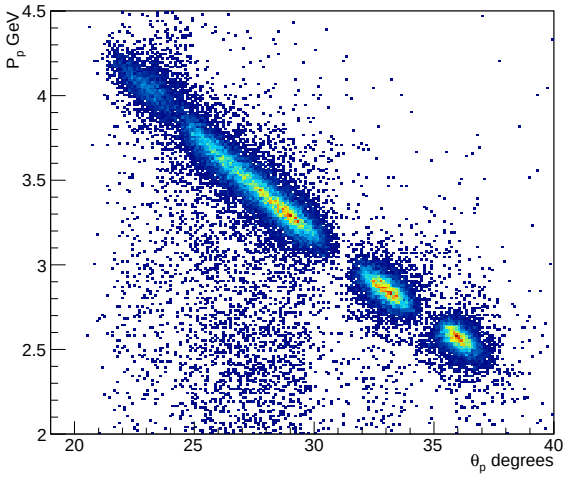

Figure 4.29: p_p as a function of θ_p for sector 5 after the fiducial cuts.

4.4 Kinematic corrections

The motivation for kinematical corrections comes from the observed ϕ-dependence of the elastic peak in the invariant mass W. As can bee seen in Fig. 4.30, the distribution for the W elastic peak fluctuates as a function of ϕ with respect to the proton mass. The badly reconstructed momentum could arise from mis-alignment of the DC or lack of understanding of the magnetic field, but the cause of this effect is not precisely known so that it is not possible to reproduce it by simulation. As a consequence, we need to introduce ad-hoc corrections at the data level.

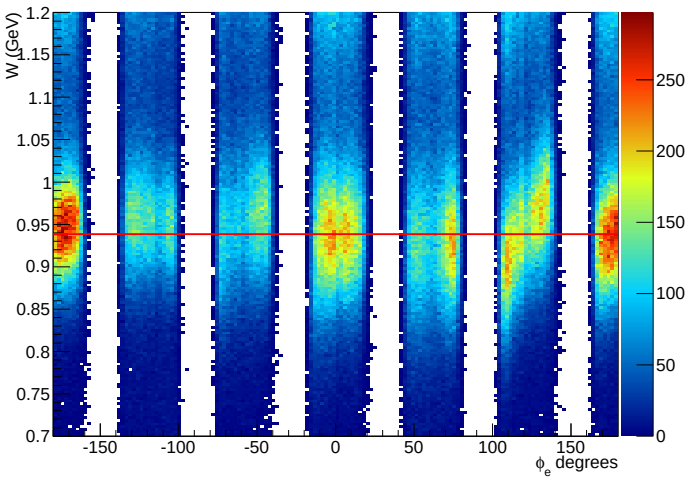

Figure 4.30: W distribution as a function ϕ. The six CLAS sectors can be seen. An azimuthal ϕ dependence of W can be observed with respect to the proton mass (red line).

The following work is based on the procedure described in [Par06]. We assume that we have the correct proton angles and momentum, and we will use those to correct the electron kinematics with the constraints of the elastic-scattering kinematics. The assumption that the proton kinematics is correct is based on the fact that most of the DC mis-alignments could happen in the forward region, affecting the protons less than the electrons. The procedure consists in correcting the electron kinematics in two successive steps. The first step will be to correct the electron angle, and the second will be to correct the electron momentum. In the following, elastic events are selected with a cut on W: $0.7 < W < 1.1$ GeV.

4.4.1 Electron angle correction

Knowing the electron beam energy E_B and the proton polar angle θ_p, the constraints of the elastic scattering kinematics allow to calculate the electron polar angle $\theta_{e_{calc}}$. From the two-body kinematics, one calculates the polar angle of the electron as:

$$\theta_{e_{calc}} = 2\,tan^{-1}\left(\frac{m_p}{(E_B + m_p)\,tan\theta_p}\right) \tag{4.4}$$

We computed the difference $\delta\theta_e$ between the electron polar angle measured in the experiment $\theta_{e_{meas}}$ and the one calculated $\theta_{e_{calc}}$ from the proton angle. A systematic study has been done for each of the six sectors of CLAS, with bins in ϕ_e (2°-wide) and θ_e (various bin widths from 20° to 35°). The differences $\delta\theta_e = \theta_{e_{calc}} - \theta_{e_{meas}}$ were fitted with a Gaussian distribution. Figure 4.31 shows the result for the first sector.

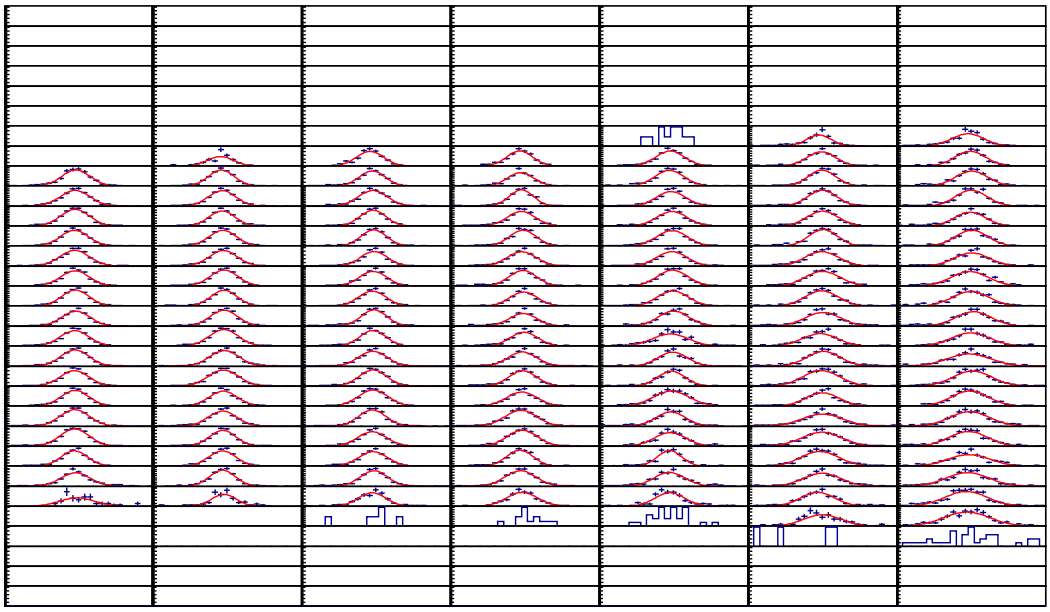

Figure 4.31: $\delta\theta_e$ calculated in the first sector for each bin in ϕ_e (y-axis, from $-30°$ to $+30°$) and θ bins (x-axis, from 20° to 35°). The red curves are the Gaussian fits.

The mean value of the Gaussian fit was then used to derive the ϕ and θ dependence of $\delta\theta_e$. The distribution $\delta\theta_e$ can be described by the following 4-th order equation:

$$\begin{aligned}
\delta\theta_e &= \theta_{e_{calc}} - \theta_{e_{meas}} \\
&= A(\theta_e, s) * \phi_e^4 + B(\theta_e, s) * \phi_e^3 + C(\theta_e, s) * \phi_e^2 + D(\theta_e, s) * \phi_e + E(\theta_e, s) \\
&= (\alpha_s^A * \theta_e^2 + \beta_s^A * \theta_e + \gamma_s^A) * \phi_e^4 \\
&+ (\alpha_s^B * \theta_e^2 + \beta_s^B * \theta_e + \gamma_s^B) * \phi_e^3 \\
&+ (\alpha_s^C * \theta_e^2 + \beta_s^C * \theta_e + \gamma_s^C) * \phi_e^2 \\
&+ (\alpha_s^D * \theta_e^2 + \beta_s^D * \theta_e + \gamma_s^D) * \phi_e \\
&+ (\alpha_s^E * \theta_e^2 + \beta_s^E * \theta_e + \gamma_s^E)
\end{aligned} \tag{4.5}$$

where s represents the sector number, (α, β, γ) are the coefficient of the 2-nd order θ polynomial, and the (A, B, C, D, E) parameters are related to the power of the 4-th order ϕ polynomial.

We first studied the ϕ dependence of $\delta\theta_e$ by fitting the distribution with a 4-th order polynomial with the (A, B, C, D, E) parameters. The reason for using a high order polynomial is to reproduce the distribution at small polar angles, which has a more complicated shape than at higher angles. Fig. 4.32 shows for the first sector the $\delta\theta_e$ distribution with its associated fit in different θ bins. We can see that

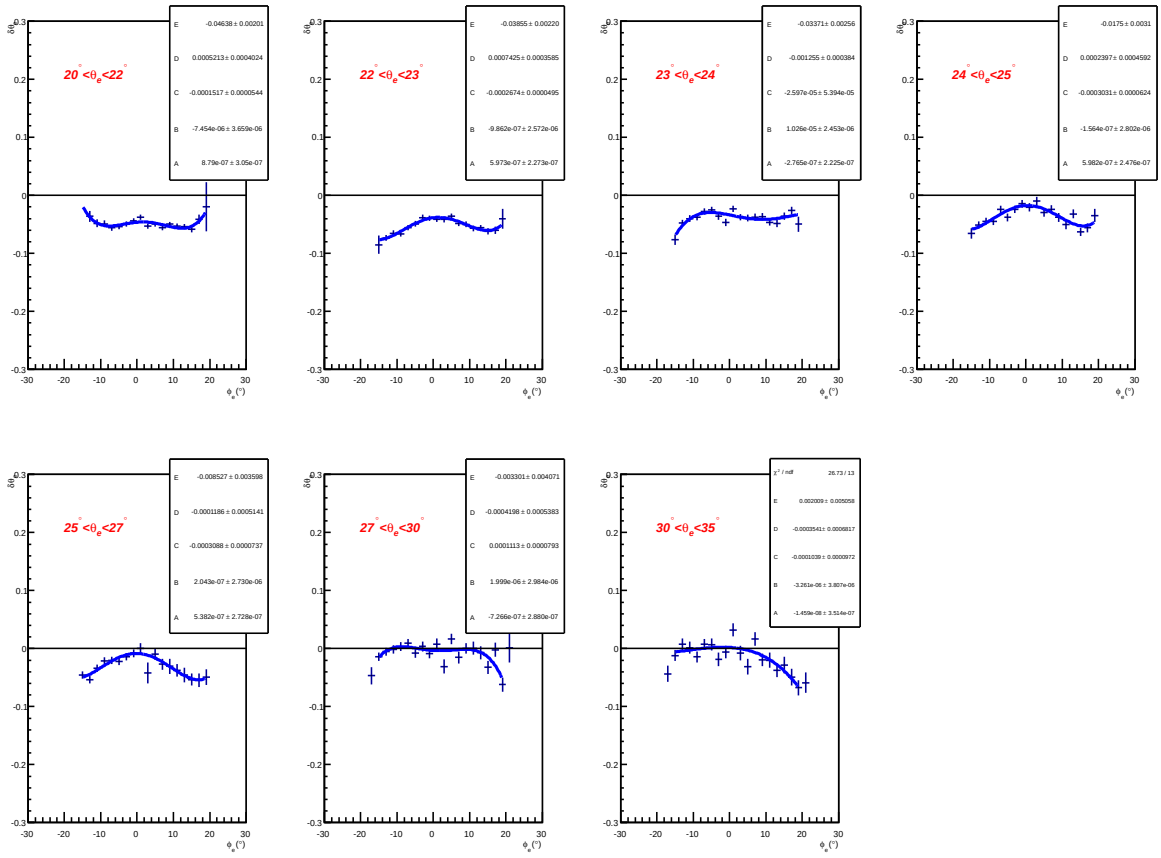

Figure 4.32: $\delta\theta_e$ as a function of ϕ_e for different bins in θ. The fit function (in blue) is defined as: $f = A * \phi_e^4 + B * \phi_e^3 + C * \phi_e^2 + D * \phi_e + E$. The fit parameters are also displayed.

the shifts and the azimuthal dependences are well reproduced by the fitting function. The maximal deviation that we observe in sector one is around 2 mrad.

We then studied the θ dependence of the parameters A, B, C, D, and E. A 2-nd order polynomial (with α, β and γ parameters) has been used to fit the distributions. Fig. 4.33 shows the distributions and the fits for the first sector. With the fit results of α, β γ for each of the A, B, C, D, E parameters, one can construct the function $\delta\theta_e$ presented in Eq. 4.5 that is used to correct the electron angle $\theta_{e_{meas}}$. Figure 4.34 shows a superposition of $\delta\theta_e$ for the uncorrected and corrected data. We see a clear improvement of $\delta\theta_e$, specially at small θ_e values where the distributions were shifted with respect to $\delta\theta_e = 0$.

One did not notice any significant improvement of the invariant mass W using the electron angular correction. Shifts and azimuthal dependences of W are mainly due to wrong momentum reconstruction. The next sub-section describes the procedure to correct the electron momentum.

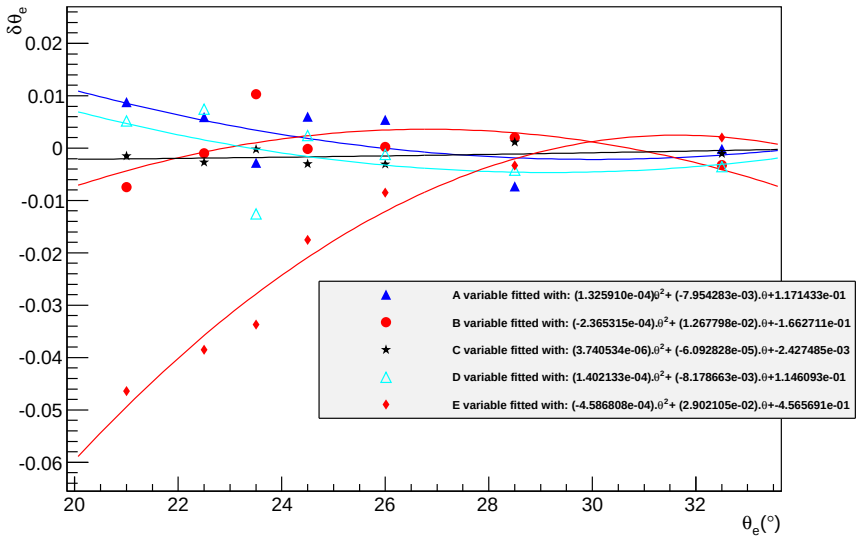

Figure 4.33: The (A, B, C, D, E) ϕ_e fit parameters of $\delta\theta_e$ plotted as a function of θ_e in sector 1. The fit function is defined as: $f_{A,B,C,D,E} = \alpha_{A,B,C,D,E} * \theta_e^2 + \beta_{A,B,C,D,E} * \theta_e + \gamma_{A,B,C,D,E}$. The fitting parameters are also displayed. A scaling factor (10^3 for A and B, 10 for C and D) has been applied to each distributions for display purpose.

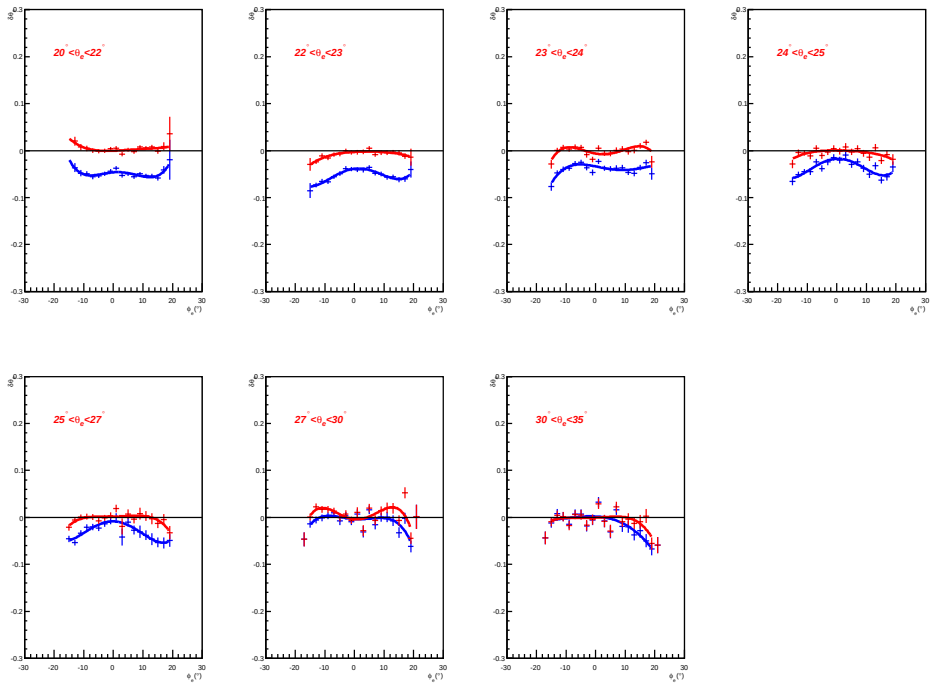

Figure 4.34: $\delta\theta_e$ as a function of ϕ_e for different bins in θ. The blue curve is a fit to the data before angular correction. The red curve is a fit to the data after correction.

4.4.2 Electron momentum correction

The electron momentum $p_{e_{calc}}$ can be calculated from the beam energy E_B and the corrected electron polar angle θ_e as in the previous sub-section. With the constraints of the elastic scattering kinematics, we have:

$$p_{e_{calc}} = \frac{E_B}{1 + 2\,\frac{E_B}{m_p} sin^2(\theta_e/2)} \tag{4.6}$$

Similarly to the angular correction, the momentum correction is a function of θ_e, ϕ_e and of the sector number. The correction function δp_e can be written as:

$$\begin{aligned}
\delta p_e &= p_{e_{calc}}/p_{e_{meas}} \\
&= A(\theta_e, s) * \phi_e^3 + B(\theta_e, s) * \phi_e^2 + C(\theta_e, s) * \phi_e + D(\theta_e, s) \\
&= (\alpha_s^A * \theta_e^2 + \beta_s^A * \theta_e + \gamma_s^A) * \phi_e^3 \\
&+ (\alpha_s^B * \theta_e^2 + \beta_s^B * \theta_e + \gamma_s^B) * \phi_e^2 \\
&+ (\alpha_s^C * \theta_e^2 + \beta_s^C * \theta_e + \gamma_s^C) * \phi_e \\
&+ (\alpha_s^D * \theta_e^2 + \beta_s^D * \theta_e + \gamma_s^D)
\end{aligned} \tag{4.7}$$

where s is the sector number, (α, β, γ) are the coefficients of the 2-nd order θ polunomial, and (A, B, C, D) parameters are related to the 3-rd order ϕ polynomial. Similarly to the $\delta\theta_e$ distributions, δp_e has been fitted with Gaussian distributions for all sectors in different bins in θ_e and ϕ_e. The results of the Gaussian fits are then used to determine the correlations between ϕ_e and θ_e in δp_e. Figure 4.35 shows the ϕ_e dependence of δp_e in the third sector of CLAS, fitted with a 3-rd order polynomial in ϕ with the A, B, C, D parameters. The first bins in θ_e show a strong azimuthal dependence, which then decreases for higher θ_e values.

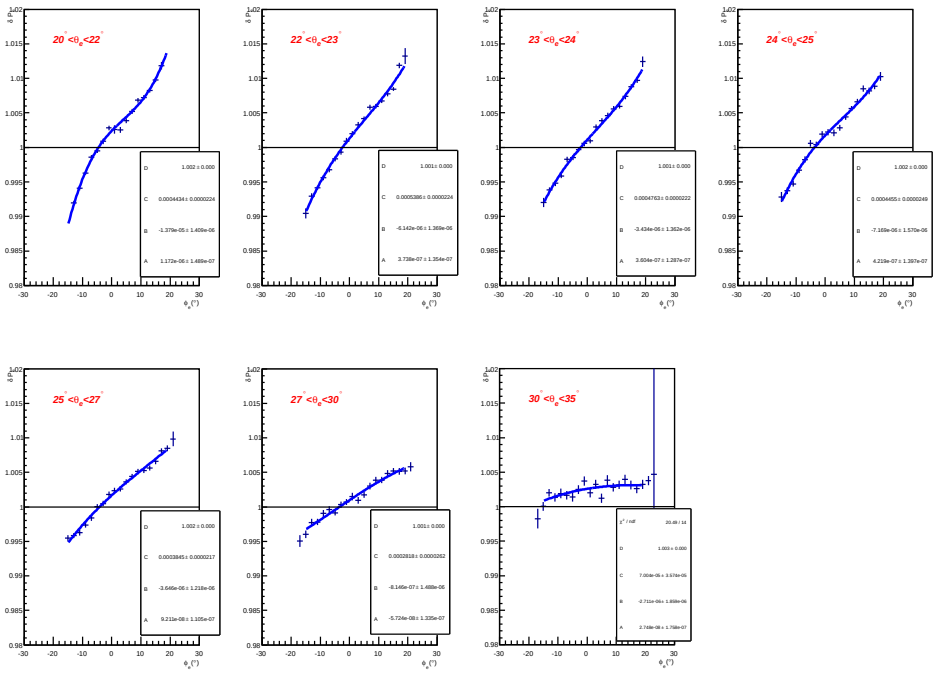

Figure 4.35: δp_e plotted as a function of ϕ_e for different bins in θ_e. The fit function (in blue) is defined as: $f = A * \phi_e^3 + B * \phi_e^2 + C * \phi_e + D$. The fit parameters are also displayed.

The θ-dependences of the parameters A, B, C, and D are then studied with a 2-nd order polynomial in θ (with the α, β γ parameters). Fig. 4.36 shows the distributions and the fits for the third sector.

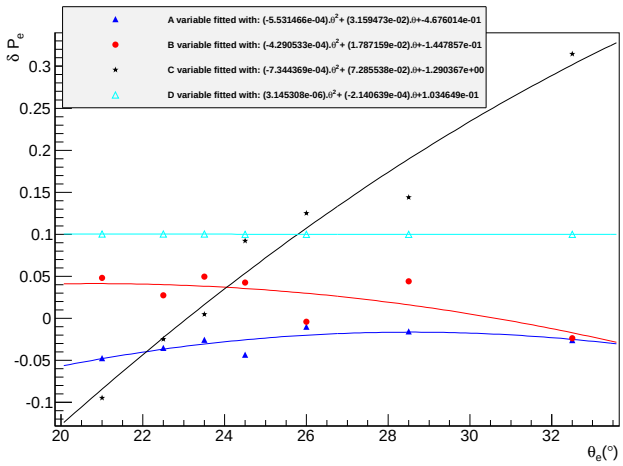

Figure 4.36: The (A, B, C, D) ϕ_e fit parameters of δp_e as a function of θ_e. The fit function is defined as: $f_{A,B,C,D,E} = \alpha_{A,B,C,D} * \theta_e^2 + \beta_{A,B,C,D} * \theta_e + \gamma_{A,B,C,D}$. The Fit parameters are also displayed. A scaling factor (10^4 for A and B, 100 for C) has been applied to each distribution for display purpose.

The momentum correction function is then implemented following Eq. 4.7 with the parameters coming from the fits. Figure 4.37 shows δp_e before and after the momentum-correction procedure. The azimuthal dependence of δp_e is very small, as expected.

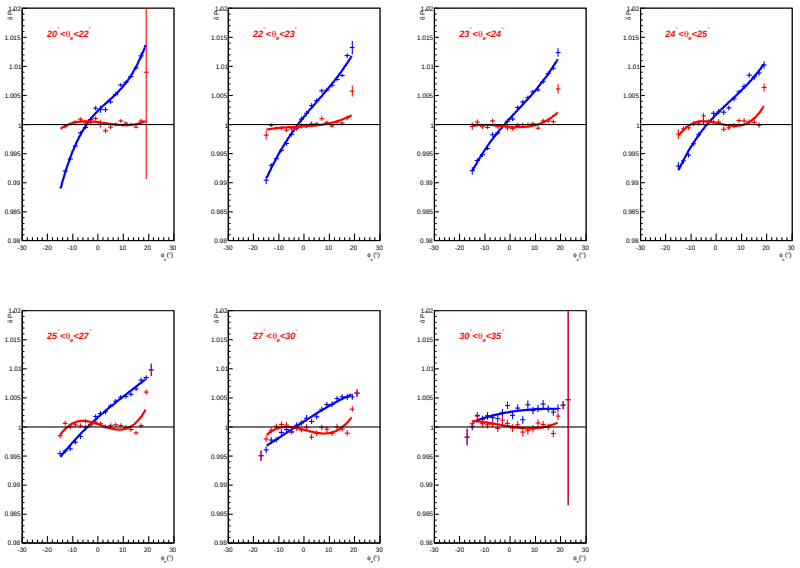

Figure 4.37: δp_e as a function of ϕ_e for different bins in θ. The blue curve is a fit to the data before angular corrections. The red curve is a fit to the data after corrections.

4.4.3 Results

At this stage, the angle and momentum of the electrons have been corrected according to the previous procedures. The correction functions have been developed for all CLAS sectors and applied to the whole DVCS2 data set. In Fig. 4.38, we show the results of these corrections for the W distribution. The elastic peak has been fitted with a Gaussian + background. Fig. 4.39 and 4.40 show respectively

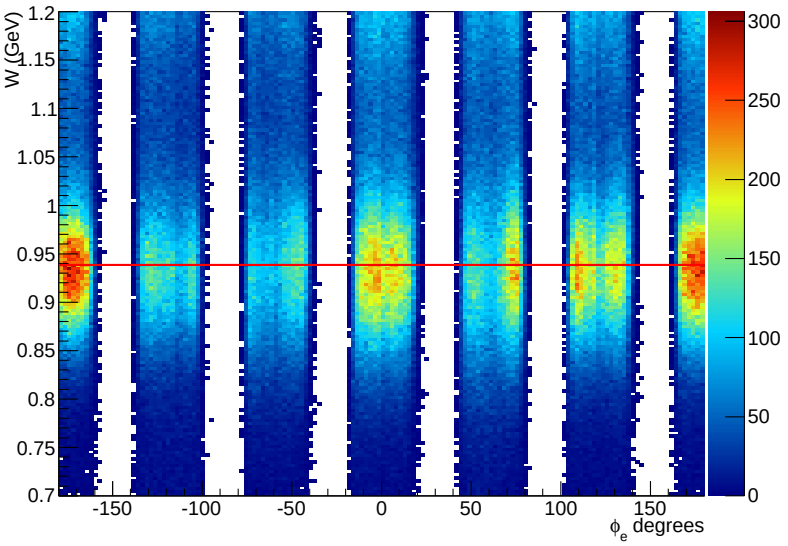

Figure 4.38: W distribution after corrections. The red line is the proton mass.

the mean and the sigma value of these fits, before and after corrections, for the six sectors of CLAS. The corrections applied show a significant improvement of the mean value of the elastic distribution W.

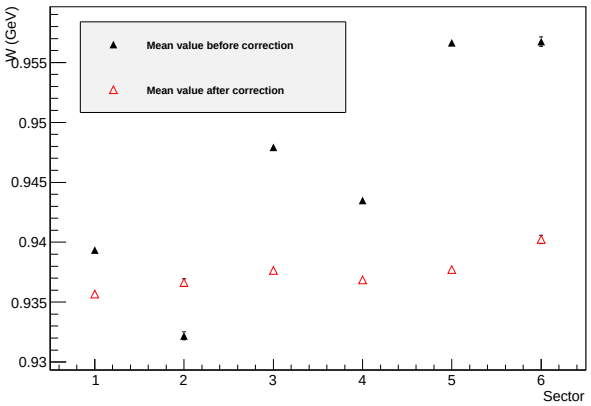

Figure 4.39: Mean value of the elastic W distribution as a function of sector number, before and after corrections.

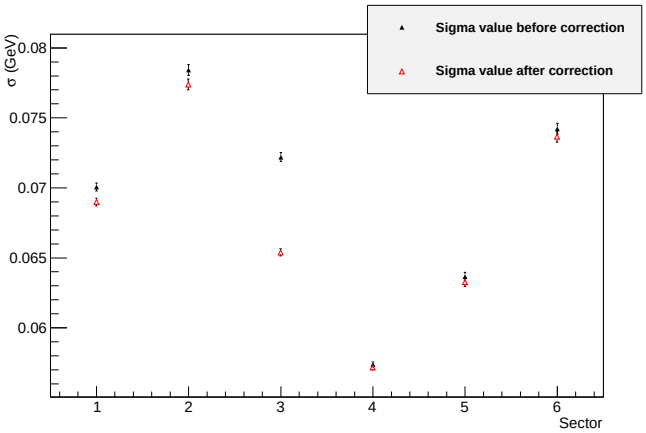

Figure 4.40: Sigma value of the elastic W distribution as a function of sector number, before and after corrections.

However, we did not get any improvement for the resolution σ (except for the third sector). Concerning

the beam energy, one can see the effects of the electron kinematics corrections in Fig. 4.41. The precision is improved significantly and the final value of the beam energy is $E_B = 5.883 \pm 0.003$ GeV.

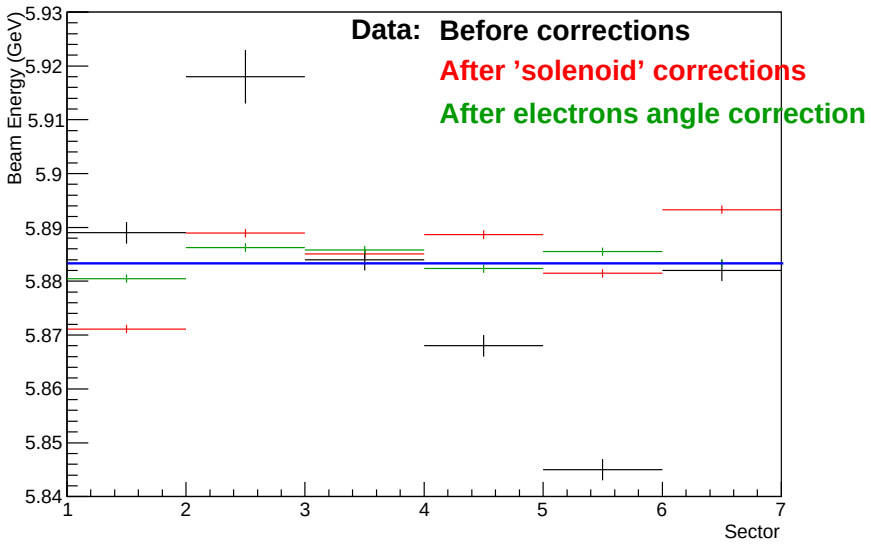

Figure 4.41: Mean of the beam energy value as a function of the sector number. The uncorrected data are in black. The corrected data taking into account a shift of the solenoid are in red. The corrected data taking into account the shift of the solenoid and the electron kinematical correction are in green.

4.5 Elastic cross-section

The elastic cross section has been measured by many experiments and can be considered to be precisely known. Extracting the elastic cross section is therefore a good preliminary test to check the normalization of the data. In this section, we calculate the elastic cross section. Experimentally, it can be obtained as:

$$\frac{d\sigma}{dQ^2} = \frac{N_{ep}}{Acc \times L_{int} \times \Delta Q^2} \tag{4.8}$$

where N_{ep} is the total number of ep events in a Q^2 bin (in this analysis the width ΔQ^2 is 0.2 GeV^2, L_{int} is the integrated luminosity, and Acc is the acceptance of the detector. The acceptance is calculated by simulations (we used a phase-space event generator), and is defined for each bin as the number of reconstructed events divided by the number of generated events. The procedure to compute the two normalization factors L_{int} and Acc is common to both elastic and DVCS channels and will be discussed in detail in Chap. 5 when we will describe the DVCS cross section normalization.

Figure 4.42 shows the theoretical elastic cross section computed with and without radiative effects, using the FF parametrization of Ref. [BKLH02]. The radiative corrections have been computed ac-

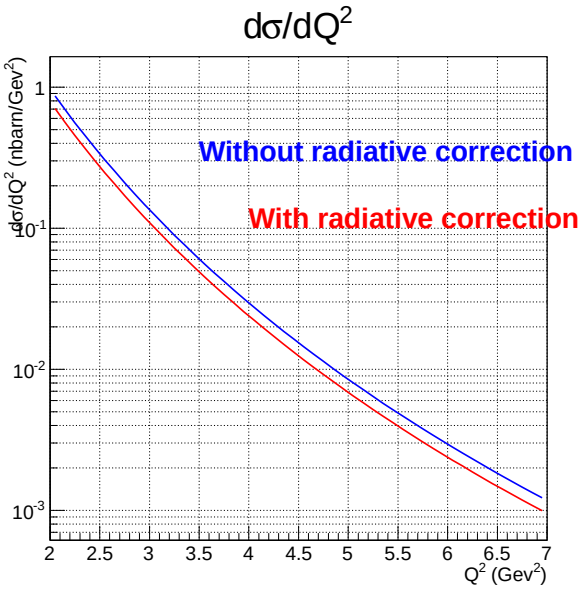

Figure 4.42: Theoretical elastic cross section computed with and witout radiative effects. The blue curve is the Born term. The red curve is the Born term with the radiative effects calculated from Ref. [MT69].

cording to Ref. [MT69]. Their effect lowers the cross section by 19% approximately.

The number of elastic events N_{ep} is shown in Fig. 4.43 as a function of Q^2 for each sector. The acceptance Acc is shown in Fig. 4.43 as a function of Q^2 for each sector. The distributions show some "holes" corresponding to the fiducial cuts that have been applied to some parts of the detectors (mainly DC) to remove the low-efficiency regions of CLAS. Especially, one can notice that sector 2 (linked to sector 5 in the elastic kinematics) suffers from important low-efficiency regions that remove a large part of the elastic peak.

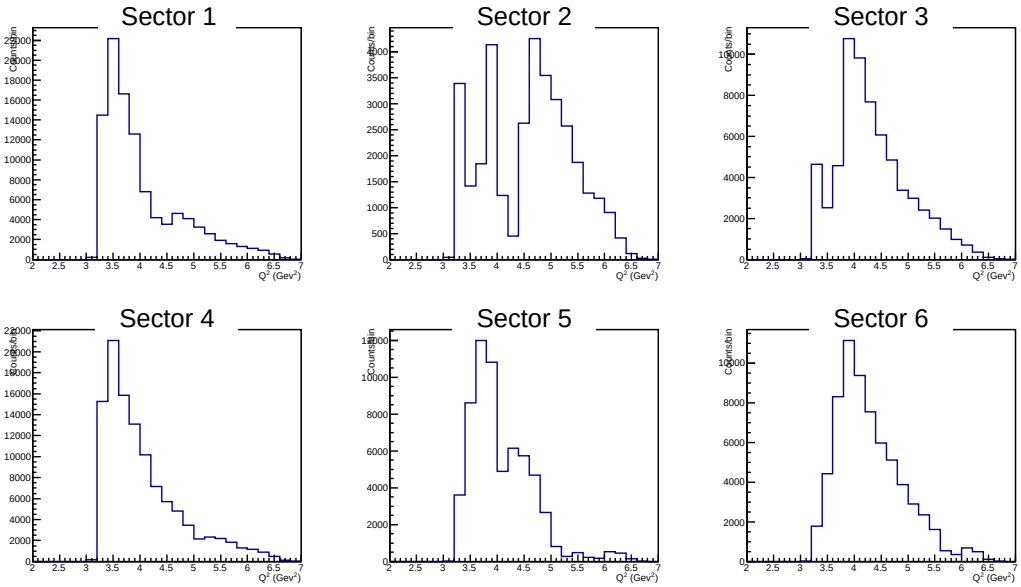

Figure 4.43: N_{ep} as a function of Q^2 for each sector.

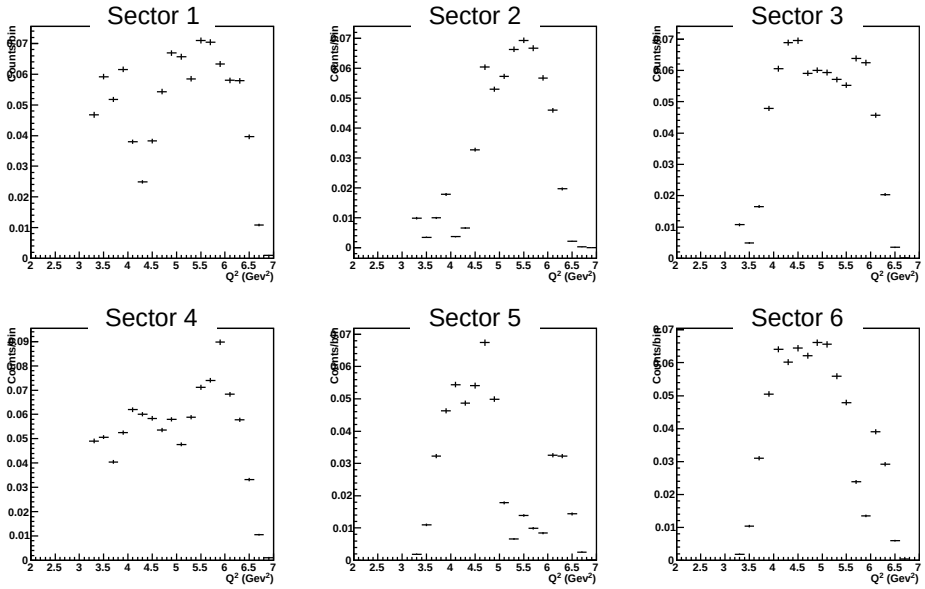

Figure 4.44: Acc as a function of Q^2 for each sector.

The cross section has been computed for each sector according to Eq. 4.8. The experimental results are compared to the theoritical elastic cross section with radiative effects in Fig. 4.45.

Figure 4.46 shows for each sector the ratio between the extracted elastic cross section and the theoretical calculation including radiative effects. The ratio for each sector has been fitted with a constant (α) to estimate the deviation from the nominal value. We can observe that our elastic cross section differs from the expected value by approximately 5% in the best case (sector 1), and by approximately

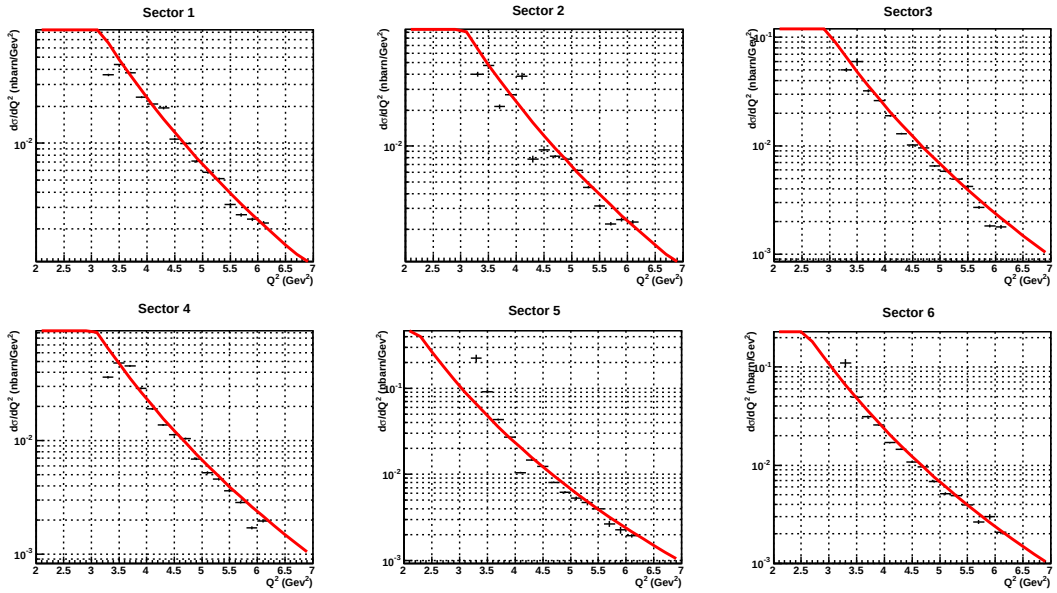

Figure 4.45: Comparison, for each sector, between the elastic cross section (in black) and the theoretical calculation with radiative effects.

15% in the worst case (sector 2). The fluctuations that can be observed in the ratios (especially in sectors 2 and 5) point to the difficulties that one has to get a correct acceptance in the regions of the holes where the Q^2 distributions vary a lot. As we will see, such distribution do not appear for the DVCS process that is a three body reaction.

Figure 4.47 shows the results when the cross-section computation is integrated over the 6 sectors. The global discrepancy observed in the normalization of the elastic cross section is about 7%. This problem of normalization will be taken into account for the computation of the DVCS cross section (Sec. 5.3).

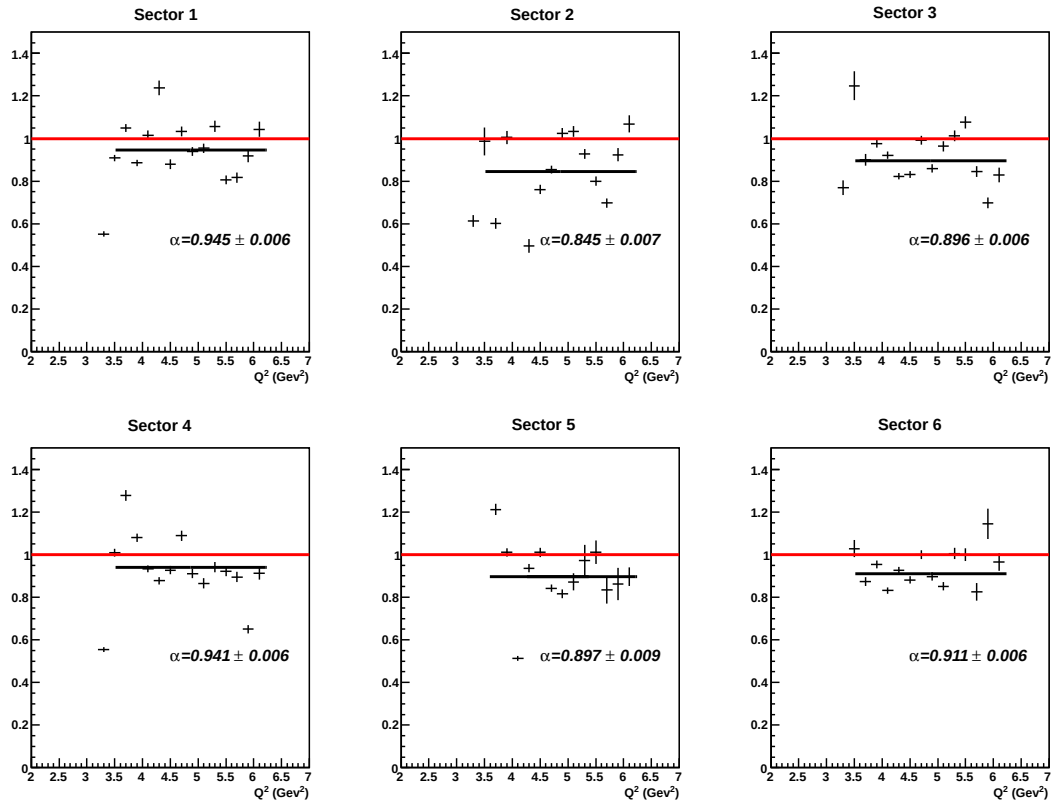

Figure 4.46: Extracted elastic cross section divided by the theoretical calculation. The black curves are the constant fits performed to the ratio.

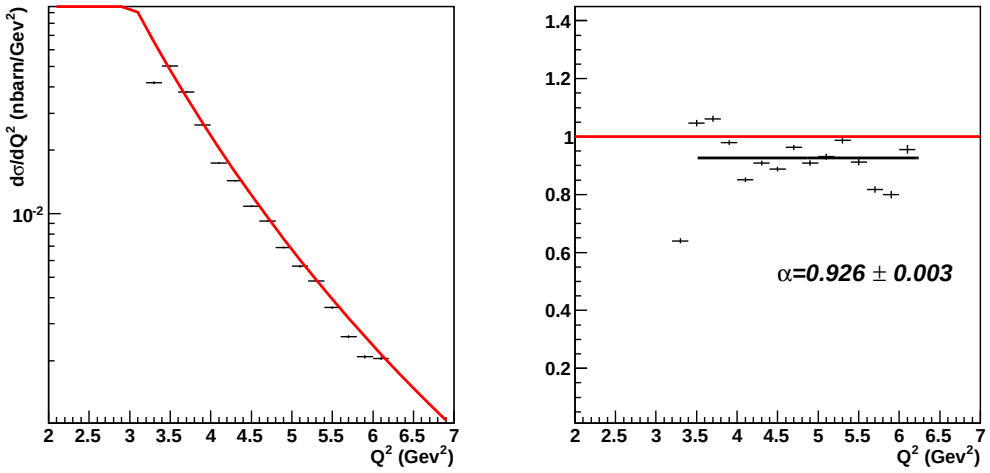

Figure 4.47: Left: comparison between the elastic cross section (in black) and the theoretical calculation with radiative effects, integrated over all the six sectors. Right: extracted elastic cross section divided by the theoretical calculation. The black line is the constant fit performed to the data.

Chapter 5

DVCS cross section analysis

We describe in this section the data analysis that has been performed on the second part of the e1-DVCS experiment [BEG$^+$03]. The goal is to extract the DVCS cross section over a wide phase space.

The selection of the electrons and the protons have been described in Sec. 4.1. We present herafter the selection cuts applied to identify the photon of the DVCS final state.

We will then describe the exclusivity cuts used to select the DVCS channel, and the different terms that enter in the cross section normalization.

5.1 Photon selection

The photon detection is performed by both the EC and IC calorimeters. The role of the latter one is to ensure the detection at low polar angles, where most of the DVCS/BH photons are emitted. For the events containing a "good" electron and a "good" proton, selected according to the previous cuts, we require in addition at least one neutral particle which can be a photon or a neutron, with momentum p larger than 150 MeV.

Both photons and neutrons can be detected in EC. The contamination by the neutrons is eliminated by a cut on $\beta = \frac{l}{c.t_{EC}}$, where l is the distance between the target and the EC hit and t_{EC} is the EC timing. Figure 5.1 shows the β distribution for neutral particles in EC. One requires $\beta > 0.93$ (3-σ cut) to select the photons. The fiducial cuts applied for the EC calorimeter are the same as for the electrons.

Because the particles can not be tagged as charged or neutral only with IC, one makes the assumption that all the events detected by IC are photons. Once the exclusivity cuts will be applied, this will select the high-energy photons and will remove the contamination from low-momentum Moller electrons.

Figures. 5.2 and 5.3 show the IC occupancy before and after the fiducial cuts respectively. The outer edges have been suppressed to remove low efficiency regions. The inner part, too close to the beam, is also removed by applying a cut on θ. As shown in Fig. 5.4, this latter cut corresponds to the outer edge of the first layer of cristals: we require $\theta_\gamma > 4.77°$, that we apply to both data and simulations.

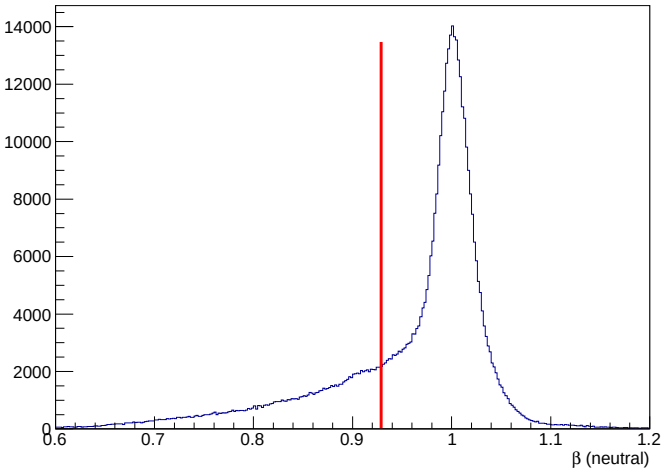

Figure 5.1: β for neutral particles in EC. The cut $\beta > 0.93$ is used to select the photons.

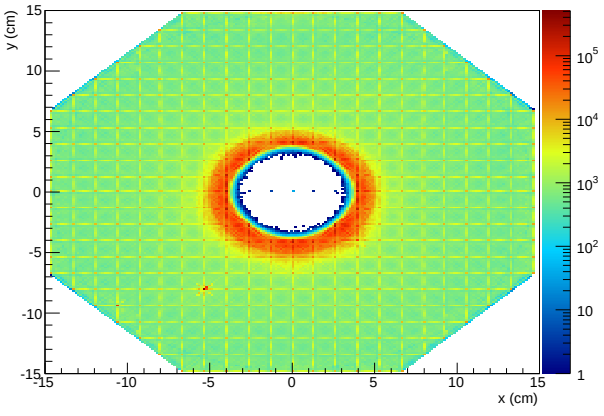

Figure 5.2: IC occupancy before the fiducial cuts.

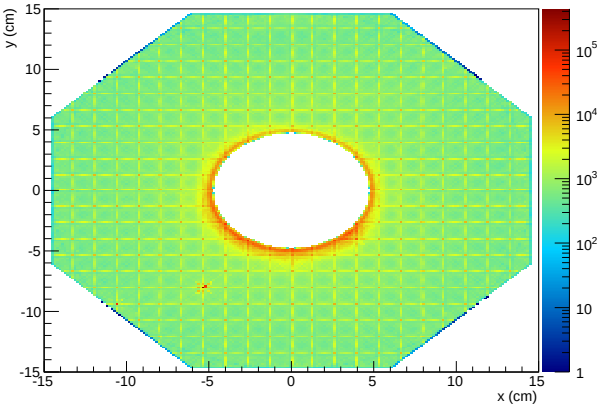

Figure 5.3: IC occupancy after the fiducial cuts.

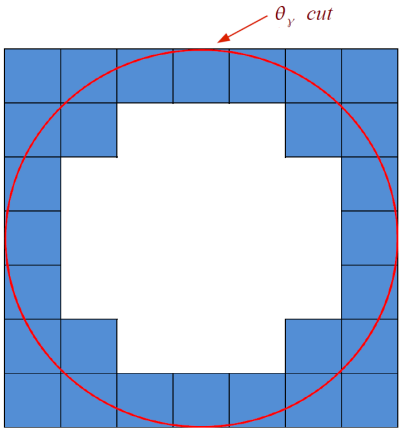

Figure 5.4: Representation of the cut $\theta_\gamma > 4.77°$.

5.2 DVCS channel selection

After the previous particle selection, the events of our data sample contain all one "good" electron, one "good" proton and one "good" photon. To study the DVCS process, we start by applying two cuts on our set of (e, p, γ) events. We want to ensure the applicability of the GPD formalism. One requires $Q^2 > 1$ GeV^2 which is meant to select the Bjorken regime, where the DVCS factorization should hold. We also require the invariant mass W to be larger than 2 GeV in order to be above the nucleon resonance region. The phase space (Q^2, x_B) thus delimited by these cuts and the acceptance of the detector is shown in Fig. 5.5.

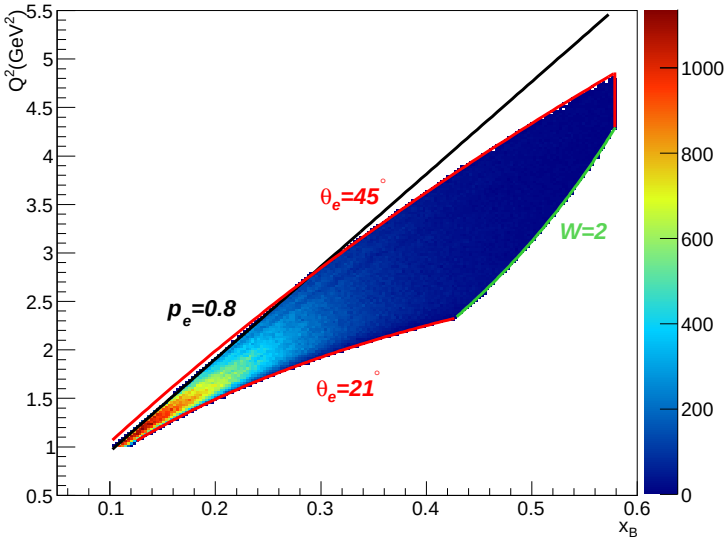

Figure 5.5: Q^2 as a function of x_B, delimited by the following cuts: $p_e > 0.8$ GeV is the minimum electron momentum requested; $Q^2 > 1$ GeV^2 and $W > 2$ GeV select the Bjorken regime, $\theta_e > 21°$ defines the region of agreement between data and Monte-Carlo, and $\theta_e < 45°$ corresponds to the edge of the acceptance of CLAS for the electrons.

We now describe the additional cuts required to ensure the exclusivity of the reaction $ep \to ep\gamma$.

5.2.1 Exclusivity cuts

The exclusivity of the DVCS channel is ensured by applying the following cuts, shown in Fig. 5.6:

- In the configuration $ep \to ep\gamma X$, we require a small missing transverse momentum $p_\perp$ of the system X: $p_\perp = \sqrt{p_x^2 + p_y^2} < 0.15$ GeV.
- One also applies a cut to the squared missing mass $MM^2_{ep\gamma} < 0.1$ GeV^2.
- A cut is applied on the missing mass squared of the system (ep): $MM^2_{ep} < 0.3$ GeV^2. We can see in Fig. 5.6 that this cut allows to remove the contamination from the mesons η, ρ or ω. However, because of the resolution of the detector, the pion peak can not be distinguished from the peak of the photon and the $ep\gamma$ channel wil remain contaminated by the $ep\pi^0$ channel.
- A cut is applied on the cone angle between the detected photon and the calculated photon in $ep \to epX$. We require $\theta_{\gamma X} < 1.5°$.

- Because $\gamma*$, p' and γ belong to the same (hadronic) plane in the DVCS process, one applies a coplanarity cut between the two planes ($\gamma*$, p') and (p', γ): $|\Delta\Phi| < 0.2°$.

We can see the effects of all these cuts in Fig. 5.6. We show the spectra before and after all the cuts represented by the red lines. We also show the missing energy of the system ($ep\gamma$) and the missing mass squared of the system ($e\gamma$). A shift from the expected values (0 and M_p respectively) can be observed in these two spectra. Especially, a 200-MeV shift can be seen in the missing energy, probably due to a wrong recontruction of the photon energy.

Effect of the exclusivity cuts on the particle identification cuts

The electron identification has been presented in Sec. 4.1. To select an electron, we applied a CC cut on the number of photo-electron, and two EC cuts on E_{cin} and E_{tot}/p. These cuts are at the strict level of particle identification, necessary to select a good electron. However, it can be seen in Figs. 5.7 and 5.8, that the exclusivity cuts have a large impact on the π^- contamination. In fact, almost all the π^- contribution is suppressed when we apply the exclusivity cuts. It was then decided to remove the N_{phe} and E_{cin} cuts from the analysis.

Figure 5.9 shows a comparison of E_{tot}/p as a function of p for the data and the simulation. It was noticed that removing the cut on E_{tot}/p increases the π^- peak in the N_{phe} distribution. This cut is kept (as defined in Eq. 4.2), and applied to data and simulations.

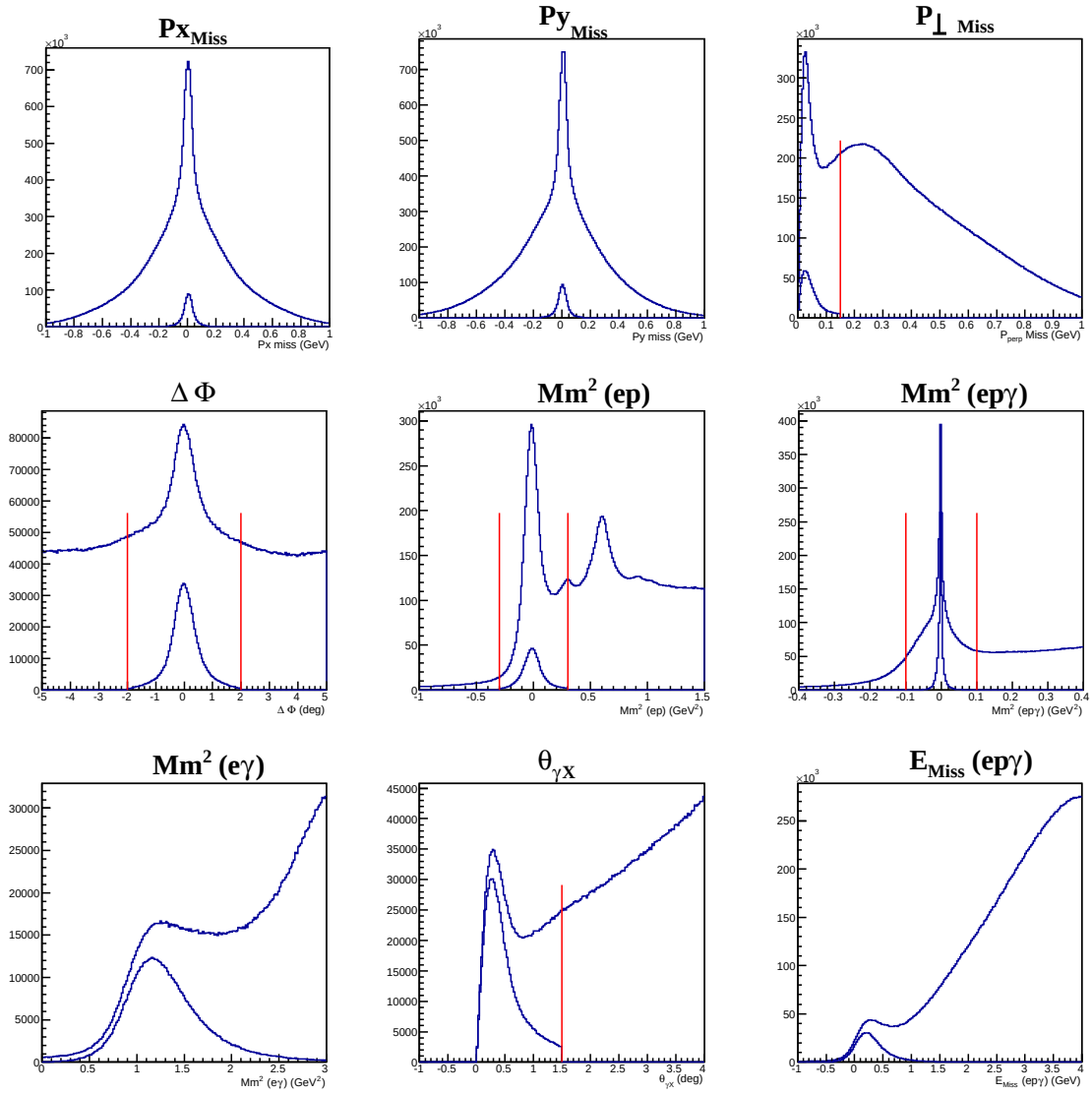

Figure 5.6: Effect of the exclusivity cuts applied on the $ep\gamma$ events. The cuts applied are presented in red. Top row: missing transverse momentum p_x, p_y and $\sqrt{p_x^2 + p_y^2}$ of the system X in the configuration $ep \to ep\gamma X$. Middle row: the left figure is the angle between the planes $(\gamma*, p')$ and (p', γ); the middle and right ones are respectively the missing mass squared of the (ep) and $(ep\gamma)$ systems. Bottom row: the left figure is the missing mass squared of the $(e\gamma)$ system, the middle one is the angle between the detected photon and the calculated photon from $ep \to epX$, and the right one is the missing energy of the $(ep\gamma)$ system.

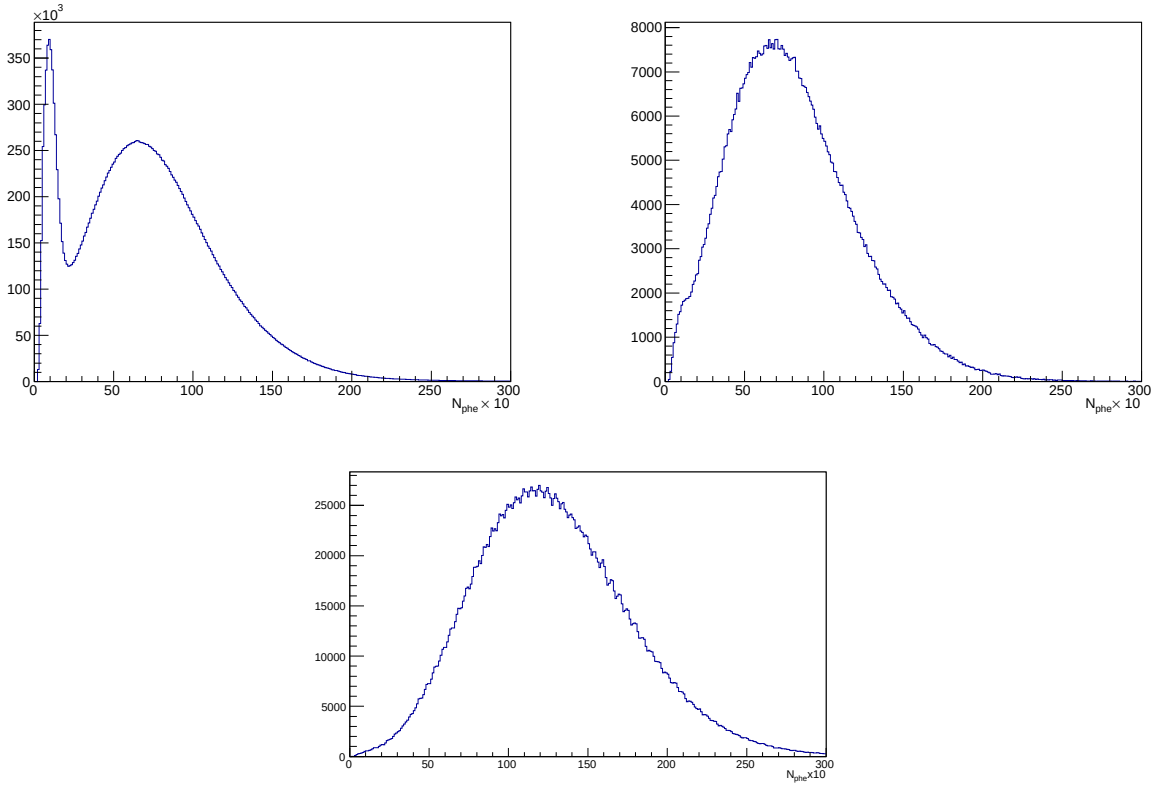

Figure 5.7: Number of photo electrons detected by CC. The top left figure is the distribution after the electron identification and before the exclusivity cuts, on which we normally cut at $N_{phe} \times 10 > 25$ (not applied here). The top right figure is after the electron identification and after the exclusivity cuts. The exclusivity cuts remove almost completely the pion peak. The bottom plot is the result from the simulation.

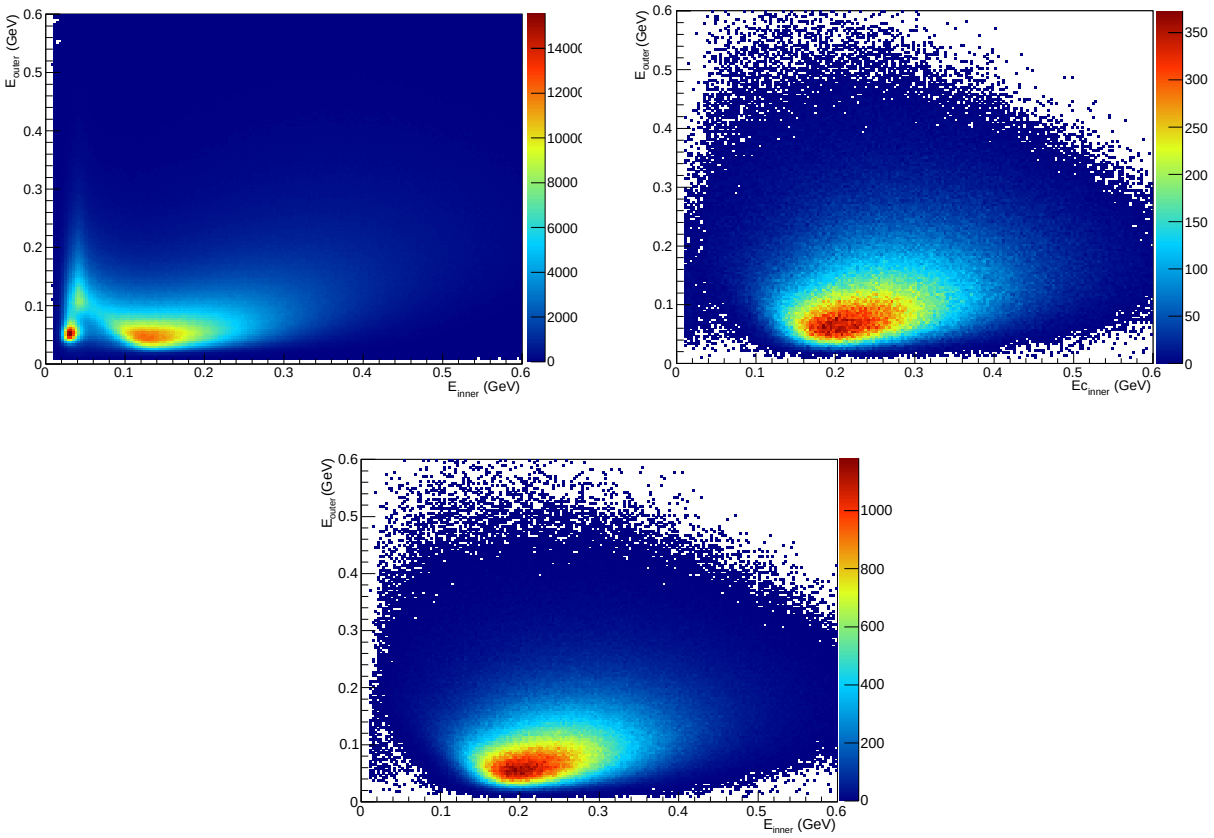

Figure 5.8: Deposited energy in the two stacks of EC: E_{outer} vs E_{inner} (GeV). The left figure is the distribution after the electron identification and before the exclusivity cuts, on which we normally cut at $E_{inner} > 60$ MeV (not applied here). The right figure is after the electron identification and after the exclusivity cuts. The exclusivity cuts remove almost completely the pion peak. The bottom plot is the result from the simulation.

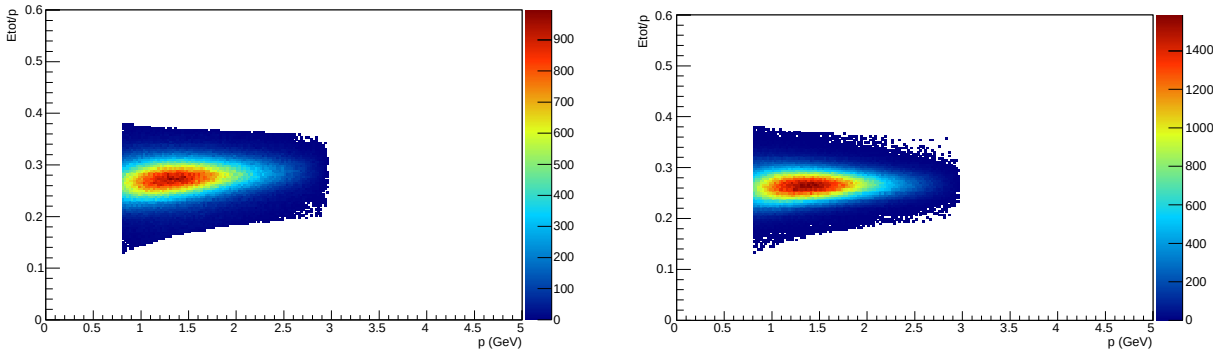

Figure 5.9: Comparison of E_{tot}/p as a function of p for data (left) and simulation (right) after the electron identification and after the exclusivity cuts.

5.3 DVCS cross section

We describe in this section the different steps necessary to extract the cross section of the $ep \to ep\gamma$ channel, described in Fig. 5.10. We will first describe the kinematical regime of the DVCS process and the binning adopted for the data analysis. We will then detail the various normalization factors entering in the cross section. We will finally describe the π^0 contamination substraction.

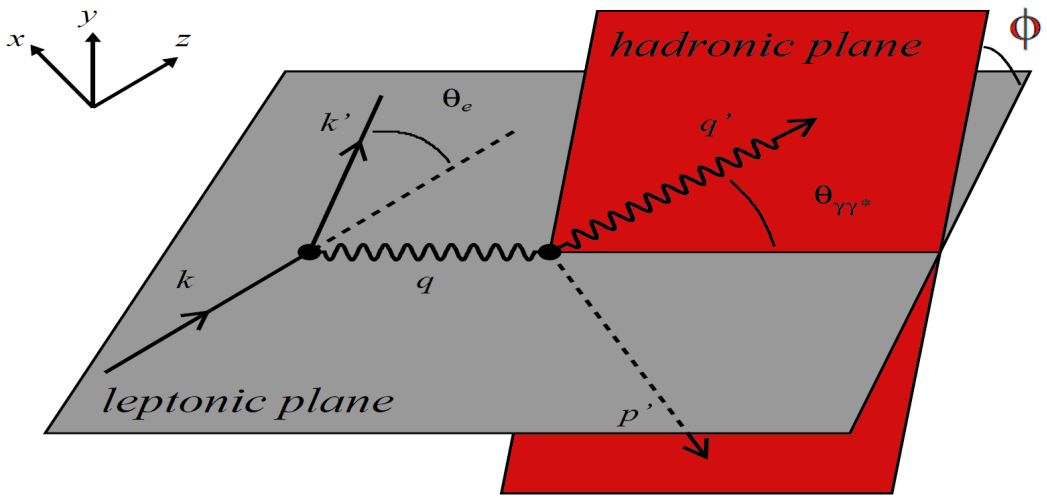

Figure 5.10: The DVCS process, where the electron beam is along the z-direction. The leptonic plane is defined by the incoming (k) and outgoing (k') electrons. The hadronic plane is formed by the final nucleon (p') and the real photon (q'). The virtual photon (q) belongs to both the leptonic and hadronic planes. θ_e is the angle between the outgoing and the incoming electron. $\theta_{\gamma\gamma*}$ is the angle between the real and the virtual photon. Φ is the angle between the leptonic and the hadronic plane.

5.3.1 Binning

The three 4-vectors used to described the final state of the three-body reaction $ep \to ep\gamma$ correspond to 12 variables. This number reduces to 7 because the reaction is independent of the electron azimuthal angle and because of the 4 equations of the energy-momentum conservation. In addition, we know the mass of the three particles so that the total number of independent variables reduces to 4.

In this work, the three-body final state reaction $ep \to ep\gamma$ is described by the four independent variables (Q^2, x_B, t, Φ) defined previously.

Fig. 5.11 shows the distribution of these variables after the particle identification and exclusivity cuts discussed previously.

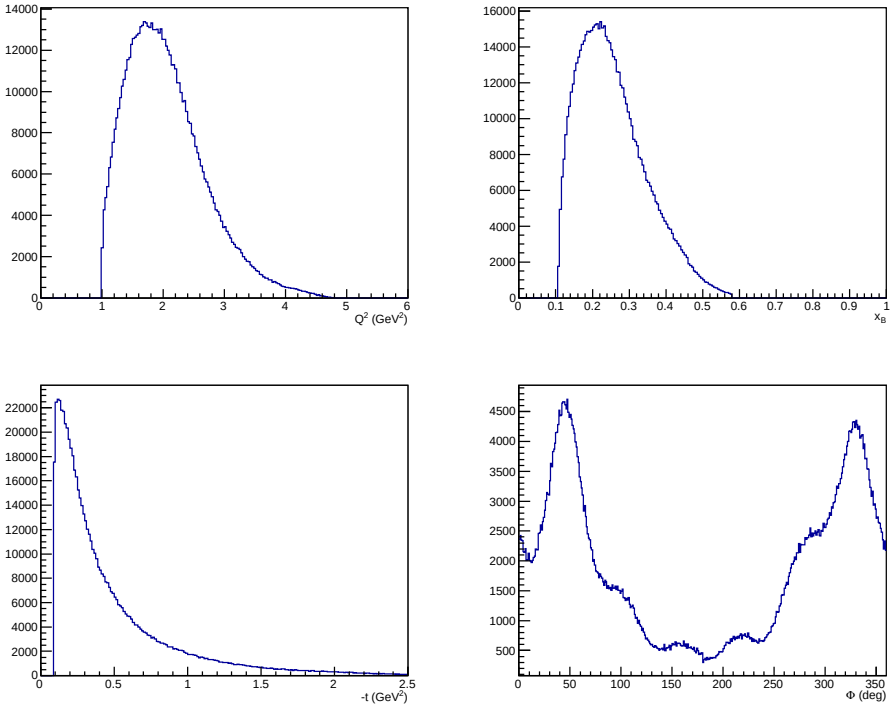

Figure 5.11: Distribution of the four independent variables: Q^2, x_B, t, Φ, for $ep\gamma$ events, after exclusivity cuts.

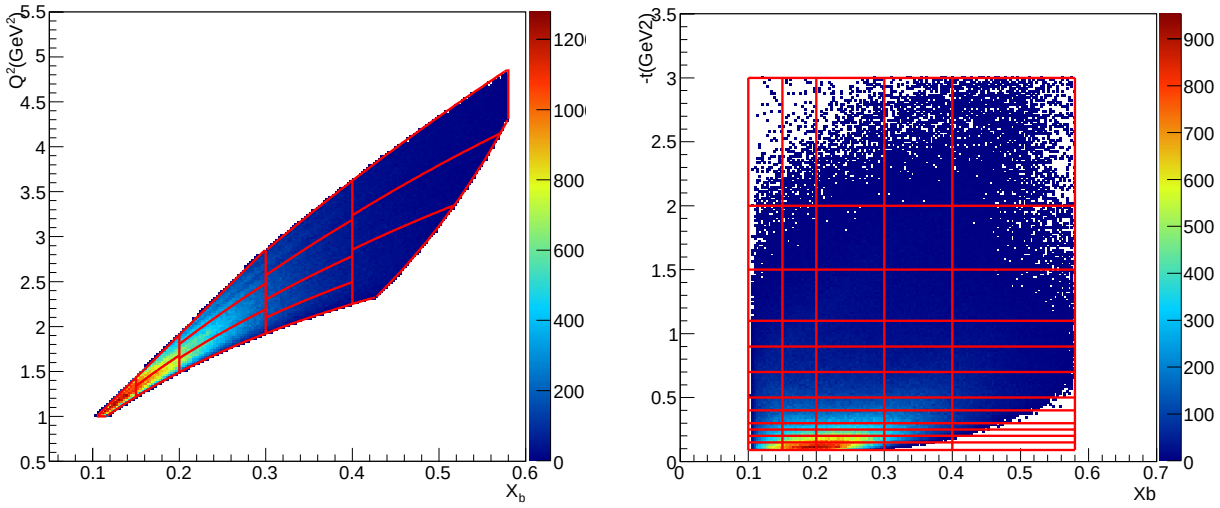

Figure 5.12: Presentation of the binning. Left figure: Q^2 as a function of x_B where one can see in red the 13 bins delimited in terms of θ_e and x_B. Right figure: $-t$ as a function of x_B.

The binning adopted in this analysis has been chosen according to the statistics and the distributions shown in Fig. 5.11. It consists in 13 bins in (Q^2, x_B), 12 bins in $-t$ and 72 bins in Φ. The binning in (Q^2, x_B) is shown in Fig. 5.12.

We give in Table. 5.1 the cuts applied to define the (Q^2, x_B) bins and in t. The binning of the variable t is presented in Table. 5.2.

	Bins in (Q^2, x_B)
Bin 1:	$0.1 < x_B < 0.15$
Bin 2:	$0.15 < x_B < 0.2$ and $21° < \theta_e < 26°$
Bin 3:	$0.15 < x_B < 0.2$ and $26° < \theta_e < 45°$
Bin 4:	$0.2 < x_B < 0.3$ and $21° < \theta_e < 25°$
Bin 5:	$0.2 < x_B < 0.3$ and $25° < \theta_e < 31°$
Bin 6:	$0.2 < x_B < 0.3$ and $31° < \theta_e < 45°$
Bin 7:	$0.3 < x_B < 0.4$ and $21° < \theta_e < 23.5°$
Bin 8:	$0.3 < x_B < 0.4$ and $23.5° < \theta_e < 27°$
Bin 9:	$0.3 < x_B < 0.4$ and $27° < \theta_e < 33.5°$
Bin 10:	$0.3 < x_B < 0.4$ and $33.5° < \theta_e < 45°$
Bin 11:	$0.4 < x_B < 0.58$ and $21° < \theta_e < 28°$
Bin 12:	$0.4 < x_B < 0.58$ and $28° < \theta_e < 34.5°$
Bin 13:	$0.4 < x_B < 0.58$ and $34.5° < \theta_e < 45°$

Table 5.1: The 13 bins in (Q^2, x_B).

The binning of the variable Φ consists in 72 bins of equal width: $\Delta\Phi = 5°$.

5.3.2 Kinematical regime

We show in Fig. 5.13 the distributions of p as a function of θ for the three particles (e, p, γ), after all the exclusivity cuts and within the binning limits.

Bins in $-t$ (GeV^2)
0.09 - 0.15
0.15 - 0.2
0.2 - 0.25
0.25 - 0.3
0.3 - 0.4
0.4 - 0.5
0.5 - 0.7
0.7 - 0.9
0.9 - 1.1
1.1 - 1.5
1.5 - 2
2 - 3

Table 5.2: The 12 bins in $-t$.

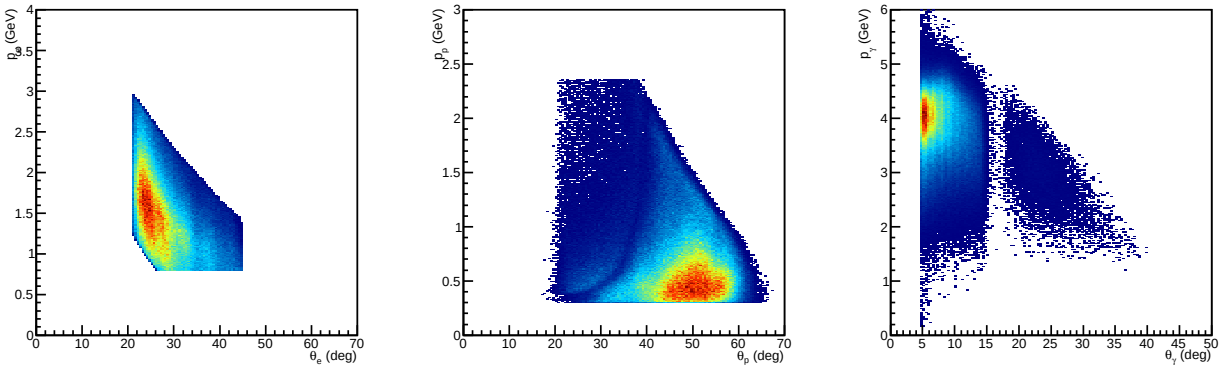

Figure 5.13: p as a function of θ for electrons (left), protons (middle) and photons (right), with all the cuts previously mentioned.

- Electrons are mostly emitted at low scattering angle ($\theta_e \approx 23°$) with momentum p between 1.5 and 2 GeV.
- Protons are scattered at higher angles, typically $\theta_p \approx 50°$, with a smaller average momentum $p \approx 0.5$ GeV.
- Photons are mostly detected by IC in the very forward region ($\theta_\gamma \lesssim 15°$) with high momentum $p \approx 4$ GeV. The gap around 17° corresponds to the transition between IC and EC.

5.3.3 Experimental $ep \to ep\gamma$ cross section

The 4-fold differential DVCS cross section is obtained from:

$$\frac{d^4\sigma}{dQ^2 dx_B dt d\Phi} = \frac{N_{ep\to ep\gamma}}{Acc\, L_{int}\, F_{vol}} \times F_{rad} \tag{5.1}$$

where:

- (Q^2, x_B, t, Φ) are the four independent variables describing the process.
- $N_{ep\to ep\gamma}$ is the number of $ep\gamma$ events in each (Q^2, x_B, t, Φ) bins, corrected for π^0 contamination.

- Acc is the acceptance of the detector. It is determined by simulation for each (Q^2, x_B, t, Φ) bin.
- L_{int} is the integrated luminosity for the whole DVCS2 data set.
- F_{vol} corresponds to the effective hyper-volume of the bin (Q^2, x_B, t, Φ).
- F_{rad} are the radiative corrections calculated in each (Q^2, x_B) bins in order to compute the cross section at the Born term.

We now give a detailed description of each of these terms.

5.3.4 Acceptance

The acceptance Acc is calculated by Monte Carlo for each quadri-dimensional (Q^2, x_B, t, Φ) bin. It corresponds to the detection efficiency of CLAS. Indeed, the angular coverage of CLAS is not perfect and some areas of CLAS can not detect the particles. In these zones which are dead or which have a very low detection efficiency, the number of particles detected is smaller than the number of particles actually created. To recover the orignal number of particles, we correct the number of detected events $N_{ep\to ep\gamma}$ by the acceptance term Acc, that is determined from simulations as the number of event reconstructed divided by the number of event generated in each 4-dimensional bins.

The different stages of the procedure are summarized in Fig. 5.14. We will now give details about

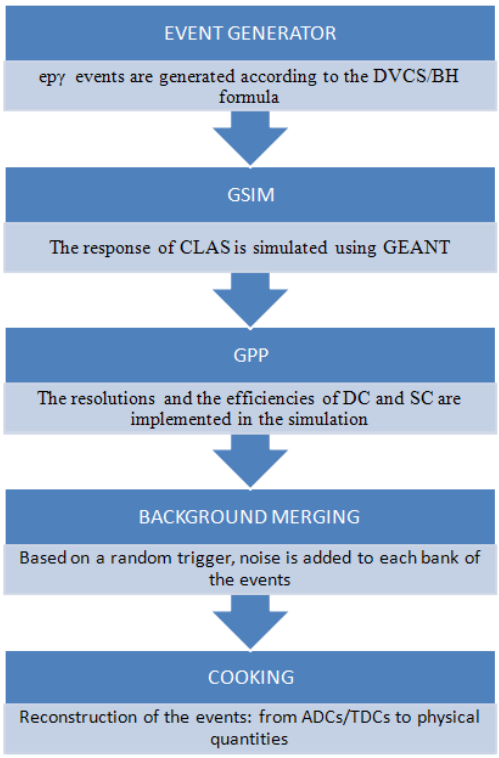

Figure 5.14: Procedure for the computation of the acceptance.

the different stages that are necessary to complete the acceptance calculation.

DVCS events generator

The event generator is based on the code written by V. Korotkov [KN02] from the HERMES collaboration. The $ep\gamma$ events are generated according to the cross section formula for the DVCS/Bethe-Heitler

process from Belitsky et al. [BMK02]. The GPD parametrization is performed according to the double distributions formalism and the D-term detailed in Sect. 2.3.6. Radiative corrections have been implemented according to [ABR99] including real radiated photons.

Approximately 75 million events have been generated in the following kinematics:

- beam energy E_B=5.88 GeV
- $0.8 < Q^2 < 6$ GeV^2
- $0 < x_B < 0.95$
- $0 < -t < 6$ GeV^2
- W >1.85 GeV
- Energy of the scattered electron: $E_{e'}$>0.35 GeV.

Two additional cuts have been applied on $\theta_{e\gamma} > 1.95°$ and $\theta_{e'\gamma} > 1.95°$, respectively the angle between the incident electron (e) with the real photon γ and the angle between the scattered electron (e') with the photon. These cuts have been added into the event generator code to remove the two poles of the Bethe-Heitler (Eq. 2.27).

GEANT simulations

The CLAS detector has been simulated using the GSIM code [GSI12] based on the GEANT3 libraries developed at CERN. GSIM mimics the CLAS geometry and it allows to compute the different physics interactions that can occur between particles and the detector. Physical phenomena are in general well reproduced by GSIM except in the EC calorimeters where the electromagnetic showers are not precisely simulated (to reduce computing time, we must apply a cut on the minimum deposited energy so that we loose part of the shower), and the Cherenkov counters that have a too complicated geometry and are not reproduced with sufficiently good precision to simulate a realistic photo electrons distribution.

Two main changes have been applied to the DVCS2 experiment with respect to DVCS1. A 5 cm long target has been used during the data taking compared to a 2.5 cm long target in DVCS1. This new target has been implemented into GSIM [Soh12]. In addition, GSIM takes into account the lead shielding that was added to shield the IC calorimeter and to trap Moller electrons behind the calorimeter [Fra12].

GSIM Post-Processing

A realistic acceptance computation must reproduce the CLAS detector efficiencies and resolutions. The output of the GSIM simulations does not perfectly match the data in terms of resolution and detection efficiency. The idea of the GSIM Post-Processing (GPP) is to include in the simulations the low-efficiency regions of DC and SC, and to smear the GSIM TOF and DC resolutions in order to obtain more realistic results.

Four parameters are used to match the resolutions of the simulations with the resolutions of the data. The parameters a, b and c are used to smear the resolutions of the DC in regions 1, 2 and 3. The parameter f is used to worsen the resolution of the time-of-flight counters. We have used the $ep \to ep\pi^0$ channel to compare the resolutions between the data and the simulations. The combination of parameters that we finally use to get a relatively good agreement between data and simulations is: $a = 1.2$, $b = 1.25$, $c = 1.3$ and $f = 2$. The result can be seen in Fig. 5.15.

We have used the fiducial cuts applied in Sec. 4.1 on the low-efficiency paddles of SC to remove the regions were the discrepancy between data and simulation were too important.

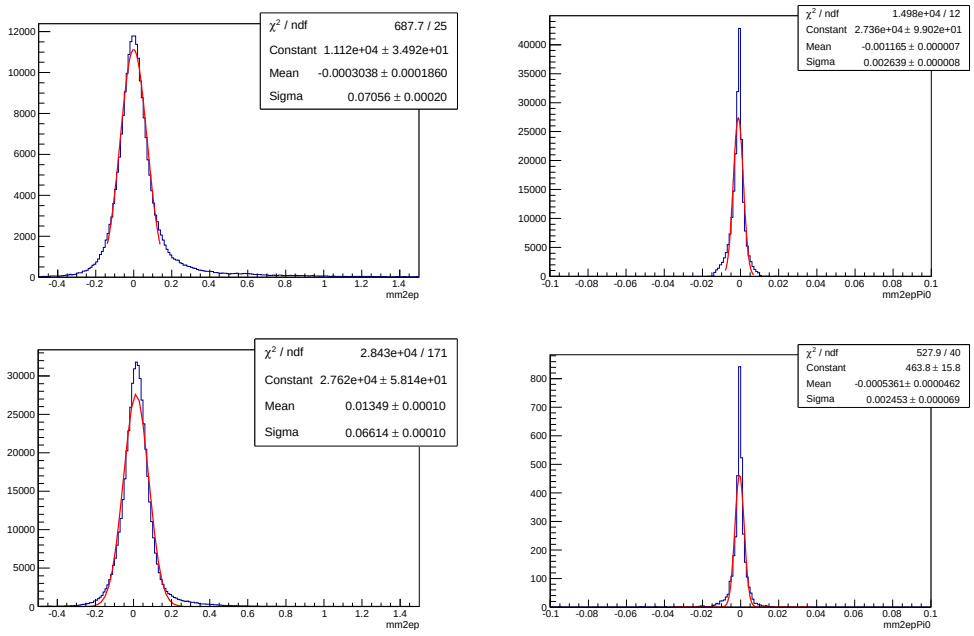

Figure 5.15: Comparison of resolutions between the distributions of MM^2_{ep} (left) and $MM^2_{ep\pi^0}$ (right) for the data (top panels) and simulations (bottom panels).

For the DC efficiency, we applied a procedure to take into account the dead, inefficient, and hot wires of the different regions. This procedure has been first described in [UL03]. For each wire i of the sector S, we build a sample of 18 wires containing the wire i with its neighboring wires $i-1$ and $i+1$, and the corresponding wires in the other sectors S'. For each wire i of this sample, we count the number n ($0 \leq n \leq 17$) of wires that have an occupancy within a certain percentage of its occupancy Occ_i. The wire that has the maximum number n is used to calculate the expectation value Exp_{val}, defined as the occupancy average in the group of wires n. The efficiency of the wire i is then defined as: $Eff_i = \frac{Occ_i}{Exp_{val}}$. If $Eff_i < 1\%$, the wire is considered to be dead and its efficiency value is set to 0.

The efficiency table of all the DC wires is then implemented into the CLAS database so that the simulated wire occupancy is realistic. The results of this analysis can be seen in Fig. 5.16.

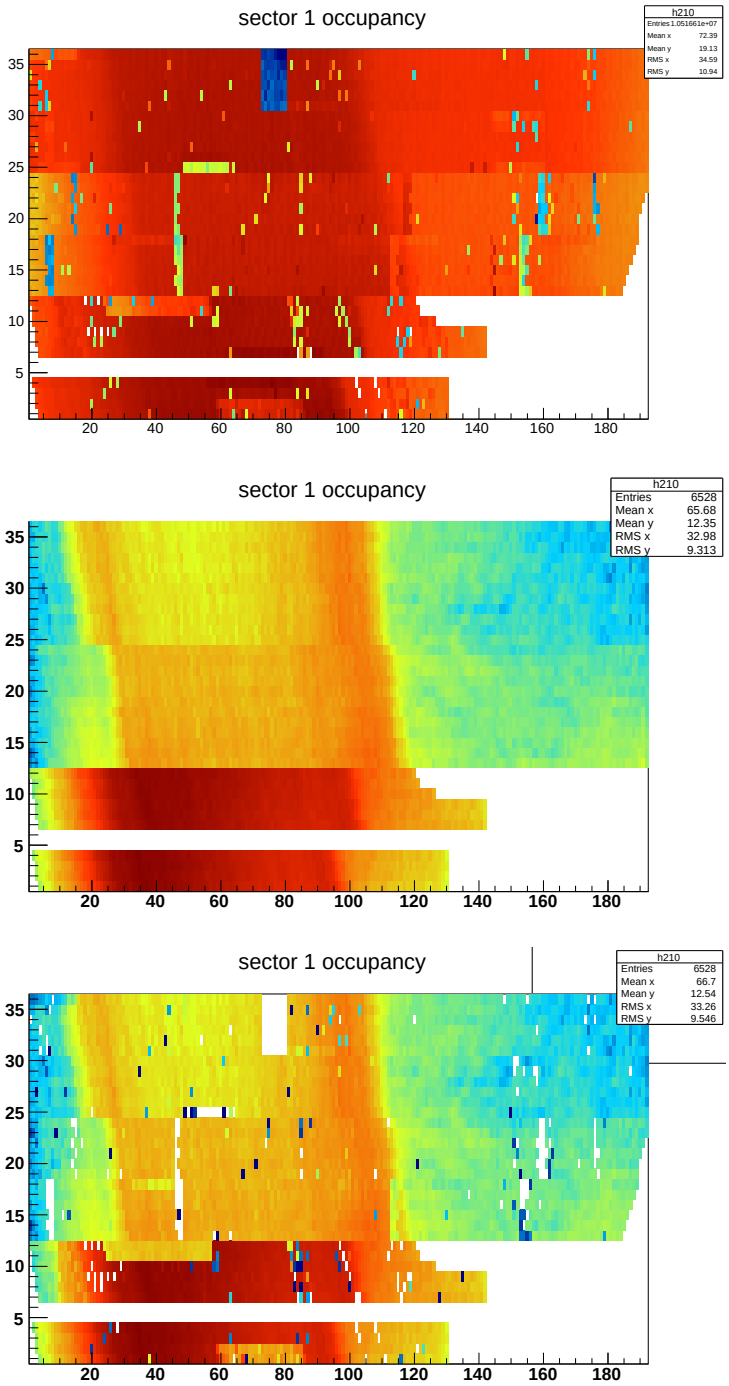

Figure 5.16: Drift chambers occupancy (layer number vs wire number) in sector 1 for three different cases: accumulated experimental raw data (top), DVCS simulation without the drift-chambers efficiency (middle), and DVCS simulation taking into account the drift-chambers efficiency (bottom). One sees that the data are well reproduced by the simulation after taking into account the inefficiencie of the wires. As an example, the block of inefficient wires in the last six layers of the region 3 (from layer 31 to 35) is well reproduced by the simulation. The fact that the occupancy is 0 for these wires is due to the fact that their efficiency is less than 1% in the data.

Background merging

During the data acquisition, Moller electrons or accidental events within TDC windows can leave signals in the detectors and create background noise. This reduces the efficiency of the reconstruction and needs to be taken into account in the normalisation of the data. The level of the background noise depends on the beam current that has been used during the experiment. The higher the beam current is, the higher the background noise is. An increase of the beam current leads to a linear decrease of the reconstruction efficiency, as can be seen in Fig. 5.17. A method to account for these background effects

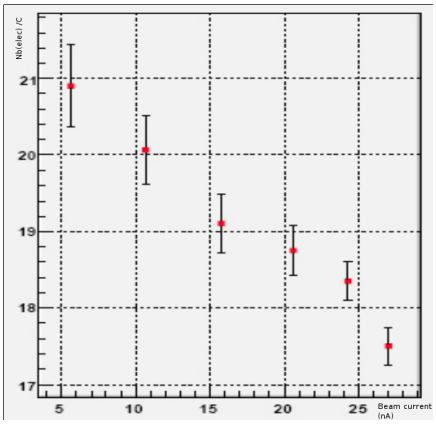

Figure 5.17: Number of electrons normalized to the Faraday Cup charge (Nb_{elec}/C) as a function of beam current (nA). The number of reconstructed electrons decreases linearly as a function of the beam current. The figure is extracted from Ref. [Yur12].

is to add background events taken from data into the simulated events.

During the e1-DVCS2 experiment, the so-called Faraday cup trigger has been created to allow a description of the background. It is a random trigger that takes snapshots of the detector state with a rate proportional to the beam current.

The background merging procedure has been described first in Ref. [Yur12]. It consists of four different stages:

- Extraction of the Faraday cup trigger (bit 8) events from raw data. All the ADC/TDC information from all the detectors banks (EC, SC, CC ...) are collected with respect to the trigger bit number. Then, to compare real data with simulations, we proceed to ADC/TDC corrections which consists in the second stage.

- In real data, the record in ADC value is "pedestal + signal" which is then converted in a physical quantity with the use of calibration coefficients (gains) which are specific to every channel. In the MC the record in ADC number is "signal" only and the pedestal is taken to be 0. Calibration coefficients are not changing from channel to channel. So these differences have to be taken into account in order to merge them. One has to subtract the pedestal from the data and to scale it with Gain(chid)/GainMC for every channel id as:

$$NewADC(chid) = [OldADC(chid) - Ped(chid)] \times \frac{Gain(chid)}{GainMC} \tag{5.2}$$

- For real data, the TDC slope was 100 ps per TDC channel. This means for instance that if TDC=300, it corresponds to 30 ns. The TDC for the MC had 50 ps per 1 TDC channel. TDC distributions have been studied [Yur12] for all detectors for MC and data in order to find some empirical offsets to correct the differences.

- Production of 1300 files with approximately 11000 events each.

The background files have been introduced into the simulations by mixing a simulated event with a background event. Each BOS banks (EC, CC, SC, DC, IC) of the simulated event is merged with the corresponding bank of the background event. Elastic simulations have been performed to evaluate the impact of the background merging. It was found that the background effects reduce the reconstruction efficiency by approximately 6%.

Reconstruction

The transformation of the raw data from the ADC/TDC signals to physical quantities is carried out by the reconstruction program RECSIS. Events reconstruction in CLAS consists in the identification of charged and neutral particles along with the computation of their 4-momenta.

Using the event start time from the accelerator RF signal to determine the beam bunch associated with the event, RECSIS reconstructs first the events of EC and IC. Then in a first stage, the DC reconstruction (the so-called Hit-Based Tracking) uses the spatial information of the three regions of DC to track the possible candidates and reject the others. A lookup table is used to find groups of hits that are consistent with a track traversing the three regions. Finally, the reconstruction of the time of flight is performed using the SC information, and the number of photo electrons is calculated for CC. A first identification of the particles is performed by combining the information of all detectors.

In a second stage, a more precise reconstruction of the charged particles is performed. For each charged particle passing through a DC cell, the Time-Based Tracking uses the drift time (TDC information) and converts it into the DOCA (distance-of-closest-approach). Using this distance from the wire, fits are applied to reconstruct precisely the trajectory.

Simulations results

Fig. 5.18 shows the comparison of the simulations with the data for the four distributions Q^2, x_B, $-t$ and Φ (normalized with the same number of events). The simulations reproduce the data with a good level of precision.

We show in Fig. 5.19 a comparison between data and simulations of the ϕ distributions as a function of θ for the three final state particles e, p and γ. In particular one can notice that the low-efficiency regions described in Sec. 4.1 are well reproduced by our simulations. At the end of the simulation chain, we have observed a small discrepancy at small θ for the electron distribution. To remove this region, we require in the following $\underline{\theta_e > 21^\circ}$.

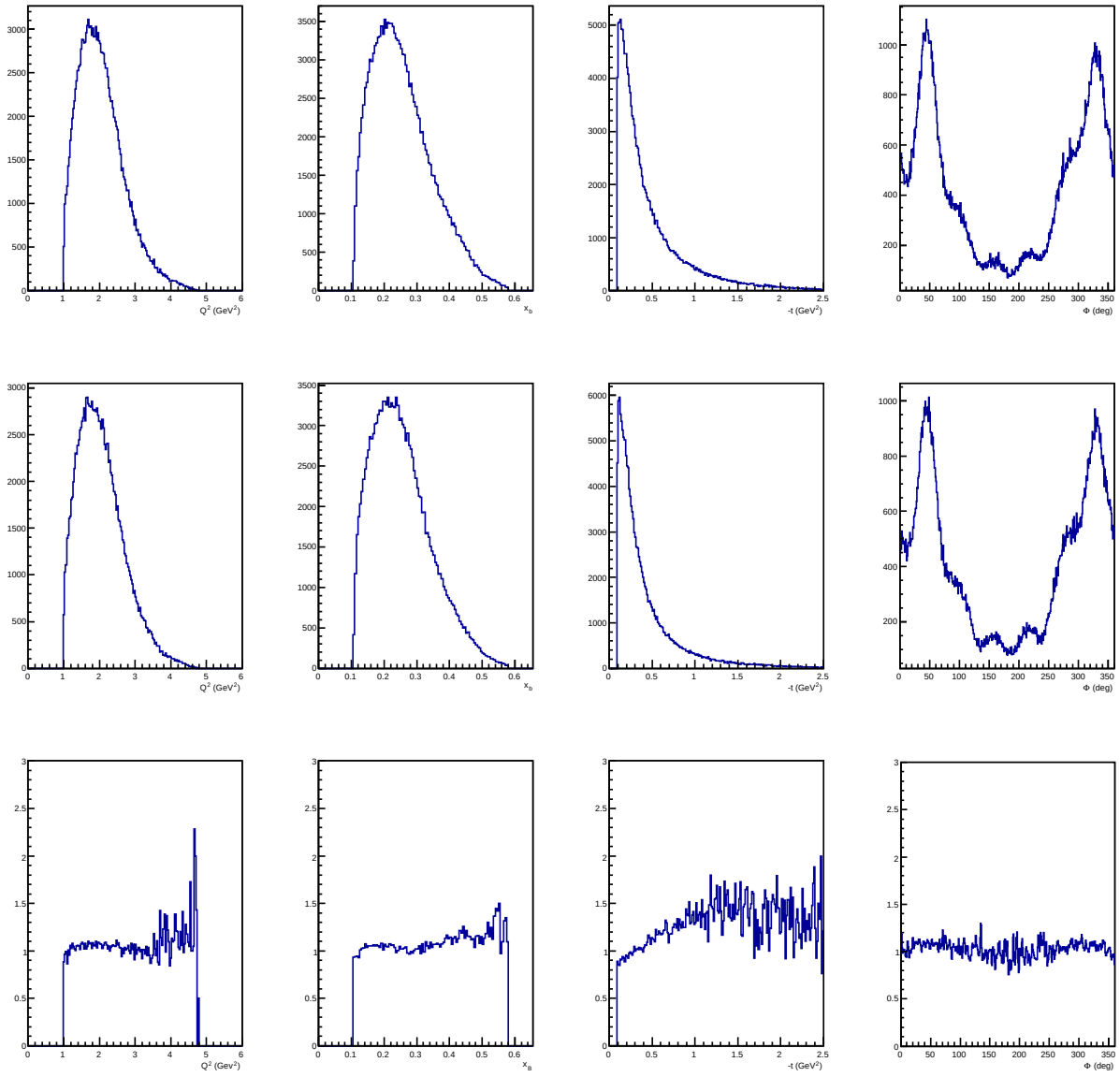

Figure 5.18: Comparison of the distributions Q^2, x_B, $-t$ and Φ for data (top panels) and simulations (middle panels). The bottom panels correspond to the ratio between data and simulations, showing a good agreement.

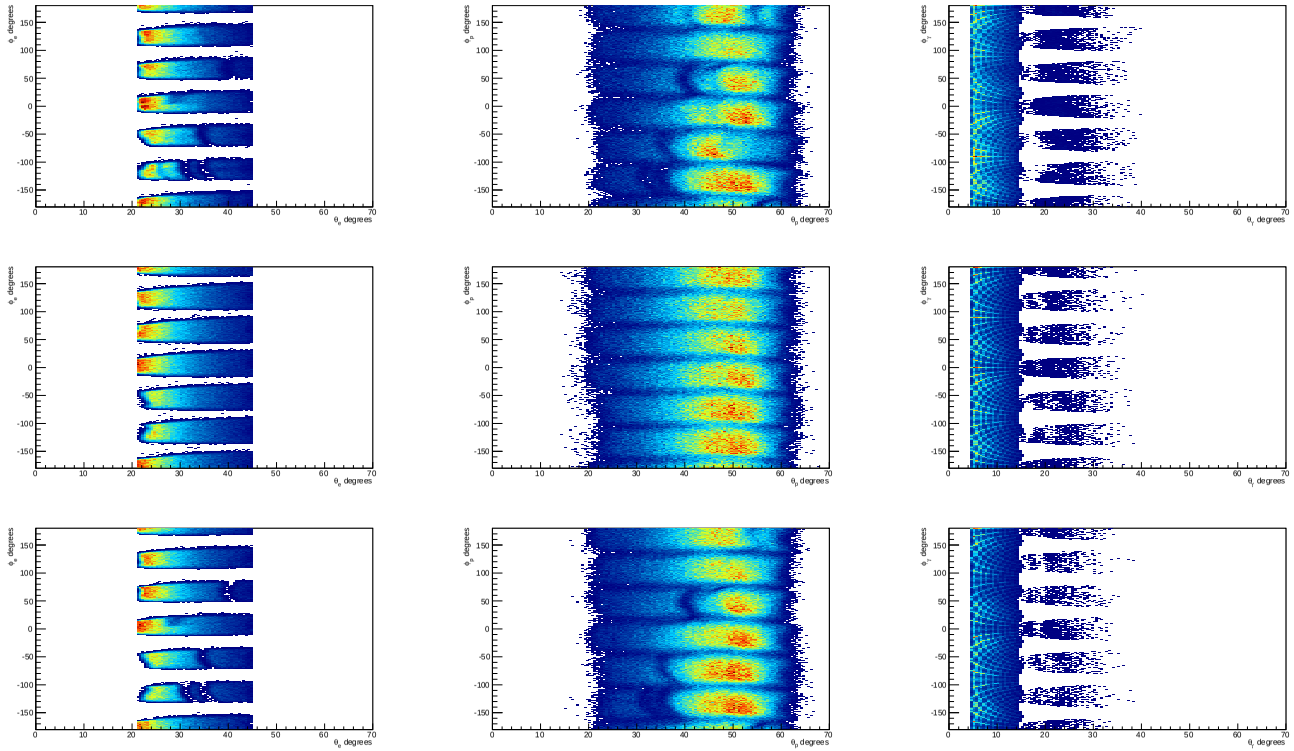

Figure 5.19: Comparison of the ϕ distributions as a function of θ for the electrons (left), protons (middle) and photons (right). Data are shown in the top row. Simulation without the fiducial cuts are shown in the middle row. The simulations result with all the fiducial cuts and exclusivity cuts included is shown in the bottom row.

Computation of the bin by bin acceptance

Using the results of the simulations, we can proceed and computate the acceptance for the DVCS cross-section normalization. It is defined for each quadri-dimensional (Q^2, x_B, $-t$, Φ) bin as:

$$Acc|_{bin} = \frac{Rec|_{bin}}{Gen|_{bin}} \tag{5.3}$$

where $Gen|_{bin}$ is the total number of $ep\gamma$ events generated within the bin, and $Rec|_{bin}$ is the number of $ep\gamma$ events reconstructed per bin.

Our acceptance takes into account the correlation between the three particles e, p, γ of our final state. In Fig. 5.20, we show the distributions of θ as a function of Φ for the three particles in the first (Q^2, x_B) bin. While the electrons are bounded within a certain θ range (limited by the Q^2 bin), one can notice that the protons tend to be emitted at smaller θ as $-t$ increases. Conversely, the DVCS photons are emitted at higher polar angle as $-t$ increases. The acceptance really depends on the photons. Firstly, they can not be detected under $\approx 5°$, so that there is no data at small Φ in some t-bins (the first t bins of the photon distribution clearly show this correlation). Secondly, one can observe that in the high-t region we have a discontinuity in the distributions around $\Phi = 180°$. The main reason is that it corresponds to the transition between the IC calorimeter that detects photons up to $\approx 15°$, and the EC that detects photons from $\approx 17 - 18°$ due to the IC shadow.

We show in Fig. 5.21 the CLAS acceptance for the 12 t bins of the bin 2 in (Q^2, x_B). All the (Q^2, x_B) bins can be found in Appendix D. It goes from 15 to 25%. The "up-and-down" structure of the acceptance reflects the CLAS geometry with its six sectors. Our acceptance drops to zero in the low-Φ region because it is highly correlated to the low-θ_γ region where there is no detector coverage.

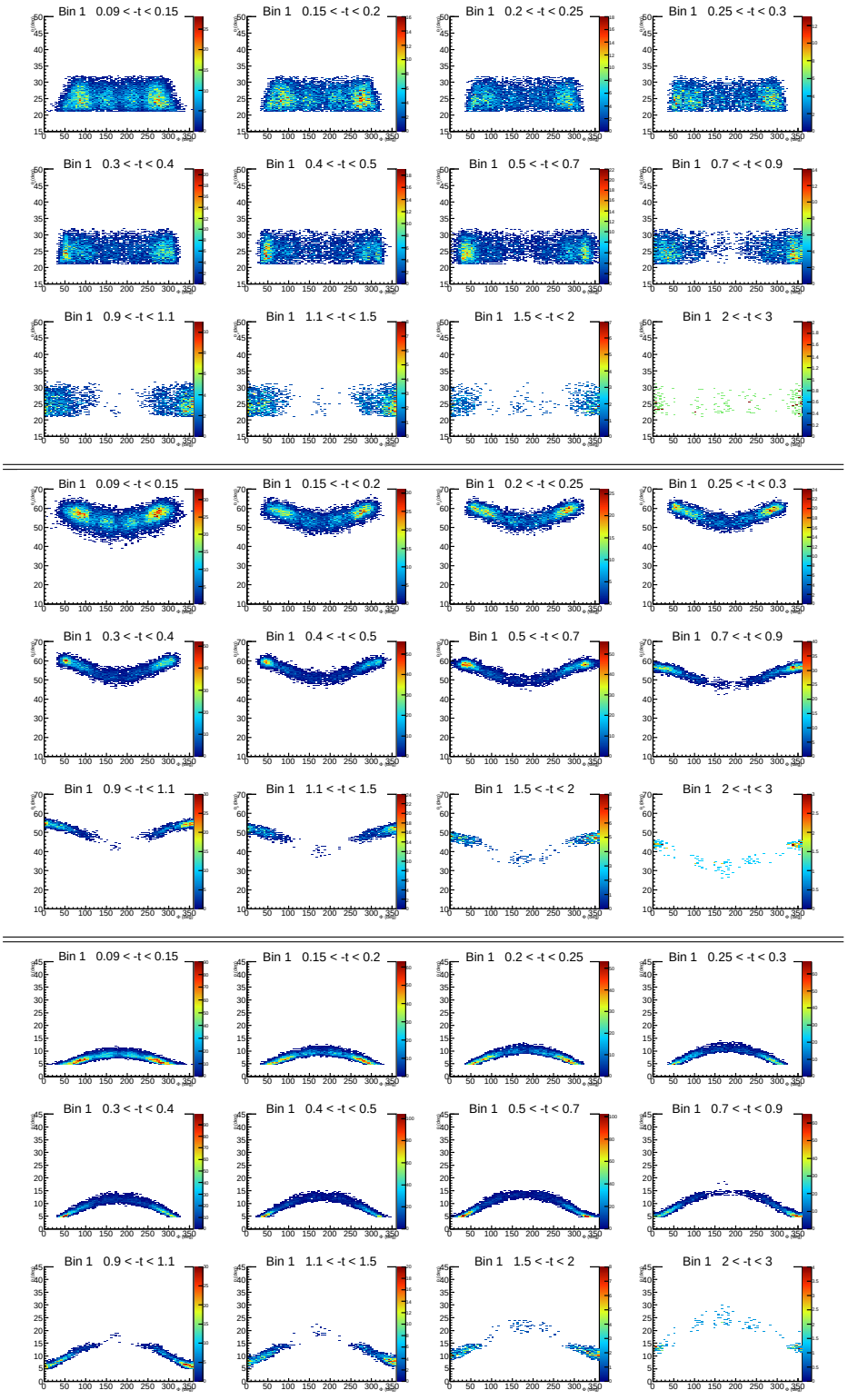

Figure 5.20: The distributions θ vs Φ for the three final state particles: e (top), p (middle) and γ (bottom). The distributions are shown for the 12 t bins of the second bin in (Q^2, x_B).

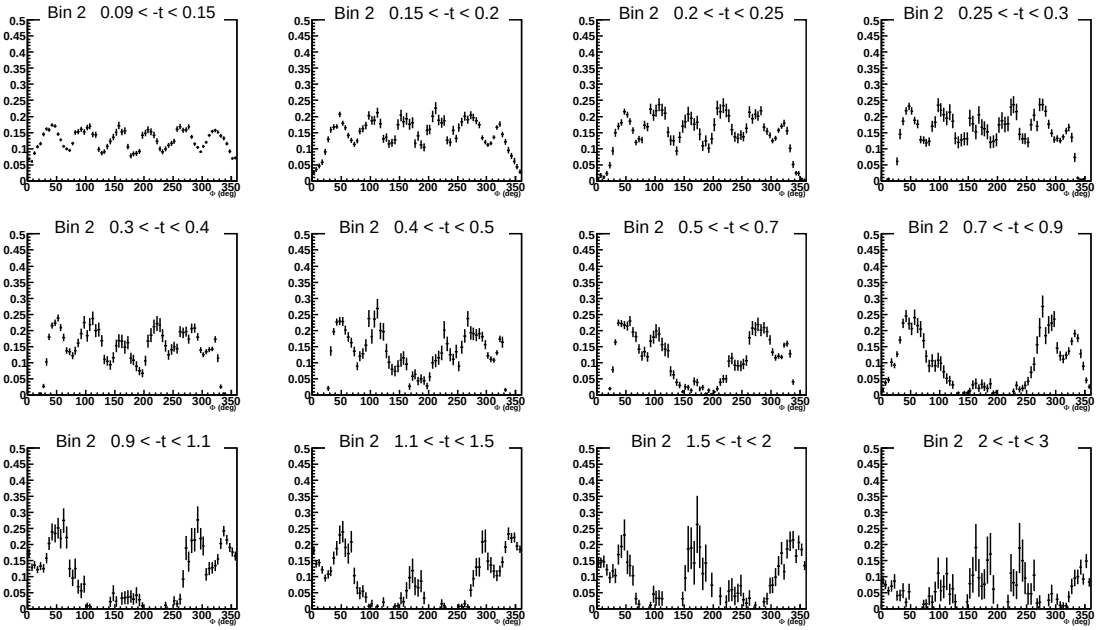

Figure 5.21: CLAS acceptance plotted as a function of Φ for the 12 t-bins of the (Q^2, x_B) bin 2.

5.3.5 Luminosity

We describe now the integrated luminosity factor L_{int} that is used to normalize the cross section. This quantity is defined as:

$$L_{int} = \eta_{target} \frac{Q_{int}}{q_e} \tag{5.4}$$

where η_{target} is the number of atoms per cm^2 in the target, q_e is the electron charge, and Q_{int} is the integrated charge accumulated during the experiment. This integrated charge is calculated from the selection of good files that is used for the data analysis.

Runs selection in DVCS2

The whole set of the e1-DVCS2 data cannot be used for the analysis. During the data taking, the quality of the data can be corrupted due to different reason. Bad calibrations, failure of one of the sub-detectors, problems in the data acquisition, ... can affect our data and their quality. The e1-DVCS2 experiment consists of 629 runs split approximately into 30000 files. The files with incorrectly recorded Faraday-Cup readings are automatically rejected from the run selection. The quality of our data is checked by looking at the electron rate for each file. The electron rate is defined as the number of detected electrons divided by the Faraday-Cup charge integrated over the file. During the experiment, this quantity should remain approximately constant. Large deviations from this constant value are interpreted as a detector malfunction or a wrong data acquisition, and the files are removed from the analysis.

Fig. 5.22, extracted from Ref. [Say12], shows the electron rate as a function of the file number. Any file out of the 3.5-σ region is removed from the analysis.

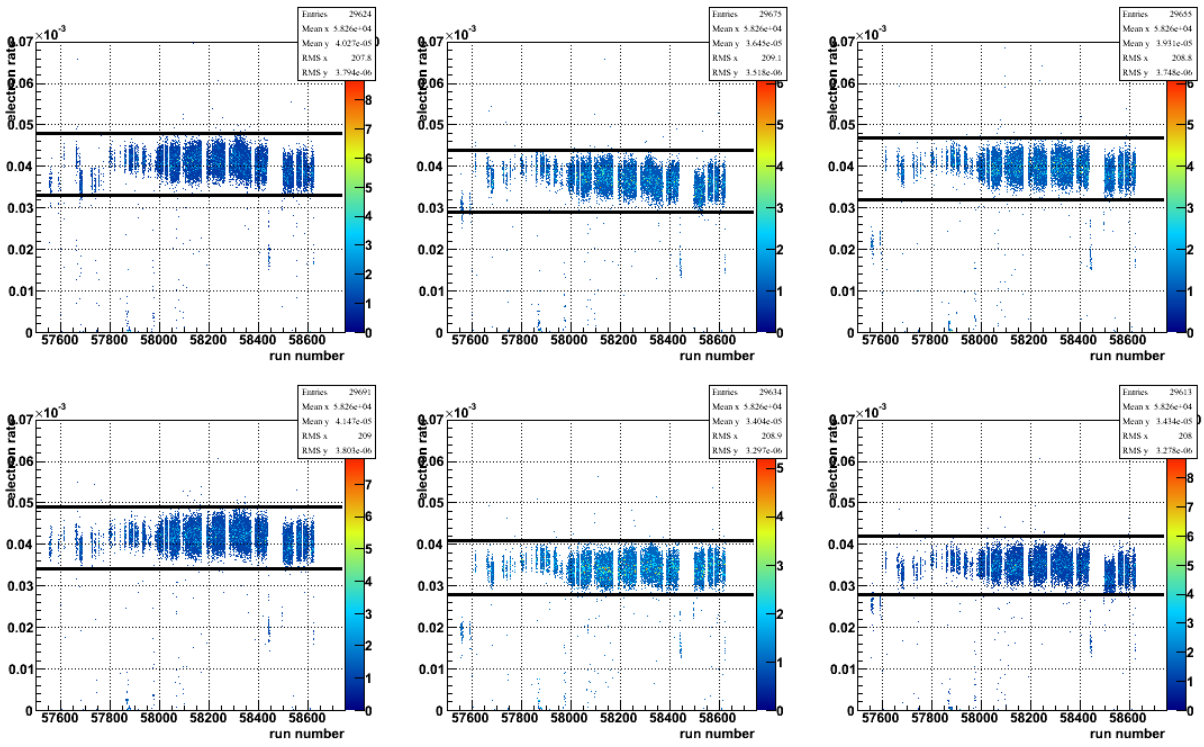

Figure 5.22: Electron rate as a function of the file number. All files out of the selection are removed from the analysis. Figure taken from Ref. [Say12].

Integrated charge

Using the list of good files described above, we can now compute the integrated charge. The measurement of the beam charge is performed by using the information of the Faraday cup. It consists of a lead cylinder weighing 4000 kg and is used to stop the electron beam and to measure the deposited charge with an efficiency of almost 100%. The charge is calculated by a capacitor that discharges when it accumulates $1/(9.264 \times 10^{12})$ of Coulomb. Every single discharge, or "click", is stored for each electron beam polarization. To compute the total charge accumulated in the Faraday cup, we sum the total number of clicks for both polarizations, that is finally converted into Coulombs with the following formula:

$$Q_{int} = [N^{\rightarrow}_{click} + N^{\leftarrow}_{click}] \times 9.264\,10^{-12}\ C \tag{5.5}$$

For the list of good files, the number of clicks is $N^{\rightarrow}_{click} + N^{\leftarrow}_{click} = 314911009416$, corresponding to an integrated charge $Q_{int} = 33993 \times 10^{-6}$ C.

Integrated luminosity

The number of atoms η_{target} per cm^2 is calculated according to the liquid hydrogen target properties as:

$$\eta_{target} = \frac{\rho\, l\ N_A}{M_H} \tag{5.6}$$

where:

- ρ is the target density: $\rho = 1.01$ g/cm^3
- l is the target length: $l = 5$ cm
- N_A is Avogadro's number: $N_A = 6.022 \times 10^{23}$ mol^{-1}
- M_H is the molar mass of the target: $M_H = 1.00794$ g/mol.

Finally, the integrated luminosity of the e1-DVCS2 experiment calculated as in Eq. 5.4 is: $L_{int} = 4.297665 \times 10^{40}$ cm^{-2}.

5.3.6 Bin volume

To compute the quadri-differential cross section $\frac{d^4\sigma}{dQ^2 dx_B dt d\Phi}$, the number of events $N_{ep\gamma}$ is normalized by the size of the bins. For a full bin in Q^2, x_B, t, and Φ, one has the volume $V = \Delta Q^2 \Delta x_B \Delta t \Delta \Phi$, i.e the product of the four bin widths. However, the hypervolume V is limited by the acceptance of the detector and is reduced by the cuts we apply during the analysis. Our phase space is delimited by the following series of cuts, applied to both data and simulations (reconstructed and generated):

- $\theta_{e\gamma} > 1.95°$ and $\theta_{e'\gamma} > 1.95°$: meant to suppress in the simulations and in the data the Bethe-Heitler singularities that diverge in these regions.
- $-t > t_{min}$: the squared momentum transfer t possesses a minimal value that needs to be implemented in the definition of our volumes. t_{min} depends on both Q^2 and x_B and is defined as:

$$t_{min} = \frac{Q^2\left[2(1-x_B)(1-\sqrt{1+\frac{4M_p x_B^2}{Q^2}}) + \frac{4M_p x_B^2}{Q^2}\right]}{4\,x_B(1-x_B) + \frac{4M_p x_B^2}{Q^2}} \tag{5.7}$$

- $\theta_{e'} > 21°$ and $\theta_{e'} < 45°$: the lower cut is needed to select the region where there is agreement between data and simulations. The latter is due to the EC acceptance.
- $\theta_p > 20°$: this cut is due to the fact that no protons are detected below that angle.
- $W > 2$ GeV: to be out of the resonance regions.
- $p_e > 0.8$ GeV: minimal momentum value required for the electrons.
- $\theta_\gamma > 4.77°$: the minimum polar-angle value for the photon detection is determined removing the first ring of crystals in IC. θ_γ is related to Φ via the formula:

$$\cos(\theta_\gamma) = \cos(\Phi)\sin(\theta_{\gamma *})\sin(\theta_{\gamma\gamma *}) + \cos(\theta_{\gamma *})\cos(\theta_{\gamma\gamma *}) \tag{5.8}$$

  where $\theta_{\gamma *}$ and $\theta_{\gamma\gamma *}$ are respectively the virtual-photon angle and the angle between the real photon and the virtual photon (see Fig. 5.10). Therefore the cut that we apply on θ_γ affects the Φ distributions. The effect of this cut can be seen in Fig. 5.23.

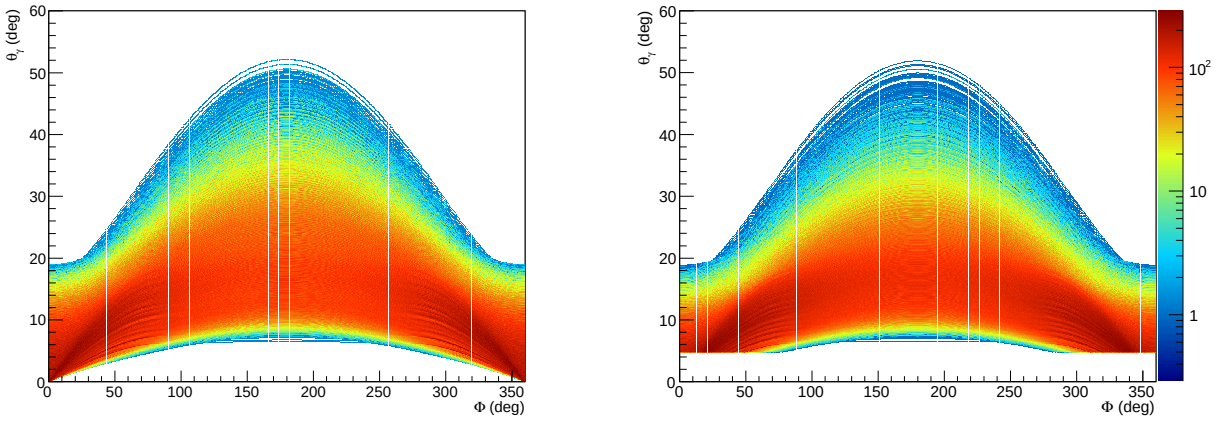

Figure 5.23: Comparison of θ_γ as a function of Φ with (right) and without (left) the θ_γ cut, integrated over all kinematics. Cutting at $\theta_\gamma > 4.77°$ removes data for $\Phi \approx 0°$ and $\Phi \approx 360°$.

As a results of these cuts, some bins are only partially filled and the effective size of the bins V_{eff} is generally smaller than V. The effective size of the bins needs to be calculated after the application of our cuts. To calculate these truncated volumes, we have applied the following procedure:

- Each bin width is divided into 50 parts. Within each quadri-dimensional bin (Q^2, x_B, t, Φ), the size of the small hyper-volumes is therefore defined as: $V_s = \frac{\Delta Q^2}{50}\frac{\Delta x_B}{50}\frac{\Delta t}{50}\frac{\Delta \Phi}{50}$. The initial hyper-volume V is therefore divided into 6.250.000 small hyper-volumes V_s.
- In each bin of volume V, we calculate the number N_s of small bins of volume V_s that are defined within our cuts.
- The effective volume V_{eff} used for the cross section normalization is computed for each bins (Q^2, x_B, t, Φ) as the number of small hyper-volume multiplied by its size: $V_{eff} = N_s \times V_s$.

We show in Fig. 5.24 an illustration of the method in the 2-dimensional plane (Q^2, x_B), which consists in this case to compute the sum of the small squares that are defined within our bins.

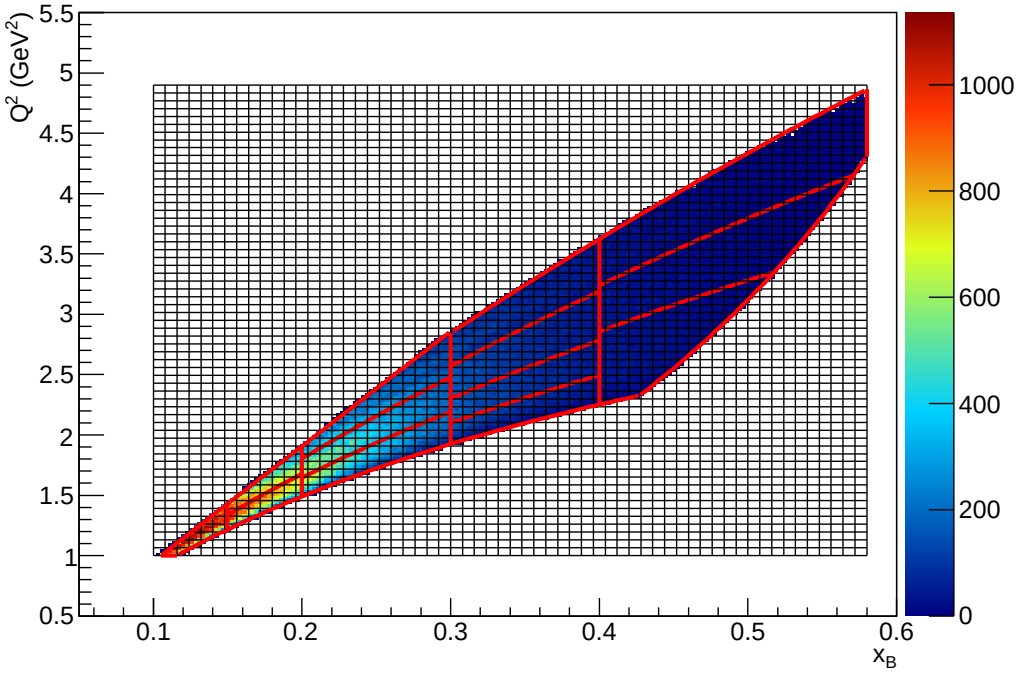

Figure 5.24: Illustration of the calculation of the effective volume V_{eff} in the plane (Q^2, x_B). The size of the small cubes is not to scale. We sum the number of the small volumes that are within our cuts to find the volume of each effective quadri-dimensional bins. This procedure is extended to the variables t and Φ.

Fig. 5.25 shows the results of the effective volume computation for our 12 t-bins of the second (Q^2, x_B) bin as defined in Table. 5.1. The results of the 12 other bins in (Q^2, x_B) are presented in Appendix E. The volume of the bins is clearly reduced at low Φ because of the θ_γ cut.

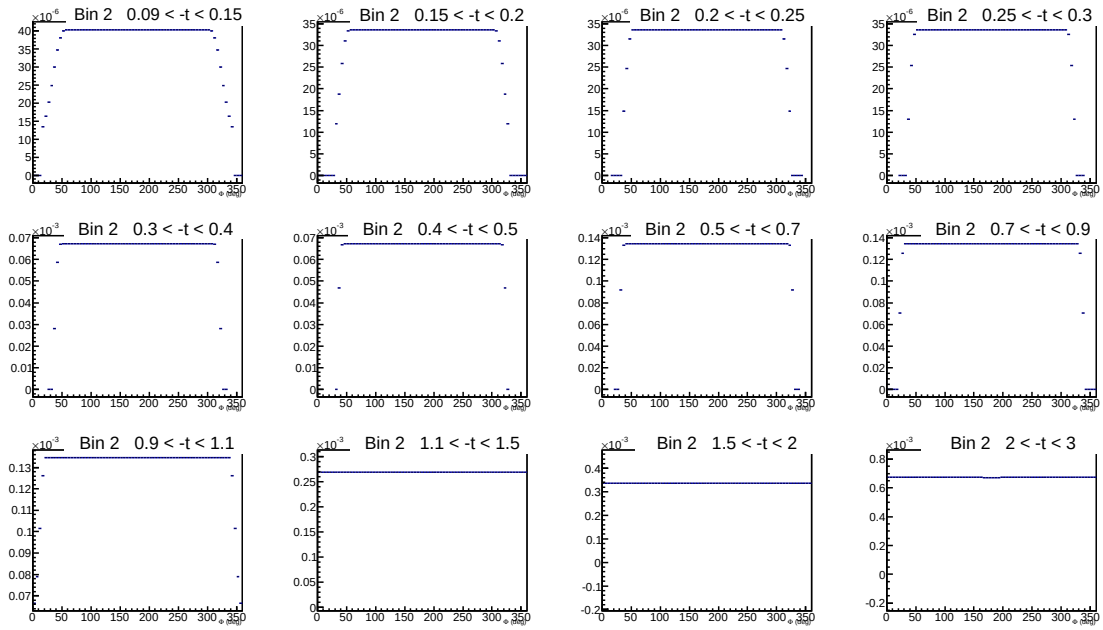

Figure 5.25: Effective bin volume ($\mathrm{GeV}^4\mathrm{rad}$) as a function of Φ for the 12 t bins of the (Q^2, x_B) bin 2.

5.3.7 Radiative corrections

The radiative corrections of electron-nucleon scattering can be calculated with a high level of precision. The Born term of the DVCS process consists of one photon exchange (the so-called handbag diagram). However, the experimental cross section that we measure contains radiative effects. In this section, we will describe the method to compute the radiative corrections in order to allow a comparison between theory and experiment. We want to correct the experimental cross section so that it corresponds to the Born term of the theory.

The radiative corrections of lepton-nucleon scattering are calculated using perturbative theory with the small electromagnetic coupling constant $\alpha_e \approx \frac{1}{137}$. The radiative corrections have two natures: they can be virtual or real. The virtual radiative corrections imply vertex (Fig. 5.26 (a)), self energy (Fig. 5.26 (b)) and vacuum corrections (Fig. 5.26 (c)). The final state is identical to the DVCS final state: all these processes interfere coherently. The real radiative corrections imply the emission of a real photon by either the incoming or the outgoing electron. By emitting an additional real photon, the kinematics (Q^2, x_B) changes and the final state ($ep\gamma\gamma_{rad}$) interferes incoherently with the DVCS.

In the following, we make the approximation that the radiative corrections to the DVCS process are to the ones of the elastic process. This is correct at a few percent level, following Ref. [ea00a]. Some of the radiative processes are shown in Fig. 5.26, where only the diagrams for the lepton side and for the vacuum polarization are displayed. The corrections for the proton side depend on a model to describe the internal structure of the proton. The proton current was taken to have the usual on-shell form, and elastic form factors were included in the calculations. The proton corrections are very small because the probability to radiate a photon is inversely proportional to the mass of the particle.

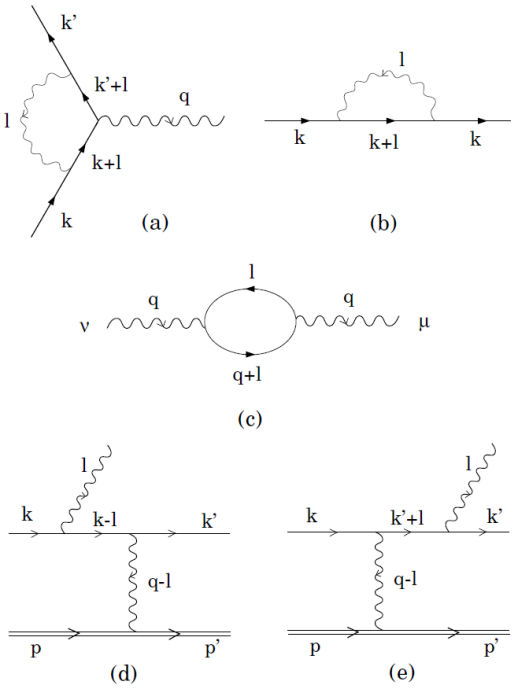

Figure 5.26: First-order virtual and real radiative processes: (a) vertex diagram, (b) lepton self-energy diagram, (c) photon-polarization diagram, (d) and (e) real-photon emission contributions to elastic lepton-nucleon scattering. Figure extracted from Ref. [ea00a].

The experimental cross section can be expressed in terms of the Born cross section, corrected for the radiative effects. These have been calculated in Ref. [ea00a], and the correction factor can be written as:

$$\sigma_{exp} = \sigma_{Born} \times \frac{e^{\delta_{vertex}+\delta_r+\delta_1+\delta_2}}{(1-\delta_{vac}/2)^2} \tag{5.9}$$

where δ_{vertex} is the vertex radiative correction:

$$\delta_{vertex} = \frac{\alpha}{\pi}\left[\frac{3}{2}ln\left(\frac{Q^2}{m_e^2}\right) - 2 - \frac{1}{2}ln^2\left(\frac{Q^2}{m_e^2}\right) + \frac{\pi^2}{6}\right] \tag{5.10}$$

δ_r the real radiative correction:

$$\delta_r = \frac{\alpha}{\pi}\left\{ln\left(\frac{(\Delta E)^2}{EE'}\right)\left[ln\left(\frac{Q^2}{m_e^2}\right) - 1\right] - \frac{1}{2}ln^2\left(\frac{E}{E'}\right) + \frac{1}{2}ln^2\left(\frac{Q^2}{m_e^2}\right) - \frac{\pi^2}{3} + Sp\left(cos^2\frac{\theta_e}{2}\right)\right\} \tag{5.11}$$

and δ_{vac} the vacuum photon polarization:

$$\delta_{vac} = \frac{\alpha}{\pi}\frac{2}{3}\left\{-\frac{5}{3} + ln\left(\frac{Q^2}{m_e^2}\right)\right\} \tag{5.12}$$

In these equations, E is the beam energy, E' and θ_e are respectively the energy and the polar angle of the outgoing electron, ΔE is the maximum energy loss of the electron, and $Sp()$ is the Spence function ($Sp(x) = -\int_0^x dt\frac{ln(1-t)}{t}$). The terms δ_1 and δ_2 contain the corrections for the proton side and can be found in Refs. [ea00a, MT00].

The radiative term δ_r is responsible for the radiative tail that one can observe in the missing-mass or missing-energy spectra. As one can see in Eq. 5.11, δ_r depends on ΔE. This latter term is the parameter that needs to be adapted to experimental conditions. It is defined as $\Delta E = \frac{M(epX)}{2}$, where $M(epX)$ is the missing mass on which we have applied a cut for the exclusivity selection. It depends on the data analysis and on the detector resolution. By applying this cut, we have removed events from the radiative tail. The number of these events can be precisely calculated using the ΔE dependance of δ_r. We can therefore compensate the loss of radiative events and eventually find the Born cross section that does not depend on the $M(epX)$ cut. In this analysis, we applied a cut on $|MM^2_{epX}| < 0.3$ GeV^2, which corresponds to $\Delta E = 0.27$ GeV in the center-of-mass system of $\gamma + \gamma_{rad}$.

The radiative effects have been computed according to Eq. 5.9 for each central value of Q^2 in our 13 bins. We correct our experimental cross section for radiative effects so that we can compare with the theory, that includes only the Born term. It is done according to the following formula:

$$\sigma_{exp} = \sigma_{Born} \times (1 + Rad_{tot}) \rightarrow \sigma_{Born} = \frac{\sigma_{exp}}{1 + Rad_{tot}} = \sigma_{exp} \times F_{rad} \tag{5.13}$$

The results for Rad_{tot} and F_{rad} are shown in Table 5.3. The results show that Rad_{tot} is smaller than 1, so that the experimental cross section is always smaller than the Born cross section. In order to compare with the Born term of the theory, we therefore mutliply σ_{exp} by F_{rad} which has the effect to increase the experimental cross section by approximately 17 to 19%.

	$< Q^2 >$ (GeV^2)	Rad_{tot}	F_{rad}
Bin 1:	1.194	-0.148	1.174
Bin 2:	1.450	-0.150	1.176
Bin 3:	1.592	-0.151	1.178
Bin 4:	1.813	-0.152	1.180
Bin 5:	2.008	-0.154	1.182
Bin 6:	2.273	-0.155	1.184
Bin 7:	2.191	-0.155	1.180
Bin 8:	2.391	-0.156	1.185
Bin 9:	2.673	-0.157	1.187
Bin 10:	3.016	-0.159	1.189
Bin 11:	2.749	-0.158	1.187
Bin 12:	3.319	-0.160	1.190
Bin 13:	3.858	-0.162	1.193

Table 5.3: Radiative corrections computed for the 13 central values Q^2 of our bins.

5.3.8 π^0 contamination subtraction

To compute the true number of DVCS events $ep \to ep\gamma$, one has to subtract the contamination from the $ep \to ep\pi^0 \to ep\gamma\gamma$ events. Indeed, when one of the two photons of the pion decay escapes the detection, the pion channel can mimi a DVCS candidate. For each bin, the true number of DVCS events N_{DVCS} corresponds to the number of $ep\gamma$ events that we have measured $N_{ep\gamma}$ minus the number of π^0 events for which one of the two photons has not been detected. It can be written as:

$$N_{DVCS} = N_{ep\gamma} - N_{ep\pi^0}(1\gamma) \tag{5.14}$$

The evaluation of the contamination $N_{ep\pi^0}(1\gamma)$ is performed by combining simulations and data. It is defined as:

$$N_{ep\pi^0}(1\gamma) = \frac{N^{MC}_{ep\pi^0}(1\gamma)}{N^{MC}_{ep\pi^0}(2\gamma)} \times N^{DATA}_{ep\pi^0}(2\gamma) \tag{5.15}$$

where:

- $N^{DATA}_{ep\pi^0}(2\gamma)$ is the number of $ep \to ep\pi^0$ events that have been measured experimentally, with two photons detected.
- $N^{MC}_{ep\pi^0}(1\gamma)$ is the number of simulated $ep \to ep\pi^0$ events, for which only one photon has passed the DVCS cuts.
- $N^{MC}_{ep\pi^0}(2\gamma)$ is the number of simulated $ep \to ep\pi^0$ events, for which the two photons have passed the π^0 cuts.

We now describe how these terms are determined.

Selection of the $N^{DATA}_{ep\pi^0}(2\gamma)$ events

After the selection of a good electron and a good proton, the selection of the π^0 events is performed by selecting events with at least 2 photons. Among all the photons in the event, we select the photon pair whose invariant mass is the closest to the π^0 mass (≈135 MeV). The number of events $N^{DATA}_{ep\pi^0}(2\gamma)$ is then selected by applying the following cuts:

- $|MM^2_{e\pi_0}| < M_p^2 \pm 3\,\sigma_{(MM^2_{e\pi_0})}$, the squared missing mass of the (e, π_0) system.
- $|MM^2_{ep\pi_0}| < 0 \pm 3\,\sigma_{(MM^2_{ep\pi_0})}$, the squared missing mass of the (e, p, π_0) system.
- $|MM^2_{ep}| < M^2_{\pi^0} \pm 3\,\sigma_{(MM^2_{ep})}$, the squared missing mass of the (e, p) system.
- $|ME_{ep\pi_0}| < 0 \pm 3\,\sigma_{(ME_{ep\pi_0})}$, the missing energy of the (e, p, π_0) system.
- $|MI_{\gamma\gamma}| < M_{\pi^0} \pm 3\,\sigma_{(MI_{\gamma\gamma})}$, the invariant mass of the two photons.

The effect of these cuts can be seen in Fig. 5.27.

Estimation of $\frac{N^{MC}_{ep\pi^0}(1\gamma)}{N^{MC}_{ep\pi^0}(2\gamma)}$ by simulations

The fraction of π^0 events that is mis-identified as DVCS events is determined by simulations and is equal to $\frac{N^{MC}_{ep\pi^0}(1\gamma)}{N^{MC}_{ep\pi^0}(2\gamma)}$. The event generator is based on a simplified GPD model where only the imaginary part is used and approximated to its forward limit in terms of the PDFs.

The simulation procedure has been described in Sec. 5.3 and is exactly the same for the π^0 channel.

The result of the π^0 contamination is shown in Fig. 5.28 as the ratio $\frac{N_{ep\pi^0}(1\gamma)}{N_{ep\gamma}}$ for the (Q^2, x_B) bin 2. All the (Q^2, x_B) bins can be found in Appendix F.The general tendency seems to indicate an increase of the π^0 contamination with an increase of $-t$, going from ≈ 10% to ≈ 30%. The size of the error bars is strongly correlated to the limited number of $N^{DATA}_{ep\pi^0}(2\gamma)$ events.

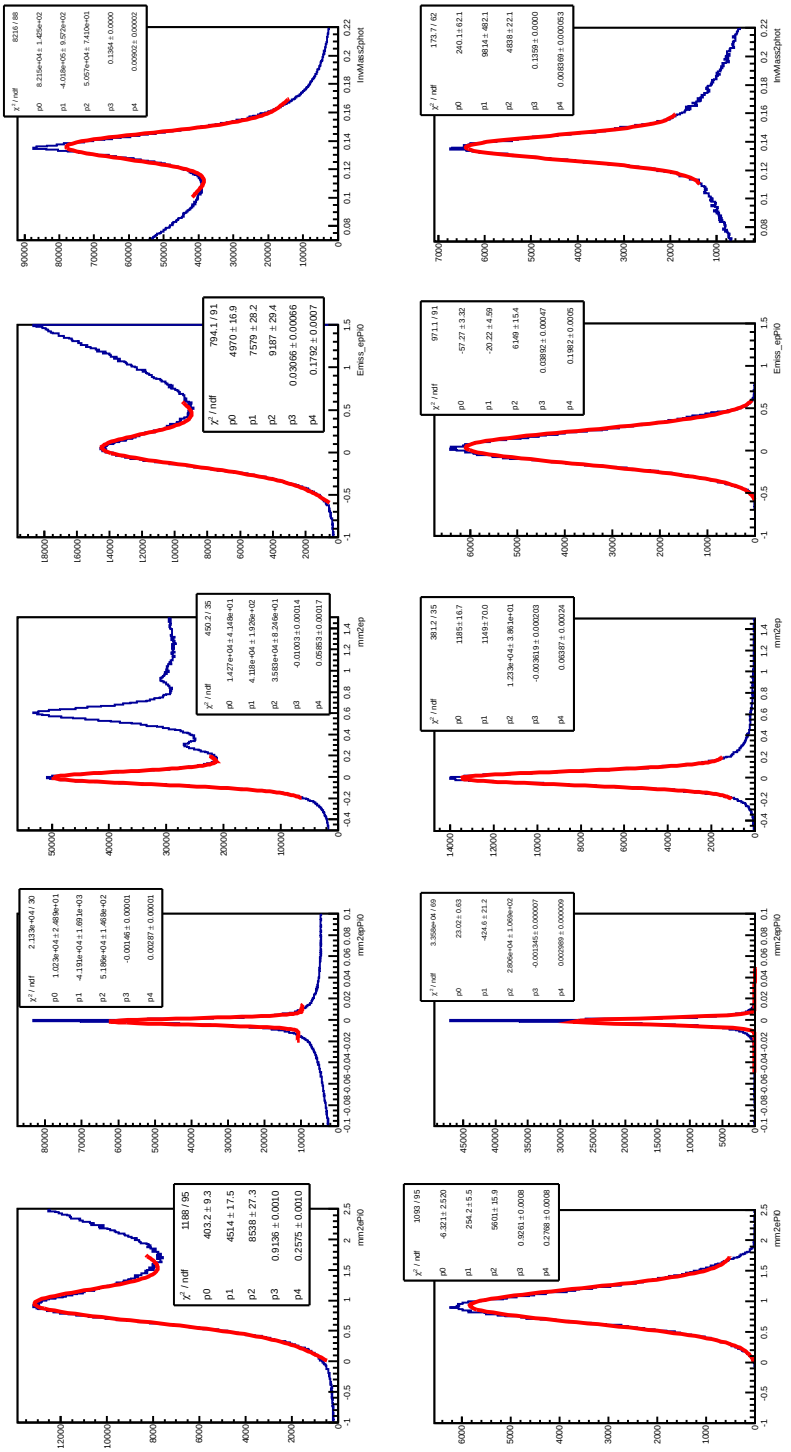

Figure 5.27: Distributions from left to right: $MM^2_{e\pi_0}$, $MM^2_{ep\pi_0}$, MM^2_{ep}, $ME_{ep\pi_0}$, $MI_{\gamma\gamma}$. The first row presents the distributions without cuts, and the second row shows the distributions after all cuts except the one on the distribution plotted. The fits have been performed with a Gaussian plus a linear background.

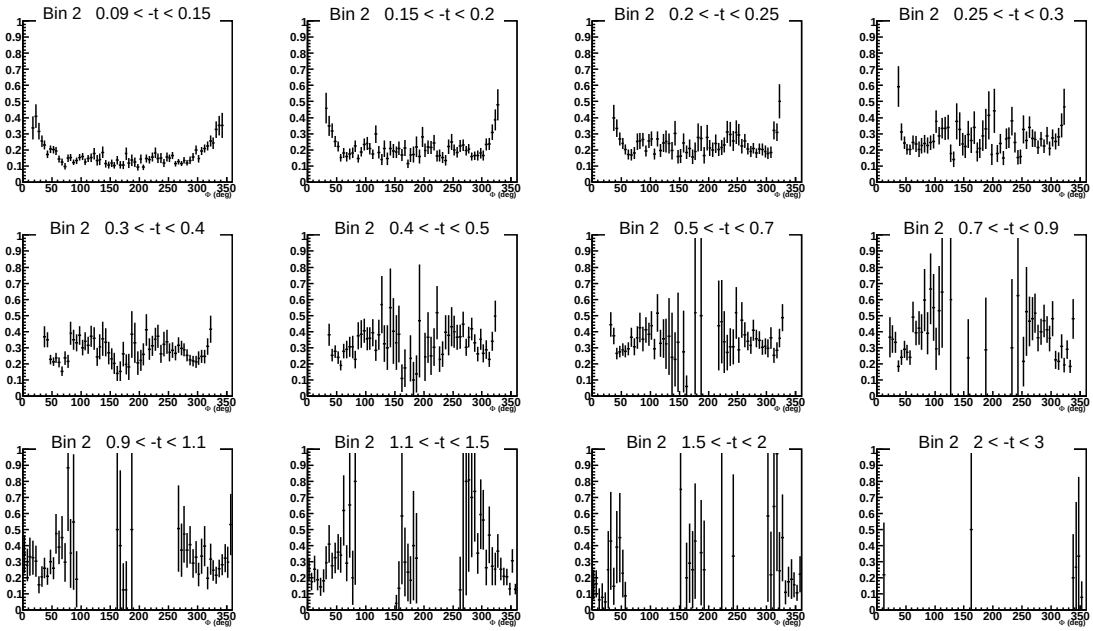

Figure 5.28: $\frac{N_{ep\pi^0(1\gamma)}}{N_{ep\gamma}}$ as a function of Φ for the (Q^2, x_B) bin 2.

5.3.9 Estimation of the uncertainties

Statistical uncertainty

As already mentioned, the DVCS cross section can be written as:

$$\frac{d^4\sigma}{dQ^2 dx_B dt d\Phi} = \frac{N_{ep\gamma} - N_{ep\pi^0(1\gamma)}}{Acc\, L_{int}\, F_{vol}} \times F_{rad} \tag{5.16}$$

Therefore, for the computation of the statistical error bars of the cross section, one has to take into account the statistical errors of:

- the number of $ep\gamma$ events $N_{ep\gamma}$ before the π^0 substraction,
- the number of $ep\gamma$ events coming from the π^0 contamination: $N_{ep\pi^0}(1\gamma) = \frac{N^{MC}_{ep\pi^0}(1\gamma)}{N^{MC}_{ep\pi^0}(2\gamma)} \times N^{DATA}_{ep\pi^0}(2\gamma)$,
- the acceptance $Acc = \frac{Rec}{Gen}$.

The relative statistical errors is then written as:

$$\frac{\Delta\sigma}{\sigma} = \sqrt{\left(\frac{\Delta N_{ep\gamma}}{N_{ep\gamma} - N_{ep\pi^0}(1\gamma)}\right)^2 + \left(\frac{\Delta N_{ep\pi^0}(1\gamma)}{N_{ep\gamma} - N_{ep\pi^0}(1\gamma)}\right)^2 + \left(\frac{\Delta Acc}{Acc}\right)^2} \tag{5.17}$$

with:

- the statistical error on the number of $ep\gamma$ events: $\Delta N_{ep\gamma} = \sqrt{N_{ep\gamma}}$
- the statistical error on the number of $N_{ep\pi^0}(1\gamma)$ events:
  $\Delta N_{ep\pi^0}(1\gamma) = N_{ep\pi^0}(1\gamma) \times \sqrt{\left(\frac{\Delta N^{MC}_{ep\pi^0}(1\gamma)}{N^{MC}_{ep\pi^0}(1\gamma)}\right)^2 + \left(\frac{\Delta N^{MC}_{ep\pi^0}(2\gamma)}{N^{MC}_{ep\pi^0}(2\gamma)}\right)^2 + \left(\frac{\Delta N^{DATA}_{ep\pi^0}(2\gamma)}{N^{DATA}_{ep\pi^0}(2\gamma)}\right)^2}$
- the statistical error on the acceptance: $\frac{\Delta Acc}{Acc} = \sqrt{\left(\frac{\Delta Rec}{Rec}\right)^2 + \left(\frac{\Delta Gen}{Gen}\right)^2}$

The statistical errors have been calculated for each quadri dimensional bin.

Systematic uncertainty

The systematic error have to be estimated and added quadratically to the statistical errors. Due to time constraints, we haven't been able to compute them. The source of our systematic uncertainties are varied. Hereafter we mention some of them, with a first estimation coming from the first part of the e1-DVCS experiment:

- the uncertainty on the computation of the acceptance. The systematic error can be computed by using a different event generator. The difference with our acceptance is used to compute bin-by-by the systematic error ($\approx 10\%$).
- the uncertainty on the π^0 background substraction. Another model can be used to computed the systematic error ($\approx 10\%$).
- the uncertainty due the the normalization factor from the elastic cross section ($\approx 5\%$).
- the uncertainty on the radiative corrections ($\approx 5\%$).
- the uncertainty on the fiducial cuts and exclusivity cuts ($\approx 1\%$).

5.3.10 Unpolarized DVCS cross section

Using Eq. 5.1, we have now all the necessary terms to extract the DVCS cross section. In Fig. 5.29, we present the results of the unpolarized DVCS cross section $\frac{d^4\sigma}{dQ^2\,dx_B\,dt\,d\Phi}$ (nbarn/GeV^4) computed for the (Q^2, x_B) bin 2, and compared (in green) to the Bethe-Heitler (BH) cross section integrated within the acceptance of 4-dimensional bins. All the (Q^2, x_B) bins can be found in Appendix G. As we showed in Sec. 2.3.4, the cross-section for the exclusive electroproduction of a photon ($eN \to eN\gamma$) receives a contribution from both the DVCS and the BH processes. It is expected that the contribution of the BH dominates almost completely the cross section in the regions where the real photon is emitted in the same direction than the incoming or the outgoing electron, which correspond to low and large Φ regions. The main contribution of the DVCS signal is in the central Φ-region.

The azimuthal decomposition of $d^4\sigma_{unp}$ can be found in Ref. [BMK02] and is expressed at leading twist (twist-2) as:

$$\frac{d^4\sigma_{unp}}{dQ^2\,dx_B\,dt\,d\Phi} = \frac{d^4|DVCS|^2}{dQ^2\,dx_B\,dt\,d\Phi} + \frac{d^4|BH|^2}{dQ^2\,dx_B\,dt\,d\Phi} + \Gamma_0 \times \Re e(A) + [\Gamma_1 - \cos(\Phi)\,\Gamma_2] \times \Re e(B) \quad (5.18)$$

where the terms A and B are combinations of CFFs defined as:

$$A = F_1\mathcal{H} - \frac{t}{4M^2}F_2\,\mathcal{E} - \xi^2(F_1+F_2)[\mathcal{H}+\mathcal{E}] \quad (5.19)$$

$$B = F_1\mathcal{H} + \xi(F_1+F_2)\tilde{\mathcal{H}} - \frac{t}{4M^2}F_2\,\mathcal{E}. \quad (5.20)$$

Here, $F_{1,2}$ are the Dirac and Pauli form factors, and $\Gamma_{0,1,2}$ are kinematic factors with a Φ-dependence coming from the electron propagators of the Bethe Heitler amplitude. The $|DVCS|^2$ term does not have a Φ-dependence at leading twist and is a bilinear combination of the CFFs. The twist-3 contribution of the interference, not written here, consists of a linear combination of the CFFs with a $\cos(2\Phi)$-dependence. The contributions in the interference terms of the CFFs $\tilde{\mathcal{H}}$ and $\mathcal{E}$ are reduced because $x_B \approx 0.2$ (proportional to ξ) and $-t \approx 0.3$ GeV^2 in our typical kinematics. As a consequence, we expect the unpolarized cross section to be mainly sensitive to the CFF $\mathcal{H}_{Re}$.

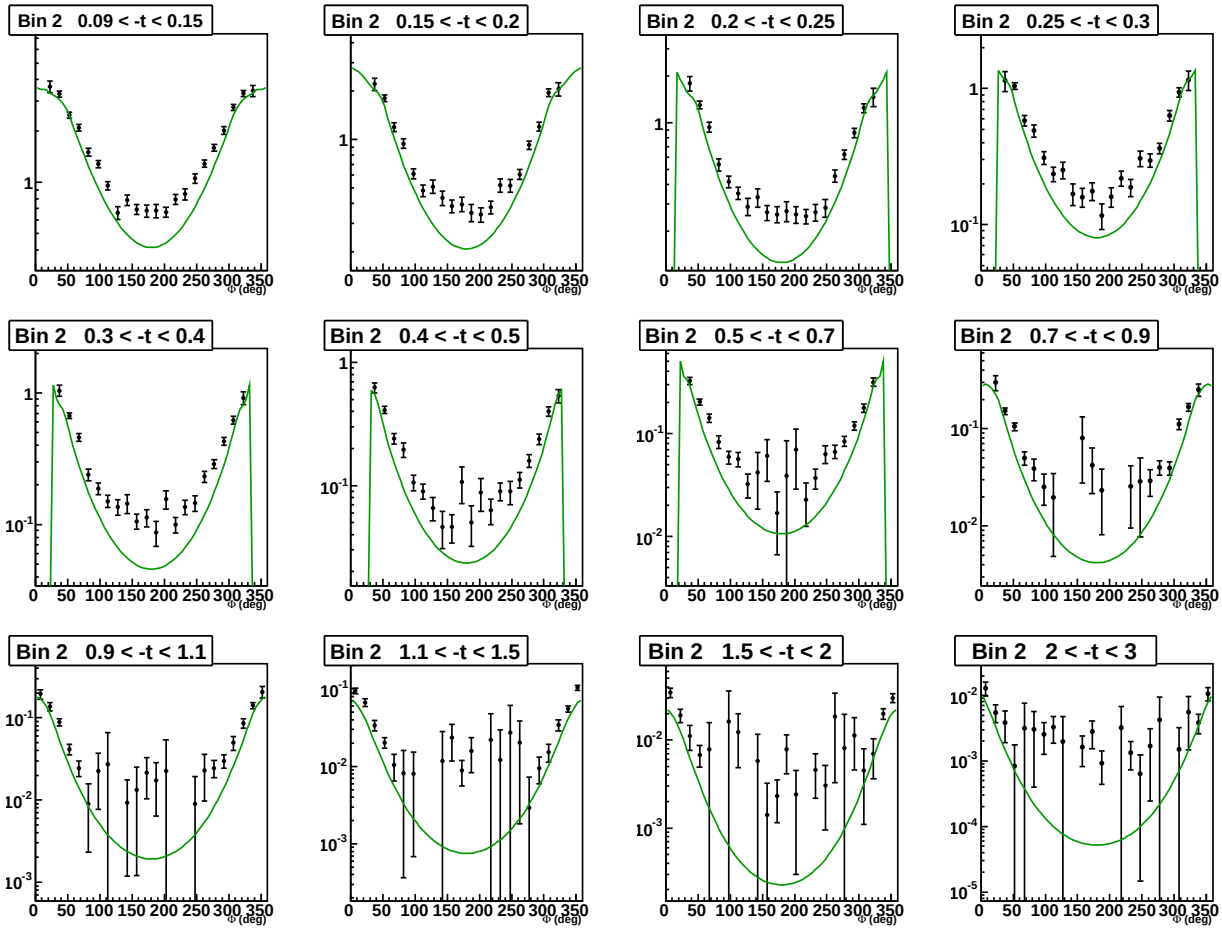

Figure 5.29: DVCS cross section (nbarn/GeV^4) as a function of Φ for the 12 t bins of the (Q^2, x_B) bin 2, compared to the BH cross-section (green) integrated over the bins size.

5.3.11 Comparison of DVCS1 and DVCS2 unpolarized cross sections

As we mentioned previously, the goal of the e1-DVCS experiment is to extract the DVCS unpolarized and polarized cross sections over a large phase space and with high precision. The data have been taken in two times. The first data set is called e1-DVCS1, and we propose in this section to compare the cross-section results of DVCS1 and DVCS2, the final goal being to merge the two sets of data.

In Fig. 5.30, we show a comparison of the cross-section distributions for the 12 t-bins of the (Q^2, x_B) bin 2. The 13 (Q^2, x_B) bins can be found in Appendix H. The first figure is the superposition of the DVCS1 (blue) and DVCS2 (red) results. One can see a really good agreement between the two data sets. The second figure shows the ratio of the DVCS1 cross section over the DVCS2 cross section. Most of the points are compatible within the error bars.

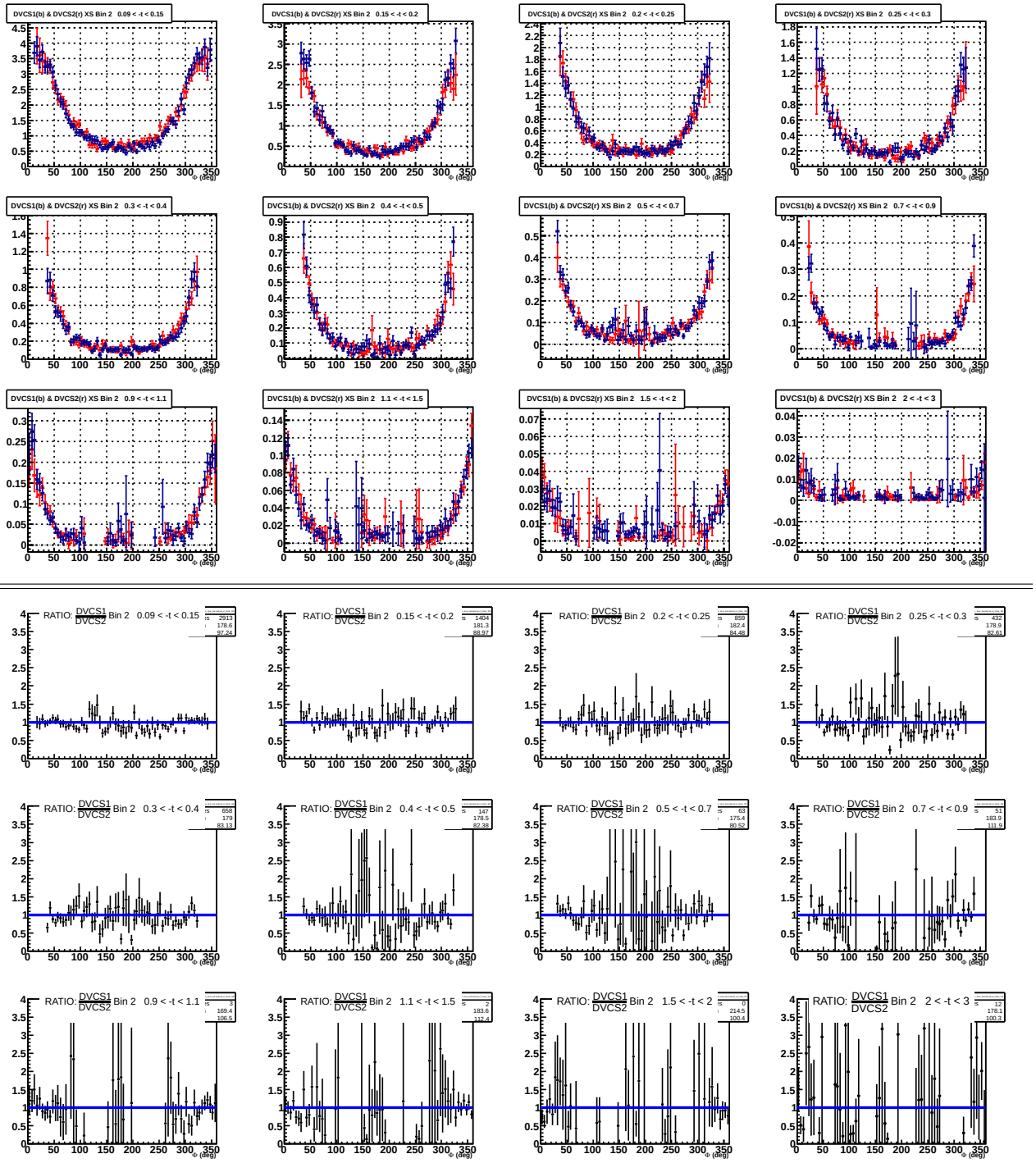

Figure 5.30: Top: Comparison of the DVCS cross section for e1-DVCS1 (blue) e1-DVCS2 experiments. The cross section are shown as a function of Φ for the 12 t-bins of the (Q^2, x_B) bin 2. Bottom: ratio of the two experimental cross sections.

Statistical approach

To compare the two DVCS cross sections, we have performed a χ^2-test to check the compatibility between the two distributions. Our binning consists of 13 bins in (Q^2, x_B) and 12 bins in t. In total, the χ^2 has been calculated for each of the 156 Φ distributions. For two binned distributions Y_1 and Y_2, the normalized χ^2 is defined as:

$$\chi^2 = \frac{1}{N_{tot}} \sum_{i=1}^{N_{tot}} \frac{[Y_1(i) - Y_2(i)]^2}{[\sigma_1^2(i) + \sigma_2^2(i)]} \tag{5.21}$$

where $\sigma_1(i)$ and $\sigma_2(i)$ are the error bars of the bin i of $Y_1(i)$ and $Y_2(i)$ respectively. We are comparing two distributions that consist of 72 bins, so the maximum number of degree of freedom N_{tot} is equal to 72. We remove one degree of freedom each time that Y_1 and Y_2 are equal to zero for a bin i.

In Fig. 5.31, we show the results of the normalized χ^2/ndf as a function of the 12 t-bin for each of the 13 bins in (Q^2, x_B). From these figures, we can see that the two distributions are in good agreement for most of the bins. However, the general trend seems to indicate that the agreement decreases at large t where the statistics is really small. Some particular cases, like the first two t-bins of the (Q^2, x_B) bin 4, show substantial deviations between the two distributions. At the moment of writing, these discrepancies are still not understood.

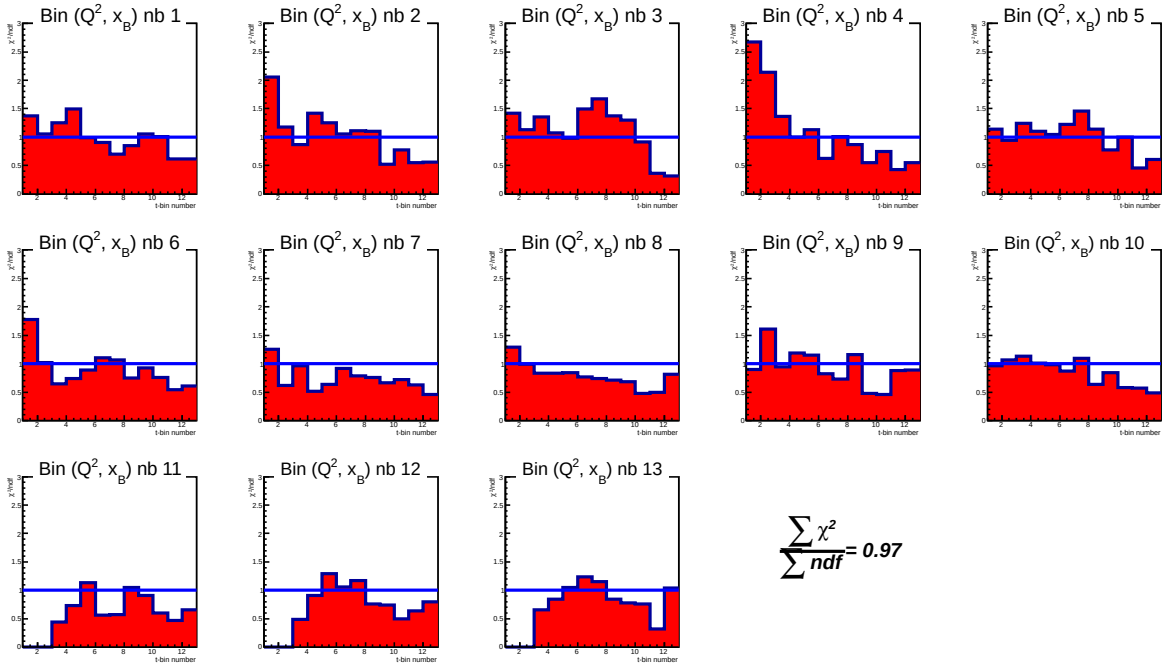

Figure 5.31: χ^2/ndf as a function of the 12 t bins, for the 13 bins in (Q^2, x_B).

The global normalized χ^2 has been computed for the 156 distributions. It was calculated as: $\frac{\sum \chi^2}{\sum ndf} = 0.97$. We conclude that the two distributions are compatible within the error bars for most of our bins.

5.3.12 Difference of polarized cross sections

The e1-DVCS experiment used a polarized electron beam. Selecting the helicity of the incident electrons, one can then extract one other obvervable: the difference of polarized cross sections σ_{pol} and the beam spin asymmetry $\mathcal{A}_{LU}$ for a longitudinaly polarized beam and a unpolarized target.

To compute these observables, one has to separate the analysis in two sets of data according to the beam helicity value. The total number of DVCS events taking into account the pion contamination (Sec. 5.3.8) and corresponding to the beam helicity state $\overrightarrow{e}$ is defined as:

$$\overrightarrow{N}_{DVCS} = \overrightarrow{N}_{ep\gamma} - \frac{N^{MC}_{ep\pi^0}(1\gamma)}{N^{MC}_{ep\pi^0}(2\gamma)} \times \overrightarrow{N}^{DATA}_{ep\pi^0}(2\gamma) \tag{5.22}$$

and the total number of DVCS events corresponding to the beam helicity $\overleftarrow{e}$ is defined as:

$$\overleftarrow{N}_{DVCS} = \overleftarrow{N}_{ep\gamma} - \frac{N^{MC}_{ep\pi^0}(1\gamma)}{N^{MC}_{ep\pi^0}(2\gamma)} \times \overleftarrow{N}^{DATA}_{ep\pi^0}(2\gamma) \tag{5.23}$$

The number of events $\overrightarrow{N}_{DVCS}$ ($\overleftarrow{N}_{DVCS}$) is normalized with the luminosity $L_{\overrightarrow{int}}$ ($L_{\overleftarrow{int}}$) which is calculated taking into account only the $\overrightarrow{e}$ ($\overleftarrow{e}$) events. Figure 5.32 shows the difference of integrated charge detected in the Faraday cup for the electrons with helicity state ($\rightarrow$) and helicity state ($\leftarrow$). The deviation from 0 is really small ($< 10^{-6}$): the number of polarized electrons $\overrightarrow{e}$ is truly comparable to the number of polarized electrons $\overleftarrow{e}$ accumulated for the e1-DVCS2 experiment.

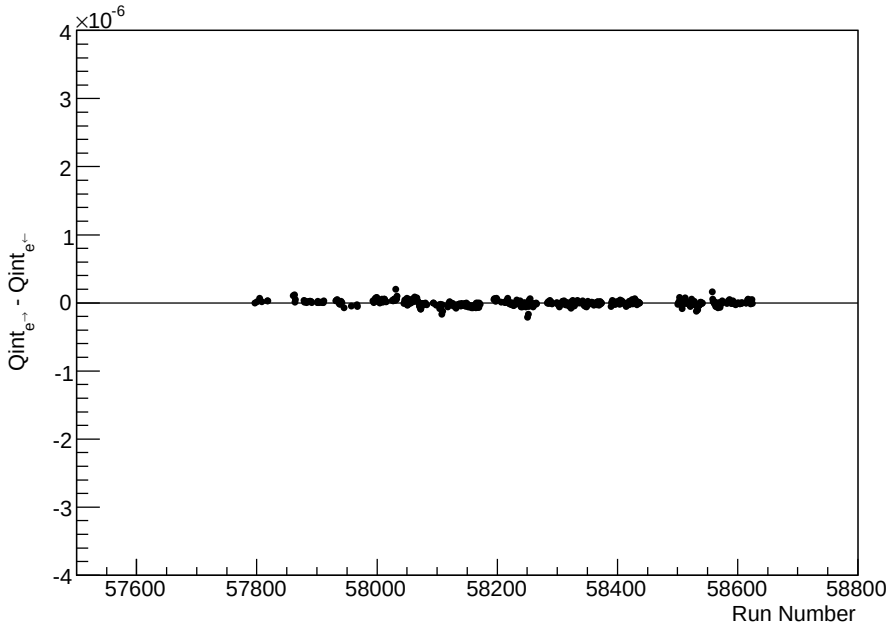

Figure 5.32: Difference of the integrated charge corresponding to the two helicity states as a function of the run number.

In addition, the normalization needs to take into account the fact that the beam is not 100% polarized. During the data taking, a polarimeter measures the angular asymmetry distributions in elastic

electron-electron Møller scattering to measure the beam polarization. The typical polarization P measured during the e1-DVCS2 experiment was between 83 to 87%. Therefore, in order to get the number of DVCS events that one would have with a 100% polarized beam, one normalizes σ_{pol} by the polarization P.

The difference of polarized cross sections can be computed for each quadri-dimmensional bins as:

$$\begin{aligned} \frac{d^4\sigma_{pol}}{dQ^2\,dx_B\,dt\,d\Phi} &= \frac{1}{2}\left[\frac{d^4\overrightarrow{\sigma}}{dQ^2\,dx_B\,dt\,d\Phi} - \frac{d^4\overleftarrow{\sigma}}{dQ^2\,dx_B\,dt\,d\Phi}\right] \\ &= \frac{1}{2\,P}\left(\frac{\overrightarrow{N}_{DVCS}}{L_{\overrightarrow{int}}} - \frac{\overleftarrow{N}_{DVCS}}{L_{\overleftarrow{int}}}\right)\frac{F_{rad}}{\Delta Q^2\,\Delta x_B\,\Delta t\,\Delta\Phi\,Acc\,F_{vol}} \end{aligned} \tag{5.24}$$

The azimuthal decomposition of $d^4\sigma_{pol}$ can be found in [BMK02] and is expressed at leading twist (twist-2) as:

$$\frac{d^4\sigma_{pol}}{dQ^2\,dx_B\,dt\,d\Phi} = \sin(\Phi)\,\Gamma_\Phi\,\Im m\left[F_1\mathcal{H} + \xi(F_1+F_2)\tilde{\mathcal{H}} - \frac{t}{4M^2}F_2\mathcal{E}\right] \tag{5.25}$$

where $F_{1,2}$ are the Dirac and Pauli form factors, Γ_Φ is a kinematic factor with a Φ-dependence coming from the electron propagators of the Bethe Heitler amplitude. The twist-3 contribution, not written here, consists of a linear combination of the CFFs with a $\sin(2\Phi)$-dependence. The term $|DVCS|^2$ is a twist-3 contribution and the term $|BH|^2$ vanishes because the BH does not depend on the beam helicity (for an unpolarized target). The contributions of $\tilde{\mathcal{H}}$ and $\mathcal{E}$ to $d^4\sigma_{pol}$ are reduced because $x_B \approx 0.2$ (proportional to ξ) and $-t \approx 0.3$ GeV^2 in our typical kinematics. The difference of polarized cross section is therefore mainly sensitive to the CFF $\mathcal{H}_{Im}$. Its distribution has a sinusoidal shape modulated by the BH propagators.

In Fig. 5.33, we show the results of σ_{pol} plotted as a function of Φ for each of the 12 t-bins aof the (Q^2, x_B) bin 2. The 13 (Q^2, x_B) bins can be found in Appendix I.

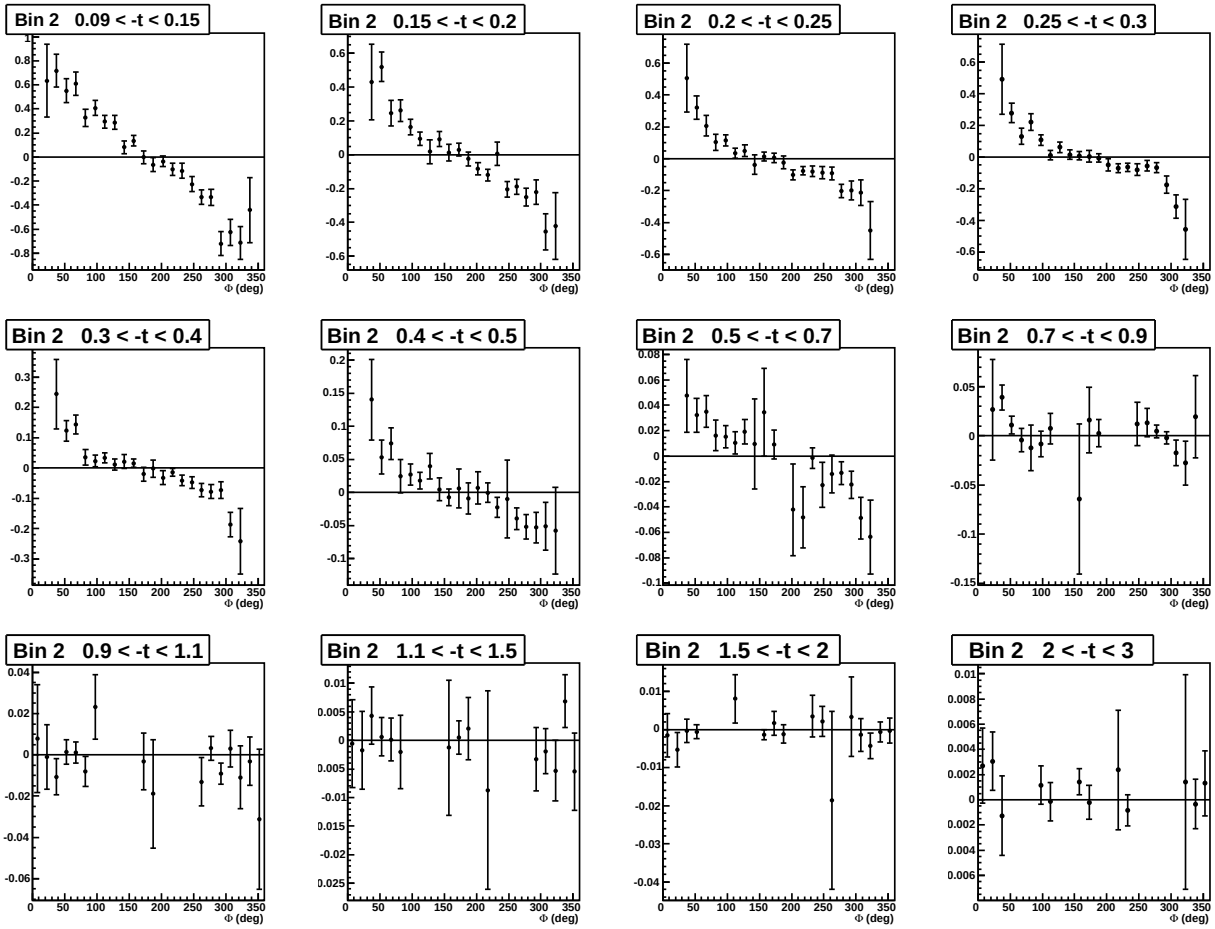

Figure 5.33: Difference of polarized cross section as a function of Φ for the 12 t-bins of the (Q^2, x_B) bin 2.

5.3.13 Comparison of DVCS1 and DVCS2 polarized cross sections

In the same spirit than the comparison between the unpolarized cross sections, we present herafter the comparison between the difference of polarized cross-sections of DVCS1 and DVCS2.

In Fig. 5.34, we show a superposition of the DVCS1 (blue) and DVCS2 (red) polarized cross-sections for the 12 t-bins of the (Q^2, x_B) bin 2. One can see a really good agreement between the two data sets. The 13 (Q^2, x_B) bins can be found in Appendix J.

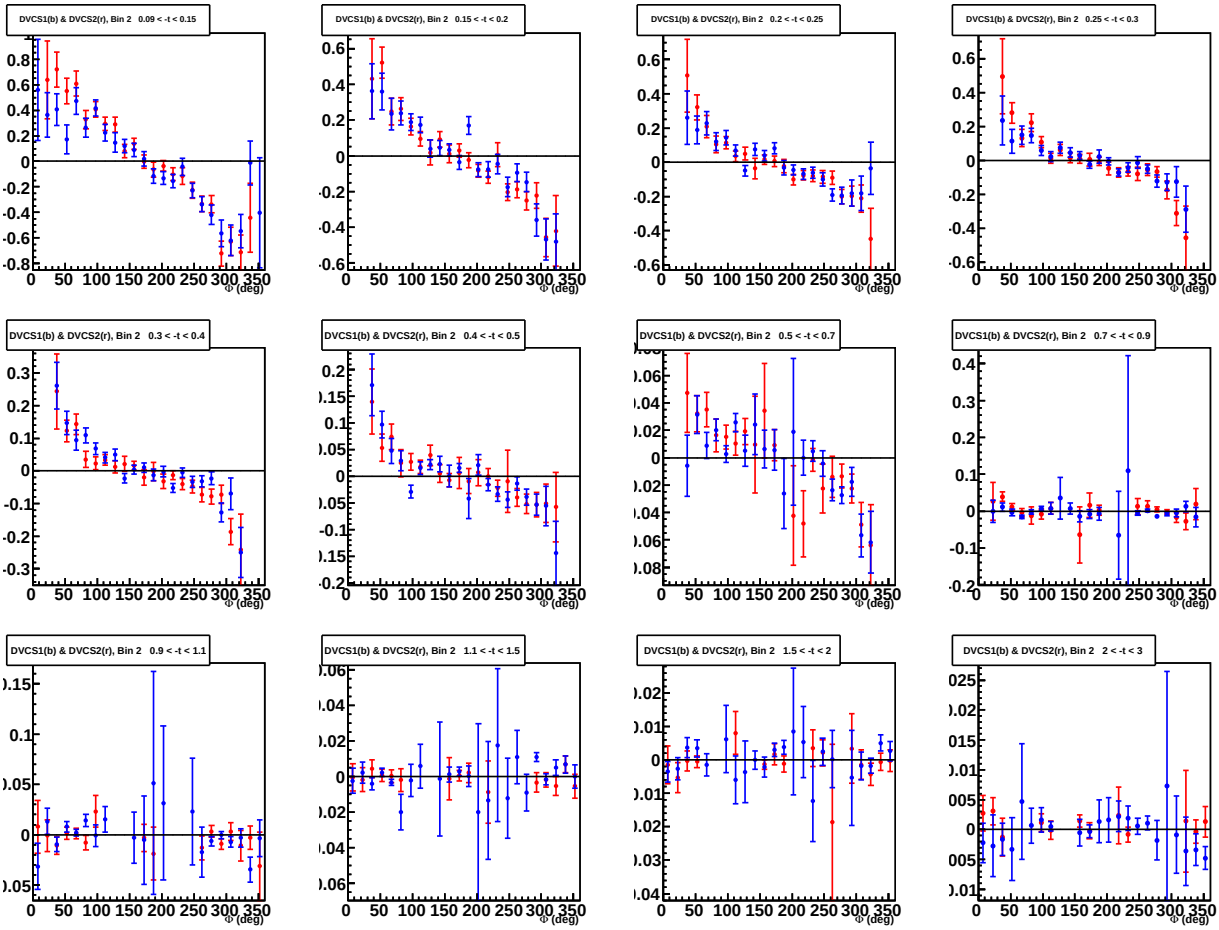

Figure 5.34: Comparison between the difference of polarized cross section of e1-DVCS1 (blue) and e1-DVCS2 (red), as a function of Φ for the 12 t-bins of the (Q^2, x_B) bin 2.

5.3.14 Beam-spin asymmetries

The beam-spin asymmetry $\mathcal{A}_{LU}$ is defined as the ratio of σ_{pol} over σ_{unp}. An important advantage of the beam-spin asymmetry is that all the normalization factors cancel out for the computation of the asymmetry. It is defined as:

$$\mathcal{A}_{LU} = \frac{1}{P}\left(\frac{\overrightarrow{N}_{DVCS} - \overleftarrow{N}_{DVCS}}{\overrightarrow{N}_{DVCS} + \overleftarrow{N}_{DVCS}}\right) \tag{5.26}$$

This latter observable has been measured and published in Ref. [ea08c], using the e1-DVCS1 data. In Fig. 5.35, we compared the results between the e1-DVCS1 and e1-DVCS2 experiments. Due to different binnings in t, we can't make a bin-by-bin comparison. In Fig. 5.35, the e1-DVCS1 bin is $-t = [0.09; 0.2]$, and is compared to two e1-DVCS2 bins $-t = [0.09; 0.1]$ and $-t = [0.1; 0.2]$.

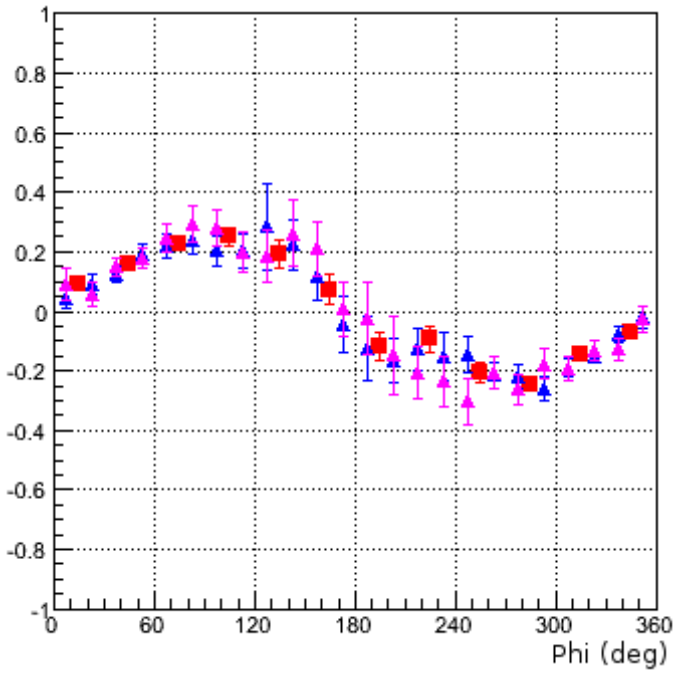

Figure 5.35: Comparison of the e1-DVCS1 and e1-DVCS2 asymmetries as a function of Φ for the (Q^2, x_B) bin 5. The sizes of the t-bins are different between the two experiments, with the e1-DVCS2 binning finer. The e1-DVCS1 points are the red squares, and the e1-DVCS2 points are blue ($-t = [0.09; 0.1]$) and pink triangles ($-t = [0.1; 0.2]$). Figure extracted from Ref. [Gir12].

Following Eqs. 5.18 and 5.25, the azimuthal decomposition of the beam-spin asymmetry $\mathcal{A}_{LU}$ can be written at leading twist as:

$$\mathcal{A}_{LU} = \frac{a\sin(\Phi)}{b + c\cos(\Phi) + d\cos(2\Phi)} \tag{5.27}$$

where the parameters a, b, c and d are expressed in terms of kinematical factors, the FFs and the CFFs. The $\cos(2\Phi)$-dependence arises from the Bethe-Heitler squared contribution $d^4|BH|^2$ to the unpolarized cross section.

We show in Fig. 5.36 our results of the beam-spin asymmetries for the (Q^2, x_B) bin 2. The 13 (Q^2, x_B) bins can be found in Appendix K.

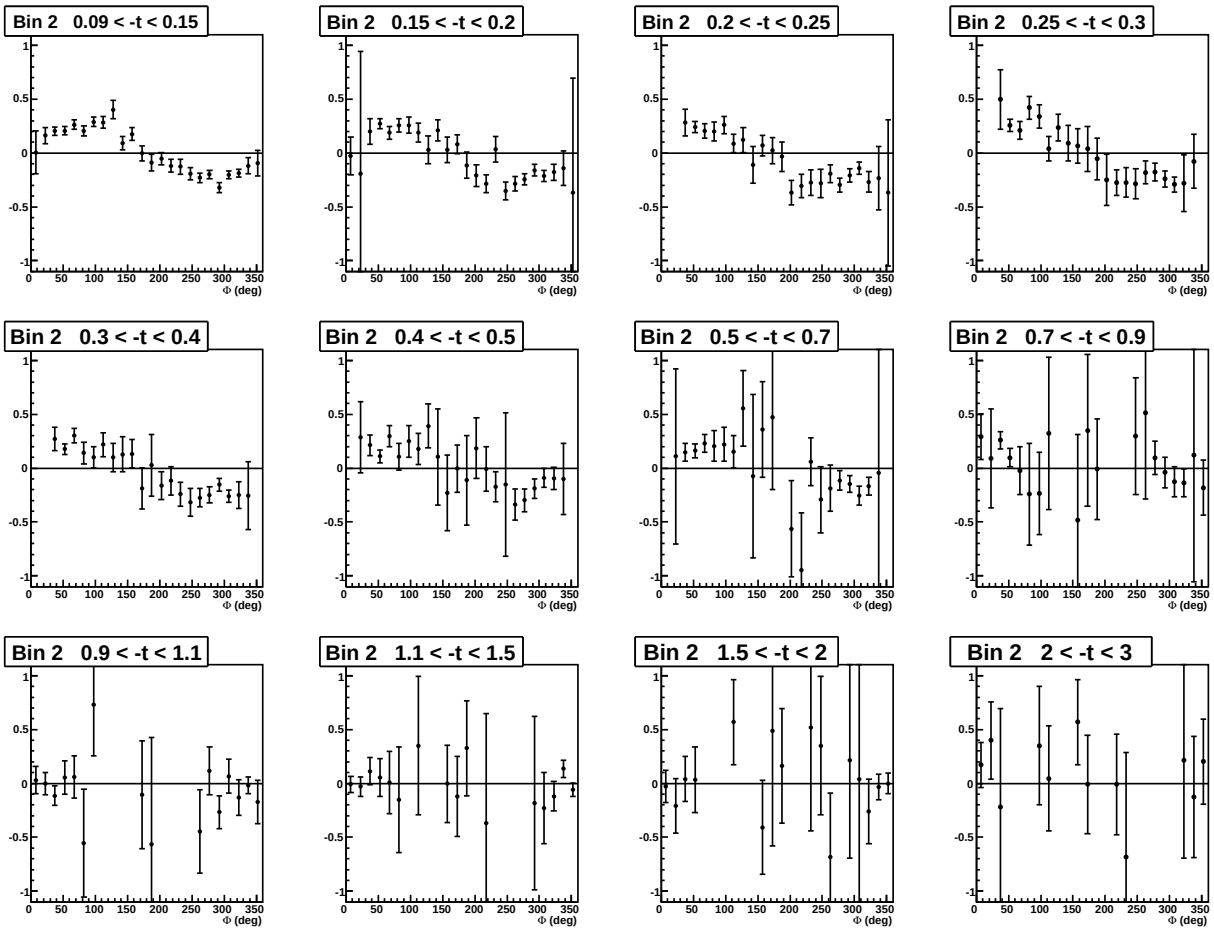

Figure 5.36: Asymmetries as a function of Φ for the 12 t-bins of the (Q^2, x_B) bin 2.

Chapter 6

Preliminary interpretation

In this chapter, our measurements (unpolarized, polarized cross-sections and beam-spin asymmetry) are going to be compared to the predictions of the VGG model described in Sect. 2.3.6. Because there are three integrals (two for the Double Distributions and one for the real part of the CFFs) in the calculation of the cross-section at a given (Q^2, x_B, t, Φ) point, it is too computing time consuming to integrate over the 4-dimensional volume of the bin. Theoretical calculation are therefore performed at a representative kinematical value of each bin. We will first discuss what should be the representative kinematical value of the bins in our analysis. Using this value, we will make a comparison of our data with the VGG predictions. Then we will discuss the model-independent fitting procedure used to extract the CFFs from our observables, and make a first interpretation of the extracted CFFs.

6.1 Representative bin abscissa for the DVCS cross section analysis

For non-linear distributions varying rapidly (like DVCS+BH cross-section) over a bin of finite width, the problem is to determine at which abscissa value the bin has to be defined in order to compare with theoritical model. The following discussion is inspired from Ref. [LW95]. Simplifying our cross-section analysis to one dimension, what we measure in a particular bin of width $\Delta x = x_2 - x_1$ is defined as:

$$< \sigma_{bin} >= \frac{1}{\Delta x} \int_{x_1}^{x_2} \sigma(x)\, dx \tag{6.1}$$

where $\sigma(x)$ is the true frequency distribution of the cross section. The question is then to know at which value of x within the bin of width Δx, should $< \sigma_{bin} >$ be regarded as a true measurement of $\int_{x_1}^{x_2} \sigma(x)\, dx$.

The solution consists in solving (analytically or numerically) the equation

$$\sigma(\tilde{x}) = \frac{1}{\Delta x} \int_{x_1}^{x_2} \sigma(x)\, dx \tag{6.2}$$

where $\tilde{x}$ is the representative x-value defining the bin. However, this solution requires to know precisely the function $\sigma(x)$, which is actually the function that we want to measure.

Two common ways to approximate the $\tilde{x}$-value of a bin consist in taking the center value x_{center} defined as

$$x_{center} = x_1 + \frac{\Delta x}{2} \tag{6.3}$$

or the barycentre $\bar{x}$ (weighted average) of the bin

$$\bar{x} = \frac{\int_{x_1}^{x_2} x\, f(x)\, dx}{\int_{x_1}^{x_2} f(x)\, dx} \tag{6.4}$$

However, for a non-linear problem with finite bins width, the two values x_{center} and $\bar{x}$ actually differ from the expected value $\tilde{x}$.

To illustrate this, we take the following one-dimensional example. We naively modelize the Φ-dependence of the DVCS+BH cross-section as $\sigma(\Phi) = e^{-\frac{\Phi}{30}}$. The aim is to reproduce the sharp variation of the distribution at low Φ. In Fig. 6.1, we show this one-dimensional modelling of the cross section for $\Phi \in [0, 180°]$. For the particular $[15°, 30°]$ bin, we obtain the results of $\bar{x} = 21.88°$, $\tilde{x} = 22.19°$ and $x_{center} = 22.5°$, calculated as in Eqs. 6.2-6.3-6.4.

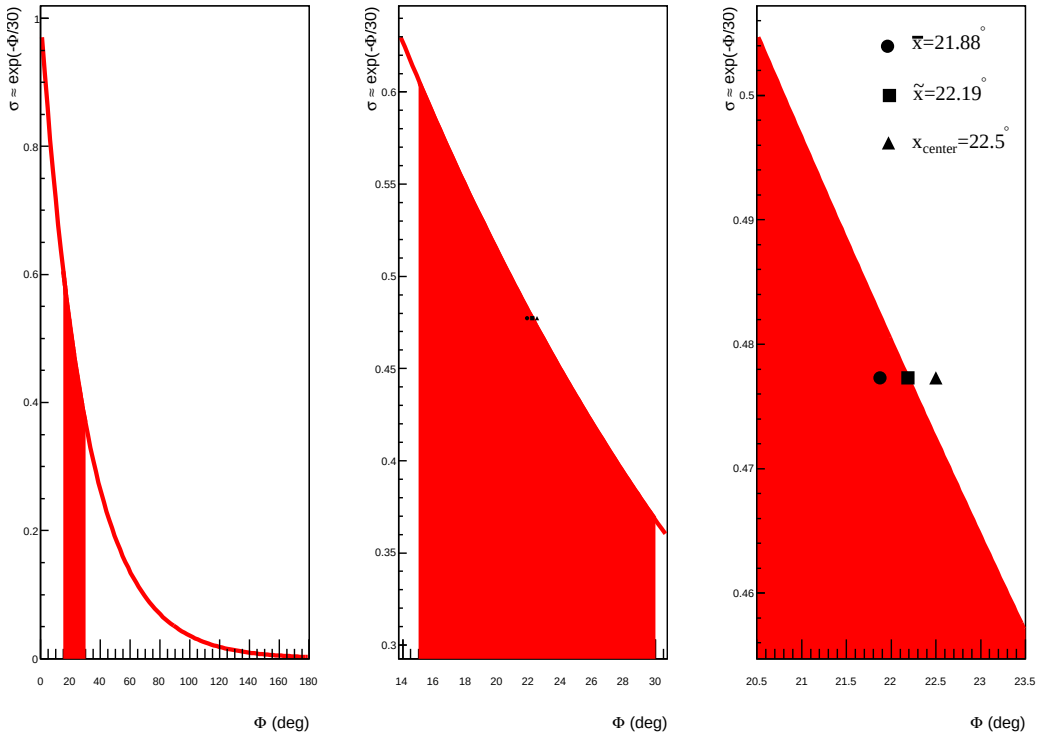

Figure 6.1: Example of a one-dimensional modelling of the Φ-dependence of the DVCS+BH cross-section. $\bar{x}$, $\tilde{x}$ and x_{center} are computed for the $[15°, 30°]$ bin. We see that taking the center value overestimates the cross section while taking the average value underestimates the cross section. The "true" reference value is in-between.

For a given bin of width 15°, the value x_{center} and $\bar{x}$ equivalently differ from $\tilde{x}$ of 0.31°. In these low-Φ regions where the cross section varies extremely rapidly, such a small variation in the definition of the representative x-value of a bin creates significant significant variations in the cross-section. In reality, we recall that we are dealing with a 4-dimensional problem and this is also true for small variations of x_B, t or Q^2.

In Fig. 6.2, the same analysis is done for different bin width (from 1° to 30°), at the same central bin value $x_{center} = 22.5°$. We can see that the values of x_{center} and $\bar{x}$ deviate from $\tilde{x}$ as the bin-width increases. Conversely, for bins with a small enough size, x_{center} and $\bar{x}$ convert to $\tilde{x}$.

For the DVCS cross section analysis, there is a priori no reason to know whether x_{center} is a better

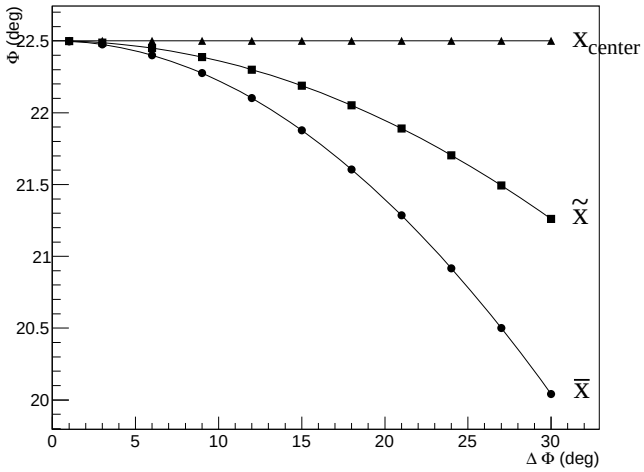

Figure 6.2: Values of $\bar{x}$, $\tilde{x}$ and x_{center} as a function of the bin width at the central value $x_{center} = 22.5°$.

approximation to $\tilde{x}$ than $\bar{x}$. In order to know at which kinematical value should be used to define our bins, we show in Fig. 6.3 a comparison between the BH integrated BH_{int} over the four-dimensional bin size, and the BH calculated at the weighted average BH_{wa} and central BH_c kinematics. The results are presented as the ratio: $\frac{BH_{int}}{BH_{wa}}$ (red) and $\frac{BH_{int}}{BH_c}$ (blue), for one t-bin. We can draw the conclusion

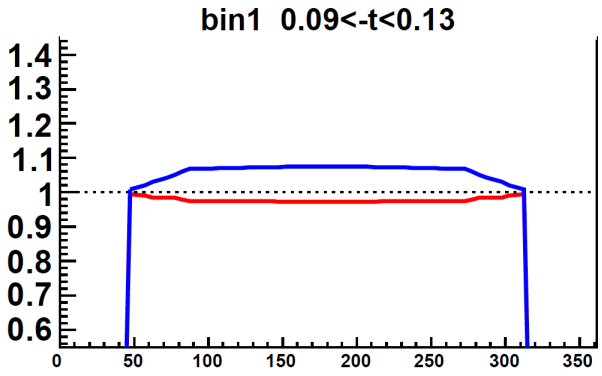

Figure 6.3: Comparison bewteen the BH calculated at the weighted average BH_{wa} and central BH_c kinematics, for one t-bin. In red: BH_{int}/BH_{wa}. In blue: BH_{int}/BH_c. Figure extracted from Ref. [Jo12]

that the BH calculated at the weighted average kinematics is very close to the BH integrated, much closer than the BH calculated at the central kinematics. In the following, we will therefore carry out the calculations of the VGG model, and perform the fits, at the weighted average kinematics.

6.2 Comparison of the unpolarized cross section with VGG predictions

In Fig. 6.4, we present a comparison of our four-fold differential cross-sections $\frac{d^4\sigma}{dQ^2\,dx_B\,dt\,d\Phi}$ (nbarn/GeV^4) computed for the second (Q^2, x_B) bin (see Appendix L for the other bins), to four different calculations:

- In green: the Bethe-Heitler (BH) cross section integrated within the acceptance of 4-dimensional bins.
- In maroon dashed: the BH calculated at the weighted average kinematics $< Q^2 >$, $< x_B >$, $< -t >$. As discussed in the previous section, this cross section can differs from the integrated BH because the size of our bins is not sufficiently small. Especially, in the low and large-Φ regions where the BH varies rapidly (and thus depends a lot on small variations of $< x_B >$, $< Q^2 >$ ...), one can see some significant deviations between the integrated and the BH calculated at the weighted average kinematics. To reduce this difference, the size of our binning has to be reduced.
- In pink: the DVCS+BH cross section calculated with the VGG model at the weighted average kinematics, taking into account the four GPDs H, E, $\tilde{H}$ and $\tilde{E}$. The shape of the experimental distributions is well reproduced by VGG, and in several cases the normalization also.
- In blue: DVCS+BH cross section calculated with the VGG model at the weighted average kinematics, taking only into account the GPD H. According to this model, one can observe that at low t the main contribution to the unpolarized cross section arises from the GPD H. The sensitivity to the other GPDs appears at higher t.

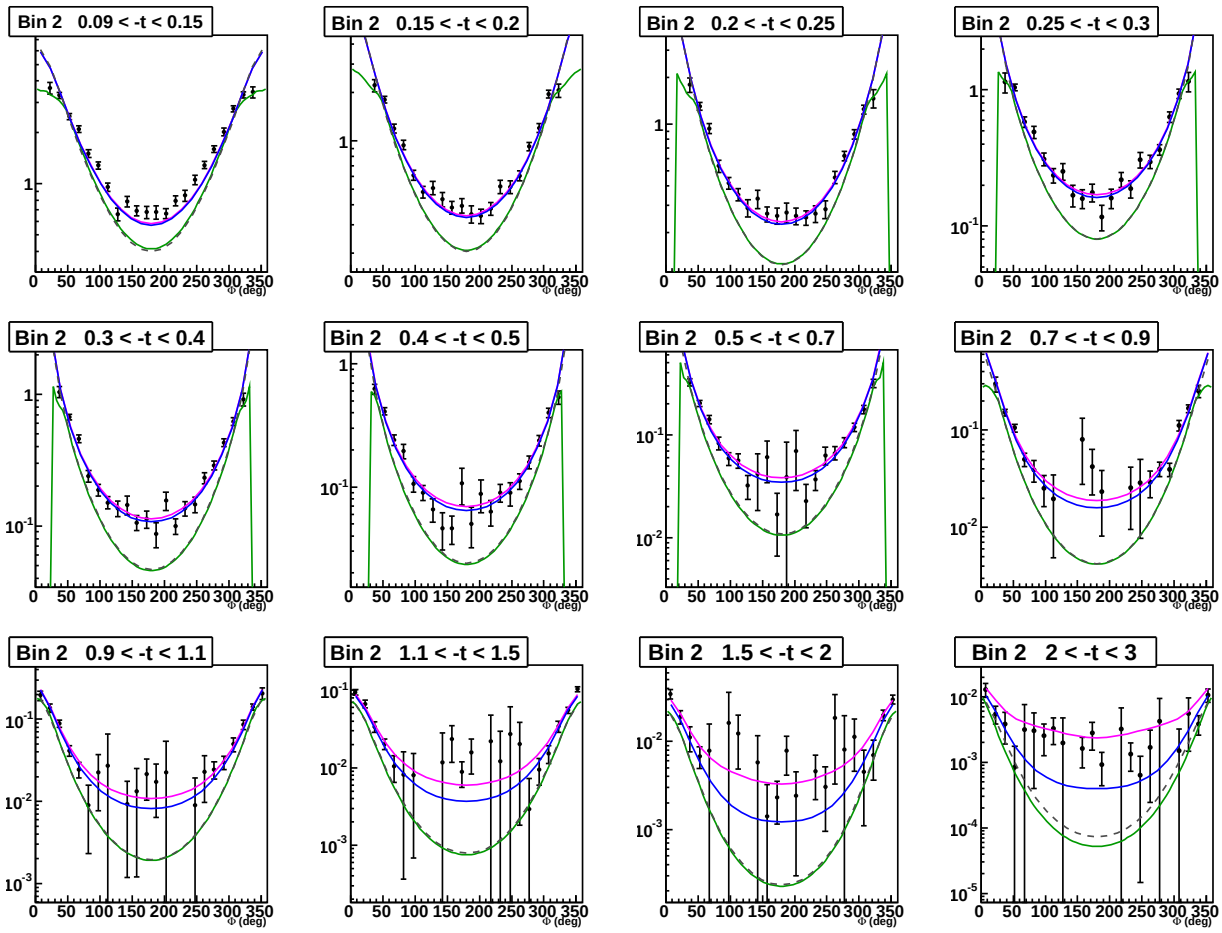

Figure 6.4: DVCS cross section (nbarn/GeV^4) as a function of Φ for the 12 t bins of the (Q^2, x_B) bin 2, compared to the BH cross-section and the VGG model predictions. The different curves are described in the text.

6.3 Comparison of the polarized cross section with VGG predictions

In Fig. 6.5, we show the results of the difference of polarized cross-sections σ_{pol} plotted as a function of Φ for each of the 12 t-bins of the (Q^2, x_B) bin 2. The 13 (Q^2, x_B) bins can be found in Appendix M. They are compared to two calculations from VGG:

- In pink: the difference of polarized cross sections calculated with the VGG model at the weighted average kinematics, taking into account the four GPDs H, E, $\tilde{H}$ and $\tilde{E}$. The shape of the experimental distributions is well reproduced by VGG. However, we can notice that at small t, the prediction of the amplitude is bigger than the one observed in the data. This amplitude goes to zero as t increases.
- In blue: the difference of polarized cross sections calculated with the VGG model at the weighted average kinematics, taking into account the GPD H only. According to this model, one can see that σ_{pol} is almost completely dominated by the contribution of the GPD H on all the phase space.

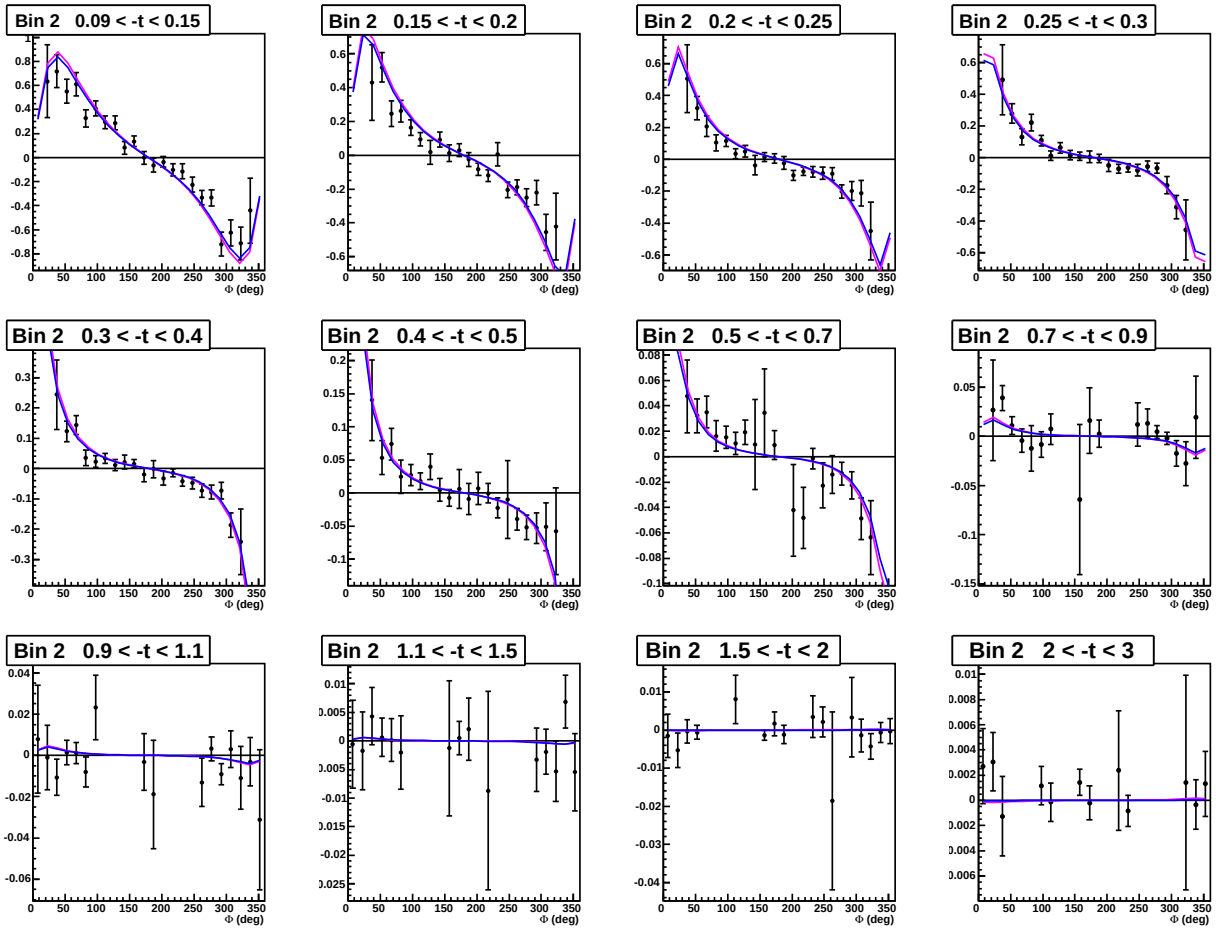

Figure 6.5: Difference of polarized cross section as a function of Φ for the 12 t-bins of the second (Q^2, x_B) bin. The curves correspond to VGG predictions and are described in the text.

6.4 Comparison of the BSA with VGG predictions

We show in Fig. 6.6 our results of the beam-spin asymmetries $\mathcal{A}_{LU}$ for the (Q^2, x_B) bin 1. The 13 (Q^2, x_B) bins can be found in Appendix N. They are compared to two asymmetries from VGG:

- In pink: the asymmetry calculated with the VGG model at the weighted average kinematics, taking into account the four GPDs H, E, $\tilde{H}$ and $\tilde{E}$. One can see that the shape of the experimental distributions is well reproduced by VGG, with slight difference in the amplitude though.
- In blue: the asymmetry calculated with the VGG model at the weighted average kinematics, taking into account the GPD H only. According to this model, one can see that the beam-spin aymmetry is almost completely dominated by the contribution of the GPD H on all the phase space.

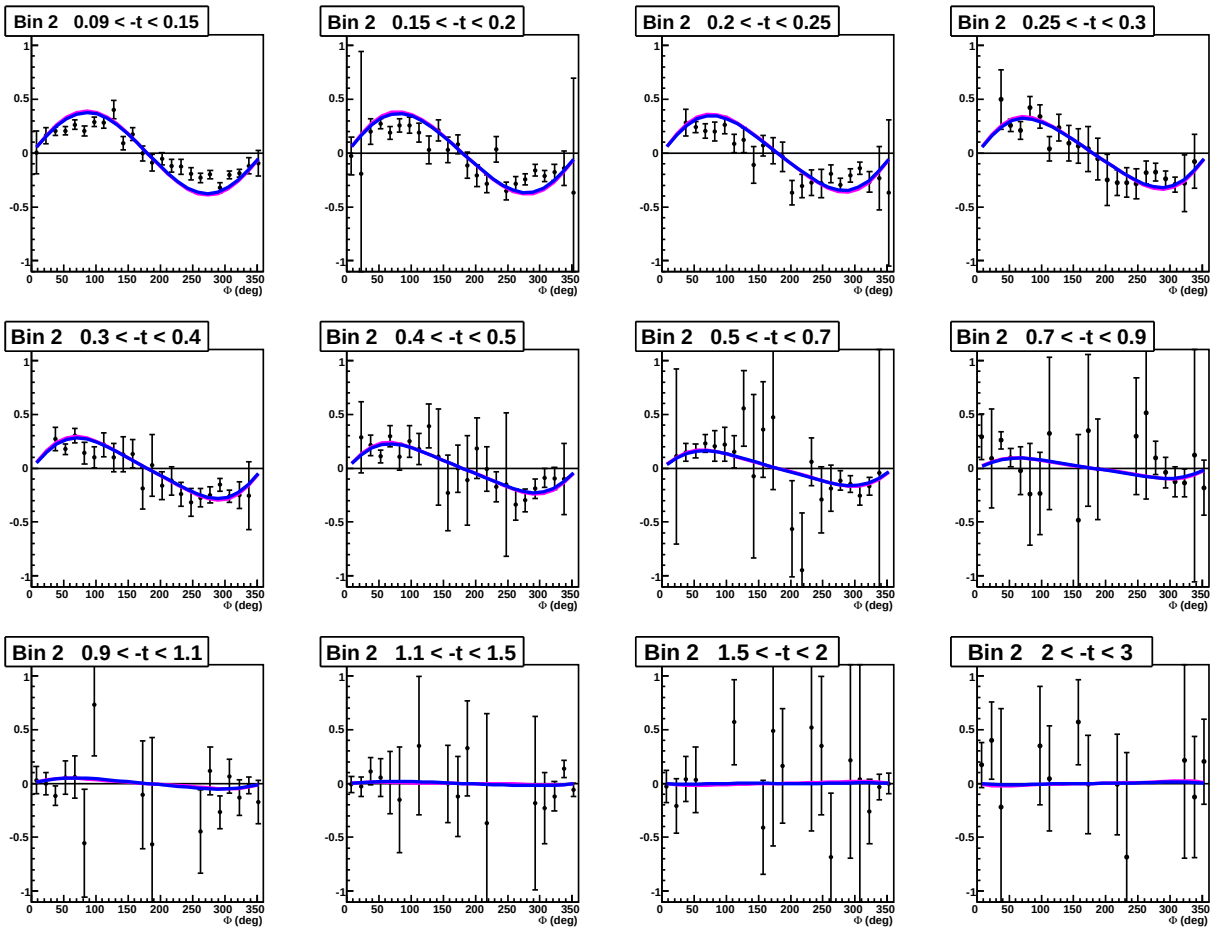

Figure 6.6: Asymmetries as a function of Φ for the 12 t-bins of the second (Q^2, x_B) bin. The curves correspond to VGG predictions and are described in the text.

6.5 Fitting procedure

In this section, we make a preliminary extraction of the Compton Form Factors from the e1-DVCS2 data. As we mentionned in Sec. 2.3.3, the quantities that can be extracted model-independently from the DVCS process are the eight CFFs. They are either weighted GPDs integrated over x or GPDs at the line $x = \pm\xi$, so that they only depend on ξ (or equivalently on x_B) and t.

The GPD $\tilde{E}$ is usually associated to the t-channel pion pole exchange, and is parametrized in terms of the pseudoscalar form factor and the pion distribution amplitude. The pion exchange contributes only in the region $-\xi \leq x \leq \xi$, and therefore to the real part of the DVCS amplitude. Therefore if the imaginary part of the amplitude is neglected for the GPD $\tilde{E}$, we can neglect also the contribution of the CFF $\tilde{\mathcal{E}}_{Im}$, reducing the total number of CFFs to seven.

Each of the eight observables (see Table 2.2) that can be measured with the DVCS process are function of the seven CFFs, with a different sensitivity though. In theory, the problem is therefore analog to solve eight equations with seven unknowns. In practice, all the observables are not available for all the kinematics so that there is not hope to extract all the CFFs yet.

In the following, we will extract the CFFs from only the two independant observables that we have measured in this thesis, i.e. the unpolarized cross section σ_{unp} and the difference of polarized cross-section σ_{pol}. The problem is therefore largely under-constrained with only two constraints for seven unknowns. We will use the model-independant fitting procedure that has been developed in Refs. [Gui08a, Mou09]. The procedure is that for a given experimental point $(x_B, -t)$, the seven CFFs are taken as free parameters and are extracted from the DVCS experimental observables.

The procedure consists in fitting the 2×24 points of the Φ distributions of σ_{unp} and σ_{pol}, in a given (Q^2, x_B, t) bin. There are 156 such bins so that one can extract in principle the CFF at 156 different kinematics. The quantity to be minimized is:

$$\chi^2 = \sum_{i=1}^{n} \frac{[\sigma_i^{theo} - \sigma_i^{exp}]^2}{(\delta\sigma_i^{exp})^2} \tag{6.5}$$

where σ^{theo} and σ^{exp} are respectively the theoretical and the experimental cross-sections (unpolarized and polarized), $\delta\sigma^{exp}$ it the experimental error bar and i is the number of points to be fitted. The theoretical calculation DVCS+BH is given at leading twist by the VGG code described in Chap 2.3.6, where the seven CFFs are the free parameters to be fitted to the data.

The fitting procedure is non trivial, because the relation between the CFFs and the observables is non-linear, there can be correlations between the CFFs, and the problem is under-constrained with only two observables to be fitted. To overcome the lack of constrains, the range over which the values of the seven CFFs are allowed to vary is bounded. The domain of variation allowed for the CFFs is defined as an hypervolume of $\{-5, 5\}$ times the values of the CFFs calculated by the VGG code which therefore serves as a reference. This condition is very conservative because it allows the cross-section to vary by a factor 5^2 with respect to the value of the VGG code. Solving the problem of seven unknowns with two equations becomes possible then, if some of them happen to be suppressed kinematically.

We show the results of the fitting procedure in Fig. 6.7 for the second bin in (Q^2, x_B). The 13 (Q^2, x_B) bins can be found in Appendix O.

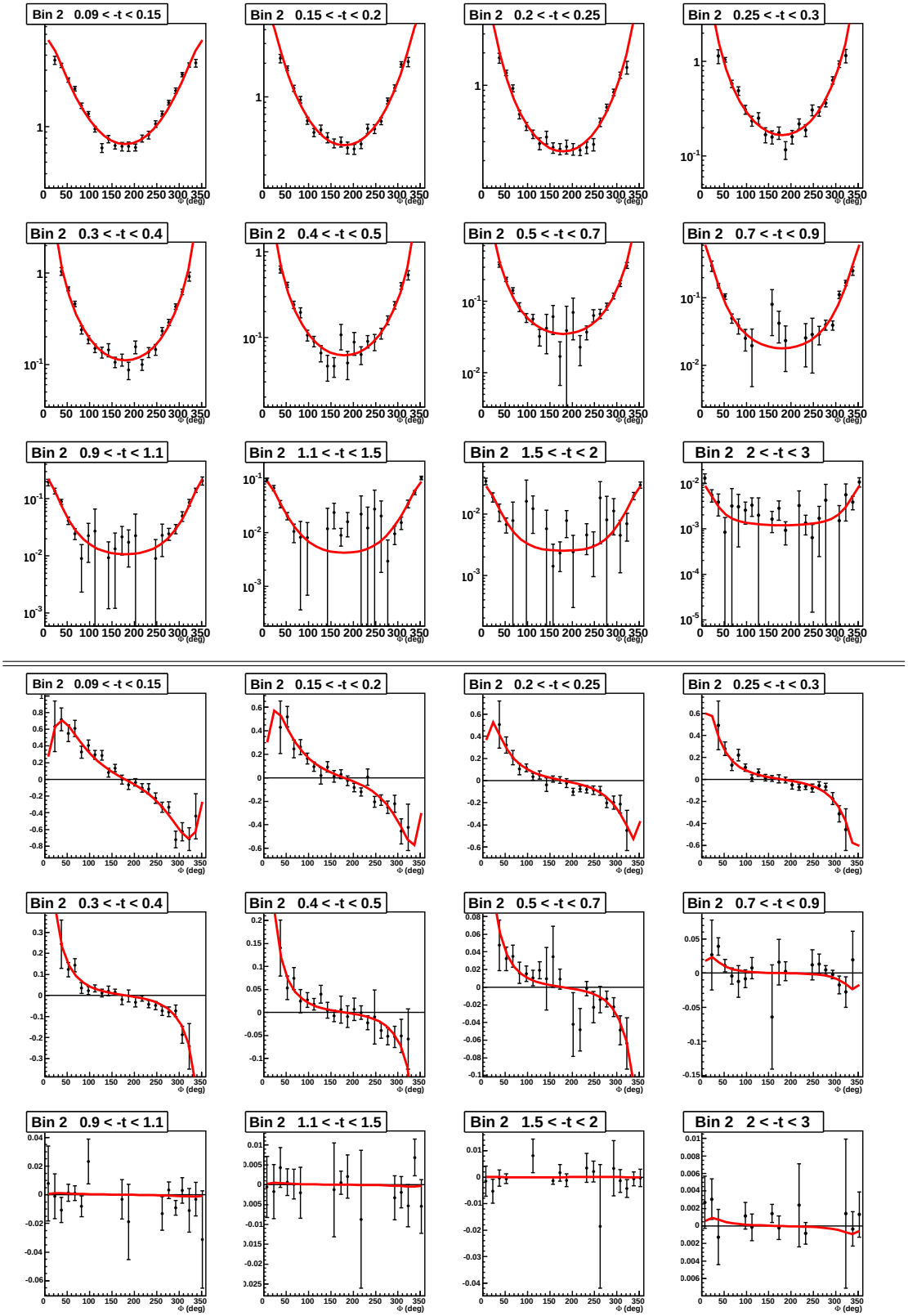

Figure 6.7: Simultaneous fits of the unpolarized (top) and polarized (bottom) cross sections as a function of Φ for the 12 t-bins of the (Q^2, x_B) bins 2.

6.6 Extraction of the Compton Form Factors

As we mentionned in Sec. 2.3.3, σ_{unp} and σ_{pol} are expected to be mainly sensitive to $\mathcal{H}_{Re}$ and $\mathcal{H}_{Im}$ respectively, the other CFFs being subdominant in these observables. Using the previous results of the fitting procedure, $\mathcal{H}_{Im}$ and $\mathcal{H}_{Re}$ are indeed the two CFFs which come out, as expected, with well defined χ^2 minima and finite error bars in the fit. They are plotted in Figs. 6.8 and 6.9, as a function of t for each of the 13 (Q^2, x_B) bins.

These preliminary results indicate that the t-slope of $\mathcal{H}_{Im}$ decreases with x_B increasing. If we neglect the ξ-contribution, this can be interpreted as follows: as the momentum transfer t is the conjugate variable of the impact parameter $b_\perp$, a small t-slope means that the valence-quarks (high-x) tend to remain in the center of the nucleon. Conversely, the sea-quarks (low-x) extend to the periphery of the nucleon.

A comparison between $\mathcal{H}_{Im}$ extracted from the fits and the VGG model (solid lines) shows a relatively good agreement within the error bars. We also compare the CFFs that have been extracted from our data with those extracted from previous measurements (the points at $x_B = 0.33$ arise from the fits of σ_{pol} and σ_{unp} from Hall-A, the points at $x_B = 0.24$ arise from the fits of $\mathcal{A}_{LU}$ and $\mathcal{A}_{UL}$ from Hall-B), and we find a fair agreement within the error bars. It is a good consistency check to see that by fitting different observables from different experiments, one extracts CFFs which are compatible. The coverage of the phase space has been considerably improved compared to the previous measurements.

The interpretation of $\mathcal{H}_{Re}$ is not so intuitive because it represents a GPD integrated over x and weighted by a factor $\frac{1}{x \pm \xi}$. It mainly serves as a strong constraint for the the modelisation of the GPD H. We observe that the prediction of the VGG model is in fair agreement with the data.

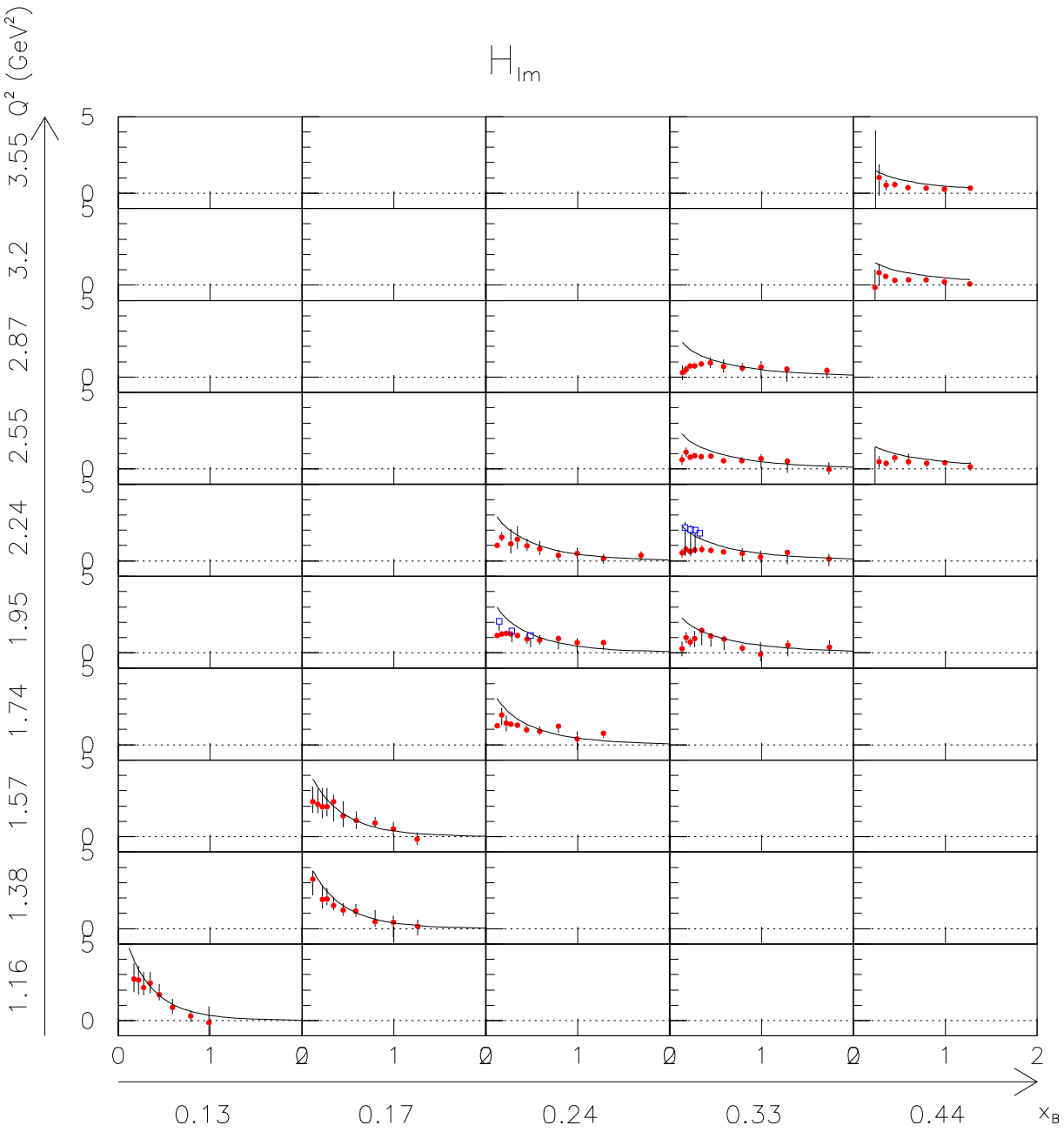

Figure 6.8: The red points show the extraction of $\mathcal{H}_{Im}$ as a function of t, for each of the 13 bins in (Q^2, x_B). The solid lines are the results from the VGG model. The blue points at $x_B = 0.33$ are the extractions from the Hall-A data [ea06a]. The blue points at $x_B = 0.24$ are the extractions from the Hall-B data [ea08c, ea06b].

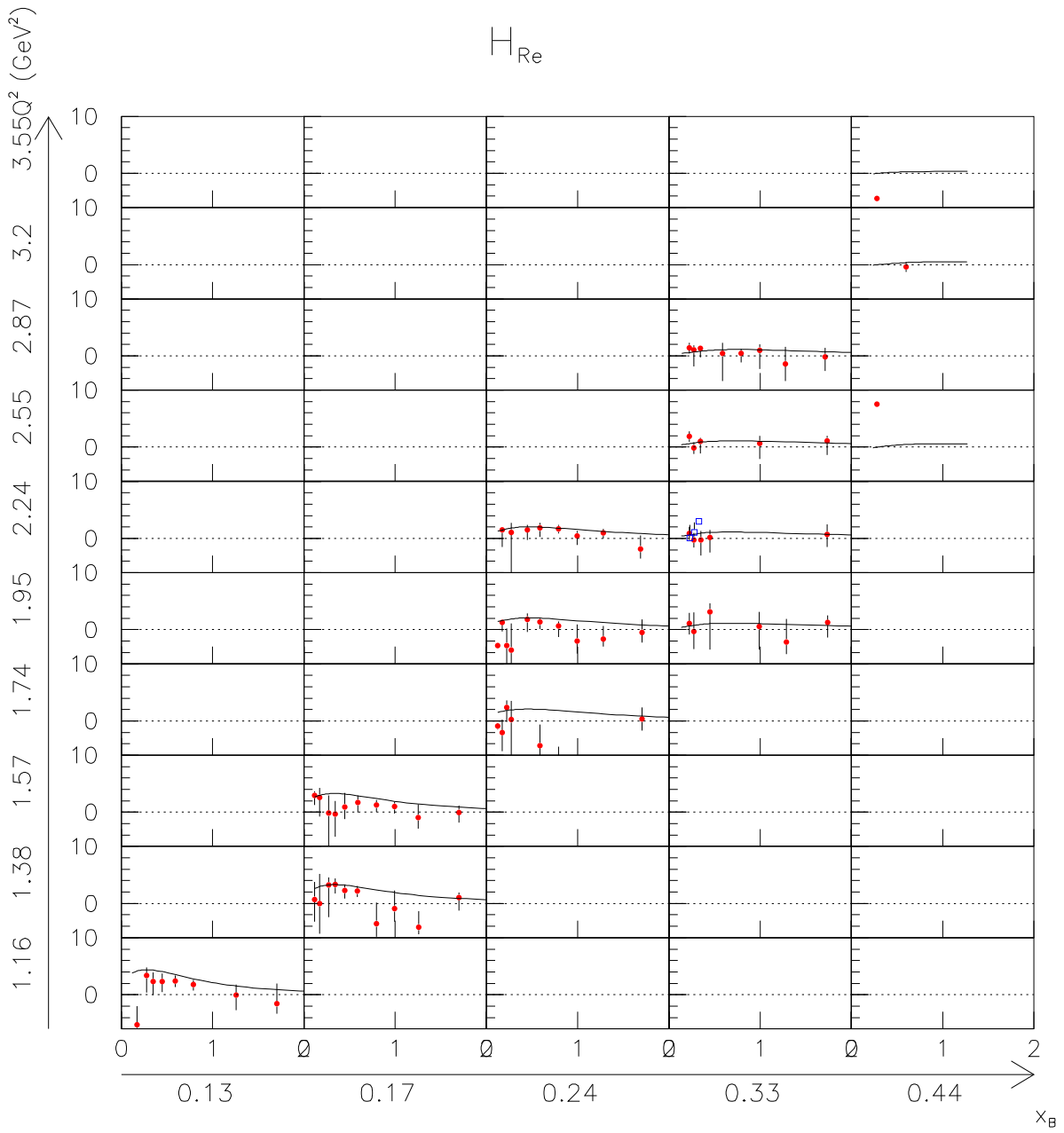

Figure 6.9: The red points show the extraction of $\mathcal{H}_{Re}$ as a function of t, for each of the 13 bins in (Q^2, x_B). The solid lines are the results from the VGG model. The blue points are the extractions from the Hall-A data [ea06a].

6.7 Proton charge density extraction

As mentionned in Sec. 2.3.2, for $\xi = 0$ ($t = -\Delta_\perp^2$) the 2-dimensional Fourier transform of the GPD $H(x,0,t)$ is equal to the parton density distribution $\rho(x, b_\perp)$. It provides a simultaneous measurement of the longitudinal momentum x at a given tranverse position (impact parameter $b_\perp$) for unpolarized quarks in the target. The density distribution can be obtained from H with the following equation:

$$\rho(x,0,b_\perp) = \int_0^\infty \frac{dt}{4\pi} J_0(b\sqrt{t})\, H(x,0,t) \tag{6.6}$$

where J_n is the regular cylindrical Bessel function. Using the unpolarized and polarized cross sections, we have been able to extract the CFF $\mathcal{H}_{Im}$ on a very wide kinematical regime. As shown in Table. 2.1, $\mathcal{H}_{Im}$ is a combination of the GPD H at the line $x = \pm\xi$: $\mathcal{H}_{Im}(\xi,t) = H(\xi,\xi,t) - H(-\xi,\xi,t)$. In the following, we make the approximation that the anti-quark contribution (negative x) is negligeable, so that $\mathcal{H}_{Im}(\xi,t) = H(\xi,\xi,t)$.

What we measure is $H(\xi,\xi,t)$, but what appears in Eq. 6.6 is the function $H(x,0,t)$. To make the link between the two functions, we have to introduce the model dependent correction factor $\frac{H(\xi,0,t)}{H(\xi,\xi,t)}$. This factor corresponds to a correction of 10 to 20% according to the VGG model.

In the upper part of Fig. 6.10, we show the t-dependence of $\mathcal{H}_{Im}$ for five different x_B bins (fixed Q^2). The t-dependence has been fitted with an exponential: $\mathcal{H}_{Im}(t) = e^{a+bt}$. One can then use Eq. 6.6 to obtain the proton charge density $\rho(b_\perp)$ for different $x = x_B$ values. We show the results in the lower part of Fig. 6.10.

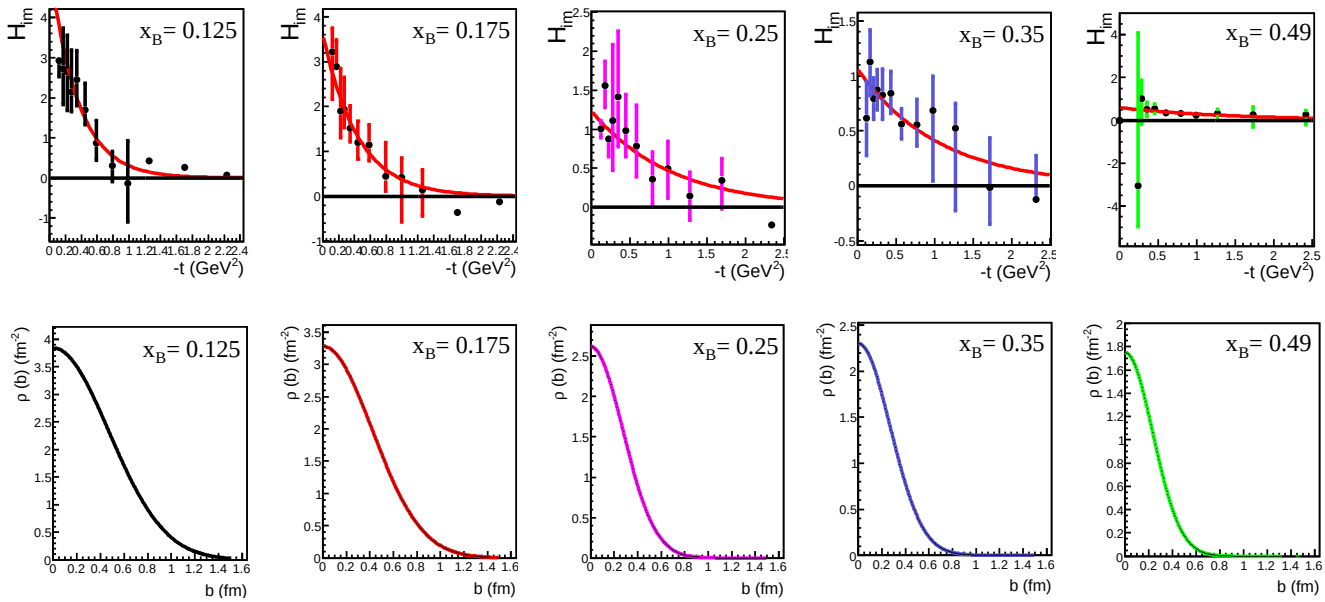

Figure 6.10: Upper part: t-dependence of $\mathcal{H}_{Im}$ for five different values of x_B. The red curve is the exponential fit. Lower part: proton charge density $\rho(b_\perp)$ as a function of the impact parameter $b_\perp$, as defined by the Eq. 6.6.

Fig. 6.11 shows the superpostion of the these proton charge densities. For large momentum fraction x, the t slope is small. The Fourier transform gives then a narrow proton charge density as a function of $b_\perp$. It means that the valence quarks that have large momentum fractions are localized in the core

of the nucleon. For small momentum fraction x, the t-slope of the GPDs becomes large. The density distribution becomes broader and it means that the sea quark with small momentum fraction can extend to large values of $b_\perp$.

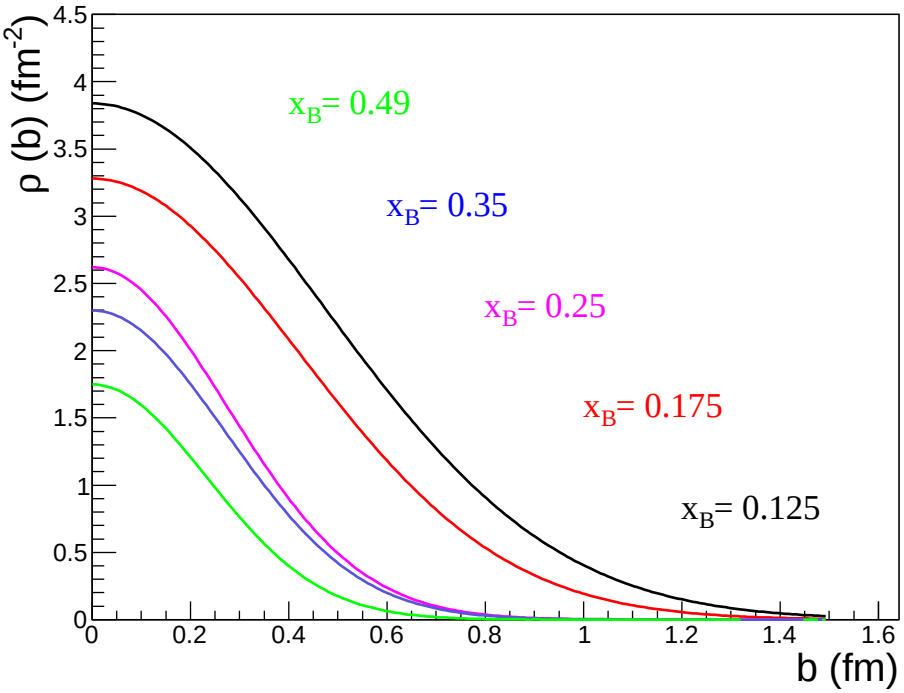

Figure 6.11: Proton charge density as a function of the impact parameter $b_\perp$, for five different values of x_B.

Chapter 7

Neutron DVCS for CLAS12

7.1 Introduction

Most of our current knowledge on GPDs comes from exclusive measurements of DVCS on the proton. So far, these measurements have provided enough contraints to extract only information about H_p and $\tilde{H}_p$.

To improve our description of nucleon structure in terms of GPDs, we need to measure DVCS on the neutron as well. n-DVCS measurements would allow one to access some combinations of GPDs that are supressed in DVCS on a proton target, and also to carry out a quark-flavor separation of the GPDs.

7.1.1 Physical interest for DVCS on the neutron

As we showed in Table 2.2, DVCS can be studied with many observables. Each of them being sensitive to a particular CFF (hence to a GPD).

The n-DVCS program at CLAS12 plans to study the beam-spin asymmetry (BSA) observable. Using a longitudinally polarized electron beam (L) and a unpolarized target (U), the asymmetry $\mathcal{A}_{LU}$ can be approximated as :

$$\mathcal{A}_{LU}(\phi) \propto \Im m\left\{ F_1\,\mathcal{H} + \xi(F_1+F_2)\,\tilde{\mathcal{H}} - \frac{t}{4M^2}F_2\,\mathcal{E} \right\} \sin(\phi). \tag{7.1}$$

where ϕ is the angle between the leptonic and hadronic planes, and $F_{1,2}$ the form factors as defined in Eq. 2.1.

In the case of a proton target, the $\tilde{\mathcal{H}}$ and $\mathcal{E}$ contributions are reduced because $x_B \approx 0.2$ (proportional to ξ) and $-t \approx 0.3$ GeV^2 in our typical kinematics. The main contribution to $\mathcal{A}_{LU}$ arises therefore from $\mathcal{H}_{Im}$.

With a neutron target, the sensitivity differs because the form factor F_1 (linked to the charge distribution) is almost zero. $\tilde{\mathcal{H}}$ is suppressed because of the cancellation of the polarized PDFs of u and d quarks ($\Delta u + 2\Delta d \approx 0$). So the main contribution to the BSA with a neutron target is arising from $\mathcal{E}_{Im}$, that is the GPD E along the line $x = \pm\xi$, the least known and least constrained of the GPDs.

Moreover, E is one of the two GPDs entering Ji's sum rule (Eq. 2.18) which links the total angular momentum J_q carried by each quark q to the second moment in x of the sum of the GPDs H and E.

Measuring neutron GPDs is also necessary to attenpt a quark-flavor (u, d) separation of GPDs. In fact, the GPD H of the proton can be decomposed as:

$$H^p(x,\xi,t) = \frac{4}{9}H^u + \frac{1}{9}H^d \tag{7.2}$$

, while the one of the neutron is decomposed as:

$$H^n(x,\xi,t) = \frac{1}{9}H^u + \frac{4}{9}H^d \tag{7.3}$$

Measuring both H_p and H_n will allow one to carry out a flavor separation.

7.1.2 Neutron DVCS with CLAS12

The CEBAF accelerator in the near future will be upgraded from 6 to 12 GeV. With a higher beam energy, we will extend the kinematical domain for GPD measurement. More precisely, we will have access to smaller values of x_B where the beam-spin asymmetry for DVCS on a neutron target is supposed to be larger.

Along with the upgrade of CEBAF, the CLAS detector will also need to be upgraded (CLAS12 will be the name of the new detector). Our group will add a neutron detector to the central part of CLAS12 in order to study DVCS on the neutron.

We will measure the n-DVCS reaction using a deuterium target ($ed \rightarrow enp\gamma$) and detecting the scattered e^-, γ and the recoil neutron. Neutrons interact with matter through nuclear interaction, unlike charged particles that mainly interact electromagnetically with matter. During the interaction of a neutron with a nucleus, charged particles can be produced and leave a signal in the detector through ionisation and production of light in the scintillators. For the detection of the recoil neutron, which is necessary to ensure the exclusivity of the reaction, the design of a scintillator-barrel detector in the central part of the future CLAS12 has been studied. In particular, Monte-Carlo simulations were performed in order to define the requirements of the central neutron detector (CND).

The kinematics of the n-DVCS reaction and the neutron detector resolution requirements have been studied. Also, we evaluated the contamination of the n-DVCS events by the exclusive neutral pion production channel, and we estimated the count rates that are expected with 80 days running at 11-GeV.

This work has been used to write a proposal (Deeply Virtual Compton Scattering on the Neutron with CLAS12 at 11 GeV) [NKAM11] that has been approved by the JLab Program Advisory Committee (PAC-37) with maximum rating (A).

7.2 Requirements of the neutron detector

We describe here our study of the n-DVCS process on the deuterium target ($ed \to epn\gamma$) to be measured at 11 GeV with the CLAS12 detector. The following results are based on simulations. The GENEPI [AV09] event generator has been used to simulate DVCS and exclusive π^0 electro-production off free and bound nucleons. The DVCS amplitude is computed using the BKM formalism [BMK02]. The GPDs are parametrized with the double distributions including the D-term introduced in [VGG99, GPV01]. The exclusive π^0 electroproduction off a nucleon is calculated from J. M. Laget model [Lag11]. This model is based on Regge theory with the inclusion of rescattering processes. It provides estimations of cross sections which are in agreement with the ones measured by the JLab collaborations of Hall-A [ea11b] and Hall-B [BK10] on the proton. In this model, in the kinematical domain considered for this proposal, the exclusive π^0 cross section on the proton is assumed to be equal to the one on the neutron.

Cuts have been applied on the simulated events to be in the kinematic regime of the GPD aaplicability. Specifically, we applied the following cuts:

- $Q^2 \geq 1$ GeV to be in the Bjorken regime.
- $-t \leq 1.2$ GeV^2 to reduce the higher-twist contributions.
- $W \geq 2$ GeV to be out of the resonance region.

Figs. 7.1 and 7.2 show the physical region that we will cover with the 12 GeV upgrade. In particular, we will be able to reach smaller x_B values: ≈ 0.05 compared to 0.1 in the current JLab setting, and higher Q^2: ≈ 10 GeV^2 instead of ≈ 5 GeV^2.

On Figs. 7.3, 7.4 and 7.5 are plotted the momentum p versus θ for each detected particle of the final state: e, γ, n.

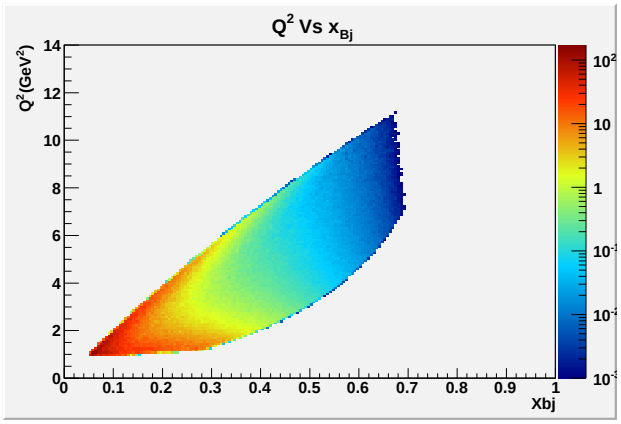

Figure 7.1: Q^2 as a function of x_B.

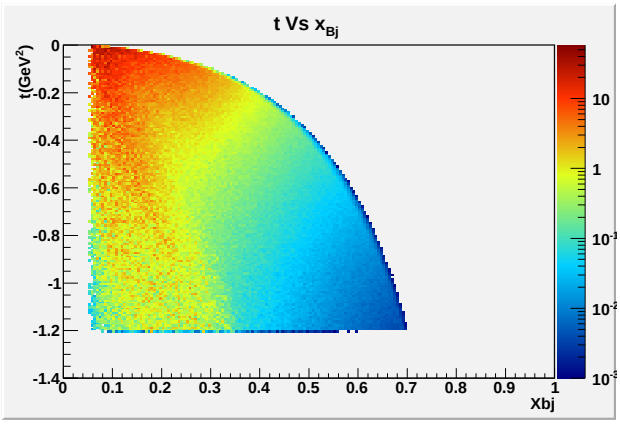

Figure 7.2: t as a function of x_B.

Electrons and photons are mostly emitted at high energy and forward angles and thus will be detected in the calorimeters located in the forward part of CLAS12. The cut on Fig. 7.4 around 4.5° correspond to the overlap between the Forward Tagger[1] (FT) detecting photons below 4.5°, and the Electromagnetic Calorimeter (EC). Fig. 7.5 shows that the neutron is emitted mostly (for $\sim 80\%$ of the events) at $\theta \geq 40°$ in the laboratory frame. In the baseline of CLAS12, neutrons can be detected in the forward region (between 5° to 40°) by the electromagnetic calorimeters with $\sim 30\%$ efficiency, while in the central part (from 35° to 125°) they can be detected by the central time-of-flight, with only 3% of efficiency. This points to the necessity to add a neutron detector to the central part of CLAS12 in order

[1] Calorimeter similar to IC. It will be located in the very forward region of CLAS12. See Ref. [BVS+05] for more details.

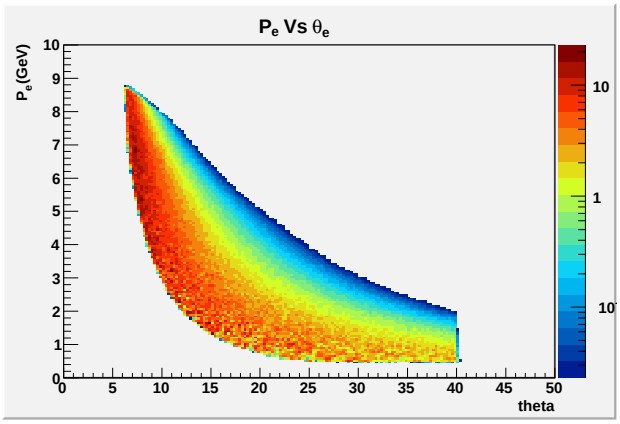

Figure 7.3: Electron momentum as a function of electron polar angle, for n-DVCS events. Forward-CLAS12 acceptance cuts and physics cuts are included.

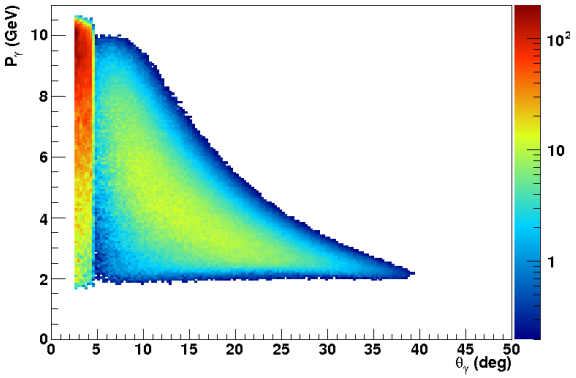

Figure 7.4: Photon momentum as a function of photon polar angle, for n-DVCS events. Forward-CLAS12 acceptance cuts and physics cuts are included.

to increase the neutron detection efficiency. It must be sensitive to the momentum range $0.2 \leq p_n \leq 1.2$ GeV, and have an angular coverage $40° \leq \theta_n \leq 80°$.

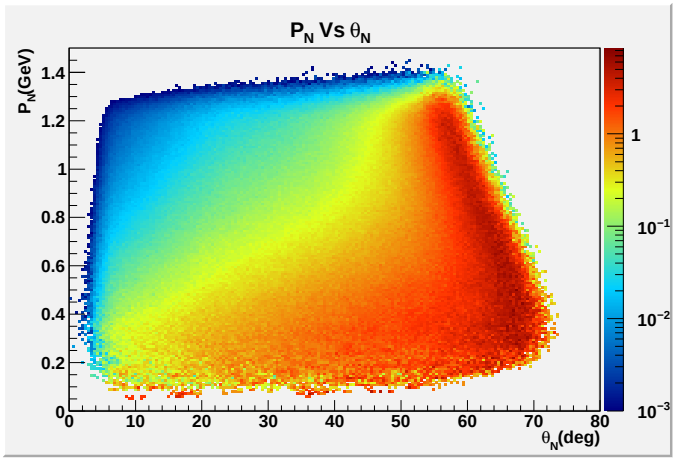

Figure 7.5: Neutron momentum as a function of neutron polar angle, for n-DVCS events. Forward-CLAS12 acceptance cuts and physics cuts are included. The neutrons are emitted mostly (for $\sim 80\%$ of the events) at $\theta \geq 40°$.

7.3 Resolutions and GEANT simulations

In order to determine the requirements of the central neutron detector in terms of momentum and angular (θ, ϕ) resolutions, we have studied the missing mass squared of the $en\gamma$ system in the process $ed \rightarrow en\gamma[X]$, where X is the spectator proton. The electron beam is set at 11 GeV along the z-axis, and hits a deuterium target at rest. The final state is consequently the scattered electron, the photon, the neutron and the spectator proton which is not detected.

GEANT4 simulations have been performed for a realistic design of the CND [Sok12]. As an input, a timing resolution of $\sigma_t \sim 150$ ps, coming from experimental measurements on a prototype, has been used to extract realistic angular and momentum resolutions for neutrons detected in the CND. Both θ_N and P_N depend on the time measurements of the photodetectors. They are defined as:

$$\theta_N = \frac{180}{\pi} \arccos(\frac{z}{l}), \qquad P_N = \frac{\beta\, M_N}{\sqrt{1-\beta^2}} \tag{7.4}$$

where $l = \sqrt{z^2 + h^2}$ is the path length with componants z and h the hit positions in the direction along the z-axis (beam direction) and in the radial direction (see Fig. 7.6). z is calculated by measuring the hit timing at both sides of the scintillator bar:

$$\begin{aligned} t_{left} &= t_l + t_{\frac{L}{2}+z} \\ t_{right} &= t_l + t_{\frac{L}{2}-z} \end{aligned} \tag{7.5}$$

where L is the length of the paddle. So $z = \frac{v_{eff}}{2}(t_{left} - t_{right})$, where v_{eff} is the effective velocity of light propagation in the scintillator. h is given by the distance between the target and the middle of the hit paddle. β also strictly depends on timing measurements and is defined as: $\beta = \frac{l}{TOF.c}$, with TOF the reconstructed time of flight and c the speed of light.

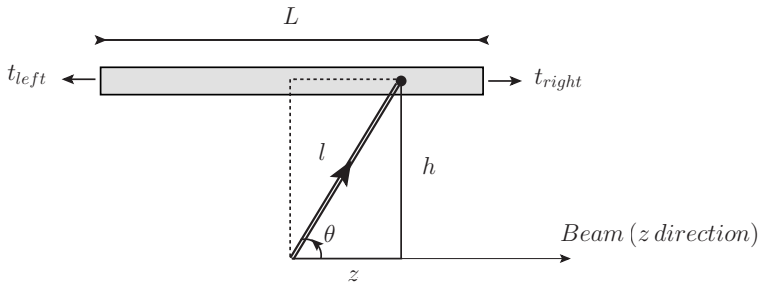

Figure 7.6: Description of a hit in one scintillator bar.

For a timing resolution of 150 ps, the angular and momentum resolutions for neutrons are:

$$\Delta\theta_N = 2.5°, \Delta\phi_N = 3.75°, \frac{\Delta P_N}{P_N} = 5\% \tag{7.6}$$

One of the goals of this study was to find out which kinematical variable (θ, ϕ, p) of the neutron affects the resolution of the missing mass $M_m^2(en\gamma)$ the most, which is the only quantity we can cut on to minimize the π^0 contamination. Our approach has been first to remove the electron and the photon resolutions, and to vary the smearing of the kinematical variables of the neutron. It is then possible to see which neutron variable affects the resolution of $M_m^2(en\gamma)$ the most. The results are shown on Figs. 7.7, 7.8 and 7.9.

In Fig. 7.7, the squared missing mass of the enγX system for various values of the θ_N resolution is displayed. $\frac{\Delta P_N}{P_N} = 5\%$ and $\Delta\phi_N = 3.75°$ are kept constant. Similarly, Fig. 7.8 shows the squared missing mass of the enγX system for various values of the ϕ_N resolution for fixed θ_N and momentum resolutions. From these plots, we can conclude that the effect of the angular resolutions ϕ_N and θ_N are negligeable. Indeed, varying the angular resolutions (either θ or ϕ) from 0.1° to 20° only increases the standard deviation of the missing mass from 22 to 30 MeV.

Fig. 7.9 shows the effect of varying the relative neutron momentum resolution $\frac{\Delta P_N}{P_N}$ from 0.1% to 20%, keeping fixed the angular resolutions ($\Delta\theta_N = 2.5°$, $\Delta\phi_N = 3.75°$). It shows a strong effect on

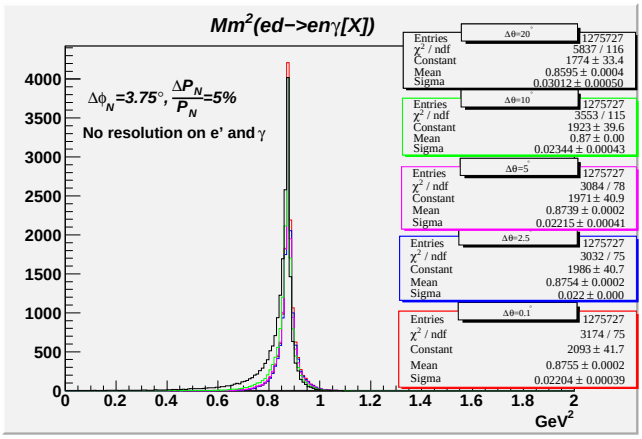

Figure 7.7: Missing mass squared of the enγ system, for fixed neutron $\Delta\phi_N$ and $\frac{\Delta P_N}{P_N}$ resolutions, and $\Delta\theta_N$ varying between 0.1° and 20°.

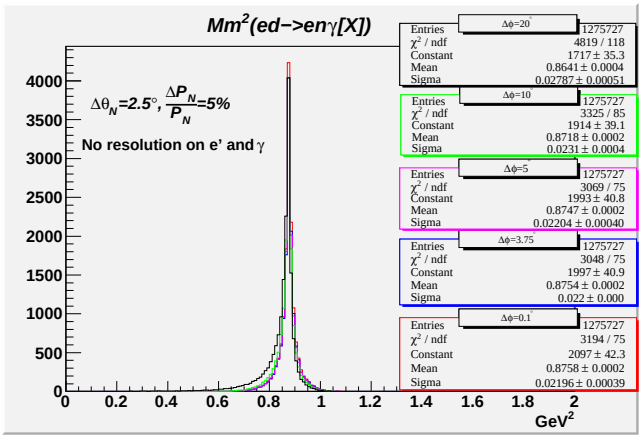

Figure 7.8: Missing mass squared of the enγ system, for fixed neutron $\Delta\theta_N$ and $\frac{\Delta P_N}{P_N}$ resolutions, and $\Delta\phi_N$ varying between 0.1° and 20°.

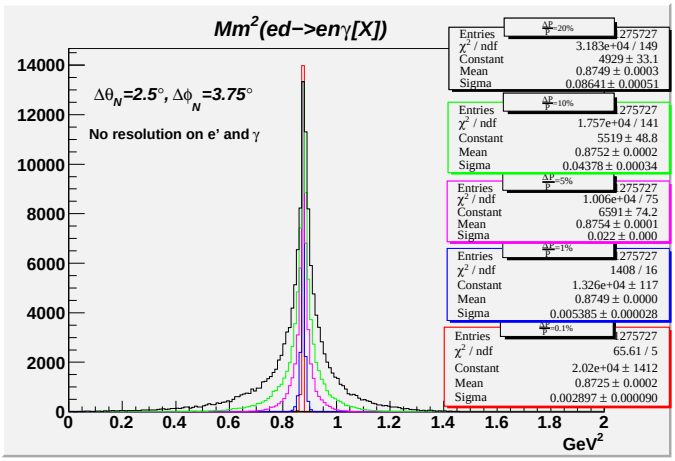

Figure 7.9: Missing mass squared of the enγ system, for fixed neutron $\Delta\phi_N$ and $\Delta\theta_N$ resolutions, and $\frac{\Delta P_N}{P_N}$ varying between 0.1% and 20%

the enγX squared missing mass. Unlike the two previous results, the missing mass resolution increases from 2 MeV to 86 MeV.

We then introduced realistic resolutions on the kinematical variables of the photon and electron, which have been smeared according to the expected CLAS12 sub-detectors resolutions (for the momentum: $\frac{\Delta P_e}{P_e} \sim 1\%$ and $\frac{\Delta P_\gamma}{\sqrt{P_\gamma}} \sim 5\%$).

In Fig. 7.10, the curves correspond to different combinations of particles being detected with absolute precision or with realistic resolutions.

In Fig. 7.11, the electron and photon resolutions are kept constant and we vary the neutron momentum resolution $\frac{\Delta P_N}{P_N}$, while looking at the effect on $M_m^2(en\gamma)$.

We clearly see that the effect of the neutron momentum resolution is negligeable compared to the others. More precisely, for a 10% neutron momentum resolution, one can see that 94% of the missing mass width is due to the photon resolution.

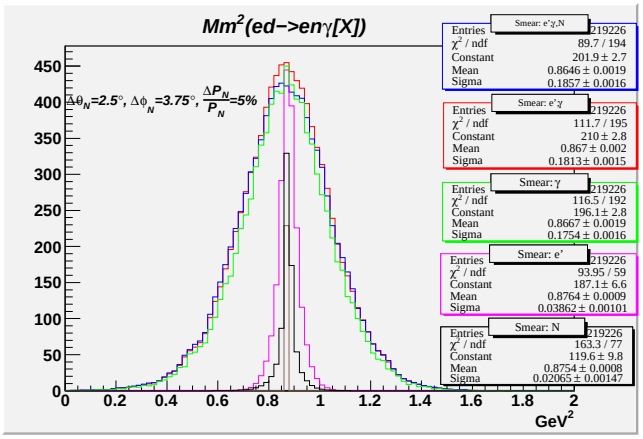

Figure 7.10: Missing mass squared of the $en\gamma$ system for fixed neutron kinematical resolutions. The curves correspond to different combinations of particles being detected with absolute precision or with realistic resolutions. The black curve is obtained with only the neutron resolutions. The red curve is due to the electron resolutions only. The green curve is due to the photon kinematical resolutions only, and the blue curve is when we consider all the kinematical resolutions from the three detected particles.

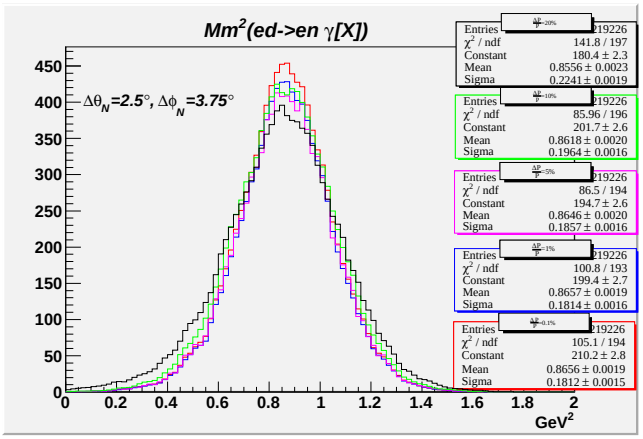

Figure 7.11: Missing mass squared of the enγ system, for fixed electron, photon and neutron $\Delta\theta_N$ and $\Delta\phi_N$ resolutions. The curves correspond to the variation of $\frac{\Delta P_N}{P_N}$ between 0.1% and 20%.

To summarize, $\Delta\phi_N$ and $\Delta\theta_N$ do not have a major impact on the neutron detector resolution, while the neutron momentum resolution is more important (albeit it is still negligeable compared to the effect of the resolutions of the electron and the photon). Since the final cost of the detector is proportional to the number of scintillators, we want to minimize their number. As we saw, a large number of segments of the detector will not give us a much better resolution. Because the ϕ resolution ($\Delta\phi = \frac{360^\circ}{N_{paddles}}$) is not crucial, we shall therefore aim at minimizing the number of paddles $N_{paddles}$. However, the final segmentation in ϕ (48 in the final design) has been chosen to allow an optical matching for light collection between the size of the PMTs and the cross section of the paddle. Also, because $\frac{\Delta P_N}{P_N}$ depends on the number of layers (related to h), we need to have several layers of paddles in order to have a good momentum resolution.

7.4 Design of the central neutron detector

The final design (Fig. 7.12) of the neutron detector consists of a barrel of plastic scintillator bars of trapezoidal shape parallel to the beam direction. The segmentation consists of 48 azimuthal segments and 3 layers in the radial direction, for a total of 144 scintillator bars (66 cm long, 3 cm thick and 3.5 cm wide). Because of the high magnetic field in the central region, the signals detected in the barrel will be transported by light guides from the backward end of each scintillator bar to a lower magnetic field region, and read out by PMTs. The front end of each bar is connected via a "U-turn" light guide to the neighboring paddle. The light emitted at the front end is therefore read out by the PMT of the neighboring paddle.

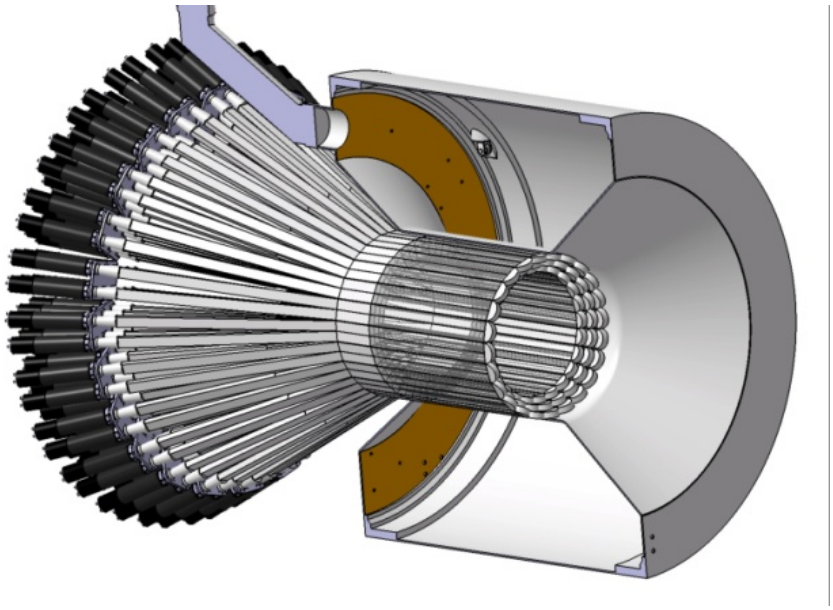

Figure 7.12: Design of the Central Neutron Detector. One can see the barrel of scintillator paddles in the central region. The light guides in the left side transport the signal from the paddles to the PMTs, located in a low magnetic field region.

7.5 Pi0 contamination

The DVCS channel consists in the production of a real photon radiated from one of the nucleons. After the selection of the events containing one electron, one photon and one neutron, one can make the identification of a good n-DVCS event by applying a cut on the $en\gamma$ missing mass.

However, the remaining $en\gamma$ events will still be contaminated by events coming from the $en\pi^0(p)$ channel, in which one photon coming from the π^0 decay (98.79% into two photons) is detected by CLAS12 while the other escapes detection.

With the GENEPI event generator, π^0 and n-DVCS events have been generated. Angular and momentum resolutions have been applied to the neutrons according to the GEANT4 simulations of the CND. Electron and photon resolutions, as well as fiducial cuts on the three final state particles have been implemented with the aid of the CLAS12 fast-MC detector simulation.

The expected level of π^0 contamination has been calculated. Fig. 7.13 shows the missing mass $en\gamma$ for both n-DVCS (red) and $en\pi^0$ (black) channel, integrated over the full kinematic range. The long right tail in the $en\pi^0$ distribution arises from the undetected photon.

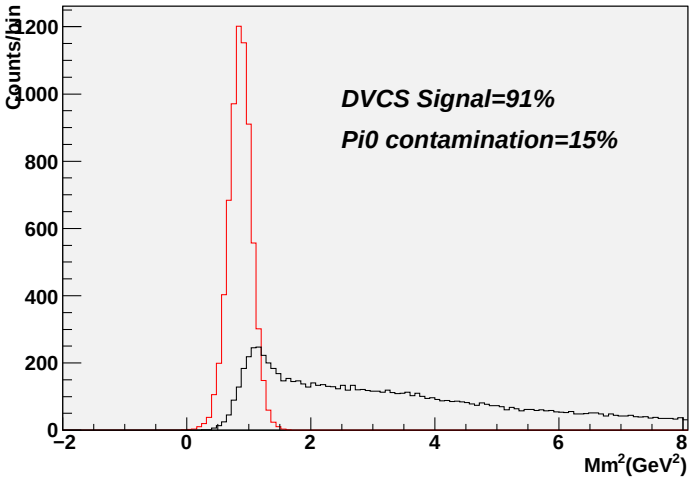

Figure 7.13: Missing mass of the $en\gamma$ system, for the n-DVCS channel (in red), and the $en\pi^0$(p) channel (black).

Due to the kinematical resolutions of the detected particles, the two distributions overlap. To reduce the contamination of the pion channel, we apply a cut on the missing mass. With a cut at 1.05 GeV^2, the π^0 contamination is reduced to 15% while around 91% of the n-DVCS events are kept.

7.6 Count rate estimate

In this session, we describe the way the count rate has been estimated for the n-DVCS reaction with the CLAS12 detector (JLab experiment [NKAM11]). We provide the expected number of reconstructed events for n-DVCS.

Using our GEANT4 simulations, we have found about 10% neutron detection efficiency for the CND (corresponding to $\sim 1\%$ per cm of scintillator).

For each 4-dimensional bin (Q^2, x_B, t, ϕ), the count rate can be calculated as:

$$N = \frac{d^4\sigma}{dQ^2 dx_B dt d\phi} \cdot \Delta Q^2 \cdot \Delta x_B \cdot \Delta t \cdot \Delta\phi \cdot L \cdot T \cdot Acc \cdot Eff \tag{7.7}$$

where $\frac{d^4\sigma}{dtdQ^2 dx_B d\phi}$ is the 4-fold differential cross section for n-DVCS given by [BMK02], T is the running time assumed to be 80 days, $L = 10^{35}\text{cm}^{-2}\text{s}^{-1}$ is the luminosity expected, Acc is the bin-by-bin acceptance of the electron and photon, and Eff is the neutron detection efficiency.

In our analysis, we adopted the following grid of bins:

- 4 bins in $Q^2(GeV^2) : [1, 2, 3.5, 5, 10]$
- 4 bins in $x_B(GeV) : [0.05, 0.15, 0.3, 0.45, 0.7]$
- 4 bins in $-t(GeV^2) : [0, 0.2, 0.5, 0.8, 1.2]$
- 12 bins of 30° in ϕ from 0° to 360°.

In Table. 7.1 and Fig. 7.14, we give the expected values (for one particular bin: $\langle t\rangle = -0.35$ GeV^2, $\langle Q^2\rangle = 2.75$ GeV^2, $\langle x_B\rangle = 0.275$ GeV) of the 4-fold cross section, the acceptance and the corresponding counts, as a function of ϕ.

$\phi(^\circ)$	$\frac{d\sigma}{dtdQ^2 dx_B d\phi}(nb/GeV^4)$	Acc×Eff	Nb events
15	0.138	2.6%	87924
45	0.027	2.1%	13491
75	0.015	2.0%	7414
105	0.011	2.8%	7248
135	0.009	4.0%	8473
165	0.008	4.0%	7643
195	0.008	3.1%	5691
225	0.008	1.8%	3610
255	0.011	1.1%	2730
285	0.015	1.0%	3719
315	0.028	1.1%	7567
345	0.297	1.8%	128645

Table 7.1: Simulation results for each ϕ bin: 4-fold differential cross section, 4-dimensional acceptance times neutron detection efficiency and number of events for n-DVCS with CLAS12 and the CND, for one particular bin: $\langle t\rangle = -0.35$ GeV^2, $\langle Q^2\rangle = 2.75$ GeV^2, $\langle x_B\rangle = 0.275$ GeV.

In each kinematic bin, the n-DVCS beam-spin asymmetry has been computed using the VGG model [VGG99]. Fig. 7.15 shows the result for the bin of Table. 7.1. A beam polarization $P = 85\%$ has been assumed. The error bars (in average of the order of 20%) depend on the values of the BSA itself (A) estimated by the VGG model, the beam polarization (P) and the number of counts:

$$\sigma_A = \frac{1}{P}\frac{\sqrt{(1-PA)^2}}{\sqrt{N}} \tag{7.8}$$

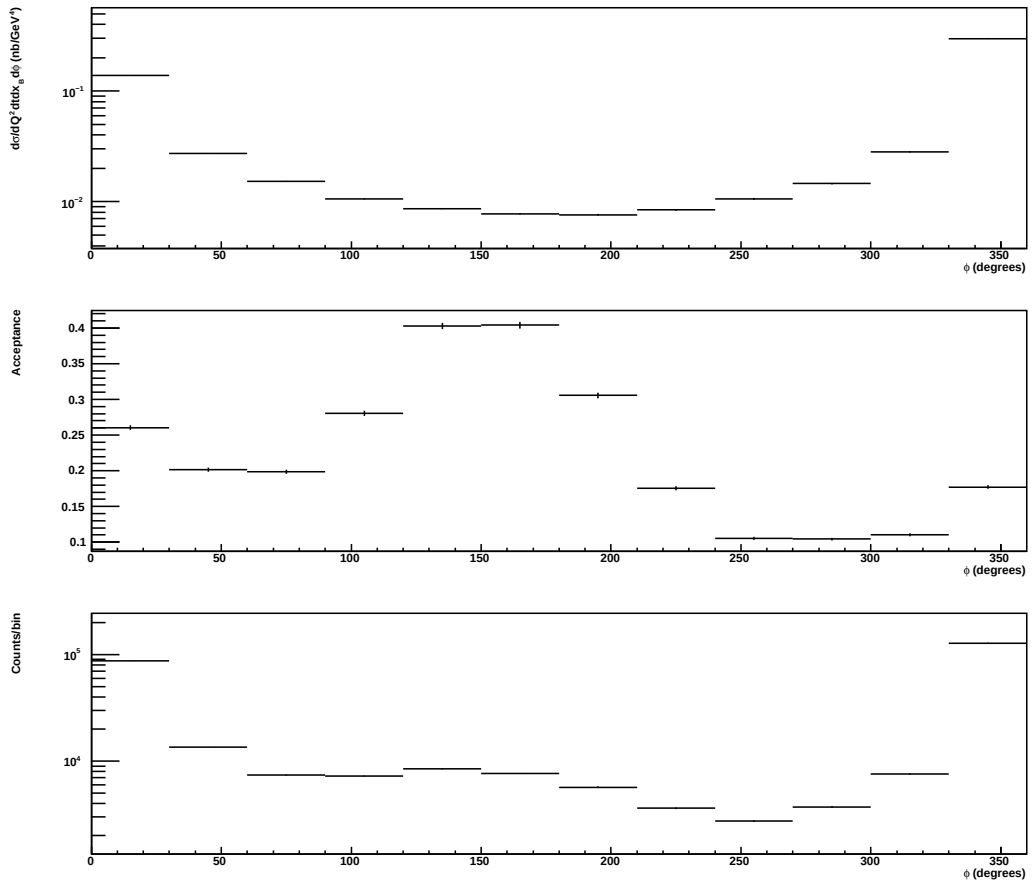

Figure 7.14: Top: cross section for n-DVCS. Middle: acceptance for the $e\gamma(p)$ final state. Bottom: expected number of counts for 80 days of beam time.

By summing all the events obtained for the full grid of bins, we can estimate the total expected number of n-DVCS counts. Overall, roughly 25 millions of n-DVCS events are expected to be collected over the full kinematic range.

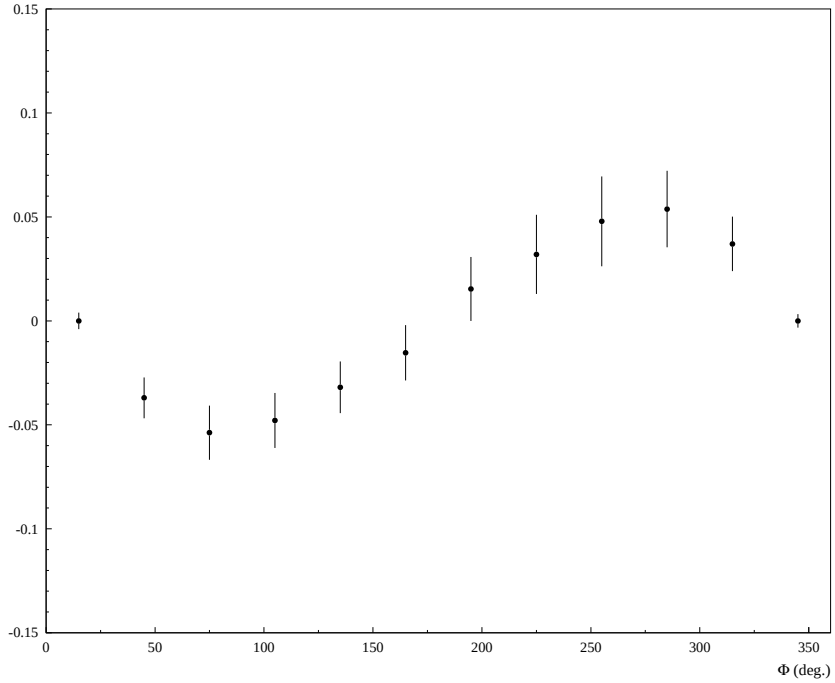

Figure 7.15: Beam-spin asymmetry for n-DVCS as predicted by the VGG model (for $J_u = 0.3$ and $J_d = 0.1$), for the bin of Table. 7.1. The error bars show the expected statistical precision of our experiment.

Chapter 8

Conclusion

We have studied the Deeply Virtual Compton Scattering process on the protonin the largest kinematic regime ever explored in the valence region. The exclusivity of the process has been ensured by detecting the three final state particles with CLAS. Using the JLab polarized electron beam operating at 5.88 GeV and an unpolarized hydrogen target, we have extracted the unpolarized cross section and the difference of beam-polarized cross section for the kinematics: $1 < Q^2 < 5$ GeV^2, $0.1 < x_B < 0.6$ and $0.09 < -t < 3$ GeV^2.

Our experimental results have been compared to the Bethe-Heitler cross section which has served as a check of normalization of our data. We also made comparisons with the VGG model, and found a relatively good agreement for the shape of the distributions, but with some differences for the normalisation. We have also compared the unpolarized and polarized cross-section of the two parts of the e1-DVCS experiement. We have found compatible results within the error bars for most of the bins. We have used these observables to extract the Compton Form Factors, the only quantities that can be extracted model independently from the DVCS experiments. The unpolarized cross section is sensitive to the real part of the amplitude, and a fitting procedure has been used to extract the $\mathcal{H}_{Re}$ CFF, which is the dominant contribution to the amplitude. The difference of polarized cross section is sensitive to the imaginary part of the amplitude, and we have the dominant CFF $\mathcal{H}_{Im}$. With these results, a preliminary physics interpretation has been made in terms of nucleon imaging over a large kinematic domain.

So far, most of DVCS measurements have been performed on a hydrogen target, providing information about the GPDs of the proton. To access the GPDs at the quark level, a necessary step is to use a deuterium target in order to access the GPDs of the neutron, thus allowing a quark flavor separation by isospin decomposition. Such an experiment is planned for the upgrade of JLab at 12 GeV. We have shown in this thesis that a neutron detector will be added in the central region of the future CLAS12 detector, allowing to ensure the exclusivity of the n-DVCS process. Studying the beam-spin asymmetry with a neutron target will provide information about $\mathcal{E}_{Im}$, that is the GPD E along the line $x = \pm\xi$. The GPD E is the least known and is one of the two GPDs entering Ji′s sum rule giving access to to the total (spin + orbital) angular momentum carried by the quarks. Ultimately, this sum rule will give access experimentally for the first time to the quark orbital momentum contribution to the nucleon spin.

The e1-DVCS experiment is part of a large program that aims to study the nucleon structure through the GPDs formalism. Along with HERMES at DESY, JLab already contributed to measure observables that are used to extract the various CFFs. With the shut-down of HERMES and JLab at 6 GeV, the future experimental program turns now to JLab at 12 GeV and COMPASS. The upgrade to 12 GeV will allow to open a new kinematic regime ($1 < Q^2 < 11$ GeV and $0.05 < x_B < 0.7$), where proposals for experiments have already been accepted to study DVCS in particular with transversally polarized targets. With its naturally polarized muon beam of 200 GeV, the COMPASS collaboration

will study DVCS at very small x_B ($0.01 < x_B < 0.3$), and therefore add constraints in a kinematic region not explored yet. It will allow one to obtain more information on the sea quark GPDs through the measurement of cross section differences and mixed beam charge and spin asymetries. Another collaboration could possibly start the study of the nucleon structure in a not too far future: the PANDA collaboration could study the time-like GPDs with $p\bar{p}$ annihilation processes in a crossed kinematics ($p\bar{p} \to \gamma\gamma*$). Finally, for the long term future, the hadronic physics community has started to work on the design of an electron-ion collider. This project will allow to reach much higher Q^2 and lower x_B due to the collision kinematics.

Chapter 9

French summary

9.1 Processus exclusif: DVCS

Les expériences de diffusion élastique et profondément inélastique permettent d'accéder respectivement aux Facteurs de Forme (FF) électromagnétique liés aux distributions spatiales des quarks dans le plan transverse, et aux distributions de partons (PDF) qui contiennent l'information sur les distributions en impulsion longitudinale des quarks dans le nucléon.

La Diffusion Compton profondément virtuelle (DVCS) nous permet d'obtenir davantage d'informations sur les constituants des nucléons. Elle offre un accès à de nouvelles fonctions de structure, les Distributions de Partons Généralisées (GPD), qui corrélent les distributions spatiales des partons dans le plan transverse avec leur fraction d'impulsion longitudinale. On peut ainsi obtenir une image tridimensionnelle (tomographie) du nucléon.

Il y a environ quinze ans, D. Muller et al. [MRG$^+$94], X. Ji [Ji97] et A. Radyushkin [Rad96] ont montré que dans le régime Bjorken, il est possible de factoriser l'amplitude DVCS en deux parties. On peut séparer une partie «dure» qui correspond au processus Compton au niveau des quarks ($\gamma^* q \to \gamma q$) calculable perturbativement en QED, et une partie "molle" non perturbative qui est paramétrisée en fonction de quatre GPDs au premier ordre et au premier twist.

La figure 9.1 montre le diagramme "sac à main" du processus DVCS sur un nucléon: $eN \to e'N'\gamma$. Un nucléon initial d'impulsion p absorbe un photon virtuel d'impulsion q émis par un électron incident, produisant dans l'état final un photon réel d'impulsion $q' = q - \Delta$ et un nucléon de recul avec une quantité de mouvement $p' = p + \Delta$. Le quark qui absorbe le photon virtuel devient virtuel et se propage perturbativement. Ce quark émet alors un photon réel (processus Compton) et retourne dans le nucléon laissé dans son état fondamental.

Les quantités $x + \xi$ ($x - \xi$) de la Fig. 9.1 référent aux fractions d'impulsion longitudinale du quark initial (final) respectivement. x est la fraction d'impulsion du proton du quark frappé, et -2ξ est la fraction d'impulsion longitudinale du transfert Δ. Ces fractions d'impulsion sont définis dans le repére du moment infini par rapport à l'impulsion moyenne du nucléon $P = \frac{p+p'}{2}$, tels que $k^+ = x\,P^+$ et $\Delta^+ = -2\xi\,P^+$, où (+) est la composante plus des vecteurs du cône de lumière. Dans la limite de Bjorken, ξ est liée à la variable de Bjorken x_B par la formule $\xi \sim \frac{x_B}{2-x_B}$. La variable $t = \Delta^2 = (p' - p)^2$ est le transfert d'impulsion au carrée entre le nucléon initial et final.

Pour chaque saveur des quarks (u, d, s), il y a quatre GPDs, H, E, $\tilde{H}$, $\tilde{E}$, ce qui correspond à chacune des quatre configurations possibles de spin-hélicité du proton et du quark (Fig. 9.2). Les GPDs H and E sont indépendantes de l'hélicité du quark et sont donc appelés GPDs non polarisées tandis que $\tilde{H}$ and $\tilde{E}$ sont dépendantes de l'hélicité du quark et sont appelés GPDs polarisés.

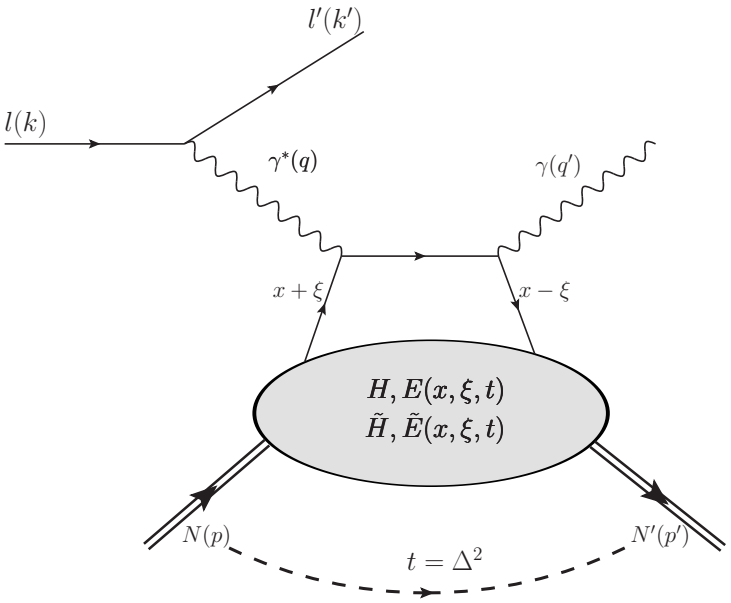

Figure 9.1: Diagramme du "sac à main" du processus DVCS dans la région DGLAP $x \in [\xi, 1]$, correspondant à la diffusion sur un quark.

H et $\tilde{H}$ conservent le spin du proton, tandis que E et $\tilde{E}$ renversent le spin du proton. Dans ce dernier cas, l'hélicité globale n'est pas conservé (le proton change d'hélicité, mais pas le quark), et la conservation du moment angulaire implique la présence d'un moment angulaire orbital.

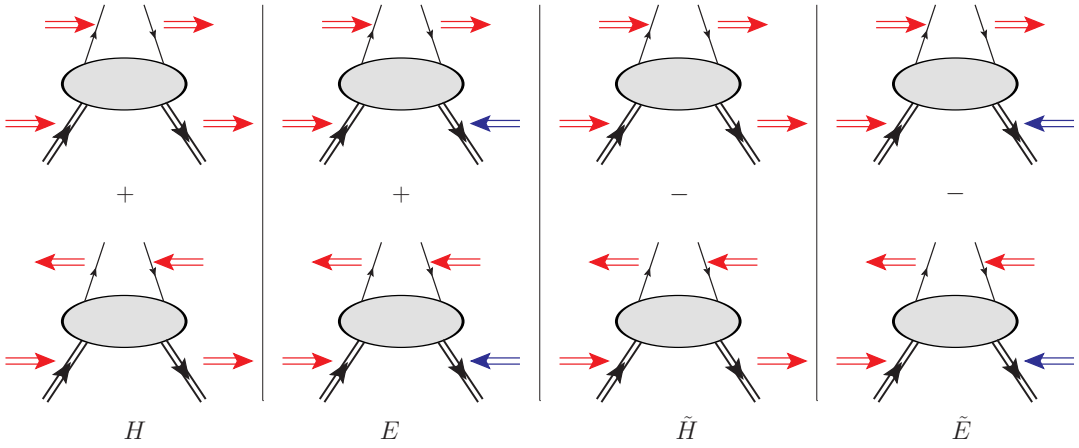

Figure 9.2: Les quatre états d'hélicité des nucléons/quark avec les GPDs associées. Les flèches indiquent les états d'hélicité du proton et du quark. Les flèches bleues indiquent le renversement de spin du proton. Les GPDs H and E sont indépendantes de l'hélicité du quark et se composent de la somme des états d'hélicité du proton et du quark. Les GPDs $\tilde{H}$ et $\tilde{E}$ dépendent de l'hélicité du quark et consistent en la différence d'états d'hélicité du proton et du quark.

Les GPDs dépendent de trois variables: x, ξ et t. Les GPDs représentent l'amplitude de probabilité

de trouver un quark (anti-quark) dans le nucléon avec une fraction d'impulsion longitudinale $x+\xi$ et de le remettre dans le nucléon avec une fraction d'impulsion longitudinale $x-\xi$. Les GPDs sont définies pour ξ et $x \in [-1,1]$. Les valeurs relatives de ces deux variables permettent de distinguer l'interaction entre le photon virtuel et le nucléon dans trois régions différentes:

- Les régions $x > \xi$ et $x < -\xi$ sont appelés la région DGLAP. Elle correspond à l'équation d'évolution de QCD en Q^2 pour les PDFs définies dans les réactions DIS. Si $x \in [\xi, 1]$ ($x \in [-1, -\xi]$), les deux fractions d'impulsion $x+\xi$ et $x-\xi$ sont positives (négatives) et les GPDs décrivent l'émission et la réabsorption d'un quark (antiquark) avec différentes impulsions.

- La région $|x| < \xi$ est appelé la région ERBL[1]. Elle correspond à l'équation d'évolution de QCD en Q^2 pour les Distributions d'Amplitudes (DA). Dans cette région, $x+\xi$ est positif (ce qui correspond à un quark) et $x-\xi$ est négatif (ce qui correspond à un anti-quark). Cette région est sensible à la teneur en meson (ie $q\bar{q}$) du nucléon et n'est pas accessible dans le processus de DIS (car $\xi \to 0$ dans la limite avant). Les GPDs représentent alors l'amplitude de probabilité de trouver une paire $q\bar{q}$ dans le nucléon.

Les GPDs ne sont pas totalement inconnues et possédent les propriétes suivantes:

- Dans la limite avant ($\Delta = p - p' = 0, \xi = 0$), le théorème optique relie la partie imaginaire de l'amplitude DVCS à la section efficace du DIS.

- Des règles de somme indépendantes de modèle relient le premier moment en x des GPDs aux Facteurs de Formes élastiques [Ji97].

- X. Ji a dérivé une règle de somme qui lie dans la limite avant ($t \to 0$) le second moment en x des GPDs H et E au moment angulaire total (spin + orbital) porté par les quarks J_{quarks}.

De plus, il a été démontré [Bur03] que la dépendence en t des GPDs peut être liée à la répartition spatiale transverse des partons dans le nucléon. Les Facteurs de Formes correspondent aux GPDs mais intégrées sur la fraction d'impulsion x. Si l'on utilise la même transformée de Fourier pour les GPDs que pour les facteurs de forme (Eq. 2.4), il est alors possible d'interpréter les GPDs comme une décomposition en x des facteurs de forme: nous avons accès aux FFs à différentes valeurs de x, plutôt qu'intégré sur x.

Ainsi, les informations provenant des PDFs des expériences DIS et les FFs mesurées en ES sont désormais unifiés dans le formalisme des GPDs. Cela donne la possibilité d'avoir une image à trois dimensions (deux spatiales et une en impulsion) du nucléon.

En plus de l'amplitude DVCS, la section efficace de l'électroproduction exclusif d'un photon ($eN \to eN\gamma$) reçoit également la contribution du processus Bethe-Heitler (BH) (Fig. 9.3). Dans ce cas, le photon réel est émis soit par l'électron entrant ou par l'électron diffusé, mais pas par le nucléon lui-même, à la différence du DVCS.

[1] Efremov-Radyushkin, Brodsky-Lepage.

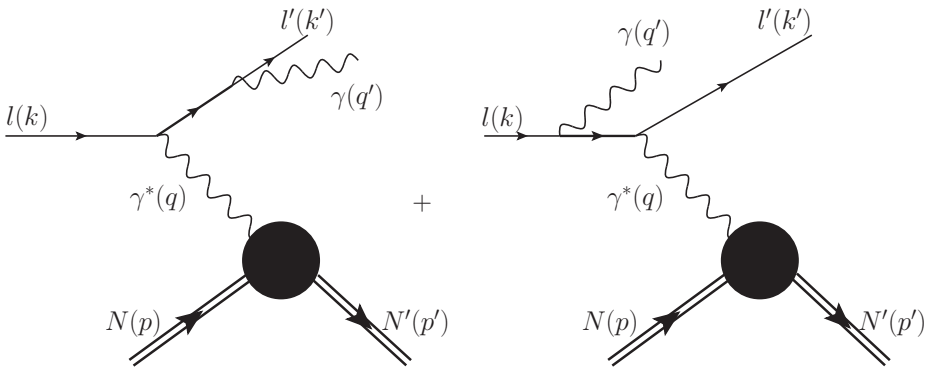

Figure 9.3: Processus Bethe-Heitler.

9.2 Appareillage expérimental

CEBAF (Fig. 9.4) est un accélérateur d'électrons de haute intensité dont l'énergie maximale est environ 6 GeV. Il est constitué d'un injecteur d'électrons (67 MeV) et de deux accélérateurs linéaires (linacs) reliés entre eux par des arcs de recirculation contenant des aimants de guidage.

Après chaque passage, le faisceau peut être séparé en trois faisceaux délivrés simultanément dans les salles expérimentales de JLab: à savoir, Hall A, B et C. Chacune de ces salles peut fonctionner avec sa propre intensité de faisceau et d'énergie, ce qui permet d'effectuer des mesures simultanées avec différents appareillages.

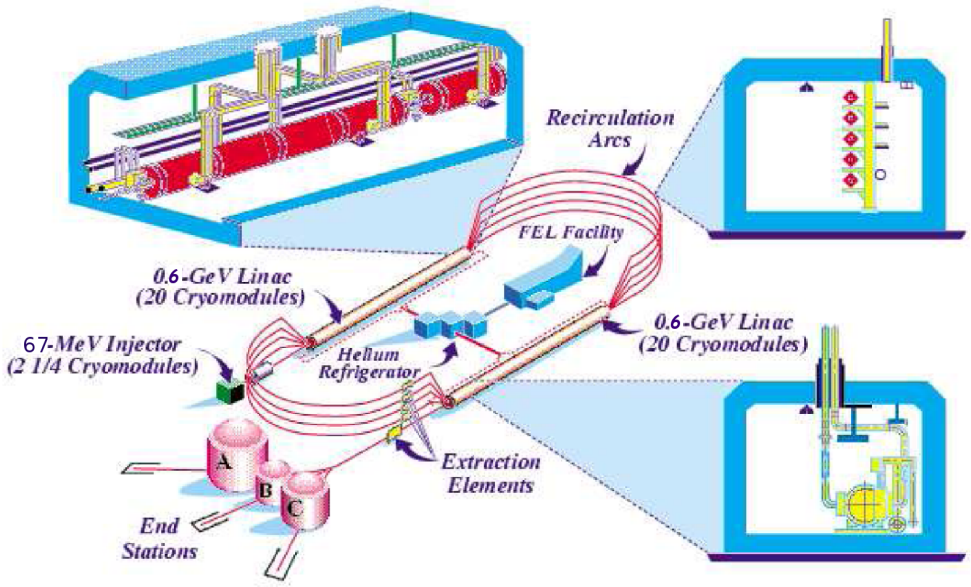

Figure 9.4: Configuration du "Continuous Electron Beam Accelerator Facility (CEBAF)" avec les différentes salles d'experiences A, B et C.

Le spéctrometre CLAS [ea03a] (Figs. 9.5 et 9.6) permet l'identification et la mesure cinématique des particules chargées et neutres. Il a un rayon d'environ 5 mètres et sa structure comprend six bobines supraconductrices, situées autour de la ligne de faisceau, qui produisent un champ magnétique toroïdal. CLAS a une structure en sous-couches de détecteurs qui sont répartis en six secteurs symétriques.

Ce détecteur a une grande acceptance couvrant la majeure partie de l'angle solide, particulièrement adapté pour l'étude des procéssus exclusifs. Les particules chargées peuvent être détectées entre 5° et 140° et les particules neutres entre 8° and 45°. La résolution en impulsion est de l'ordre du pour cent ($0.5\% \leq \frac{\Delta P}{P} \leq 2\%$) et les résolutions angulaires sont de $1 \leq \Delta\theta \leq 1.5$ mrad et $2 \leq \Delta\phi \leq 3$ mrad. La résolution temporelle est $100 \leq \Delta t \leq 250$ ps.

Une particule provenant du vertex d'interaction traverse plusieurs couches de détecteurs permettant sa détection et son identification. Ces détecteurs sont constitués de:

- 3 couches de chambres à dérive qui permettent de mesurer l'impulsion des particules chargées grâce a la trajectographie dans le champ magnétique
- des compteurs Cherenkov qui permettent de distinguer les électrons des pions
- des scintillateurs qui fournissent l'information pour le déclenchement et le temps de vol des particules

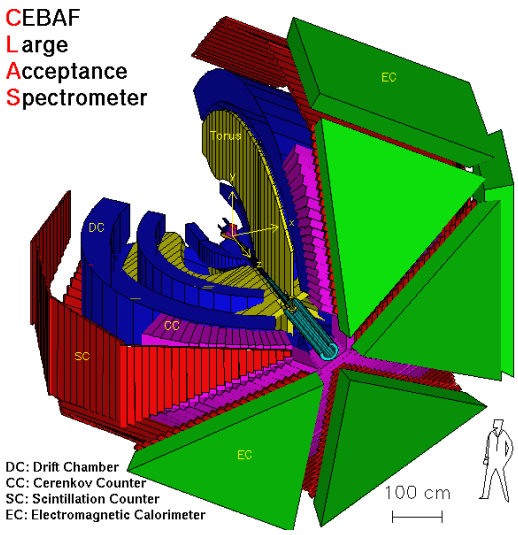

Figure 9.5: Schéma de CLAS. Quatre des six secteurs du CLAS sont affichées, avec leurs différentes couches de sous-détecteurs.

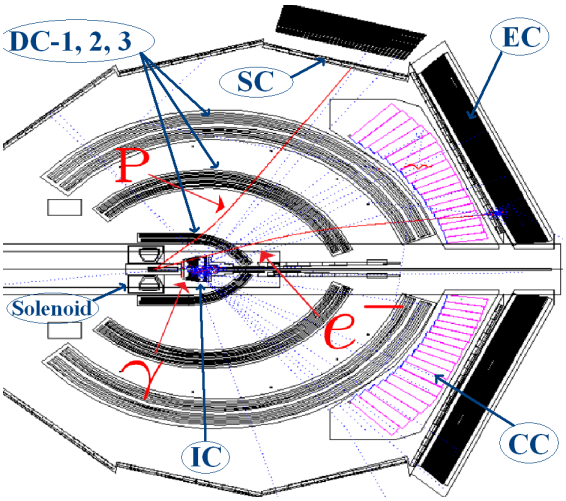

Figure 9.6: Evénement $ep\gamma$ typique dans une vue de côté de CLAS. Le solénoïde et le calorimètre intérieur, qui ne font pas partie de l'équipement standard du CLAS, peuvent être vus dans la partie centrale.

- l'identification et les mesures d'énergie des particules chargées et neutres sont fournis par les calorimètres électromagnétiques, situés dans la région à l'avant.

9.3 Vérification de la qualité des données et corrections en utilisant le processus de diffusion élastique

La sélection des électrons et des protons a été presentée dans cette section. Nous fournissons aussi l'ensemble des coupures fiducielles utilisées dans l'analyse pour ne garder que les régions des détecteurs où l'on a un bon accord entre les données et les simulations.

Pour le canal DVCS, il est important de connaître avec précision la valeur de l'énergie du faisceau car la section efficace DVCS peut varier très rapidement en fonction des quantités cinématiques x_B, Q^2, t (dans lesquelles la valeur de l'énergie du faisceau apparait).

L'énergie du faisceau peut être extraite à partir de l'analyse de la diffusion élastique $ep \to ep$ avec la connaissance de seulement deux variables cinématiques. On peut montrer qu'avec la connaissance des angles de diffusion des deux particules de l'état final, il est possible de calculer l'énergie du faisceau avec la formule suivante:

$$E_B = M_p.\left[\left(\frac{1}{tan(\theta_p).tan(\frac{\theta_e}{2})}\right) - 1\right] \tag{9.1}$$

Nous avons trouvé à partir de cette étude une valeur reconstruite de l'énergie du faisceau égale à $E_B = 5.883 \pm 0.035$ GeV.

La motivation des corrections cinématiques vient de l'observation d'une dépendance en ϕ du pic élastique dans la masse invariante W. En effet, la distribution W présente une fluctuation du pic de l'élastique en fonction de ϕ par rapport à la masse du proton. En conséquence, nous avons besoin d'introduire des corrections ad-hoc au niveau des données.

Connaissant l'énergie du faisceau d'électrons E_B et l'angle polaire du proton θ_p, les contraintes cinématique de la diffusion élastique permettent de calculer l'angle polaire de l'électron $\theta_{e_{calc}}$. De la cinématique à deux corps, on calcule l'angle polaire de l'électron avec:

$$\theta_{e_{calc}} = 2\,tan^{-1}\left(\frac{m_p}{(E_B + m_p)\,tan\theta_p}\right) \tag{9.2}$$

L'impulsion des électrons $p_{e_{calc}}$ peut être calculée à partir de l'énergie du faisceau E_B et l'angle polaire de l'électron corrigé θ_e. Avec les contraintes de la cinématique de diffusion élastique, nous avons:

$$p_{e_{calc}} = \frac{E_B}{1 + 2\,\frac{E_B}{m_p} sin^2(\theta_e/2)} \tag{9.3}$$

Le pic de l'élastique a été ajusté aux données avec une fonction gaussienne. Fig. 9.7 et 9.8 montrent respectivement la moyenne et la valeur sigma de ces ajustements, avant et après correction, pour les six secteurs de CLAS.

Les corrections appliquées montrent une amélioration significative de la valeur moyenne de la distribution élastique W. Cependant, nous n'avons pas obtenu une amélioration de la résolution σ (à l'exception du troisième secteur).

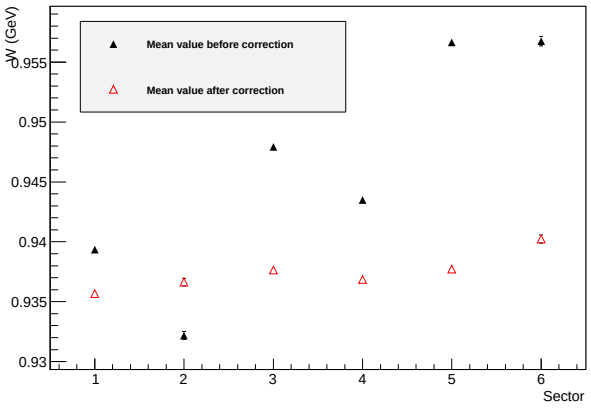

Figure 9.7: Valeur moyenne de la distribution élastique W en fonction du numéro de secteur, avant et après les corrections.

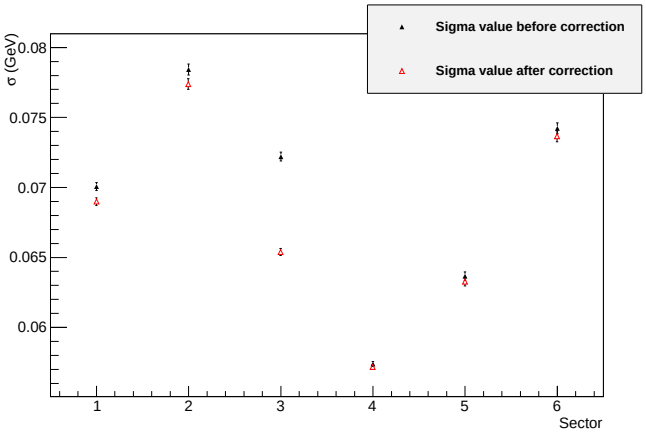

Figure 9.8: Valeur sigma de la distribution élastique W en fonction du numéro de secteur, avant et après correction.

9.4 Analyse de la section efficace DVCS

Dans cette section, nous montrons la sélection des photons DVCS ainsi que les coupures fiducielles appliquées dans l'analyse concernant les photons. Nous montrons aussi les différentes coupures d'exclusivité pour séléctionner le canal DVCS.

La section efficace DVCS 4 fois différentielle est obtenue à partir de:

$$\frac{d^4\sigma}{dQ^2 dx_B dt d\Phi} = \frac{N_{ep\to ep\gamma}}{Acc\, L_{int}\, F_{vol}} \times F_{rad} \tag{9.4}$$

où:

- (Q^2, x_B, t, Φ) sont les quatre variables indépendantes décrivant le processus DVCS.
- $N_{ep\to ep\gamma}$ est le nombre d'événements $ep\gamma$ dans chaque bin (Q^2, x_B, t, Φ), corrigés par la contamination des π^0.
- Acc est l'acceptance du détecteur CLAS. Elle est déterminée par simulation pour chacun des bins (Q^2, x_B, t, Φ).
- L_{int} est la luminosité intégrée pour l'ensemble des données.
- F_{vol} correspond à l'hyper-volume utile du bin (Q^2, x_B, t, Φ).
- F_{rad} sont les corrections radiatives calculées dans chaque bin en (Q^2, x_B) afin de calculer la section efficace au terme de Born.

Dans la Fig. 9.9, nous présentons les résultats de la section efficace DVCS non polarisée $\frac{d^4\sigma}{dQ^2\, dx_B\, dt\, d\Phi}$ (nbarn/GeV^4) calculée pour le bin 2 en (Q^2, x_B), et comparé (en vert) à la section efficace intégrée du Bethe-Heitler (BH). La section efficace de l'électroproduction exclusif d'un photon ($eN \to eN\gamma$) reçoit la contribution à la fois du DVCS et du BH. Il est attendu que la contribution du BH domine presque complètement la section efficace dans les régions où le photon réel est émis dans la même direction que l'électron incident ou sortant, ce qui correspond aux régions à petit et grand Φ. La principale contribution du signal DVCS est dans la région centrale en Φ.

La différence de section efficace polarisées peut être calculée pour chacuns des bins quadri-dimmensional comme:

$$\begin{aligned}\frac{d^4\sigma_{pol}}{dQ^2\, dx_B\, dt\, d\Phi} &= \frac{1}{2}\left[\frac{d^4\overrightarrow{\sigma}}{dQ^2\, dx_B\, dt\, d\Phi} - \frac{d^4\overleftarrow{\sigma}}{dQ^2\, dx_B\, dt\, d\Phi}\right] \\ &= \frac{1}{2\,P}\left(\frac{\overrightarrow{N}_{DVCS}}{L_{\overrightarrow{int}}} - \frac{\overleftarrow{N}_{DVCS}}{L_{\overleftarrow{int}}}\right)\frac{F_{rad}}{\Delta Q^2\, \Delta x_B\, \Delta t\, \Delta\Phi\, Acc\, F_{vol}}\end{aligned} \tag{9.5}$$

La différence de section efficace polarisées est sensible principalement à la CFF $\mathcal{H}_{Im}$. Sa distribution a une forme sinusoïdale modulée par les propagateurs du BH.

Dans la Fig. 9.10, nous montrons les résultats de σ_{pol} tracés en fonction de Φ pour chacun des 12 bin en t pour le bin numéro deux en (Q^2, x_B).

L'asymétrie de faisceau $\mathcal{A}_{LU}$ est définie comme le rapport de σ_{pol} sur σ_{unp}. Un avantage important de l'asymétrie de faisceau est que tous les facteurs de normalisation s'annulent durant le calcul de l'asymétrie. Cette observable est définie comme:

$$\mathcal{A}_{LU} = \frac{1}{P}\left(\frac{\overrightarrow{N}_{DVCS} - \overleftarrow{N}_{DVCS}}{\overrightarrow{N}_{DVCS} + \overleftarrow{N}_{DVCS}}\right) \tag{9.6}$$

Nous montrons dans la figure. 9.11 les résultats des asymétries faisceau pour le bin numéro deux en (Q^2, x_B).

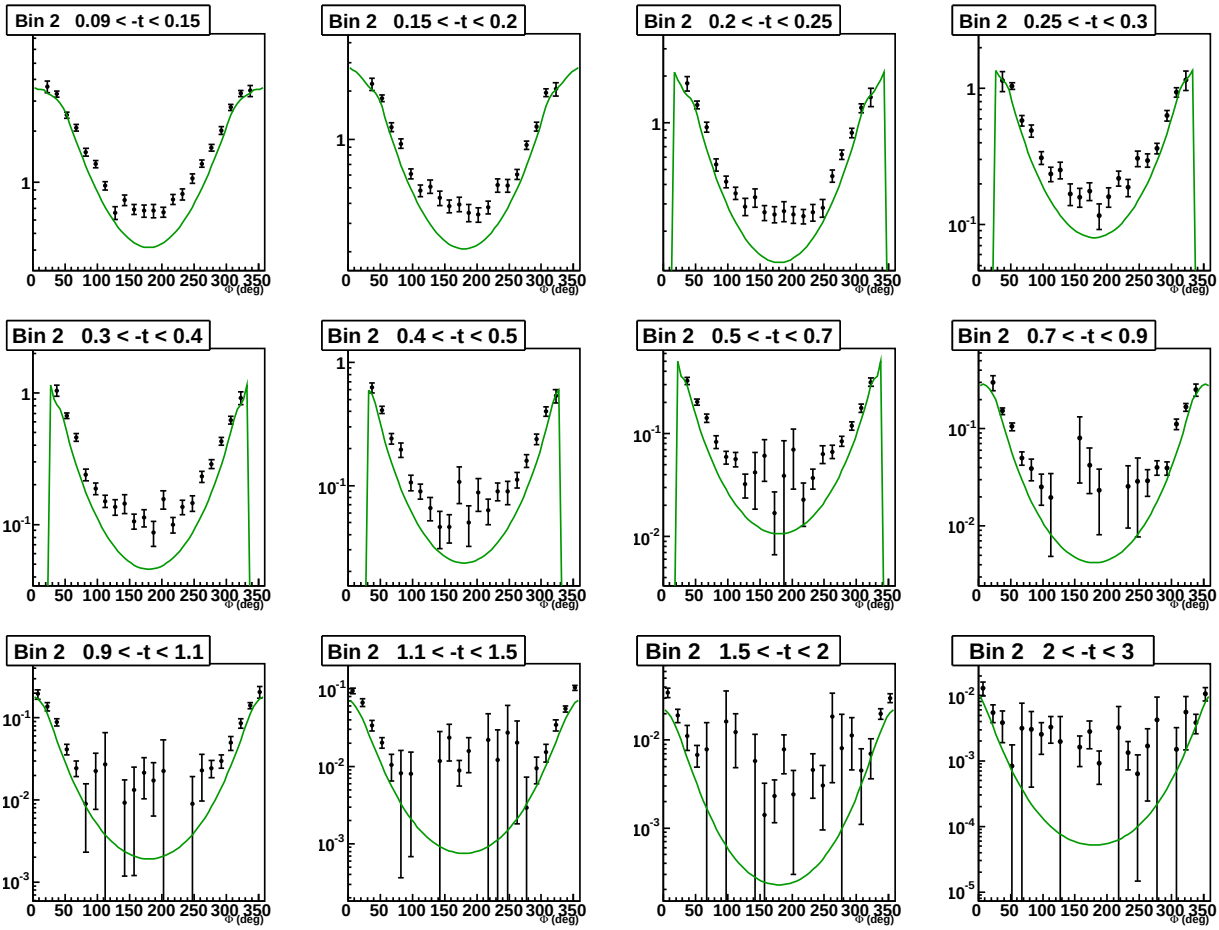

Figure 9.9: Section efficace du DVCS (nbarn/GeV^4) en fonction de Φ pour les 12 bins en t du bin numéro deux en (Q^2, x_B), comparé à la section efficace du BH (vert) intégrée sur la taille des bins.

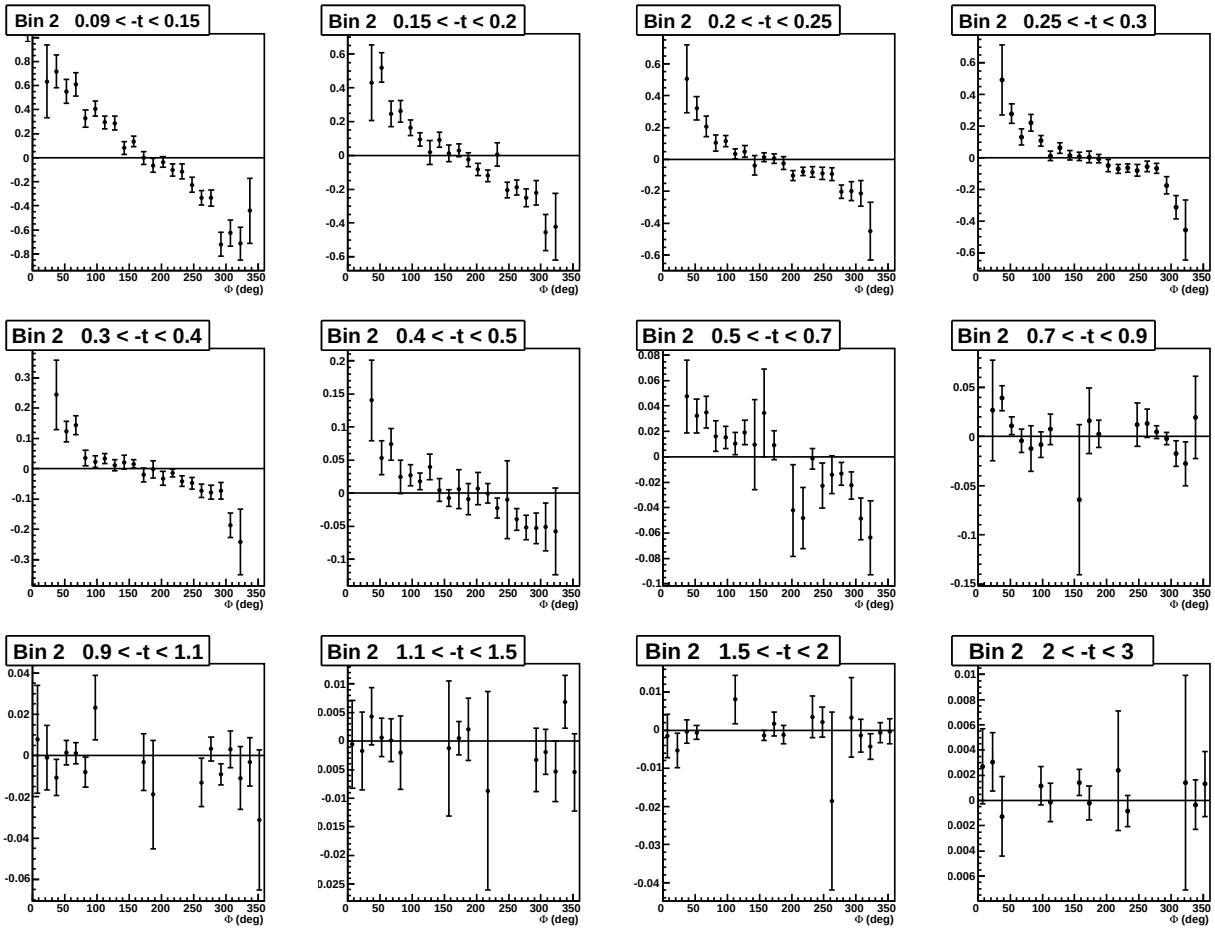

Figure 9.10: Différence de section efficace polarisée en fonction de Φ pour les 12 bins en t du bin numéro deux en (Q^2, x_B).

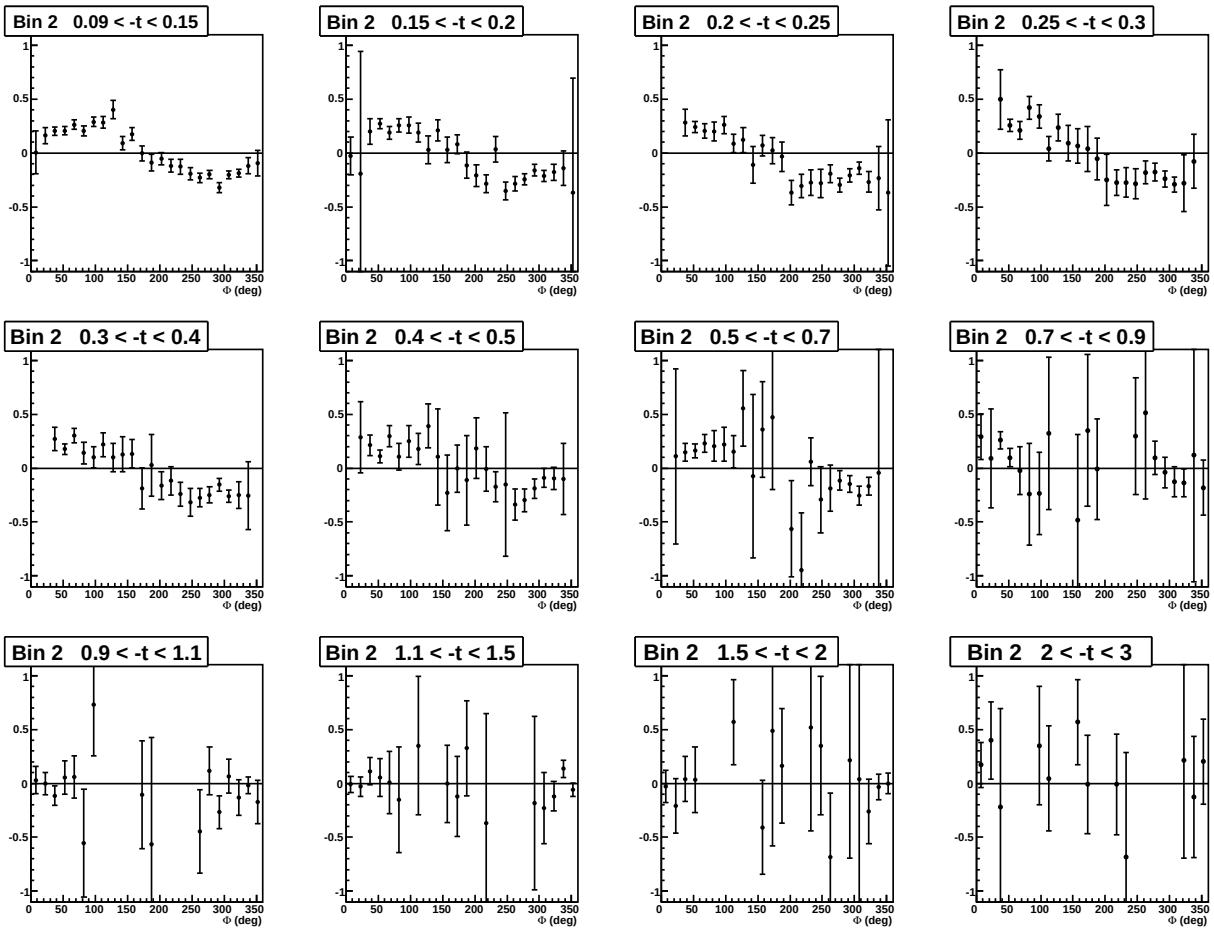

Figure 9.11: Asymétries en fonction de Φ pour les 12 bins en t du bin numéro deux en (Q^2, x_B).

9.5 Interpretation préliminaire

Chacune des trois observables précédentes ont été comparées aux résultats d'un model de GPD. Nous avons utilisé dans ce travail le model VGG qui a montré un accord raisonnable en terme d'amplitude et de forme. Pour extraire l'information liée aux GPDs, nous avons utilisé la procédure d'ajustement modèle-indépendante qui a été développé dans les références. [Gui08a, Mou09]. La procédure est que, pour un point expérimental donné (x_B, t), les sept CFFs sont pris comme paramètres libres et sont extraits des observables expérimentales DVCS.

σ_{unp} et σ_{pol} sont surtout sensibles à $\mathcal{H}_{Re}$ et $\mathcal{H}_{Im}$ respectivement, les autres CFFs étant sous-dominants dans ces observables. En utilisant les résultats précédents de la procédure d'ajustement, on a extrait les CFFs $\mathcal{H}_{Im}$ et $\mathcal{H}_{Re}$ sur un domaine cinématique trés étendu. Ils sont représentés dans les figures. 9.12 et 9.13, en fonction de t pour chacun des 13 bin en (Q^2, x_B).

Ces résultats préliminaires indiquent que la pente en t de $\mathcal{H}_{Im}$ diminue avec l'augmentation de x_B. Si nous négligeons la contribution en ξ, ceci peut être interprété comme suit: le transfert d'impulsion t est la variable conjugué du paramètre d'impact $b_\perp$, une petite pente en t signifie que les quarks de valence (grand x) ont tendance à rester dans le centre du nucléon. A l'inverse, les quarks de la mer (faible x) s'étendent jusqu'à la périphérie du nucléon.

L'interprétation de $\mathcal{H}_{Re}$ n'est pas si intuitive, car elle représente une GPD intégrée sur x et pondérée par un facteur $\frac{1}{x\pm\xi}$. Il sert principalement comme une contrainte forte pour la modélisation de la GPD H. Nous observons que la prédiction du modèle VGG est en bon accord avec les données.

Pour $\xi = 0$, la transformée de Fourier 2-dimensionnelle de la GPD $H(x, 0, t)$ est égale à la distribution de la densité de parton $\rho(x, b_\perp)$. Elle fournit une mesure simultanée de l'impulsion longitudinale x à une position donnée (paramètre d'impact transverse $b_\perp$) pour les quarks non polarisés. La distribution de la densité peut être obtenue à partir de H avec l'équation suivante:

$$\rho(x, 0, b_\perp) = \int_0^\infty \frac{dt}{4\pi} J_0(b\sqrt{t})\, H(x, 0, t) \tag{9.7}$$

où J_n est la fonction de Bessel cylindrique régulière. En utilisant les sections efficaces non polarisée et polarisée, nous avons été en mesure d'extraire la CFF $\mathcal{H}_{Im}$ sur un régime cinématique très large.

La figure 9.14 montre la superpostion des densités de charge de protons pour différente valeur en x. Pour une fraction d'impulsion x élevée, la pente en t est petite. La transformée de Fourier donne alors une densité de charge du proton étroite en fonction de $b_\perp$. Cela signifie que les quarks de valence qui ont une grande fraction d'impulsion sont localisés dans le centre du nucléon. Pour les fractions d'impulsion x petites, la pente en t des GPDs devient grande. La distribution de la densité devient plus large et signifie que les quarks de la mer avec petite fraction d'impulsion sont étendus à de grandes valeurs de $b_\perp$.

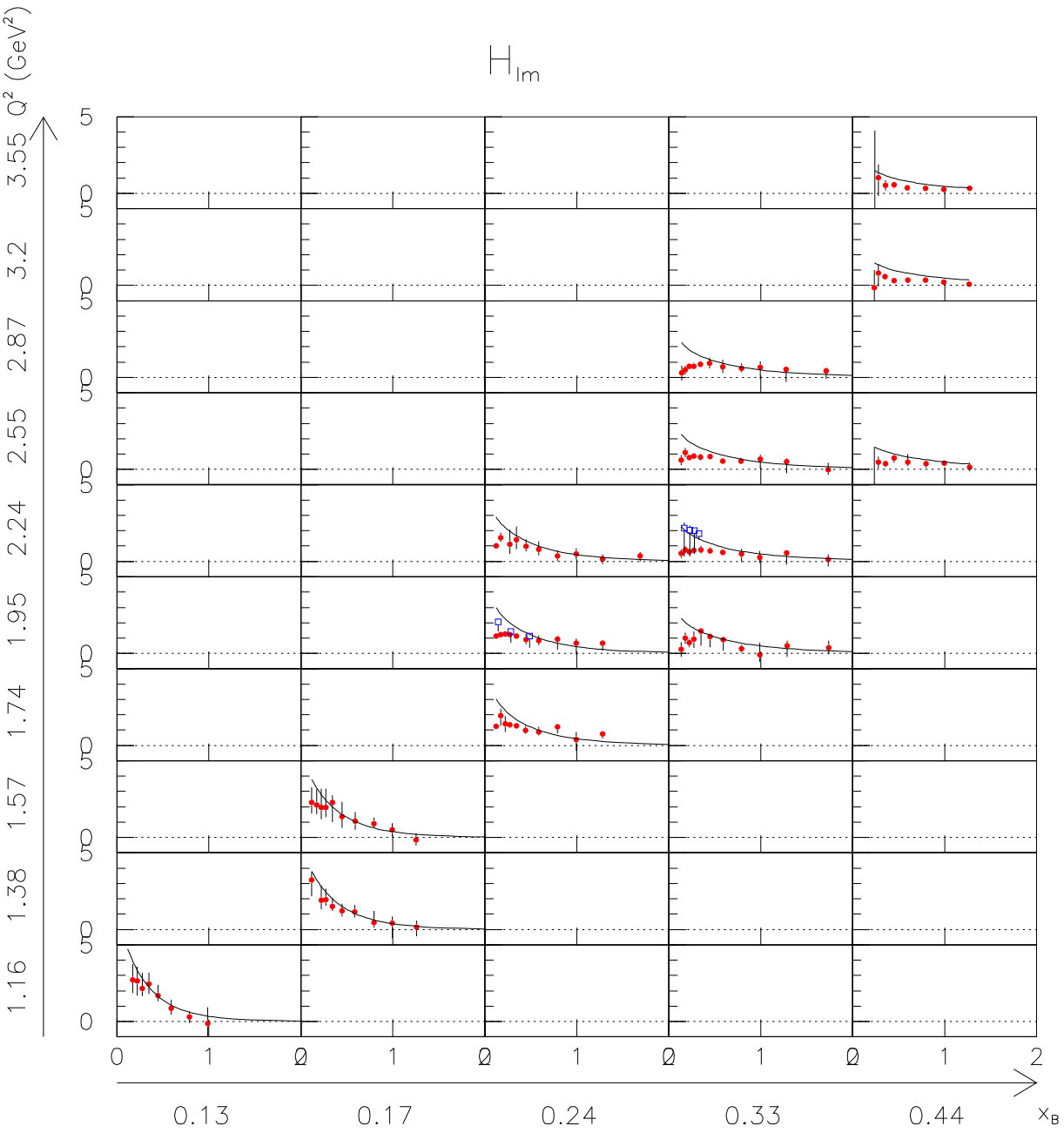

Figure 9.12: Les points rouges indiquent l'extraction de $\mathcal{H}_{Im}$ en fonction de t, pour chacun des 13 bins en (Q^2, x_B). Les lignes continues sont les résultats du modèle VGG. Les points bleus à $x_B = 0,33$ sont les extractions à partir des données du Hall-A [ea06a]. Les points bleus à $x_B = 0,24$ sont les extractions du Hall-B [ea08c, ea06b].

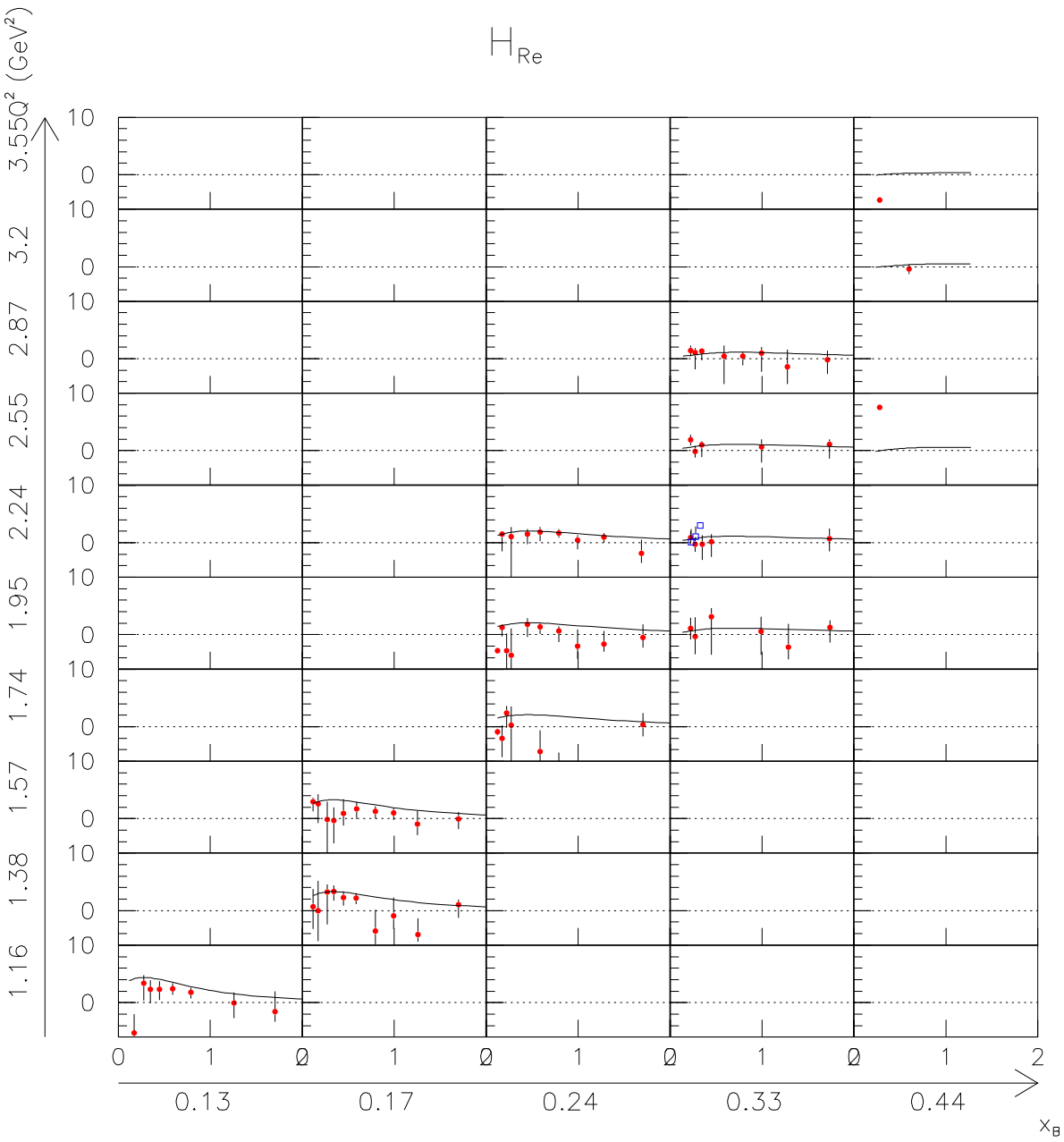

Figure 9.13: Les points rouges indiquent l'extraction de $\mathcal{H}_{Re}$ en fonction de t, pour chacun des 13 bins en (Q^2, x_B). Les lignes continues sont les résultats du modèle VGG. Les points bleus sont les extractions à partir des données du Hall-A [ea06a].

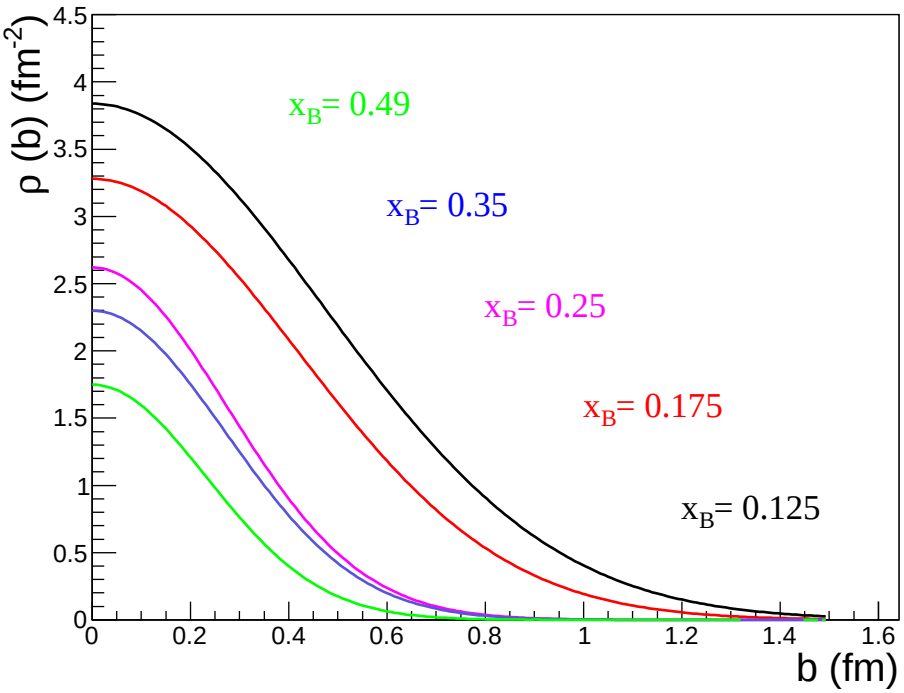

Figure 9.14: La densité de charge du proton en fonction du paramètre d'impact $b_\perp$, pour cinq valeurs différentes de x_B.

Appendix A

Elastic scattering

A.1 Amplitudes and cross sections

Elastic scattering off a point-like proton

We define the elastic scattering (Fig. A.1) process as: $l(k)+N(p) = l'(k')+N'(p')$, with $k = (E, \overrightarrow{k})$ ($k' = (E', \overrightarrow{k'})$) the four vector of the incoming (outgoing) electron respectively.

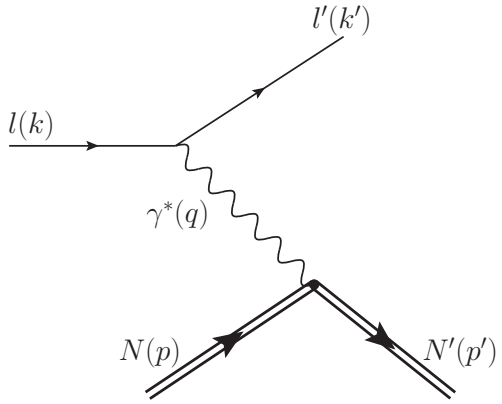

Figure A.1: Point-like elastic scattering.

For an elastic scattering of an electron off a point-like particle, the invariant amplitude follows from the Feynman rules:

$$i\mathcal{M} = \bar{u}(k')(-ie\gamma_\mu)u(k)\frac{-i}{q^2}\bar{u}(p')(ie\gamma^\mu)u(p) \tag{A.1}$$

which consists of the product of the electromagnetic current of the electron $\bar{u}(k')(-ie\gamma_\mu)u(k)$, the photon propagator $\frac{-i}{q^2}$ and the nucleon electromagnetic current $\bar{u}(p')(ie\gamma^\mu)u(p)$ in the case it is a point-like particle. Taking into account the phase space, the differential cross section is:

$$\left.\frac{d\sigma}{d\Omega}\right|_{lab} = \left(\frac{E'}{8\pi ME}\right)^2 \times \frac{1}{4}\sum_{spins}|\mathcal{M}|^2. \tag{A.2}$$

Combining with Eq. A.1, we compute the unpolarized cross section of this process (for $m_e = 0$) as:

$$\left.\frac{d\sigma}{d\Omega}\right|_{lab} = \frac{\alpha^2}{4E^2\sin^4\frac{\theta_e}{2}}\frac{E'}{E}\left[\cos^2\frac{\theta_e}{2} - \frac{q^2}{2M^2}\sin^2\frac{\theta_e}{2}\right] \tag{A.3}$$

Elastic scattering off a proton

We know from Stern and collaborators experiment (magnetic deflection of molecular beam employing H_2, performed in 1932 [EOO37]) that the proton has a magnetic moment that is approximately a factor 2.79 (measured 2.46 in 1932) larger than predicted for a Dirac particle. The consequence is that the proton can not be considered as a point-like spin-$\frac{1}{2}$ particle. It has an extended structure.

By estimating the deviation of the elastic cross section between data and theoretical models (taking into account different root-mean-square radius of the charge), Hofstadter and collaborators experiments [MH56] proved that the nucleon had a spatial extent of the order of the Fermi ($\langle r \rangle_{charge} = (0.78 \pm 0.20) \times 10^{-13}$ cm at that time).

As a consequence, the computation of the cross section can not be done with the amplitude A.1. One has to take into account the inner structure of the nucleon, which is parametrized in terms of the FFs. For a proton target, the invariant amplitude is computed as:

$$i\mathcal{M} = \bar{u}(k')(-ie\gamma_\mu)u(k)\frac{-i}{q^2}\langle p'|J^\mu_{em}(0)|p\rangle \tag{A.4}$$

where $\langle p'|J^\mu_{em}(0)|p\rangle$ is the local non-forward matrix element of the hadronic current J^μ_{em}. It can be written as $\langle p'|J^\mu_{em}(0)|p\rangle = \bar{u}(p')(ie\Gamma^\mu)u(p)$, where Γ^μ parametrizes the nucleon structure and is built from the 16 independants Dirac matrices $(1, \gamma^\mu, \sigma^{\mu\nu}, \gamma^\mu\gamma^5, \gamma^5)$ (see also Appendix C).

Since Γ^μ transforms as a vector, it must be a linear combination of possible vectors $\gamma^\mu, p^\mu, p'^\mu$. The parity-conservation of the reaction implies to remove the axial and the pseudo-scalar terms (involving the γ^5 matrix). Then, by using the gauge invariant condition[1] and the Gordon identity[2] (allows to write the vector structure in terms of the scalar and tensor structures), we finally restrict the general form of the hadronic current as:

$$\langle p'|J^\mu_{em}(0)|p\rangle = \bar{u}(p')\left[F_1(q^2)\gamma^\mu + \frac{F_2(q^2)}{2M}i\sigma^{\mu\nu}q^\nu\right]u(p) \tag{A.5}$$

where $\sigma^{\mu\nu} = i/2(\gamma^\mu\gamma^\nu - \gamma^\nu\gamma^\mu)$.

In this part, we have only mentionned the two Dirac and Pauli form factors (Eq. A.5). They describe the nucleon structure probed with an electromagnetic current. To complete the description of the nucleon structure, one can use an axial probe allowing to access the axial structure of the nucleon. We can use νN scattering or pion electroproduction to have access to the axial part of the nucleon. One introduce two other form factors (G_A and G_P) that parametrize the axial current and can be written as:

$$J^\mu_{Axial} = \bar{u}(p')\left[G_A(q^2)\gamma^\mu\gamma^5 + \frac{G_P(q^2)}{M}\gamma^5 q^\mu\right]u(p) \tag{A.6}$$

A.2 From F_1 and F_2 to G_E and G_M

Another set of nucleon form factors exists. They are combinations of the Dirac and Pauli FFs and allow to write Eq. 2.1 without interference term. We introduce G_E and G_M, respectively the Sachs electric and magnetic FFs [ESW60]:

$$\begin{cases} G_E = F_1 - \tau F_2 \\ G_M = F_1 + F_2 \end{cases}$$

[1] $q_\mu\Gamma^\mu = 0$

[2] $\bar{u}(p')\gamma^\mu\bar{u}(p) = \bar{u}(p')\left[\frac{p^\mu + p'^\mu}{2m} + \frac{i\sigma^{\mu\nu}q^\nu}{2m}\right]u(p)$

with $\tau = \frac{-q^2}{4M^2}$. In the static limit, Sachs FFs have the values of the charge and the magnetic moment of the proton and the neutron, i.e: $G_E^p = 1$, $G_M^p = \mu_p$ and $G_E^n = 0$, $G_M^n = \mu_n$.

We re-express the Rosenbluth formula (Eq. 2.1) in terms of the Sachs FFs as:

$$\frac{d\sigma}{d\Omega} = \left(\frac{d\sigma}{d\Omega}\right)_{Mott} \times \frac{E'}{E}\frac{1}{(1+\tau)}\left[G_E^2 + \frac{\tau}{\epsilon}G_M^2\right], \tag{A.7}$$

where $\epsilon = [1+2(1+\tau)\tan^2(\frac{\theta_e}{2})]^{-1}$ is the virtual photon polarization, and $\left(\frac{d\sigma}{d\Omega}\right)_{Mott} = \frac{\alpha^2}{4E^2\sin^4\frac{\theta_e}{2}}\cos^2(\frac{\theta_e}{2})$ is the Mott cross section (scattering of a spin $\frac{1}{2}$ electron by a point-like spin-less proton).

A.3 Extraction of the form factors

Rosenbluth separation

We can determine the two form factors by fixing q^2 and varying θ_e and E. We form the following reduced cross section [PPV07]:

$$\left(\frac{d\sigma}{d\Omega}\right)_{reduced} = \frac{E}{E'}\frac{\epsilon(1+\tau)}{\tau}\left(\frac{d\sigma}{d\Omega}\right)_{exp} / \left(\frac{d\sigma}{d\Omega}\right)_{Mott} = G_M^2 + \epsilon\frac{G_E^2}{\tau} \tag{A.8}$$

with $\left(\frac{d\sigma}{d\Omega}\right)_{exp}$ the measured cross section for different values of θ and E at fixed q^2.

At fixed q^2, the reduced cross section is linear in ϵ. A fit to the data allows to extract the y-intercept G_M^2 and the slope $\frac{G_E^2}{\tau}$. This method, called the Rosenbluth separation, is efficient to extract G_M^2, but due to the factor $\frac{1}{\tau}(\propto \frac{M^2}{-q^2})$, is much less adequate to extract G_E^2 at large q^2. Indeed, the precision on G_E^2 strongly decreases when $-q^2 \gg M^2$, typically for $-q^2$ larger than 1 GeV^2.

Experimentally, it was found that the FFs were compatible with an exponential model that correspond to the dipole parametrization in the momentum space. The fit obtained is:

$$G_E(q^2) \simeq \frac{G_M(q^2)}{\mu_p} \simeq G_D(q^2) = \left(1 - \frac{q^2}{0.71}\right)^{-2}. \tag{A.9}$$

This dipole form can be interpreted as a charge and magnetic moment distribution with an exponential decrease with the distance to the center.

Polarization method

The second method relies on the polarization technique [AR68]. When the beam and the target are polarized, or if the beam is polarized and the polarization of the outgoing proton is measured, then the corresponding cross section provides an interference term of the form $G_E G_M$, allowing to extract the ratio G_E/G_M with a high precision.

Using an initial electron beam longitudinally polarized, one can measure the polarization of the outgoing proton by studying the asymmetry of the azimuthal angle distribution. In the one-photon exchange approximation, the proton has two non-vanishing polarization components in the scattering plane: P_l which is parallel to the emitted proton momentum, and P_t which is perpendicular:

$$\begin{aligned} P_t &= -2\sqrt{\tau(1+\tau)}\, G_E G_M \tan(\theta_e/2) \\ P_l &= \frac{E+E'}{M}\sqrt{\tau(1+\tau)}\, G_M^2 \tan^2(\theta_e/2) \end{aligned} \tag{A.10}$$

G_E/G_M is obtained by computing the ratio of the polarization components P_t/P_l [AdJP11]:

$$\frac{G_E}{G_M} = -\frac{P_t}{P_l}\frac{(E+E')}{2M}\tan(\frac{\theta}{2}) \tag{A.11}$$

This ratio can be measured without changing either the beam energy or the diffusion angle, thus reducing many sources of systematic errors.

For $-q^2 \geq 1GeV^2$, the recent accumulated data at JLab exhibit a discrepancy with the dipole parametrization, and the picture of a proton described by an exponential distribution of charge and magnetic moments is not correct. As shown in Fig. A.2, these two methods give incompatible results for the $\frac{G_E}{G_M}$ ratio. One can see that $\mu_p G_{Ep}/G_{Mp}$ is rather flat and compatible with unity for the Rosenbluth separation while results from the polarization method decrease almost linearly as a function of q^2.

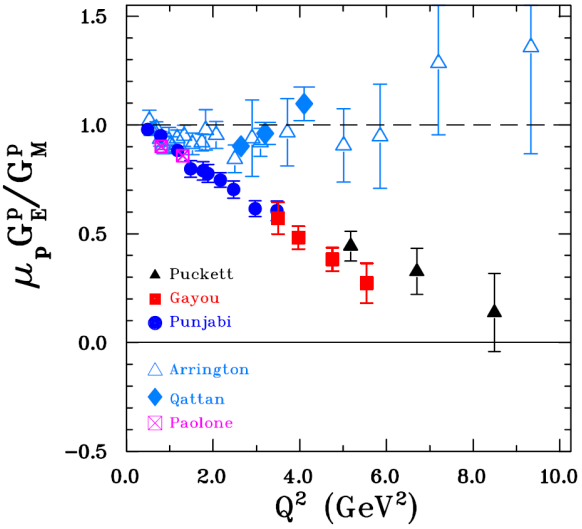

Figure A.2: Comparison of $\mu_p G_{Ep}/G_{Mp}$ as a function of q^2 using the JLab polarization data (Gayou [ea02a], Punjabi [ea05c], Paolone [PMS+10], Puckett [ea10b]) and the JLab Rosenbluth separation (world data analysis: Arrington [Arr04], and Qattan [ea05d]). Plot extracted from [AdJP11].

A possibility to explain the difference of results could be that the above computations of the Rosenbluth (Eq. 2.1) and the polarization formula, assume the exchange of a single photon between the electron and the proton. If radiative effects are largely supressed in the polarization method because of the ratio, it is not the case for the Rosenbluth separation. The discrepancy observed could therefore arise from radiative effects. Taking into account the exchange of two photons in the radiative corrections could reconcile these two results [BMT05].

Several experiments ([ea04a] and [ea05b] for instance) are planned to analyse the 2γ exchange at JLab in order to study the discrepancy. Experimentally, the 2γ exchange amplitude can be accessed by studying the cross section difference between the elastic scattering using an electron ($e^- p \to e^- p$) and a positron ($e^+ p \to e^+ p$) beam.

A.4 Interpretation of the Sachs FFs in the Breit frame

The nucleon electromagnetic current can be expressed in any reference system. The Breit frame is defined as the system where there is no energy transfered to the nucleon. Consequently, the energy of the virtual photon vanishes and its four-momentum squared q^2 coincides with its 3-momentum squared.

Working in the Breit frame allows to work in a three-dimension space. In this case, one has an analogy with a non-relativistic description of the nucleon electromagnetic structure. Using a three-dimensional Fourier transformation, one can then make an identification with the classical charge and magnetization densities:

$$\rho_{ch}(\overrightarrow{r}) = \int \frac{d^3q}{(2\pi)^3} e^{i\overrightarrow{q}\cdot\overrightarrow{r}} G_E(q^2) \tag{A.12}$$

that represents the three-dimensional charge distribution of the partons inside the nucleon (a similar identification is done for the magnetic distribution).

However, this interpretation of the Sachs FFs is spoiled by relativistic effects. Indeed, the interpretation is non-relativistic because the Breit frame varies with q^2.

Appendix B

Deep inelastic scattering

B.1 Amplitude and cross section

The final hadronic state is unknown so that the computation of the inelastic amplitude is defined as:

$$i\mathcal{M} = \bar{u}(k')(-ie\gamma_\mu)u(k)\frac{-i}{q^2}\int d^4z\, e^{iq\cdot z}\langle X|J^\mu(z)|p\rangle \tag{B.1}$$

where $J^\mu(z)$ is the quark electromagnetic current at the space-time z, and is defined as:

$$J^\mu(z) = \sum_i Q^i\, \bar{q}_i(z)\gamma^\mu q_i(z) \tag{B.2}$$

with i the quark flavor, Q its charge, and $(\bar{q},\, q)$ are the quark fields. With the phase-space term, the inelastic cross section is the product of the leptonic and the hadronic tensors:

$$\frac{d^2\sigma}{d\Omega d\nu} = \frac{\alpha^2}{q^4}\left(\frac{E'}{E}\right)^2 L_{\mu\nu}T^{\mu\nu} \tag{B.3}$$

The leptonic tensor descbribes the interaction of a Dirac particle in an electromagnetic field:

$$\begin{aligned} L_{\mu\nu} &= \frac{1}{2}Tr[(\not{k}' + m_e)\gamma_\mu(\not{k} + m_e)\gamma_\nu] \\ &= 2(k'_\mu k_\nu + k'_\nu k_\mu - (k\cdot k' - m_e^2)). \end{aligned} \tag{B.4}$$

The hadronic tensor is expressed in term of the Fourier transform of the forward matrix element of two electromagnetic currents at two separate points [SG94]:

$$T^{\mu\nu} = \frac{1}{4\pi}\sum_{spins}\int d^4z e^{iq\cdot z}\langle p|J^\mu(z)J^\nu(0)|p\rangle \tag{B.5}$$

The only independant quantities available are p_μ, q_μ and $g_{\mu\nu}$. From current conservation and the fact that $T^{\mu\nu}$ is a second-rank Lorentz tensor, the hadronic tensor decomposes as:

$$T^{\mu\nu}(p,q) = \left(-g^{\mu\nu} + \frac{q^\mu q^\nu}{q^2}\right)W_1(\nu,q^2) + \frac{1}{M^2}\left(p^\mu - \frac{pq}{q^2}q^\nu\right)\left(p^\nu - \frac{pq}{q^2}q^\nu\right)W_2(\nu,q^2) \tag{B.6}$$

where $W_{1,2}(\nu,q^2)$ are the structure functions of the nucleon and depend upon the two independent scalars ν and q^2.

From the current conservation of the leptonic part: $q_\mu L^{\mu\nu} = q_\nu L^{\mu\nu} = 0$, we finally get the effective formula for the hadronic tensor (all the terms in $q_{\mu,\nu}$ are suppressed):

$$T^{\mu\nu}_{eff}(p,q) = -W_1(\nu,q^2)g^{\mu\nu} + \frac{W_2(\nu,q^2)}{M^2}p_\mu p_\nu, \tag{B.7}$$

and we finally compute the cross section of this process as:

$$\frac{d^2\sigma}{d\Omega d\nu} = \frac{\alpha^2}{4E^2\sin^4\frac{\theta}{2}}\frac{E'}{E}\left(W_2\,\cos^2\frac{\theta}{2} + 2W_1\,\sin^2\frac{\theta}{2}\right) \tag{B.8}$$

B.2 The parton model

This model assumes that the virtual photon interacts with a point-like constituent of the nucleon. We can compare the equation of the elastic scattering on a point-like particle (Eq. A.3) where there is only one independant variable, to the inelastic scattering one (Eq. B.8) where there are two independant variables. Differentiating Eq. A.3 with respect to the variable ν, and applying the required condition of elasticity $-q^2 = 2M\nu$, we write Eq. A.3 as:

$$\left.\frac{d^2\sigma^i}{d\Omega d\nu}\right|_{lab} = \frac{\alpha^2}{4E^2\sin^4\frac{\theta}{2}}\frac{E'}{E}\left[e_i^2\cos^2\frac{\theta}{2} - e_i^2\frac{q^2}{2m_i^2}\sin^2\frac{\theta}{2}\right]\delta(\frac{q^2}{2m_i}+\nu) \tag{B.9}$$

where we subsitute $\alpha^2 \to \alpha^2 e_i^2$ with e_i the fractional charge of the parton, and where we introduced $m_i = xM$ the mass of the parton. i is the quark flavor (i= u, d, s ...), and x is the momentum fraction carried by the parton.

If we identify this result with the inclusive cross section (Eq. B.8), we can extract the contribution to W_1 and W_2 of the parton i:

$$\begin{aligned} W_1^i &= e_i^2\frac{-q^2}{4x^2M^2}\delta(\frac{q^2}{2xM}+\nu) \\ W_2^i &= e_i^2\delta(\frac{q^2}{2xM}+\nu) \end{aligned} \tag{B.10}$$

To obtain the total contribution of the partons, we sum over all types of partons i, and integrate over all values of x:

$$W_1(\nu,q^2) = \sum_i \int_0^1 dx f_i(x) W_1^i(\nu,q^2) \tag{B.11}$$

where $f_i(x)$ describes the probability that the struck parton i carries a fraction x of the proton's momentum p. These functions are called the parton distribution functions (PDF). By using the relations of the Dirac delta function:

$$\delta(g(x)) = \frac{\delta(x-x_0)}{|dg/dx|_{x=x_0}} \quad , \quad \int_0^1 dx\, G(x)\delta(x-x_0) = G(x_0) \tag{B.12}$$

we obtain:

$$W_1(\nu,q^2) = \sum_i e_i^2\frac{f_i(x_B)}{2M} \equiv \frac{1}{M}F_1(x_B) \tag{B.13}$$

and similarly for W_2:

$$W_2(\nu,q^2) = \sum_i \frac{2x_B^2M}{-q^2}e_i^2 f_i(x_B) \Rightarrow \nu W_2(\nu,q^2) = \sum_i e_i^2 x_B f_i(x_B) \equiv F_2(x_B) \tag{B.14}$$

The conservation of the 4-vector energy-momentum at the quark vertex gives the condition :

$$(xp^\mu + q^\mu)^2 = (xp'^\mu)^2 = m_i^2 \Rightarrow x = \frac{-q^2}{2M\nu} = x_B. \tag{B.15}$$

So in DIS, the momentum fraction x is equal to the Bjorken variable x_B, so that $F_2(x_B) = F_2(x)$.

Appendix C

DVCS cross section derivation

We propose here to derive the Deeply Virtual Compton Scattering amplitude according to the Feynman rules. According to our discussion in Section 2.3, the cross section at leading order is dominated by the single-quark scattering, shown in Fig. C.1.

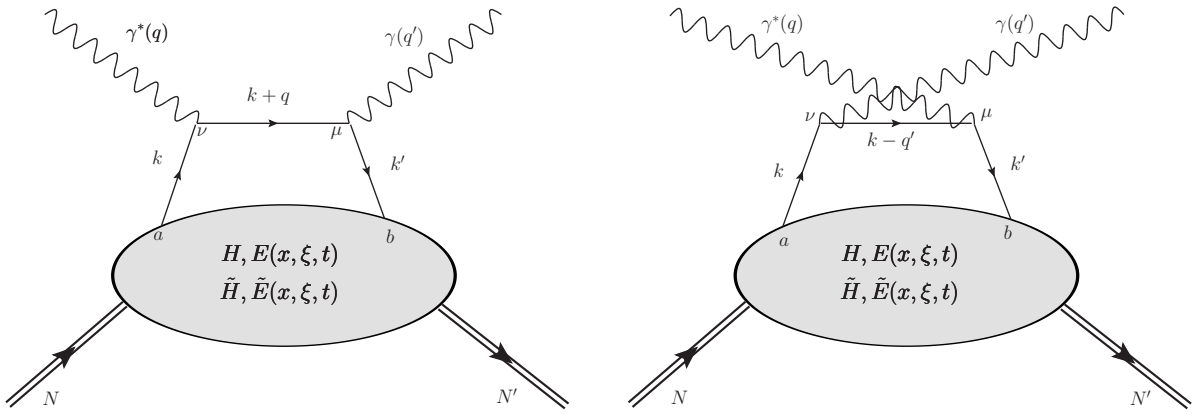

Figure C.1: Handbag diagram (and the crossed-term) of the DVCS process.

Following the Feynman rules, the invariant amplitude can be written as:

$$\begin{aligned} i\mathcal{M} &= \sum_q \int \frac{d^4k}{(2\pi)^4}(-i|e|Q_q)^2 \left[\gamma^\mu \epsilon^*_\mu \left(i\frac{\not{k}+\not{q}+m_q}{(k+q)^2-m_q^2+i\varepsilon}\right)\gamma^\nu \epsilon_\nu + \gamma^\nu \epsilon_\nu \left(i\frac{\not{k}-\not{q}'+m_q}{(k-q')^2-m_q^2+i\varepsilon}\right)\gamma^\mu \epsilon^*_\mu\right]_{ba} \\ &\times \langle p'| \int d^4z e^{iz\cdot k} T[\bar{q}_b(0) q_a(z)] |p\rangle \end{aligned} \tag{C.1}$$

where a and b are spinor indices, and $\bar{q}(0)$ $q(z)$ are the quark fields at the space-time points 0 and z respectively. They are defined as:

$$\begin{aligned} q(z) &= \int \frac{d^3k}{(2\pi)^3\sqrt{2k_0}} \sum_s \left[c(k,s)u(k,s)e^{-iz\cdot k} + d^\dagger(k,s)v(k,s)e^{iz\cdot k}\right] \\ \bar{q}(z) &= \int \frac{d^3k}{(2\pi)^3\sqrt{2k_0}} \sum_s \left[d(k,s)\bar{v}(k,s)e^{-iz\cdot k} + c^\dagger(k,s)\bar{u}(k,s)e^{iz\cdot k}\right] \end{aligned} \tag{C.2}$$

with (c, d) and ($c^\dagger$, $d^\dagger$) the annihilation and the creation operators respectively.

The term $\int \frac{d^4k}{(2\pi)^4}$ corresponds to the integration of the loop momentum. T is the time-ordering operator. The first line of Eq. C.1 corresponds to the perturbative part of the DVCS amplitude, while the non-local non-forward operator of the second line parametrize our ignorance about the nucleon structure.

Using the Fierz decomposition[1], we express the quark current in terms of the 16 Dirac matrices listed in table C.1:

$$\begin{aligned}\bar{q}_b(0)q_a(z) &= \bar{q}_{b'}(0).\delta_{b'b}.q_{a'}(z).\delta_{a'a} = \bar{q}_{b'}(0)q_{a'}(z).\delta_{b'b}\delta_{a'a} \\ &= \bar{q}_{b'}(0)q_{a'}(z)\frac{1}{4}\sum_\alpha(\Gamma_\alpha)_{b'a'}.(\Gamma^\alpha)_{ab} = \frac{1}{4}\sum_\alpha(\Gamma^\alpha)_{ab}.\bar{q}_{b'}(0)(\Gamma_\alpha)_{b'a'}q_{a'}(z) \\ &= \frac{1}{4}\Big((\mathbb{1})_{ab}.\bar{q}q + (\gamma^\lambda)_{ab}.\bar{q}\gamma_\lambda q + (\sigma^{\alpha\beta})_{ab}.\bar{q}\sigma_{\alpha\beta}q + (\gamma^5\gamma^\lambda)_{ab}.\bar{q}\gamma_\lambda\gamma^5 q + (\gamma^5)_{ab}.\bar{q}\gamma^5 q\Big) \quad \text{(C.3)}\end{aligned}$$

$\Gamma^\alpha(\alpha = S,V,T,A,P)$	$\Gamma_\alpha = (\Gamma^\alpha)^{-1}$
$\Gamma^S = \mathbb{1}$	$\Gamma_S = \mathbb{1}$
$\Gamma^V = \gamma^\mu = \gamma^0,\gamma^1,\gamma^2,\gamma^3$	$\Gamma_V = \gamma_\mu = \gamma_0,\gamma_1,\gamma_2,\gamma_3$
$\Gamma^T = \sigma^{\mu\nu} = \sigma^{01},\sigma^{02},\sigma^{03},\sigma^{12},\sigma^{13},\sigma^{23}$	$\Gamma_T = \sigma_{\mu\nu} = \sigma_{01},\sigma_{02},\sigma_{03},\sigma_{12},\sigma_{13},\sigma_{23}$
$\Gamma^A = \gamma^5\gamma^\mu = \gamma^5\gamma^0,\gamma^5\gamma^1,\gamma^5\gamma^2,\gamma^5\gamma^3$	$\Gamma_A = \gamma_\mu\gamma^5 = \gamma_0\gamma^5,\gamma_1\gamma^5,\gamma_2\gamma^5,\gamma_3\gamma^5$
$\Gamma^P = i\gamma^5$	$\Gamma_P = -i\gamma^5$

Table C.1: Basis made of 16 Dirac matrices. Every 4×4 matrix can be decomposed in the basis of 5 structures: Scalar($\mathbb{1}$), Vector(γ^μ), Tensor($\sigma^{\mu\nu}$), Pseudoscalar($i\gamma^5$) and Axial($\gamma^5\gamma^\mu$), with $\gamma^5 = i\gamma^0\gamma^1\gamma^2\gamma^3$ and $\sigma^{\mu\nu} = \frac{i}{2}[\gamma^\mu,\gamma^\nu]$.

In principle, all these structures are possible. However, we develop here the DVCS amplitude by making the approximation that the quark mass is equal to zero. It results in removing all the structures that have an even number of γ-matrices because they lead to a trace of an odd number of γ-matrices that is equal to zero. If one keeps the quark mass, the tensor and the pseudoscalar structures survive and lead to the so called chiral-odd GPDs (transversity GPDs) [HJ98], not described in this thesis. Finally, only the vector structure γ^λ and the axial structure $\gamma^5\gamma^\lambda$ survive from Eq. C.3.

Summing over the spinor indices, the amplitude C.1 becomes:

$$\begin{aligned}i\mathcal{M} &= -i\sum_q\int\frac{d^4k}{(2\pi)^4}(|e|Q_q)^2\epsilon^*_\mu\epsilon_\nu\frac{1}{4}\times\Bigg\{ \\ &\quad \left(Tr\left[\gamma^\mu\frac{\not k+\not q}{(k+q)^2+i\varepsilon}\gamma^\nu\boldsymbol{\gamma^\lambda}\right] + Tr\left[\gamma^\nu\frac{\not k-\not q'}{(k-q')^2+i\varepsilon}\gamma^\mu\boldsymbol{\gamma^\lambda}\right]\right)\times\langle p'|\int d^4z e^{iz\cdot k}T[\bar{q}(0)\boldsymbol{\gamma_\lambda}q(z)]|p\rangle \\ &+ \left(Tr\left[\gamma^\mu\frac{\not k+\not q}{(k+q)^2+i\varepsilon}\gamma^\nu\boldsymbol{\gamma^5\gamma^\lambda}\right] + Tr\left[\gamma^\nu\frac{\not k-\not q'}{(k-q')^2+i\varepsilon}\gamma^\mu\boldsymbol{\gamma^5\gamma^\lambda}\right]\right)\times\langle p'|\int d^4z e^{iz\cdot k}T[\bar{q}(0)\boldsymbol{\gamma_\lambda\gamma^5}q(z)]|p\rangle\Bigg\}\end{aligned} \quad \text{(C.4)}$$

We will now use the light-cone coordinates. Light-cone coordinates show what are the large and small components of momentum so that the calculations can be simplified. Light-cone coordinates are defined by a change of variables from the usual (t, x, y, z) coordinates. Given a vector a^μ= (a^0, a^1, a^2, a^3), its light-cone components are defined by:

$$a^+ = \frac{1}{\sqrt{2}}(a^0+a^3), \quad a^- = \frac{1}{\sqrt{2}}(a^0-a^3), \quad a^\perp = (a^1,a^2) \quad \text{(C.5)}$$

so that a^μ is written as $a^\mu = (a^+,a^\perp,a^-)$. The scalar product of two light-cone vectors is defined as:

$$a\cdot b = a^+b^- + a^-b^+ - a^\perp\cdot b^\perp \quad \text{(C.6)}$$

[1] $\delta_{il}\delta_{jk} = \frac{1}{4}\sum_\alpha(\Gamma_\alpha)_{ij}.(\Gamma^\alpha)_{kl}$

and the norm is:

$$a^2 = 2a^+a^- - a^{\perp 2} \tag{C.7}$$

For the DVCS process, it is possible to define two light-cone vectors p_1 and p_2 so that the proton and the virtual photon are colinear along z with opposite direction. In this frame, the proton flies almost only along the direction of p_1 (Fig. C.2). We introduce the two lightlike vectors $p_1 = \frac{P^+}{\sqrt{2}}(1,0,0,1)$ and $p_2 = \frac{1}{\sqrt{2}\,P^+}(1,0,0,-1)$, with $P = \frac{p+p'}{2}$ the average nucleon 4-momentum. The vectors $p_{1,2}$ satisfy the following properties: $p_1^2 = p_2^2 = 0$ and $p_1 \cdot p_2 = 1$.

We use the Sudakov decomposition for a vector:

$$\begin{aligned} a^\mu &= \alpha p_1^\mu + \beta p_2^\mu + a^{\perp\mu} \\ &= (a \cdot p_2)p_1^\mu + (a \cdot p_1)p_2^\mu + a^{\perp\mu} \\ &= \left(\frac{a^+}{P^+}\right)p_1^\mu + (a^-P^+)p_2^\mu + a^{\perp\mu} \end{aligned} \tag{C.8}$$

where a^+ is called the $(+)$ component of a^μ in the direction p_1, and a^- is the $(-)$ component of a^μ in the direction p_2.

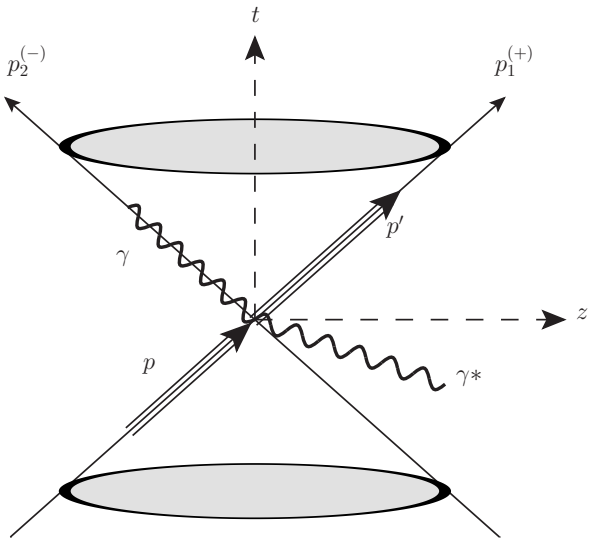

Figure C.2: Light-cone frame: the proton goes at the speed of light along the $(+)$ light cone axis while the real photon goes along the $(-)$ axis. The virtual photon, off-shell, has both $(+)$ and $(-)$ components.

In terms of the Sudakov vectors, we define the average nucleon 4-momentum P^μ and the 4-momentum of the virtual photon q^μ as in Table C.2. The other vectors are expanded in the light-cone basis using $\Delta = p' - p = q - q'$. x is defined as the momentum fraction of the average nucleon momentum P^μ, $\bar{M}^2 = m_N^2 - \frac{\Delta^2}{4}$ and (ξ, ξ') tend to the same limit $\frac{x_B}{2-x_B}$ in the Bjorken limit as:

$$2\xi' = \frac{P \cdot q}{\bar{M}^2}\left[-1 + \sqrt{1 + \frac{Q^2\bar{M}^2}{(P \cdot q)^2}}\right] \to \frac{x_B}{1 - \frac{x_B}{2}} \tag{C.9}$$

$$2\xi = 2\xi' \frac{Q^2 - \Delta^2}{Q^2 + \bar{M}^2(2\xi')^2} \to \frac{x_B}{1 - \frac{x_B}{2}} \tag{C.10}$$

Light-cone vectors:	In Bjorken limit: $Q^2 \gg m^2, -t$	
$P^\mu = \frac{p^\mu + p'^\mu}{2} = p_1 + \frac{\bar{M}^2}{2} p_2$	$\to p_1$	$+$
$q^\mu = -2\,\xi'\,p_1 + \frac{Q^2}{4\xi'} p_2$	$\to -2\,\xi\,p_1 + \frac{Q^2}{4\xi} p_2$	$+\ -$
$\Delta^\mu = p'^\mu - p^\mu = -2\,\xi\,p_1 + \xi\,\bar{M}^2\,p_2 + \Delta^\mu_\perp$	$\to -2\,\xi\,p_1$	$+$
$q'^\mu = q^\mu - \Delta^\mu = 2(\xi - \xi')\,p_1 + (\frac{Q^2}{4\xi'} - \xi\bar{M}^2)\,p_2 - \Delta^\mu_\perp$	$\to \frac{Q^2}{4\xi} p_2$	$-$
$p^\mu = P^\mu - \frac{\Delta^\mu}{2}$	$\to (1+\xi)\,p_1$	$+$
$p'^\mu = P^\mu + \frac{\Delta^\mu}{2}$	$\to (1-\xi)\,p_1$	$+$
$k^\mu = x\,P^\mu - \frac{\Delta^\mu}{2}$	$\to (x+\xi)\,p_1$	$+$
$k'^\mu = x\,P^\mu + \frac{\Delta^\mu}{2}$	$\to (x-\xi)\,p_1$	$+$

Table C.2: Declaration of the vectors in the light-cone frame.

At leading order and leading twist, the contribution in the hard part of the $\Delta_\perp$ and $\bar{M}^2$ terms are neglected because they appear in the computation as divided by Q^2 that is supposed to be very large. In this sense, one shows in the right side of Table C.2 the expansion of the DVCS vectors keeping only the dominant contributions that are used to calculate the amplitude at leading twist and leading order.

Fig. C.3 shows the handbag diagram associated to its large momentum components.

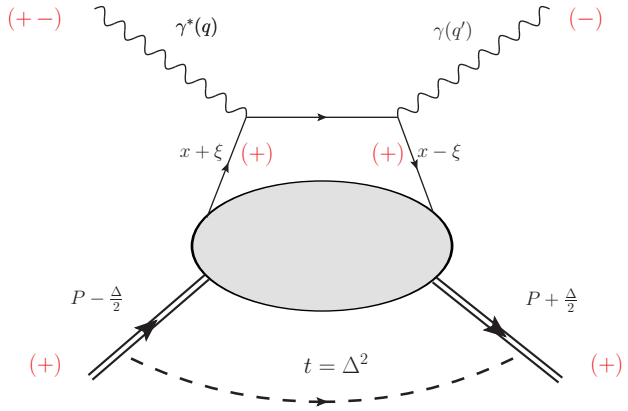

Figure C.3: Handbag diagram. The picture indicates the large momentum components: a $(+)$ indicates that the large momentum is along the vector p_1, while a $(-)$ indicates that the large momentum is along the vector p_2. The hadronic part is flying along the $(+)$ direction. The virtual photon has both components $(+\ -)$ and the final real photon has only a $(-)$ component.

Using the large components, one can calculate the numerators of Eq. C.4:

$$k + q = (x - \xi)\,p_1 + \frac{Q^2}{4\xi}\,p_2, \tag{C.11}$$

$$k - q' = (x + \xi)\,p_1 - \frac{Q^2}{4\xi}\,p_2 \tag{C.12}$$

and the denominators:

$$(k+q)^2 + i\epsilon = 2(x-\xi+i\epsilon)\frac{Q^2}{4\xi} \tag{C.13}$$

$$(k-q')^2 + i\epsilon = -2(x+\xi-i\epsilon)\frac{Q^2}{4\xi} \tag{C.14}$$

To pursue the derivation of the amplitude, it is important to notice several points:

- At first order, for Eq. C.4 to be non-zero, γ^μ and γ^ν have to be transverse. Indeed, if γ^μ or γ^ν have a (+) or (−) component (introducing $\not{p}_1$ and $\not{p}_2$ terms)[2], the amplitude vanishes up to mass correction term. Therefore, $\gamma^\mu = \gamma^\mu_\perp$ and $\gamma^\nu = \gamma^\nu_\perp$, which means that the only possible transition is between two transversely polarized photons.
- Because the proton flies along p_1 (+), the correlators in the soft part are dominated by their $\lambda = +$ component: so $\gamma_\lambda = \gamma^+$.
- Because of Eq. C.6, it also means that the perturbative part should be evaluated with a $\lambda = -$ component: so $\gamma^\lambda = \gamma^- = \frac{\not{p}_1}{P^+}$.
- Because $\gamma^\lambda = \frac{\not{p}_1}{P^+}$, the contribution along the (+) direction of the numerator Eqs. C.11 and C.12 automatically vanishes ($p_1 \cdot p_1 = 0$).

The amplitude C.4 becomes:

$$\begin{aligned} i\mathcal{M} &= -i\sum_q \int \frac{dk^+}{P^+}(|e|Q_q)^2 \epsilon^*_\mu \epsilon_\nu \frac{1}{4} \times \Bigg\{ \\ &\left(Tr\left[\gamma^\mu_\perp \frac{\not{p}_2}{2(x-\xi+i\epsilon)}\gamma^\nu_\perp \not{p}_1\right] + Tr\left[\gamma^\nu_\perp \frac{-\not{p}_2}{-2(x+\xi-i\epsilon)}\gamma^\mu_\perp \not{p}_1\right]\right) \times \int \frac{dk^- d^2k^\perp}{(2\pi)^4}\langle p'| \int dz^4 e^{iz\cdot k} T[\bar{q}(0)\gamma^+ q(z)]|p\rangle \\ &+ \left(Tr\left[\gamma^\mu_\perp \frac{\not{p}_2}{2(x-\xi+i\epsilon)}\gamma^\nu_\perp \gamma^5 \not{p}_1\right] + Tr\left[\gamma^\nu_\perp \frac{-\not{p}_2}{-2(x+\xi-i\epsilon)}\gamma^\mu_\perp \gamma^5 \not{p}_1\right]\right) \times \int \frac{dk^- d^2k^\perp}{(2\pi)^4}\langle p'| \int dz^4 e^{iz\cdot k} T[\bar{q}(0)\gamma^+\gamma^5 q(z)]|p\rangle \Bigg\} \end{aligned} \tag{C.15}$$

Using $dk^+ = P^+ \int dx$, and the following integral properties:

- $\int dk^- e^{iz^+k^-} = 2\pi\delta(z^+)$
- $\int d^2k_\perp e^{iz_\perp k_\perp} = (2\pi)^2\delta(z_\perp)$

with the following trace properties:

- $\mathrm{Tr}[\gamma^\mu_\perp \not{p}_2 \gamma^\nu_\perp \not{p}_1] = 4(p_1^\mu p_2^\nu + p_1^\nu p_2^\mu - g^{\mu\nu}_\perp)$
- $\mathrm{Tr}[\gamma^\mu_\perp \not{p}_2 \gamma^\nu_\perp \gamma^5 \not{p}_1] = -4i\epsilon^{\mu\nu\alpha\beta}(p_1)_\alpha (p_2)_\beta = -4i\epsilon^{\mu\nu+-}$

one finally finds:

$$\begin{aligned} i\mathcal{M} &= -i\sum_q \int_{-1}^{1} dx (|e|Q_q)^2 \epsilon^*_\mu \epsilon_\nu \Bigg\{ \\ &(p_1^\mu p_2^\nu + p_1^\nu p_2^\mu - g^{\mu\nu}_\perp)\left[\frac{1}{x-\xi+i\epsilon} + \frac{1}{x+\xi-i\epsilon}\right]\frac{1}{2} \times \int \frac{dz^-}{2\pi} e^{iz^-k^+}\langle p'|T[\bar{q}(0)\gamma^+ q(z)]|p\rangle\Big|_{z^+=z^\perp=0} \\ &+ i\epsilon^{\mu\nu+-}\left[-\frac{1}{x-\xi+i\epsilon} + \frac{1}{x+\xi-i\epsilon}\right]\frac{1}{2} \times \int \frac{dz^-}{2\pi} e^{iz^-k^+}\langle p'|T[\bar{q}(0)\gamma^+\gamma^5 q(z)]|p\rangle\Big|_{z^+=z^\perp=0} \Bigg\} \end{aligned} \tag{C.16}$$

[2] The Sudakov decomposition for γ matrice is: $\gamma = (\gamma^- P^+)\, p_2 + (\frac{\gamma^+}{P^+})\, p_1 + \gamma_\perp = (\gamma.p_1)\, p_2 + (\gamma.p_2)\, p_1 + \gamma_\perp = \not{p}_1 p_2 + \not{p}_2 p_1 + \gamma_\perp$

Using the Gordon identities and the parity, hermiticity and time-reversal properties, the parametrization of the correlators can be written as:

$$\int \frac{dz^-}{2\pi} e^{ixP^+z^-} \langle p'|T[\bar{q}(0)\gamma^+ q(z)]|p\rangle\Big|_{z^+=z^\perp=0} = \frac{1}{P^+}\left[H^q(x,\xi,t)\bar{u}(p')\gamma^+ u(p) + E^q(x,\xi,t)\bar{u}(p')i\sigma^{+\alpha}\frac{\Delta_\alpha}{2m_N}u(p)\right] \tag{C.17}$$

and

$$\int \frac{dz^-}{2\pi} e^{ixP^+z^-} \langle p'|T[\bar{q}(0)\gamma^+\gamma^5 q(z)]|p\rangle\Big|_{z^+=z^\perp=0} = \frac{1}{P^+}\left[\tilde{H}^q(x,\xi,t)\bar{u}(p')\gamma^+\gamma_5 u(p) + \tilde{E}^q(x,\xi,t)\bar{u}(p')\gamma_5\frac{\Delta^+}{2m_N}u(p)\right] \tag{C.18}$$

where $\bar{u}(p')$ and $u(p)$ are the spinors of the nucleon, and H, $\tilde{H}$, E, $\tilde{E}$ are the GPDs parametrizing the nucleon structure.

One can finally write the DVCS amplitude as:

$$\begin{aligned} i\mathcal{M} = -i\sum_q (|e|Q_q)^2 \epsilon^*_\mu \epsilon_\nu \Bigg\{ & \\ (p_1^\mu p_2^\nu + p_1^\nu p_2^\mu - g_\perp^{\mu\nu}) \int_{-1}^{1} dx \left[\frac{1}{x-\xi+i\epsilon} + \frac{1}{x+\xi-i\epsilon}\right] \times \frac{1}{2P^+}\left[H^q(x,\xi,t)\bar{u}(p')\gamma^+ u(p) + E^q(x,\xi,t)\bar{u}(p')i\sigma^{+\alpha}\frac{\Delta_\alpha}{2m_N}u(p)\right] & \\ + i\epsilon^{\mu\nu+-}\int_{-1}^{1} dx \left[\frac{1}{x+\xi-i\epsilon} - \frac{1}{x-\xi+i\epsilon}\right] \times \frac{1}{2P^+}\left[\tilde{H}^q(x,\xi,t)\bar{u}(p')\gamma^+\gamma_5 u(p) + \tilde{E}^q(x,\xi,t)\bar{u}(p')\gamma_5\frac{\Delta^+}{2m_N}u(p)\right] \Bigg\} & \end{aligned} \tag{C.19}$$

The 4-differential DVCS cross section is obtained from the amplitude with:

$$\frac{d^4\sigma}{dQ^2\, dx_B\, dt\, d\Phi} = \frac{1}{(2\pi^4)32}\frac{x_B\, y^2}{Q^4}\left(1+\frac{4M^2x_B^2}{Q^2}\right)^{-1/2}|\mathcal{M}_{DVCS}|^2 \tag{C.20}$$

where $y = \frac{E-E'}{E}$, and (Q^2, x_B, t, Φ) the four independent variables that describe the process.

Appendix D

Acceptance results

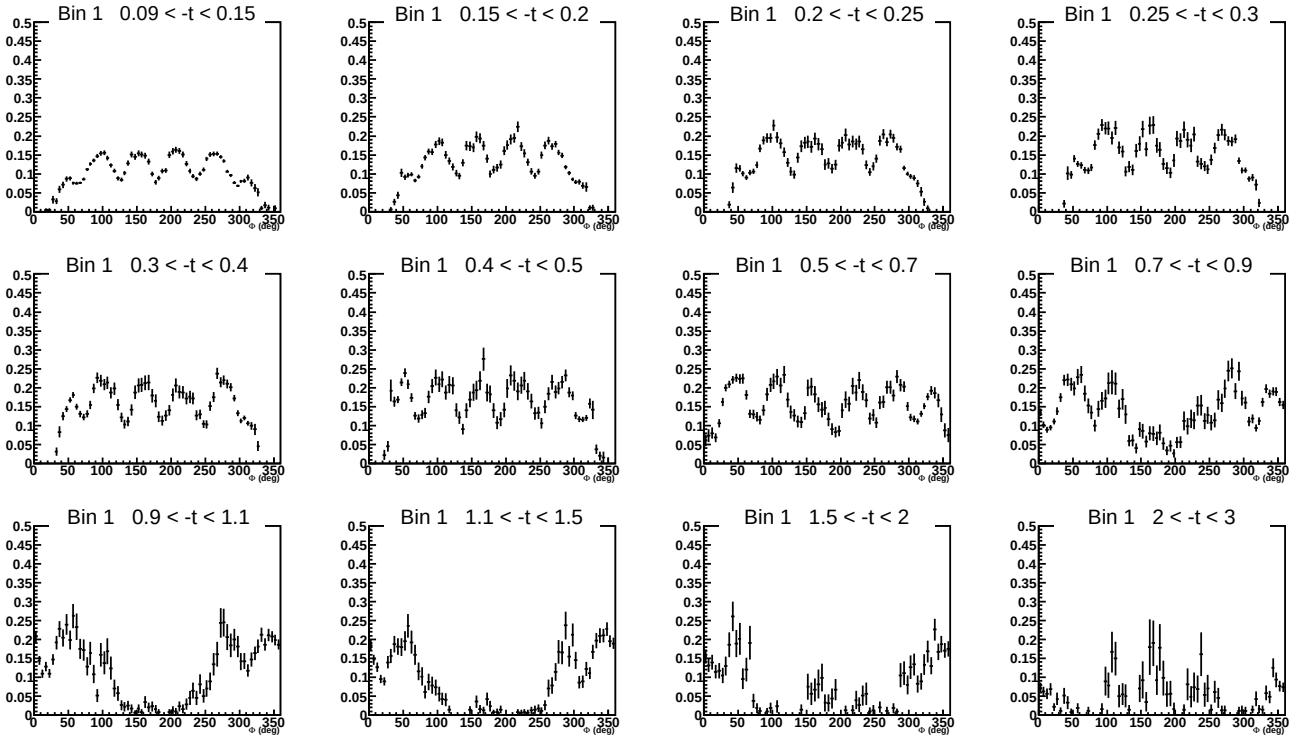

Figure D.1: CLAS acceptance plotted as a function of Φ for the 12 t-bins of the (Q^2, x_B) bin 1.

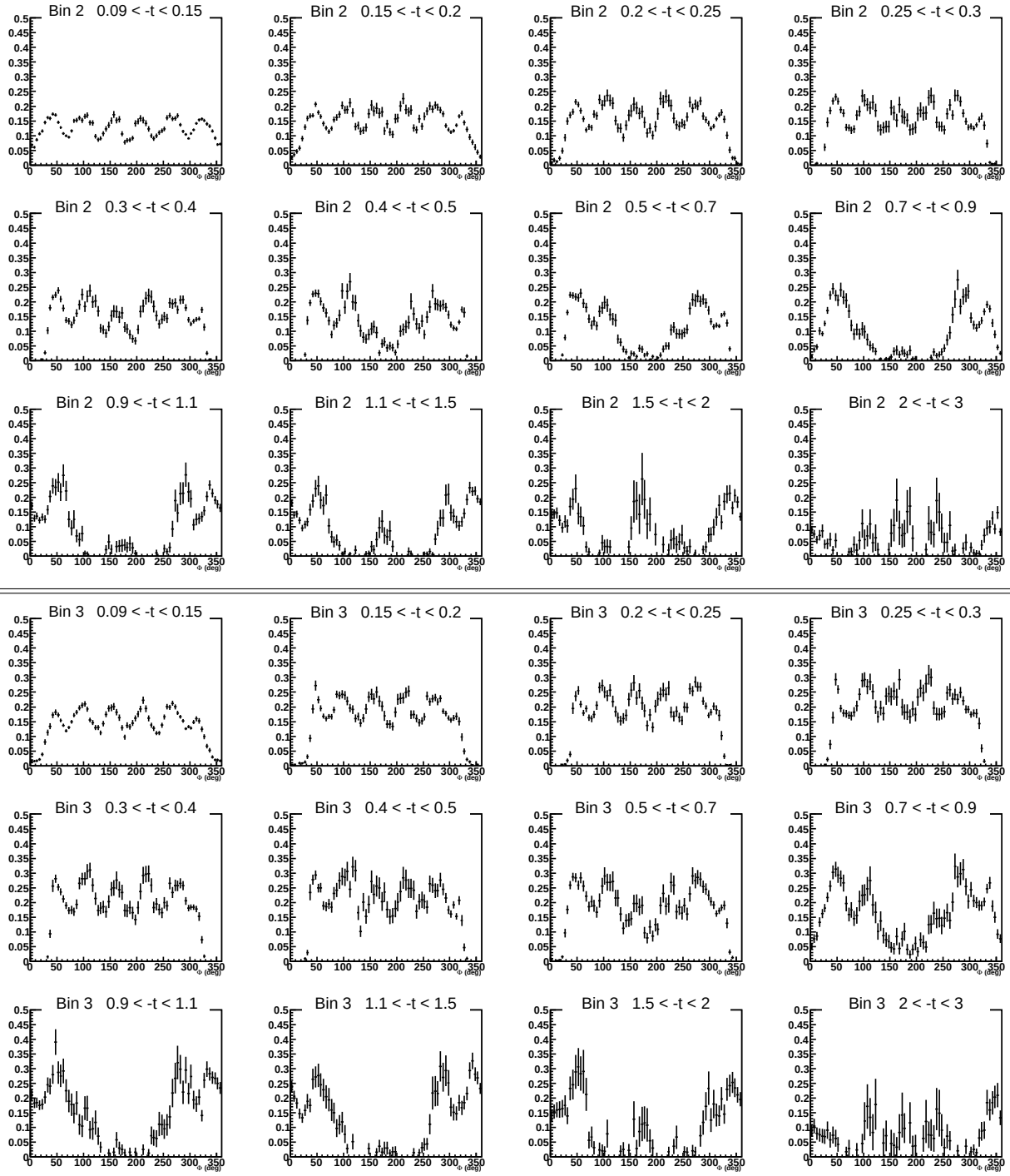

Figure D.2: CLAS acceptance plotted as a function of Φ for the 12 t-bins of the bins 2 and 3 in (Q^2, x_B).

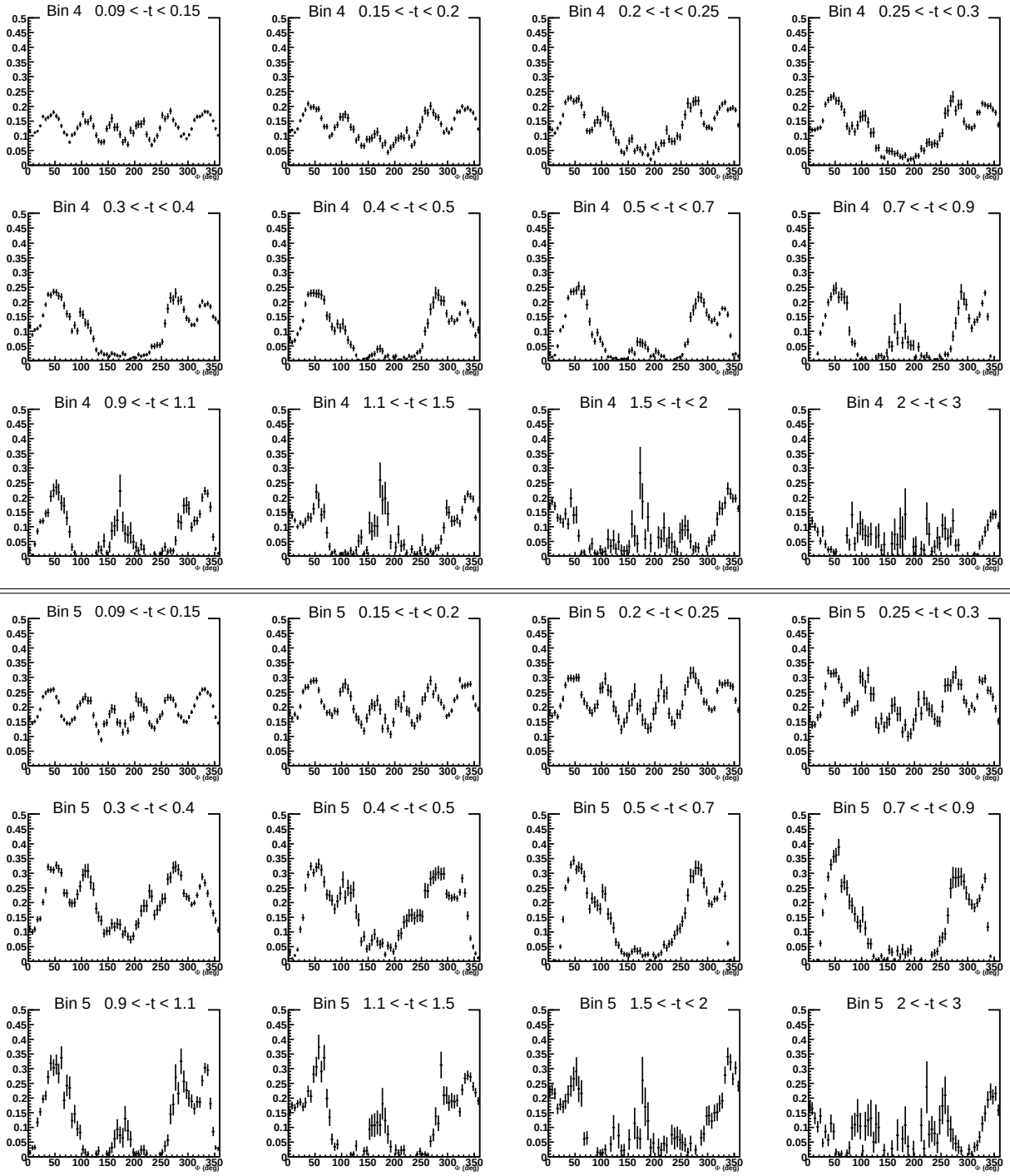

Figure D.3: CLAS acceptance plotted as a function of Φ for the 12 t-bins of the bins 4 and 5 in (Q^2, x_B).

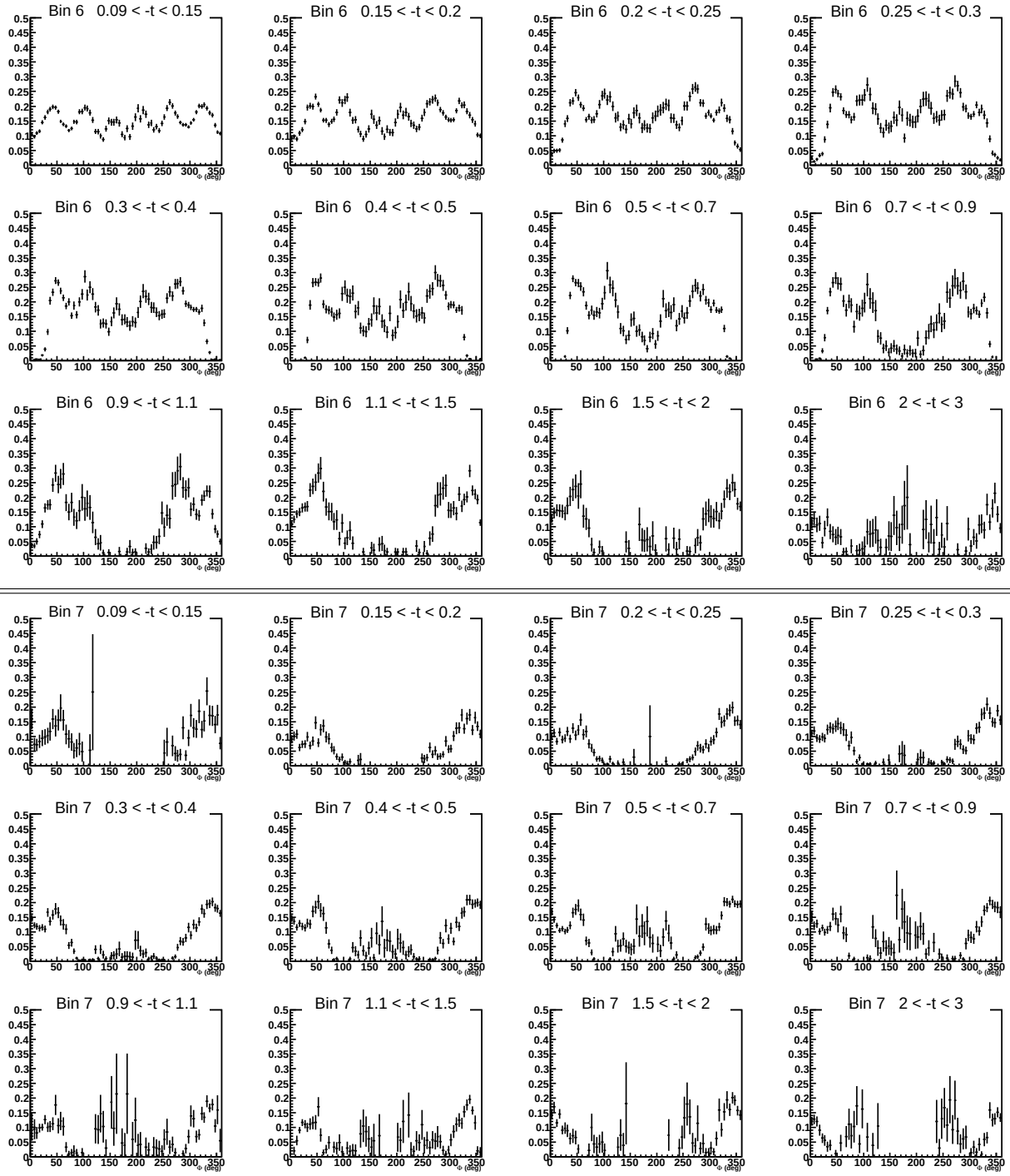

Figure D.4: CLAS acceptance plotted as a function of Φ for the 12 t-bins of the bins 6 and 7 in (Q^2, x_B).

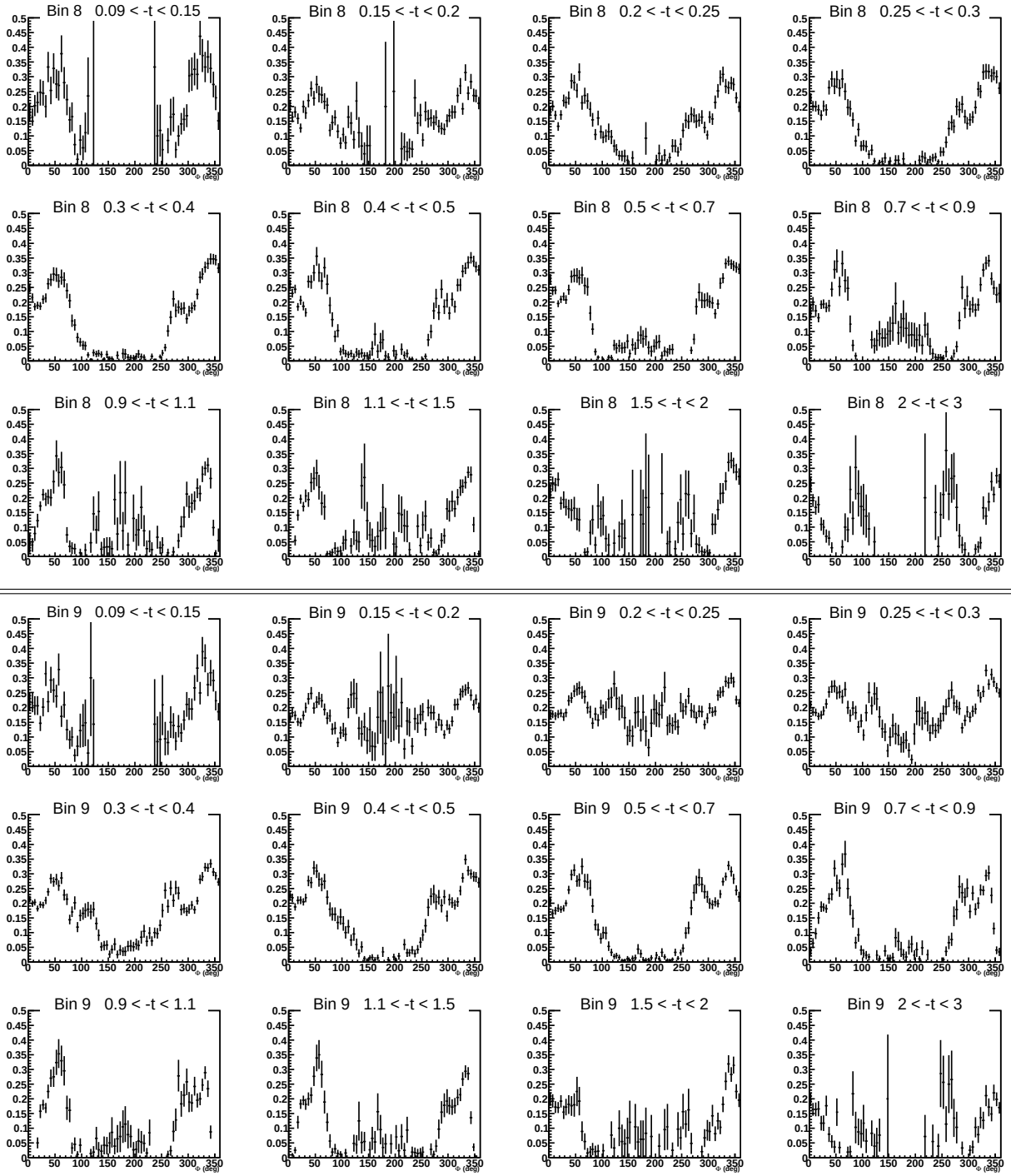

Figure D.5: CLAS acceptance plotted as a function of Φ for the 12 t-bins of the bins 8 and 9 in (Q^2, x_B).

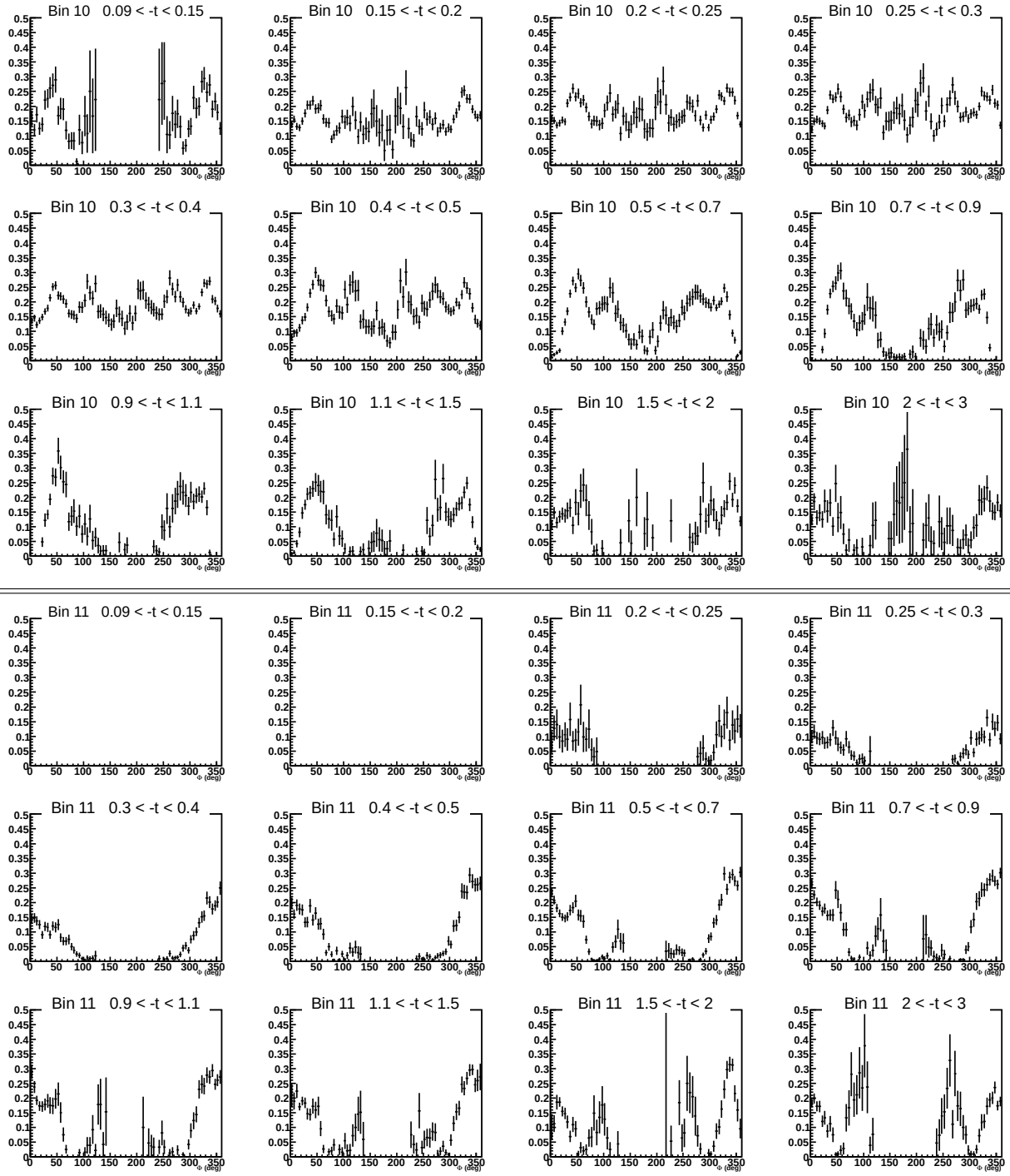

Figure D.6: CLAS acceptance plotted as a function of Φ for the 12 t-bins of the bins 10 and 11 in (Q^2, x_B).

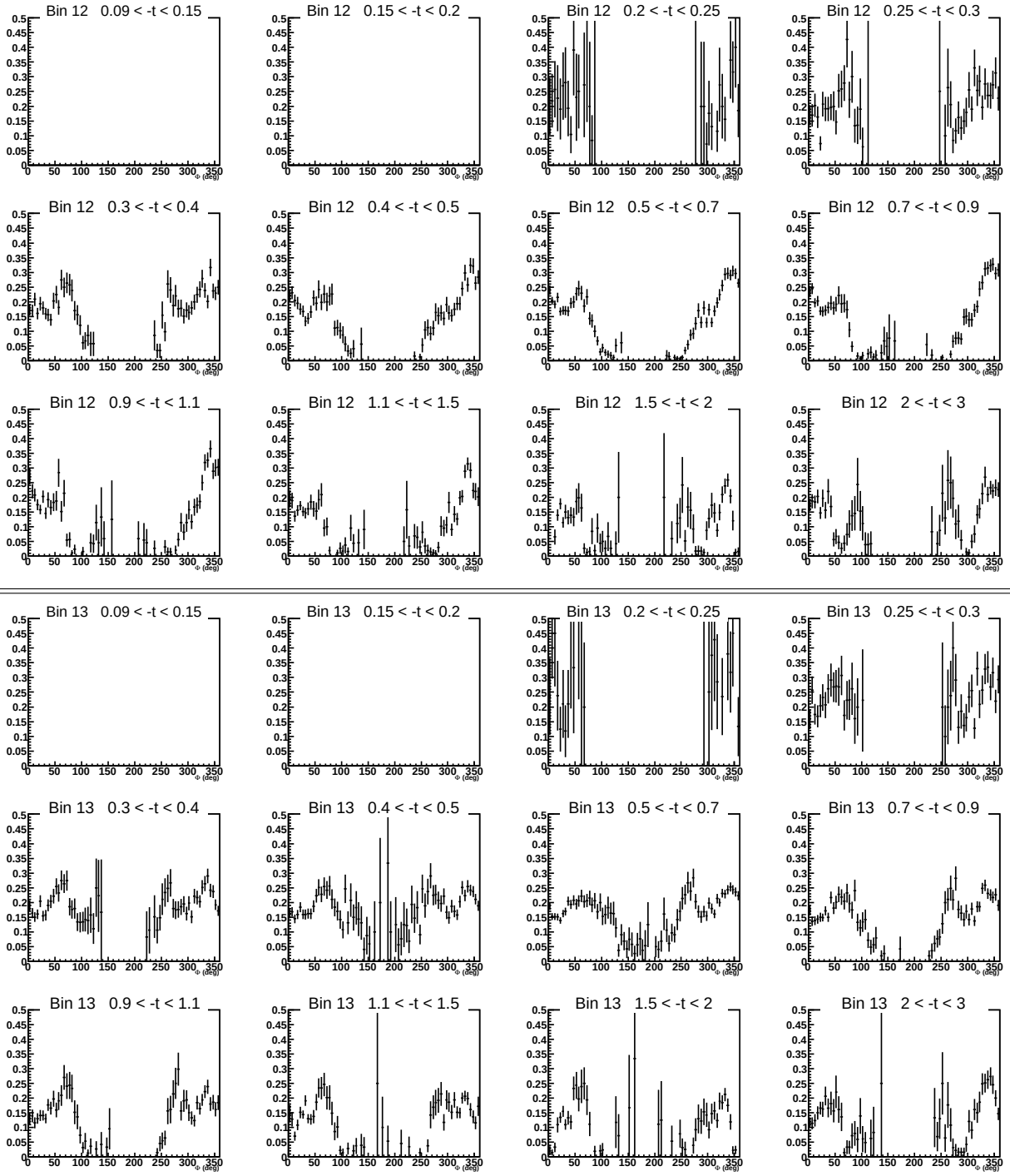

Figure D.7: CLAS acceptance plotted as a function of Φ for the 12 t-bins of the bins 12 and 13 in (Q^2, x_B).

Appendix E

Bin volume results

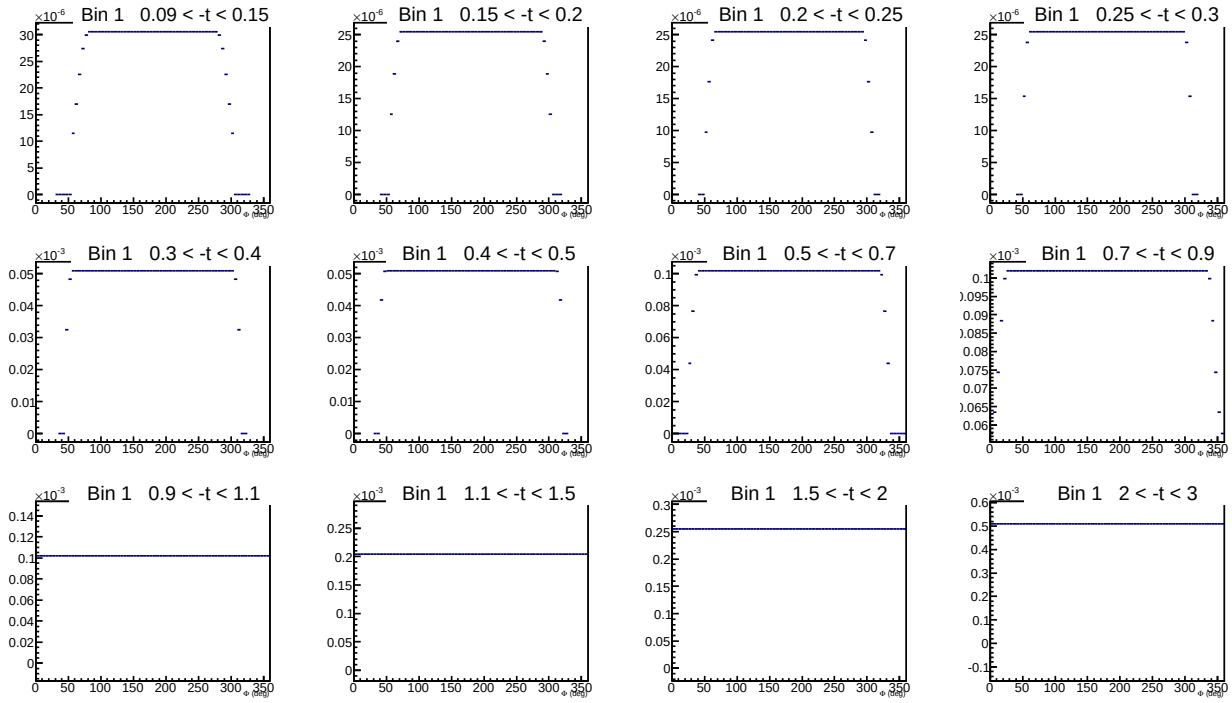

Figure E.1: Effective bin volume ($\mathrm{GeV}^4\mathrm{rad}$) as a function of Φ for the 12 t-bins of the first (Q^2, x_B) bin.

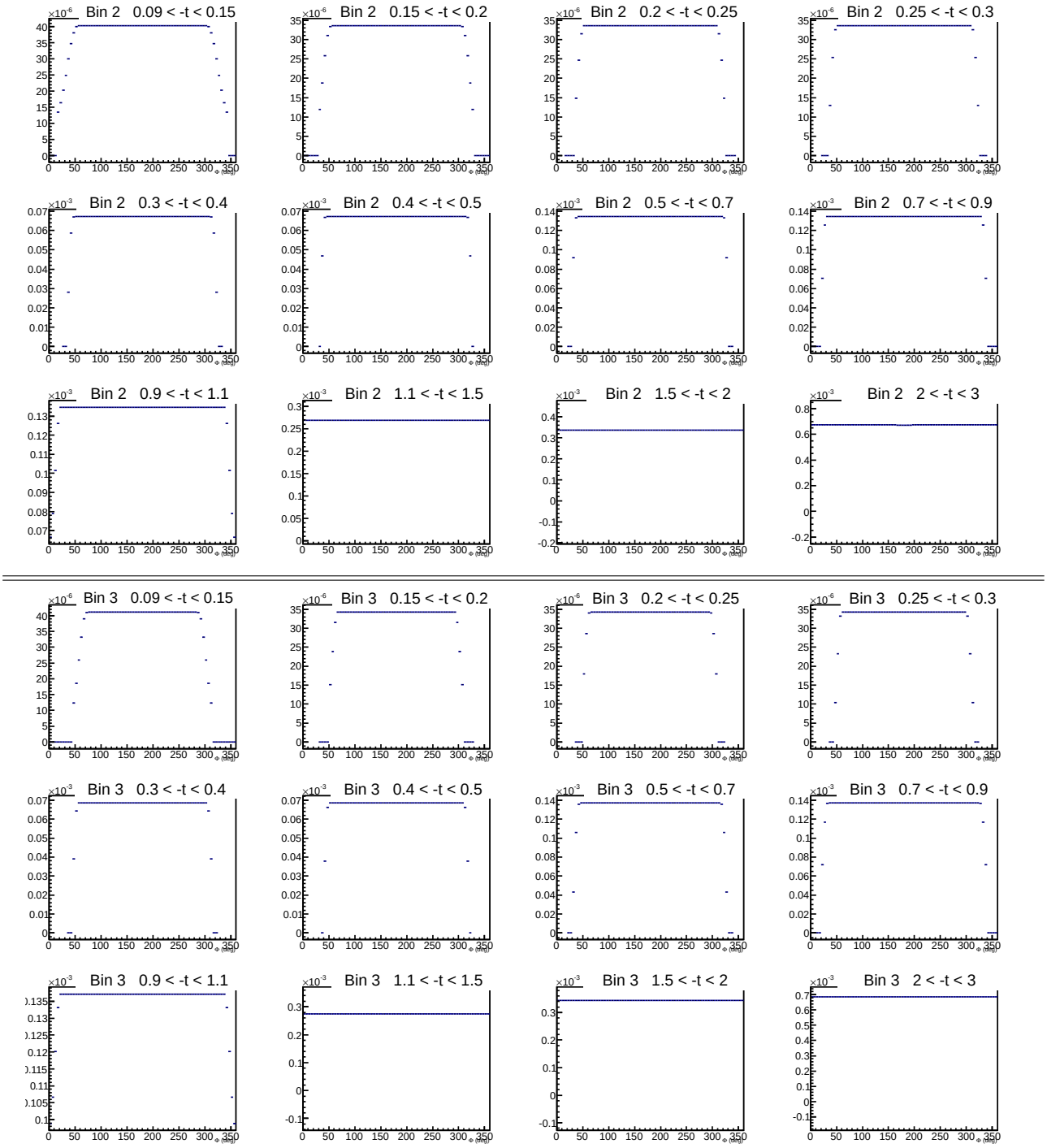

Figure E.2: Effective bin volume ($\mathrm{GeV}^4\mathrm{rad}$) as a function of Φ for the 12 t-bins of the (Q^2, x_B) bins 2 and 3.

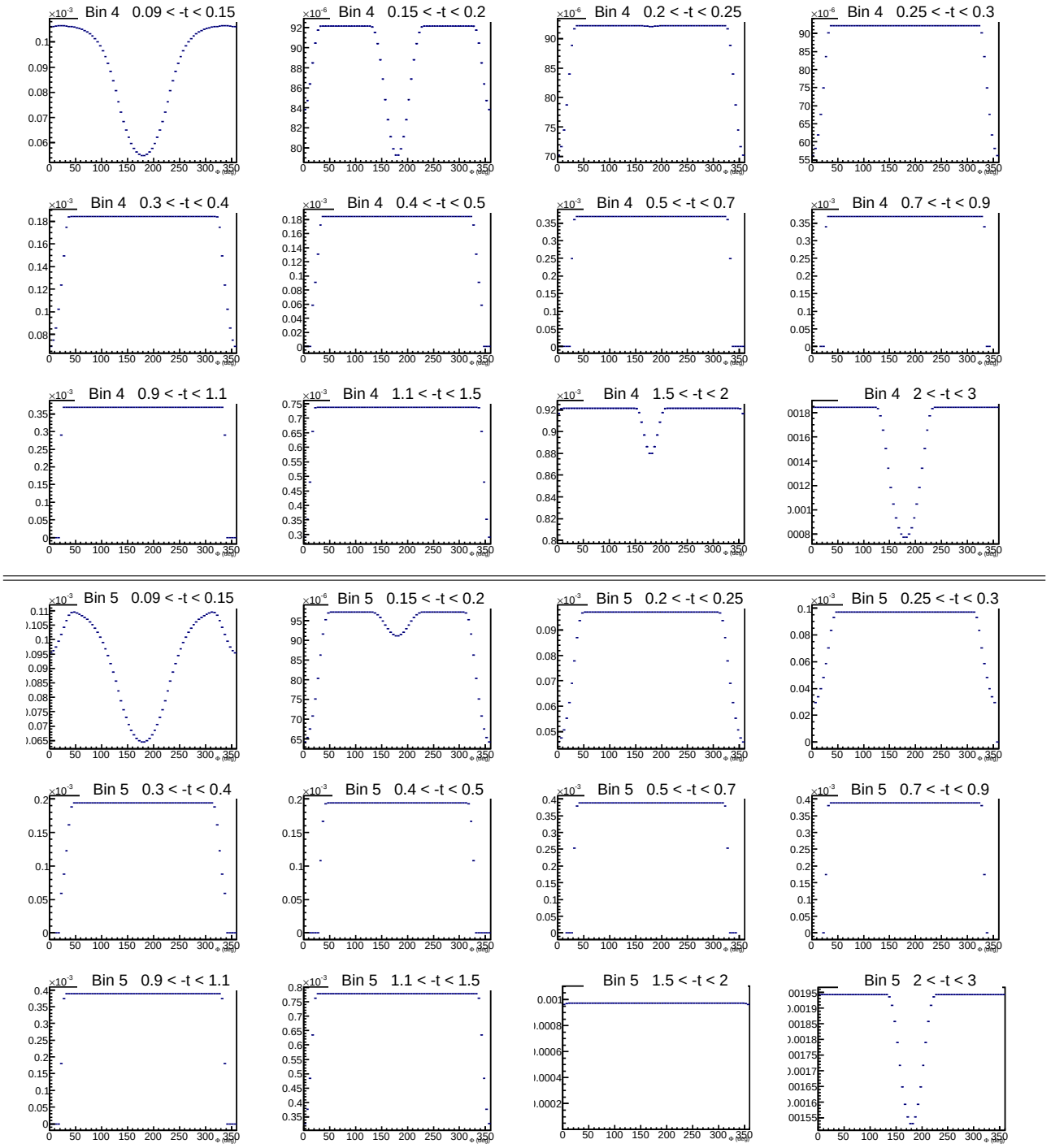

Figure E.3: Effective bin volume ($\mathrm{GeV}^4\mathrm{rad}$) as a function of Φ for the 12 t-bins of the (Q^2, x_B) bins 4 and 5.

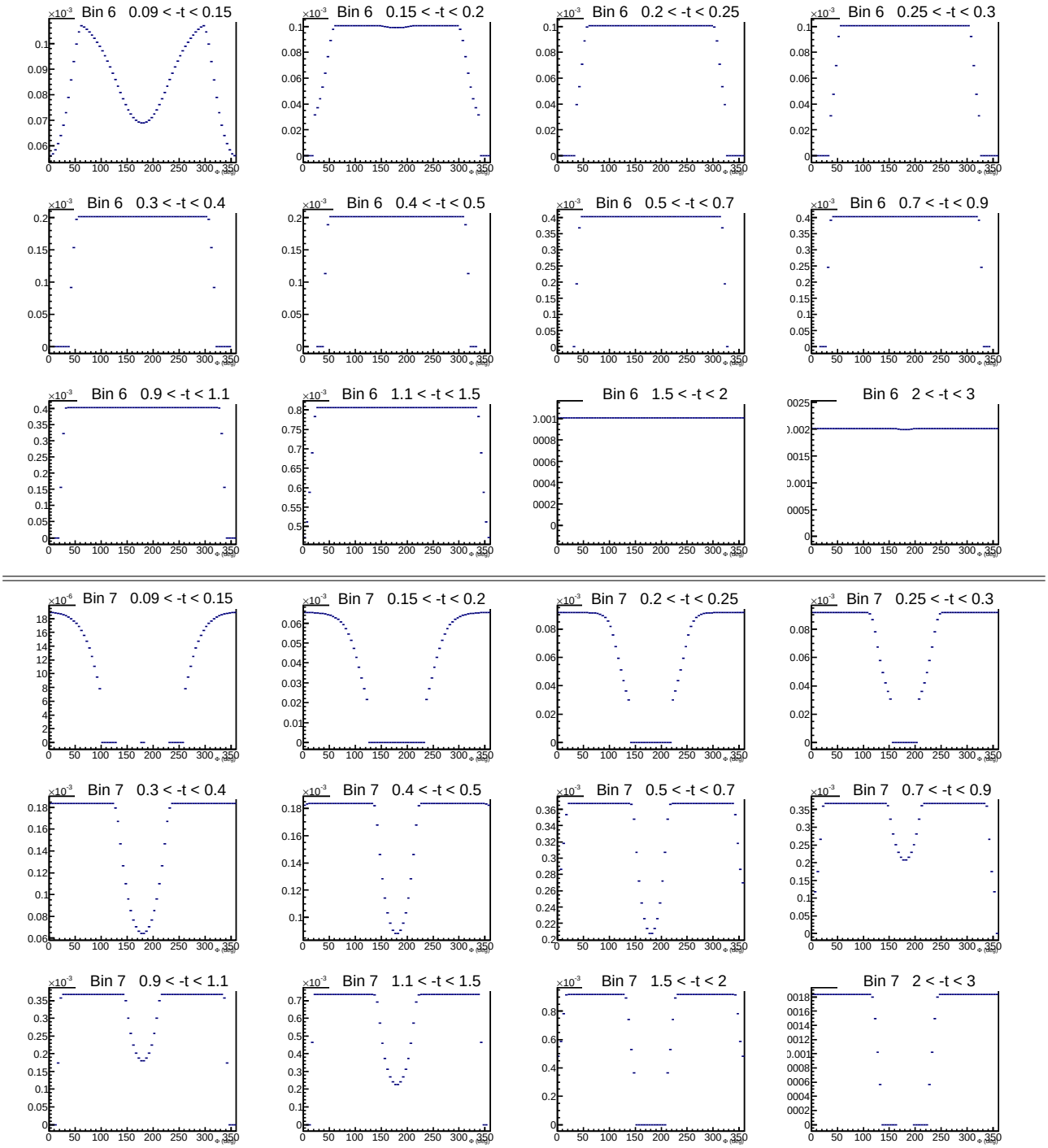

Figure E.4: Effective bin volume ($\mathrm{GeV}^4\mathrm{rad}$) as a function of Φ for the 12 t-bins of the (Q^2, x_B) bins 6 and 7.

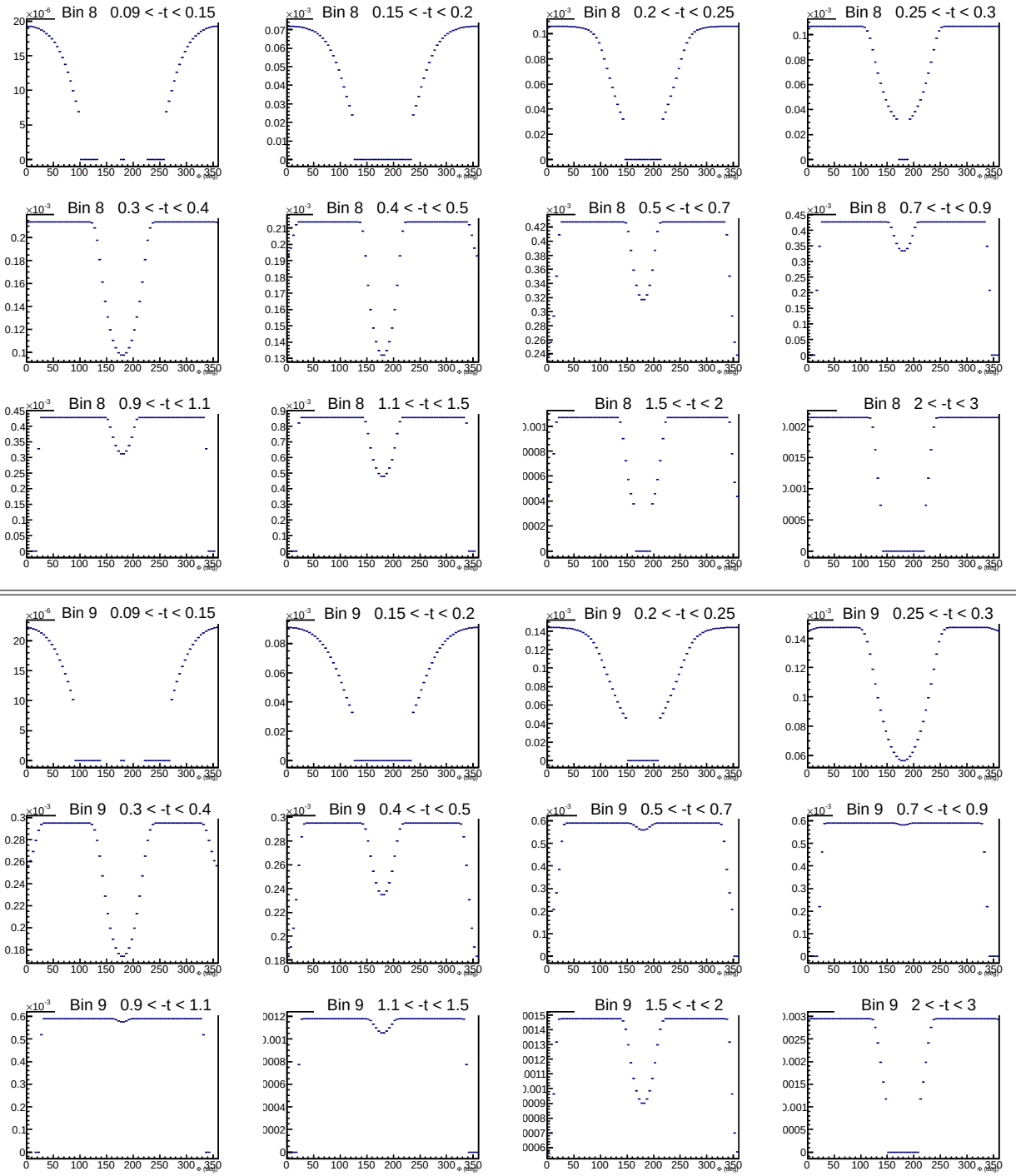

Figure E.5: Effective bin volume ($\mathrm{GeV}^4\mathrm{rad}$) as a function of Φ for the 12 t-bins of the (Q^2, x_B) bins 8 and 9.

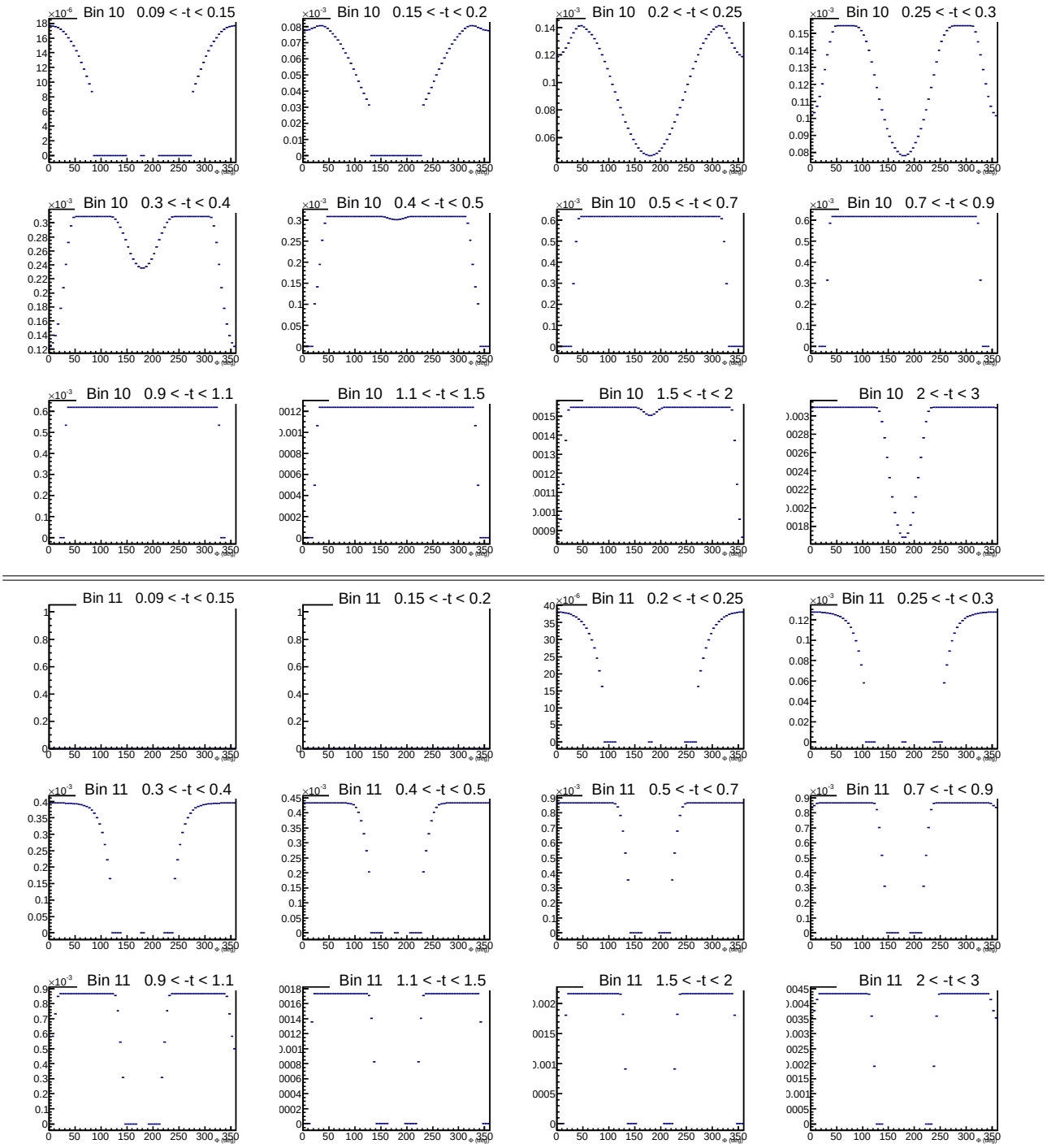

Figure E.6: Effective bin volume ($\mathrm{GeV}^4\mathrm{rad}$) as a function of Φ for the 12 t-bins of the (Q^2, x_B) bins 10 and 11.

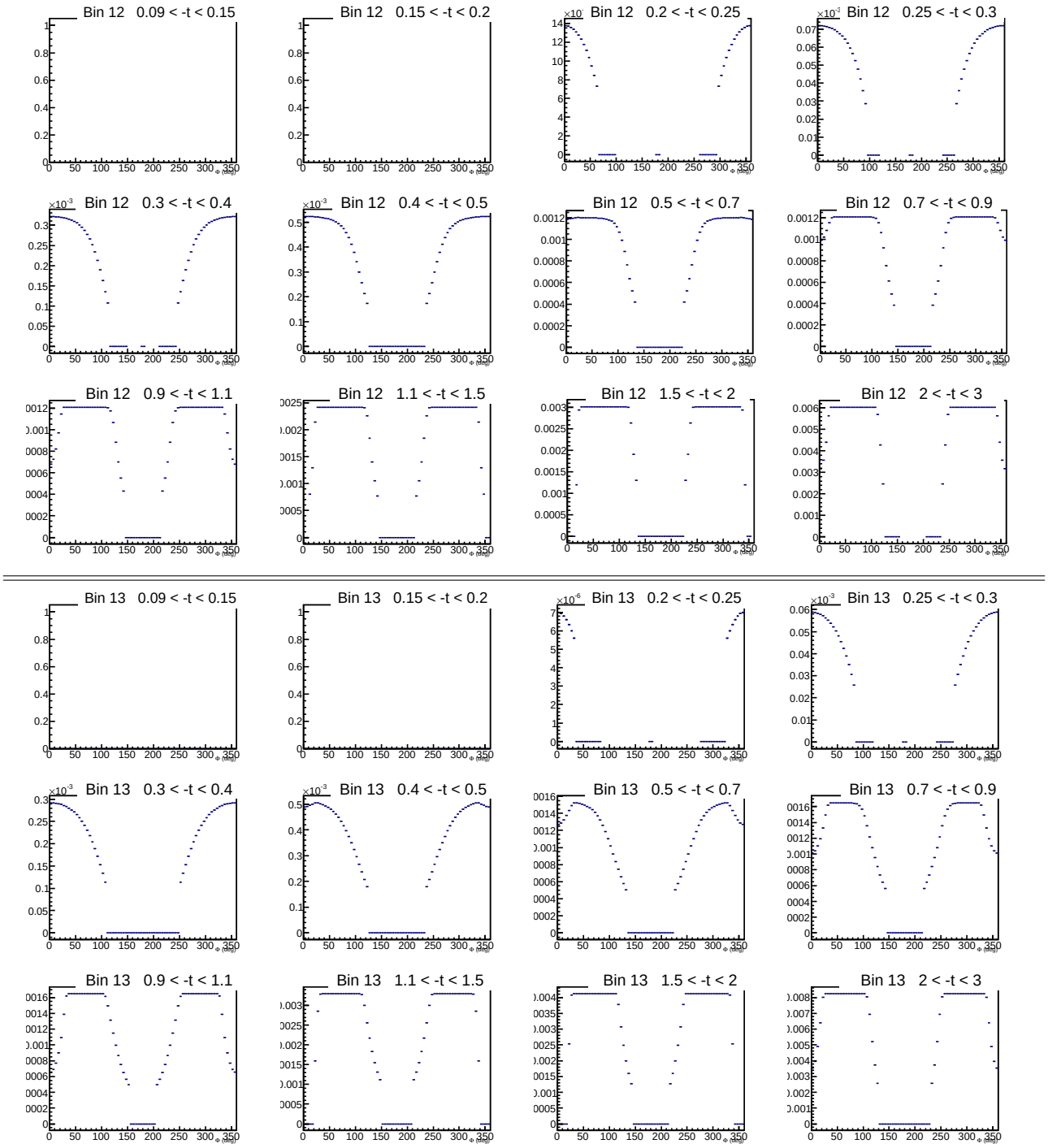

Figure E.7: Effective bin volume ($\mathrm{GeV}^4\mathrm{rad}$) as a function of Φ for the 12 t-bins of the (Q^2, x_B) bins 12 and 13.

Appendix F

Pi0 contamination results

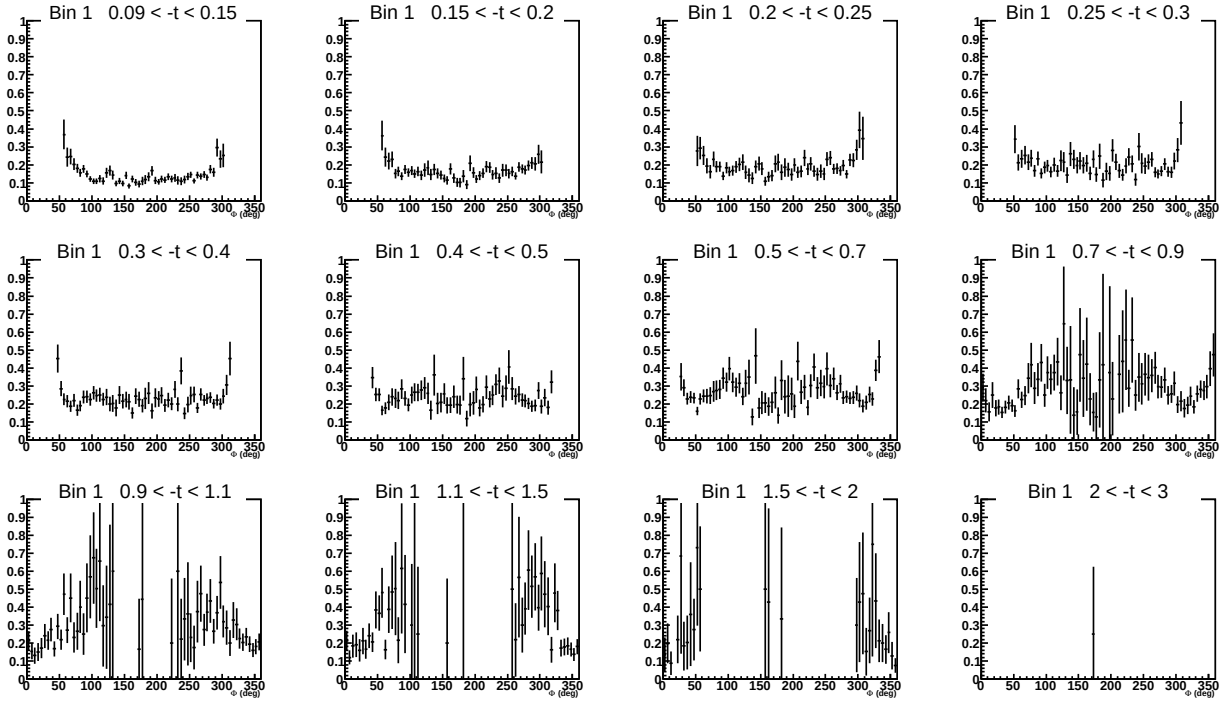

Figure F.1: $\frac{N_{ep\pi^0(1\gamma)}}{N_{ep\gamma}}$ as a function of Φ for the first (Q^2, x_B) bin.

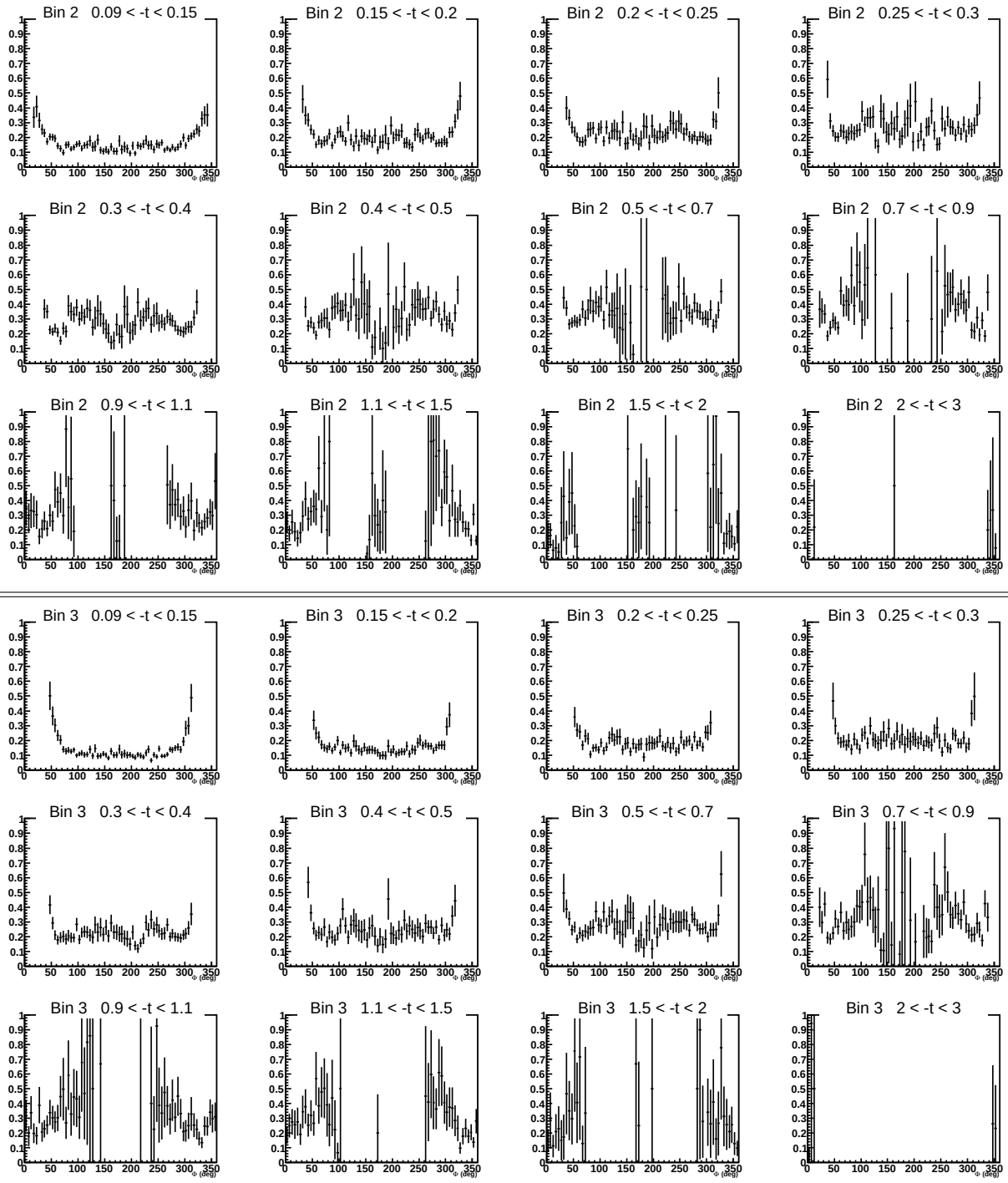

Figure F.2: $\frac{N_{ep\pi^0(1\gamma)}}{N_{ep\gamma}}$ as a function of Φ for the 12 t bins of the (Q^2, x_B) bins 2 and 3.

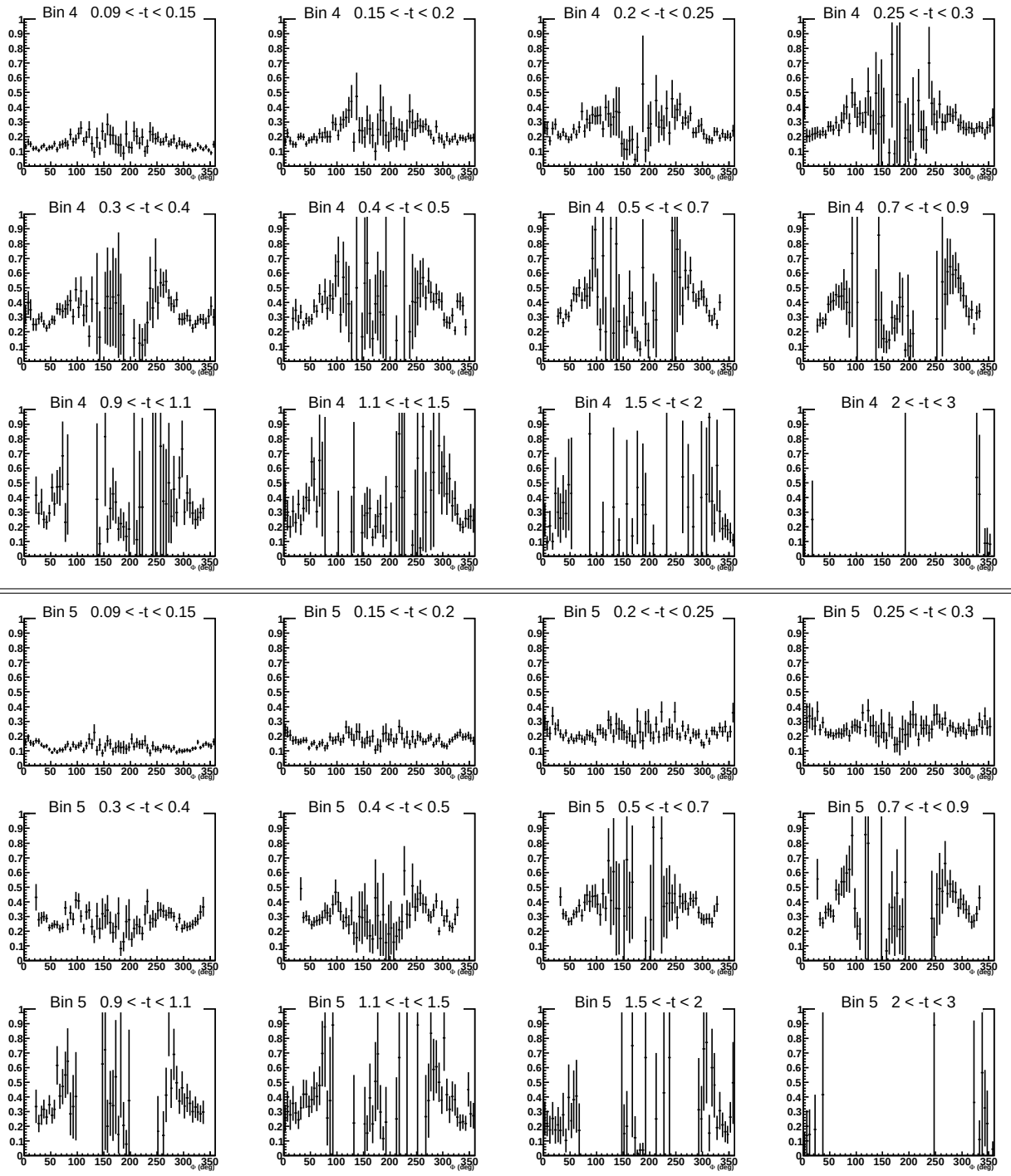

Figure F.3: $\frac{N_{ep\pi^0(1\gamma)}}{N_{ep\gamma}}$ as a function of Φ for the 12 t bins of the (Q^2, x_B) bins 4 and 5.

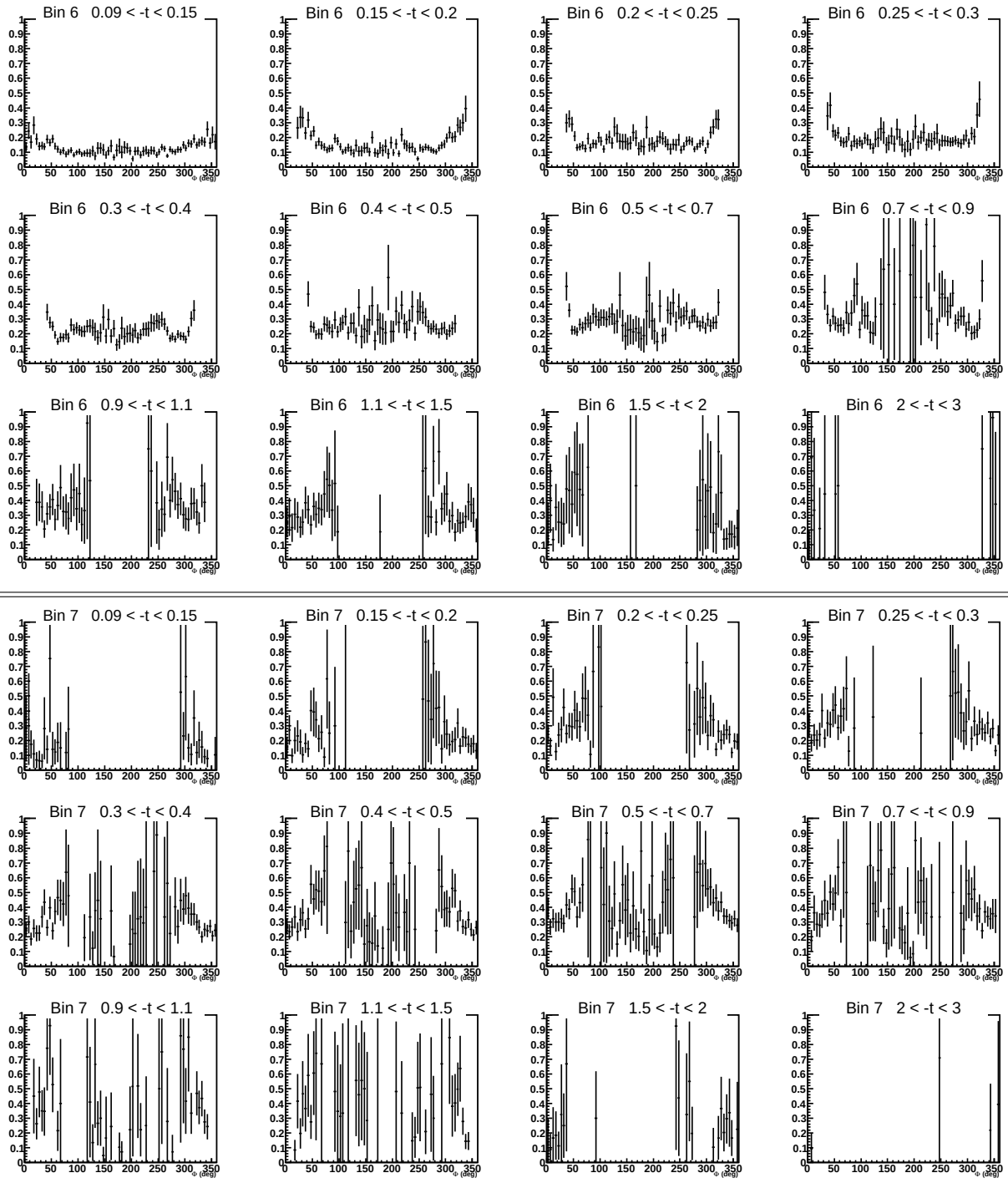

Figure F.4: $\frac{N_{ep\pi^0(1\gamma)}}{N_{ep\gamma}}$ as a function of Φ for the 12 t bins of the (Q^2, x_B) bins 6 and 7.

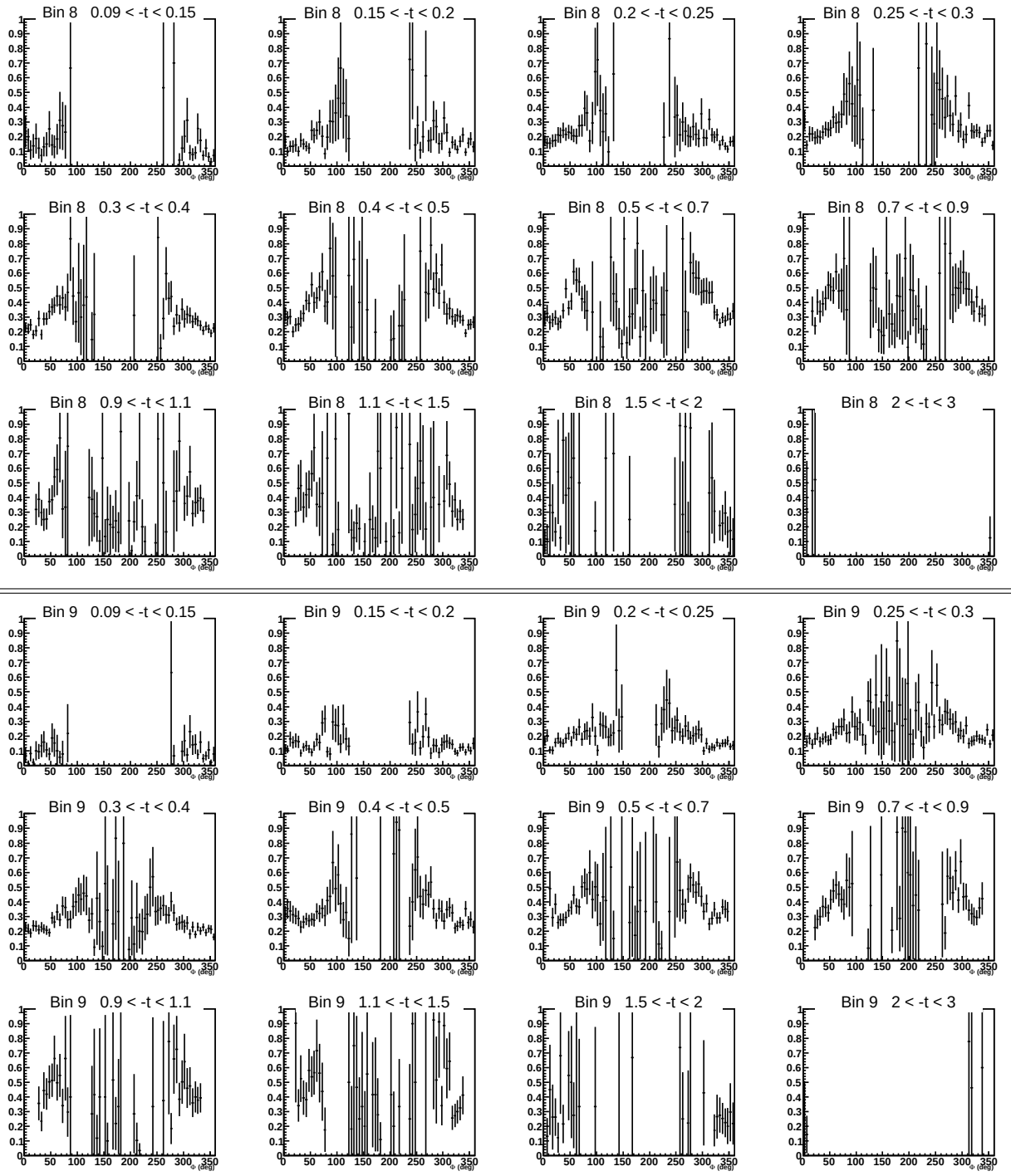

Figure F.5: $\frac{N_{ep\pi^0(1\gamma)}}{N_{ep\gamma}}$ as a function of Φ for the 12 t bins of the (Q^2, x_B) bins 8 and 9.

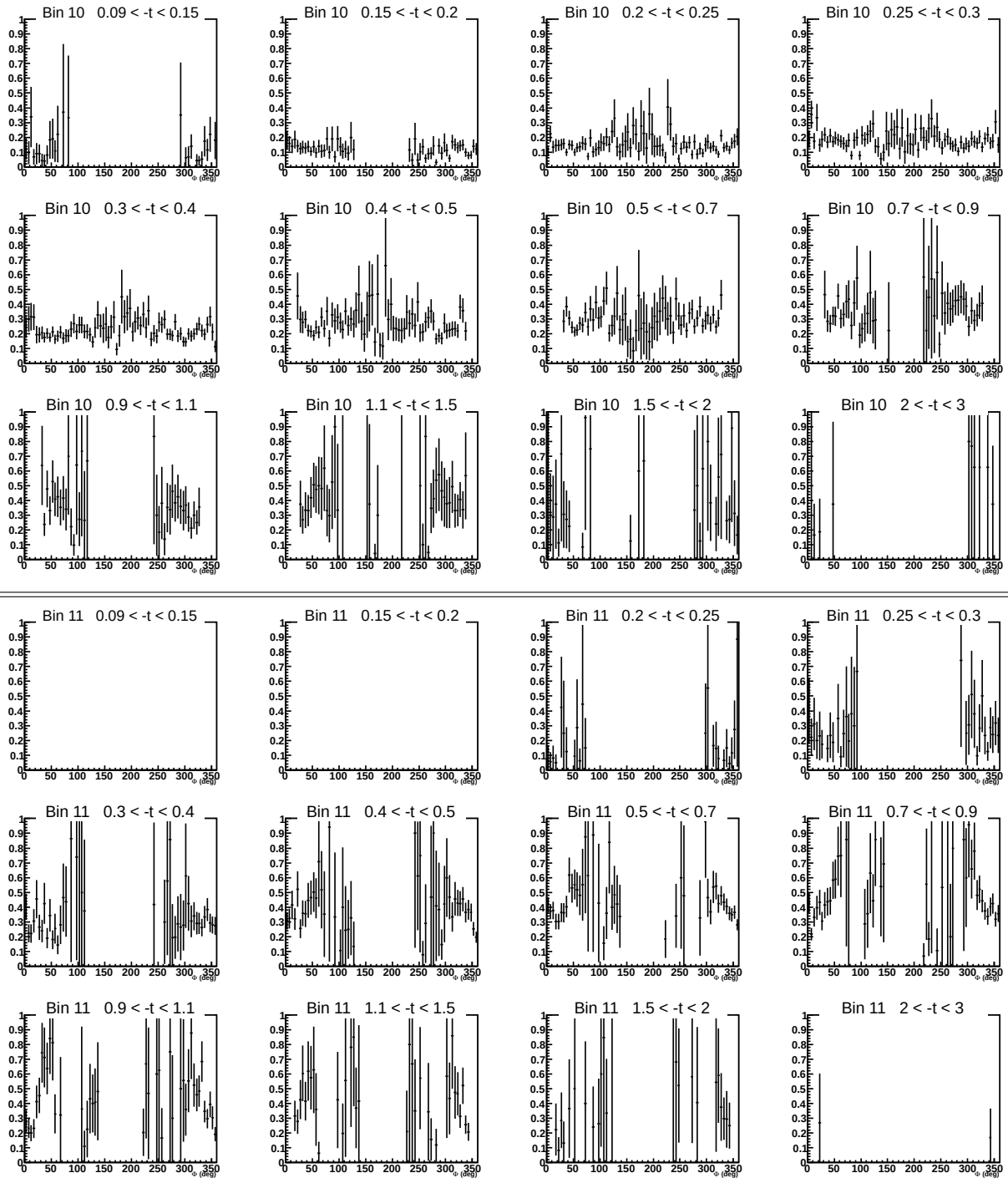

Figure F.6: $\frac{N_{ep\pi^0(1\gamma)}}{N_{ep\gamma}}$ as a function of Φ for the 12 t bins of the (Q^2, x_B) bins 10 and 11.

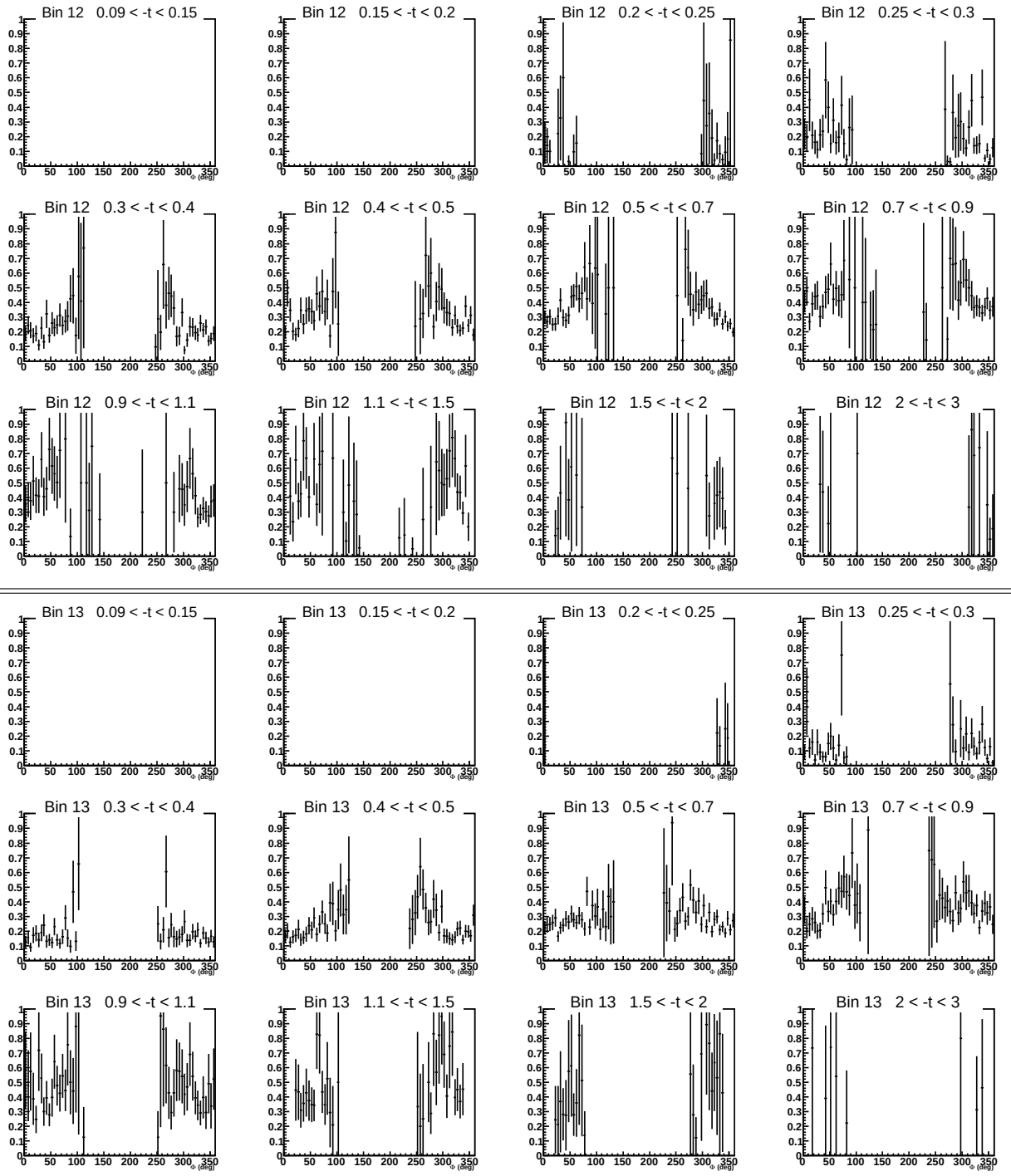

Figure F.7: $\frac{N_{ep\pi^0(1\gamma)}}{N_{ep\gamma}}$ as a function of Φ for the 12 t bins of the (Q^2, x_B) bins 12 and 13.

Appendix G

Unpolarized DVCS cross section results

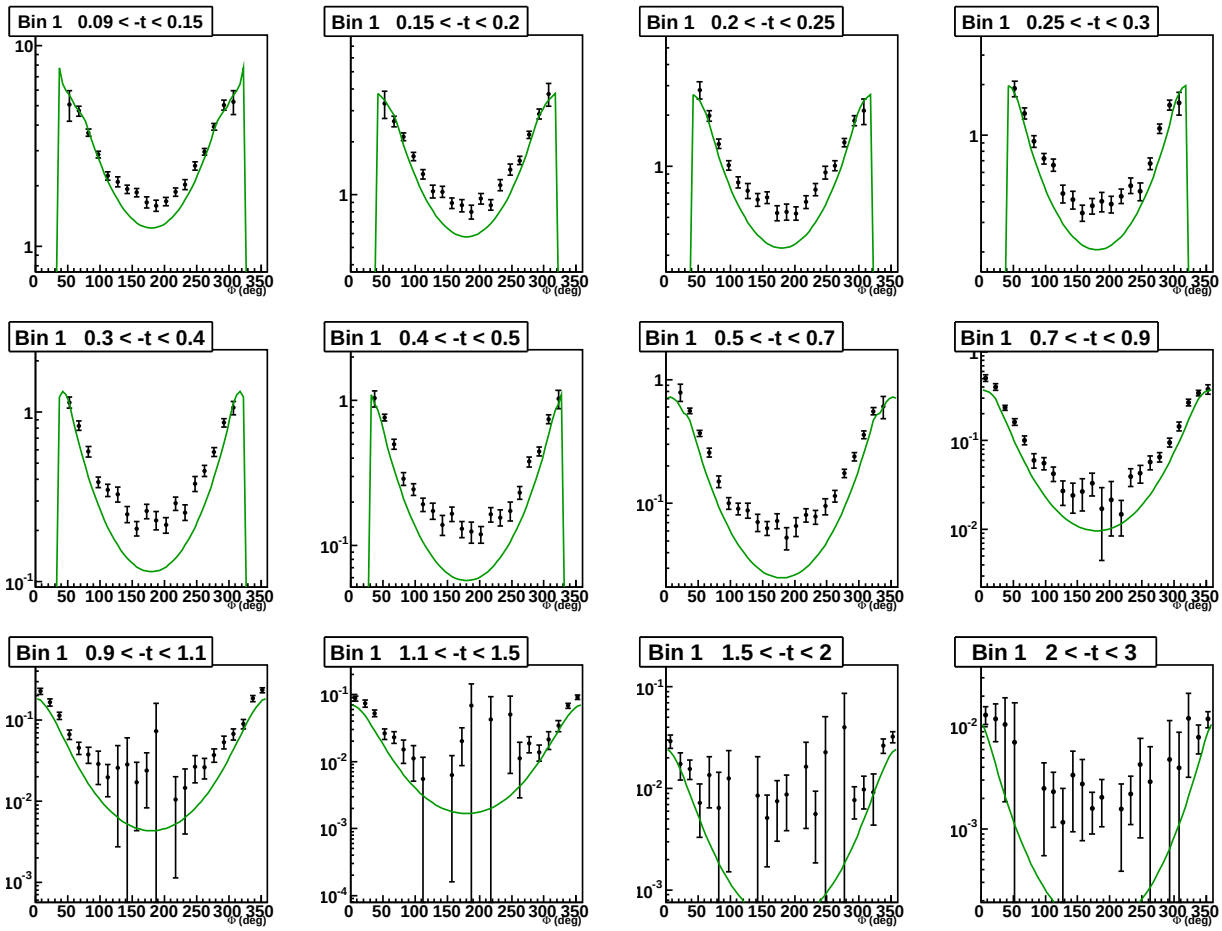

Figure G.1: DVCS cross section (nbarn/GeV^4) as a function of Φ for the 12 t bins of the first (Q^2, x_B) bin, compared to the BH cross-section (green) integrated over the bins size.

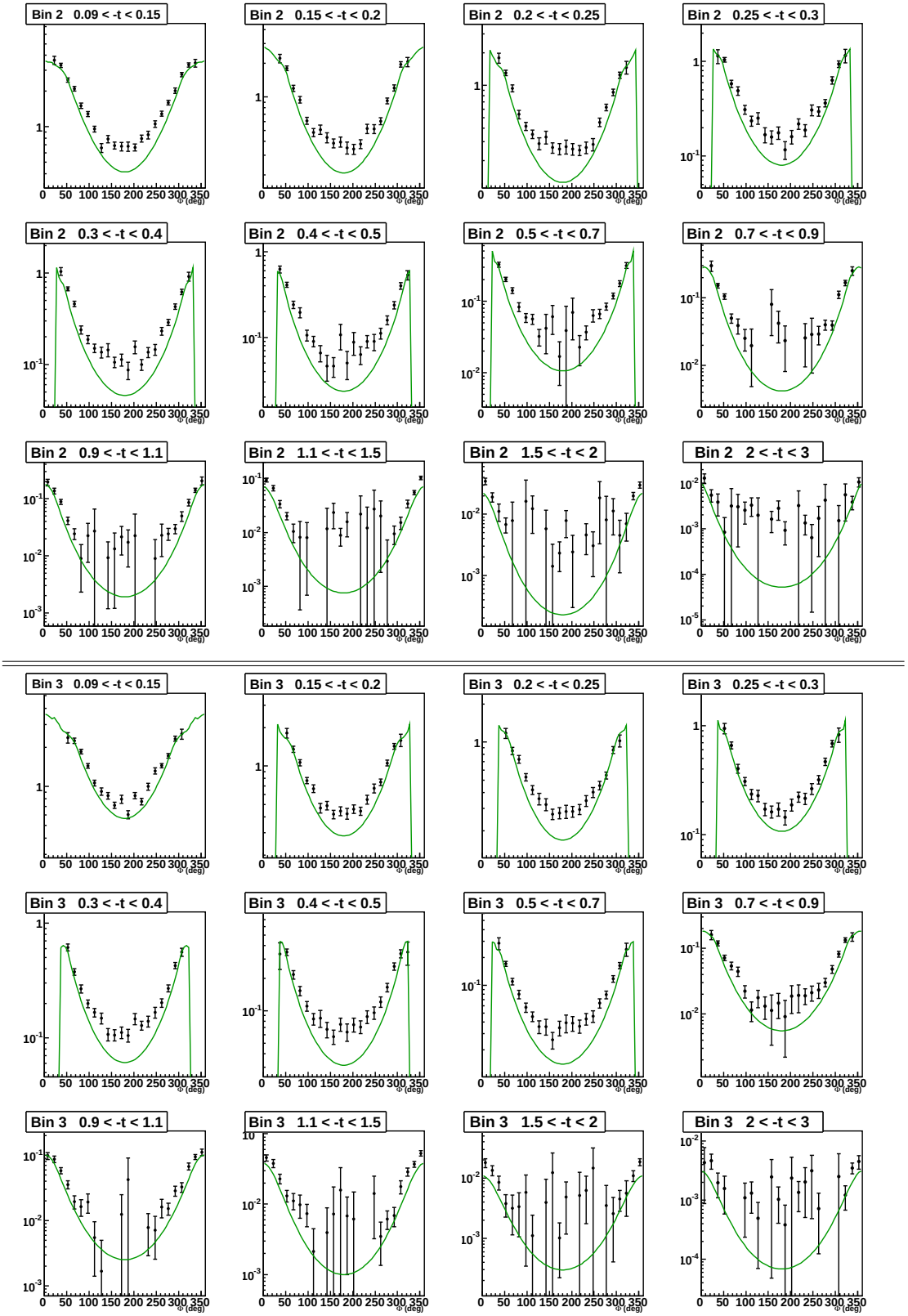

Figure G.2: DVCS cross section (nbarn/GeV^4) as a function of Φ for the 12 t bins of the (Q^2, x_B) bins 2 and 3, compared to the BH cross-section (green) integrated over the bins size.

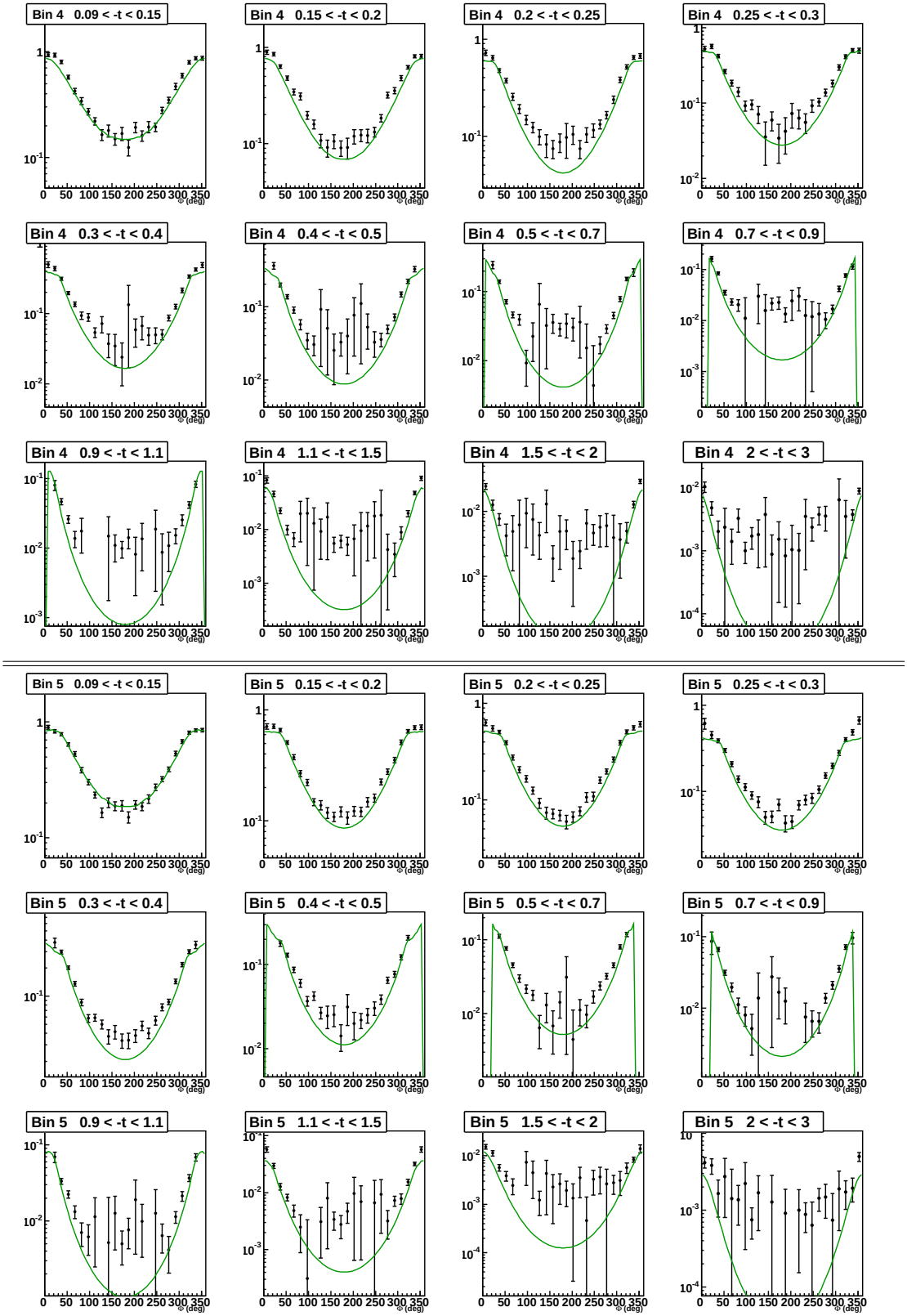

Figure G.3: DVCS cross section (nbarn/GeV^4) as a function of Φ for the 12 t bins of the (Q^2, x_B) bins 4 and 5, compared to the BH cross-section (green) integrated over the bins size.

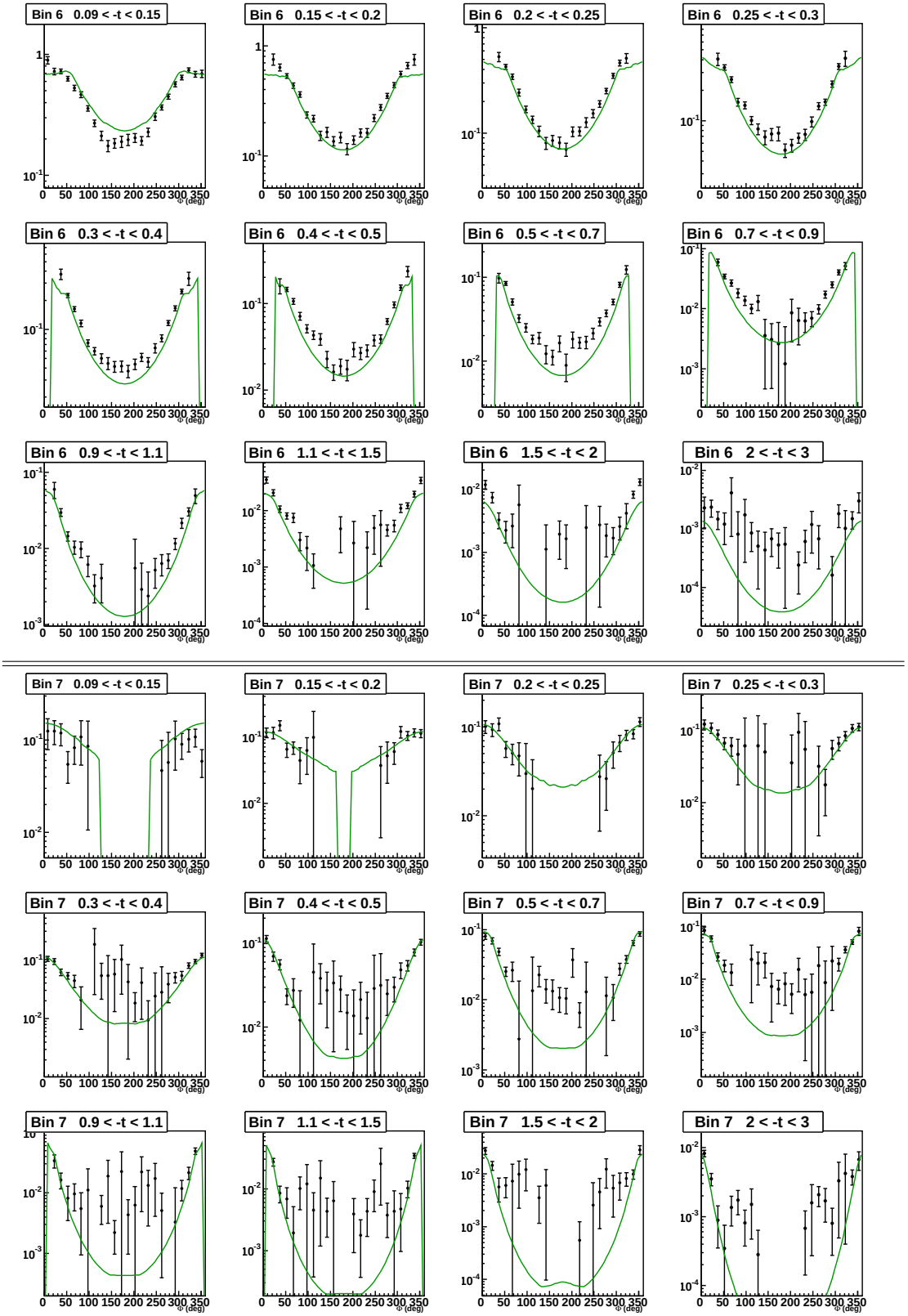

Figure G.4: DVCS cross section (nbarn/GeV^4) as a function of Φ for the 12 t bins of the (Q^2, x_B) bins 6 and 7, compared to the BH cross-section (green) integrated over the bins size.

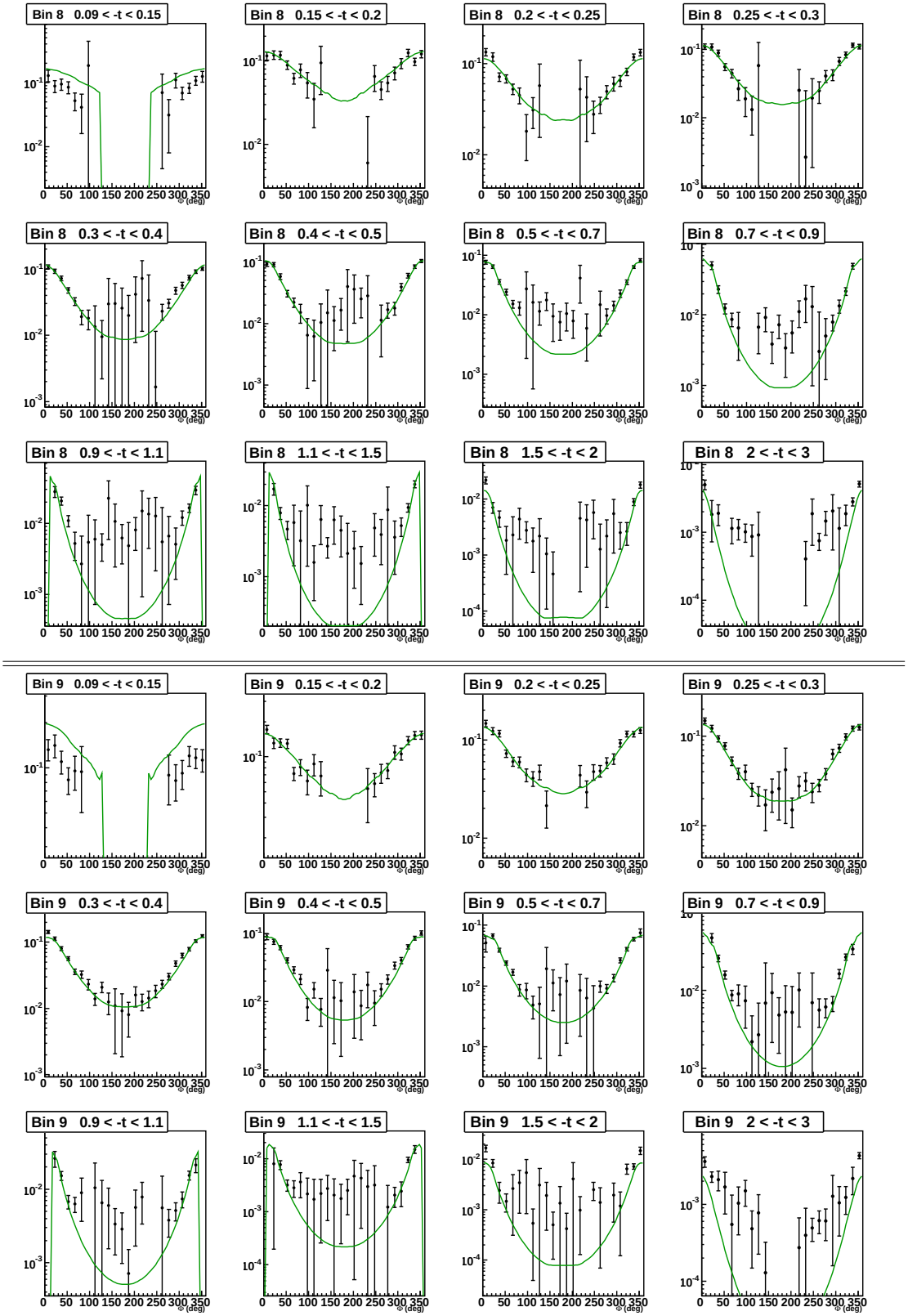

Figure G.5: DVCS cross section (nbarn/GeV^4) as a function of Φ for the 12 t bins of the (Q^2, x_B) bins 8 and 9, compared to the BH cross-section (green) integrated over the bins size.

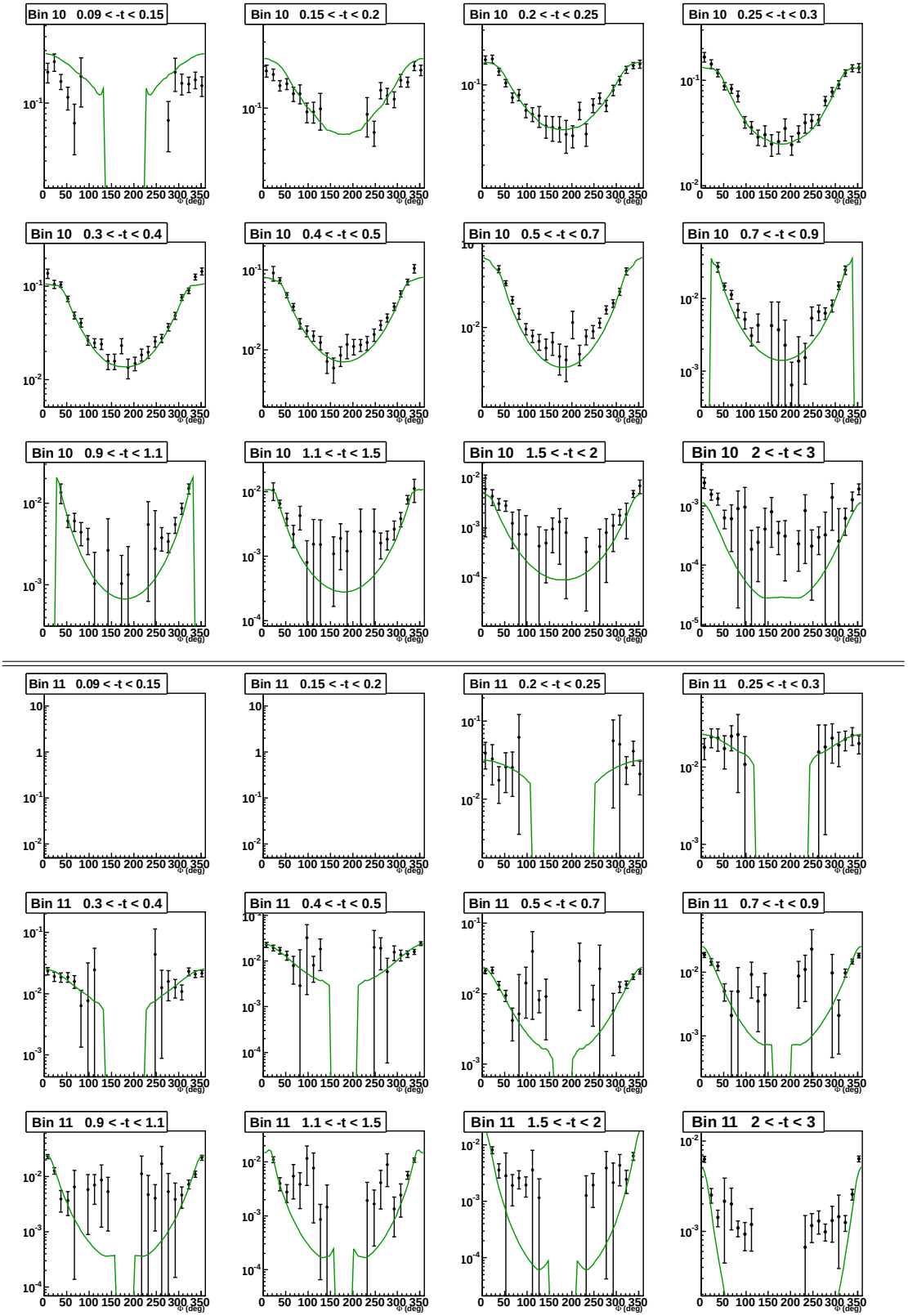

Figure G.6: DVCS cross section (nbarn/GeV^4) as a function of Φ for the 12 t bins of the (Q^2, x_B) bins 10 and 11, compared to the BH cross-section (green) integrated over the bins size.

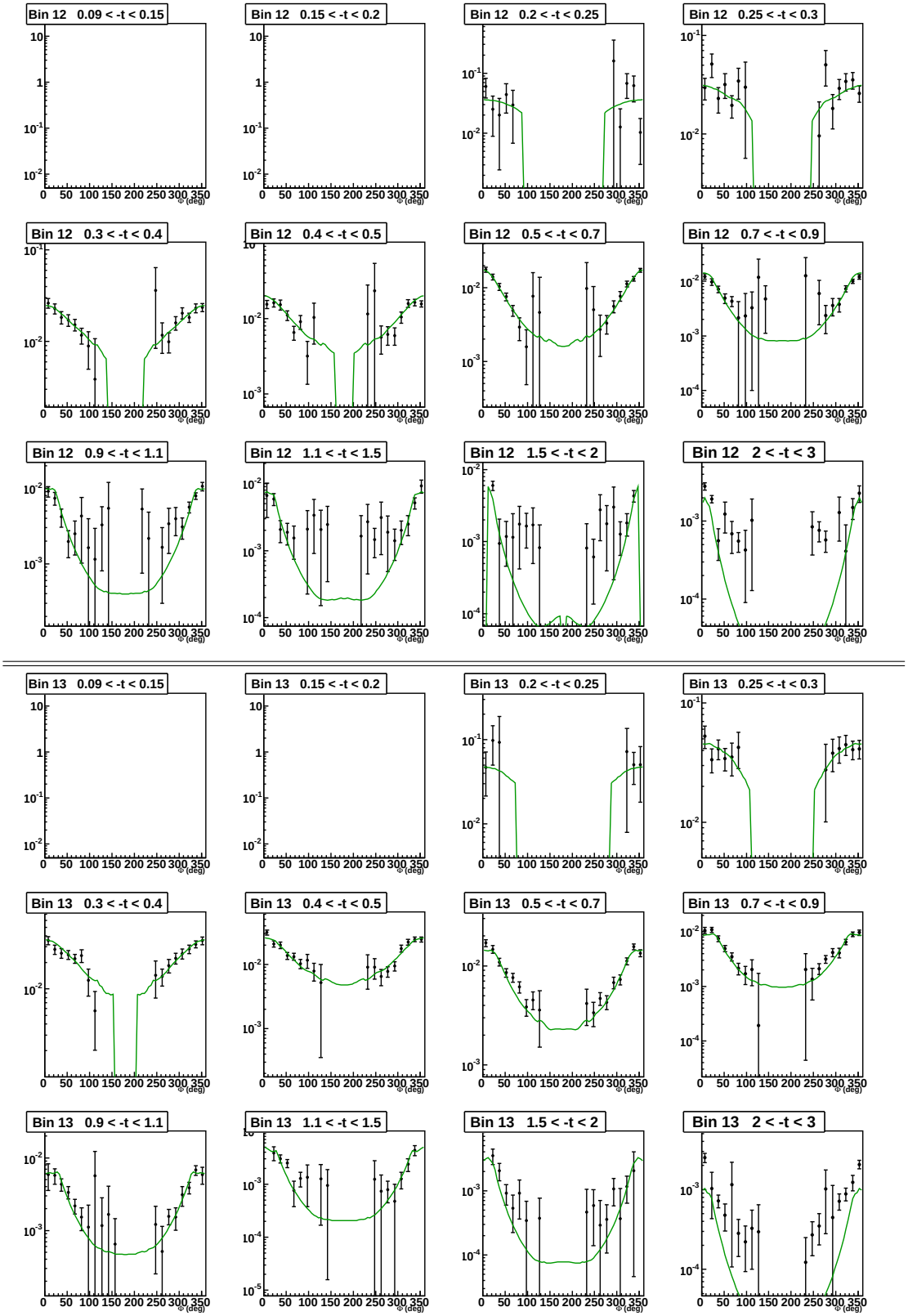

Figure G.7: DVCS cross section (nbarn/GeV^4) as a function of Φ for the 12 t bins of the (Q^2, x_B) bins 12 and 13, compared to the BH cross-section (green) integrated over the bins size.

Appendix H

Comparison of the Unpolarized cross sections

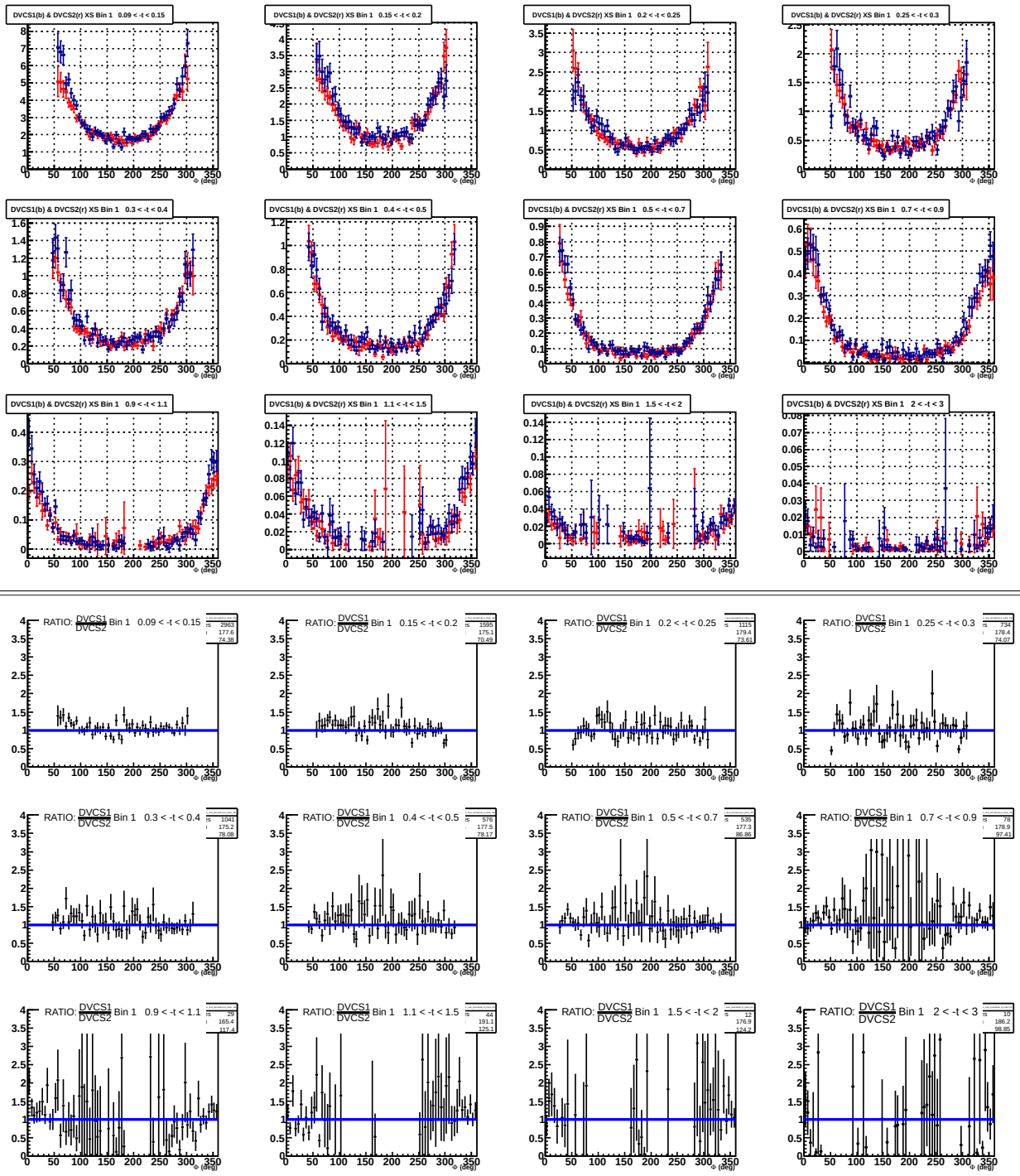

Figure H.1: Top: Comparison of the DVCS cross section of the e1-DVCS1 (blue) and e1-DVCS2 experiments. The cross sections (nbarn/GeV^4) are shown as a function of Φ for the 12 t-bins of the first (Q^2, x_B) bin. Bottom: ratio of the two experimental cross sections.

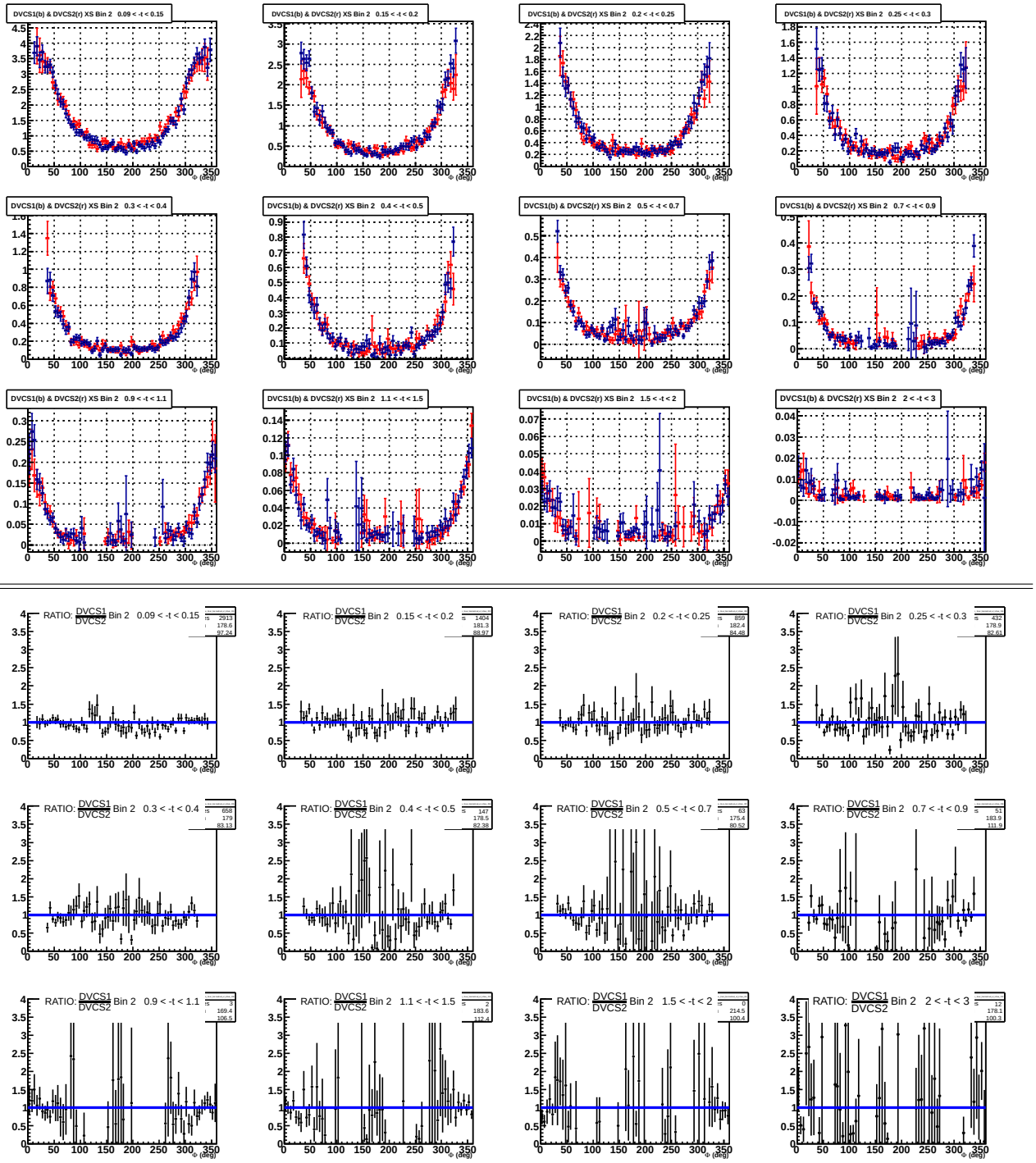

Figure H.2: Top: Comparison of the DVCS cross section for e1-DVCS1 (blue) e1-DVCS2 experiments. The cross section (nbarn/GeV^4) are shown as a function of Φ for the 12 t-bins of the (Q^2, x_B) bin 2. Bottom: ratio of the two experimental cross sections.

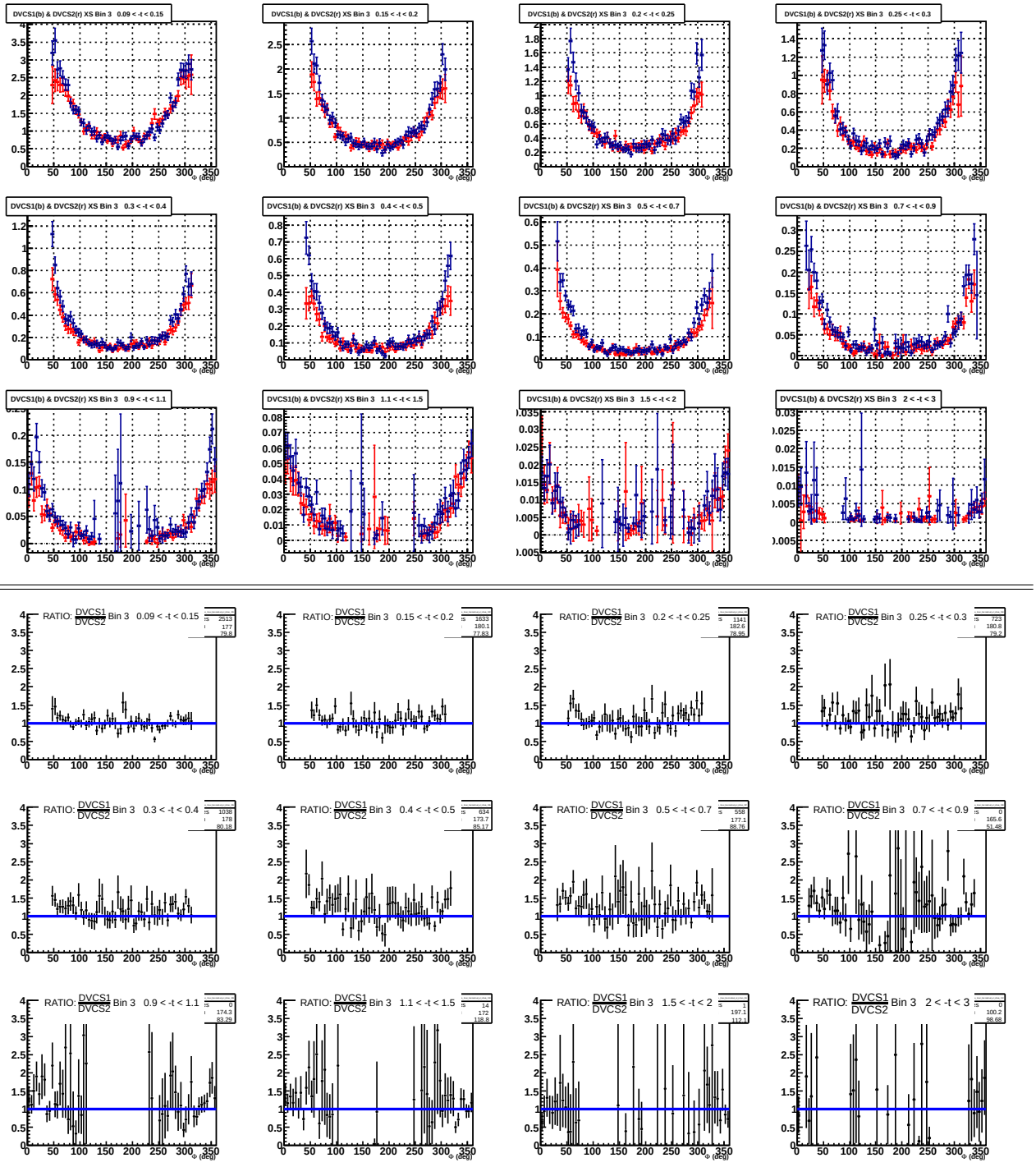

Figure H.3: Top: Comparison of the DVCS cross section for e1-DVCS1 (blue) e1-DVCS2 experiments. The cross section (nbarn/GeV^4) are shown as a function of Φ for the 12 t-bins of the (Q^2, x_B) bin 3. Bottom: ratio of the two experimental cross sections.

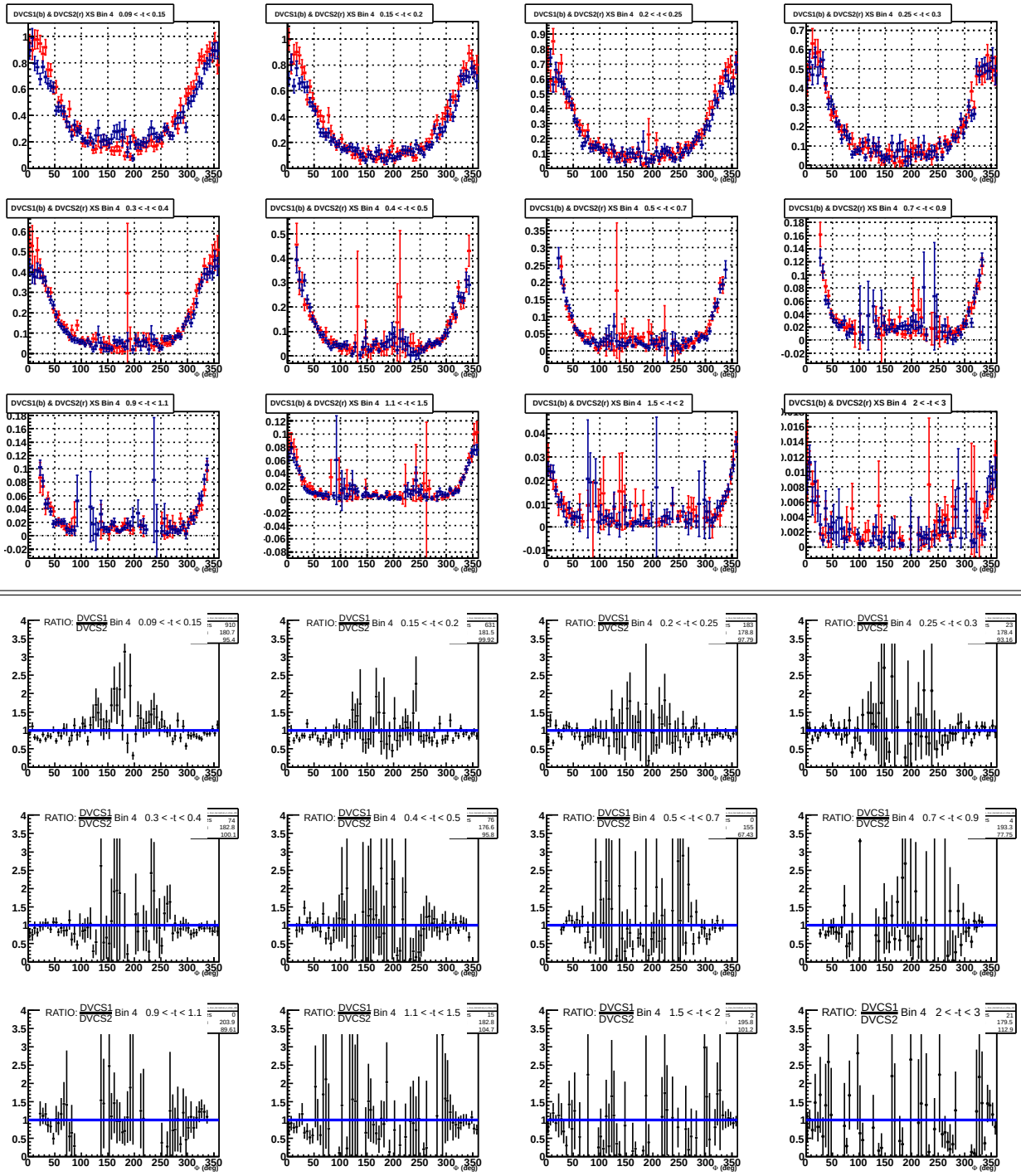

Figure H.4: Top: Comparison of the DVCS cross section for e1-DVCS1 (blue) e1-DVCS2 experiments. The cross section (nbarn/GeV^4) are shown as a function of Φ for the 12 t-bins of the (Q^2, x_B) bin 4. Bottom: ratio of the two experimental cross sections.

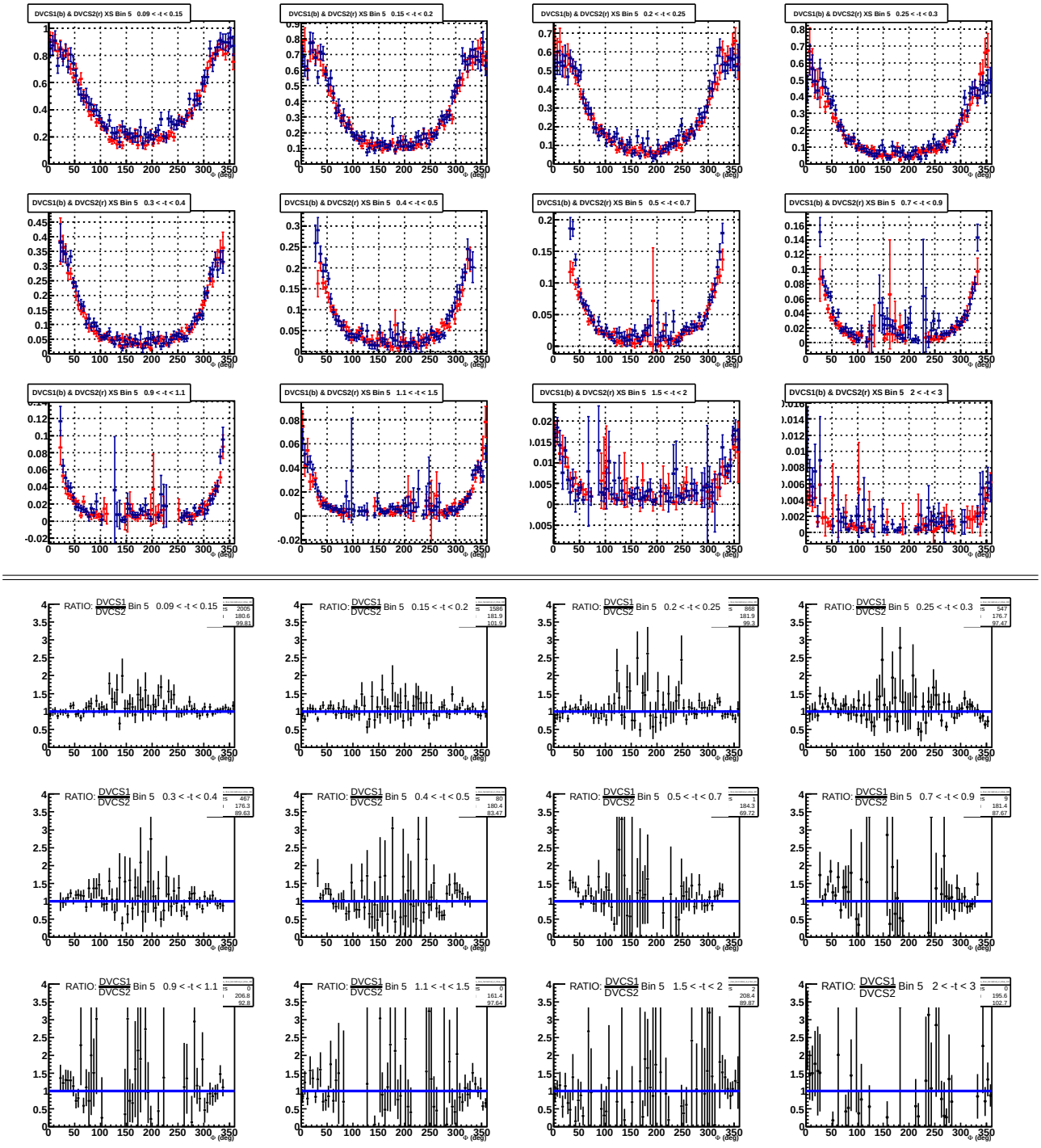

Figure H.5: Top: Comparison of the DVCS cross section for e1-DVCS1 (blue) e1-DVCS2 experiments. The cross section (nbarn/GeV^4) are shown as a function of Φ for the 12 t-bins of the (Q^2, x_B) bin 5. Bottom: ratio of the two experimental cross sections.

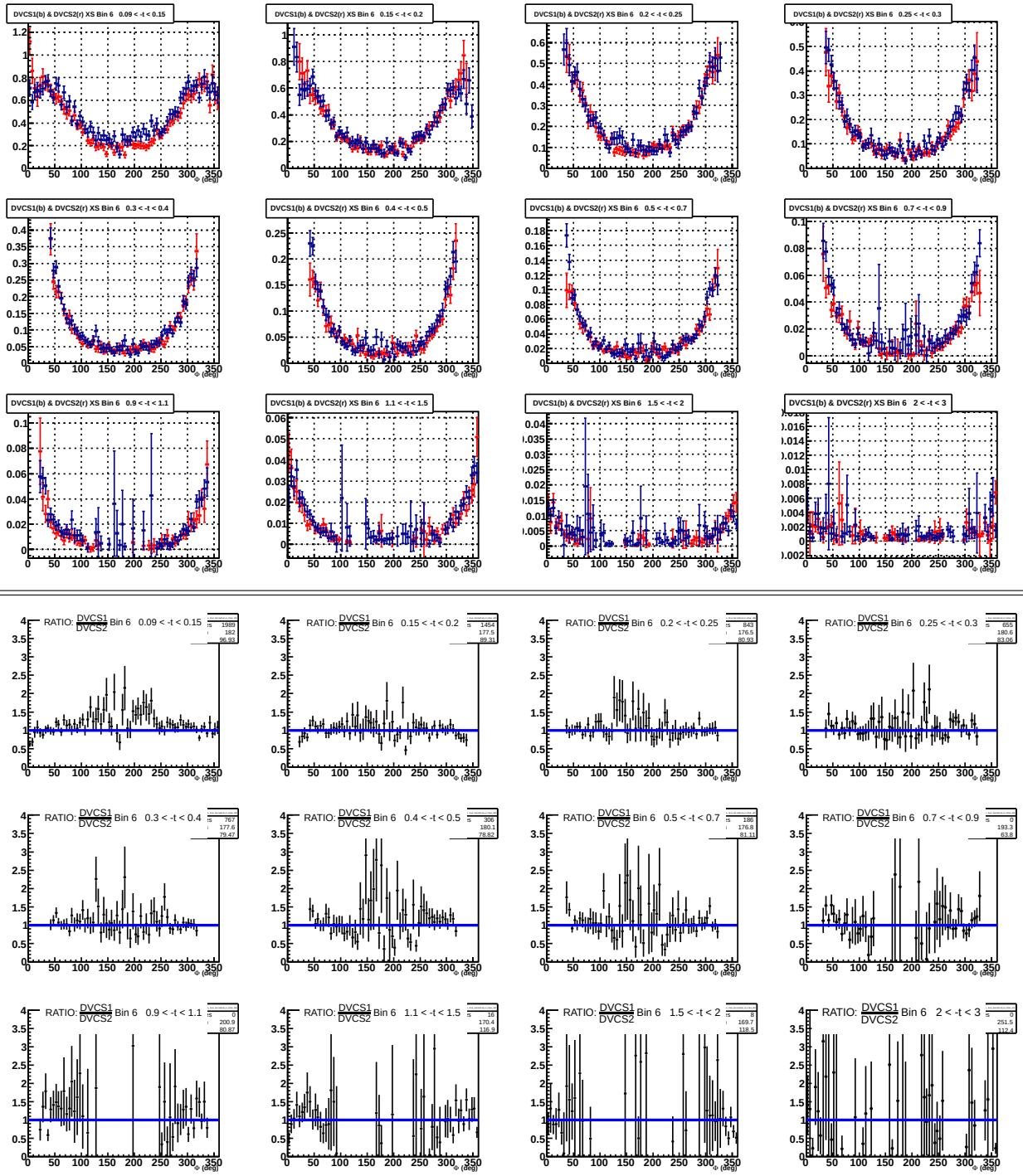

Figure H.6: Top: Comparison of the DVCS cross section for e1-DVCS1 (blue) e1-DVCS2 experiments. The cross section (nbarn/GeV^4) are shown as a function of Φ for the 12 t-bins of the (Q^2, x_B) bin 6. Bottom: ratio of the two experimental cross sections.

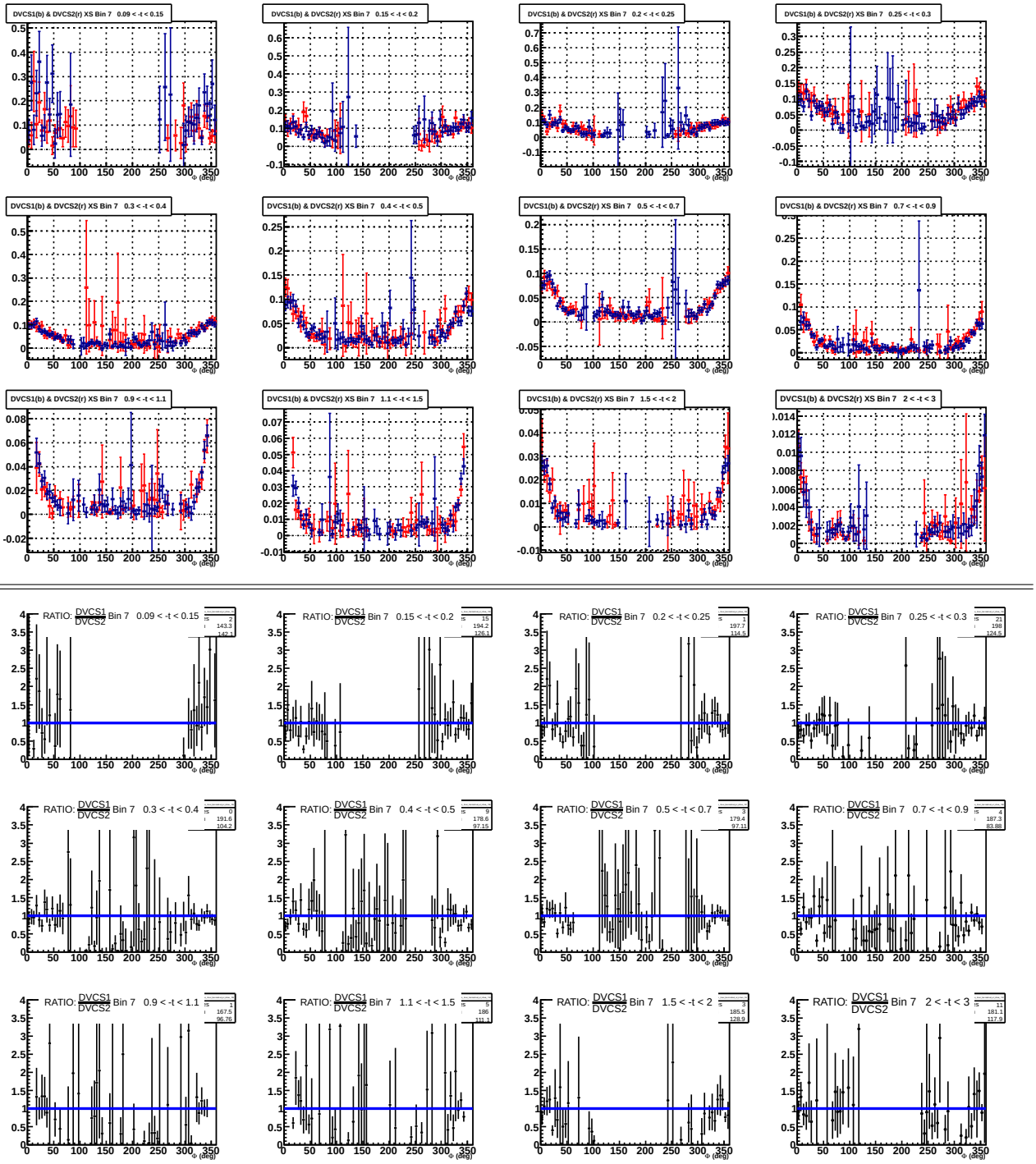

Figure H.7: Top: Comparison of the DVCS cross section for e1-DVCS1 (blue) e1-DVCS2 experiments. The cross section (nbarn/GeV^4) are shown as a function of Φ for the 12 t-bins of the (Q^2, x_B) bin 7. Bottom: ratio of the two experimental cross sections.

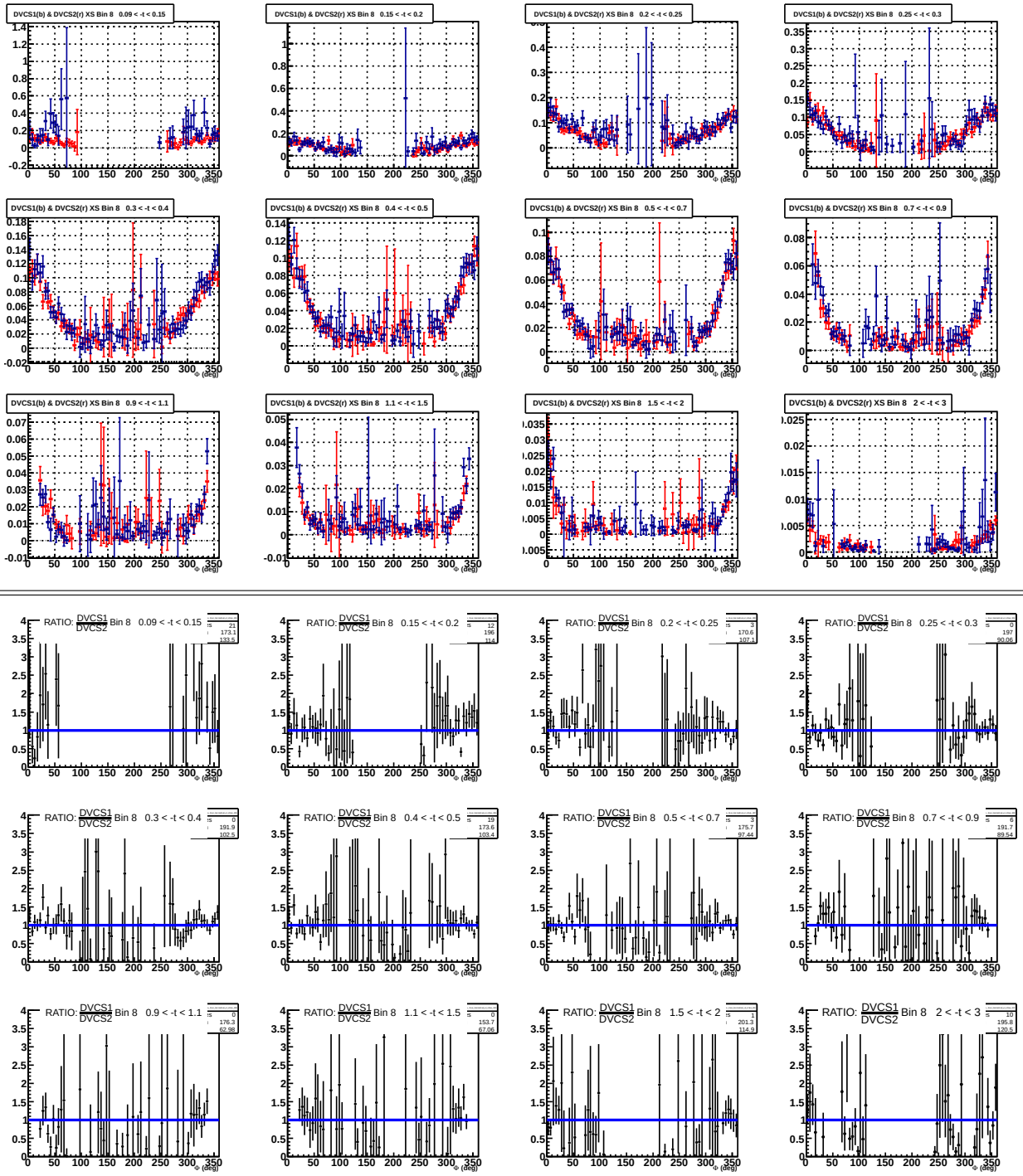

Figure H.8: Top: Comparison of the DVCS cross section for e1-DVCS1 (blue) e1-DVCS2 experiments. The cross section (nbarn/GeV^4) are shown as a function of Φ for the 12 t-bins of the (Q^2, x_B) bin 8. Bottom: ratio of the two experimental cross sections.

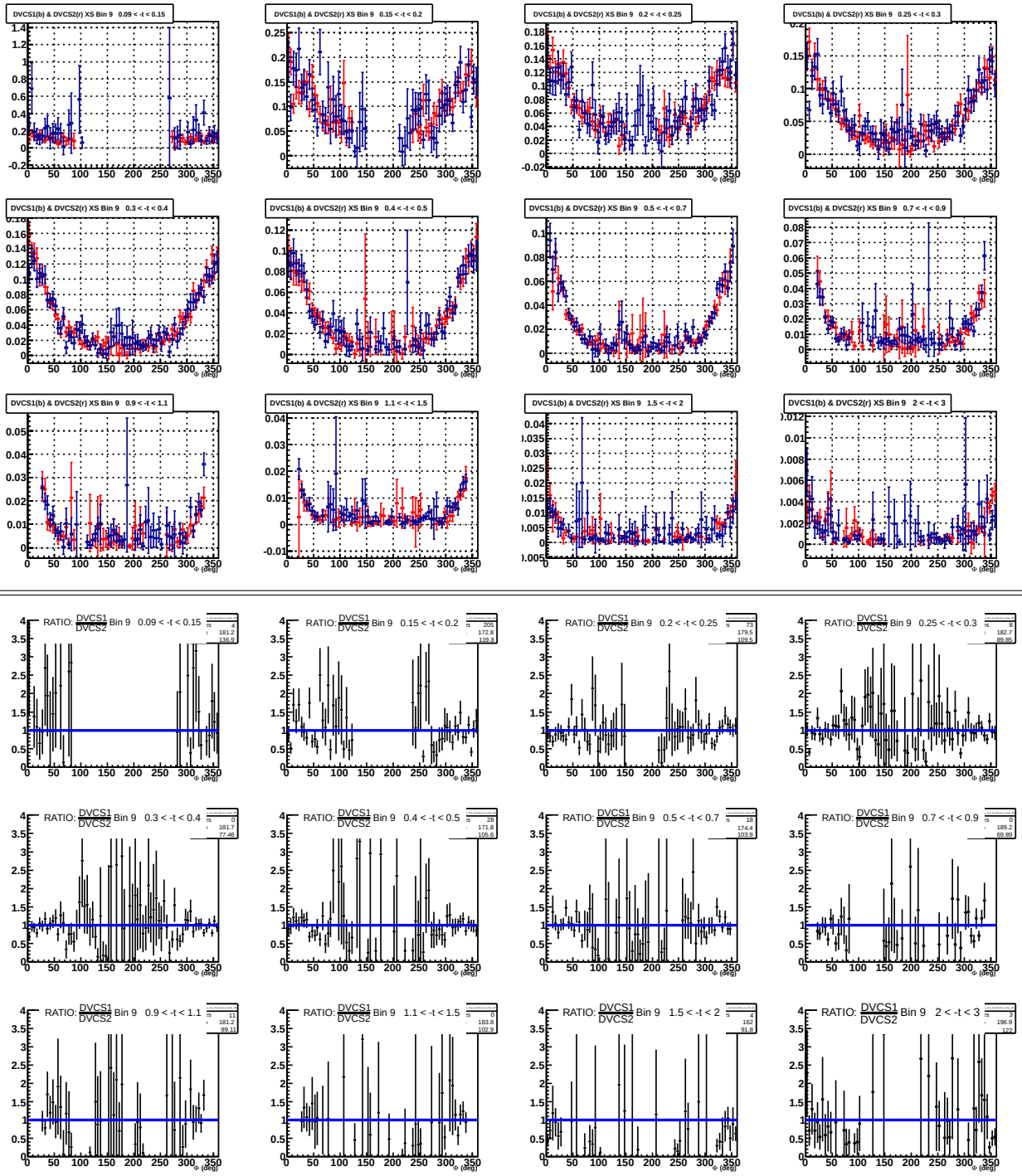

Figure H.9: Top: Comparison of the DVCS cross section for e1-DVCS1 (blue) e1-DVCS2 experiments. The cross section (nbarn/GeV^4) are shown as a function of Φ for the 12 t-bins of the (Q^2, x_B) bin 9. Bottom: ratio of the two experimental cross sections.

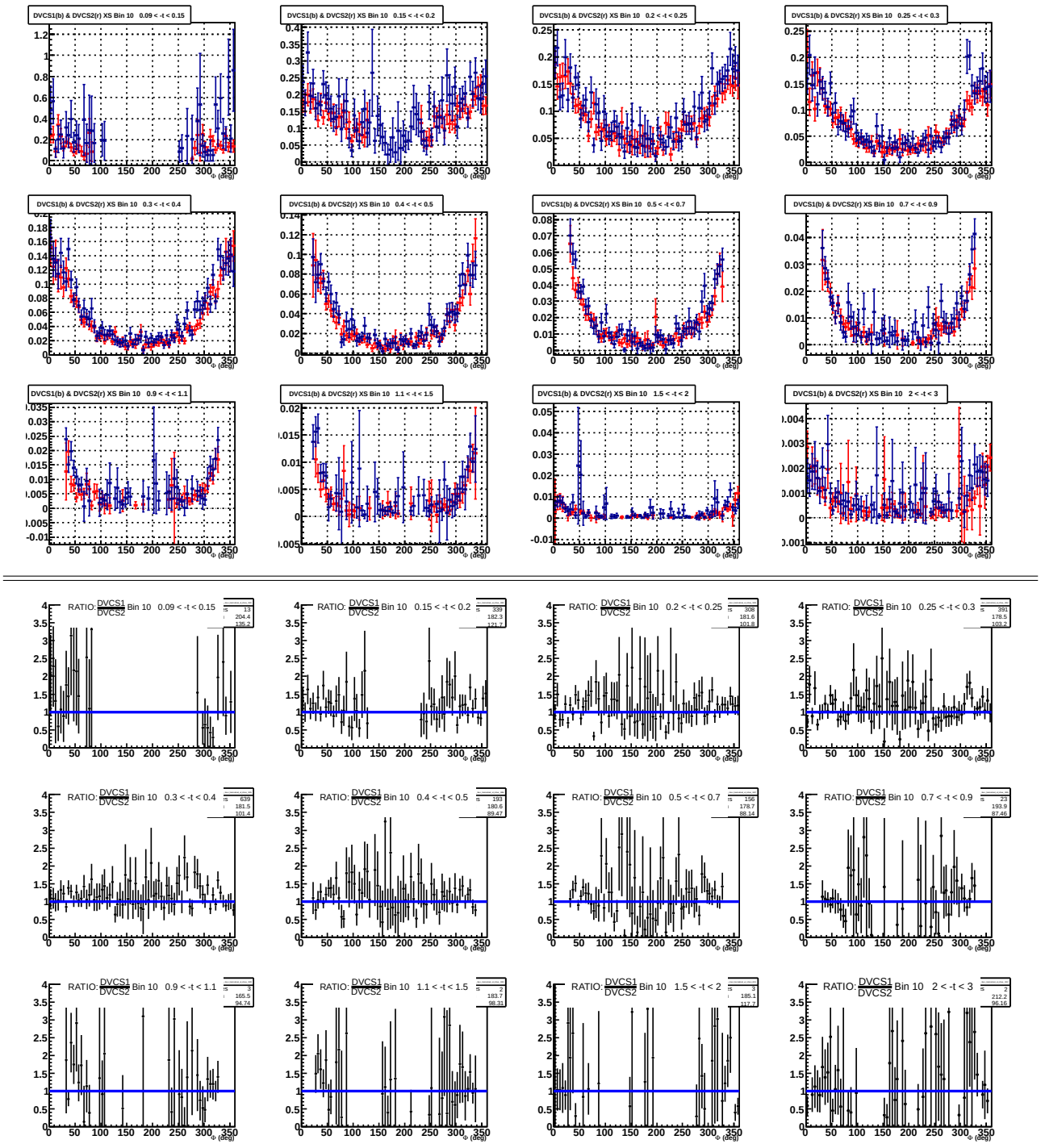

Figure H.10: Top: Comparison of the DVCS cross section for e1-DVCS1 (blue) e1-DVCS2 experiments. The cross section (nbarn/GeV^4) are shown as a function of Φ for the 12 t-bins of the (Q^2, x_B) bin 10. Bottom: ratio of the two experimental cross sections.

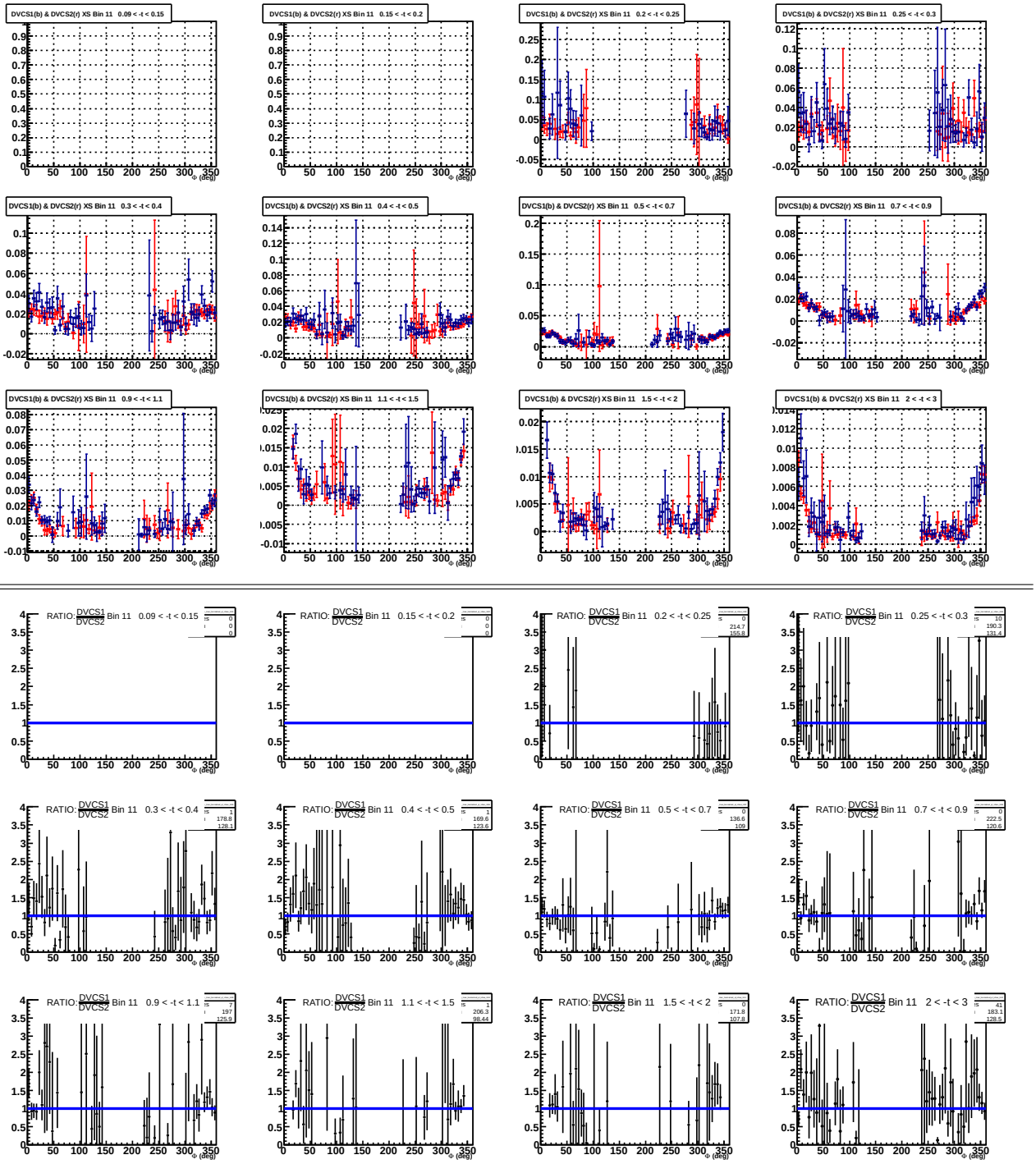

Figure H.11: Top: Comparison of the DVCS cross section for e1-DVCS1 (blue) e1-DVCS2 experiments. The cross section (nbarn/GeV^4) are shown as a function of Φ for the 12 t-bins of the (Q^2, x_B) bin 11. Bottom: ratio of the two experimental cross sections.

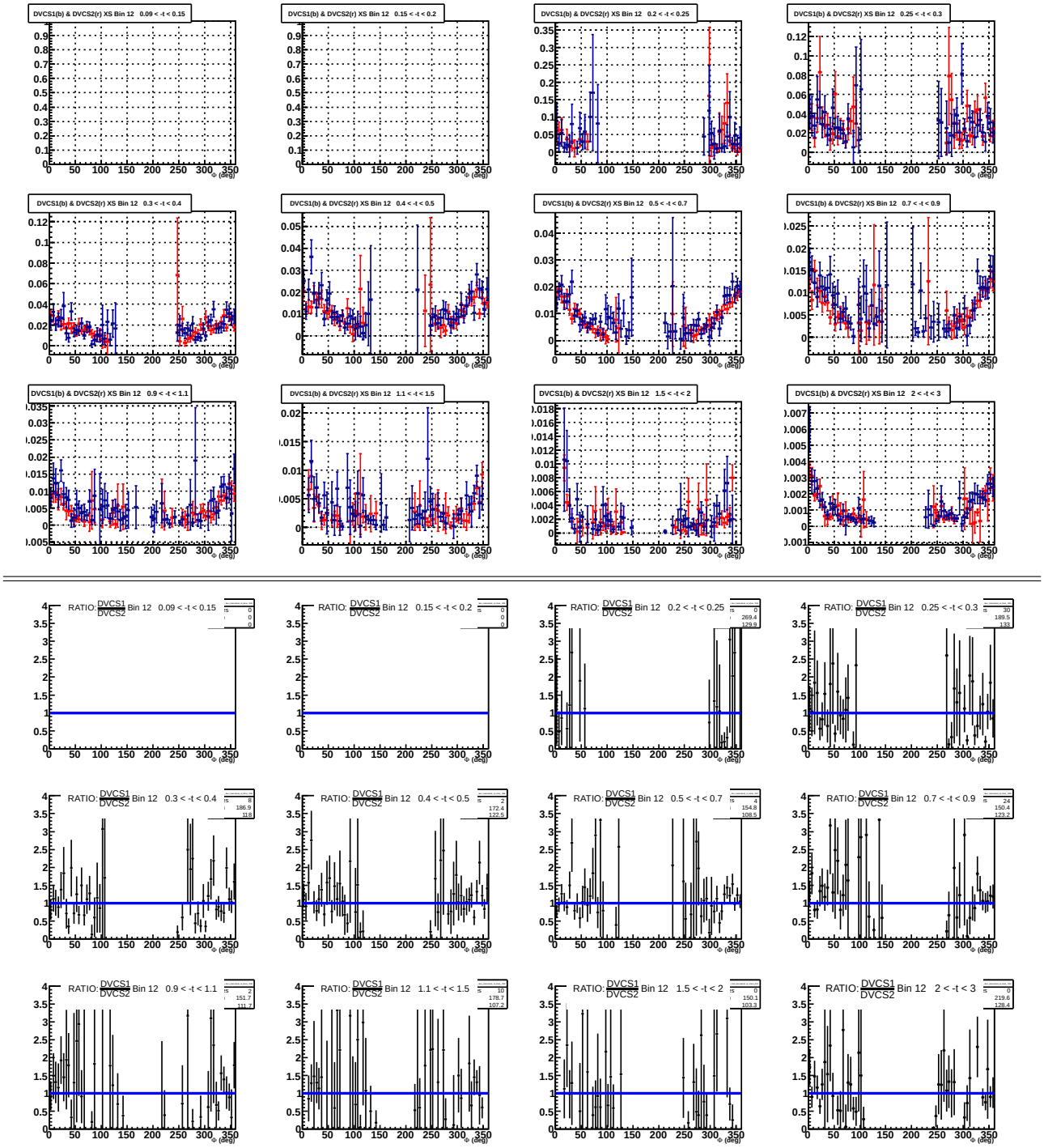

Figure H.12: Top: Comparison of the DVCS cross section for e1-DVCS1 (blue) e1-DVCS2 experiments. The cross section (nbarn/GeV^4) are shown as a function of Φ for the 12 t-bins of the (Q^2, x_B) bin 12. Bottom: ratio of the two experimental cross sections.

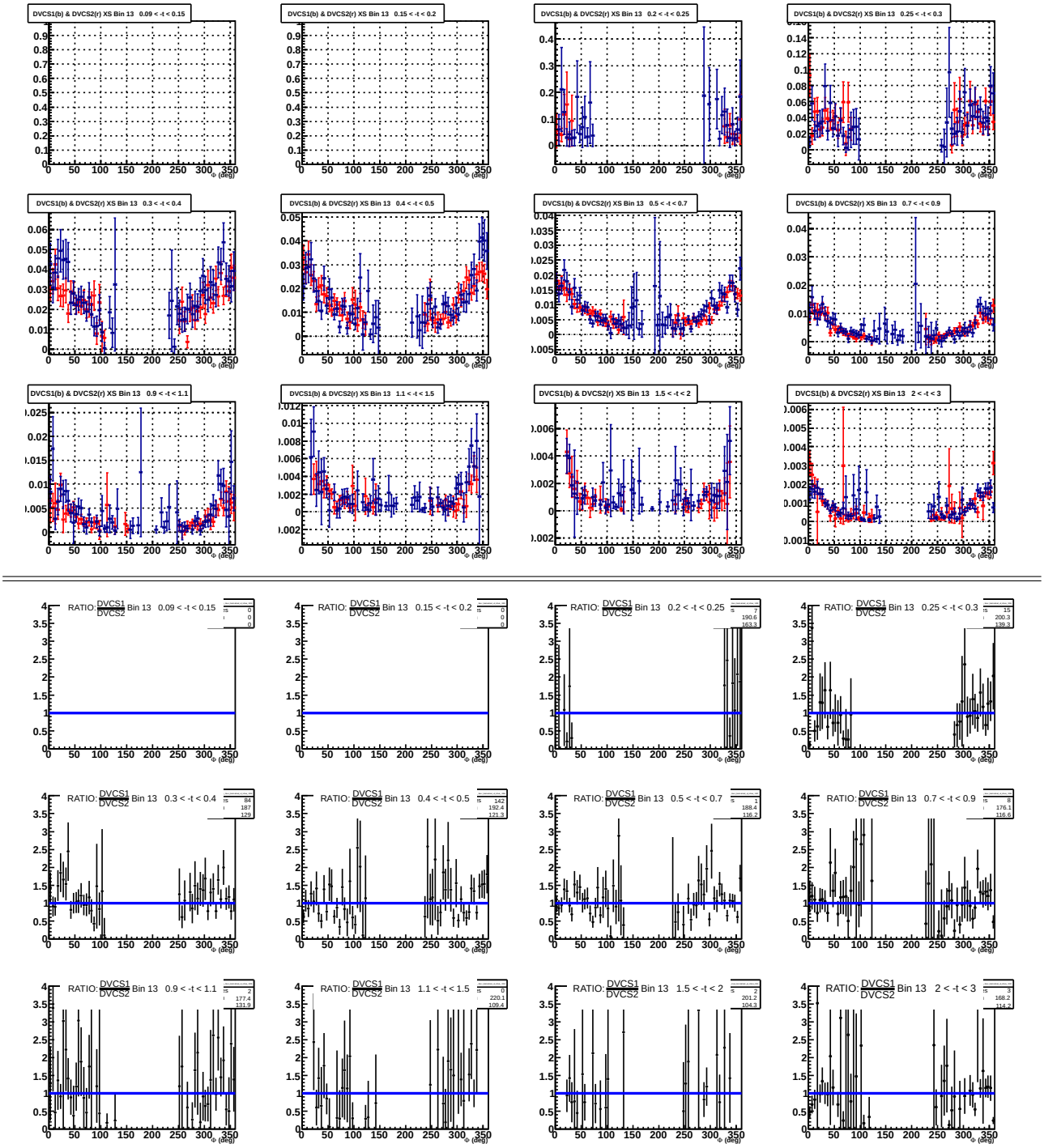

Figure H.13: Top: Comparison of the DVCS cross section for e1-DVCS1 (blue) e1-DVCS2 experiments. The cross section (nbarn/GeV^4) are shown as a function of Φ for the 12 t-bins of the (Q^2, x_B) bin 13. Bottom: ratio of the two experimental cross sections.

Appendix I

Results of the difference of polarized cross sections

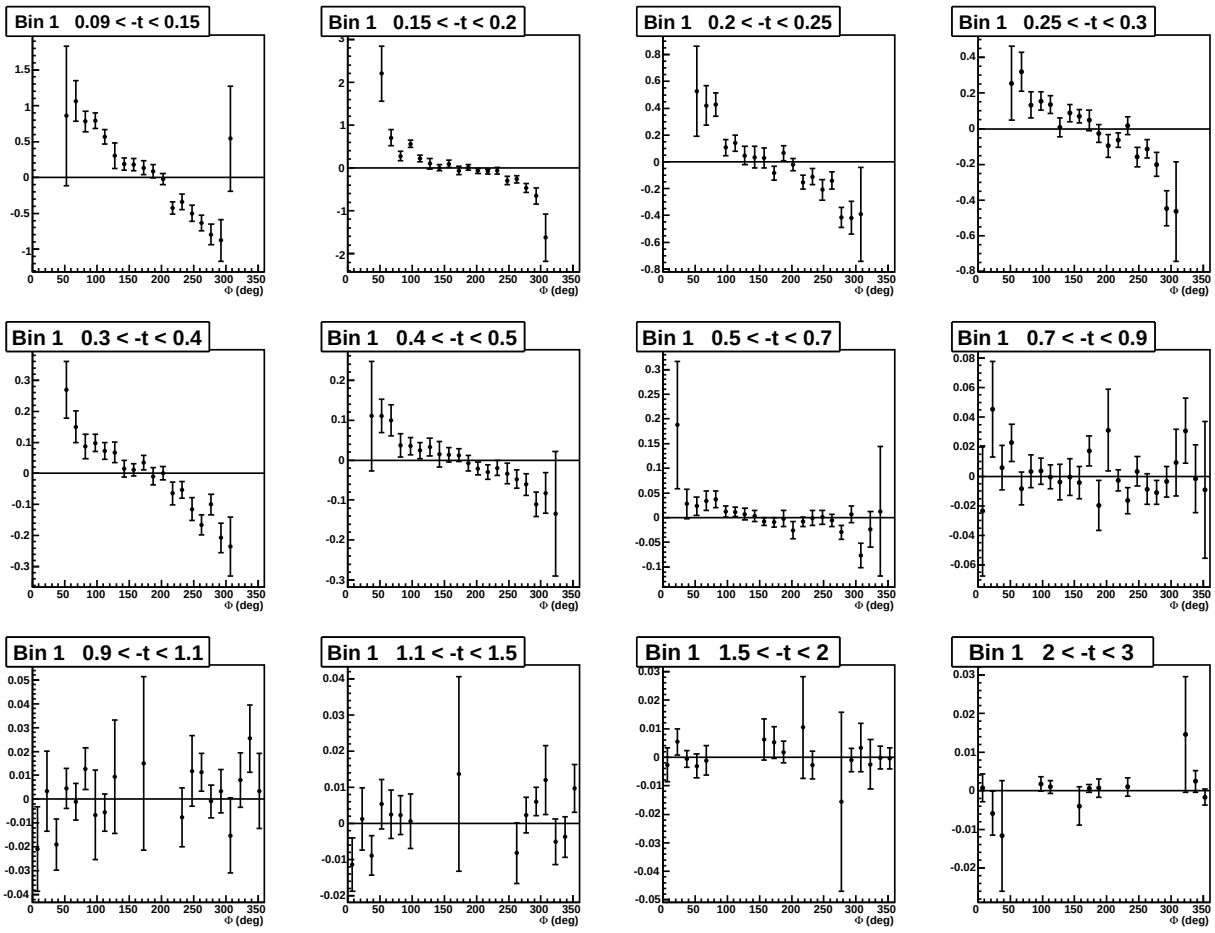

Figure I.1: Difference of polarized cross section as a function of Φ for the 12 t-bins of the (Q^2, x_B) bin 1.

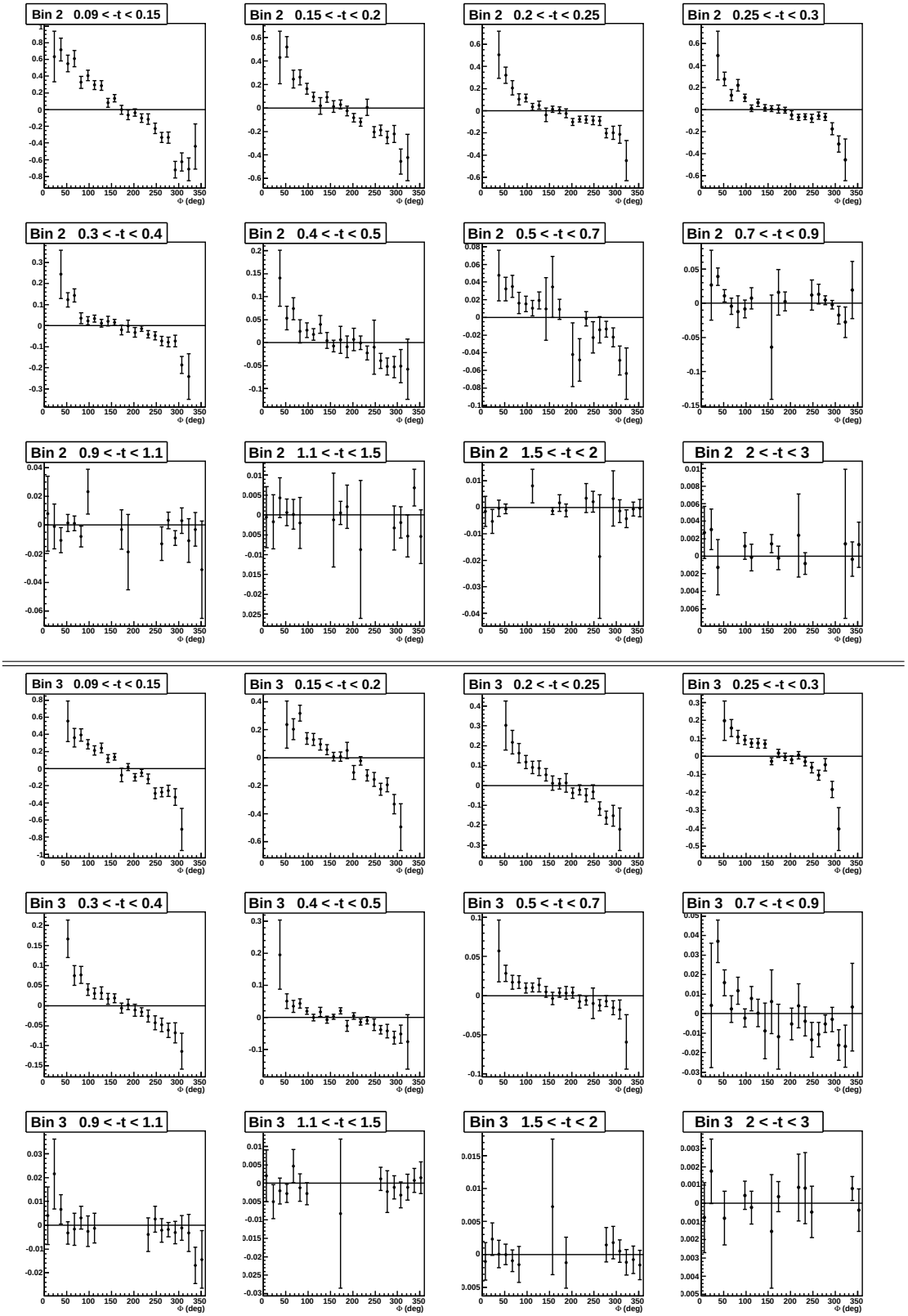

Figure I.2: Difference of polarized cross section as a function of Φ for the 12 t-bins of the (Q^2, x_B) bins 2 and 3.

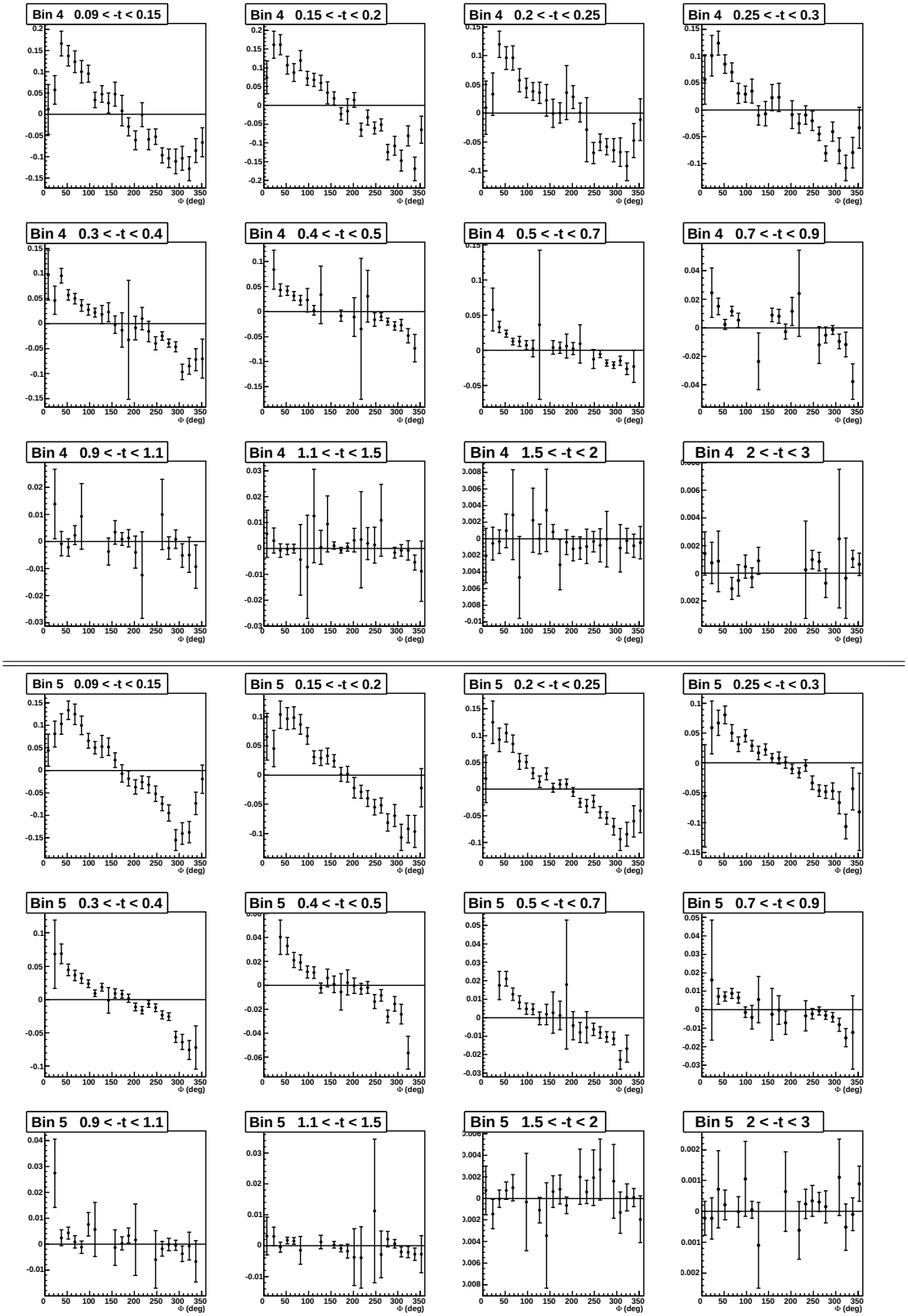

Figure I.3: Difference of polarized cross section as a function of Φ for the 12 t-bins of the (Q^2, x_B) bins 4 and 5.

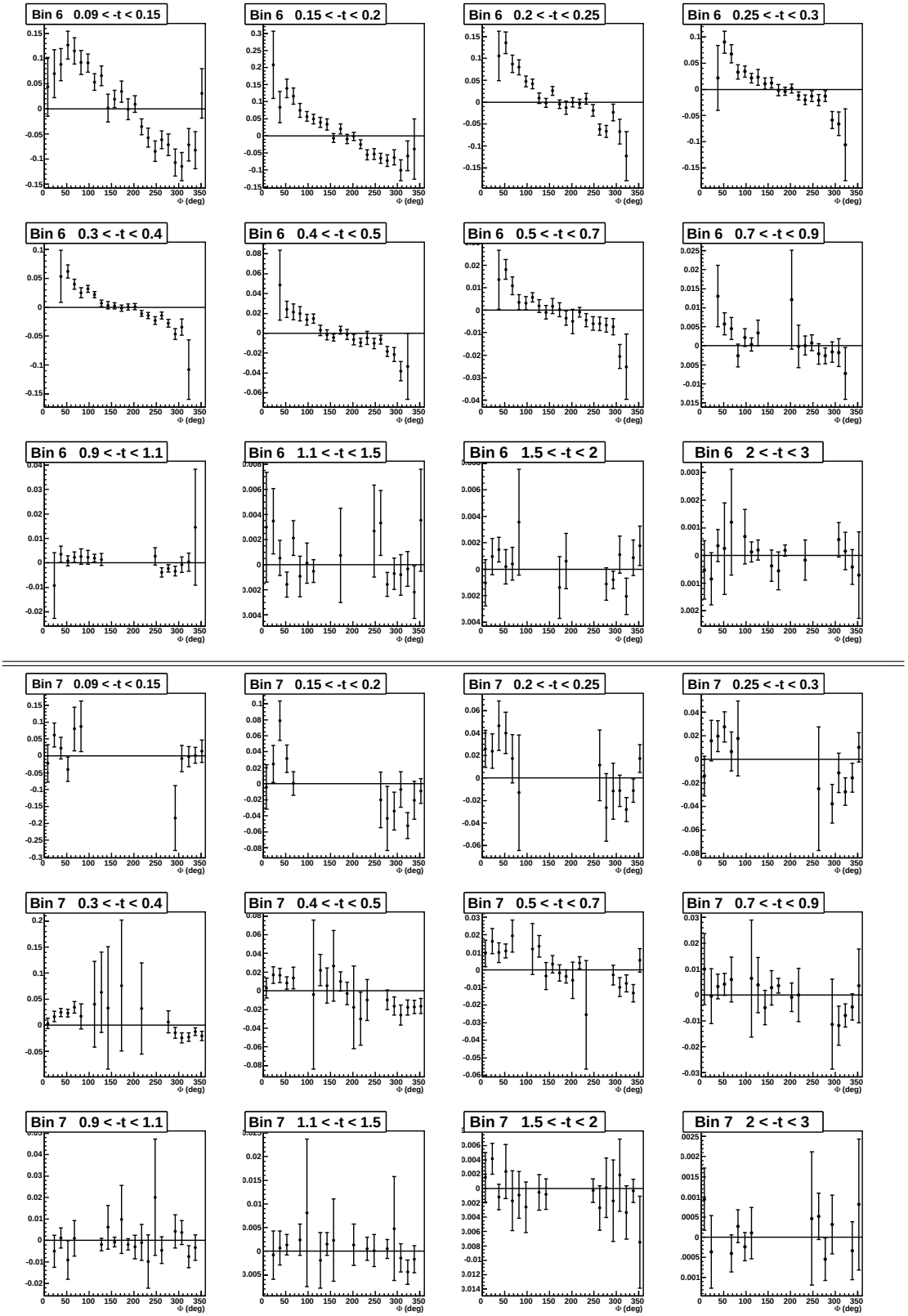

Figure I.4: Difference of polarized cross section as a function of Φ for the 12 t-bins of the (Q^2, x_B) bins 6 and 7.

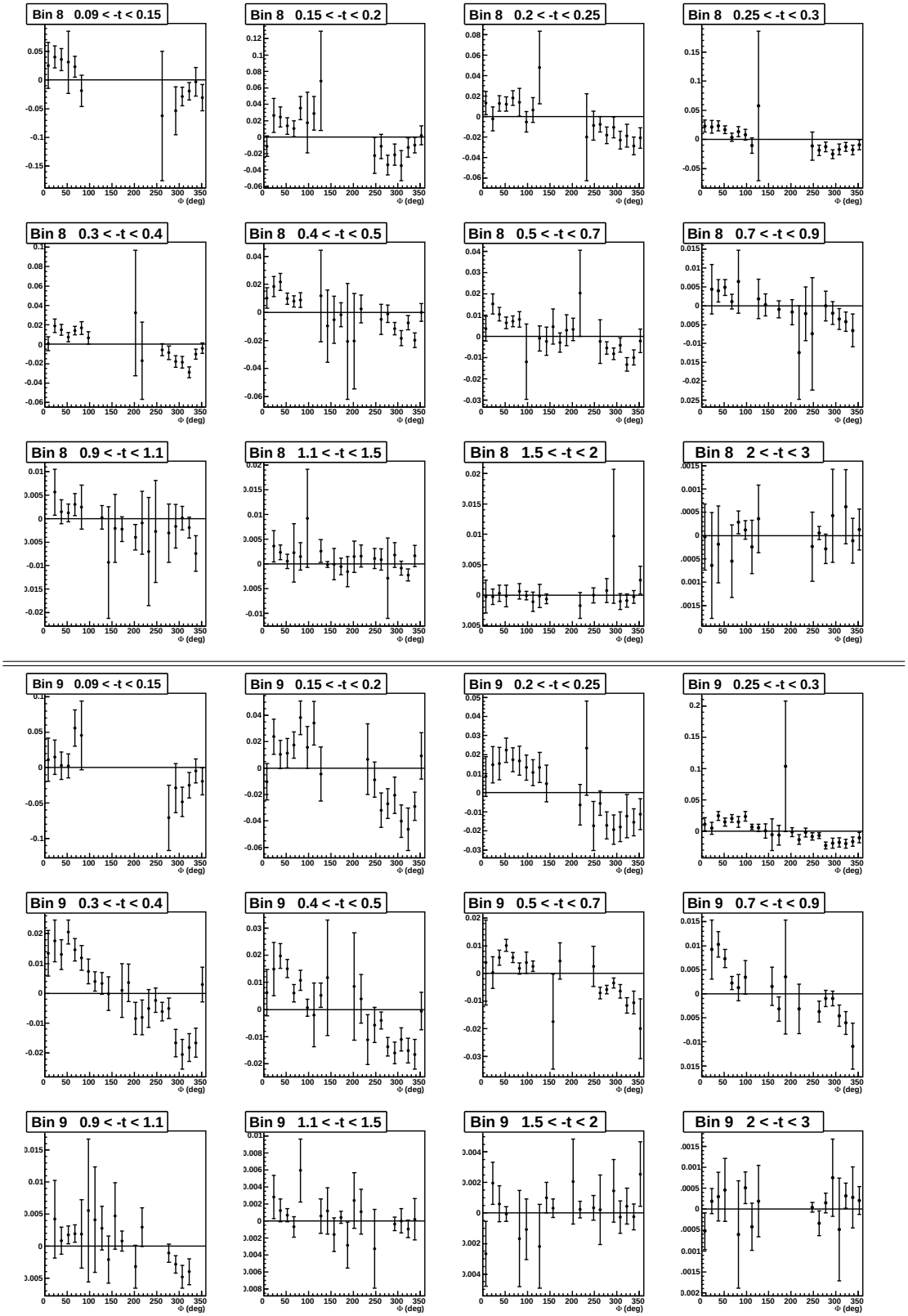

Figure I.5: Difference of polarized cross section as a function of Φ for the 12 t-bins of the (Q^2, x_B) bins 8 and 9.

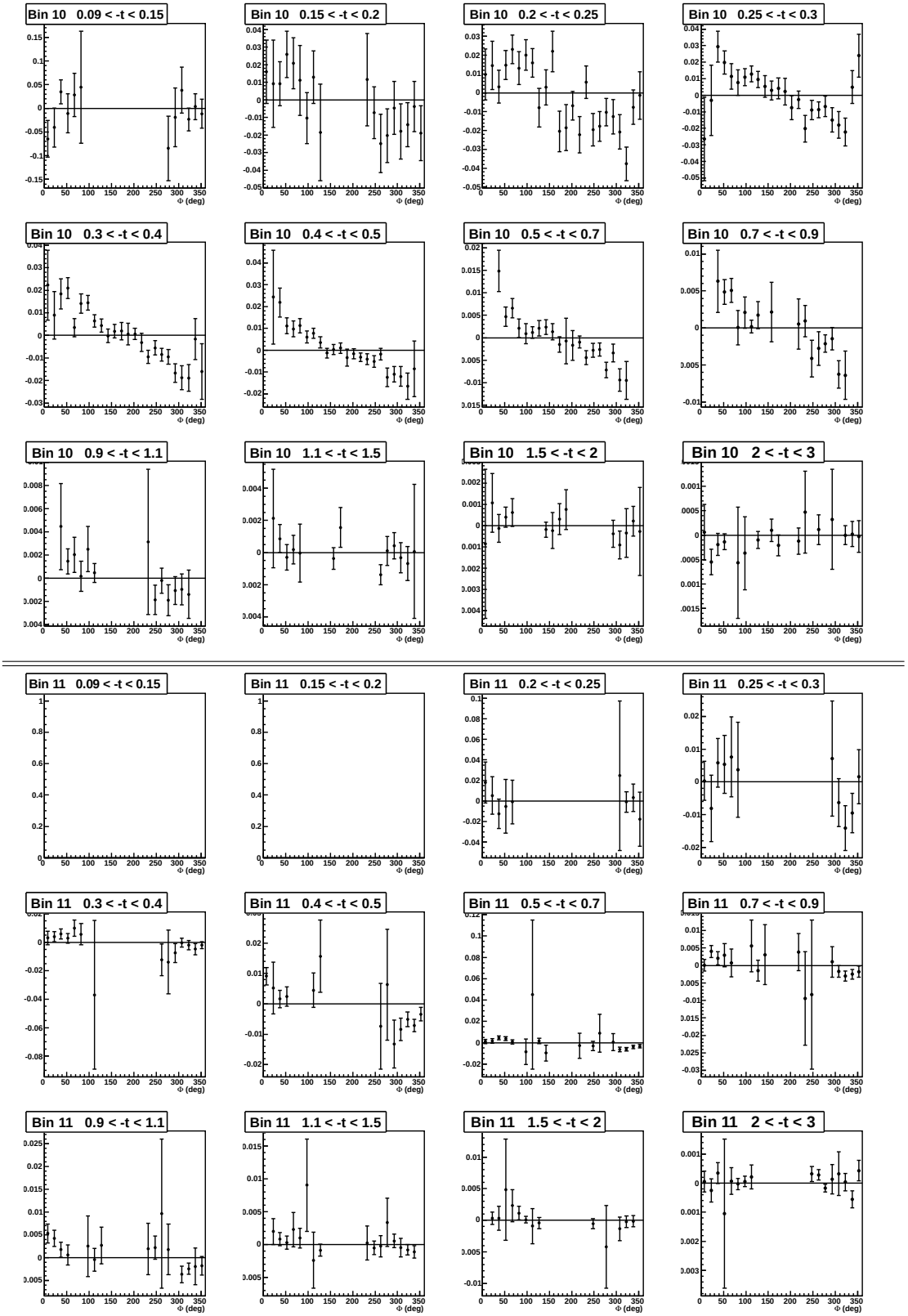

Figure I.6: Difference of polarized cross section as a function of Φ for the 12 t-bins of the (Q^2, x_B) bins 10 and 11.

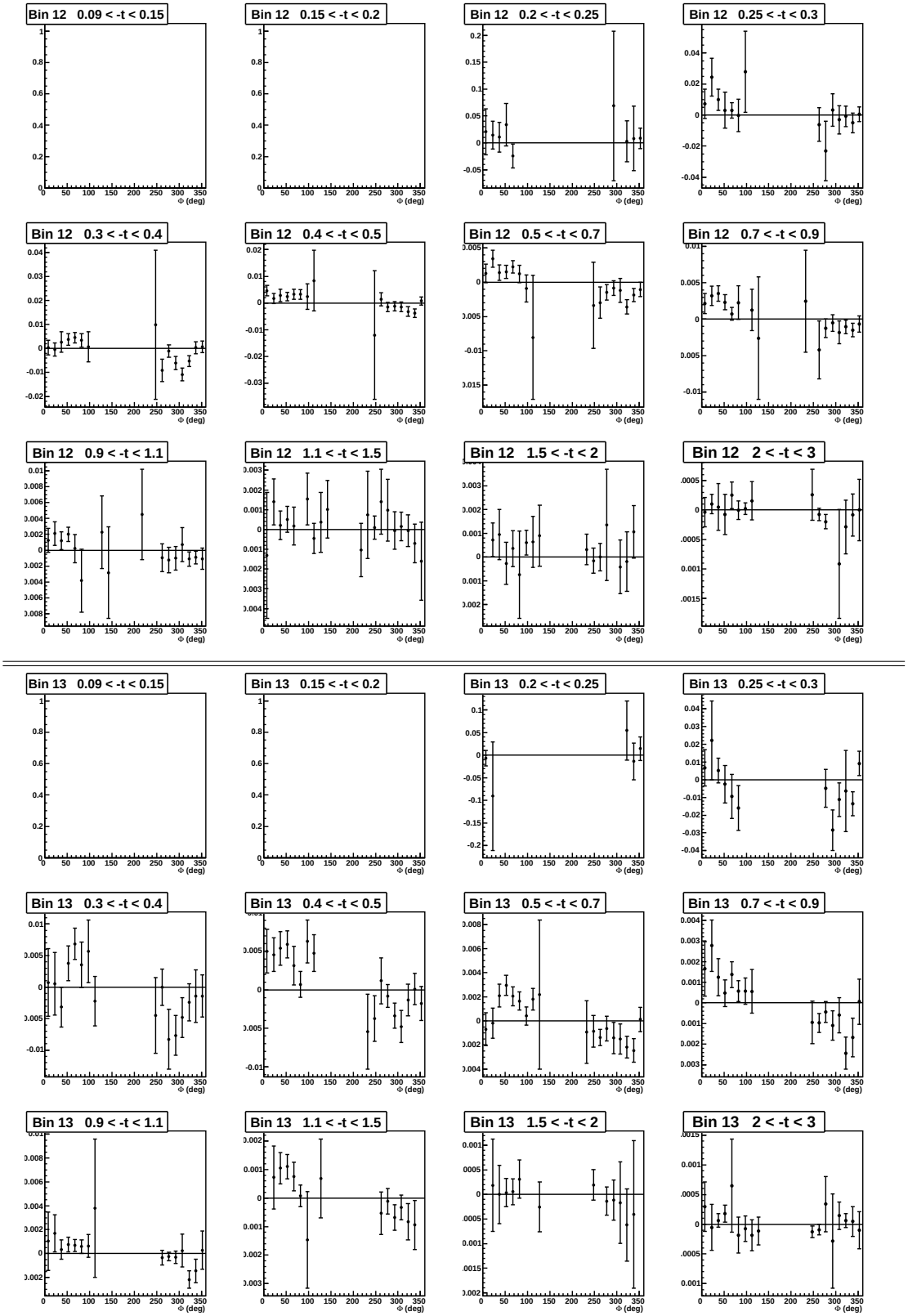

Figure I.7: Difference of polarized cross section as a function of Φ for the 12 t-bins of the (Q^2, x_B) bins 12 and 13.

Appendix J

Results of the comparison of the difference of polarized cross sections

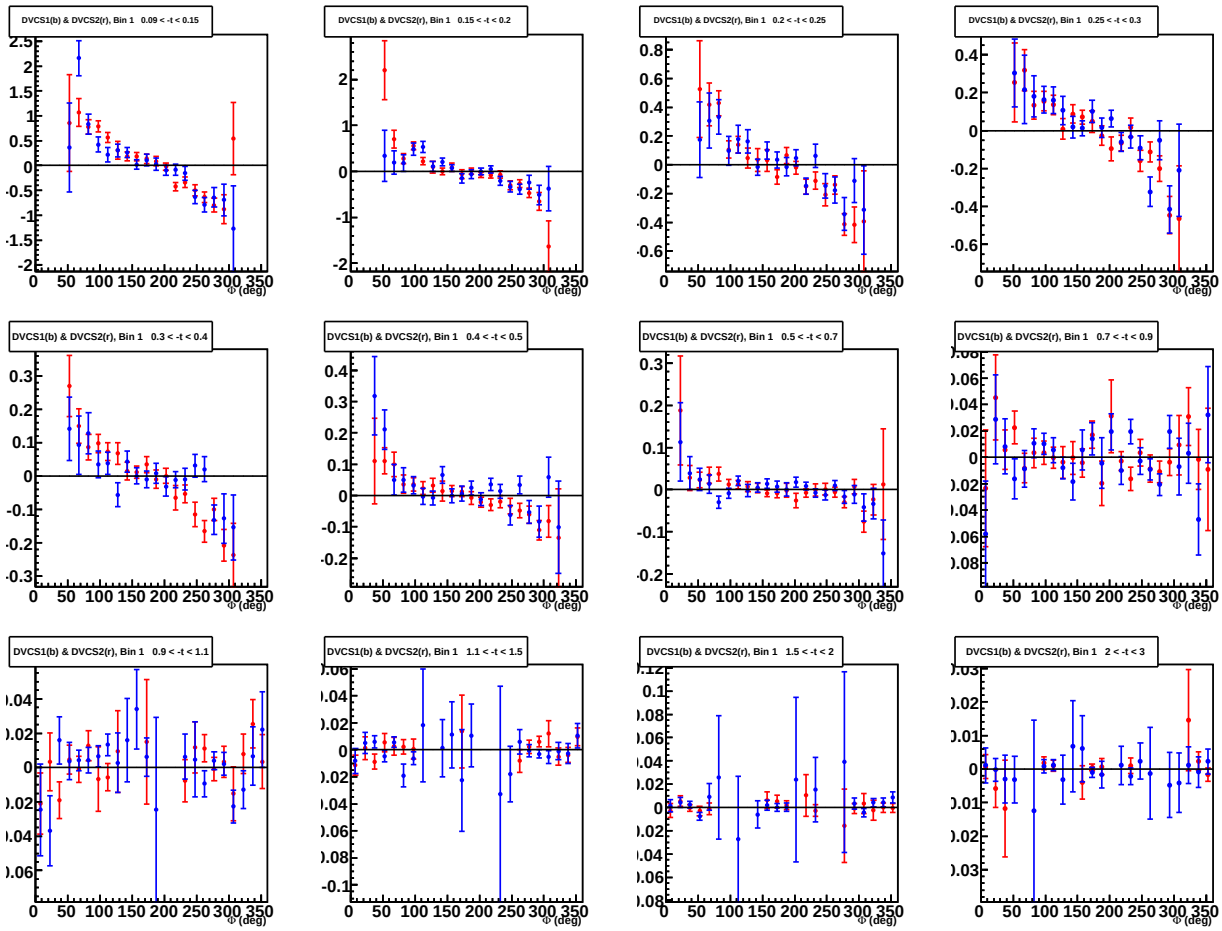

Figure J.1: Comparison between the difference of polarized cross section of e1-DVCS1 (blue) and e1-DVCS2 (red), as a function of Φ for the 12 t-bins of the (Q^2, x_B) bin 1.

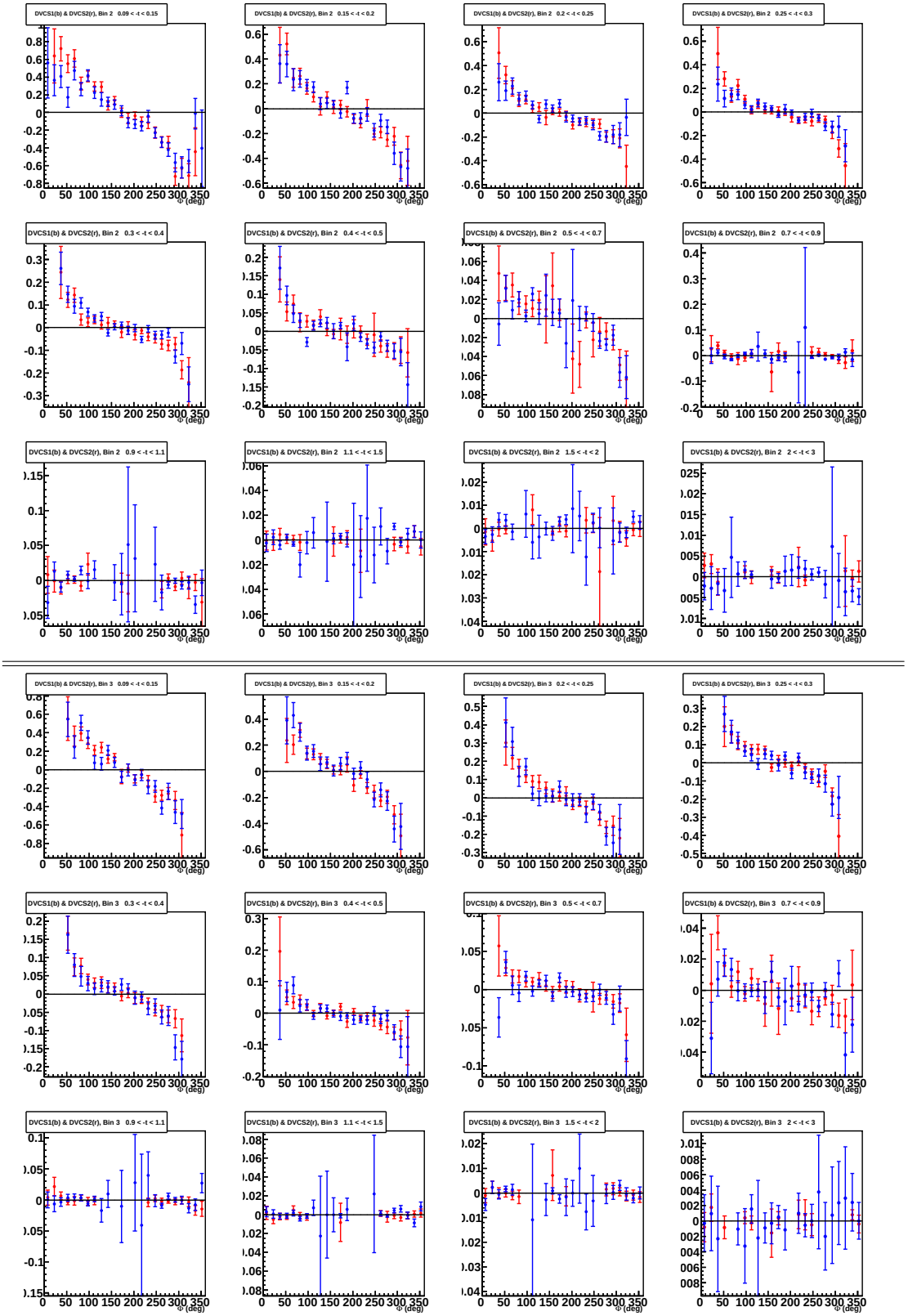

Figure J.2: Comparison between the difference of polarized cross section of e1-DVCS1 (blue) and e1-DVCS2 (red), as a function of Φ for the 12 t-bins of the (Q^2, x_B) bin 2 and 3.

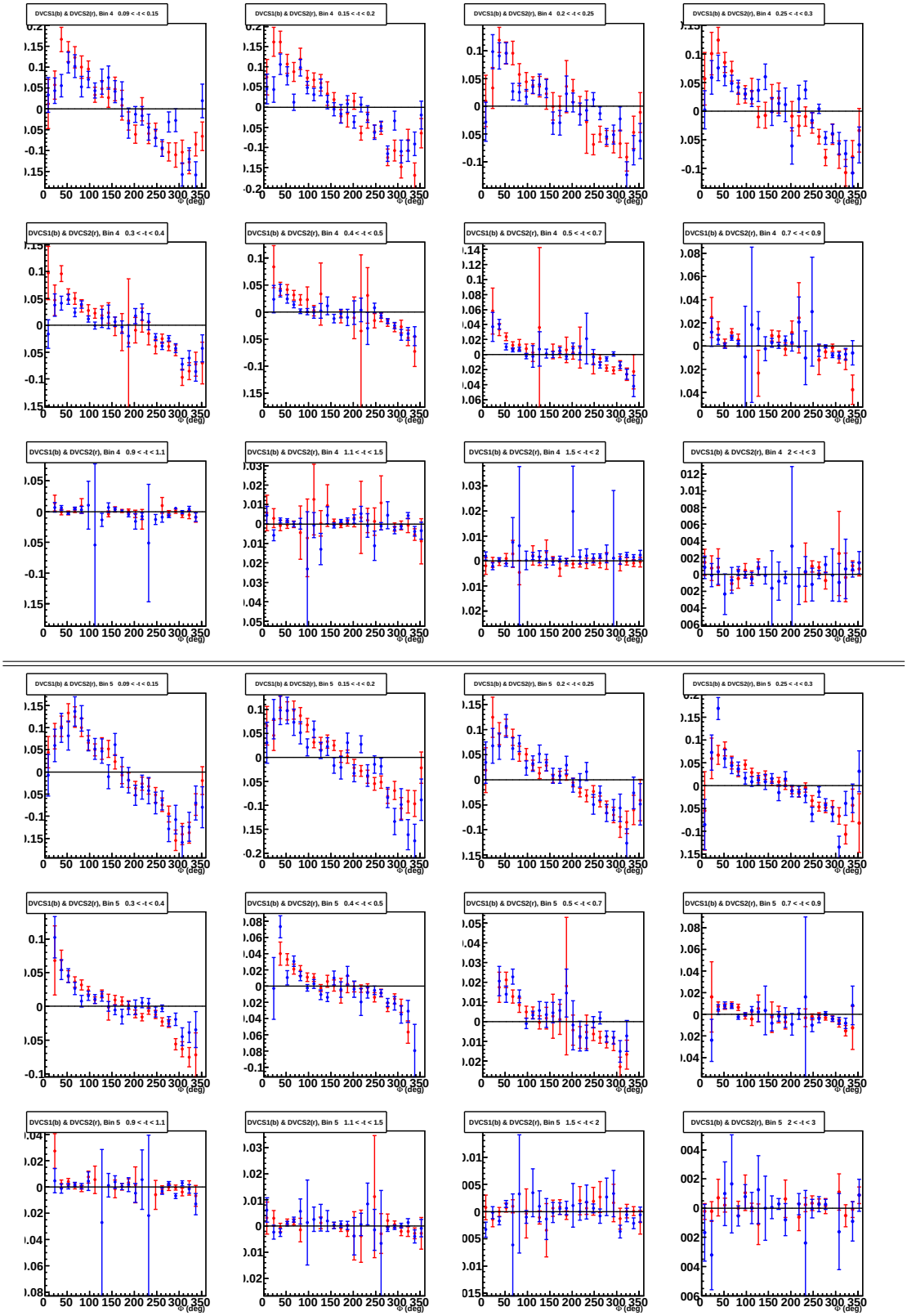

Figure J.3: Comparison between the difference of polarized cross section of e1-DVCS1 (blue) and e1-DVCS2 (red), as a function of Φ for the 12 t-bins of the (Q^2, x_B) bin 4 and 5.

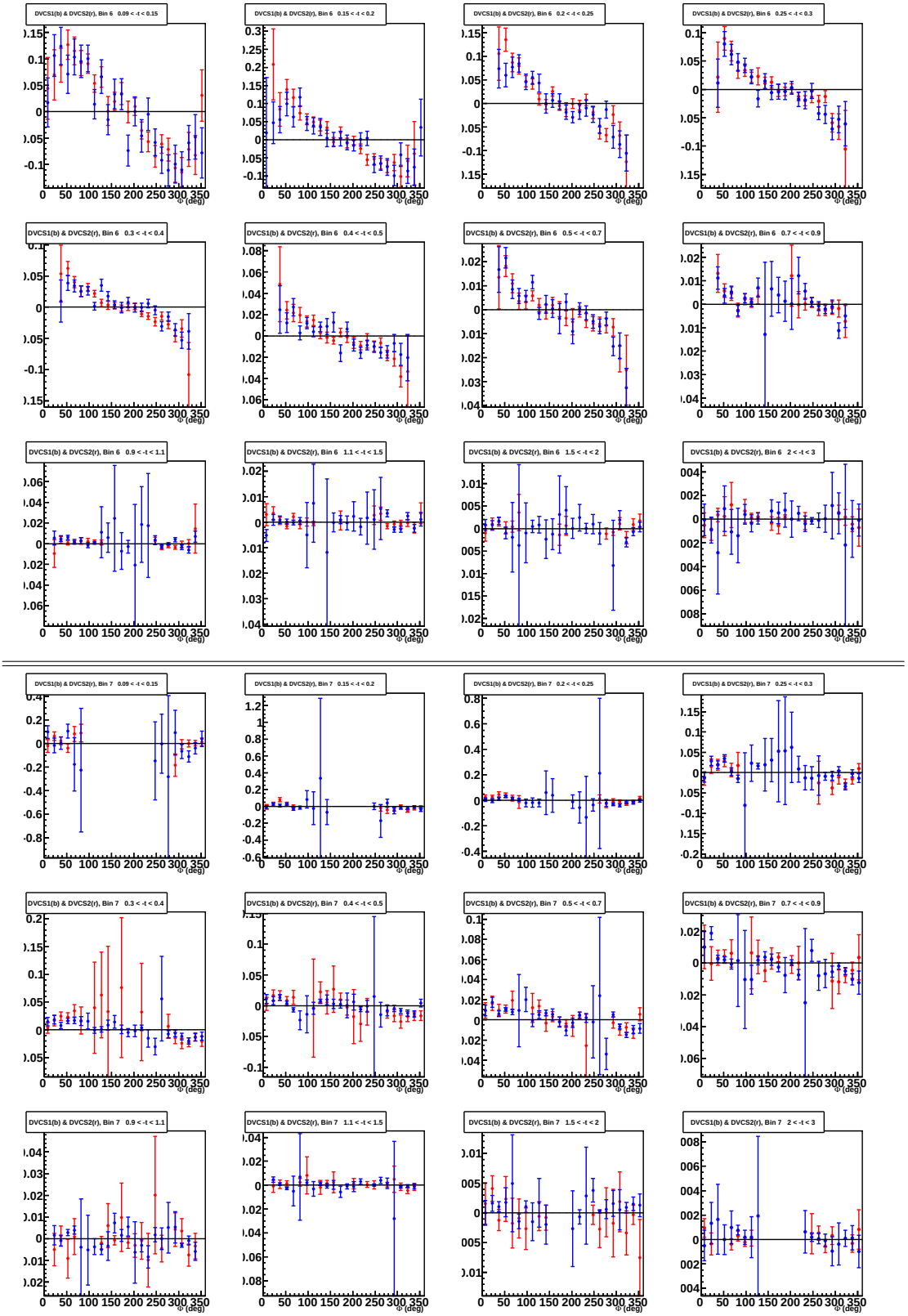

Figure J.4: Comparison between the difference of polarized cross section of e1-DVCS1 (blue) and e1-DVCS2 (red), as a function of Φ for the 12 t-bins of the (Q^2, x_B) bin 6 and 7.

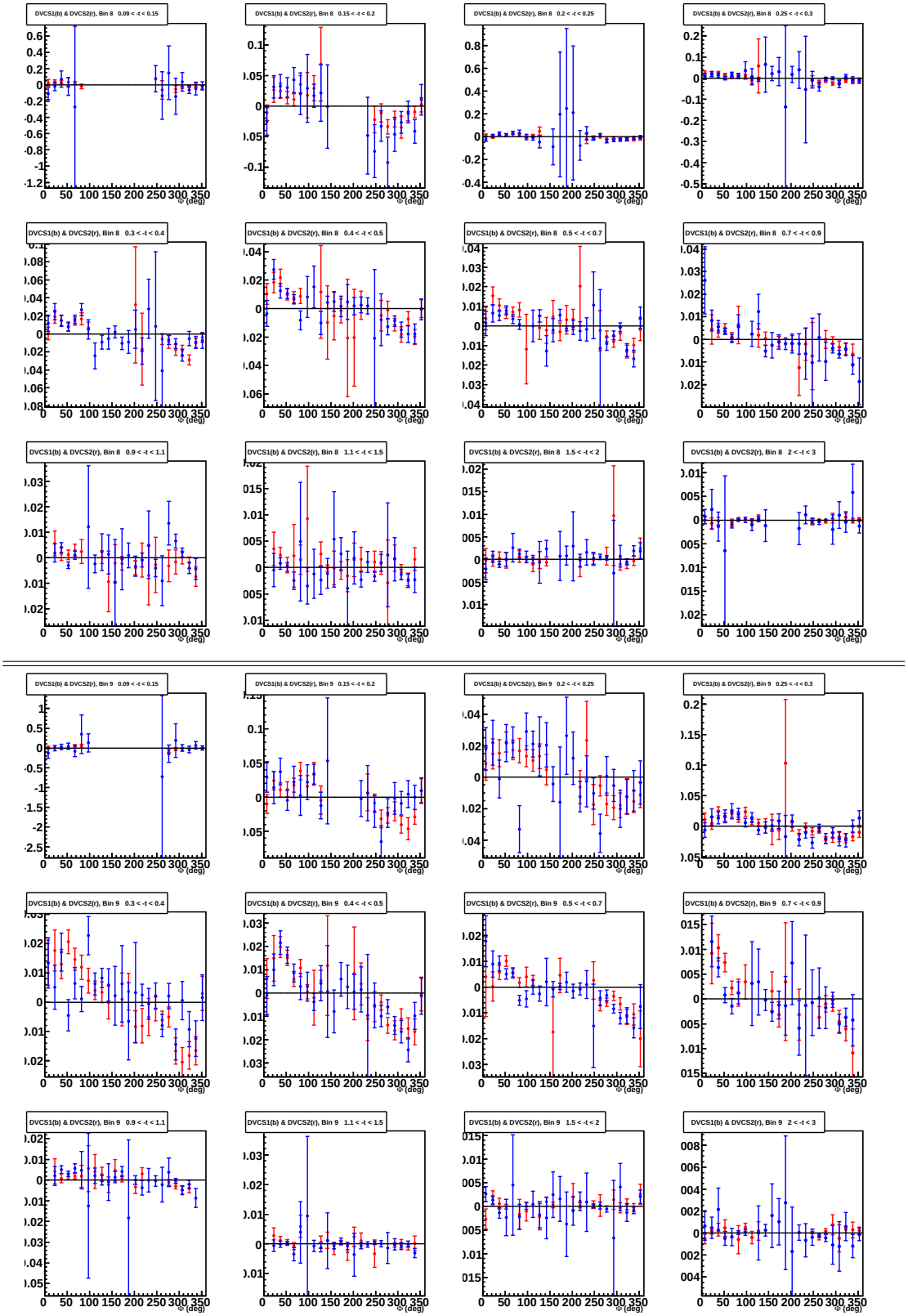

Figure J.5: Comparison between the difference of polarized cross section of e1-DVCS1 (blue) and e1-DVCS2 (red), as a function of Φ for the 12 t-bins of the (Q^2, x_B) bin 8 and 9.

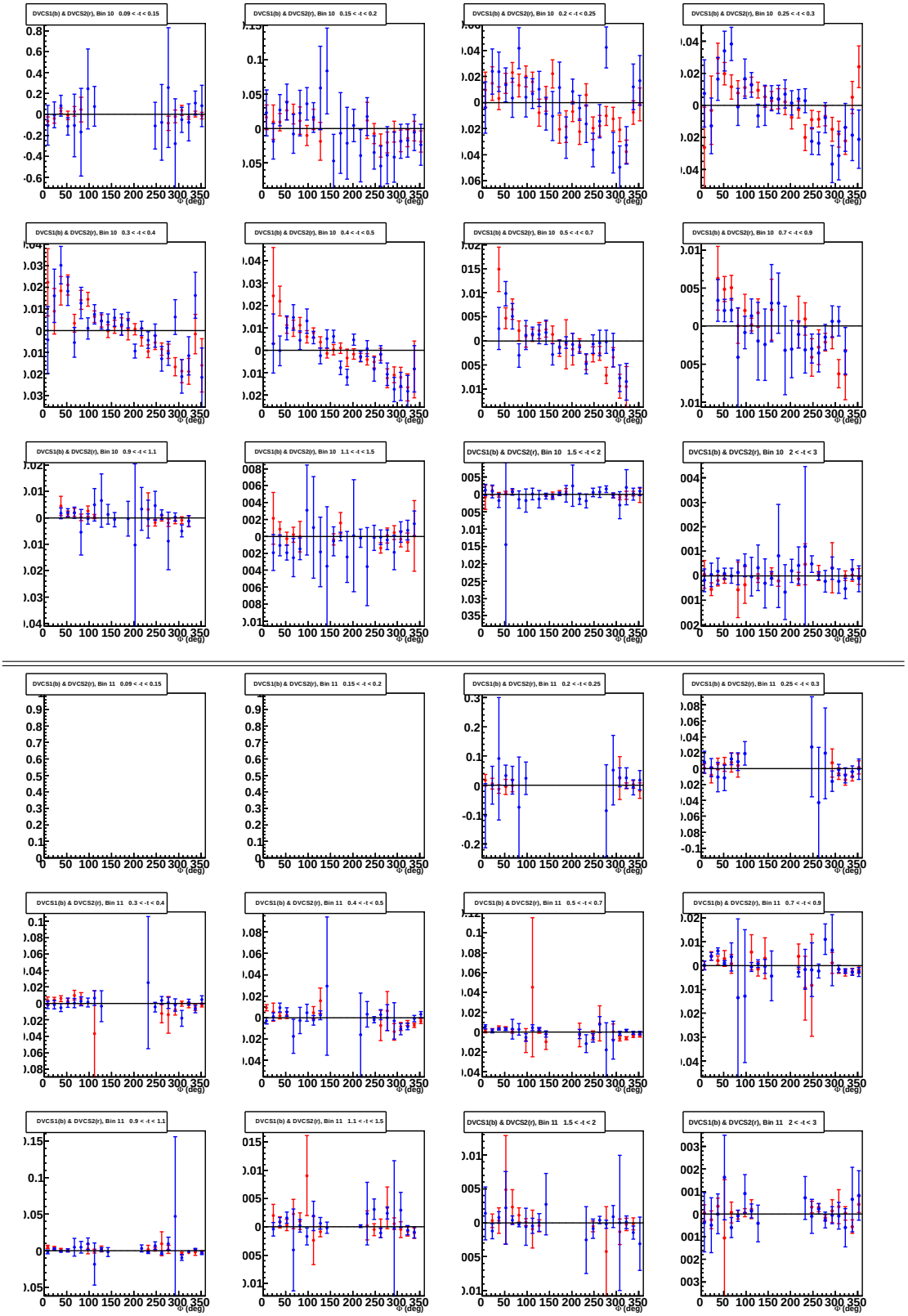

Figure J.6: Comparison between the difference of polarized cross section of e1-DVCS1 (blue) and e1-DVCS2 (red), as a function of Φ for the 12 t-bins of the (Q^2, x_B) bin 10 and 11.

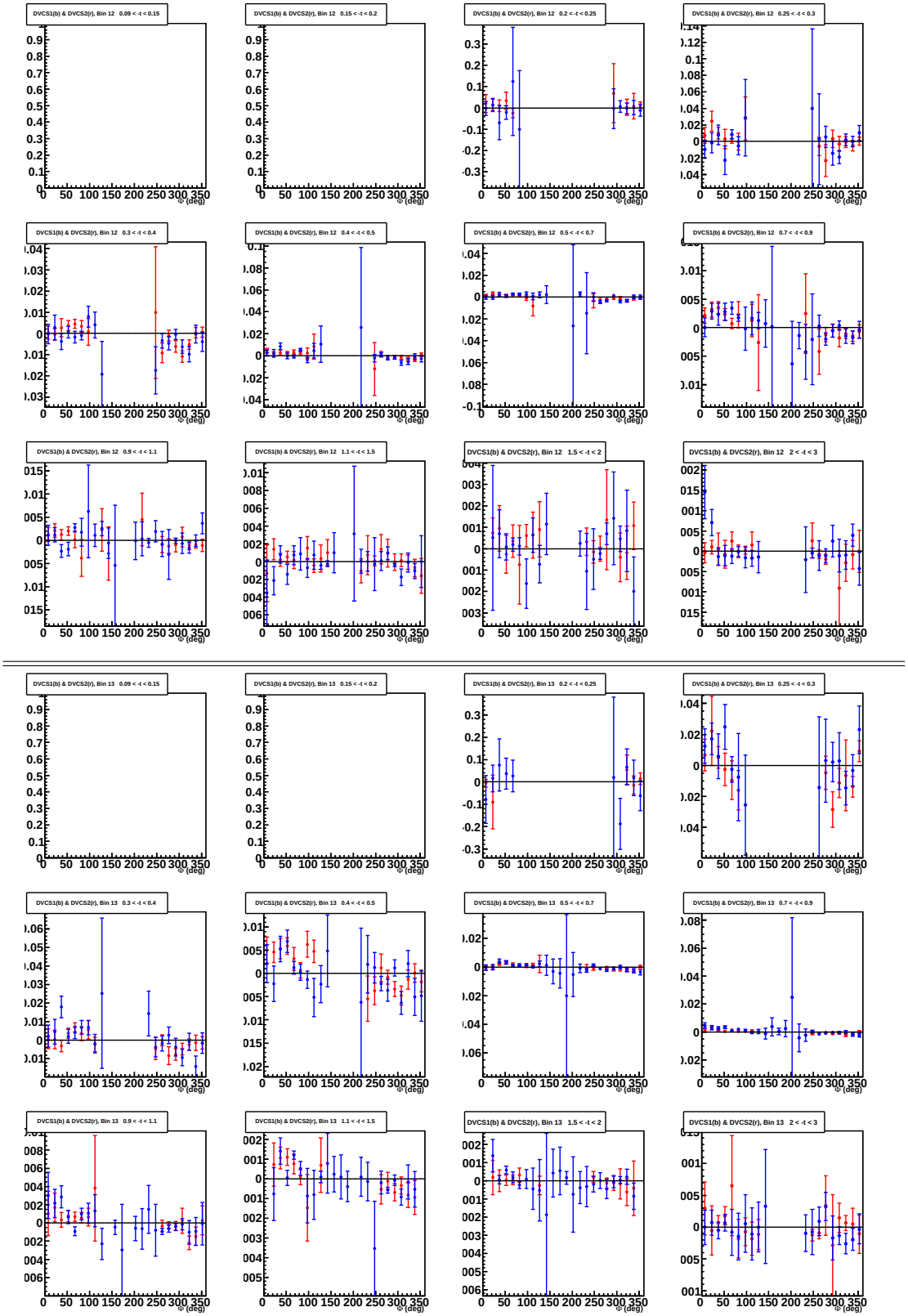

Figure J.7: Comparison between the difference of polarized cross section of e1-DVCS1 (blue) and e1-DVCS2 (red), as a function of Φ for the 12 t-bins of the (Q^2, x_B) bin 12 and 13.

Appendix K

Beam spin asymmetries results

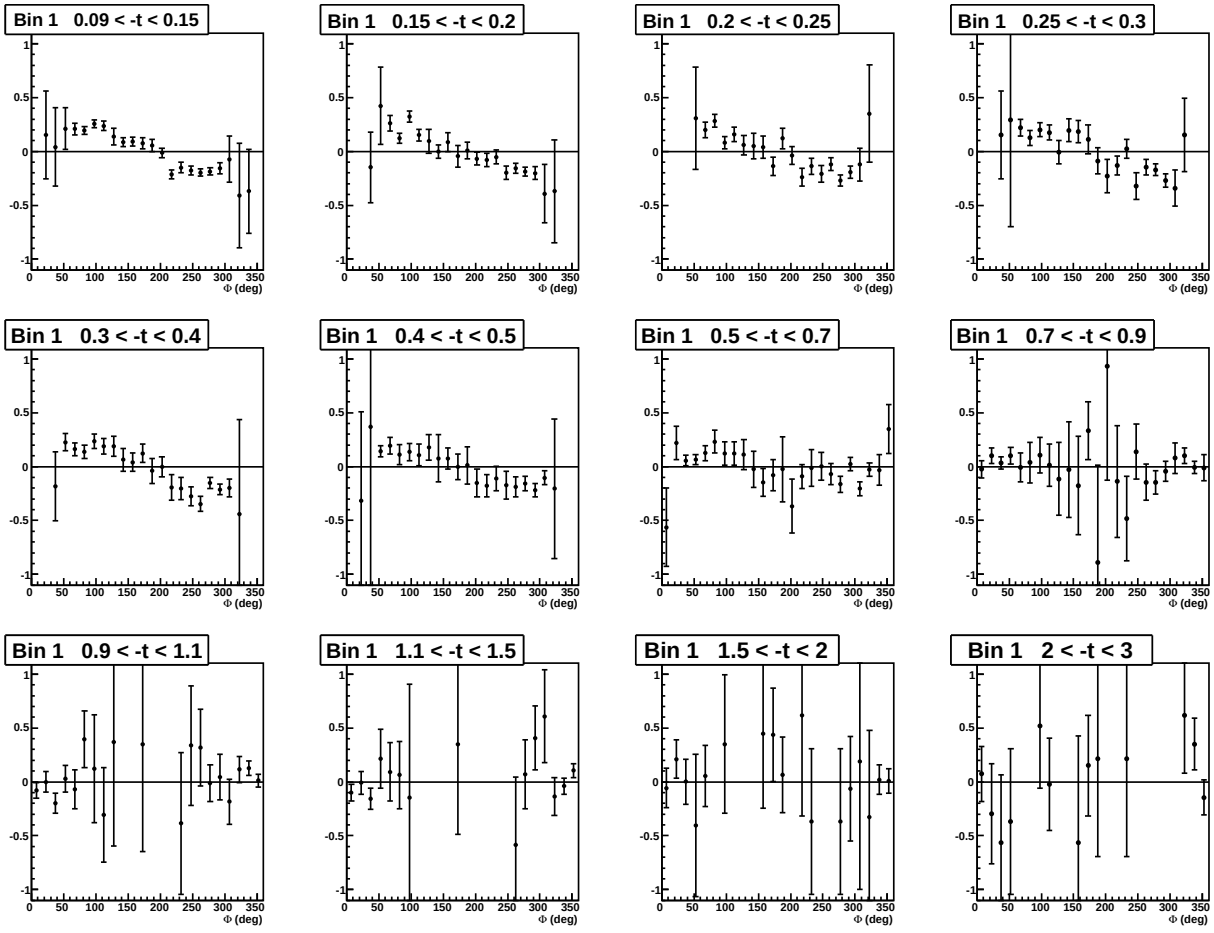

Figure K.1: Asymmetries as a function of Φ for the 12 t-bins of the (Q^2, x_B) bin 1.

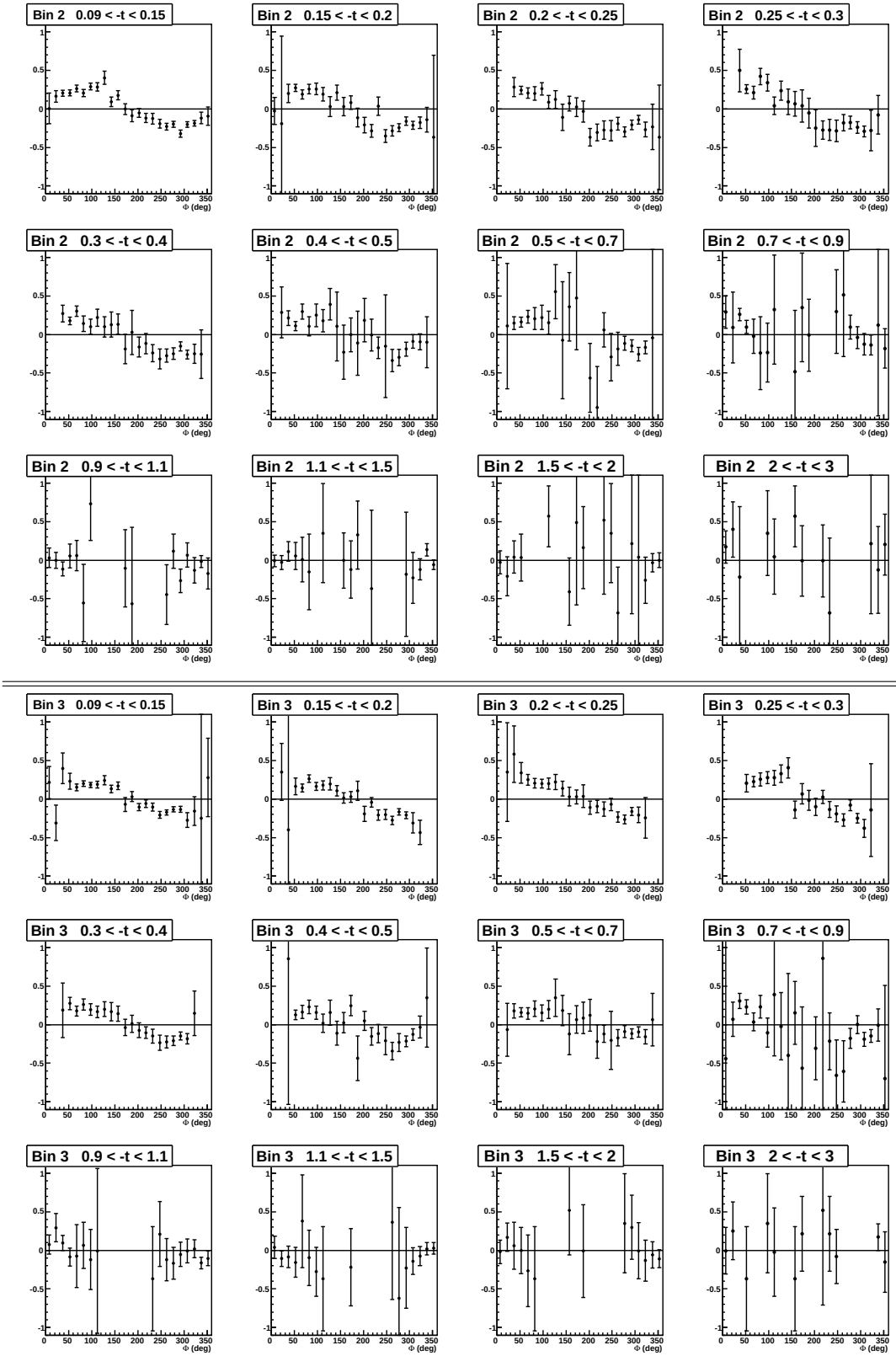

Figure K.2: Asymmetries as a function of Φ for the 12 t-bins of the (Q^2, x_B) bins 2 and 3.

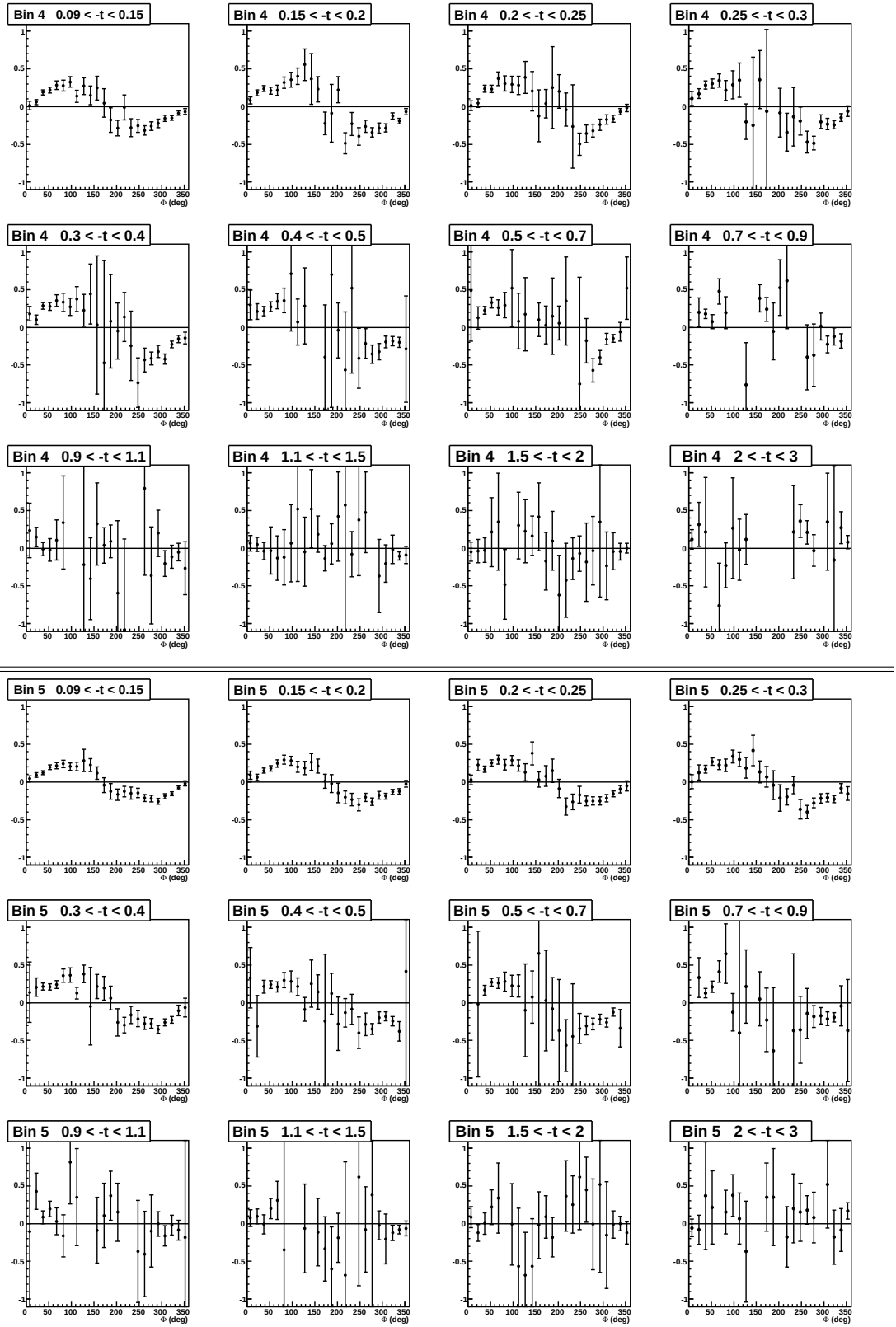

Figure K.3: Asymmetries as a function of Φ for the 12 t-bins of the (Q^2, x_B) bins 4 and 5.

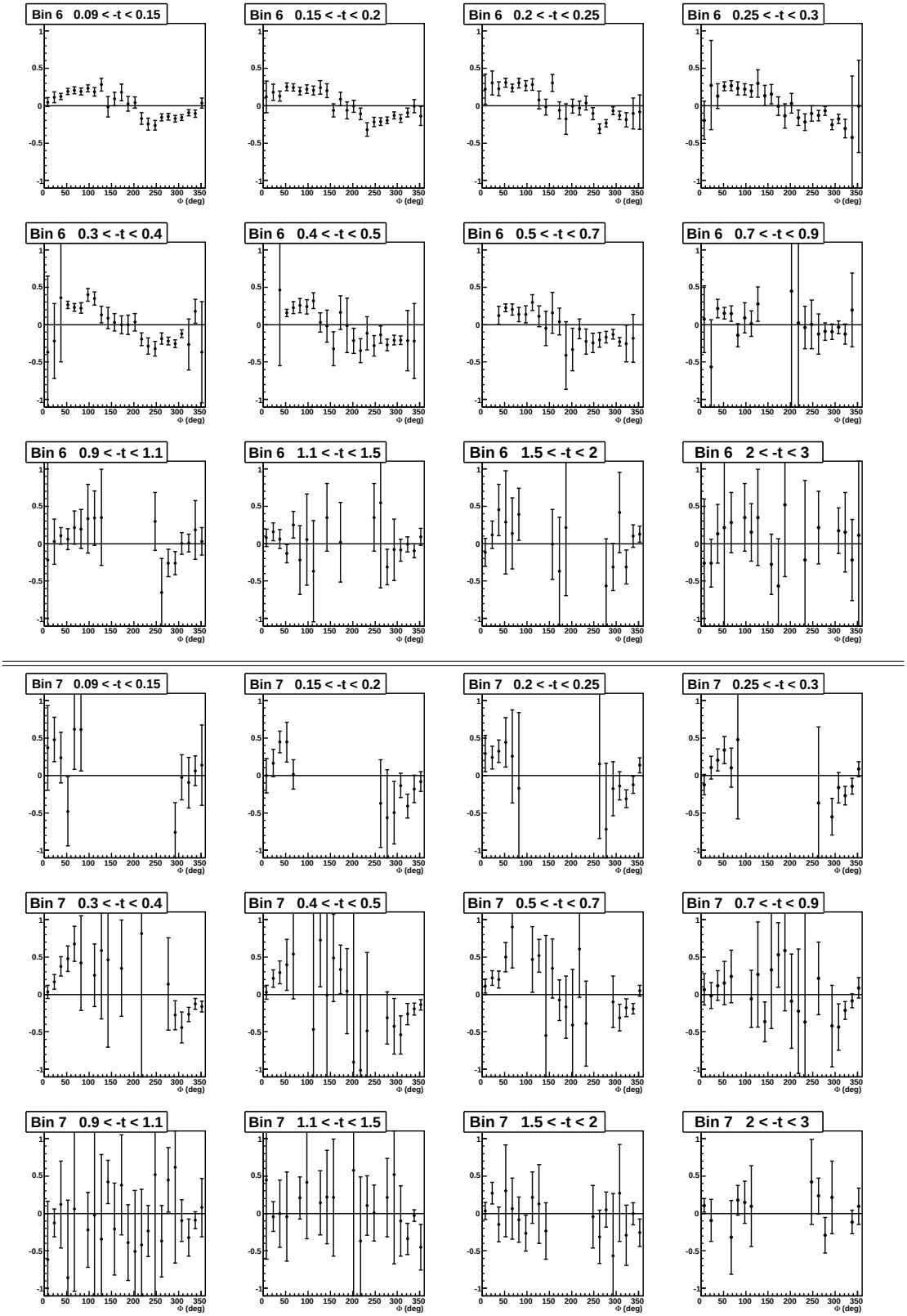

Figure K.4: Asymmetries as a function of Φ for the 12 t-bins of the (Q^2, x_B) bins 6 and 7.

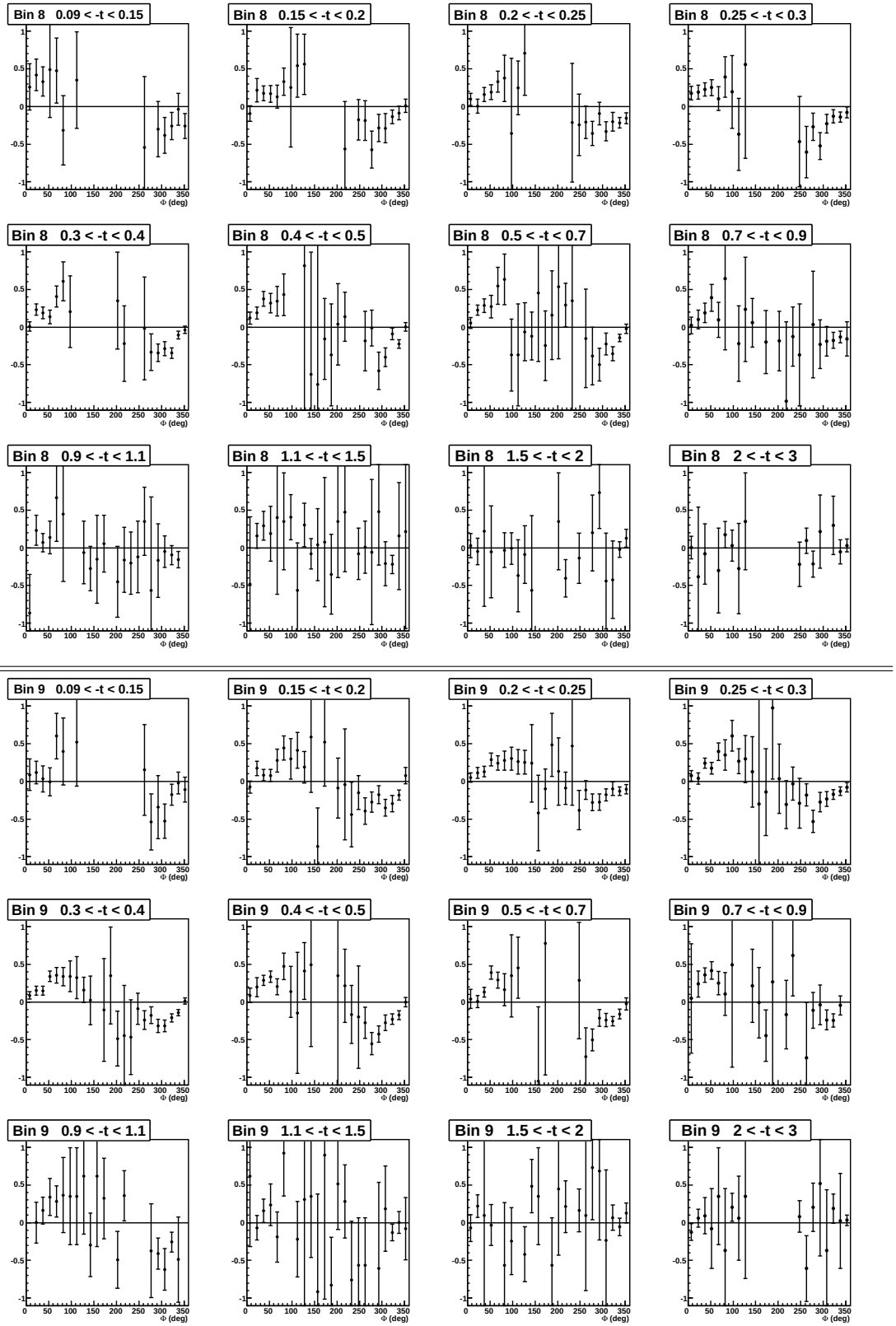

Figure K.5: Asymmetries as a function of Φ for the 12 t-bins of the (Q^2, x_B) bins 8 and 9.

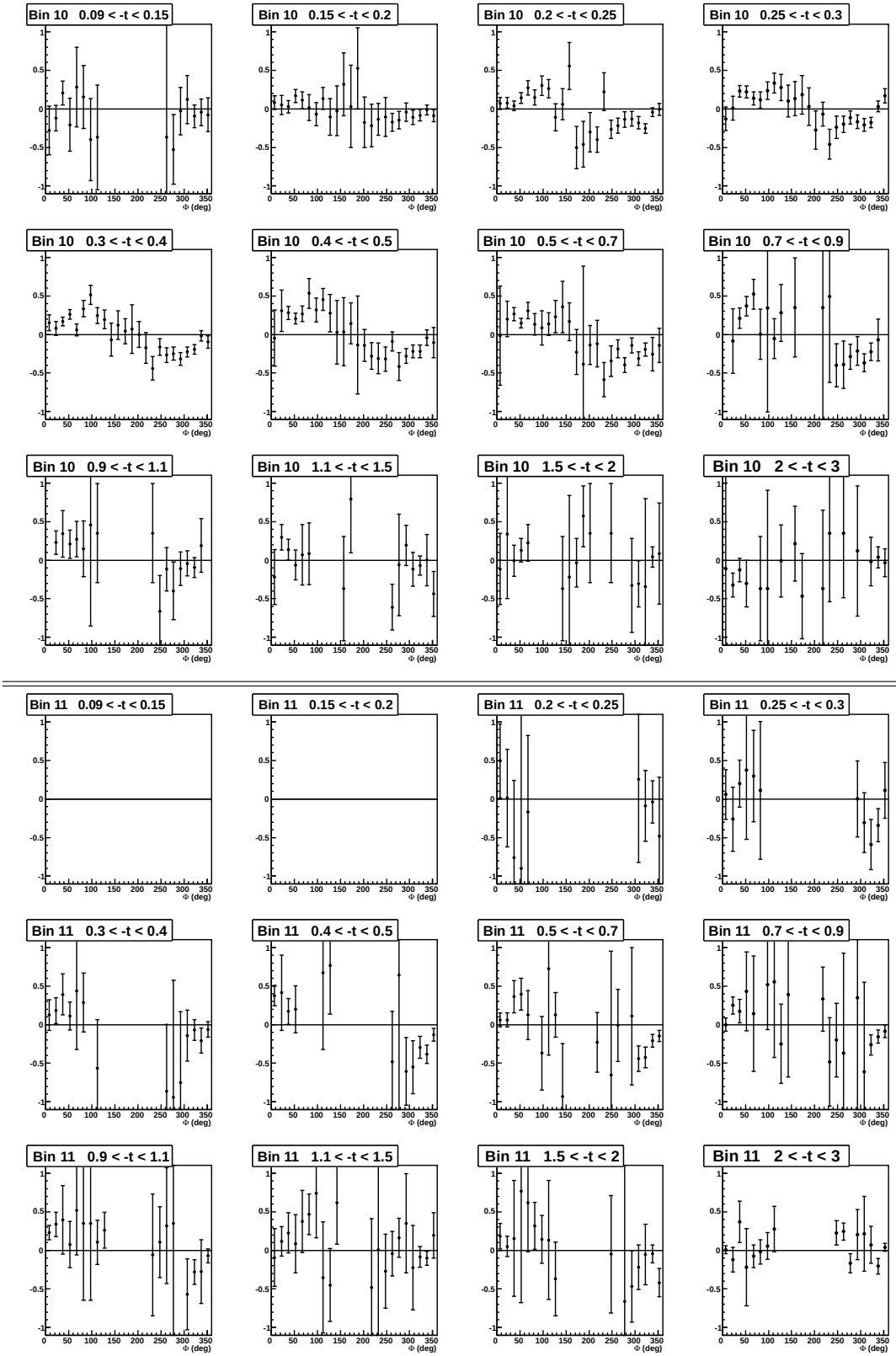

Figure K.6: Asymmetries as a function of Φ for the 12 t-bins of the (Q^2, x_B) bins 10 and 11.

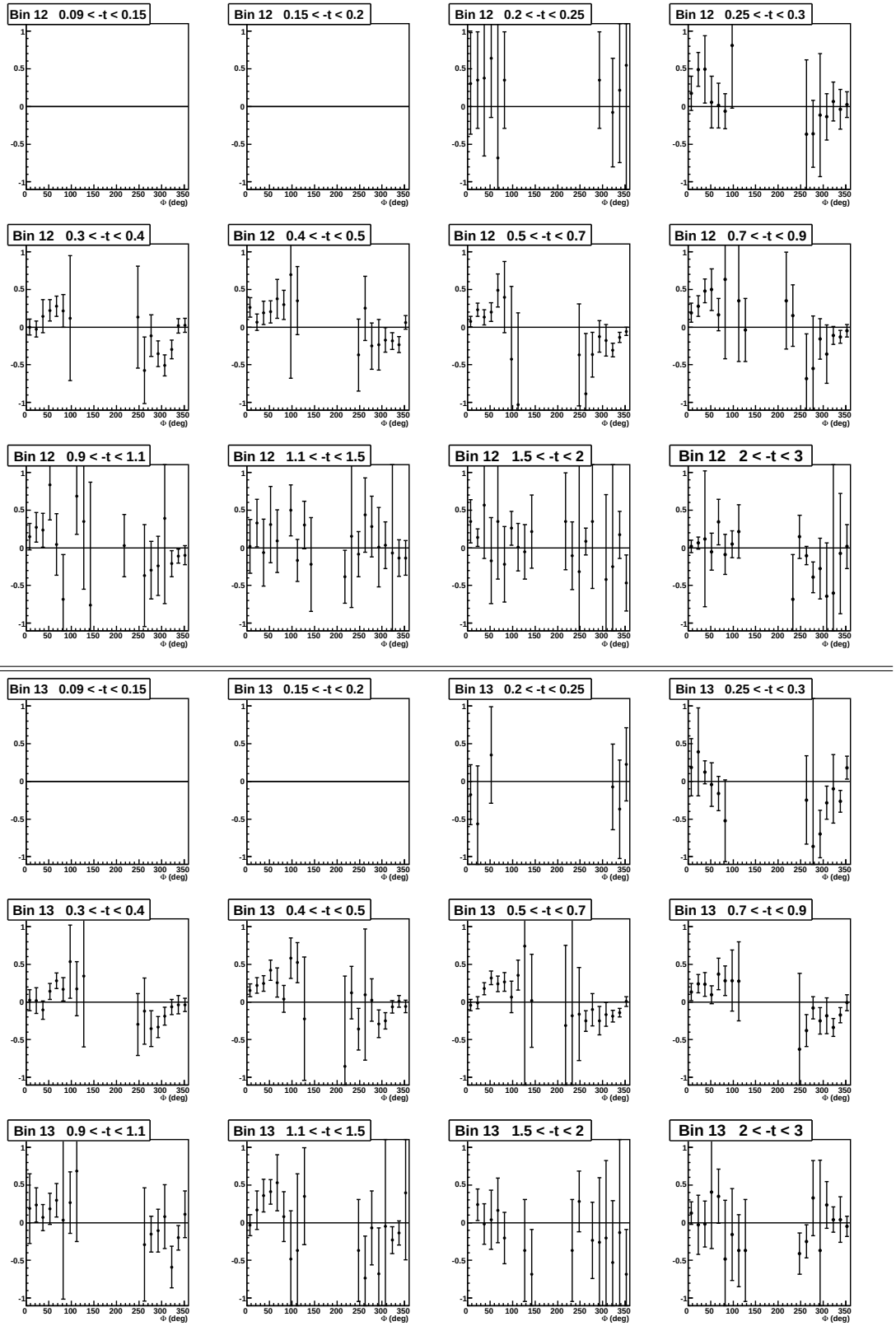

Figure K.7: Asymmetries as a function of Φ for the 12 t-bins of the (Q^2, x_B) bins 12 and 13.

Appendix L

Comparison between the unpolarized cross section and VGG model

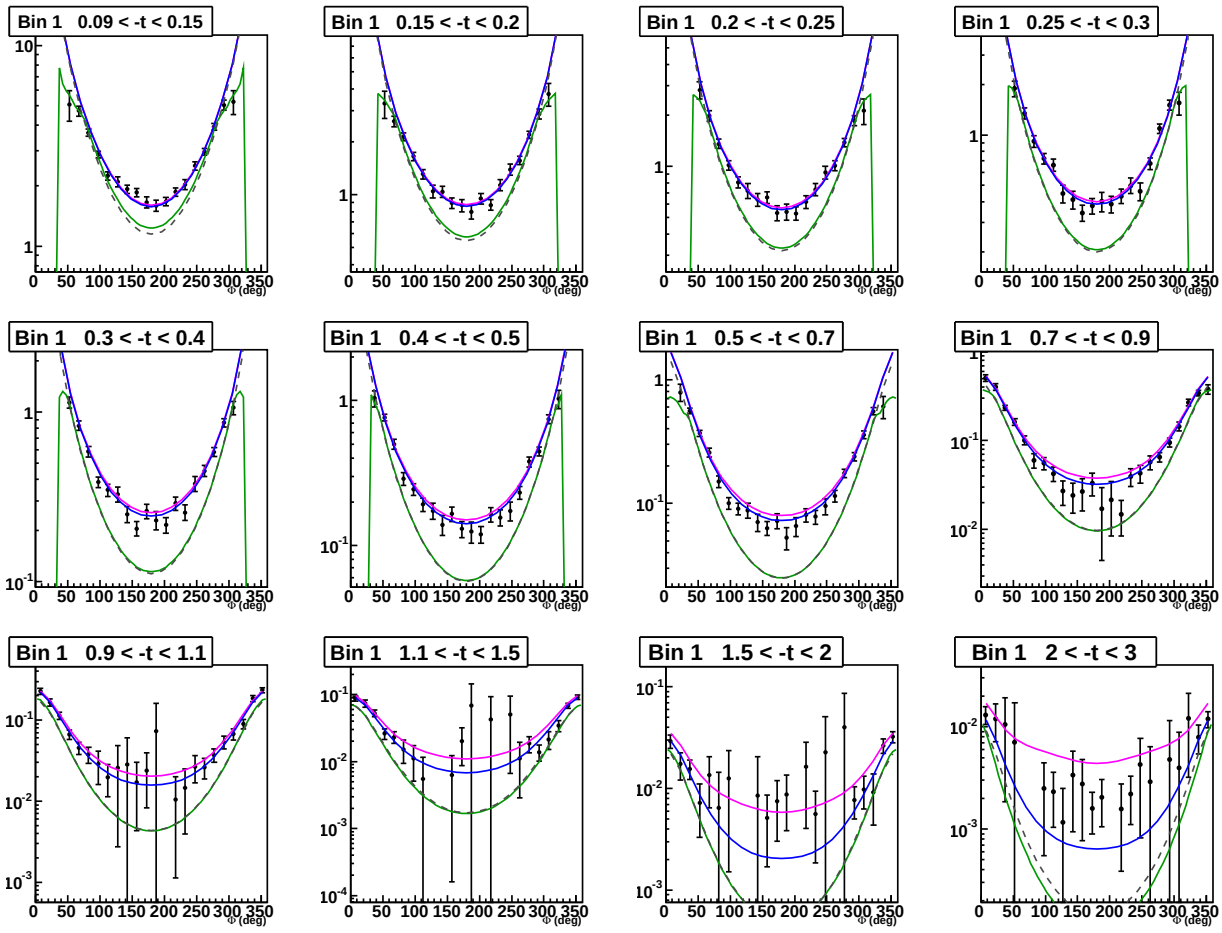

Figure L.1: DVCS cross section as a function of Φ for the 12 t bins of the (Q^2, x_B) bin 1, compared to the BH cross-section and the VGG model predictions. The different curves are described in the text.

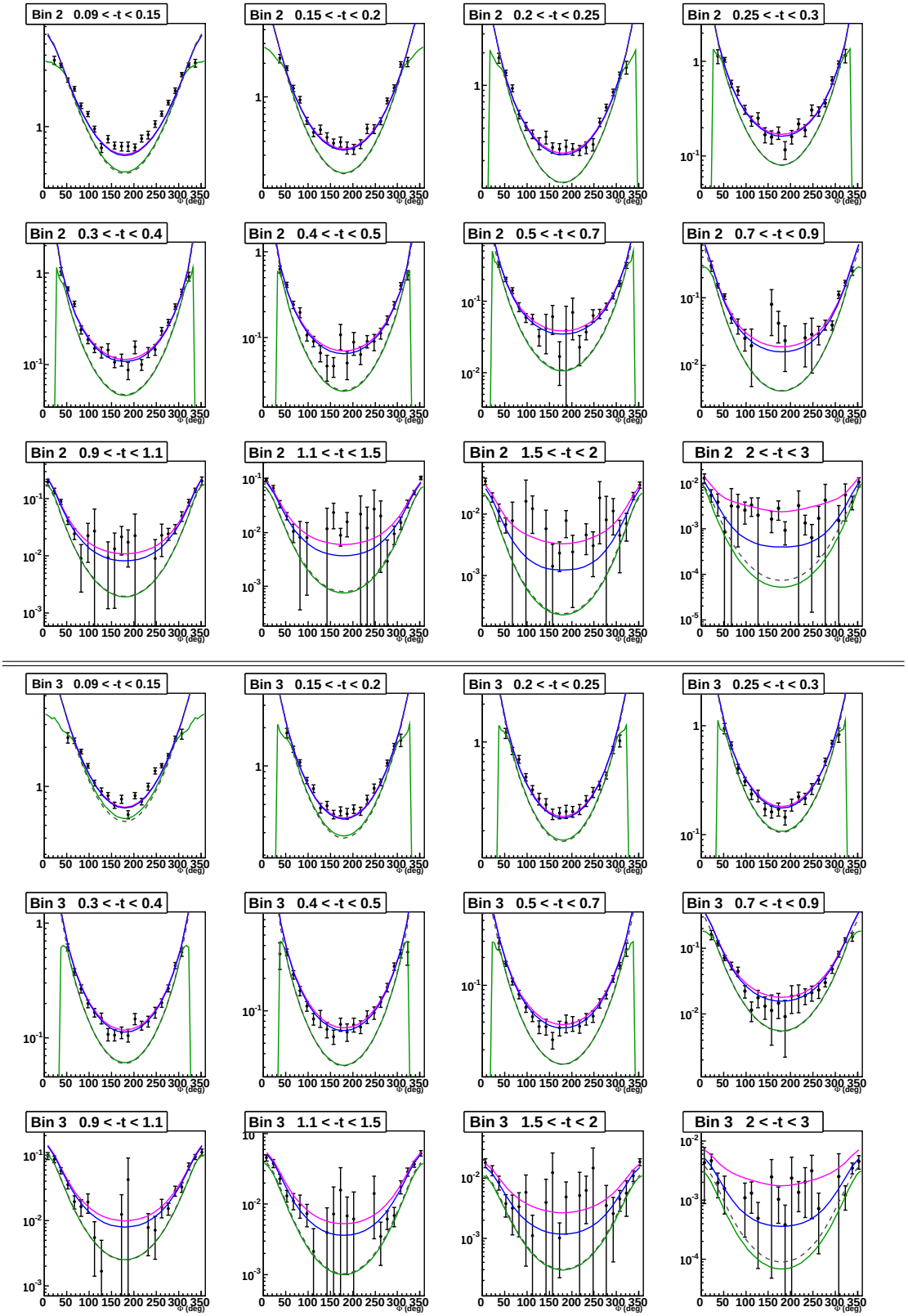

Figure L.2: DVCS cross section (nbarn/GeV^4) as a function of Φ for the 12 t bins of the (Q^2, x_B) bins 2 and 3, compared to the BH cross-section and the VGG model predictions. The different curves are described in the text.

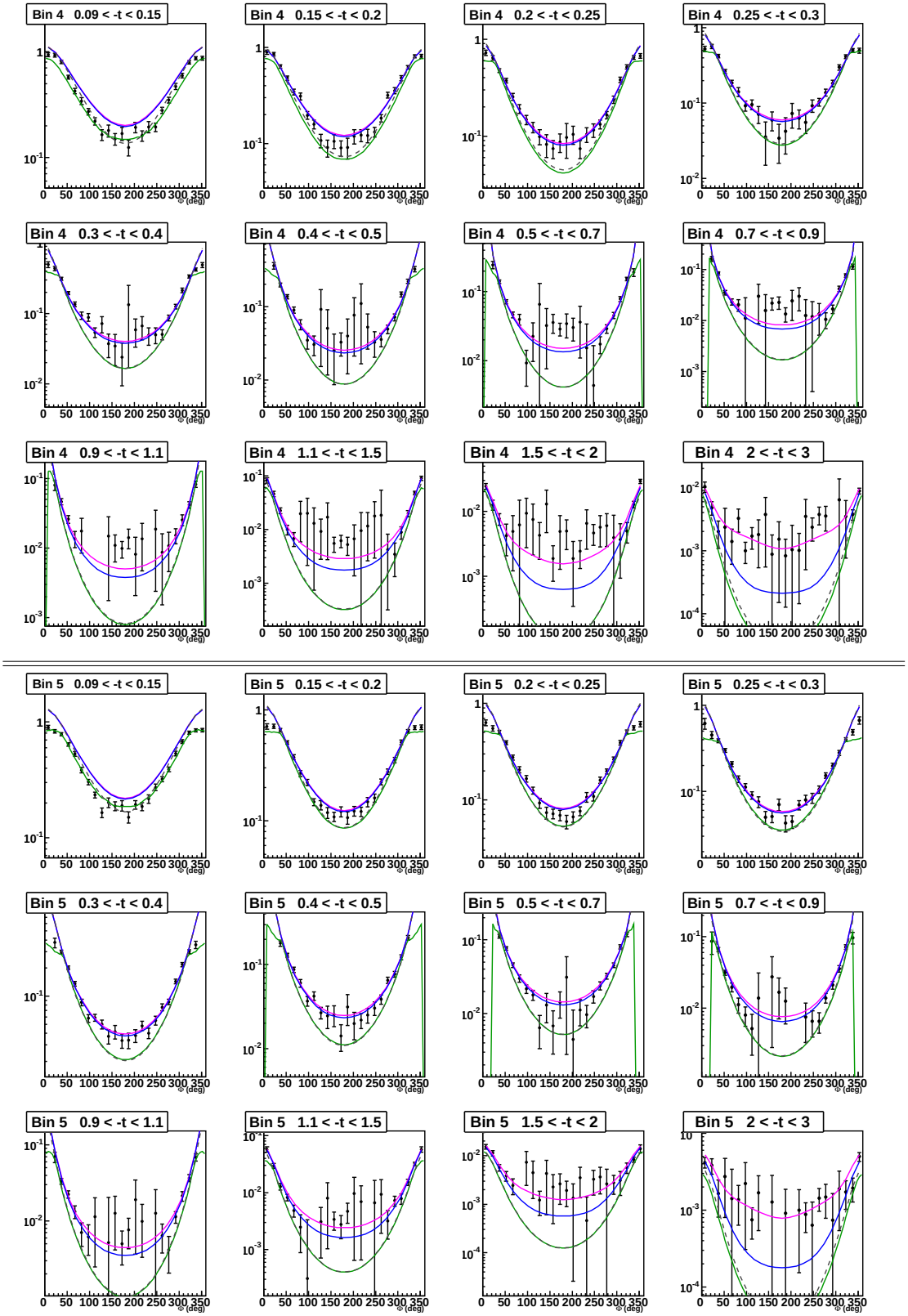

Figure L.3: DVCS cross section (nbarn/GeV^4) as a function of Φ for the 12 t bins of the (Q^2, x_B) bins 4 and 5, compared to the BH cross-section and the VGG model predictions. The different curves are described in the text.

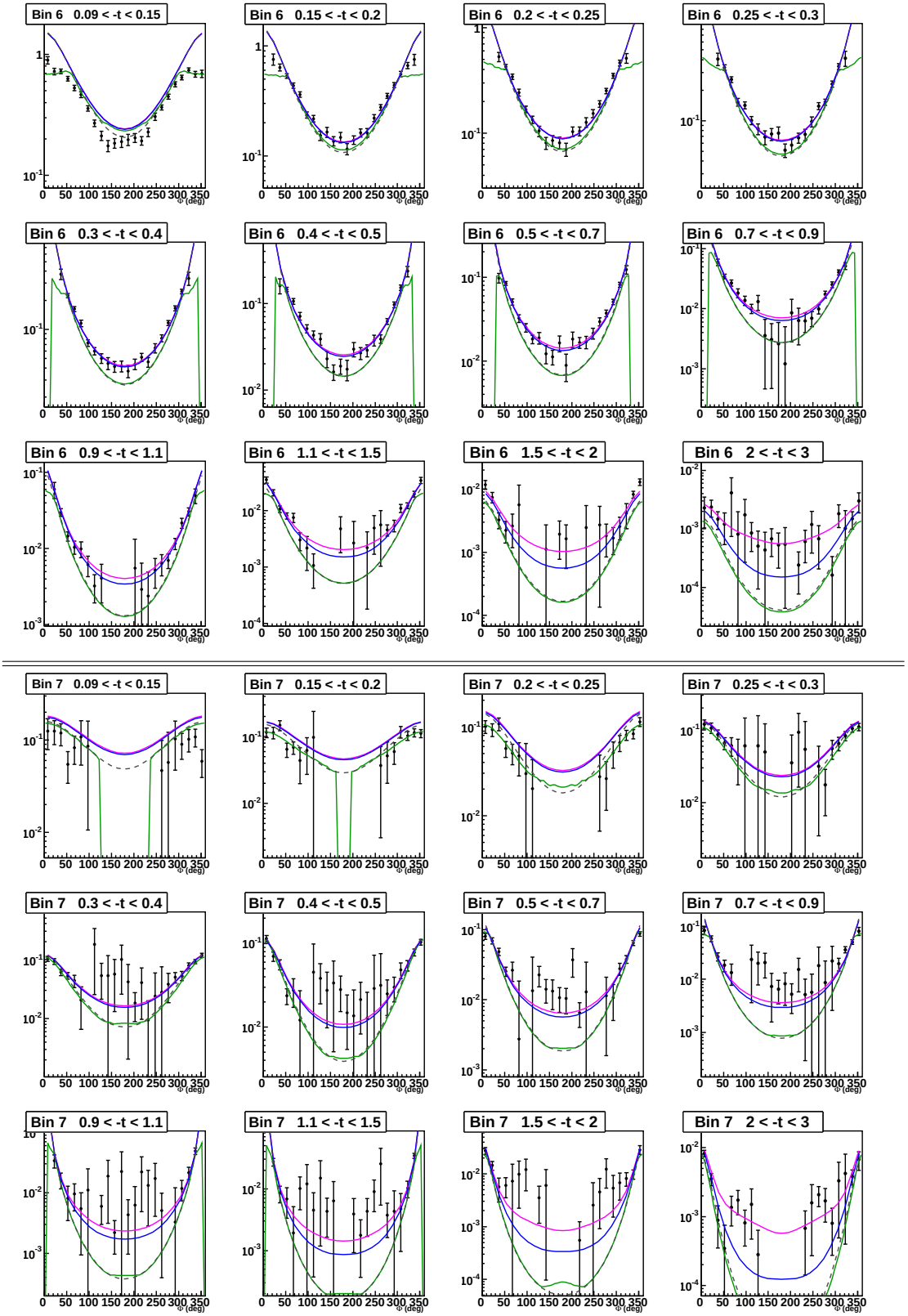

Figure L.4: DVCS cross section (nbarn/GeV^4) as a function of Φ for the 12 t bins of the (Q^2, x_B) bins 6 and 7, compared to the BH cross-section and the VGG model predictions. The different curves are described in the text.

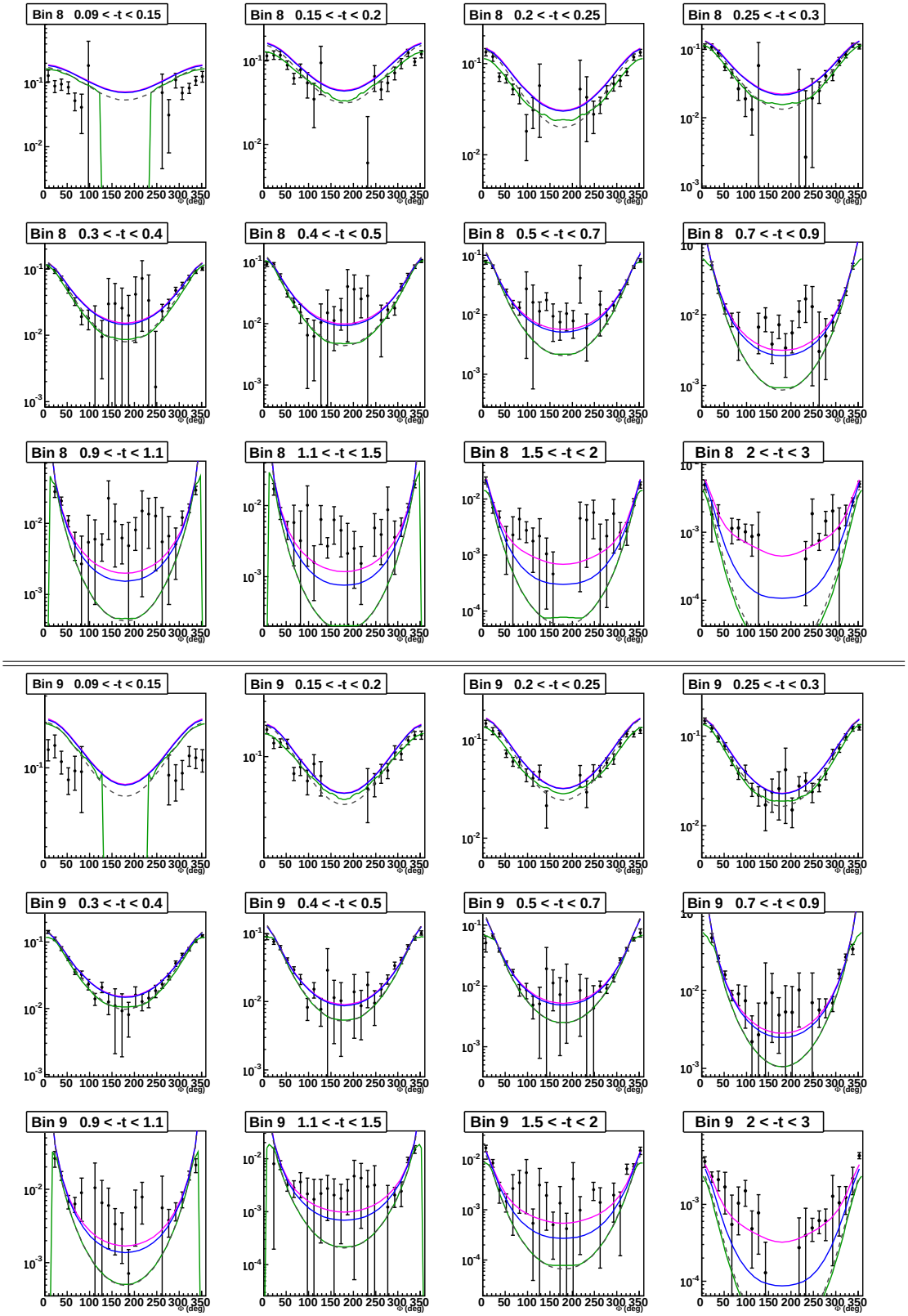

Figure L.5: DVCS cross section (nbarn/GeV^4) as a function of Φ for the 12 t bins of the (Q^2, x_B) bins 8 and 9, compared to the BH cross-section and the VGG model predictions. The different curves are described in the text.

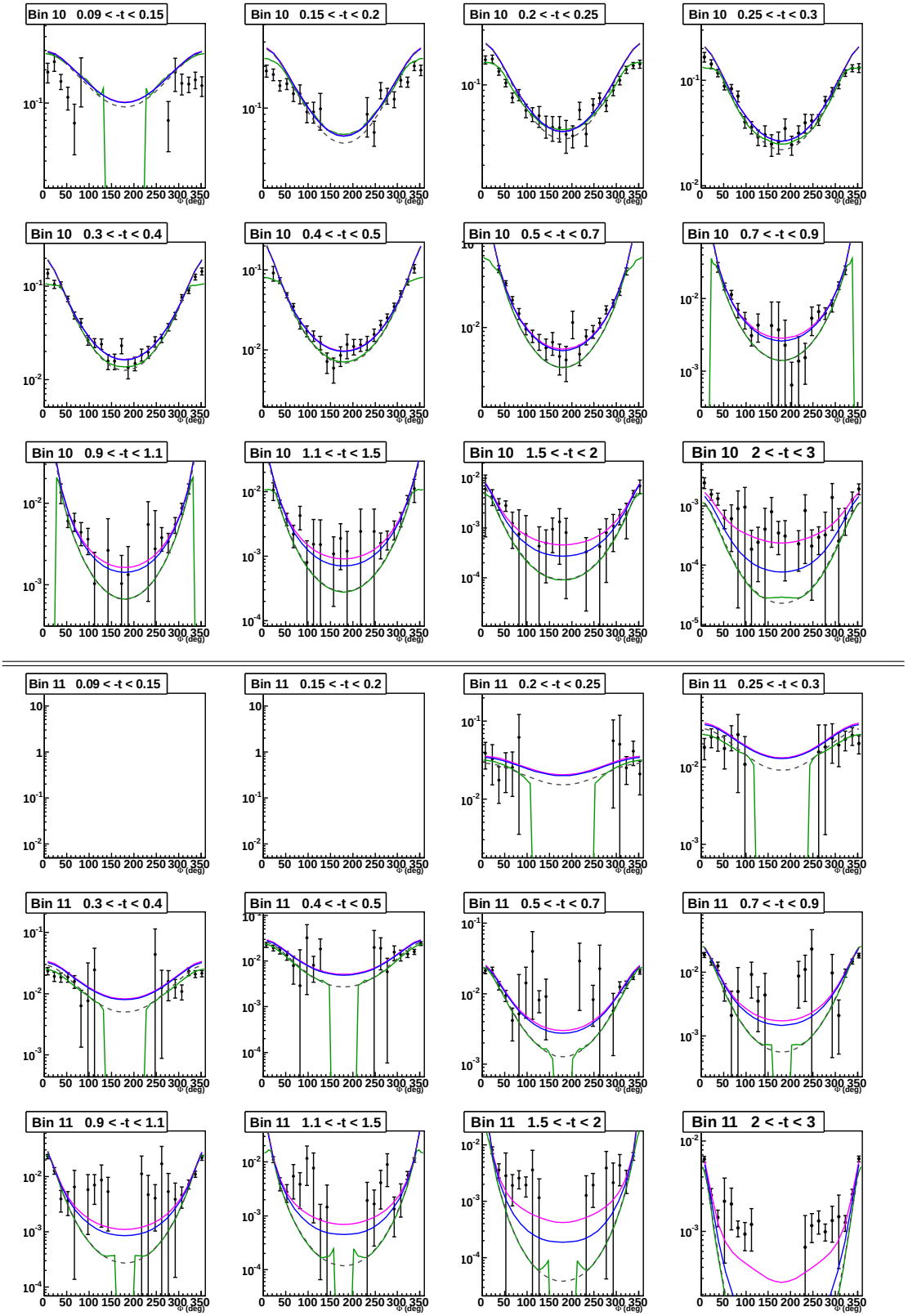

Figure L.6: DVCS cross section (nbarn/GeV^4) as a function of Φ for the 12 t bins of the (Q^2, x_B) bins 10 and 11, compared to the BH cross-section and the VGG model predictions. The different curves are described in the text.

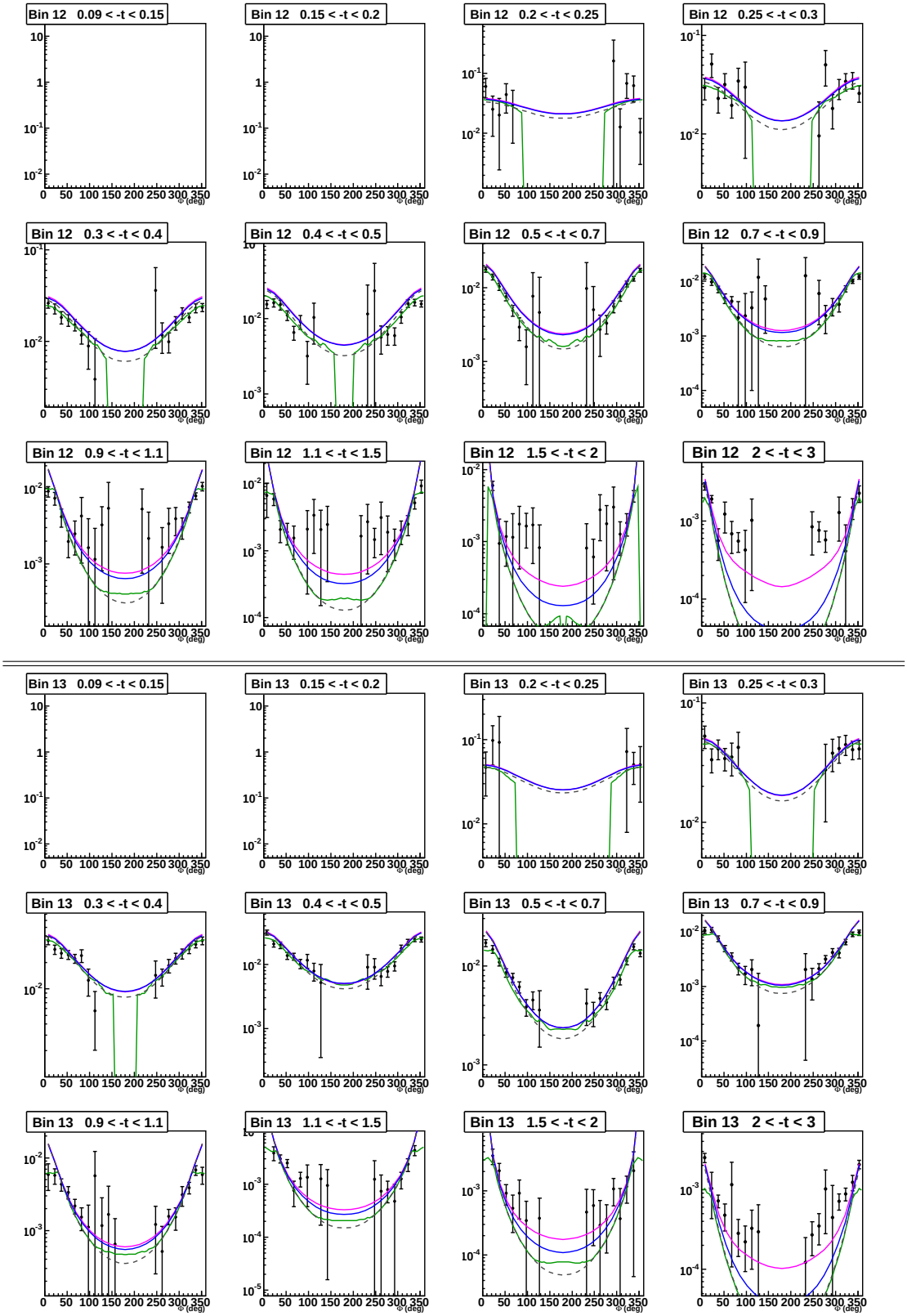

Figure L.7: DVCS cross section (nbarn/GeV^4) as a function of Φ for the 12 t bins of the (Q^2, x_B) bins 12 and 13, compared to the BH cross-section and the VGG model predictions. The different curves are described in the text.

Appendix M

Comparison of the difference of polarized cross section with VGG model

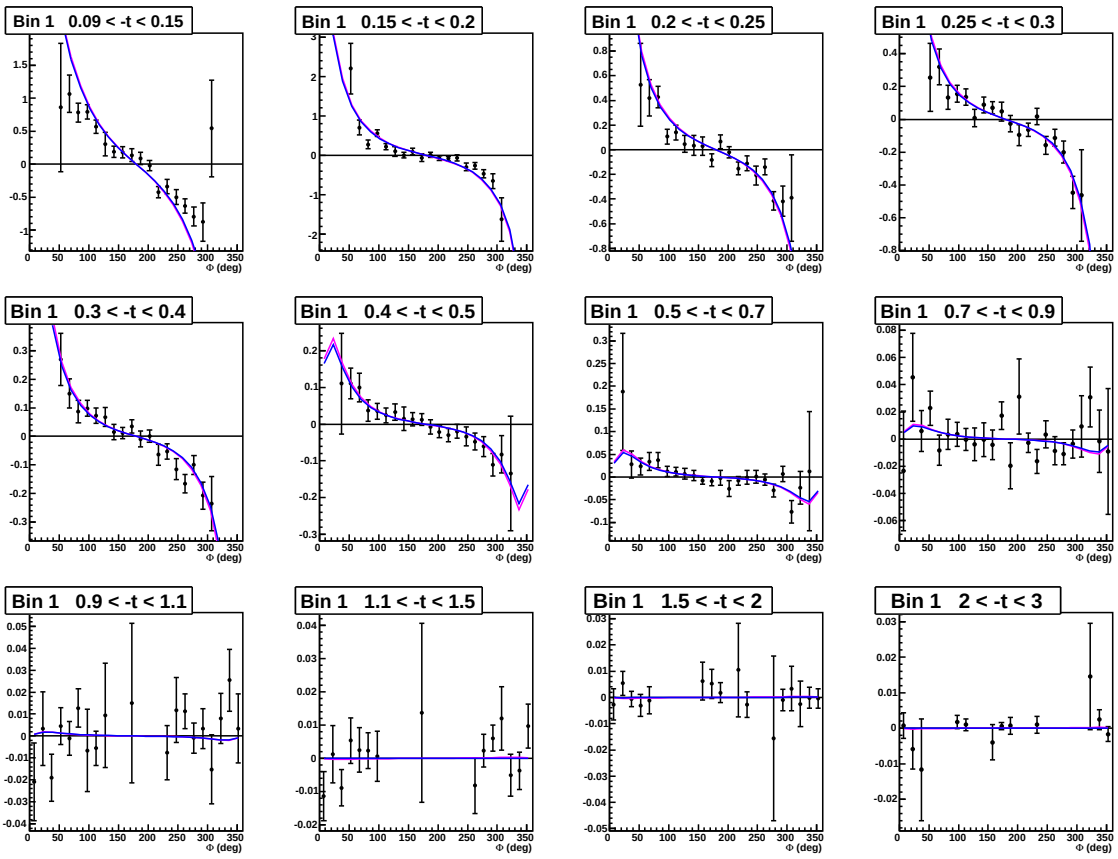

Figure M.1: Difference of polarized cross section as a function of Φ for the 12 t-bins of the first (Q^2, x_B) bin. The curves correspond to VGG predictions and are described in the text.

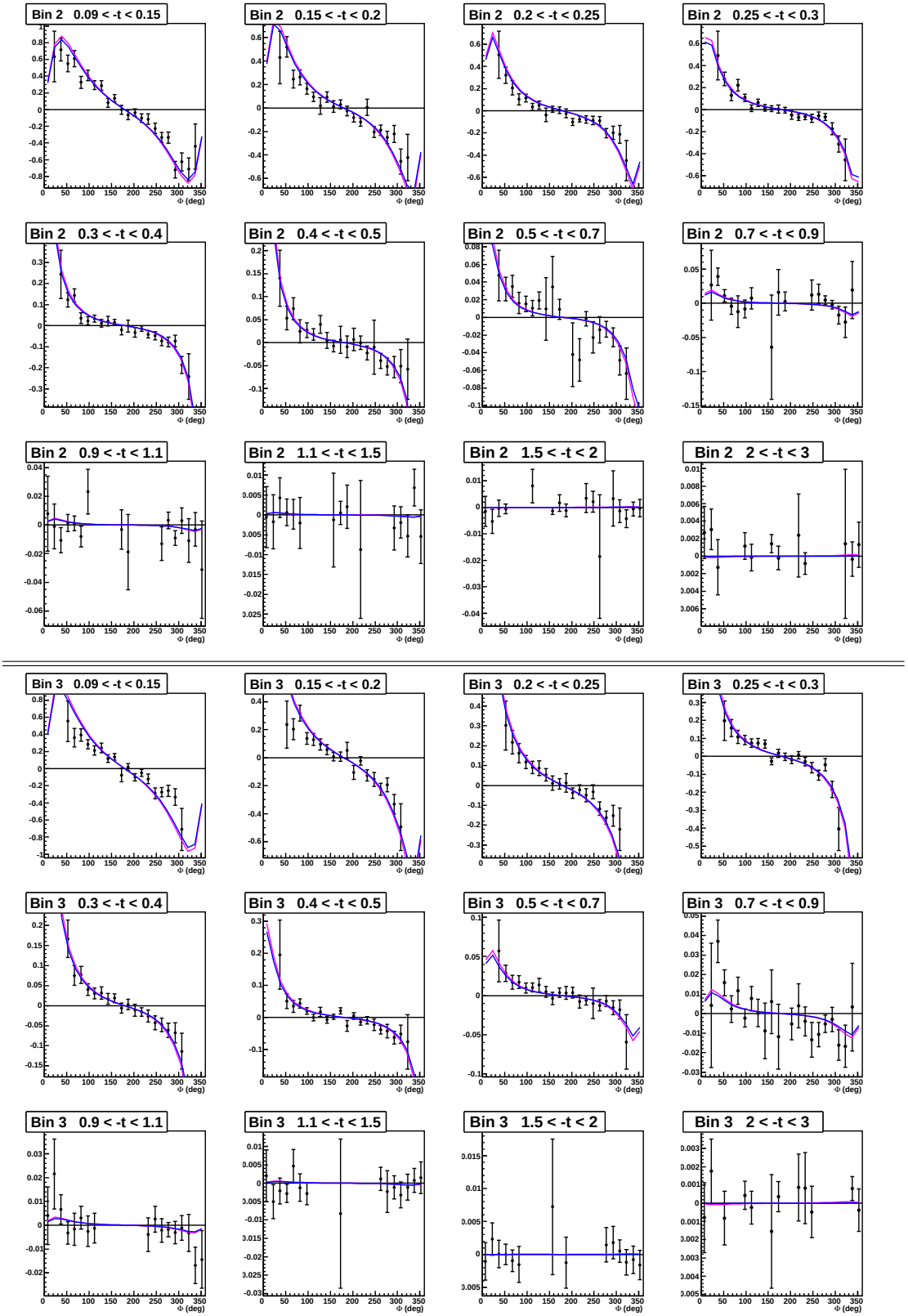

Figure M.2: Difference of polarized cross section as a function of Φ for the 12 t-bins of the (Q^2, x_B) bins 2 and 3. The curves correspond to VGG predictions and are described in the text.

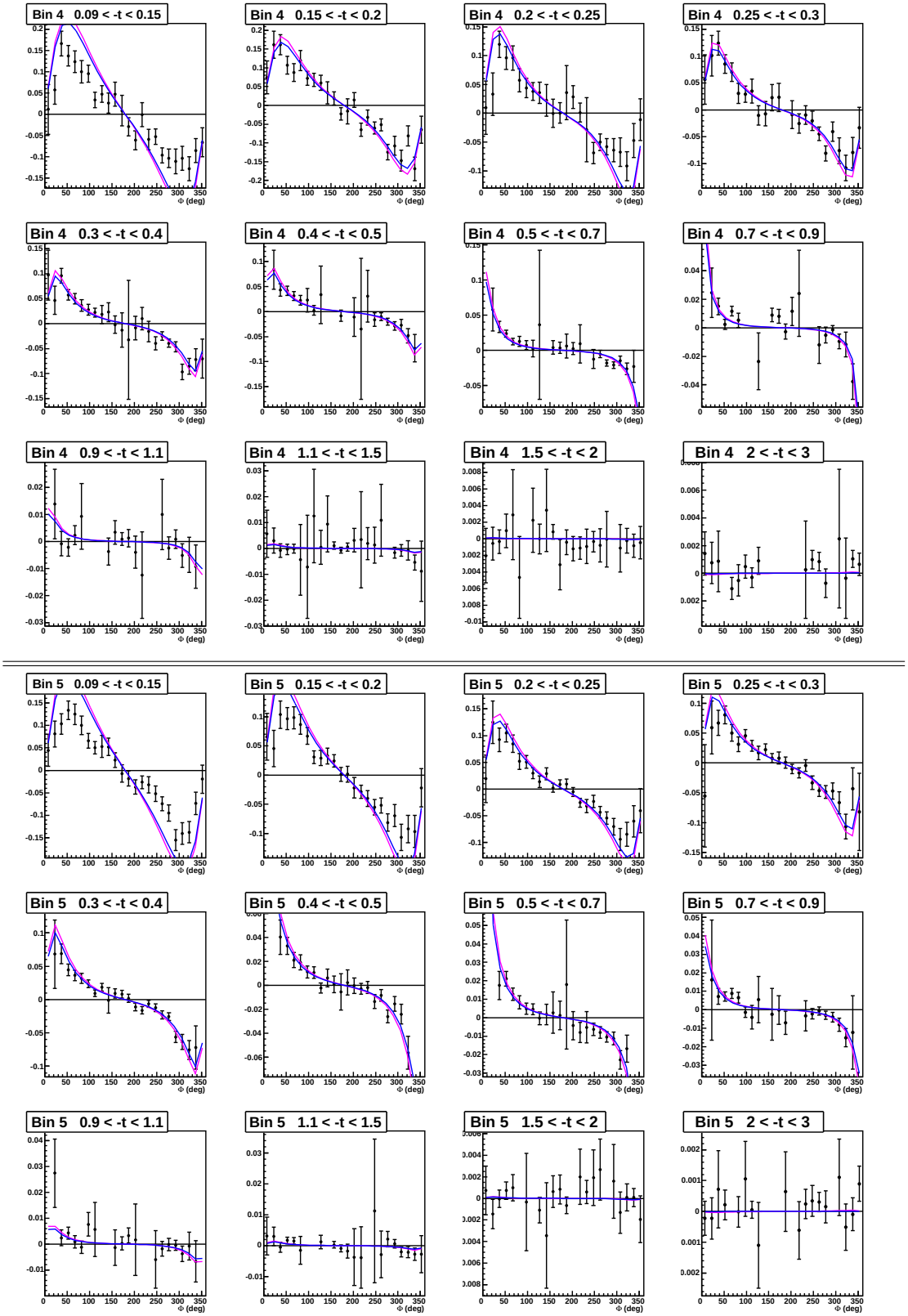

Figure M.3: Difference of polarized cross section as a function of Φ for the 12 t-bins of the (Q^2, x_B) bins 4 and 5. The curves correspond to VGG predictions and are described in the text.

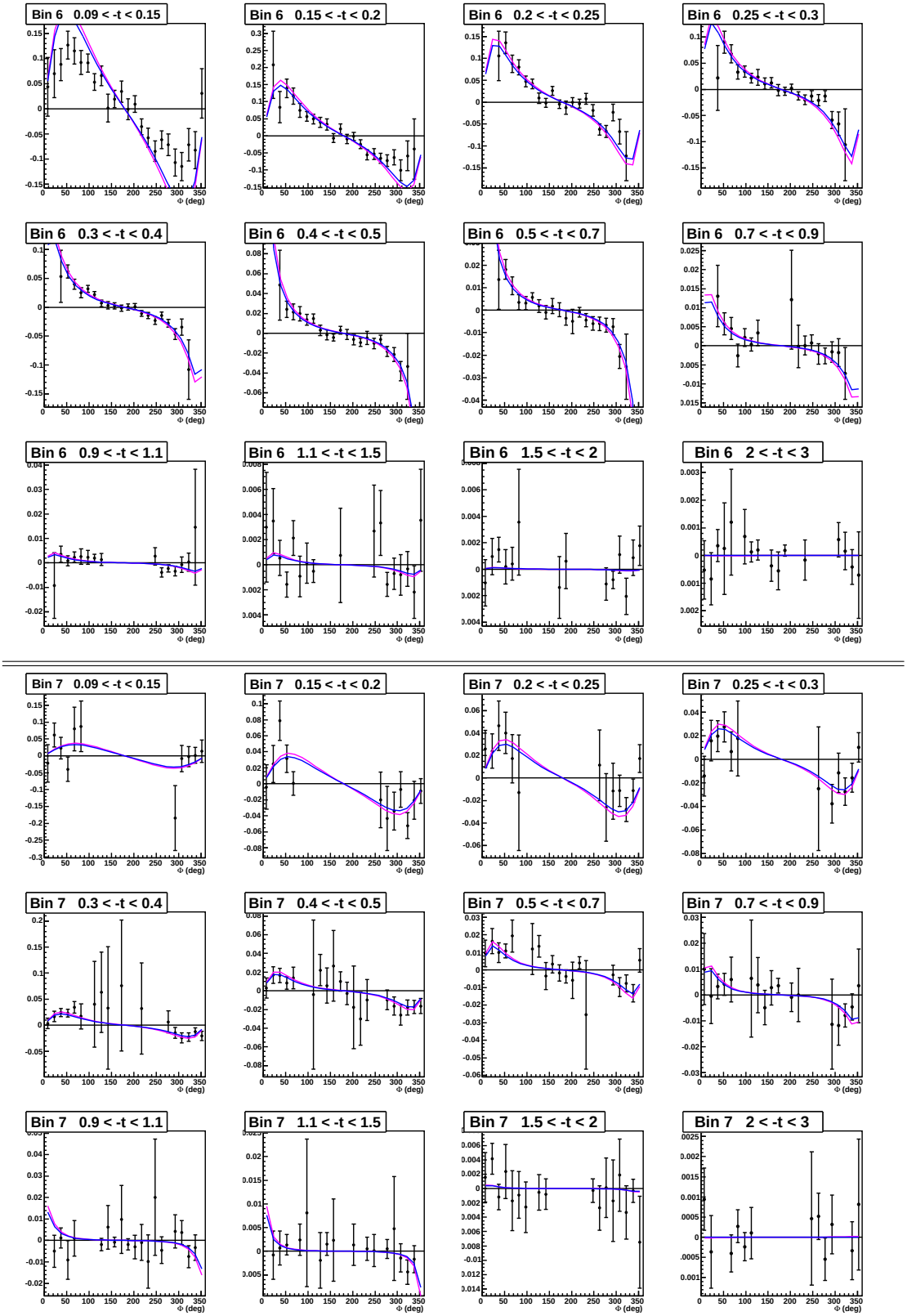

Figure M.4: Difference of polarized cross section as a function of Φ for the 12 t-bins of the (Q^2, x_B) bins 6 and 7. The curves correspond to VGG predictions and are described in the text.

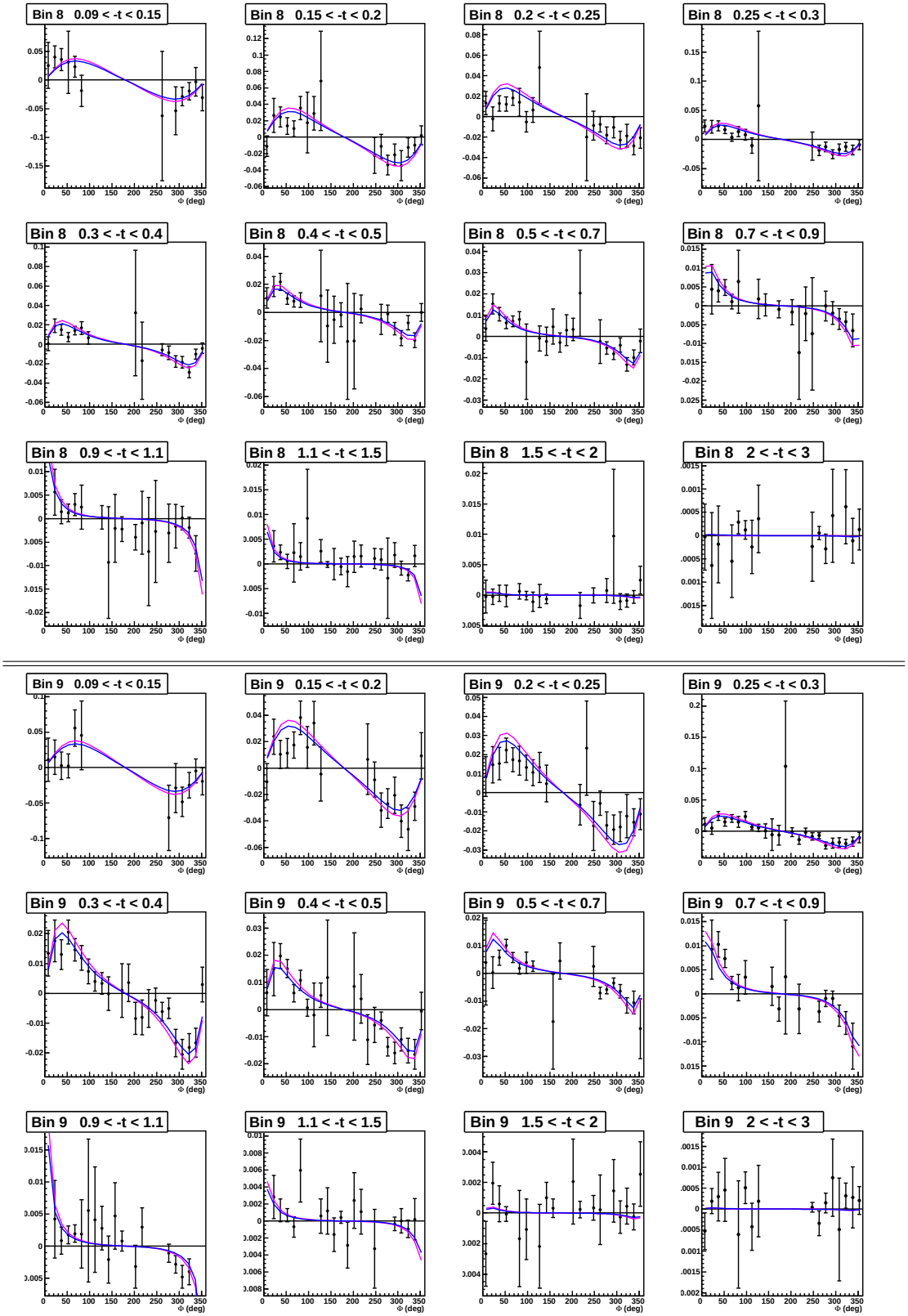

Figure M.5: Difference of polarized cross section as a function of Φ for the 12 t-bins of the (Q^2, x_B) bins 8 and 9. The curves correspond to VGG predictions and are described in the text.

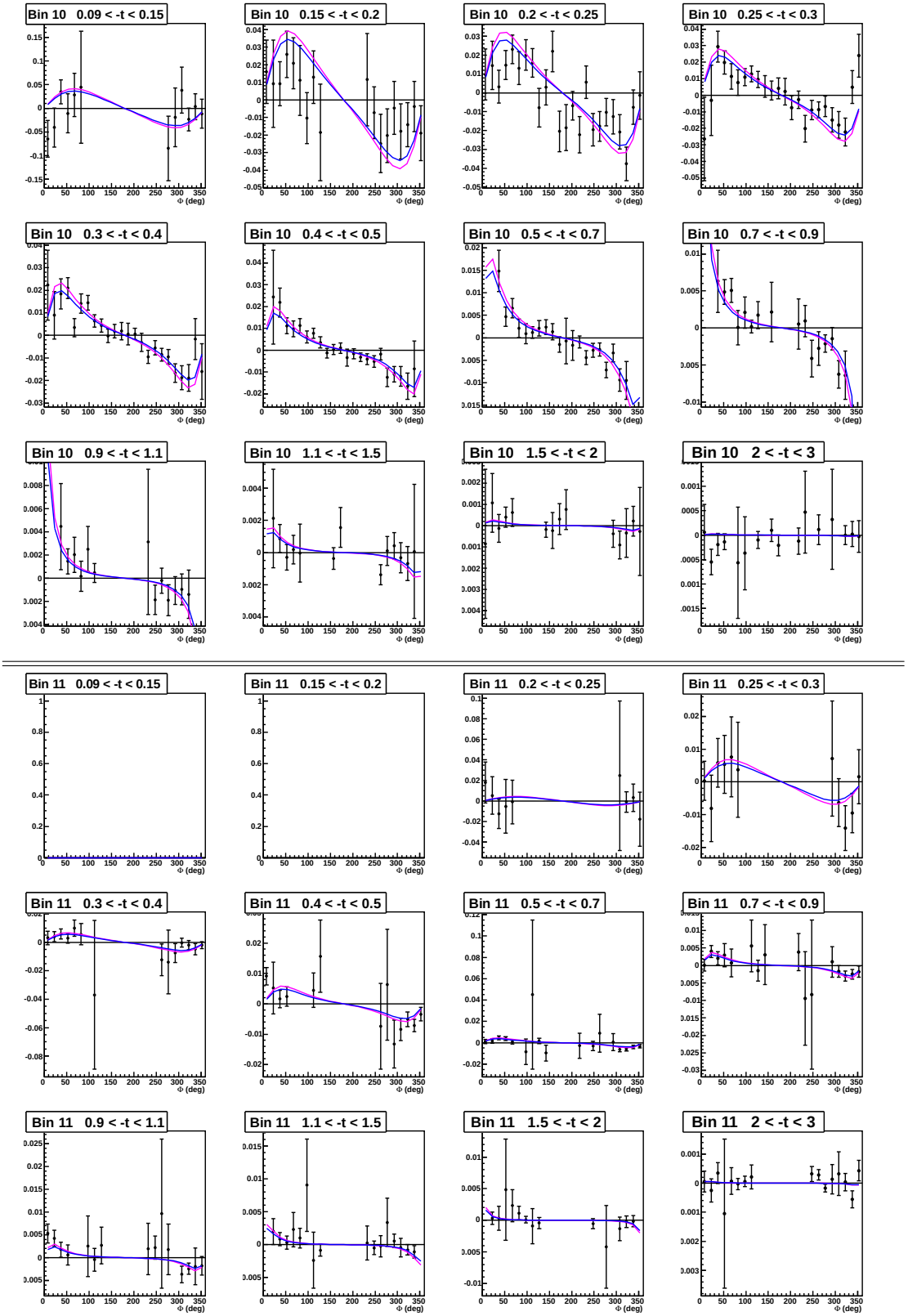

Figure M.6: Difference of polarized cross section as a function of Φ for the 12 t-bins of the (Q^2, x_B) bins 10 and 11. The curves correspond to VGG predictions and are described in the text.

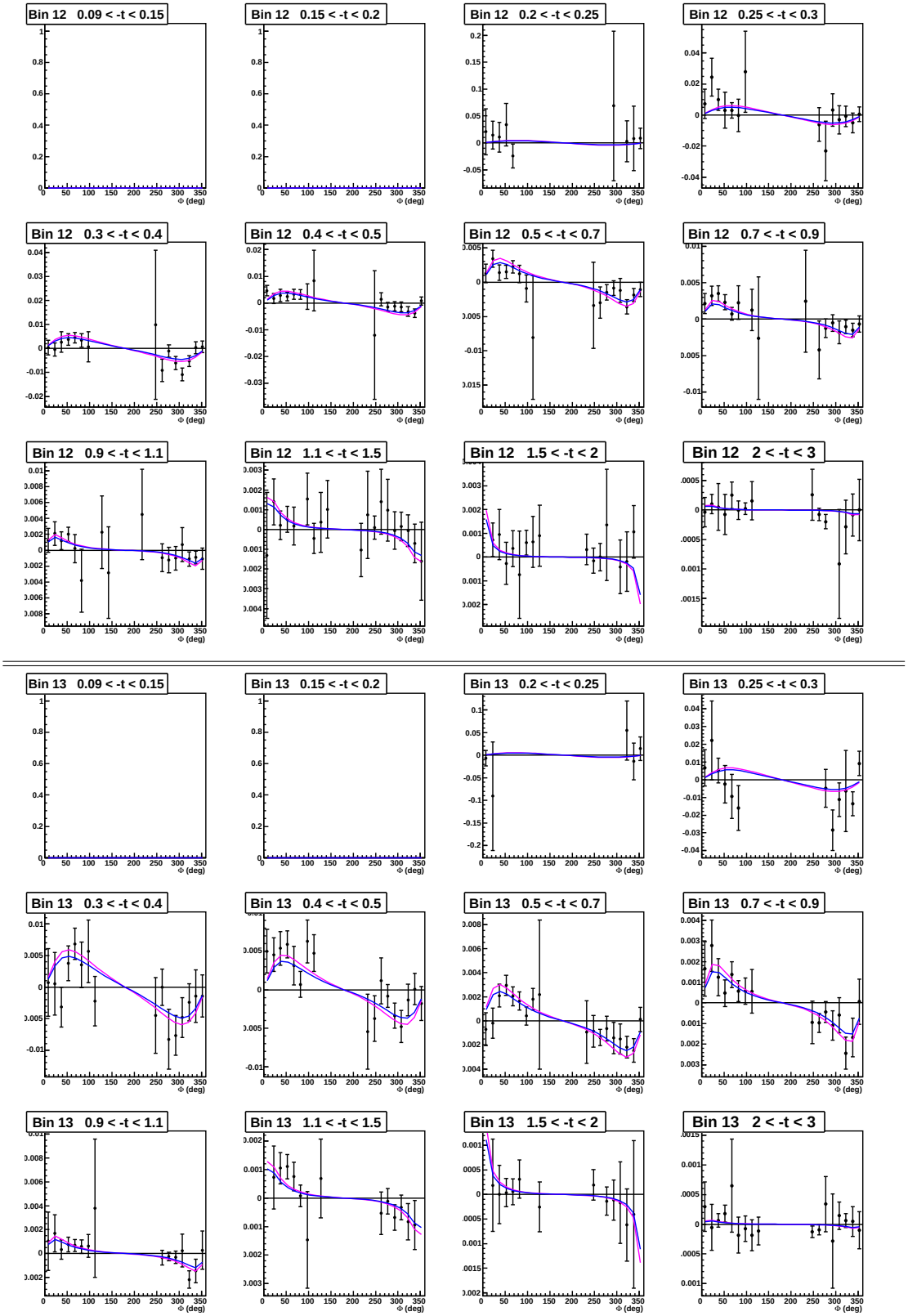

Figure M.7: Difference of polarized cross section as a function of Φ for the 12 t-bins of the (Q^2, x_B) bins 12 and 13. The curves correspond to VGG predictions and are described in the text.

Appendix N

Comparison of the asymmetries with VGG model

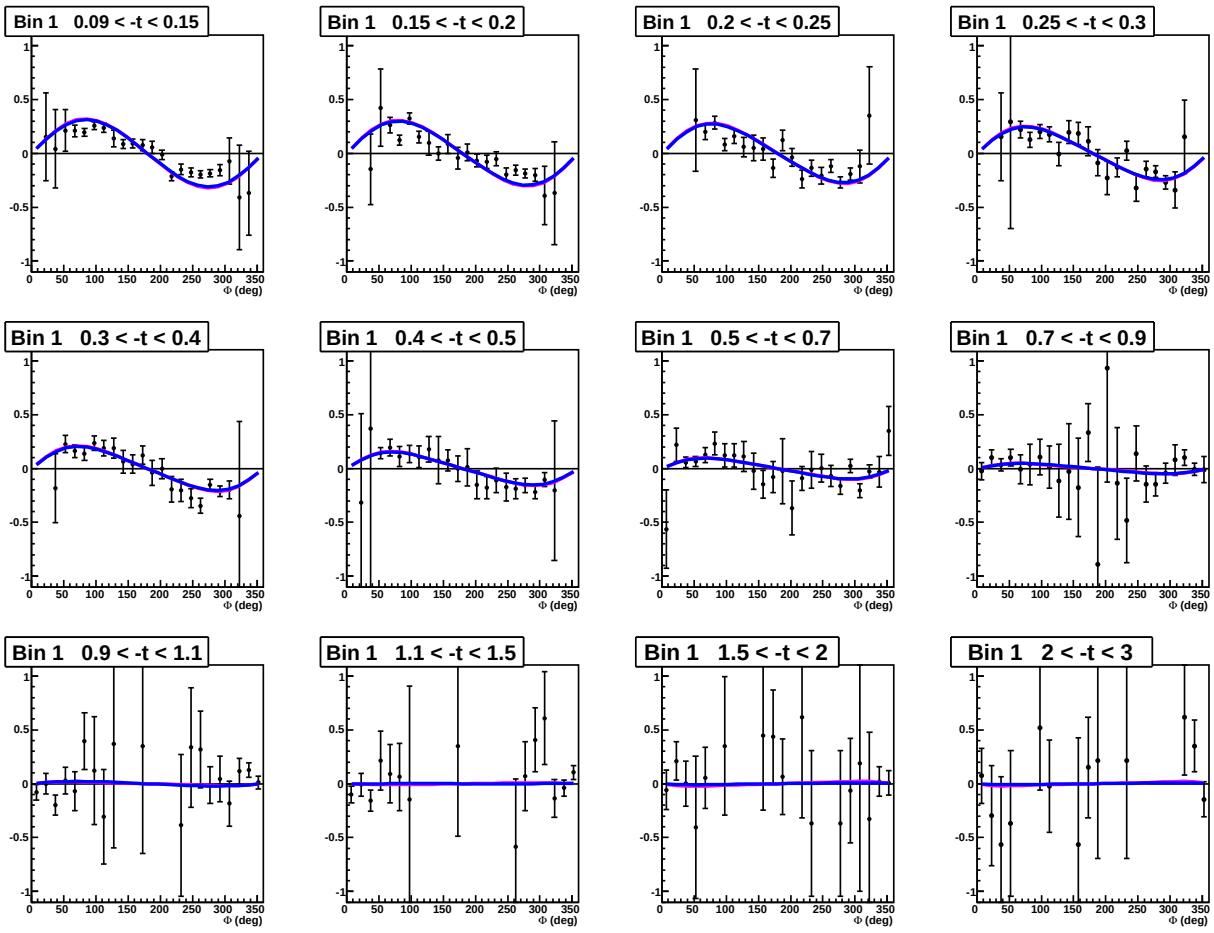

Figure N.1: Asymmetries as a function of Φ for the 12 t-bins of the first (Q^2, x_B) bin. The curves correspond to VGG predictions and are described in the text.

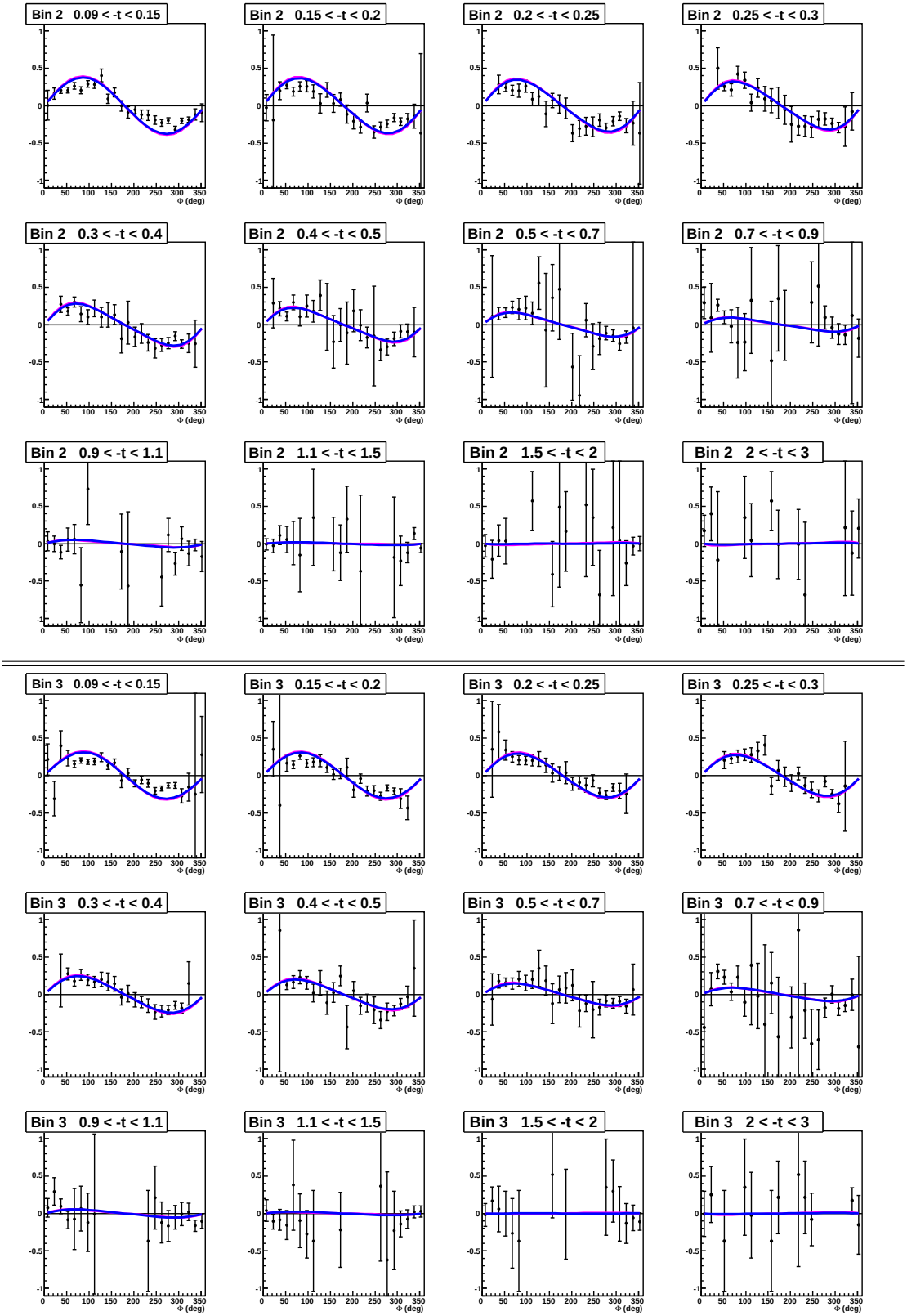

Figure N.2: Asymmetries as a function of Φ for the 12 t-bins of the (Q^2, x_B) bins 2 and 3. The curves correspond to VGG predictions and are described in the text.

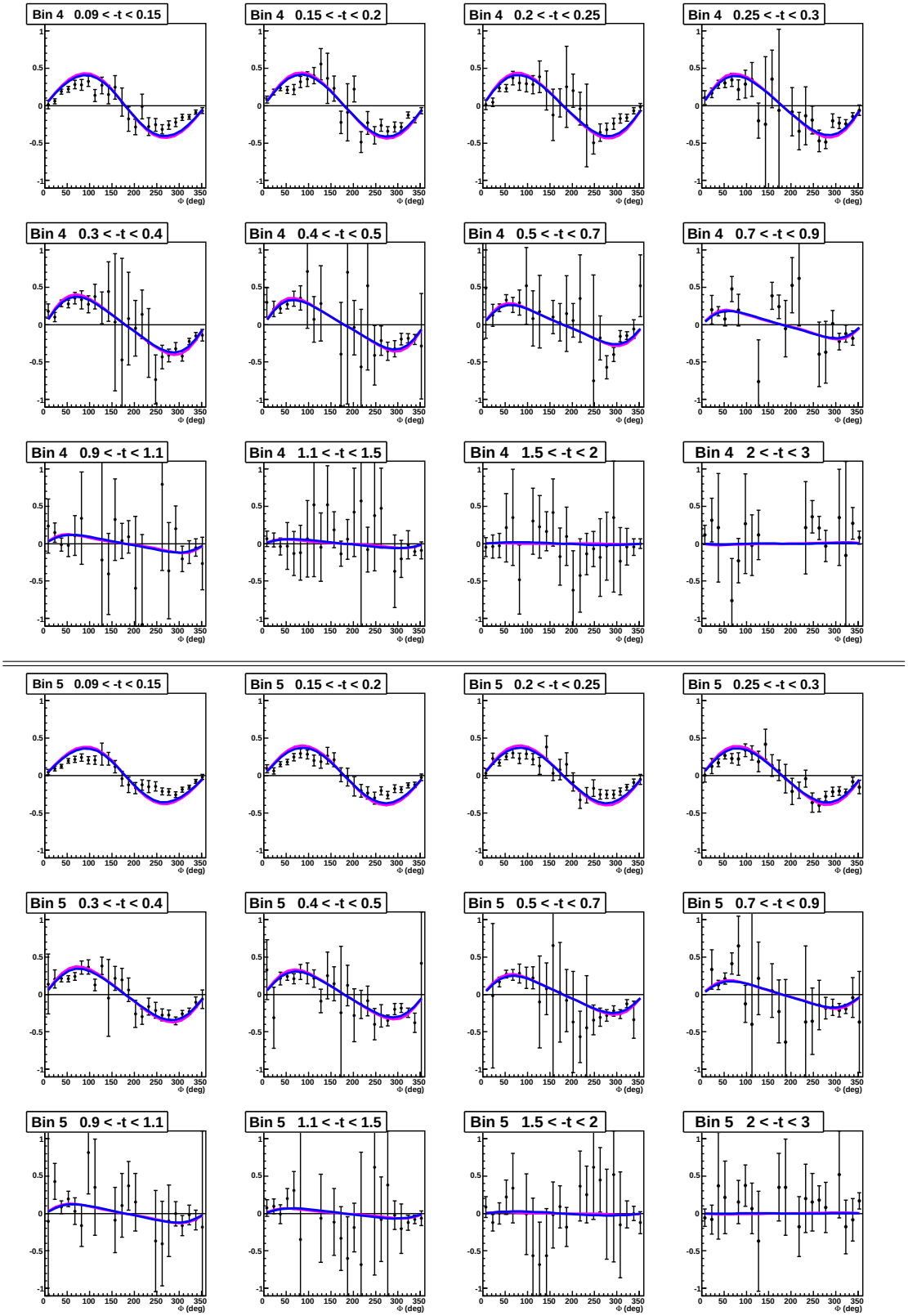

Figure N.3: Asymmetries as a function of Φ for the 12 t-bins of the (Q^2, x_B) bins 4 and 5. The curves correspond to VGG predictions and are described in the text.

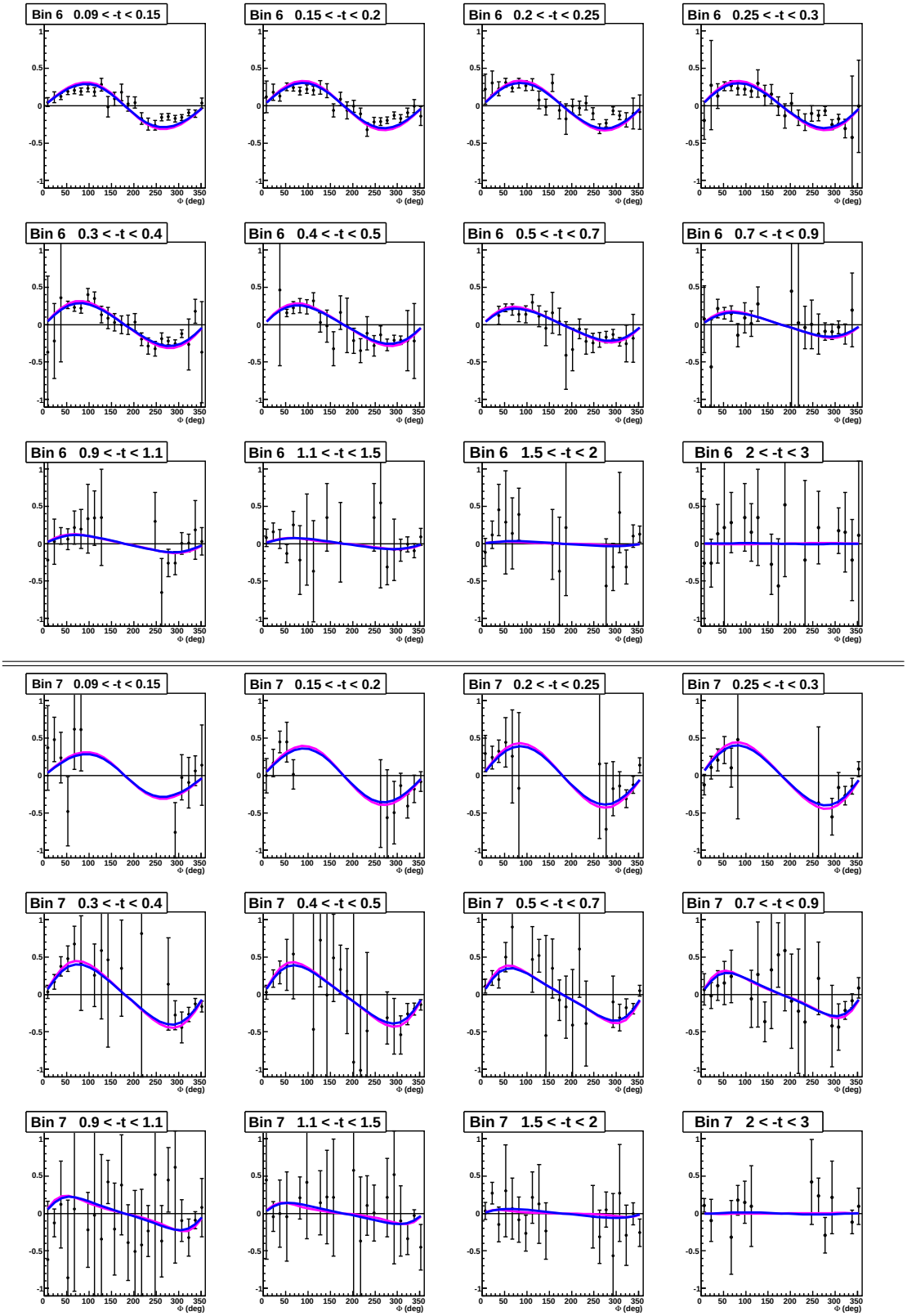

Figure N.4: Asymmetries as a function of Φ for the 12 t-bins of the (Q^2, x_B) bins 6 and 7. The curves correspond to VGG predictions and are described in the text.

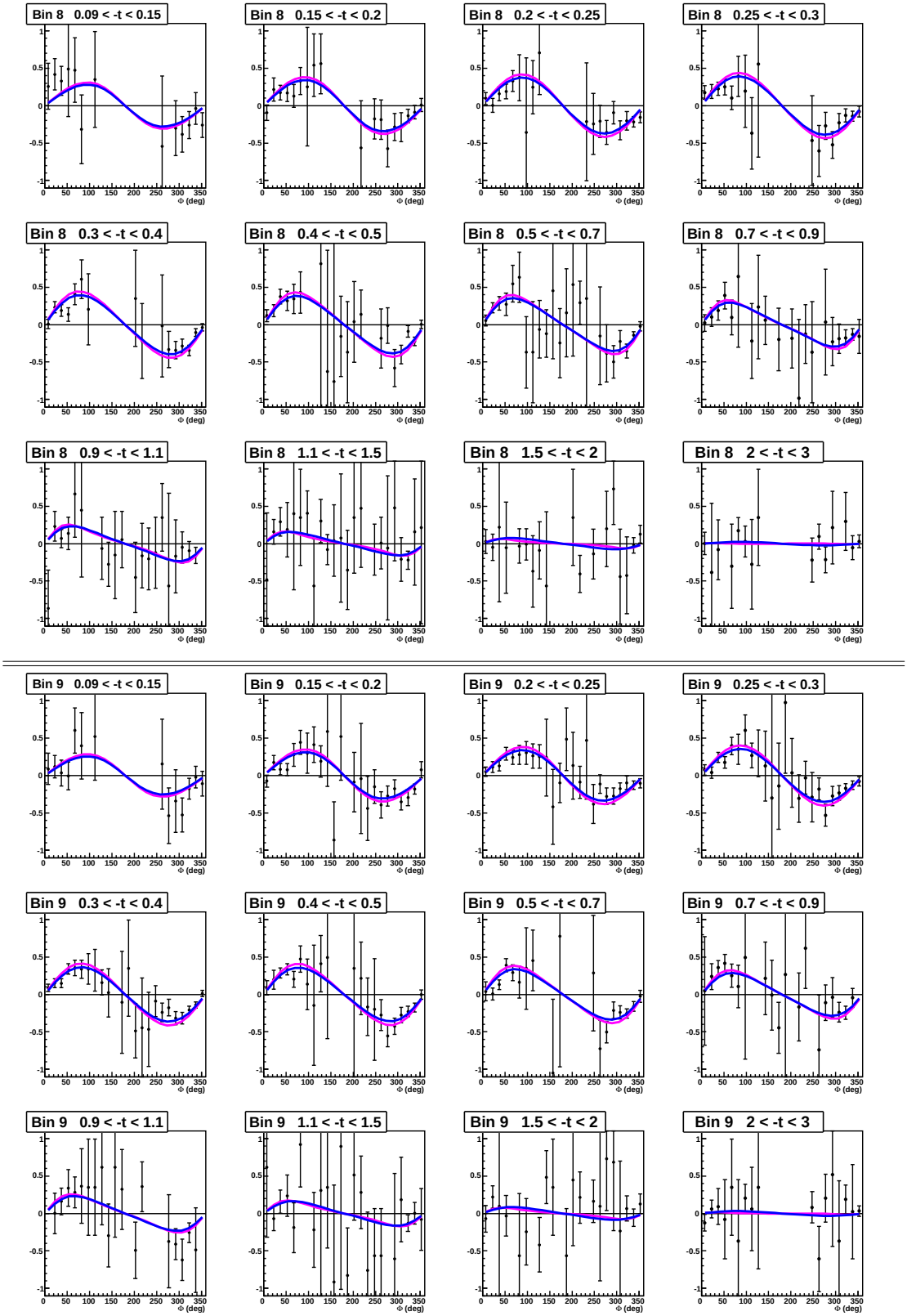

Figure N.5: Asymmetries as a function of Φ for the 12 t-bins of the (Q^2, x_B) bins 8 and 9. The curves correspond to VGG predictions and are described in the text.

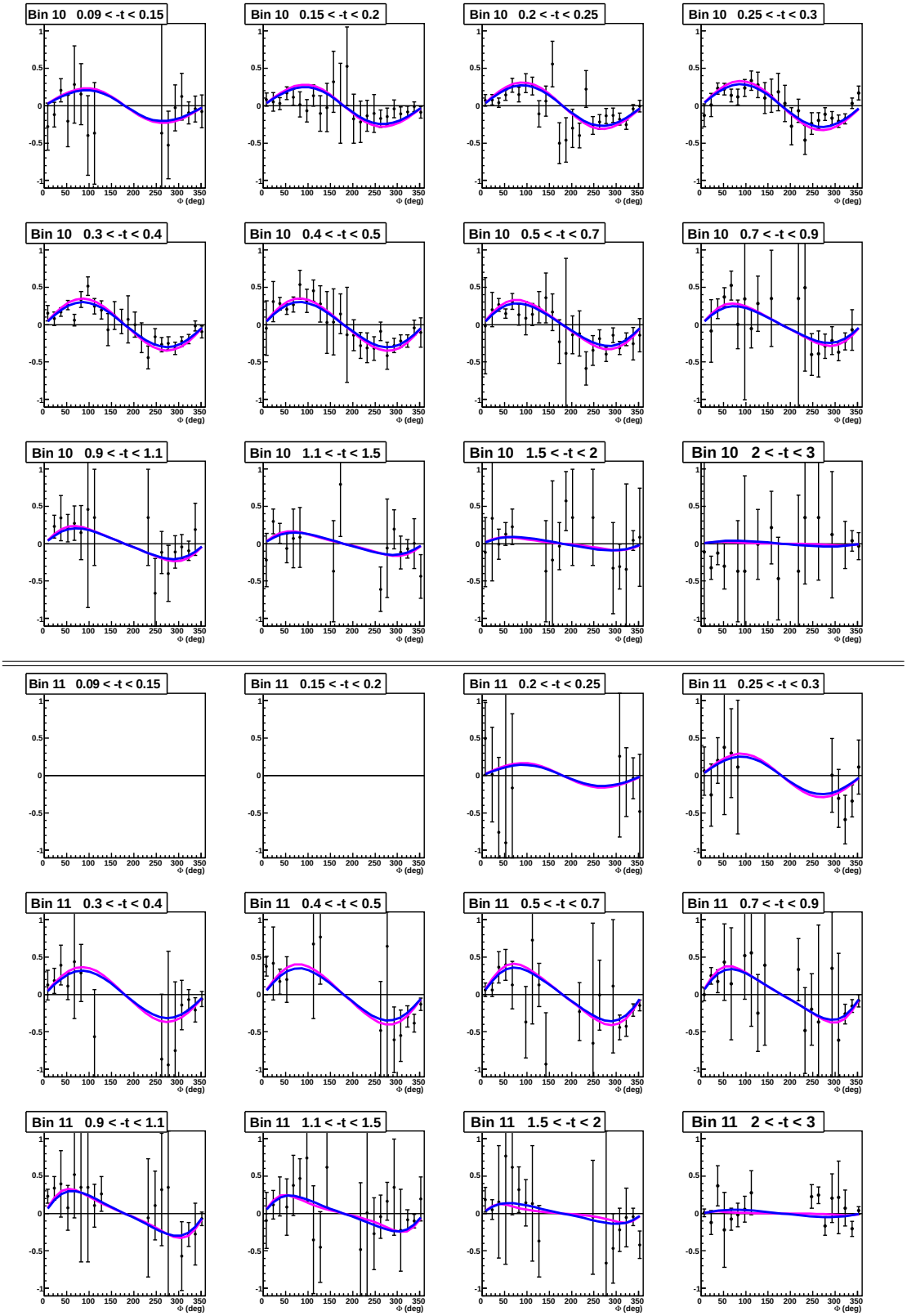

Figure N.6: Asymmetries as a function of Φ for the 12 t-bins of the (Q^2, x_B) bins 10 and 11. The curves correspond to VGG predictions and are described in the text.

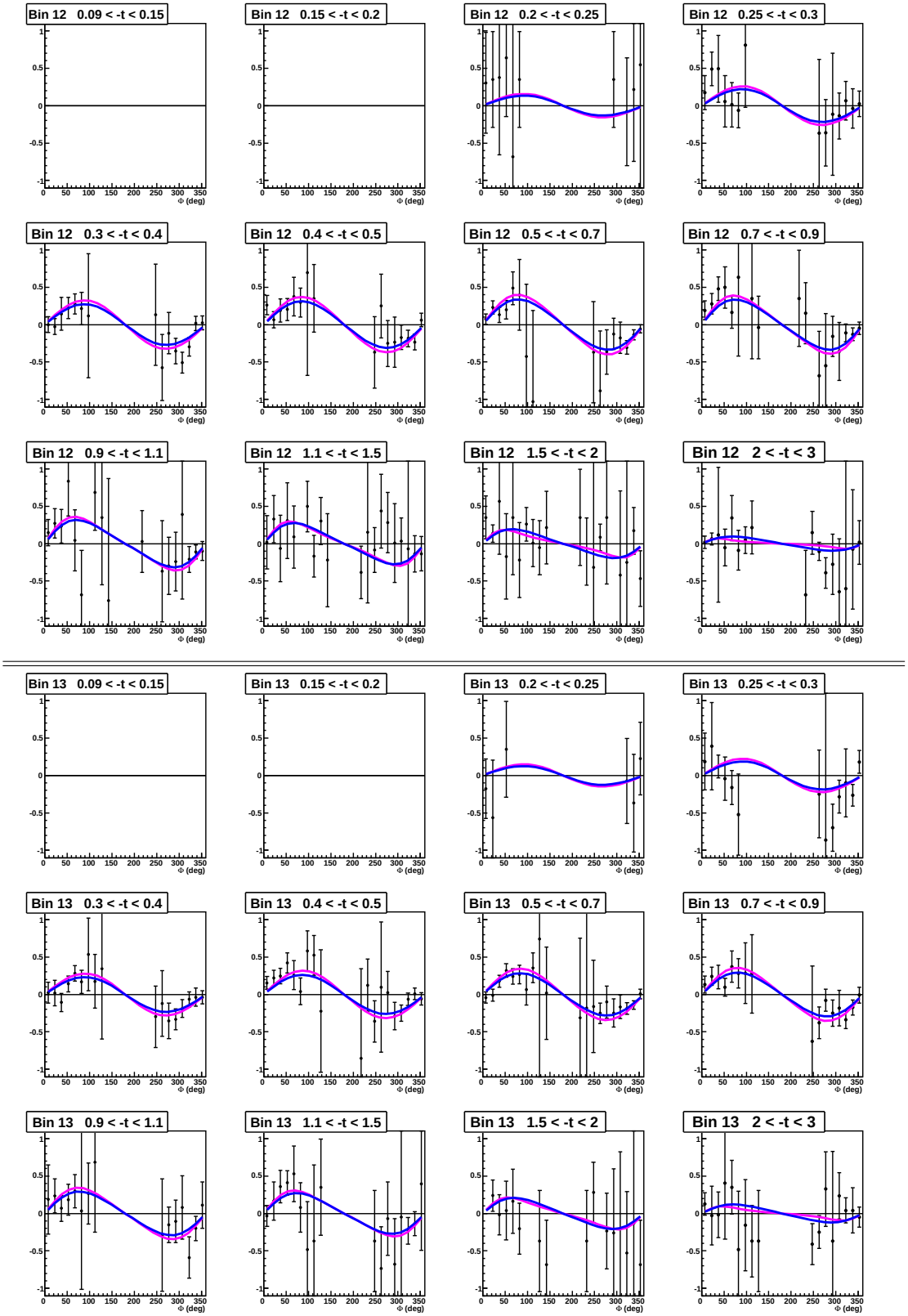

Figure N.7: Asymmetries as a function of Φ for the 12 t-bins of the (Q^2, x_B) bins 12 and 13. The curves correspond to VGG predictions and are described in the text.

Appendix O

Results of the fitting procedure

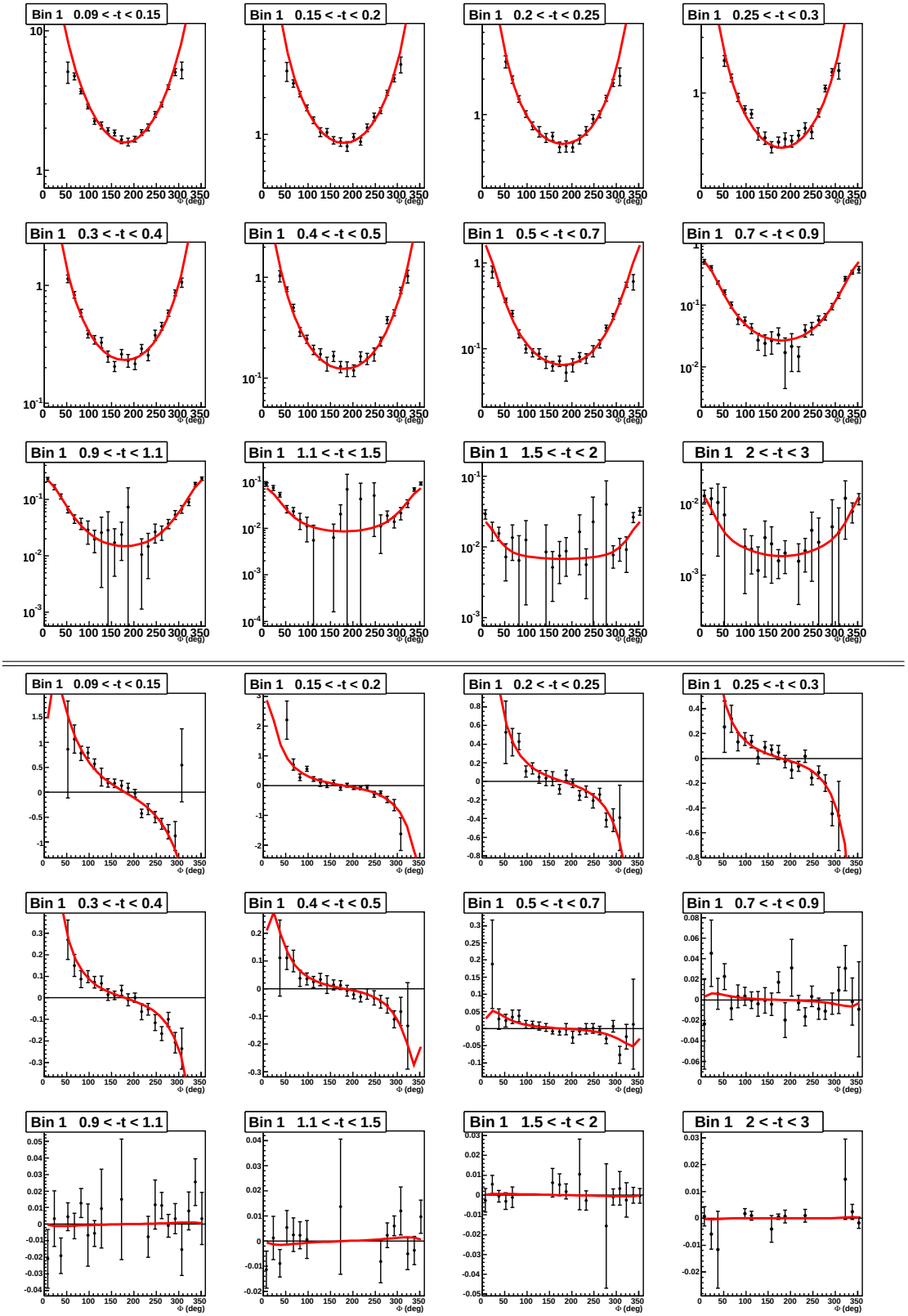

Figure O.1: Simultaneous fits of the unpolarized (top) and polarized (bottom) cross sections as a function of Φ for the 12 t-bins of the (Q^2, x_B) bins 1.

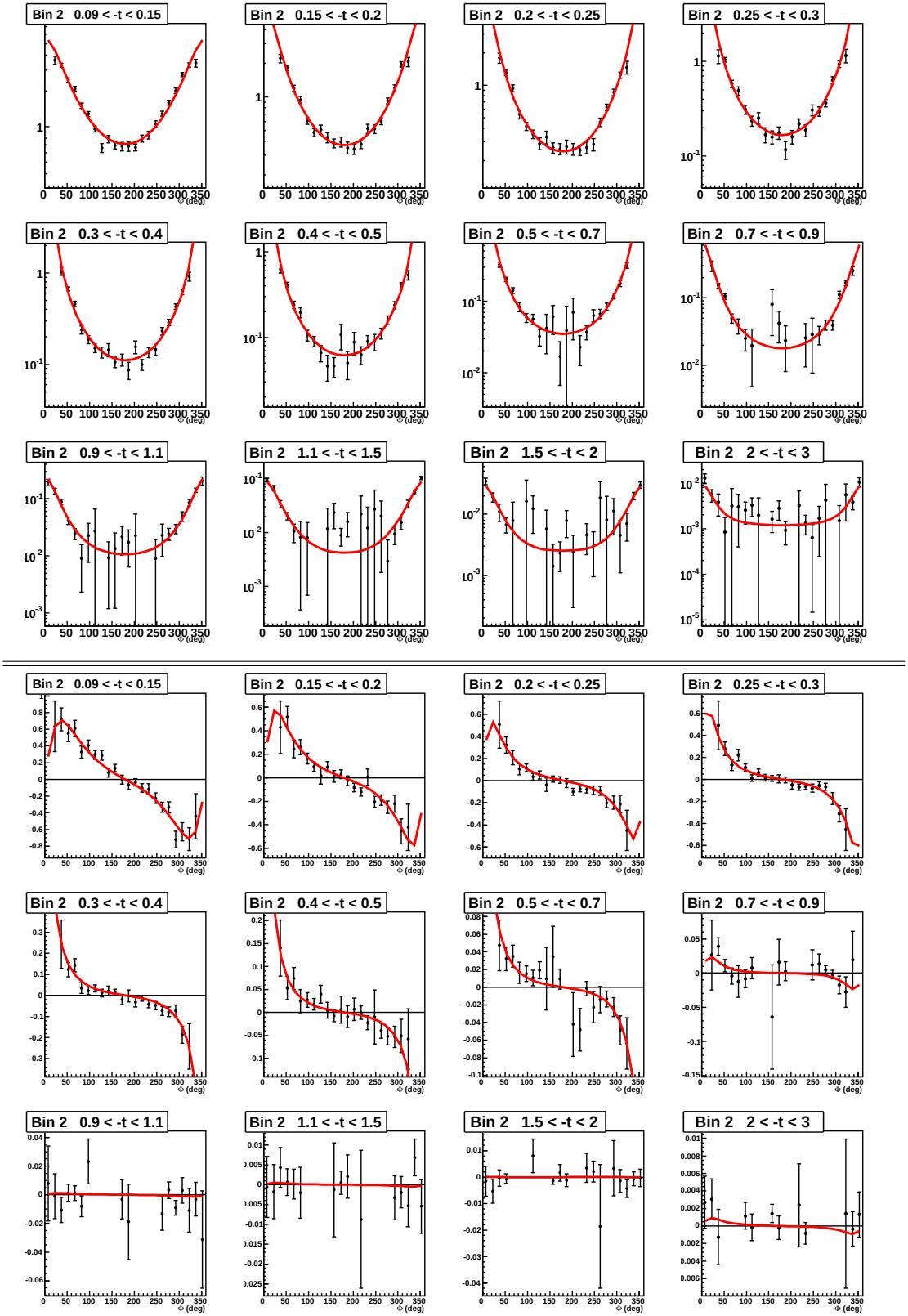

Figure O.2: Simultaneous fits of the unpolarized (top) and polarized (bottom) cross sections as a function of Φ for the 12 t-bins of the (Q^2, x_B) bins 2.

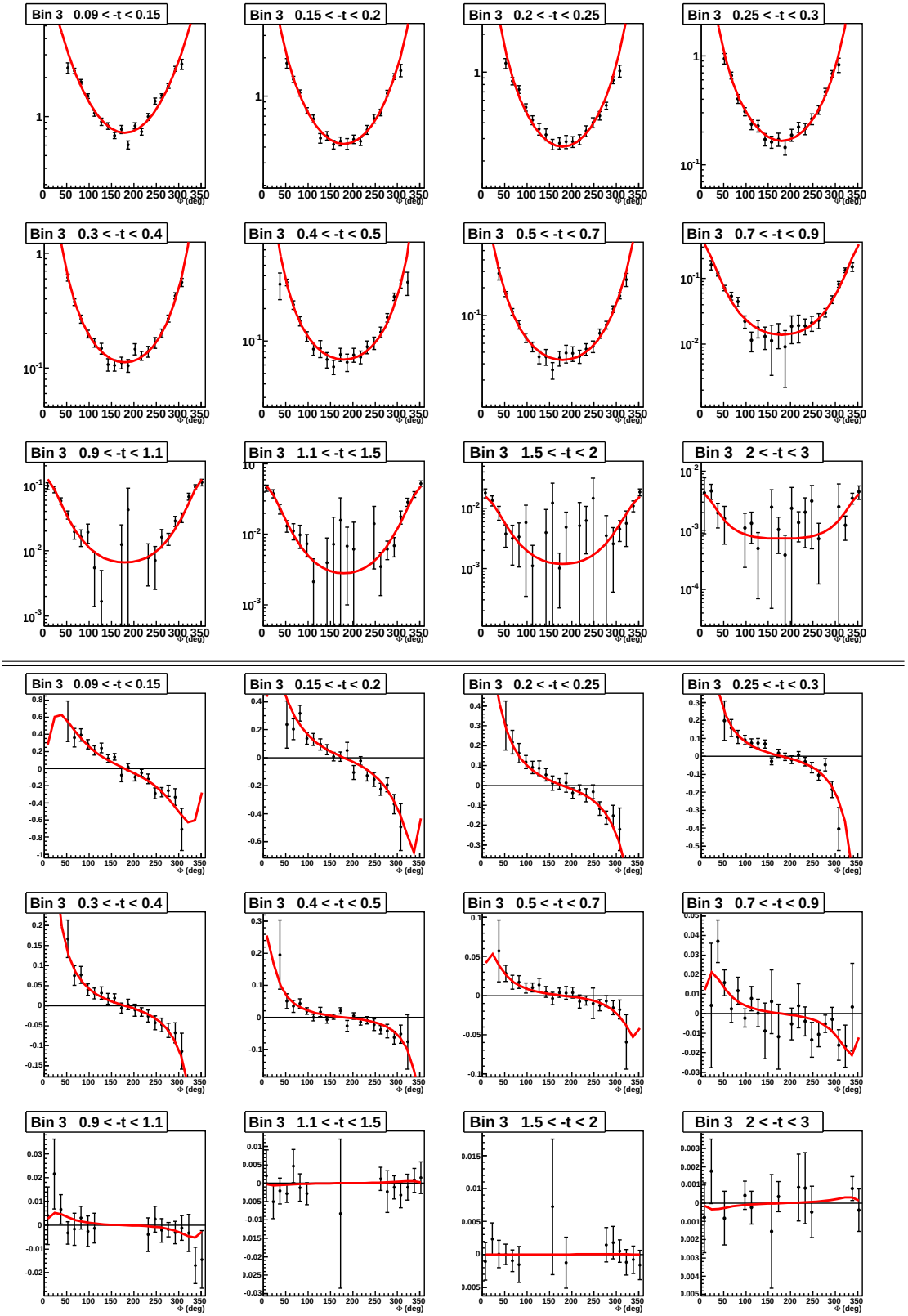

Figure O.3: Simultaneous fits of the unpolarized (top) and polarized (bottom) cross sections as a function of Φ for the 12 t-bins of the (Q^2, x_B) bins 3.

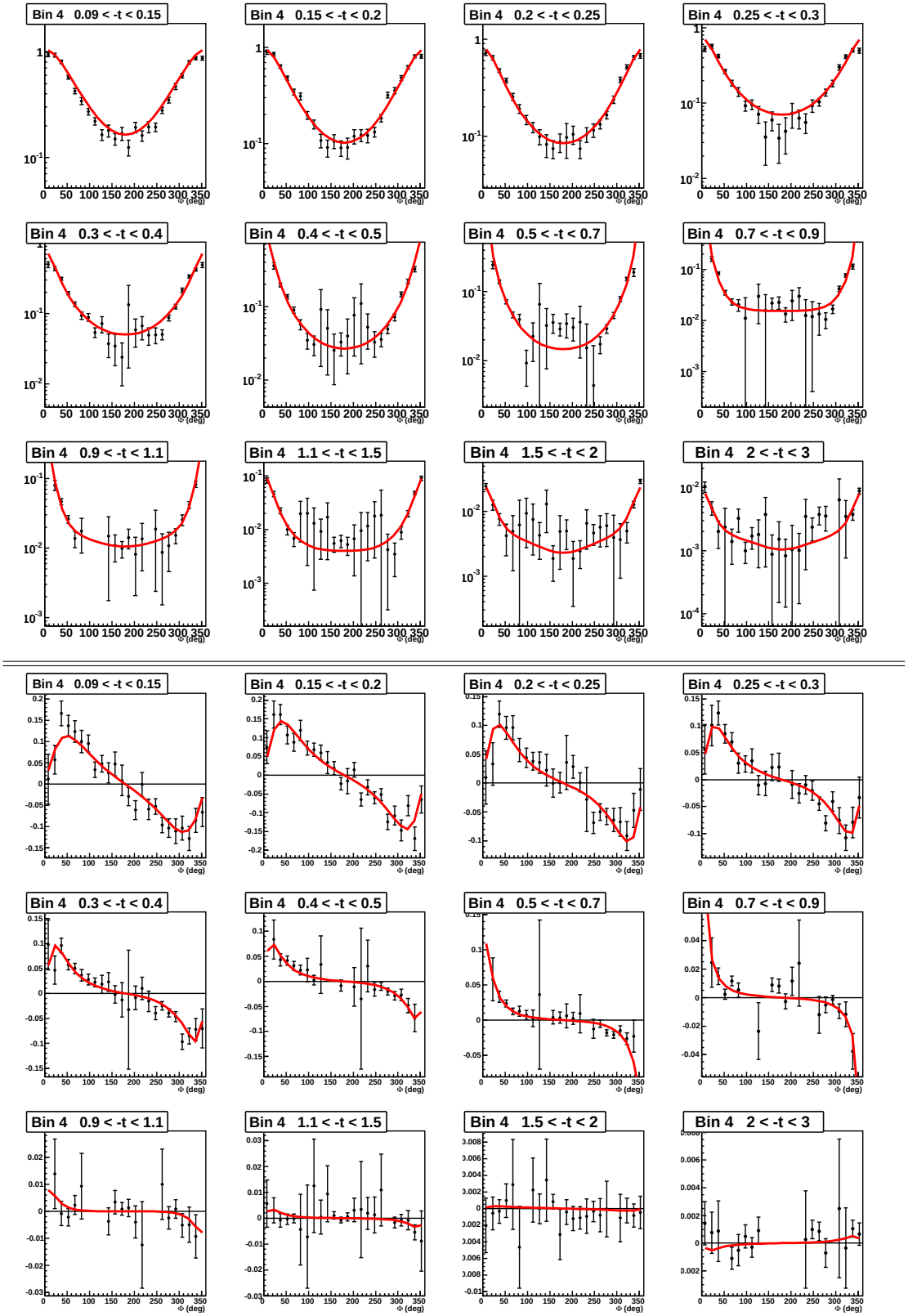

Figure O.4: Simultaneous fits of the unpolarized (top) and polarized (bottom) cross sections as a function of Φ for the 12 t-bins of the (Q^2, x_B) bins 4.

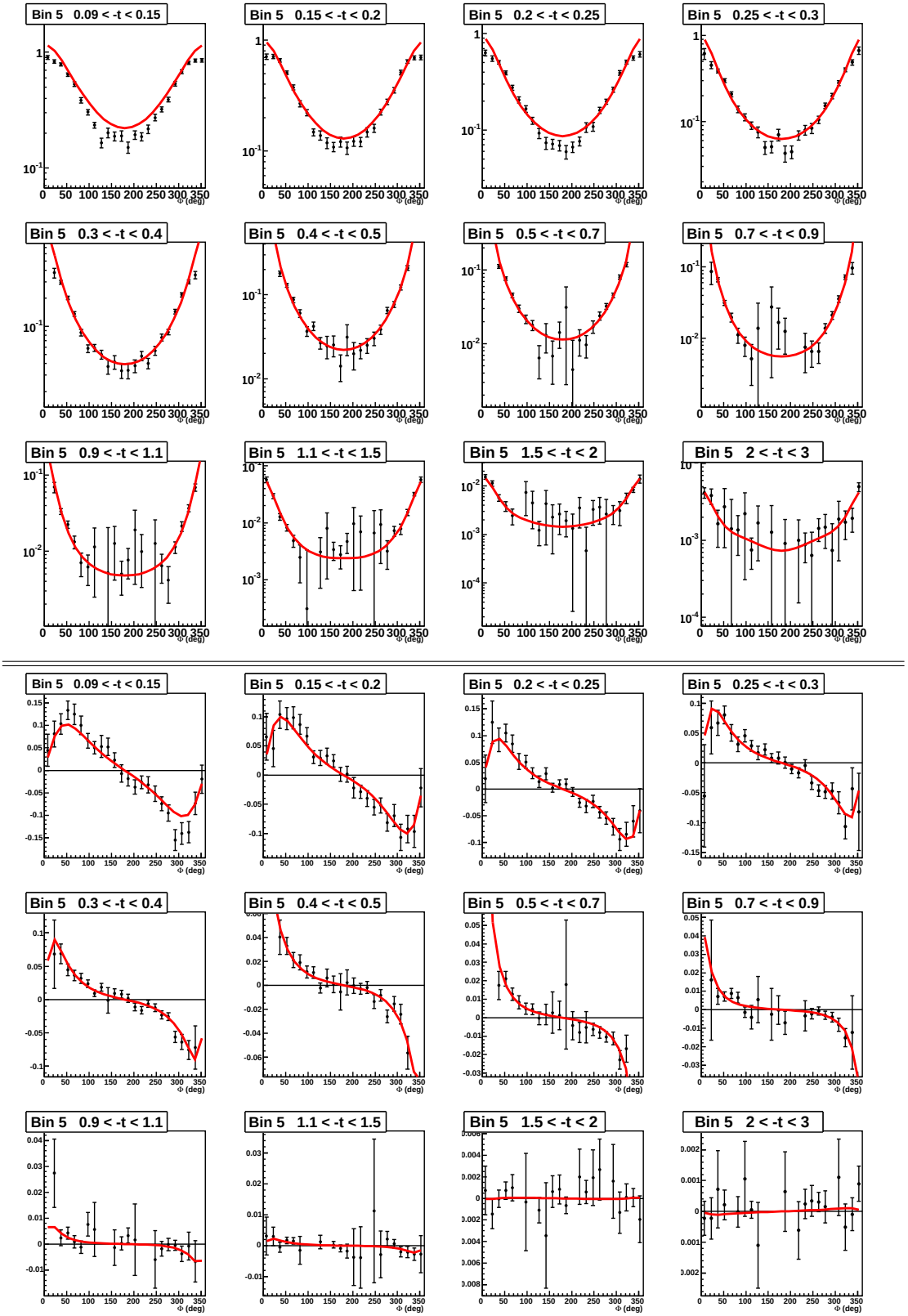

Figure O.5: Simultaneous fits of the unpolarized (top) and polarized (bottom) cross sections as a function of Φ for the 12 t-bins of the (Q^2, x_B) bins 5.

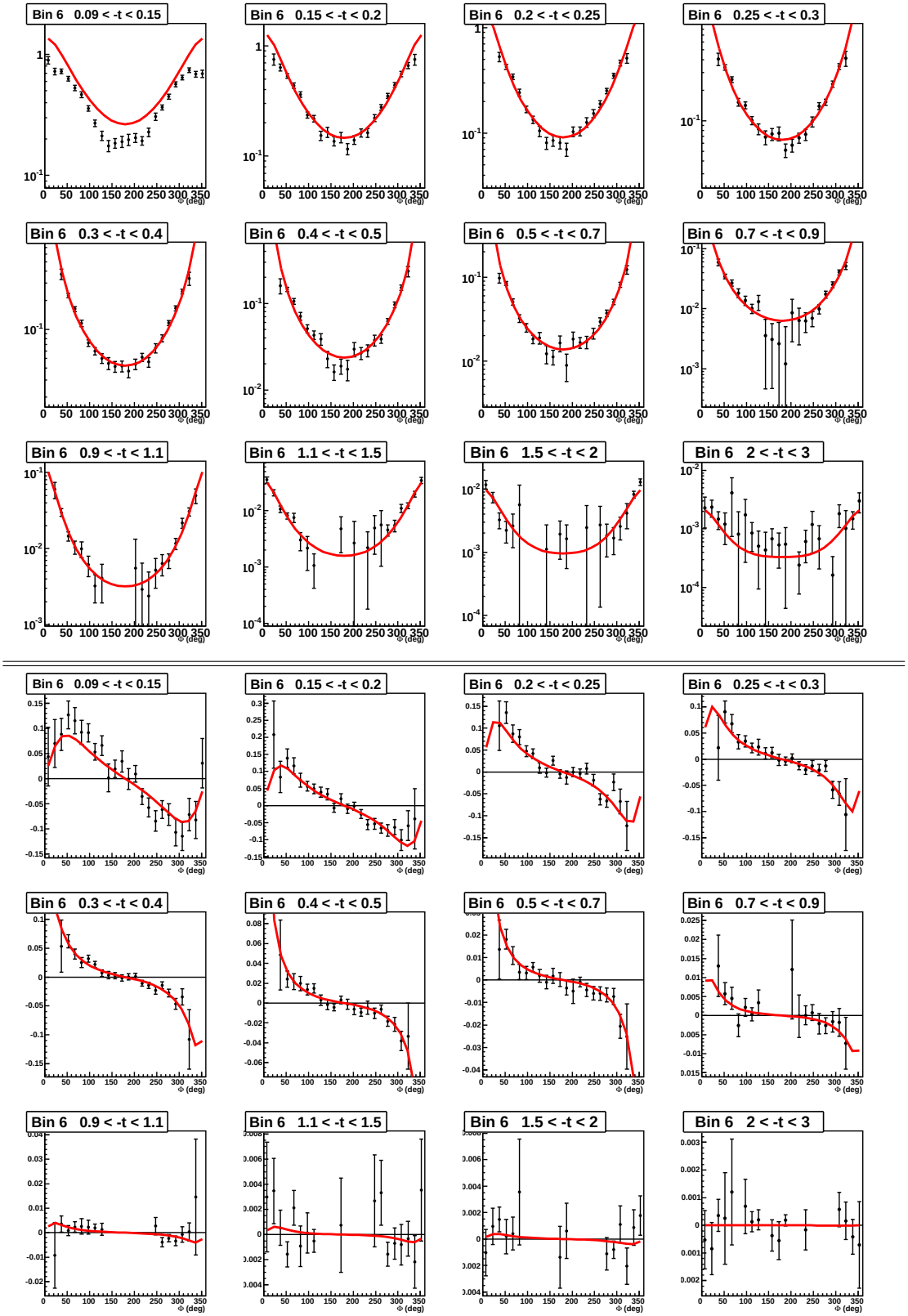

Figure O.6: Simultaneous fits of the unpolarized (top) and polarized (bottom) cross sections as a function of Φ for the 12 t-bins of the (Q^2, x_B) bins 6.

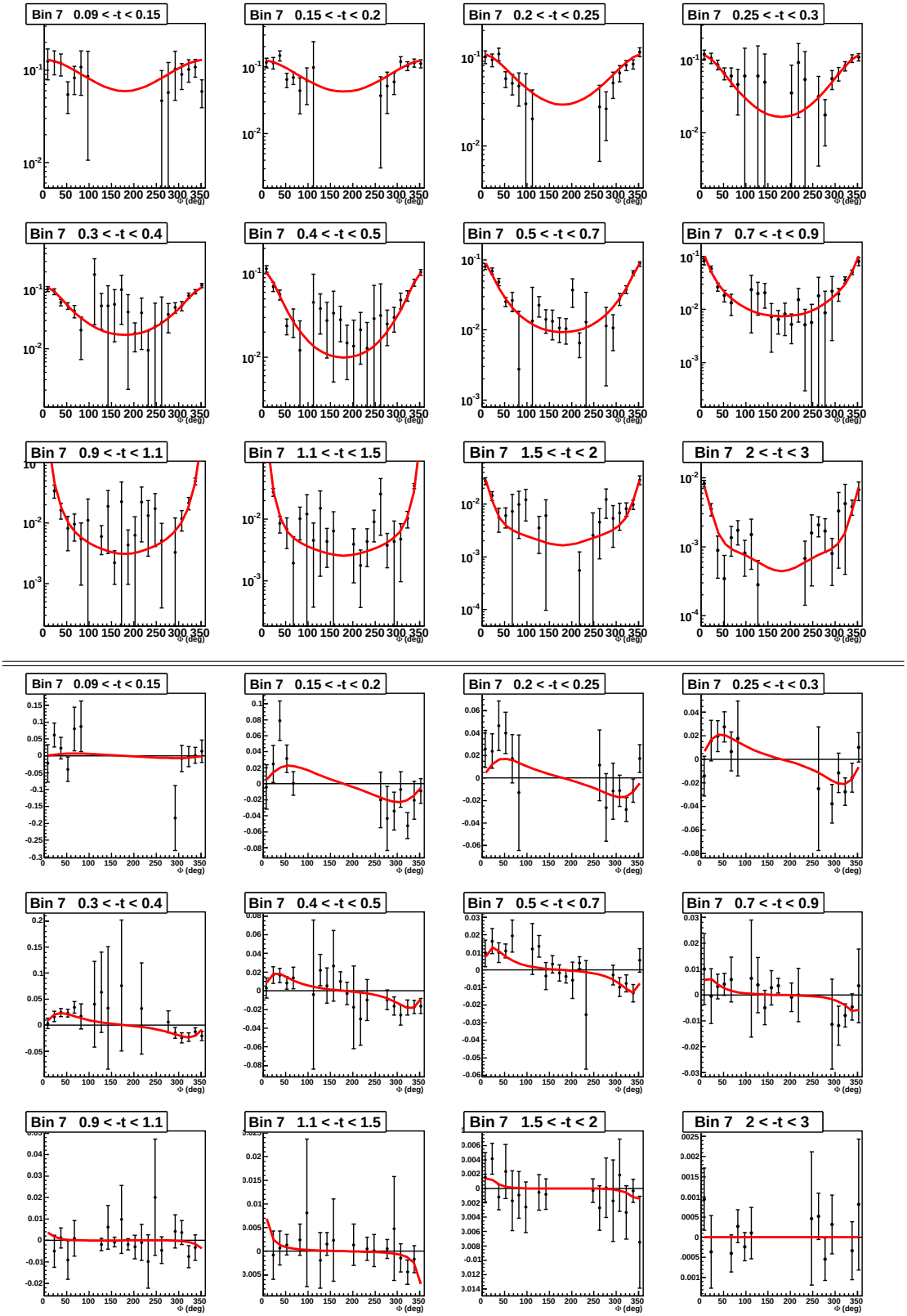

Figure O.7: Simultaneous fits of the unpolarized (top) and polarized (bottom) cross sections as a function of Φ for the 12 t-bins of the (Q^2, x_B) bins 7.

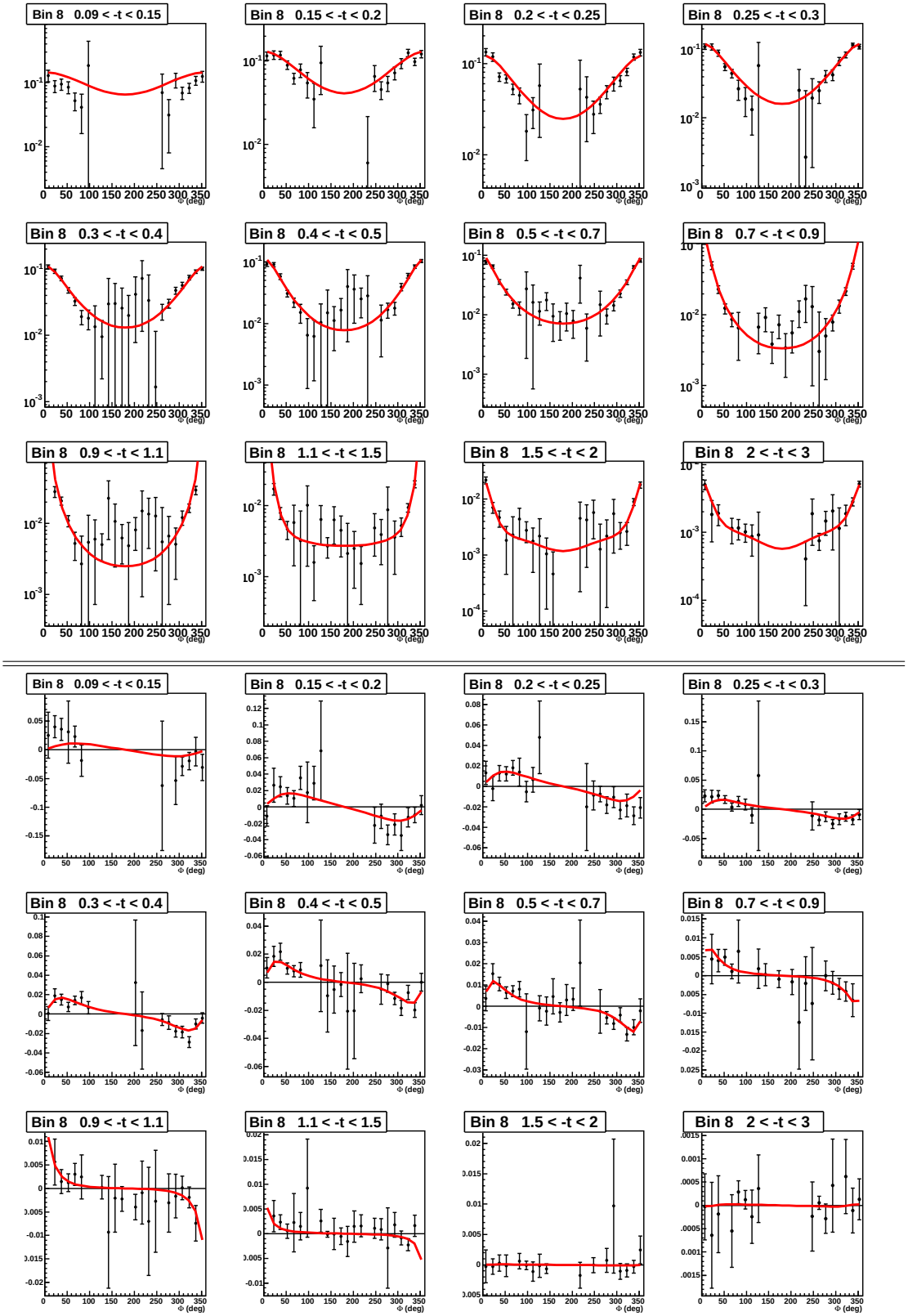

Figure O.8: Simultaneous fits of the unpolarized (top) and polarized (bottom) cross sections as a function of Φ for the 12 t-bins of the (Q^2, x_B) bins 8.

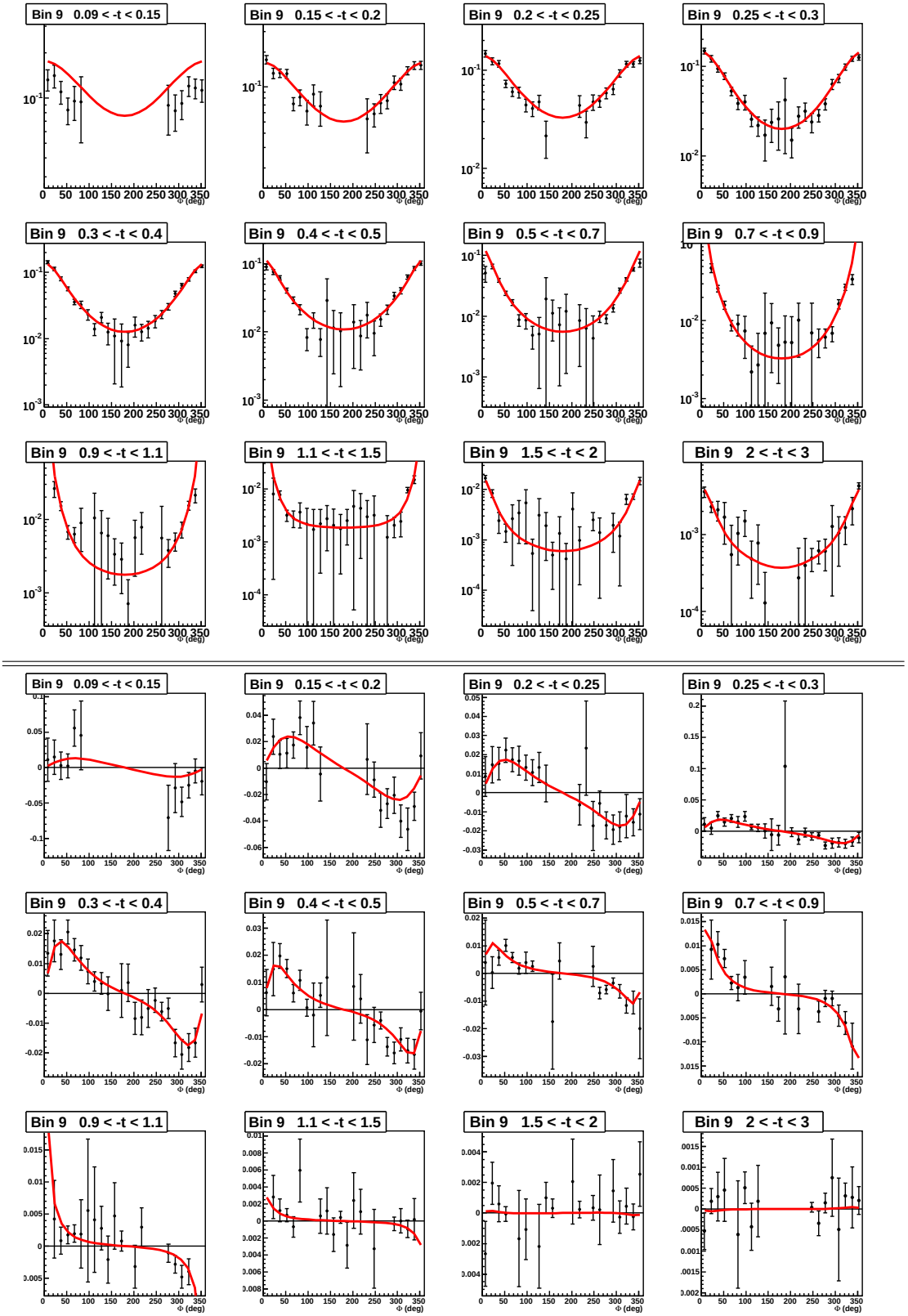

Figure O.9: Simultaneous fits of the unpolarized (top) and polarized (bottom) cross sections as a function of Φ for the 12 t-bins of the (Q^2, x_B) bins 9.

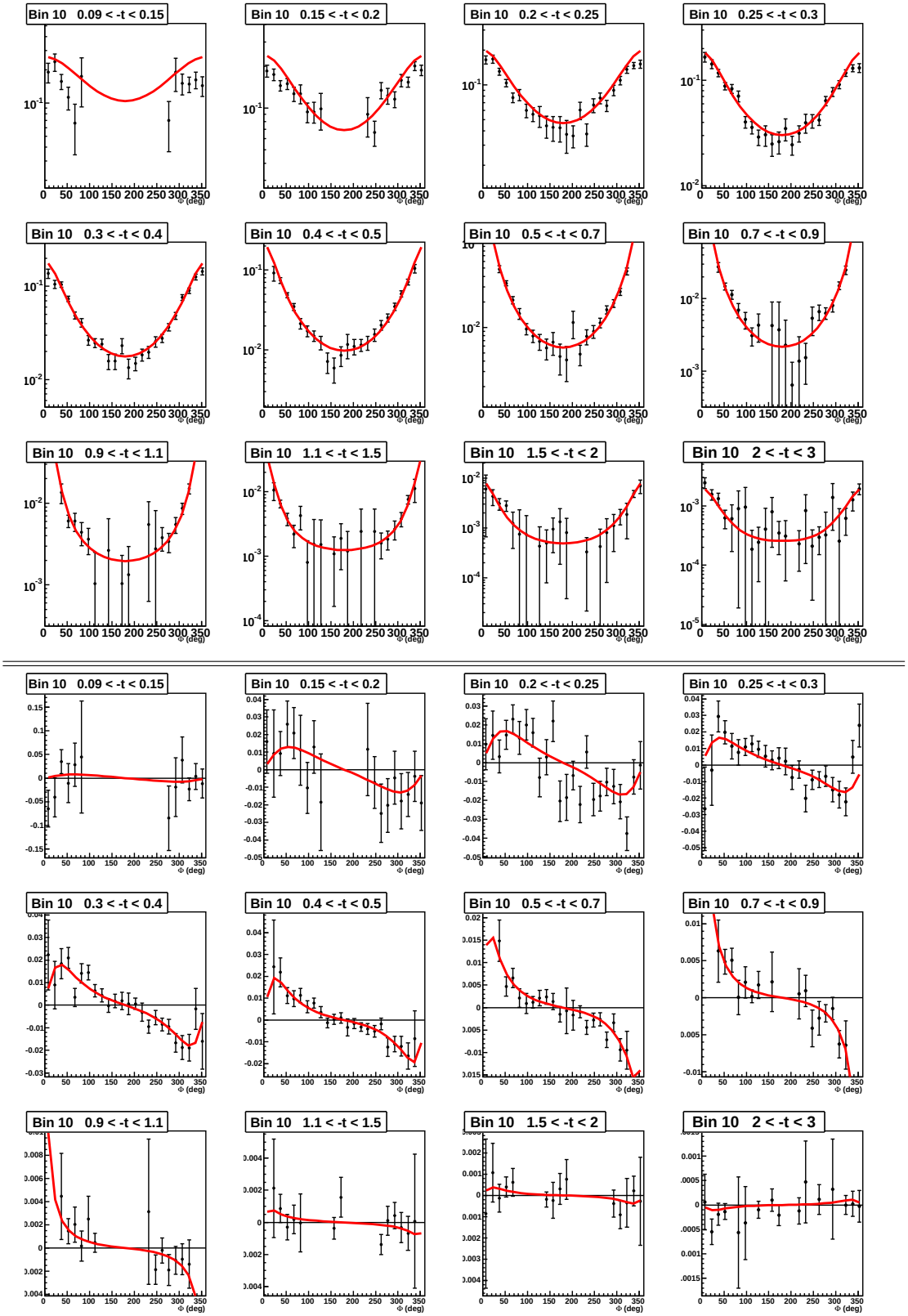

Figure O.10: Simultaneous fits of the unpolarized (top) and polarized (bottom) cross sections as a function of Φ for the 12 t-bins of the (Q^2, x_B) bins 10.

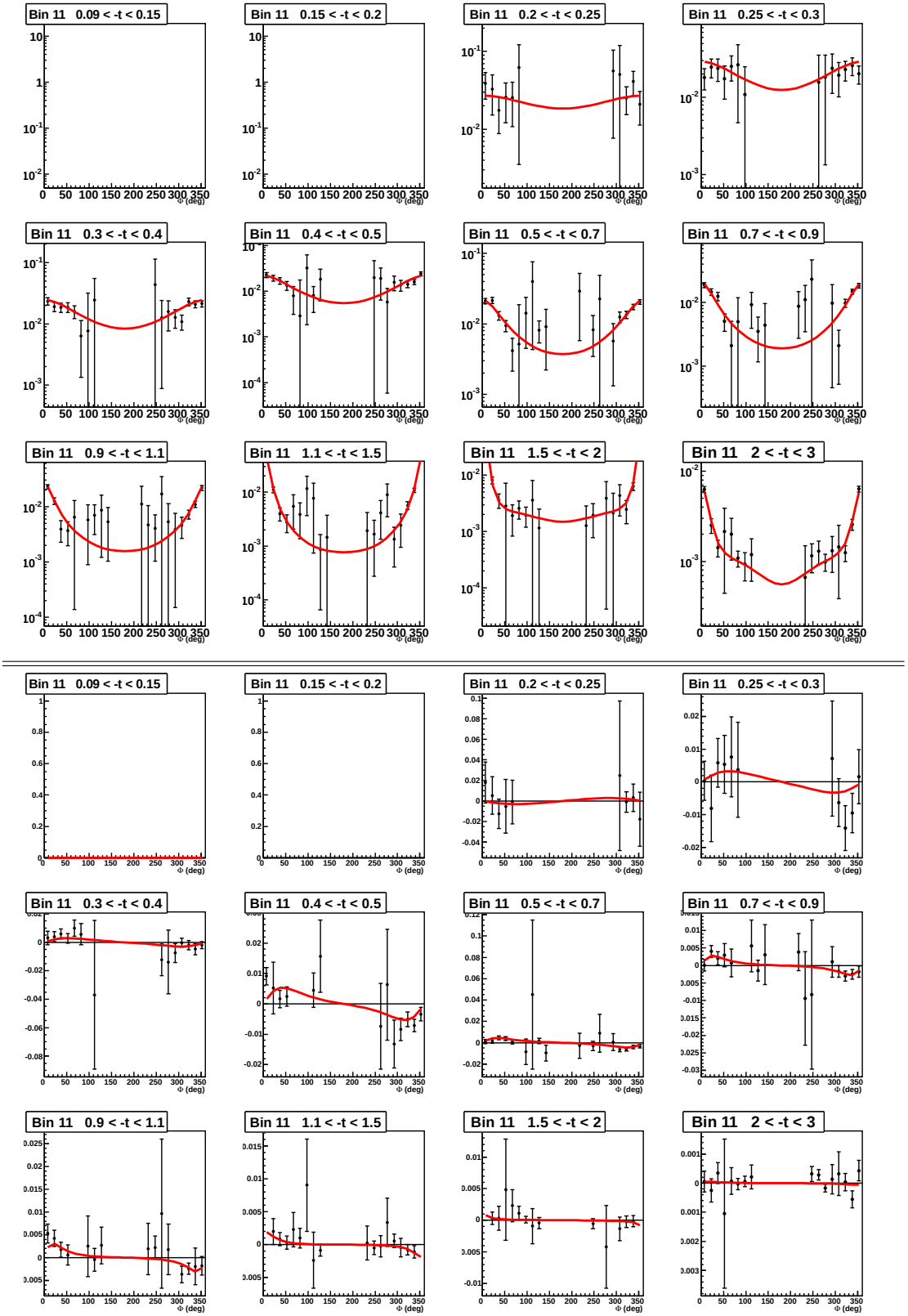

Figure O.11: Simultaneous fits of the unpolarized (top) and polarized (bottom) cross sections as a function of Φ for the 12 t-bins of the (Q^2, x_B) bins 11.

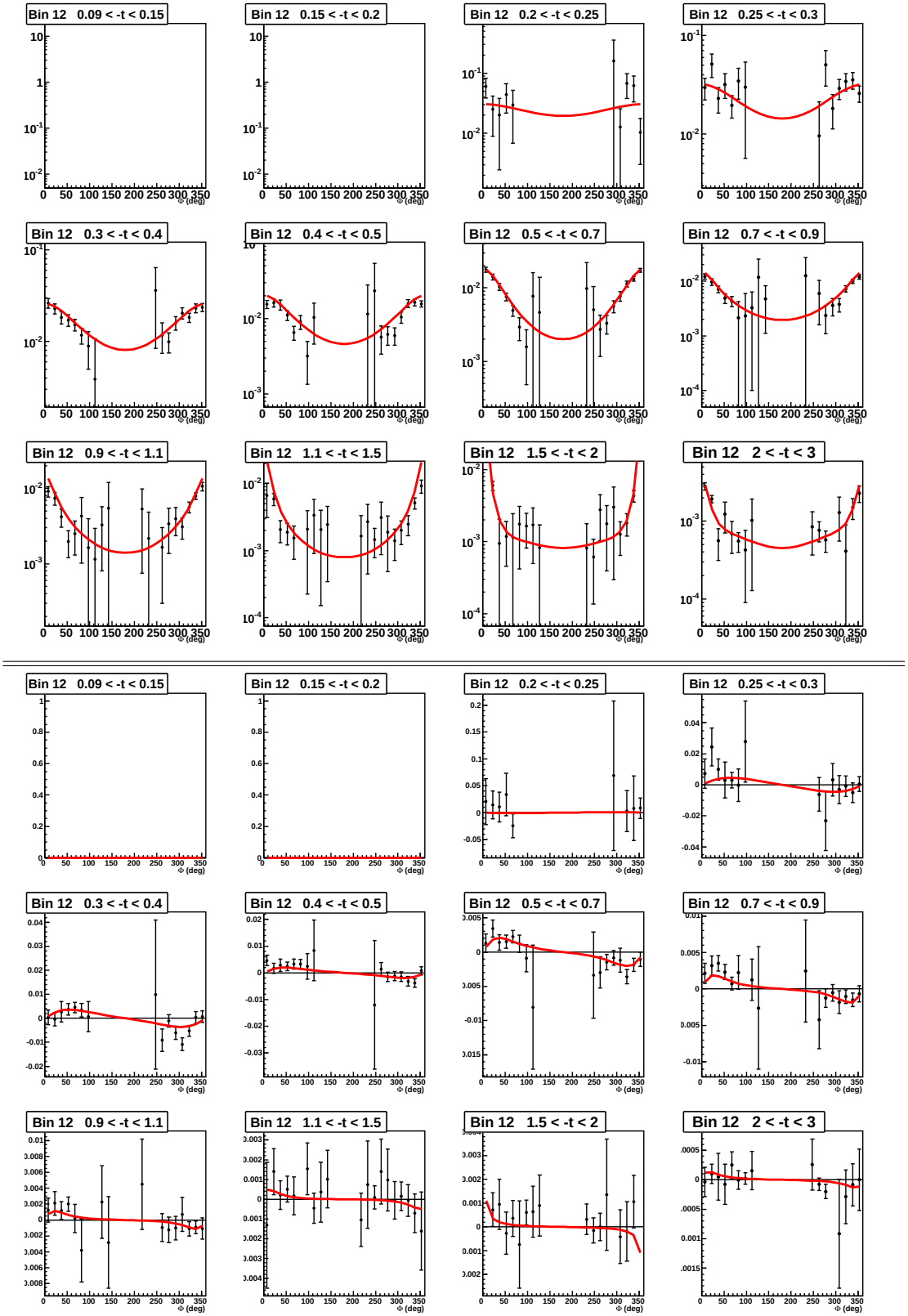

Figure O.12: Simultaneous fits of the unpolarized (top) and polarized (bottom) cross sections as a function of Φ for the 12 t-bins of the (Q^2, x_B) bins 12.

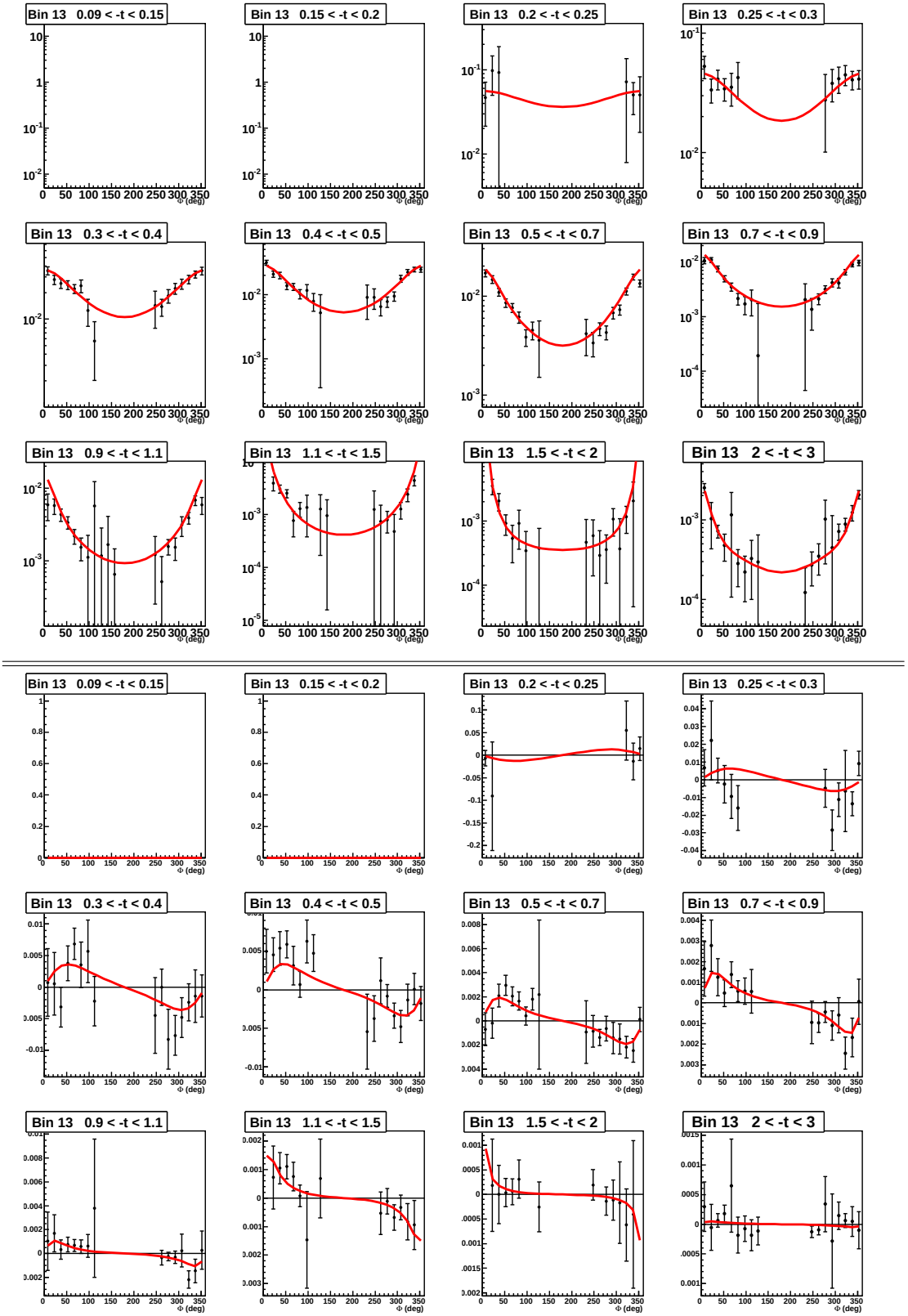

Figure O.13: Simultaneous fits of the unpolarized (top) and polarized (bottom) cross sections as a function of Φ for the 12 t-bins of the (Q^2, x_B) bins 13.

Bibliography

[ABR99] I. Akushevich, H. Boettcher, and D. Ryckbosch, *RADGEN 1.0. Monte Carlo Generator for Radiative Events in DIS on Polarized and Unpolarized Targets*, arXiv:hep-ph/9906408v1 (1999).

[AdJP11] J. Arrington, Kees de Jager, and C. F. Perdrisat, *Nucleon form factors - a jefferson lab perspective*, J. Phys.: Conf. Ser. 299 012002 (2011).

[AR68] A. I. Akhiezer and M. P. Rekalo, *Polarization phenomena in electron scattering by protons in the high energy region*, Sov. Phys. Dokl. **13** (1968), 572.

[Arr04] J. Arrington, *Implications of the discrepancy between proton form-factor measurements*, Phys. Rev. **C 69** (2004), 022201.

[AV09] A. El Alaoui and E. Voutier, *GENEPI event generator*, CLAS Note 2009-024 (2009).

[BBBA06] R. Bradford, A. Bodek, H. Budd, and J. Arrington, *A new parameterization of the nucleon elastic form factors*, Nucl. Phys. Proc. Suppl. **159** (2006), 127.

[BEG+03] V. Burkert, L. Elhouadrhiri, M. Garcon, R. Niyazov, and S. Stepanyan, *Deeply Virtual Compton Scattering with CLAS at 6 GeV*, JLab approved experiment **E-06-003** (2003).

[BEG+12] V. Burkert, L. Elouadrhiri, M. Garcona, M. Holtrop, D. Ireland, K. Joo, W. Kim, and F. Sabatie, *Deeply Virtual Compton Scattering with CLAS at 11 GeV*, JLab approved experiment **E-12-06-119** (2012).

[BEJN05] A. Biselli, L. Elhouadrhiri, K. Joo, and S. Niccolai, *Deeply Virtual Compton Scattering at 6 GeV with polarized target and polarized beam using the CLAS detector*, JLab approved experiment **E-05-114** (2005).

[BFK+69] M. Breidenbach, J. I. Friedman, H. W. Kendall, E. D. Bloom, and D. Coward et. al., *Observed behavior of highly inelastic electron-proton scattering*, Phys. Rev. Lett. **23** (1969), 935–939.

[BK10] I. Bedlinski and V. Kubarovsky, private communication (2010).

[BKLH02] E. J. Brash, A. Kozlov, Sh. Li, and G. M. Huber, *New empirical fits to the proton electromagnetic form factors*, Phys. Rev. **C 65** (2002), 051001.

[BMK02] A.V. Belitsky, D. Muller, and A. Kirchner, *Theory of deeply virtual compton scattering on the nucleon*, Nucl. Phys. **B 629** (2002), 323–392.

[BMT05] P.G. Blunden, W. Melnitchouk, and J.A. Tjon, *Two-photon exchange in elastic electron-nucleon scattering*, Phys. Rev. **C72** (2005), 034612.

[BP69] J. D. Bjorken and E. A. Paschos, *Inelastic electron-proton and γ-proton scattering and the structure of the nucleon*, Phys. Rev. (1969), 185.

[BR05] A.V. Belitsky and A.V. Radyushkin, *Unraveling hadron structure with generalized parton distributions*, Physics Reports **Volume 418, Issues 1-6** (2005), 1–387.

[Bur03] M. Burkardt, *Impact parameter space interpretation for generalized parton distributions*, Int. J. Mod. Phys. **A18** (2003), 173–208.

[BVS+05] M. Battaglieri, R. De Vita, S. Stepanyana, D. Weygand, D. I. Glazier, and C. Salgado, *Meson spectroscopy with low q^2 electron scattering in CLAS12*, JLab approved experiment **E-11-005** (2005).

[Cha32] J. Chadwick, *Possible existence of a neutron*, Nature (1932), 312.

[Col79] Mark-J Collaboration, *Discovery of three-jet events and a test of quantum chromodynamics at PETRA*, Phys. Rev. Lett. **43** (1979), 830.

[col89] EMC collaboration, *An investigation of the spin structure of the proton in deep inelastic scattering of polarised muons on polarised protons*, Nucl. Phys. **B** (1989), 328.

[Col06] COMPASS Collaboration, *Gluon polarization in the nucleon from quasi-real photoproduction of high-p_T hadron pairs*, Phys. Lett. **B633** (2006), 25–32.

[Col08] STAR Collaboration, *Longitudinal double-spin asymmetry for inclusive jet production in p+p collisions at $\sqrt{s}$=200 GeV*, Phys. Rev. Lett **100** (2008), 232003.

[Col09] PHENIX Collaboration, *The gluon spin contribution to the proton spin from the double helicity asymmetry in inclusive pi^0 production in polarized p+p collisions at $\sqrt{s}$= 200 GeV*, Phys. Rev. Lett. **103** (2009), 012003.

[CV08] C. E. Carlson and M. Vanderhaeghen, *Empirical transverse charge densities in the nucleon and the nucleon-to-delta transition*, Phys. Rev. Lett. **100** (2008), 032004.

[Die03] M. Diehl, *Generalized parton distributions*, PhD thesis (2003).

[Dok77] Y. L. Dokshitzer, *Calculation of the structure functions for deep inelastic scattering and e+ e- annihilation by perturbation theory in quantum chromodynamics*, Sov. Phys. JETP (1977), 641–653.

[ea99] E.S. Smith et al., *The time-of-flight system for CLAS*, Nucl. Instrum. Meth. **A432** (1999), 265–298.

[ea00a] M. Vanderhaeghen et al., *QED radiative corrections to virtual compton scattering*, Phys. Rev. **C62** (2000), 025501.

[ea00b] M.D. Mestayer et al., *The CLAS drift chamber system*, Nucl. Instrum. Meth. **A449** (2000), 81–111.

[ea01a] A. Airapetian et al., *Measurement of the Beam-Spin Azimuthal Asymmetry Associated with Deeply-Virtual Compton Scattering*, Phys. Rev. Lett. **87** (2001), 182001.

[ea01b] C. Adloff et al., *Measurement of deeply virtual compton scattering at HERA*, Phys. Lett. B **517** (2001), 47.

[ea01c] G. Adams et al., *The CLAS Cherenkov detector*, Nucl. Instrum. Meth. **A465** (2001), 414–427.

[ea01d] S. Stepanyan et al., *Observation of exclusive deeply virtual compton scattering in polarized electron beam asymmetry measurements*, Phys. Rev. Lett. **87** (2001), 182002.

[ea02a] Gayou O. et al, *Measurement of G_{Ep}/G_{Mp} in $ep \to ep$ to $Q^2 = 5.6GeV^2$*, Phys. Rev. Lett. **88** (2002), 092301.

[ea02b] Kubon G. et al., *Precise neutron magnetic form-factors*, Phys. Lett. **B 524** (2002), 26.

[ea03a] B.A. Mecking et al., *The CEBAF large acceptance spectrometer (CLAS)*, Nucl. Instrum. Meth. **A503** (2003), 513–553.

[ea03b] J Verdu et al, *Quark masses*, J. Phys. B: At. Mol. Opt. Phys. **36** (2003), 655.

[ea03c] Madey R. et al., *Measurement of $G_E n/G_M n$ from the d(e,e'n)p reaction to $Q^2 = 1.45$ $(GeV/c)^2$*, Phys. Rev. Lett. **91** (2003), 122002.

[ea03d] S. Chekanov et al., *Measurement of deeply virtual compton scattering at HERA*, Phys. Lett. **B 573** (2003), 46.

[ea04a] Suleiman R. et al., *Precision rosenbluth measurement of the proton elastic form-factors*, JLab proposal 04-019 (2004).

[ea04b] Warren G. et al, *Measurement of the electric form-factor of the neutron at $Q^2 = 0.5$ GeV^2/c^2 and 1.0 GeV^2/c^2* , Phys. Rev. Lett. **92** (2004), 042301.

[ea05a] A. Aktas et al., *Measurement of deeply virtual compton scattering at HERA*, Eur. Phys. J. **C 44** (2005), 1.

[ea05b] J. Arrington et al., *A measurement of two-photon exchange in unpolarized elastic electron-proton scattering*, JLab proposal E05-017 (2005).

[ea05c] Punjabi V. et al., *Proton elastic form-factor ratios to $Q^2 = 3.5$ GeV^2 by polarization transfer*, Phys. Rev. **C 71** (2005), 055202.

[ea05d] Qattan I. A. et al., *Precision rosenbluth measurement of the proton elastic form factors*, Phys. Rev. Lett. **94** (2005), 142301.

[ea06a] C. Munoz Camacho et al., *Scaling Tests of the Cross Section for Deeply Virtual Compton Scattering*, Phys. Rev. Lett. **97** (2006), 262002.

[ea06b] S. Chen et al., *Measurement of deeply virtual compton scattering with a polarized proton target*, Phys. Rev. Lett. **97** (2006), 072002.

[ea07] A. Airapetian et al, *The beam-charge azimuthal asymmetry and deeply virtual compton scattering*, Phys. Rev. **D 75** (2007), 011103.

[ea08a] A. Airapetian et al., *Measurement of azimuthal asymmetries with respect to both beam charge and transverse target polarization in exclusive electroproduction of real photons*, JHEP 0806, 066 (2008).

[ea08b] F. D. Aaron et al., *Measurement of deeply virtual compton scattering and its t-dependence at HERA*, Phys. Lett. **B 659** (2008), 796.

[ea08c] F.-X. Girod et al., *Deeply virtual compton scattering beam-spin asymmetries*, Phys. Rev. Lett. **100** (2008), 162002.

[ea09a] A. Airapetian et al., *Separation of contributions from deeply virtual Compton scattering and its interference with the Bethe-Heitler process in measurements on a hydrogen target*, JHEP 0911, 083 (2009).

[ea09b] S. Chekanov et al., *A Measurement of the Q^2, W and t dependences of deeply virtual Compton scattering at HERA*, JHEP 0905, 108 (2009).

[ea10a] A. Airapetian et al., *Exclusive leptoproduction of real photons on a longitudinally polarised hydrogen target*, JHEP 1006, 019 (2010).

[ea10b] A. J. R. Puckett et al., *Recoil Polarization Measurements of the Proton Electromagnetic Form Factor Ratio to $Q^2 = 8.5\ GeV^2$*, Phys. Rev. Lett. **104** (2010), 242301.

[ea11a] A. Airapetian et al., *Measurement of double-spin asymmetries associated with deeply virtual compton scattering on a transversely polarized hydrogen target*, Phys.Lett. **B704** (2011), 15–23.

[ea11b] E. Fuchey et al., *Exclusive neutral pion electroproduction in the deeply virtual regime*, Phys. Rev. **C 83** (2011), 025201.

[ea12] H. Avakian et al., *Deeply Virtual Compton Scattering at 11 GeV with transversely polarized target using the CLAS12 Detector*, A 12 GeV Research Proposal to Jefferson Lab PAC (PAC39) (2012).

[eaPDG08] C. Amsler et al. (Particle Data Group), Phys. Lett. **B 667** (2008).

[EOO37] I. Estermann, O.C.Simpson, and O.Stern, *The magnetic moment of the proton*, Phys. Rev. **52** (1937), 535.

[ER80] A. V. Efremov and A. V. Radyushkin, *Factorization and asymptotical behavior of pion form-factor in QCD*, Phys. Lett. **B94** (1980), 245–250.

[ESW60] F. J. Ernst, R. G. Sachs, and K. C. Wali, *Electromagnetic form factors of the nucleon*, Phys. Rev. **119** (1960), 1105.

[Fey69] R. P. Feynman, *Photon hadron interactions*, Westview Press, 1969.

[Fra12] A. Fradi, *CLAS wikipage*, http://clasweb.jlab.org/rungroups/e1-dvcs2/wiki/index.php/Ahmed (2010 [Online; accessed 02-July-2012]).

[Gir12] F.-X. Girod, *CLAS wikipage*, http://clasweb.jlab.org/rungroups/e1-dvcs/wiki/index.php/FX (2011 [Online; accessed 30-June-2012]).

[GM64] M. Gell-Mann, *A schematic model of baryons and mesons*, Phys. Lett. **8** (1964), 214.

[GPRV05] M. Guidal, M. V. Polyakov, A. V. Radyushkin, and M. Vanderhaeghen, *Nucleon form factors from generalized parton distributions*, Phys. Rev. **D72** (2005), 054013.

[GPV01] K. Goeke, M.V. Polyakov, and M. Vanderhaeghen, *Hard exclusive reactions and the structure of hadrons*, Prog. Part. Nucl. Phys. **47** (2001), 401–515.

[GSI12] *GSIM user's guide*, http://www.jlab.org/Hall-B/document/gsim/userguide.html (2011 [Online; accessed 29-July-2012]).

[Gui08a] M. Guidal, *A fitter code for deep virtual compton scattering and generalized parton distributions*, Eur. Phys. J. **A 37** (2008), 319.

[Gui08b] ———, *Generalized parton distributions and deep virtual compton scattering*, Progress in Particle and Nuclear Physics **Volume 61, Issue 1** (2008), 89–105.

[Gui10] ———, *Extraction of Compton Form Factors from DVCS data*, arXiv:1011.4195v1 (2010).

[GV03] M. Guidal and M. Vanderhaeghen, *Double deeply virtual compton scattering off the nucleon*, Phys. Rev. Lett. **90** (2003), 022001.

[GW73] D.J. Gross and F. Wilczek, *Ultraviolet behavior of non-abelian gauge theories*, Phys. Rev. Lett. **30 (26)** (1973), 1343–1346.

[HJ98] P. Hoodbhoy and X. Ji, *Helicity-flip off-forward parton distributions of the nucleon*, Phys. Rev. **D 58** (1998), 054006.

[HWMCR12] C. Hyde-Wright, B. Michel, C. Munoz Camacho, and J. Roche, *Measurements of Electron-Helicity Dependent Cross Sections of Deeply Virtual Compton Scattering with CEBAF at 12 GeV*, JLab approved experiment **E-12-06-114** (2012).

[Ji97] X. Ji, *Gauge-invariant decomposition of nucleon spin and its spin-off*, Phys. Rev. Lett. **78** (1997), 610.

[Ji98] ———, *Impact parameter space interpretation for generalized parton distributions*, J. Phys. **G24** (1998), 1181.

[Jo07] H.S. Jo, *Etude de la diffusion compton profondement virtuelle sur le nucleon avec le detecteur CLAS de jefferson lab, mesure des sections efficaces polarisees et non polarisees*, PhD thesis (2007).

[Jo12] ———, *CLAS wikipage*, http://clasweb.jlab.org/rungroups/e1-dvcs/wiki/index.php/Hyon-Suk (2011 [Online; accessed 19-July-2012]).

[Kel04] J. J. Kelly, *Simple parametrization of nucleon form factors*, Phys. Rev. **C 70** (2004), 068202.

[KM10] K. Kumericki and D. Muller, *Deeply virtual Compton scattering at small x_B and the access to the GPD H*, Nucl. Phys. **B 841** (2010), 1.

[KN02] V. Korotkov and W. D. Nowak, *Future measurements of deeply virtual compton scattering at HERMES*, Eur. Phys. J. **C 23** (2002), 455.

[KPV01] N. Kivel, M.V. Polyakov, and M. Vanderhaeghen, *Deeply virtual compton scattering on the nucleon: Study of the twist-3 effects*, Phys. Rev. D 63, 114014 **D 63** (2001), 114014.

[L.01] Lomon E. L., *Extended gari-krumpelmann model fits to nucleon electromagnetic form factors*, Phys. Rev. **C 64** (2001), 035204.

[Lag11] J.M. Laget, *Unitarity constraints on neutral pion electroproduction*, Phys. Lett. **B695** (2011), 199–204.

[LW95] G.D. Lafferty and T.R. Wyatt, *Where to stick your data points: The treatment of measurements within wide bins*, Nucl. Instrum. Meth. **A355** (1995), 541–547.

[MH56] R. W. McAllister and R. Hofstadter, *Elastic Scattering of 188Mev Electrons from the proton and the alpha particle*, Phys. Rev. **102** (1956), 851–856.

[Mil07] G. A. Miller, *Charge densities of the neutron and proton*, Phys. Rev. Lett. **99** (2007), 112001.

[Mou09] H. Moutarde, *Extraction of the Compton Form Factor H from DVCS measurements at Jefferson Lab*, Phys. Rev. **D 79** (2009), 094021.

[MRG+94] D. Muller, D. Robaschick, B. Geyer, F.M. Dittes, and J. Horejsi, Fortschr. Phys. **42** (1994), 101.

[MS10] A.V. Manohar and C.T. Sachrajda, *Quark masses*, PDG (2010).

[MT69] L. W. Mo and Y. S. Tsai, *Radiative corrections to elastic and inelastic ep and up scattering*, Rev. Mod. Phys. **41** (1969), 205–235.

[MT00] L. C. Maximon and J. A. Tjon, *Radiative corrections to electron-proton scattering*, Phys.Rev. **C62** (2000), 054320.

[NKAM11] S. Niccolai, V. Kubarovsky, A. El Alaoui, and M. Mirazita, *Deeply Virtual Compton Scattering on the Neutron with CLAS12 at 11 GeV*, A 12 GeV Research Proposal to Jefferson Lab PAC (PAC37) (2011).

[OVT] M. Osipenko, A. Vlassov, , and M. Taiuti, *Matching between the electron candidate track and the cherenkov counter hit*, CLAS-NOTE 2004-020.

[Par06] K. Park, *Measurement of cross section andelectron asymmetry of the $p(\vec{e}, e'pi+)n$ reaction in the delta(1232) and higher resonances for $q^2 < 5$ gev^2*, PhD thesis (2006).

[Pic95] A. Pich, *Quantum chromodynamics*, hep-ph/9505231 (1995).

[PMS+10] M. Paolone, S. Malace, S. Strauch, I. Albayrak, and J. Arrington et al., *Polarization transfer in the 4He(ep,e'p')3H Reaction at Q^2=0.8 and 1.3 $(GeV/c)^2$*, Phys. Rev. Lett. **105** (2010), 072001.

[Pol73] H.D. Politzer, *Reliable perturbative results for strong interactions*, Phys. Rev. Lett. **30 (26)** (1973), 1346–1349.

[PPV07] C.F. Perdrisat, V. Punjabi, and M. Vanderhaeghen, *Nucleon electromagnetic form factors*, Prog. Part. Nucl. Phys. **59** (2007), 694–764.

[PW99] M.V. Polyakov and C. Weiss, *Skewed and double distributions in pion and nucleon*, Phys. Rev. **D60** (1999), 114017.

[Rad96] A.V. Radyushkin, *Scaling limit of deeply virtual compton scattering*, Phys. Lett. **B 380** (1996), 417.

[Rad97] ———, *Nonforward parton distributions*, Phys. Lett. **D 56** (1997), 5524.

[RI04] Bijker R. and F. Iachello, *Re-analysis of the nucleon space- and time-like electromagnetic form factors in a two-component model*, Phys. Rev. **C 69** (2004), 068201.

[Ros50] M. N. Rosenbluth, *High energy elastic scattering of electrons on protons*, Phys. Rev. **79** (1950), 615–619.

[Rut19] E. Rutherford, *Collision of alpha particles with light atoms. an anomalous effect in nitrogen.*, Philosophical Magazine. 6th series 37 (1919), 581–587.

[Say12] N. Saylor, *CLAS wikipage*, http://clasweb.jlab.org/rungroups/e1-dvcs2/wiki/index.php/Nickie (2011 [Online; accessed 03-July-2012]).

[SG94] A. Schafer and W. Greiner, *Quantum chromodynamics*, Springer. ISBN 0-387-57103-5, 1994.

[Soh12] D. Sohkan, *CLAS wikipage*, http://clasweb.jlab.org/rungroups/e1-dvcs2/wiki/index.php/Daria (2010 [Online; accessed 12-June-2012]).

[Sok12] D. Sokhan., *CLAS wikipage*, http://clasweb.jlab.org/wiki/index.php/Daria (2010 [Online; accessed 01-July-2012]).

[SVS88] T. Sloan, R. Voss, and G. Smadja, *Elastic scattering of 188Mev electrons from the proton and the alpha particle*, Phys. Rept. **162** (1988), 45–167.

[UL03] M. Ungaro and J. Li, *Procedure for drift chamber inefficiencies*, CLAS-Note 2003-006 (2003).

[VGG98] M. Vanderhaeghen, P.A.M. Guichon, , and M. Guidal, *Hard electroproduction of photons and mesons on the nucleon*, Phys. Rev. Lett. **80** (1998), 5064.

[VGG99] M. Vanderhaeghen, P.A.M. Guichon, and M. Guidal, *Deeply vitual electroproduction of photons and mesons on the nucleon leading order amplitudes and power corrections*, Phys. Rev. **D 60** (1999), 094017.

[VW10] M. Vanderhaeghen and T. Walcher, *Long range structure of the nucleon*, arXiv:1008.4225v1 (2010).

[Wak10] M. Wakamatsu, *On gauge-invariant decomposition of nucleon spin*, Phys. Rev. **D81** (2010), 114010.

[WW77] S. Wandzura and F. Wilczek, *Sum rules for spin-dependent electroproduction - test of relativistic constituent quarks*, Phys. Lett. **B 72** (1977), 195.

[Yur12] M. Yurov, *CLAS wikipage*, http://clasweb.jlab.org/rungroups/e1-dvcs/wiki/index.php/Background (2008 [Online; accessed 10-July-2012]).

[Zwe64] G. Zweig, *An su(3) model for strong interaction symmetry and its breaking.*, Developments In The Quark Theory Of Hadrons **1** (1964), 22–101.

Abstract

The Generalized Parton Distributions (GPDs) provide a new description of the nucleon structure in terms of its elementary constituents, the quarks and the gluons. The GPDs give access to a unified picture of the nucleon, correlating the information obtained from the measurements of the Form Factors and the Parton Distribution Functions. They describe the correlation between the transverse position and the longitudinal momentum fraction of the partons in the nucleon. Deeply Virtual Compton Scattering (DVCS), the electroproduction of a real photon on a single quark of the nucleon $eN \to e'N'\gamma$, is the most straightforward exclusive process allowing access to the GPDs. A dedicated experiment to study DVCS with the CLAS detector of Jefferson Lab has been carried out using a 5.883 GeV polarized electron beam and an unpolarized hydrogen target, allowing to collect DVCS events in the widest kinematic range ever explored in the valence region : $1 < Q^2 < 4.6$ GeV^2, $0.1 < x_B < 0.58$, $0.09 < -t < 3$ GeV^2. In this work, we present the extraction of three different DVCS observables: the unpolarized cross section, the difference of polarized cross sections and the beam spin asymmetry. We present comparisons with GPD model. We show a preliminary extraction of the GPDs using the latest fitting code procedure on our data, and a preliminary interpretation of the results in terms of parton density.

Résumé

Les distributions de Partons Généralisées (GPDs) fournissent une nouvelle description de la structure du nucléon en terme de ses constituents élémentaires, les quarks et les gluons. Les GPDs donnent accès à une image unifiée du nucléon, corrélant l'information obtenu par les mesures des Facteurs de Forme et des Distributions de Parton. Elles décrivent la corrélation entre la position transverse et la fraction d'impulsion longitudinale des partons dans le nucléon. La Diffusion Compton Profondément Virtuelle (DVCS), ou l'électroproduction d'un photon réel sur un quark du nucléon $eN \to e'N'\gamma$, est le processus exclusif le plus direct pour accéder aux GPDs. Une experience dédié à l'étude du DVCS avec le détécteur CLAS du laboratoire Jefferson a été réalisé en utilisant un faisceau d'électron polarisé et une cible d'hydrogène non polarisée. Cette expérience a permis de collecter des évènements DVCS sur le plus large espace cinématique jamais exploré dans la région de valence: $1 < Q^2 < 4.6$ GeV^2, $0.1 < x_B < 0.58$, $0.09 < -t < 3$ GeV^2. Dans ce travail, nous présentons l'extraction de trois observables DVCS différents: la section éfficace non polarisée, la différence de section efficace polarisé et l'asymétrie de faisceau. Nous comparons nos résultats à un model de GPD. Nous présentons une extraction préliminaire des GPDs utilisant la dernière procedure d'ajustement aux données, et une interpretation préliminaire des résultats en termes de densité de parton.